Detectors in Nuclear and Particle Physics

Prof. Dr. Johanna Stachel

Department of Physics und Astronomy
University of Heidelberg

July 23, 2018

Introduction I

- Progress in nuclear and particle physics mainly driven by experimental observation
- Critically coupled with the development of new methods in particle acceleration and detection of particles
- Historical development:

1896 Discovery of X-rays w. photographic plate
(Nobel prize W.C. Röntgen 1901)
1904 Research on cathode rays (Lenard window) (Nobel prize P. Lenard 1905)
1912 Evidence for cosmic radiation (electrometer)
(Nobel prize V.F. Hess 1936)
1912 Invention of the cloud chamber
(Nobel prize C.T.R. Wilson 1927)
1929 Birth of cosmic ray physics
Observation of high energetic electrons and showers
(Nobel prize W.W. Bothe 1954 "Coincidence method and discoveries made therewith")
1931 Lawrence proposal: Cyclotron
(Nobel prize E.O. Lawrence 1939 "Invention and development of cyclotron ...")
1932 Cockroft-Walton linear accelerator for protons
(Nobel prize Sir J.D. Cockroft u. E. Walton 1951 "Transmutation of atomic nuclei by artificially accelerated atomic particles")

Introduction II

1933 Discovery of the e^+, confirmation of development of electromagnetic showers due to $e^+ - e^-$ production
(Nobel prize P.M.S. Blackett 1948 "Development of Wilson cloud chamber method and his discoveries therewith")

1934 First evidence for Cherenkov radiation
(Nobel prize P. Cherenkov, I. Frank, I. Tamm 1958 "Discovery and interpretation of the Cherenkov effect")

1939 First measurements of the proton magnetic moment
(Nobel prize O. Stern 1943 "His contribution to the development of the molecular ray method ...")

1943 Fermis first reactor

1947 Confirmation of π^-
(Nobel prize C.F. Powell 1950 "His development of the photographic method and ...")

1953 First observations of charged particle tracks in a bubble chamber
(Nobel prize D.A. Glaser 1960 "For his invention of the bubble chamber")

1959 Proposal for an experiment to distinguish ν_e and ν_μ

1960 Realisation of neutrino beams at accelerators
(Nobel prize L. Lederman, M. Schwartz, J. Steinberger 1988 "for the neutrino beam method and ...")

1960 First evidence for $\Sigma(1385)$

1961 First evidence for ω-meson
(Nobel prize L. Alvarez 1968 " ...discovery of a large number of resonance states made possible through his development of the hydrogen bubble chamber technique ...")

Introduction III

1968 Invention of the Multiwire Proportional Chamber (MPC)
(Nobel prize G. Charpak 1992 "for his invention and development of particle detectors, in particular the multiwire proportional chamber")

1983 First evidence for intermediate vector bosons W^+, W^-, Z^0
(Nobel prize C. Rubbia 1984, co-awardee S. van de Meer "stochastic cooling of proton beam ...")

1986 Precision measurement of $g-2$ of the electron
(Nobel prize H. Dehmelt and W. Paul 1989 "for the development of ion trap technique ...")

1986 Neutrino oscillations in solar and atmospheric neutrinos
(Nobel prize R. Davies and T.Koshiba 2002 " ... development of neutrino detection techniques")

1989-2000 precision measurements at LEP test QCD and establish the precise form of asymptotic freedom
(Nobel prize D.J. Gross, H.D. Politzer, F. Wilczek "for the discovery of asymptotic freedom ...")

1995 Discovery of the top quark by D0 and CDF, first $\bar{p}p$ collisions at $\sqrt{s} = 1.8$ TeV at the Tevatron in 1986

2013 Discovery of a Higgs boson by ATLAS and CMS, first pp collisions at $\sqrt{s} = 7$ TeV at the LHC 2010
(Nobel prize P. Higgs and F. Englert 2013 " for the theoretical discovery of a mechanism ... recently confirmed through the discovery of the predicted fundamental particle ...")

Units I

HEP and SI Units

Quantity	HEP units	SI Units
length	1 fm	10^{-15} m
energy	1 GeV	$1.602 \cdot 10^{-10}$ J
mass	1 GeV/c^2	$1.78 \cdot 10^{-27}$ kg
$\hbar = h/2$	$6.588 \cdot 10^{-25}$ GeV s	$1.055 \cdot 10^{-34}$ J s
c	$2.988 \cdot 10^{23}$ fm/s	$2.988 \cdot 10^{8}$ m/s
$\hbar c$	0.1973 GeV fm	$3.162 \cdot 10^{-26}$ J m

Natural units ($\hbar = c = 1$)	
mass	1 GeV
length	$1\ \mathrm{GeV}^{-1} = 0.1973$ fm
time	$1\ \mathrm{GeV}^{-1} = 6.59 \cdot 10^{-25}$ s

1.1 Beams I

- Non-controlled collisions: Cosmic radiation, beam energy and particle type cannot be controlled, many discoveries, extremely high energies
- Controlled experiments: particle accelerator - charged particle traverses potential difference
  - Particle traverses many successive potential differences
    LINAC - Linear accelerator

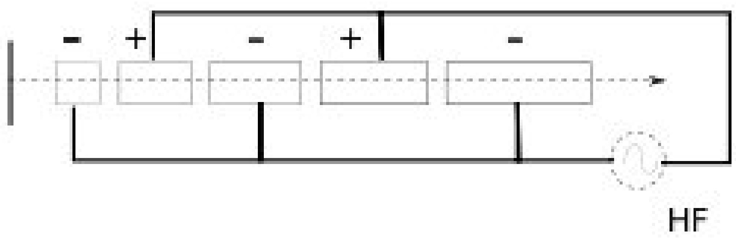

    RF cavity resonators , typically 8 MV/m
    future: e.g. ILC $>$ 35 MV/m
    The particles surf on the wavecrest through the cavities, scalable to very high energies, high cost due to length ...
  - Particle traverses the same potential difference many times
    circular accelerator (cyclotron, synchrotron)
    again acceleration in RF cavities, magnetic field keeps particles on circular orbit
    cyclotron condition :

$$\begin{aligned} p &= eBR \\ p\,(GeV/c) &= 0.3 \cdot B\,(T)R\,(m) \end{aligned}$$

1.1 Beams II

conventional coils:		1.5 T
superconducting:	Tevatron	5 T
	LHC:	10 T

The particle loses energy by synchrotron radiation, the radiated power:

$$P = \frac{2e^2 c}{3R^2} \frac{\beta^4}{(1-\beta^2)^2} \xrightarrow[(\beta \to 1)]{} \frac{2e^2 c \gamma^4}{3R^2}$$

radiated energy per turn

$$\Delta E = \frac{4\pi}{3} \frac{e^2 \gamma^4}{R}$$

e.g.: LEP $R = 4.3$ km, $E = 100$ GeV, $m_0 = 0.5$ MeV, $\gamma = 2 \cdot 10^5 \rightarrow \Delta E = 2.24$ GeV of 100 GeV
LEP maybe the last circular accelerator for electrons?
for protons, synchrotron radiation so far comparatively irrelevant
LHC in the LEP tunnel: $E = 7$ TeV, $\gamma = 7 \cdot 10^3 \rightarrow \Delta E = 3.4$ keV

- Beam hits stationary target "fixed target experiments"

$$p + p \rightarrow X \qquad \sqrt{s} = m_p \sqrt{2 + 2\gamma_p}$$

but high luminosity
e.g.: in 1 m liquid hydrogen, beam 10^{12} /s $\quad \mathcal{L} = 2 \cdot 10^{36} / \text{cm}^2\,\text{s}$

1.1 Beams III

- Colliding beams "collider experiments": high energies $\sqrt{s} = 2m_p\gamma_p$
  comparatively low luminosity
  e.g.: 10^{10} particles per bunch, 20 bunches per orbit, revolution frequency 1 MHz, beam size 10^{-2} cm^2

$$\mathcal{L} = \frac{10^6 \cdot 20 \cdot 10^{20}}{10^{-2}\mathrm{cm}^2 \cdot \mathrm{s}} = 2 \cdot 10^{29}/\mathrm{cm}^2\,\mathrm{s} \quad \mathrm{LHC}: 10^{34}/\mathrm{cm}^2\,\mathrm{s}$$

Reaction rate:

$$R = \sigma \cdot \mathcal{L}$$

typical largest cross section $\rightarrow$ total inelastic cross section

$$p + p \qquad \text{at } \sqrt{s} = 10\,(7000)\ \mathrm{GeV},\ \sigma_{\mathrm{incl}} = 30\,(60)\ \mathrm{mb}$$

1 mb = 1 millibarn = 10^{-24} cm$^2 \cdot 10^{-3}$
inelastic rate typical "fixed target" experiment: $R = 3 \cdot 10^{-26}$ cm$^2 \cdot 2 \cdot 10^{36}/$ cm^2 s $\approx 6 \cdot 10^{10}$/s
inelastic rate for pp collider: $R = 3 \cdot 10^{-26}$ cm$^2 \cdot 2 \cdot 10^{29}$/cm^2 s $\approx 6 \cdot 10^3$/s
Usually much smaller cross sections are investigated: nb, pb, ...

$\rightarrow$ 1 pb: 2 Hz for fixed target

$\rightarrow$ $2/10^7$ s (i.e. one year) for traditional colliders but 1/100 s (LHC)

Criteria for the beam energy

- Reaction rate, especially the importance of a threshold

$$e^+e^- \to Z^0 + \text{Higgs} \qquad \sqrt{s} \geq m_{Z_0} + m_{\mathrm{Higgs}}$$

$$\text{at LEP} \qquad \sqrt{s} = 208 \text{ GeV} \to m_{\mathrm{Higgs}} \leq 116 \text{ GeV}$$

- Resolution of structures
object of the dimensions Δx can be resolved with the wavelength

$$\bar{\lambda} = \frac{\hbar c}{pc} \leq \Delta x \qquad \text{or } pc \geq \frac{\hbar c}{\Delta x}$$

Tevatron	$p \approx$ 1 TeV	$\Delta x \approx 10^{-16}$ cm
LHC	$p \approx$ 10 TeV	$\Delta x \approx 10^{-17}$ cm

e^+e^- **Colliders**	$pp/p\bar{p}$ **Colliders**
	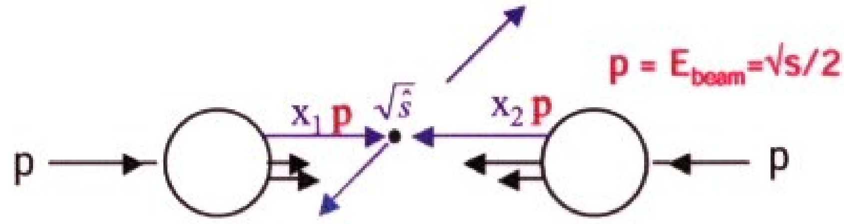
Energy of elementary interaction known $\sqrt{\hat{s}} = E(e^-) + E(e^+) = \sqrt{s}$	Energy of elementary interaction not known $\sqrt{\hat{s}} = \sqrt{x_1 x_2 s} < \sqrt{s}$
Only two elementary particles collide $\rightarrow$ clean final states	Elementary interaction (hard) + interaction of "spectator" q,g (soft) overlapp in detector
Mainly EW processes	EW processes suffer from huge backgrounds from strong processes
$\sqrt{s}$ limited by $e^\pm$ synchrotron radiation: $E_{\rm loss} \sim \frac{E^4_{beam}}{R}\frac{1}{m^4_e}$ $E_{\rm loss} \sim 2.5$ GeV/turn LEP 2 ($E_{\rm beam} \sim 100$ GeV)	Synchrotron radiation is $\sim (m_p/m_e)^4 \sim 10^{13}$ smaller
- high energy more difficult $\rightarrow$ next machine: Linear Collider (ILC, CLIC, $\sqrt{s} = 800(3000?)$ GeV) - clean environment $\rightarrow$ precision measurement machines	- high energy easier $\rightarrow$ discovery machines current machine: LHC, pp , $\sqrt{s} = 14\ TeV$ in the LEP ring more "dirty" environment, but increasingly also precision measurements

Electron Colliders Important for Testing Standard Model and Physics Beyond

	where	start	end	energy (GeV)	length/ circumf. (km)	most relevant physics
Petra	DESY	1978	1986	23.5 + 23.5	2.3	discovery of gluons
CESR	Cornell/ USA	1979	...	6 + 6	0.77	spectroscopy hadrons with b and c quarks
PEP	Stanford/ USA	1980	1990	15 + 15	2.2	top search, indirect W/Z hint
Tristan	KEK/ Japan	1987	1995	32 + 32	3	top search
LEP	CERN	1989	2000	105 + 105	26.7	precision test of standard model
SLC	Stanford/ USA	1989	1998	50 + 50	1.45 + 1.46	precision test of standard model
PEP II	Stanford/ USA	1999	2008	9 + 3.1	2.2	CP violation in B
KEK-B	KEK/ Japan	1999	2010	8 + 3.5	3	CP violation in B

Hadron Colliders Important for Testing Standard Model and Physics Beyond

	where	Beam	start	end	energy (TeV)	length/ circumf. (km)	most relevant physics
Sp$\bar{p}$S	CERN	p$\bar{p}$	1981	1990	0.45 + 0.45	6.9	W,Z bosons
Tevatron	Fermilab/ USA	p$\bar{p}$	1987	2011	0.9 + 0.9	6.3	top quark
SSC	Texas/ USA	pp	1996??		20 + 20	83.6	abandoned in 94
HERA	DESY	ep	1992	2007	0.03(e) + 0.92(p)	6.3	precise nucleon structure
RHIC	BNL/ USA	AuAu	2000	...	19.7 + 19.7	3.8	Quark-Gluon plasma
		pp			0.25 + 0.25		
LHC	CERN	pp	2009	...	7 + 7	26.7	Higgs, SUSY? ...
		PbPb			562 + 562		Quark-gluon plasma

Sources of Neutrinos Important for Testing Standard Model and Physics Beyond

source	reaction	energy range	type
solar	fusion reactions	typically below 20 MeV	ν_e
reactor	β-decay after fission	up to few MeV	ν_e
atmosphere	π- and μ-decay	GeV	ν_μ and ν_e
accelerators	μ-decay	up to 100 GeV	ν_μ

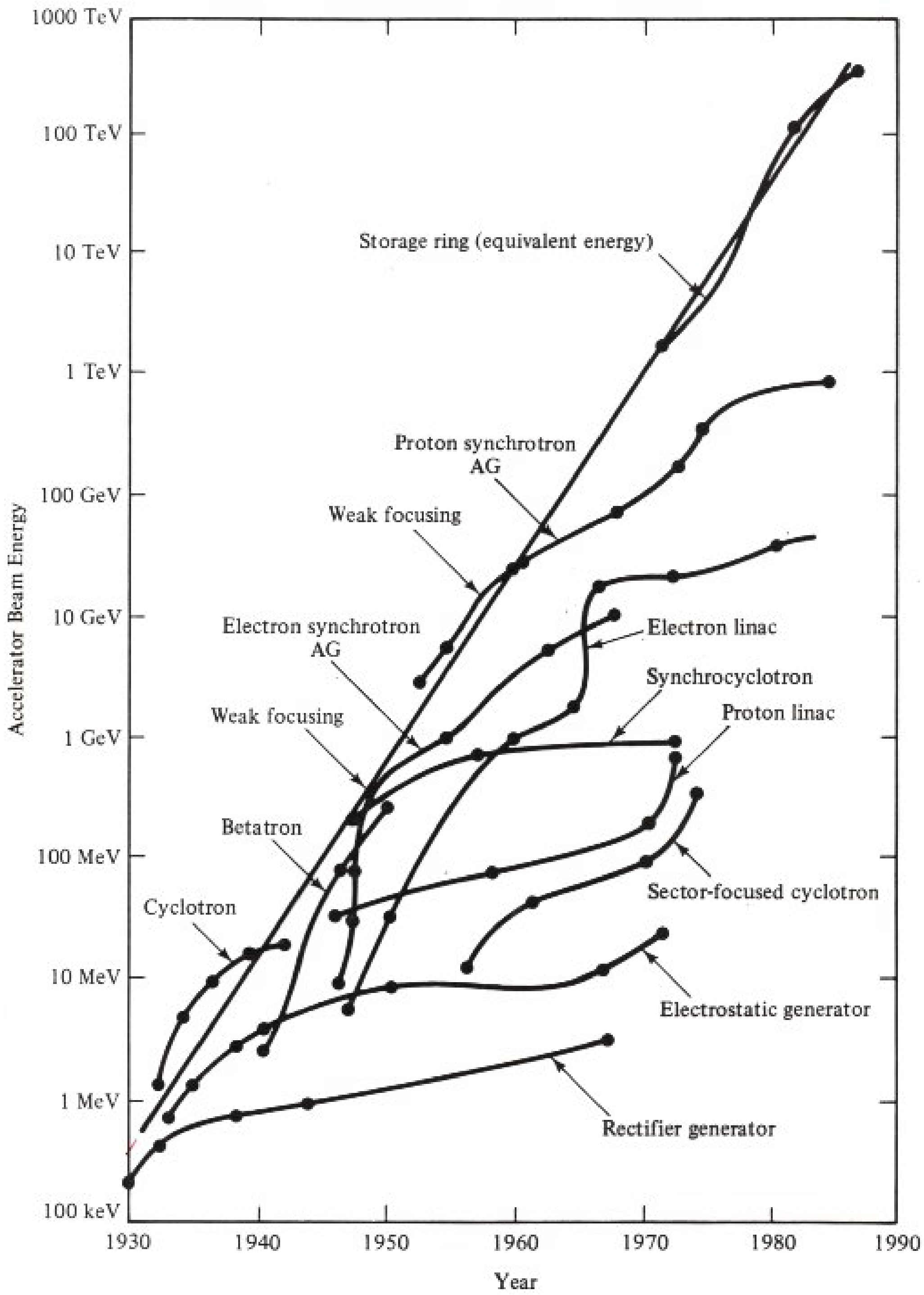

Energy growth of accelerators and storage rings. This plot, an updated version of M. Stanley Livingston's original, shows an energy increase by a factor of ten every seven years. Note how a new technology for acceleration has, so far, always appeared whenever the previous technology has reached its saturation energy. [From W. K. H. Panofsky, *Phys. Today 33, 24 (June 1980)*]

Increase: factor 10 every 7 years.

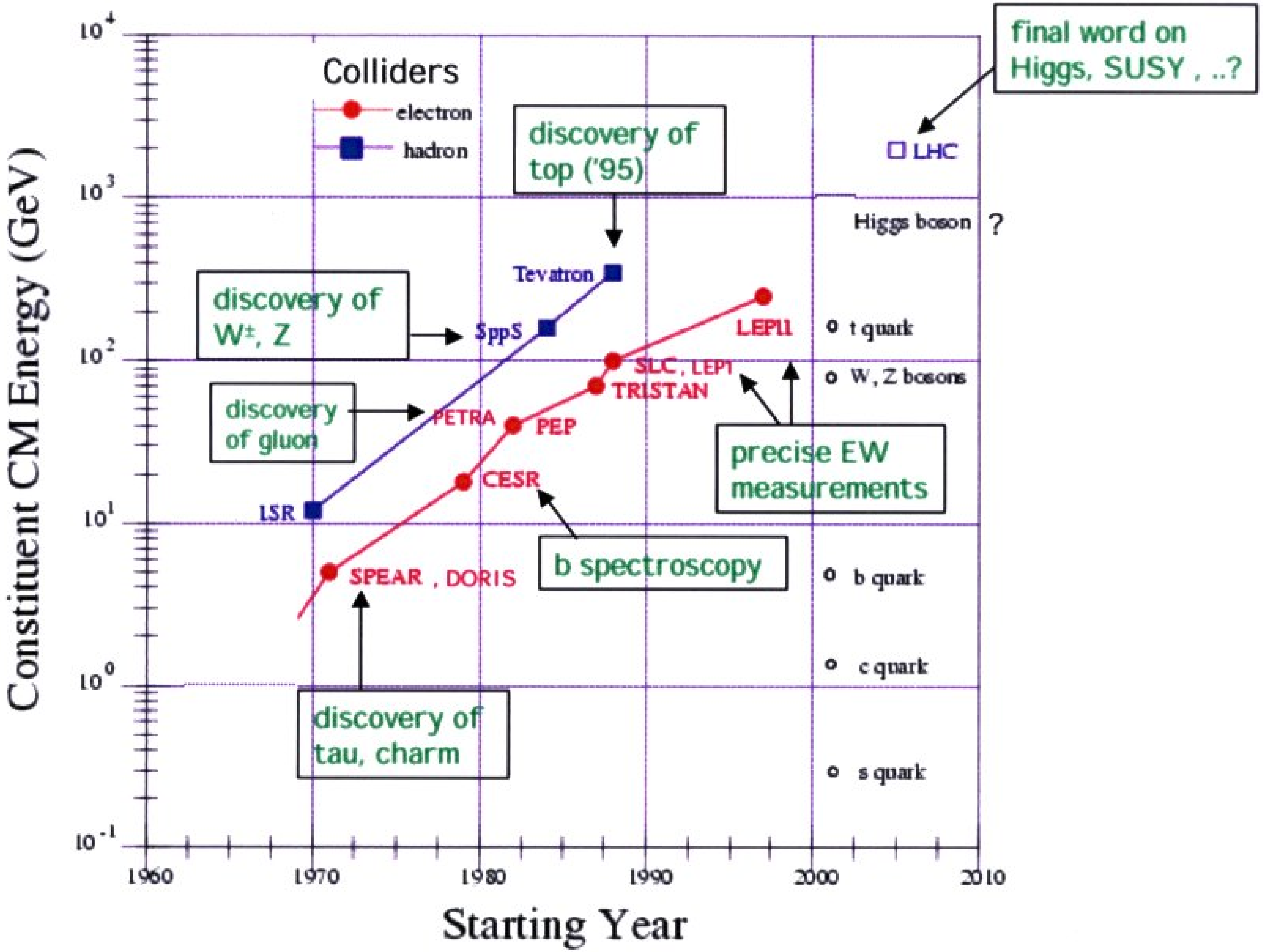

Simplified and non-exhaustive summary of SM tests at Colliders

LEP: Large Electron Positron Collider

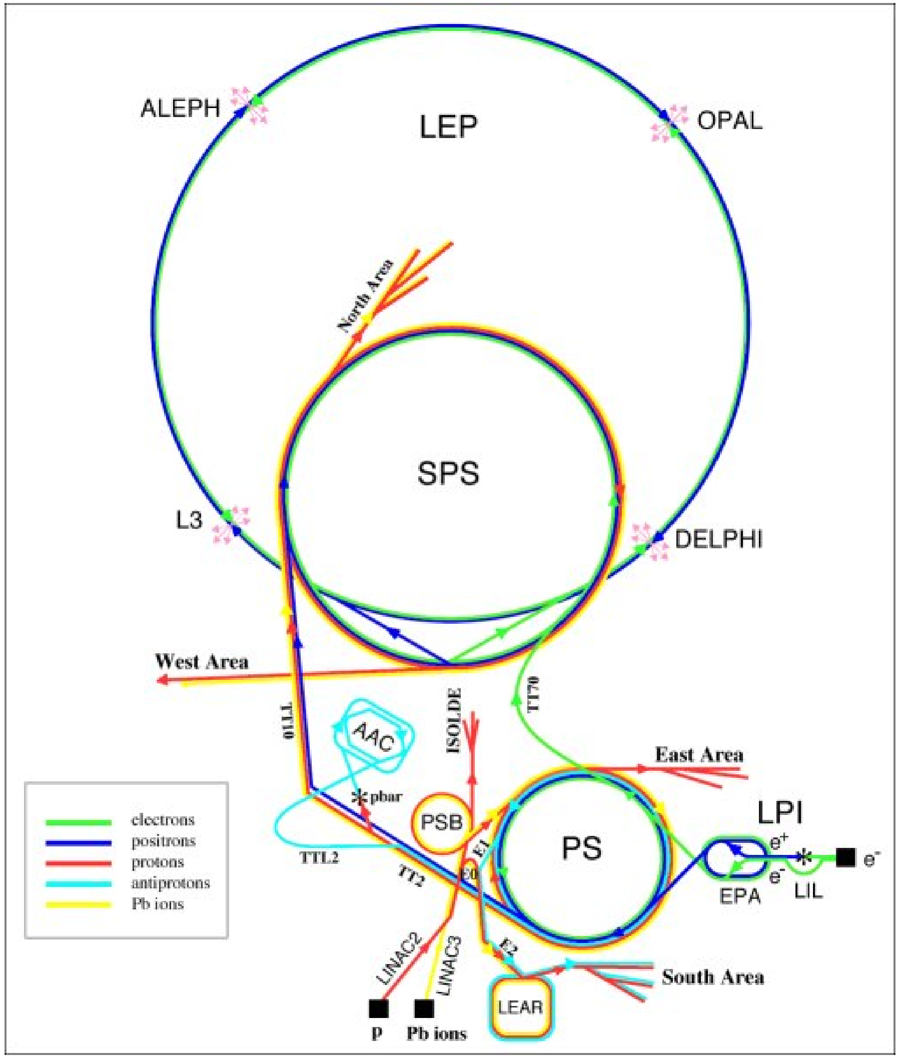

The LEP Storage Ring

Some characteristic parameters

Parameter	Value
circumference	26658.88 m
magnetic radius	3096 m
revolution frequency	11245.5 Hz
RF frequency	352 MHz
injection energy	$\approx$ 20 GeV
achieved peak energy per beam	104.5 GeV
achieved peak luminosity	4 pb^{-1} /day
number of bunches	4, 8 or 12
typical current/ bunch	0.75 mA

LEP: e^+e^- Collider at CERN

LEP1 (1989-1995) : $\sqrt{s} \approx m_z \rightarrow 2 \cdot 10^7$ Z recorded $\rightarrow$ precise Z measurements
LEP2 (1996-2000) : $\sqrt{s} \rightarrow 209$ GeV $\rightarrow$ WW production, m_W, search for Higgs and new particles

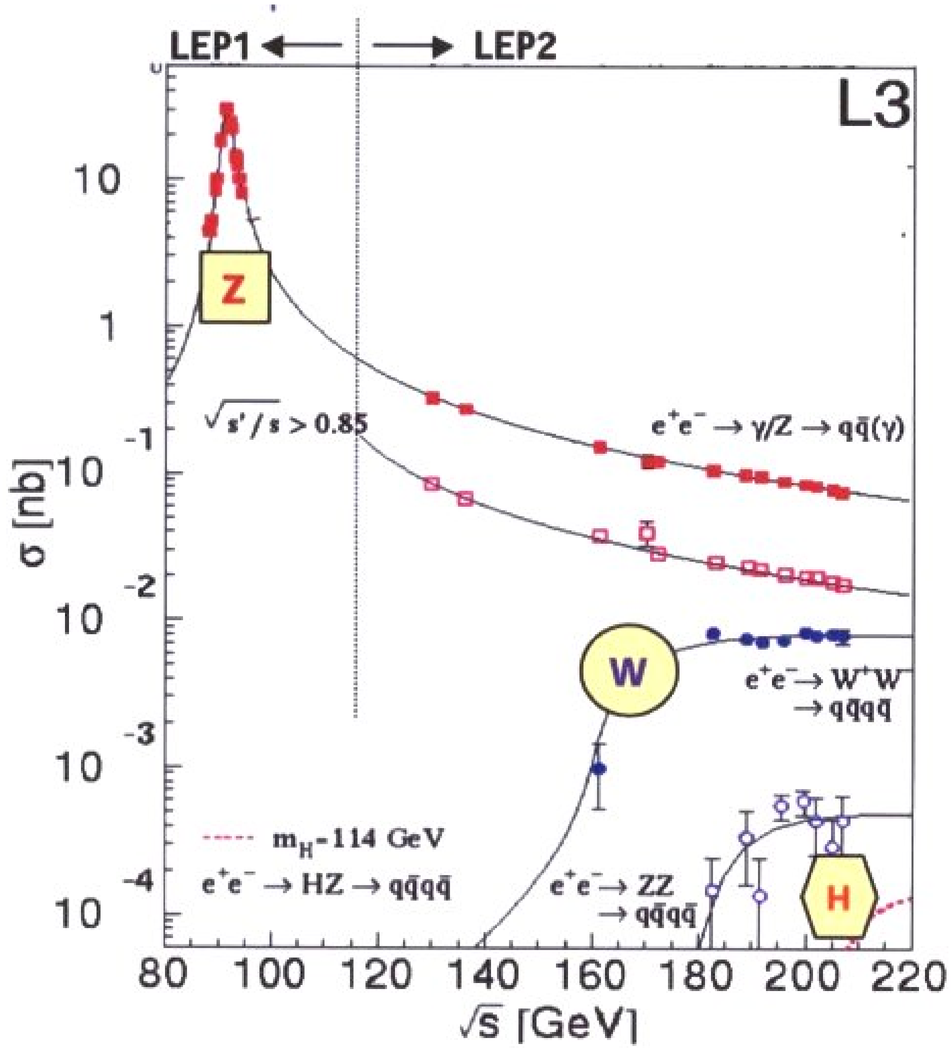

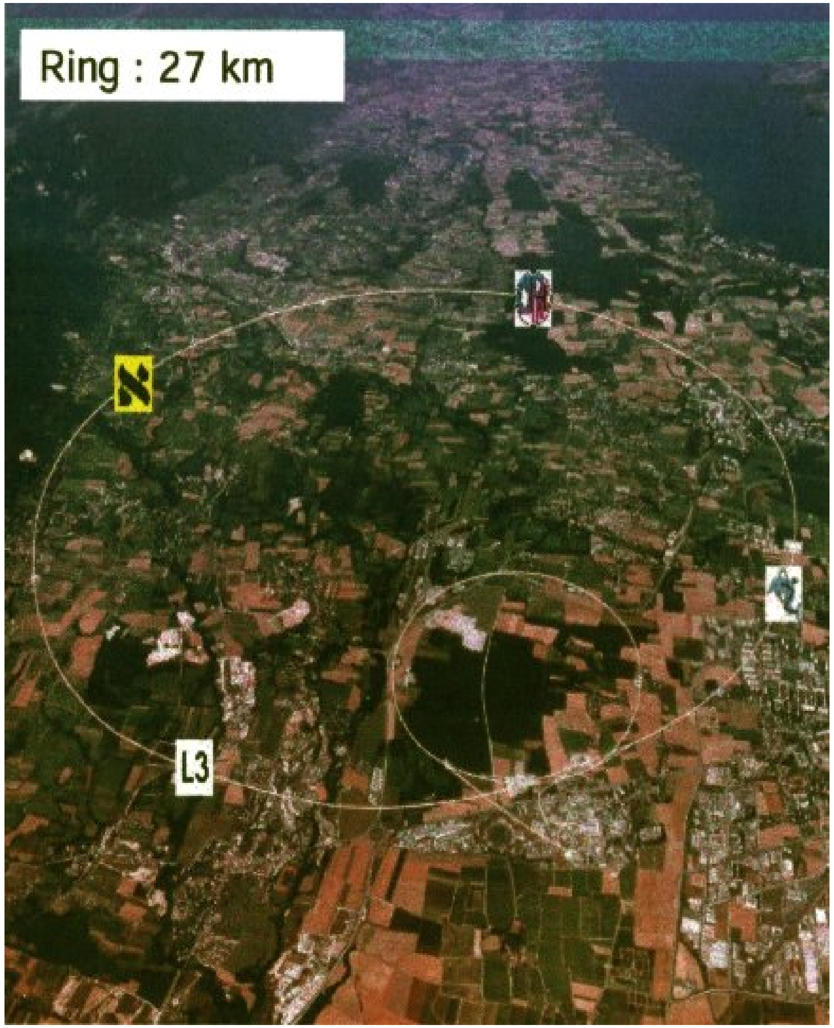

HERA: ep collider at DESY

ep collisions allow to probe efficiently the proton structure, distribution of quarks and gluons, are quarks elementary?

1994-2000 $\sim$ 0.1 fb^{-1} per experiment
2002-2006 $\sim$ 1 fb^{-1} per experiment

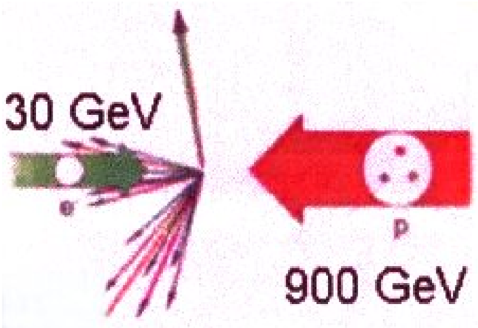

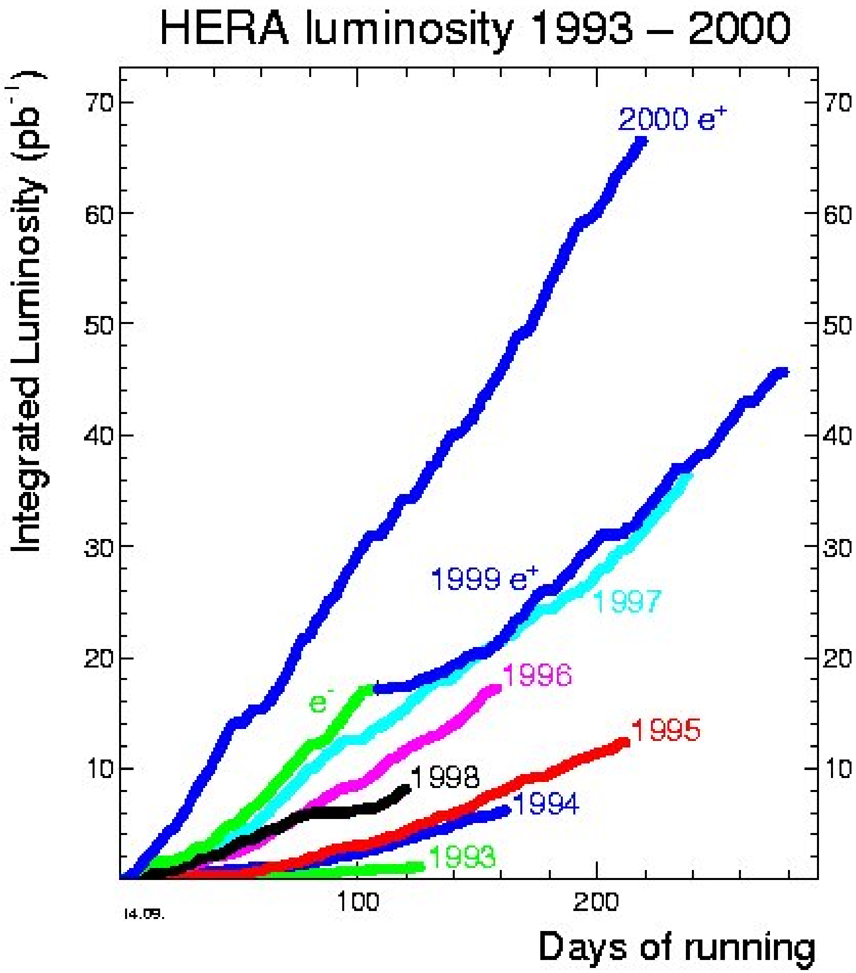

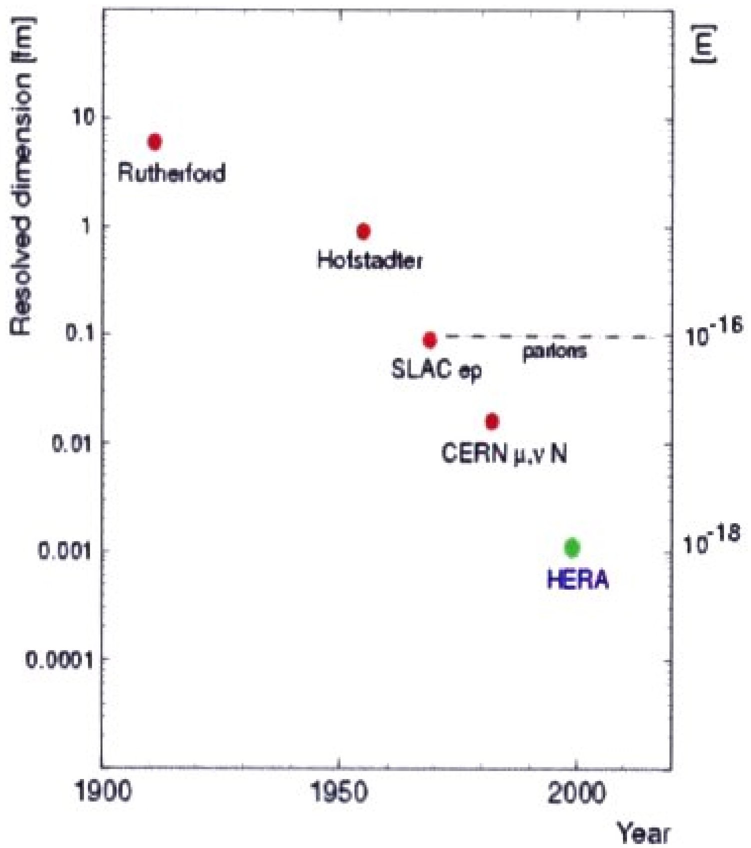

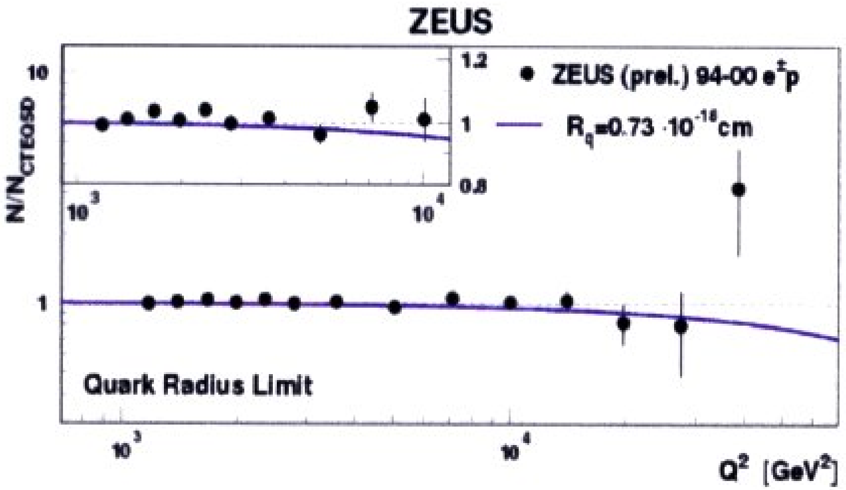

QCD with elementary quarks describes the scattering up to the highest accessible Q^2

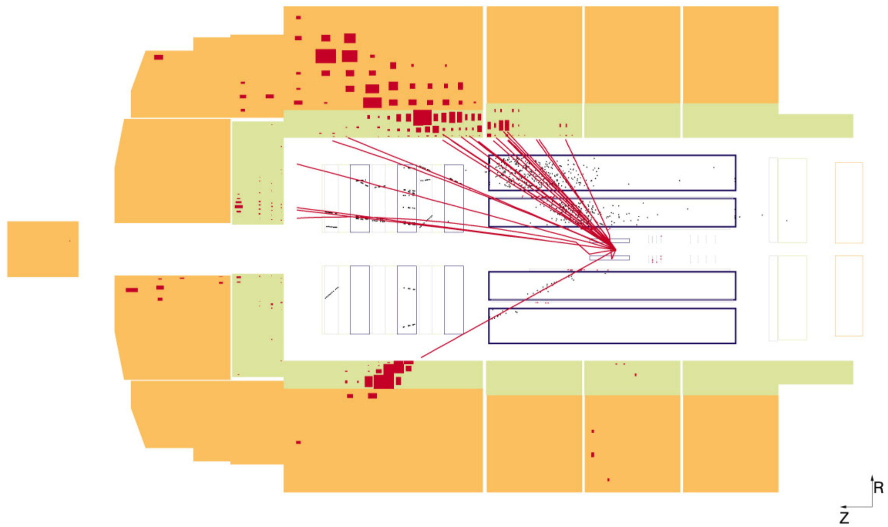

the Tevatron: $\bar{p}p$ Collider at Fermilab

$R \sim 6.5$ km

$\sqrt{s} \approx 2$ TeV

Run 1	(1989-1996)	$\approx$ 200 top events $\rightarrow$ discovery of top $\approx$ 80000 W events, measurement of m_W and m_{top}
Run 2	(2001-2011)	$\geq 100\times$ more data $\rightarrow$ better measurements of m_W and m_{top}, searches for Higgs and new particles

LHC: Hadron collider at CERN, startup in 2009

LHC: Hadron collider at CERN

LHC machine parameters		
circumference		27 km
Bending radius		3 km
Dipole field		8.33 T
Orbit frequency		11 kHz
Bunch spacing		25 ns
Protons/bunch		10^{11}
Beam energy		
	pp	$7 + 7$ TeV
	PbPb	$2.7 + 2.7$ TeV/u
Peak luminosity		
	pp	10^{34} cm^{-2} s^{-1}
	PbPb	10^{27} cm^{-2} s^{-1}

1.2 General demands on particle detectors

- Particle detection
- Momentum or energy measurement
- Particle identification *electron - pion - kaon ...*
- Reconstruction of the invariant mass of decay products $m_{\mathrm{inv}}^2 = (\sum_i p_i)^2$, four-momenta
- "Missing Mass" or "Missing Energy" for undetected particles like neutrinos
- Sensitivity to lifetime or decay length
  - stable particles: protons, $\tau \geq 10^{32} y$
    test of stability
  - unstable particles:
    decay via strong interaction: $\rho \to \pi^+\pi^-$ $\quad \Gamma = 100$ MeV

$$\tau c = \frac{\hbar c}{\Gamma} = 2 \text{ fm} \qquad \tau \approx 10^{-23} \text{ s}$$

    decay via electromagnetic interaction: $\pi^0 \to \gamma\gamma$ $\quad \tau = 10^{-16}$ s
  - quasi-stable particles:
    decay via weak interaction

Some examples for decay length

particle	τ	$c\tau$	decay length $\beta\gamma c\tau$ at $p = 10$ GeV/c
n	889 s	$2.7 \cdot 10^{8}$ km	$2.9 \cdot 10^{9}$ km
Λ	$2.6 \cdot 10^{-10}$ s	7.9 cm	71 cm
$\pi^{\pm}$	$2.6 \cdot 10^{-8}$ s	7.8 m	560 m
$D^{\pm}$	10^{-12} s	0.31 mm	1.6 mm
$B^{\pm}$	$1.6 \cdot 10^{-12}$ s	0.49 mm	0.93 mm
τ	$3 \cdot 10^{-13}$ s	0.09 mm	0.5 mm

ALEPH: Apparatus for LEP Physics

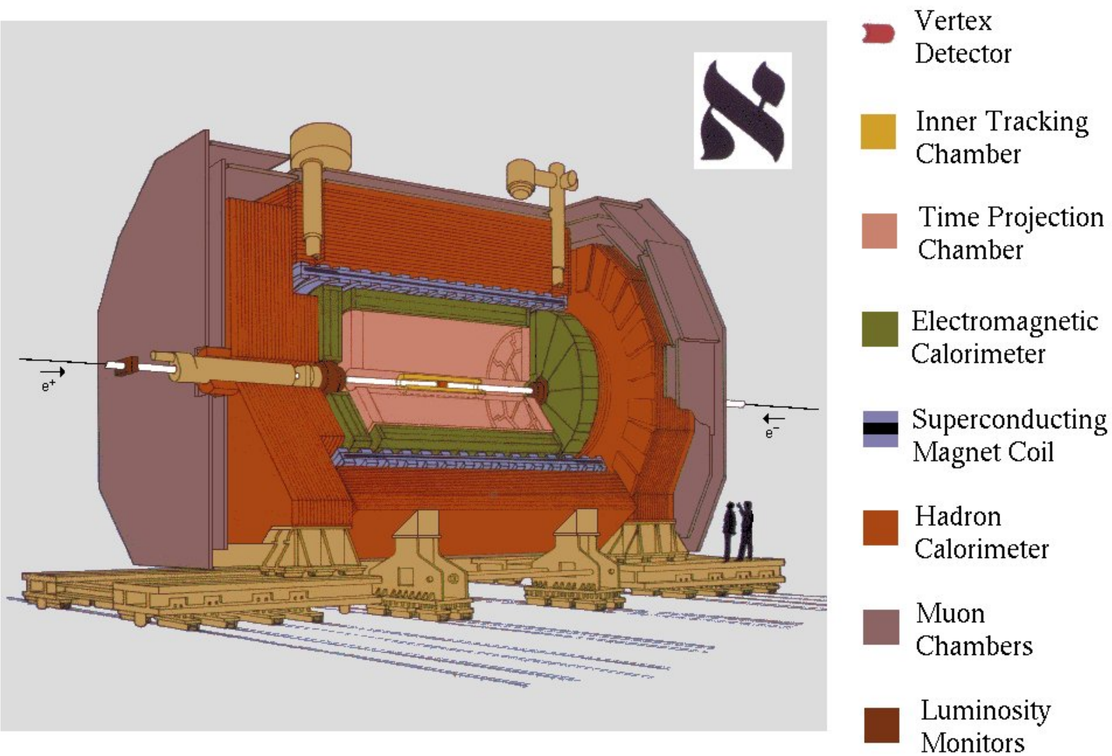

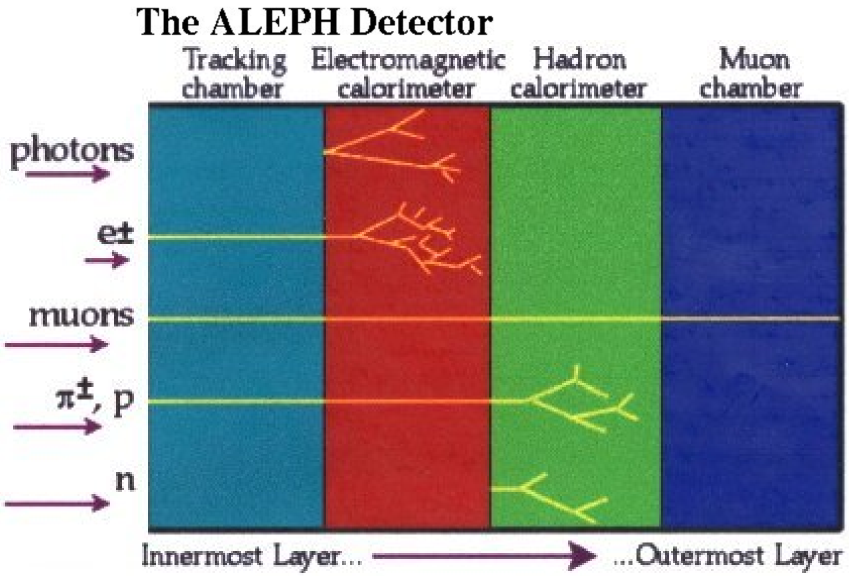

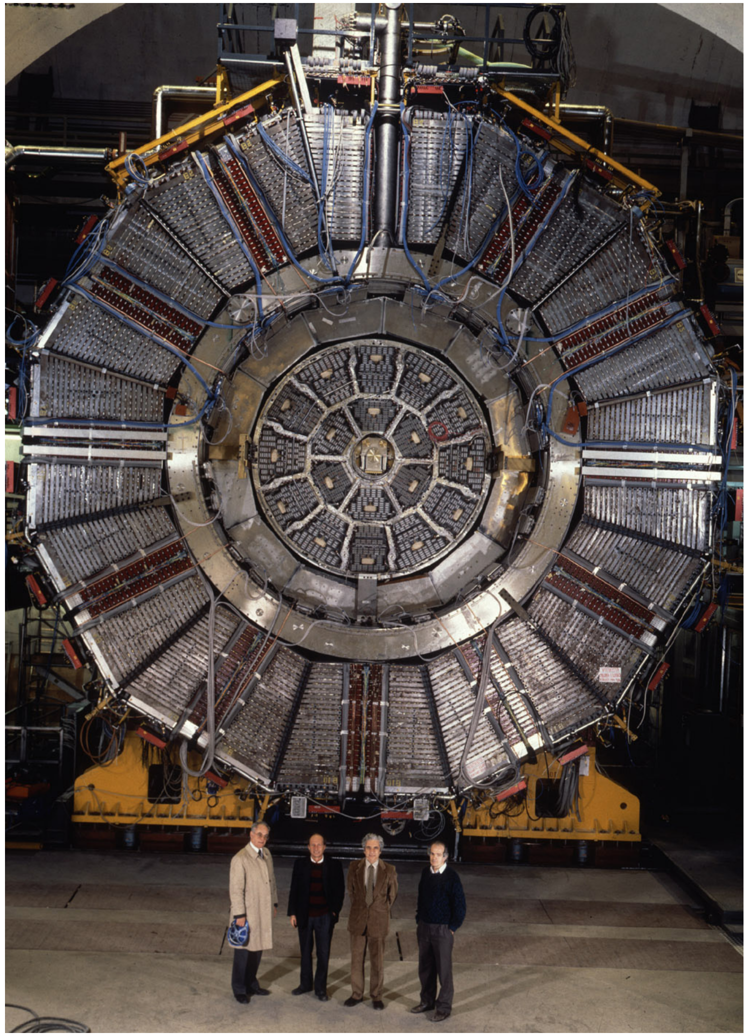

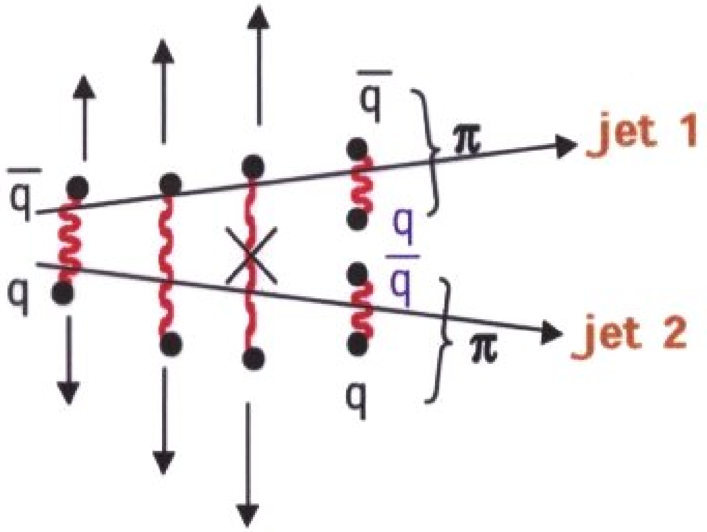

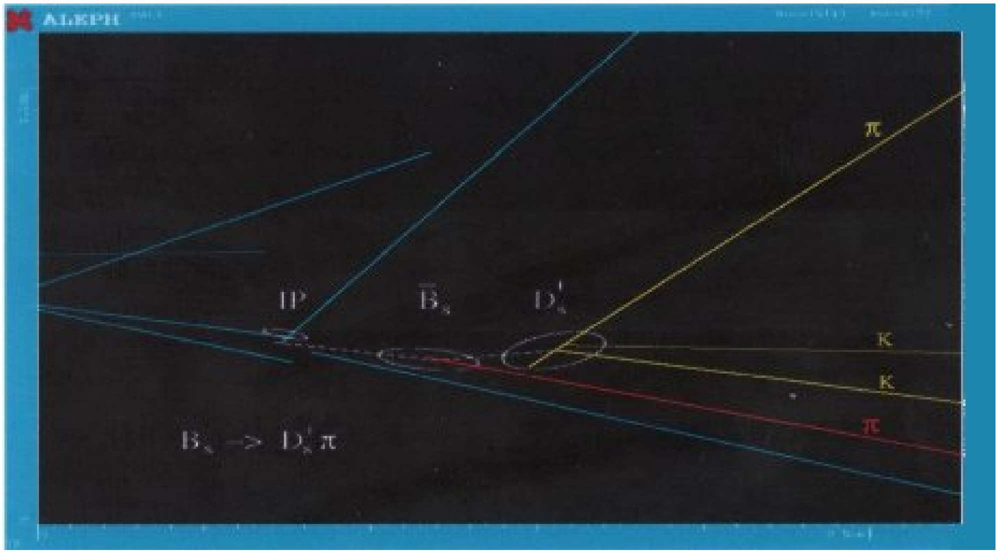

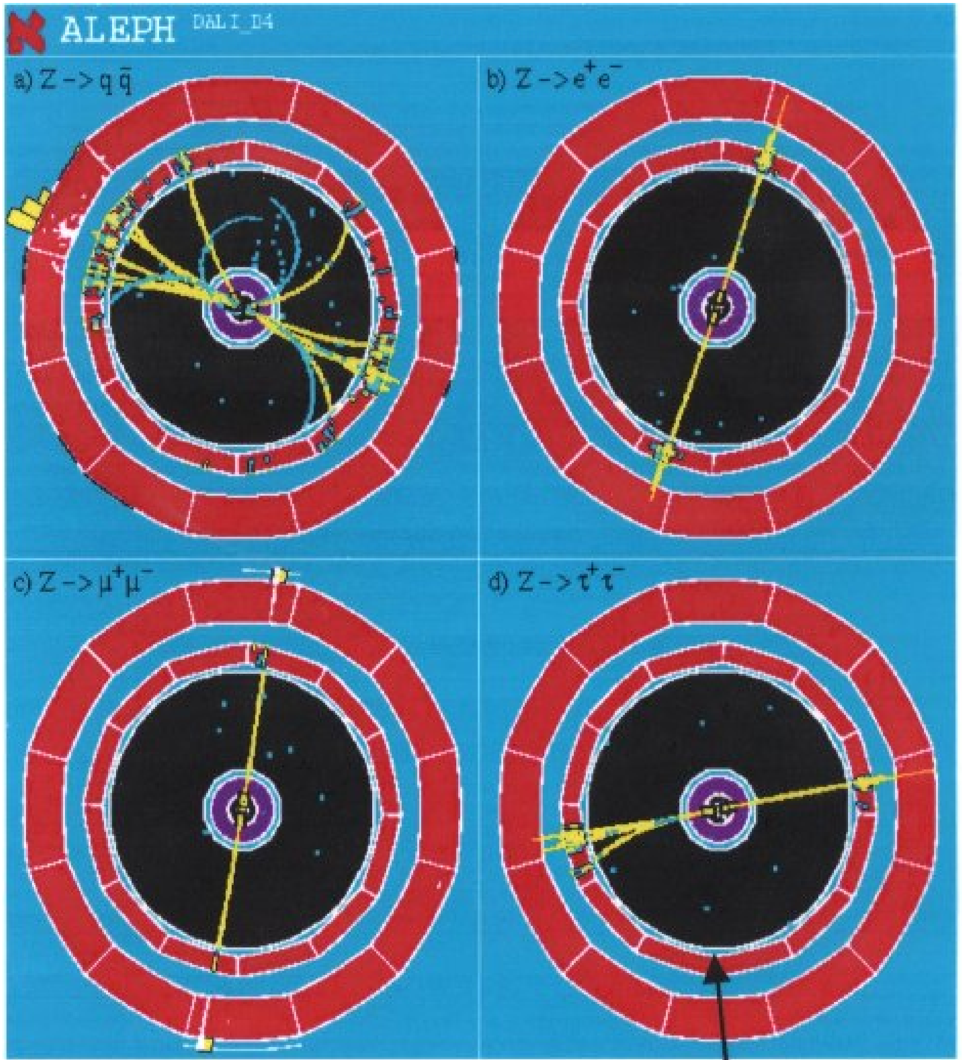

2 jets of hadrons
with low multiplicity
+ missing E carried
by neutrinos

ALEPH: Display of 2 Jet Events

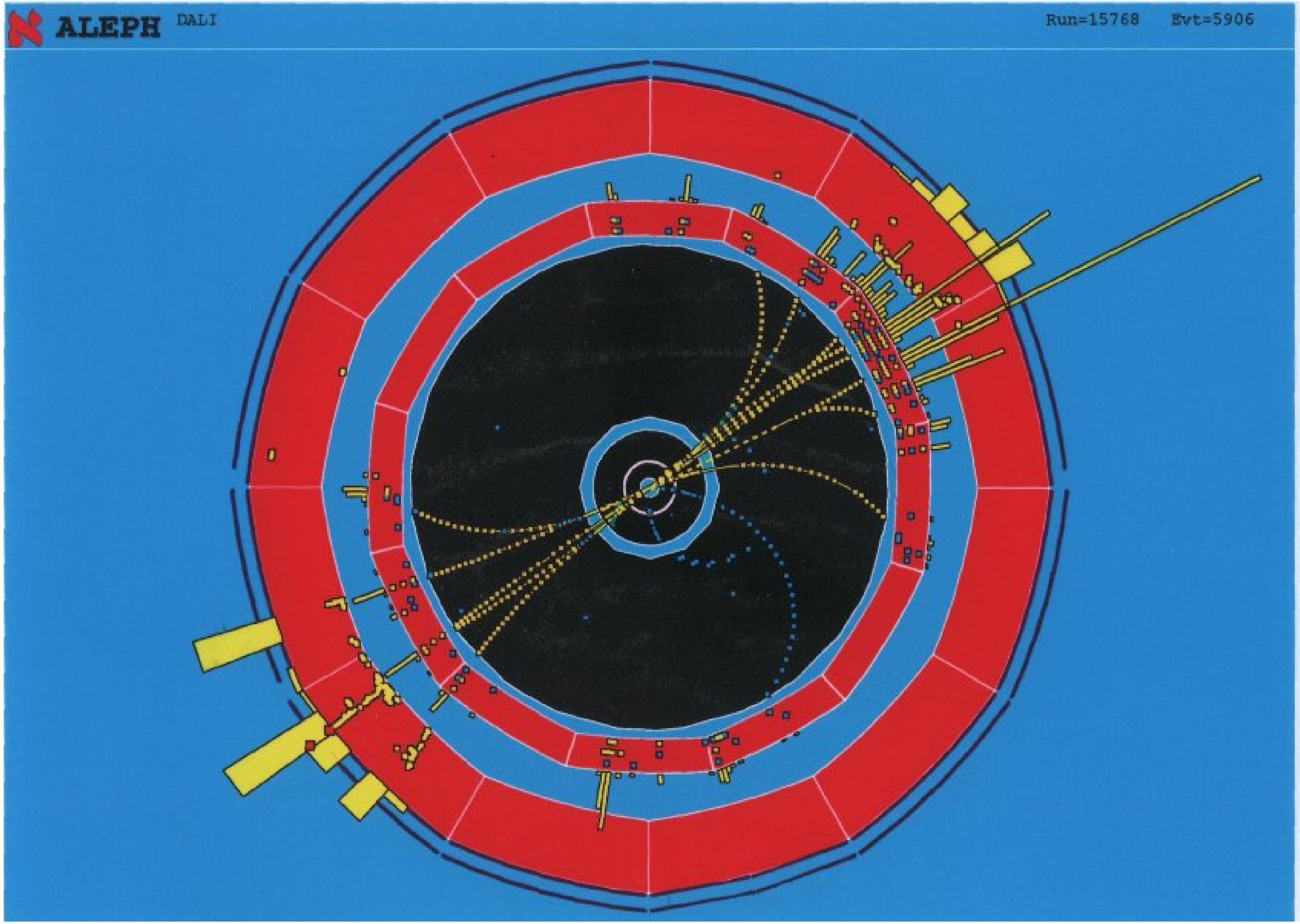

DELPHI: DEtector with Lepton, Photon and Hadron Identification

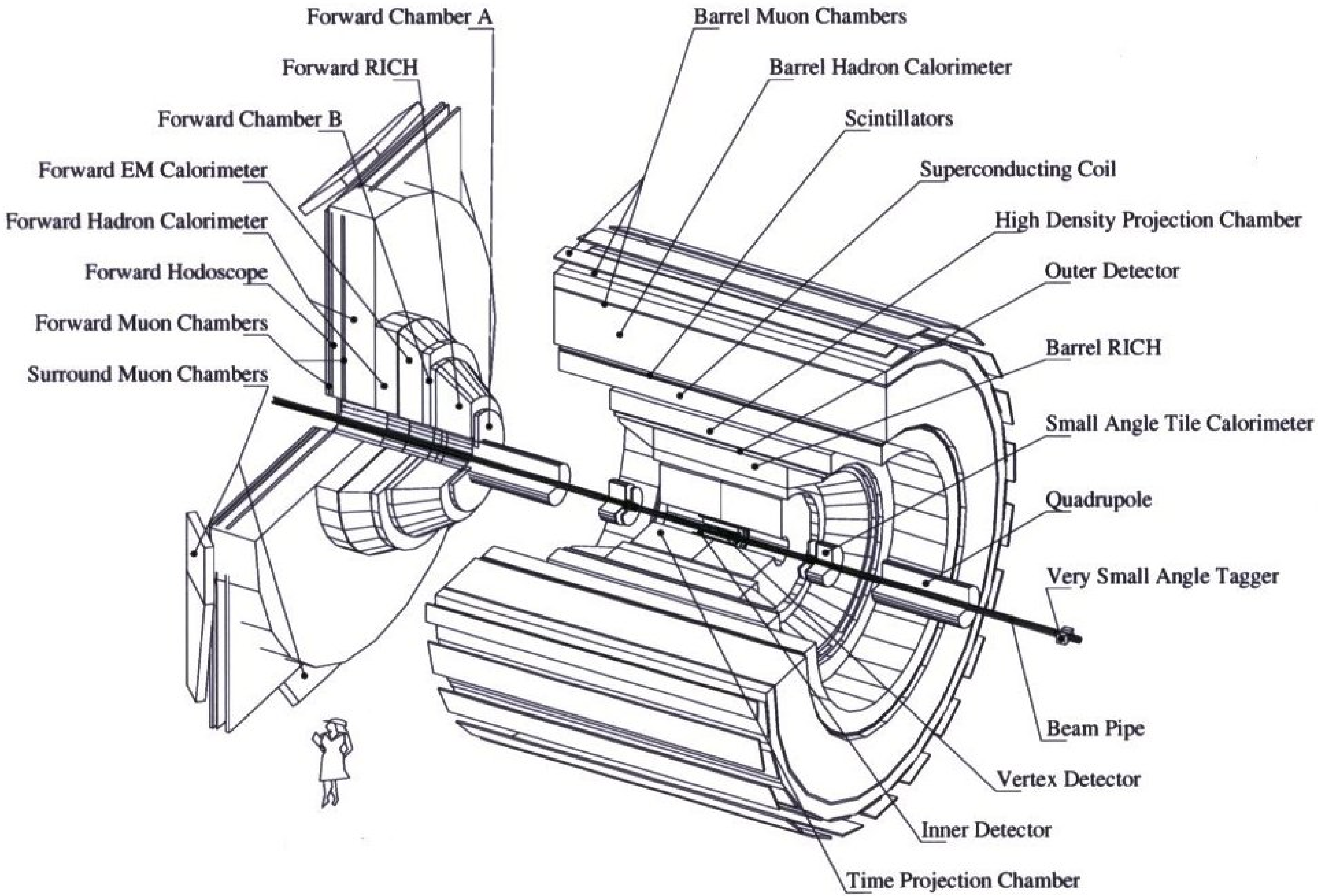

		ALEPH	DELPHI	L3	OPAL
magnet		superconducting	superconducting	normal	normal
fieldstrength		1.5 T	1.23 T	0.5 T	0.435 T
vertexdetector (SS)					
hit resolution	$r\phi$	12 μm	8 μm	7 μm	5 μm
	z	10 μm	9 μm	14 μm	13 mm
vertex detector					
hit resolution	$r\phi$	150 μm	85 μm	-	55 μm
	z	70 mm	-	-	40 mm (ΔT)
					0.7 mm (st.)
central detector		TPC	TPC	TEC	jet chamber
hit resolution	$r\phi$	180 μm	250 μm	50 μm	135 μm
	z	$\sim$ 1 mm	0.9 mm	-	45 mm
outer chambers					
hit resolution	$r\phi$	-	110 μm	-	15 mm
	z	-	35 mm	320 μm	300 μm
momentum resol.	$\sigma(\frac{1}{p_t})(\mathrm{GeV/c})^{-1}$	$0.6 \cdot 10^{-3}$	$0.6 \cdot 10^{-3}$	$0.6 \cdot 10^{-3}$	$1.3 \cdot 10^{-3}$
($\cos\theta \simeq 0$)				for $\mu^{\pm}$ only	
electromagnetic calorimeter		lead-prop. tubes	HPC /lead glass	BGO	lead glass
granularity	barrel	3×3 cm^2	$\sim 2 \times 2$ cm^2	2×2 cm^2	10×10 cm^2
	endcap	same as barrel	5×5 cm^2	same as barrel	same as barrel
energy resolution	σ_E/E	$0.18/\sqrt{E/\mathrm{GeV}}$	$0.32/\sqrt{E/\mathrm{GeV}}$	$0.02/\sqrt{E/\mathrm{GeV}}$	$0.06/\sqrt{E/\mathrm{GeV}}$
		$\oplus 0.01$	$\oplus 0.04$	$\oplus 0.01$	$\oplus 0.02$
hadronic energy resolution		$0.85/\sqrt{E/\mathrm{GeV}}$	$1.12/\sqrt{E/\mathrm{GeV}}$ $\oplus 0.21$	10% at 45 GeV	1 (at <15 GeV) to $1.2/\sqrt{E/\mathrm{GeV}}$
luminosity detector		Si-W sampling	lead-scintillating	BGO +	Si-W sampling
		+ lead sandwich	tiles & mask	Si $r\phi$ strips	+ lead sandwich
fiducial acceptance	inner/outer radius	6.1/14.5 cm	6.5/42.0 cm	7.6/15.4 cm	6.2/14.2 cm
	$\theta_{\min}/\theta\max$	30/48 mrad	44/114 mrad	32/54 mrad	31/52 mrad

ATLAS: A Toroidal LHC ApparatuS

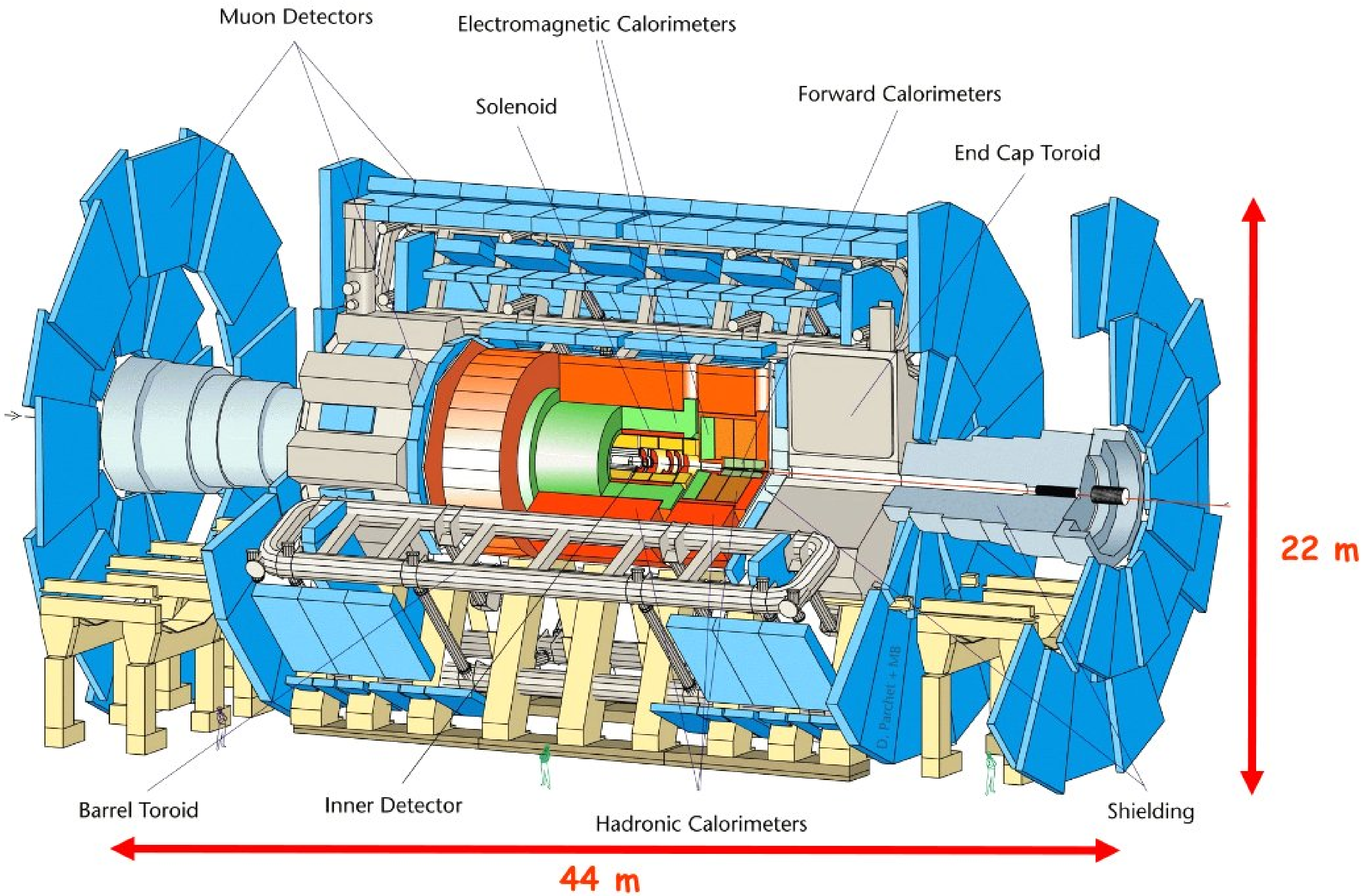

ATLAS: A Toroidal LHC ApparatuS

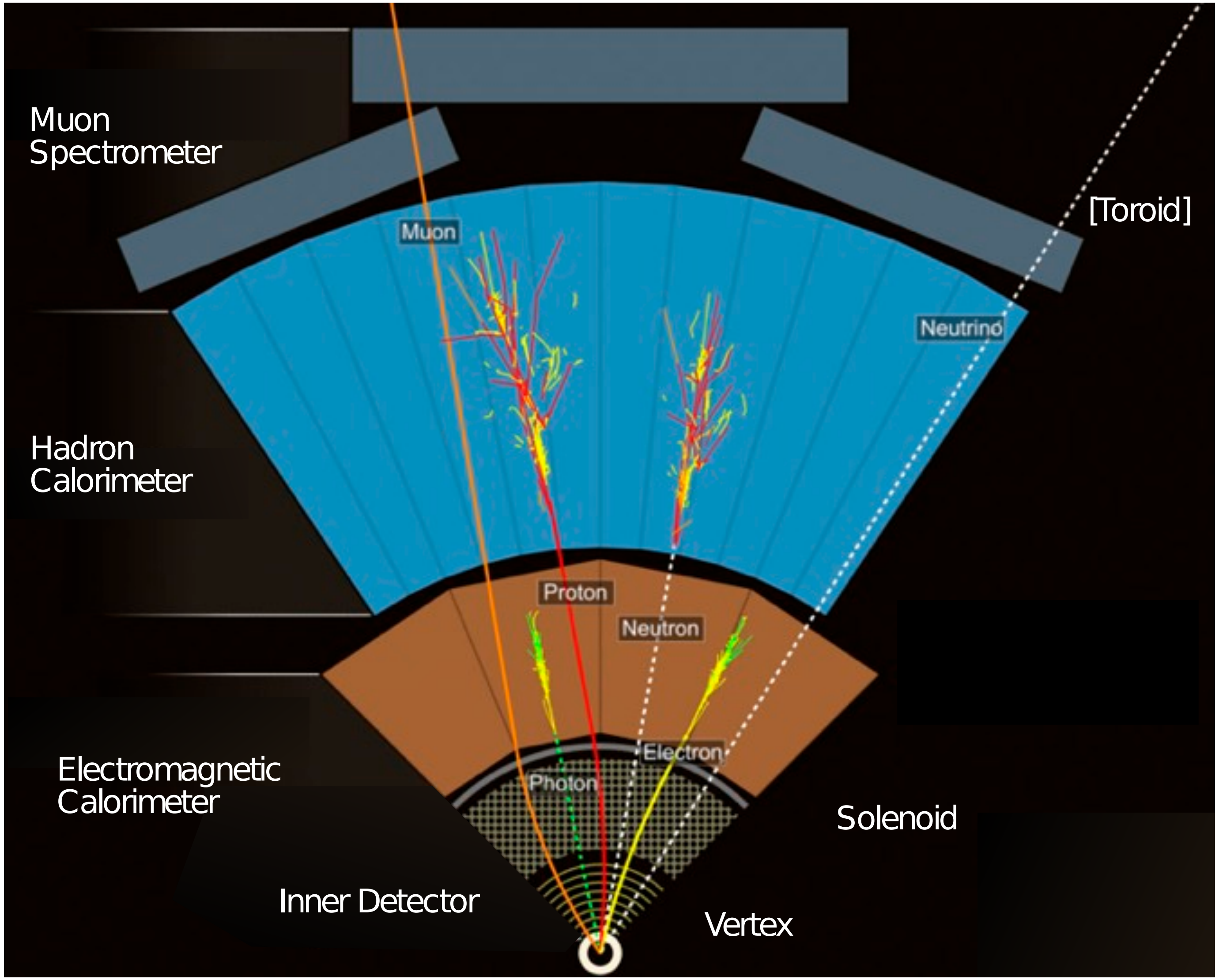

CMS: Compact Muon Spectrometer

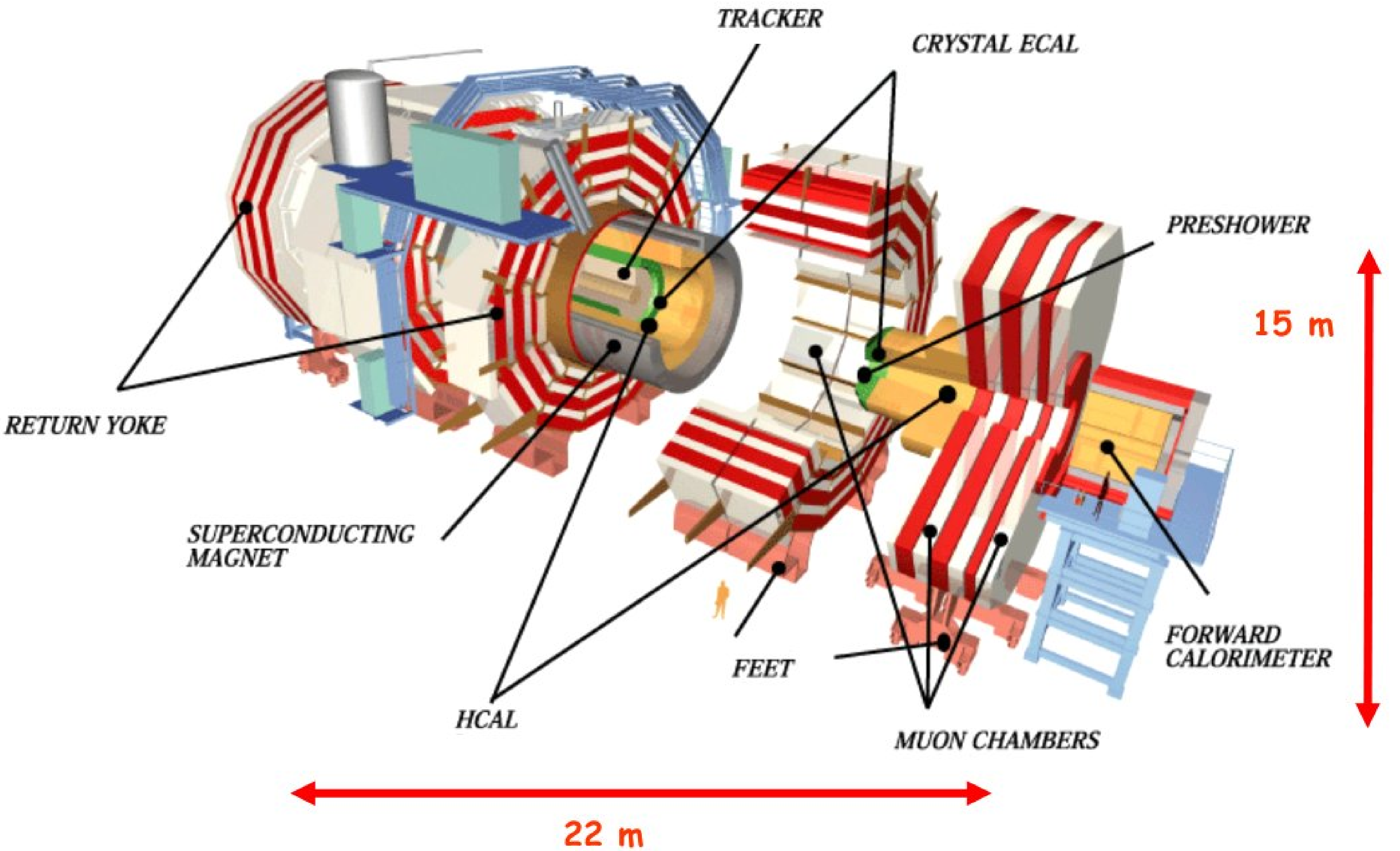

Slice through CMS

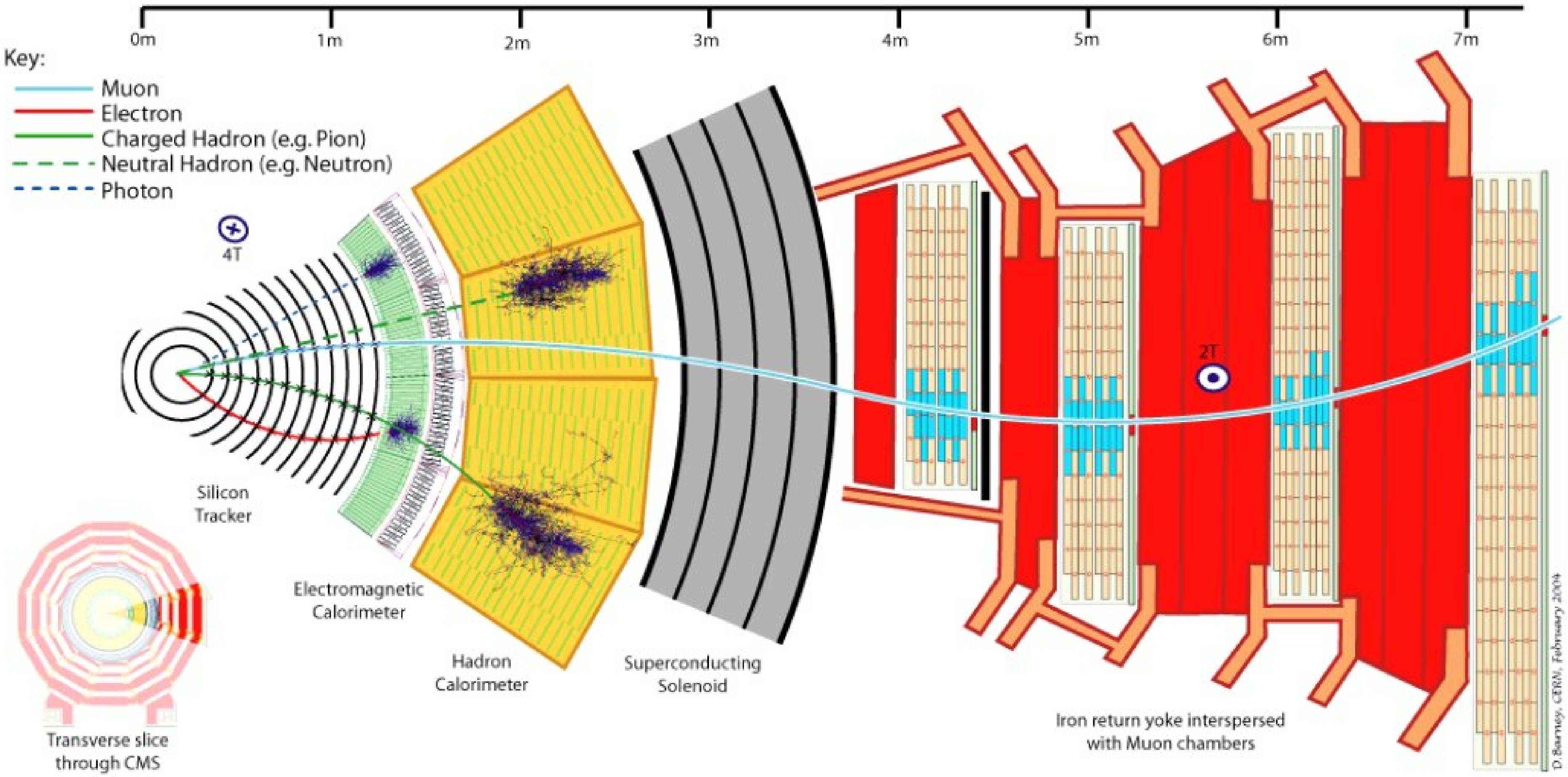

Higgs discovery $\mathrm{H} \rightarrow \mathrm{ZZ} \rightarrow \mu^+\mu^- + e^+e^-$

ATLAS event display

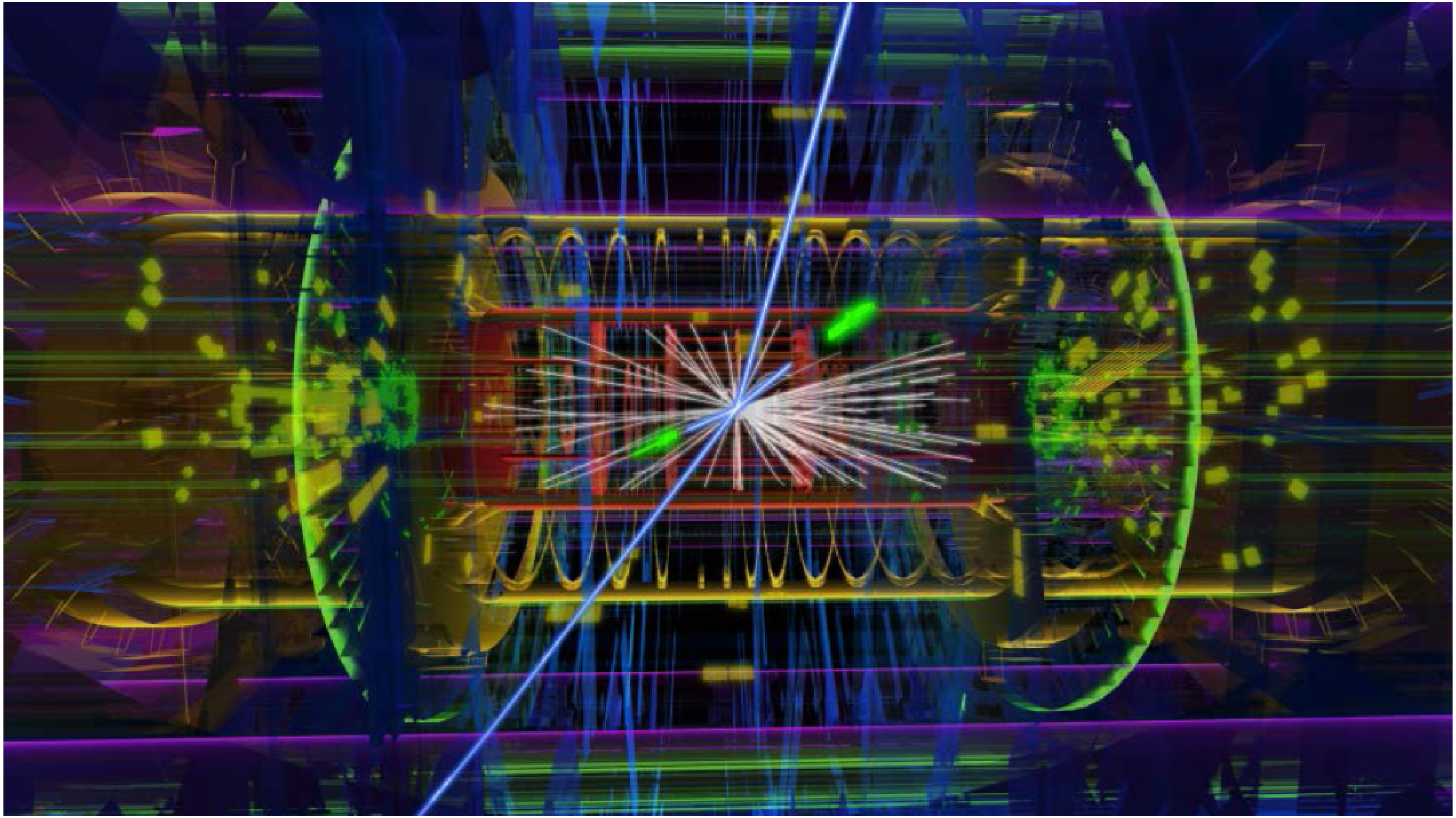

ALICE: A Large Ion Collider Experiment

Study of Quark-Gluon Plasma Matter

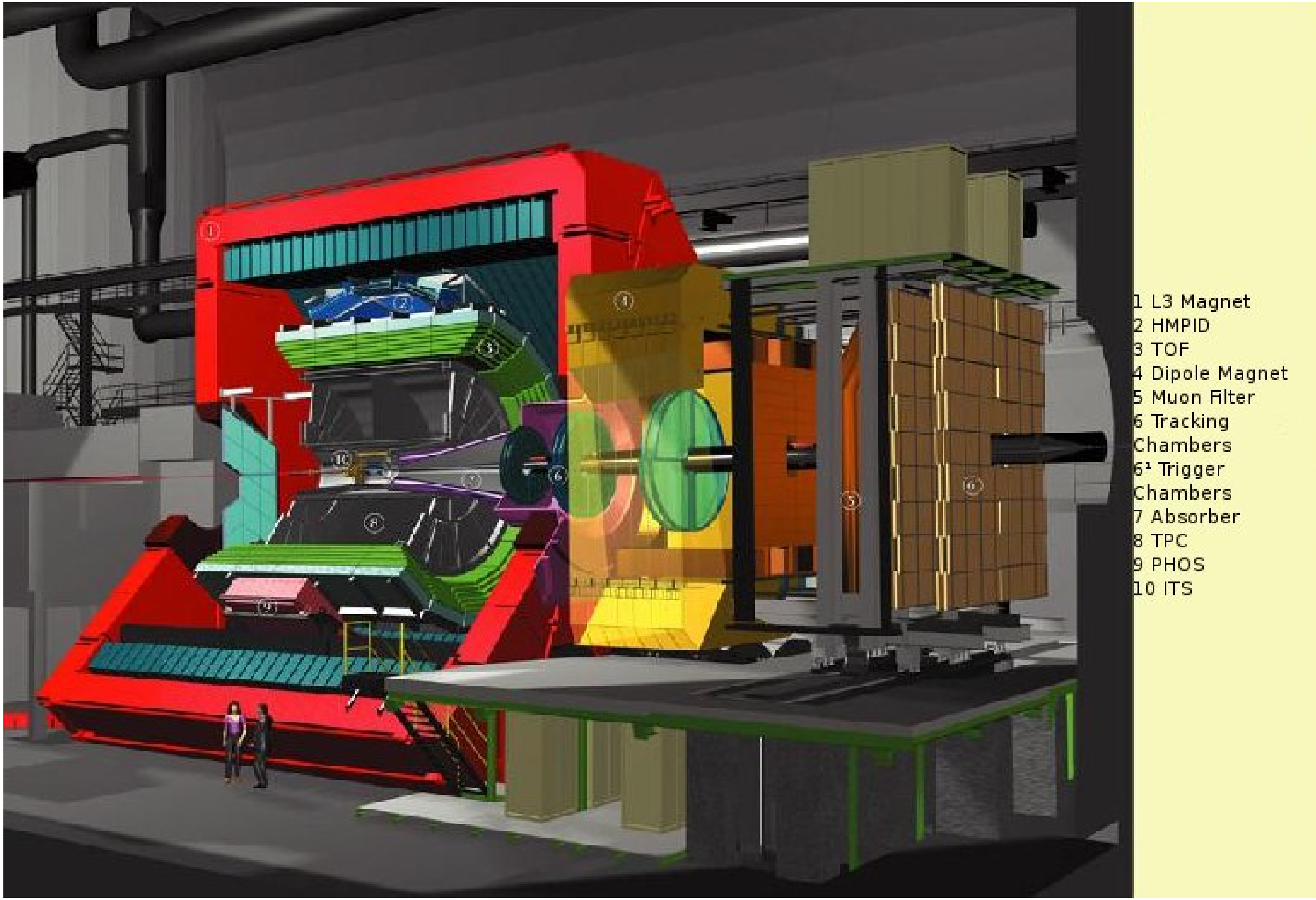

2. Interactions of particles and matter

- very compact presentation, since material should be largely known (see also chapter 3 of my lecture 'Experimentalphysik 5' WS 2008/2009 and Skript - to be found on my webpage)
- some additional material, useful relations, tables, figures[1]
- more emphasis on some aspects that are new beyond PEP4 and important for detectors

[1] Good, but very compact presentation of material, including many references in *Review of Particle Physics, Chin. Phys. C40 (2016) 100001 and 2017 update, ch. 34 "Passage of particles through matter" by P. Bichsel, D.E. Groom & S.R. Klein*

2.1 Electronic energy loss dE/dx

consider particle X with $Mc^2 \gg m_e c^2$
Coulomb interaction between particle X and atom
cross section dominated by inelastic collisions with electrons

$$
\begin{array}{llll}
\text{atom} + X & \rightarrow & \text{atom}^+ + e^- + X & \text{ionization} \\
 & \rightarrow & \text{atom}^* + X & \text{excitation} \\
 & & \quad \hookrightarrow \text{atom} + \gamma & \text{de-excitation}
\end{array}
$$

(for electrons also bremsstrahlung, see below)
classical derivation: *N. Bohr 1913*
quantum mechanical derivation: *H. Bethe, Ann. d. Physik 5 (1930) 325* and
F. Bloch, Ann. d. Physik 16 (1933) 285

Bohr: particle with charge ze moves with velocity v through medium with electron density n, electrons considered free and, during collision, at rest

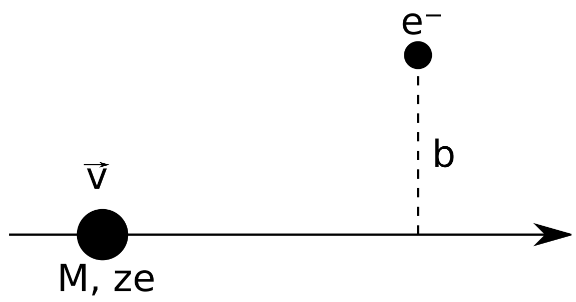

$$\Delta p_\perp = \Delta p = \frac{2ze^2}{bv} \qquad \Delta p_{||} \text{ averages to zero}$$

$$\Delta E(b) = \frac{\Delta p^2}{2m_e} \qquad \text{energy transfer onto one electron at distance } b$$

per pathlength $\mathrm{d}x$ in the distance between b and $b + \mathrm{d}b$, $n 2\pi b \, \mathrm{d}b \, \mathrm{d}x$ electrons are found [2]

[2] here and in the following $e^2 = 1.44$ MeV fm (contains $4\pi\epsilon_0$)

$$-\mathrm{d}E(b) = \frac{n4\pi z^2 e^4}{m_e v^2} \frac{\mathrm{d}b}{b} \mathrm{d}x$$

diverges for $b \to 0$ *Bohr*: choose relevant range $b_{min} - b_{max}$

$\boxed{b_{min}}$ relative to heavy particle electron is located only within the Broglie wavelength

$$\Rightarrow b_{min} = \frac{\hbar}{p} = \frac{\hbar}{\gamma m_e v}$$

$\boxed{b_{max}}$ duration of perturbation should be shorter than period of electron: $b/\gamma v \leq 1/\langle \nu \rangle$

$$\Rightarrow b_{max} = \frac{\gamma v}{\langle \nu \rangle}$$

integrate over b with these limits:

$$-\frac{\mathrm{d}E}{\mathrm{d}x} = \frac{4\pi z^2 e^4}{m_e c^2 \beta^2} n \ln \frac{m_e c^2 \beta^2 \gamma^2}{\hbar \langle \nu \rangle}$$

electron density $n = \frac{N_A \rho Z}{A}$
average revolution frequency of electron $\langle \nu \rangle \leftrightarrow$ mean excitation energy $I = \hbar \langle \nu \rangle$

Bethe-Bloch equation

considering quantum mechanical effects and some other corrections

Bethe-Bloch equation

$$-\frac{\mathrm{d}E}{\mathrm{d}x} = Kz^2 \frac{Z}{A} \rho \frac{1}{\beta^2} \left[\frac{1}{2} \ln \frac{2 m_e c^2 \beta^2 \gamma^2 T_{max}}{I^2} - \beta^2 - \frac{\delta}{2} \right]$$

describes mean rate of energy loss in the range $0.1 \leq \beta\gamma \leq 1000$

$\frac{K}{A} = \frac{4\pi N_A r_e^2 m_e c^2}{A}$ with classical electron radius $r_e = \frac{e^2}{m_e c^2}$

$T_{max} \approx 2 m_e c^2 \beta^2 \gamma^2$ max. energy transfer in a single collision, for $M \gg m_e$

$I = (10 \pm 1) \cdot Z$ eV mean excitation energy (for elements beyond aluminum)

$\delta/2$ 'density correction' (see next page) with increasing particle energy → Lorentz contraction of electric field, corresponding to increase of contribution from large *b* with ln $\beta\gamma$

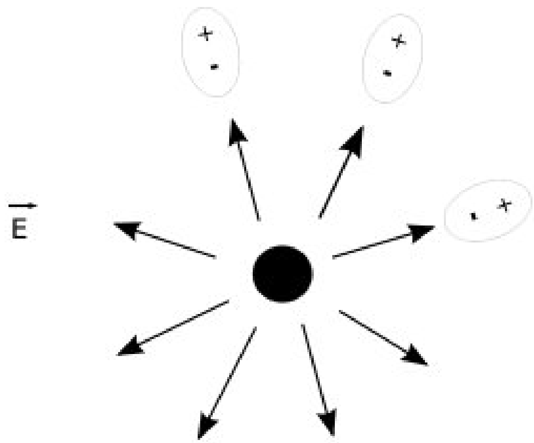

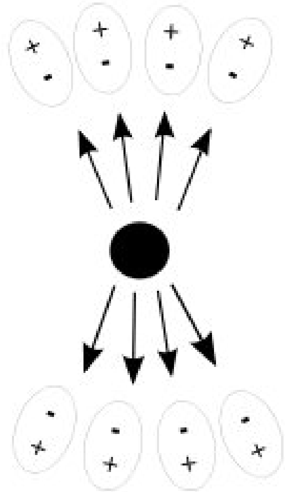

left: for small γ, right: for large γ

but: real media are polarized, effectively cuts off long-range contributions to logarithmic rise, term $-\delta/2$ leads to Fermi plateau high energy limit

$$\frac{\delta}{2} \to \ln \frac{\hbar\omega_p}{I} + \ln \beta\gamma - \frac{1}{2}$$

with plasma energy

$$\hbar\omega_p = \sqrt{4\pi n r_e^3 m_e c^2/\alpha}$$

$\Rightarrow -\frac{\mathrm{d}E}{\mathrm{d}x}$ increases more like $\ln \beta\gamma$ than $\ln \beta^2\gamma^2$ and I should be replaced by plasma energy

remark: plasma energy $\propto \sqrt{n}$
i.e. correction much larger for liquids and solids, leading to smaller relativistic rise

one more (small) correction:
'shell correction' $\Rightarrow$ for $\beta c \cong v_e$ capture processes possible

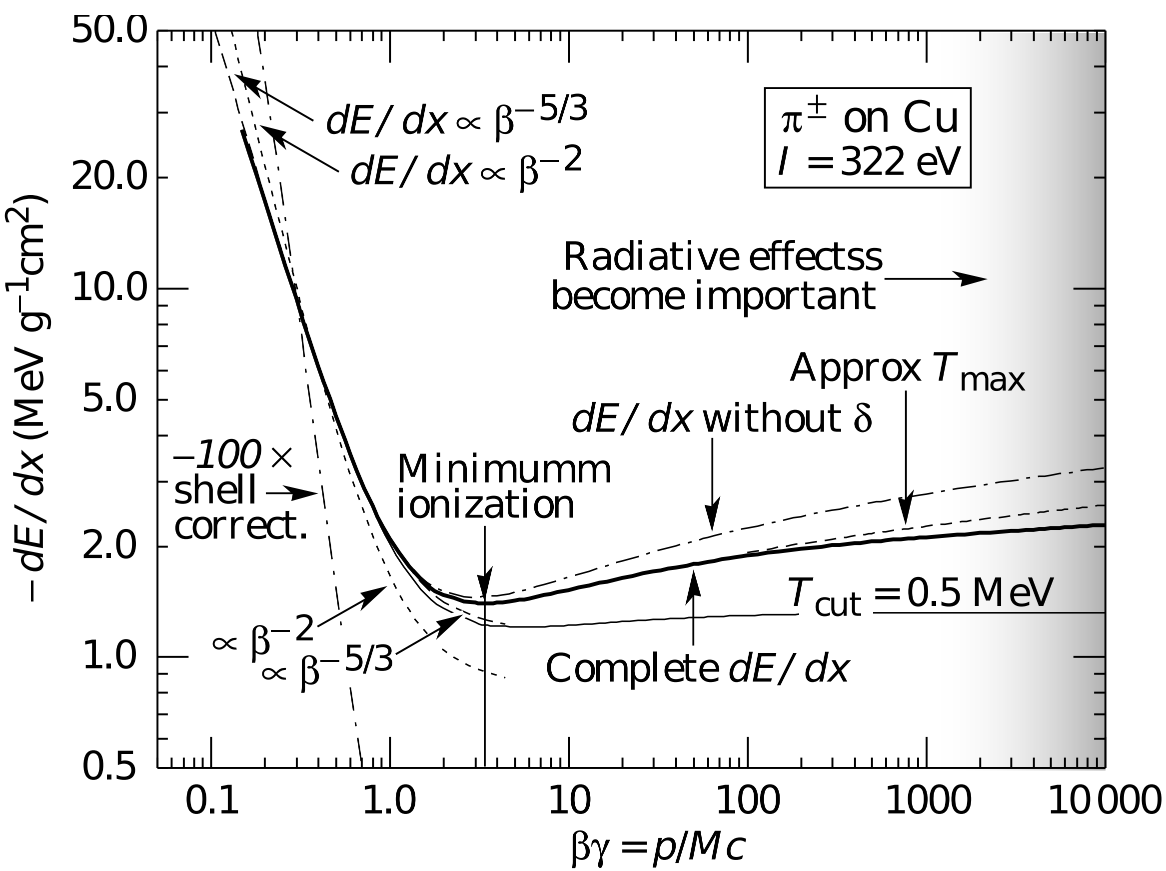

Energy loss rate in copper. The function without the density effect correction is also shown, as is the shell correction and two low-energy approximations.

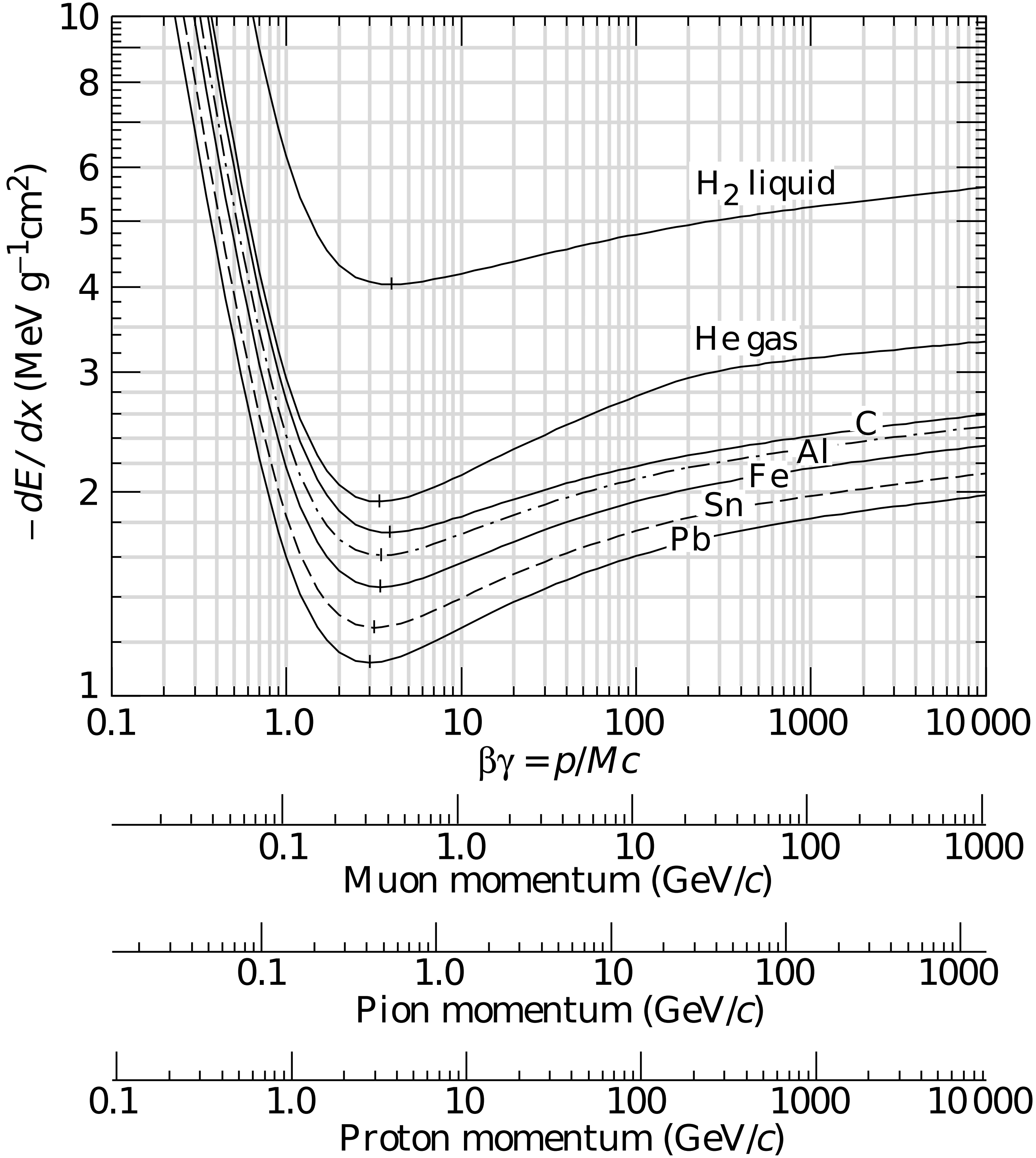
10
8
6
5
4
3
2
1
$-dE/dx$ (MeV g^{-1}cm^2)
H_2 liquid
He gas
C
Al
Fe
Sn
Pb
0.1
1.0
10
100
1000
10 000
$\beta\gamma = p/Mc$
0.1
1.0
10
100
1000
Muon momentum (GeV/c)
0.1
1.0
10
100
1000
Pion momentum (GeV/c)
0.1
1.0
10
100
1000
10 000
Proton momentum (GeV/c)

General behavior of dE/dx

- at low energies / velocities decrease as approx. $\beta^{-5/3}$ up to $\beta\gamma > 1$
- broad minimum at

$$\beta\gamma \cong \left.\begin{matrix} 3.5\ (Z=7) \\ 3.0\ (Z=100) \end{matrix}\right\} 1-2\ \frac{\text{MeV cm}^2}{g}$$

  'minimally ionizing particle'

- logarithmic rise and 'Fermi plateau'
  density correction would lead to plateau at high energy, except for energy transfer to few very energetic electrons ($T_{max} \propto \beta^2\gamma^2$). Treated explicitly beyond a certain T_{cut}
  logarithmic rise about 20% in liquids/solids and about 50% in gases
- very low velocities ($v < v_{\text{electron}}$) cannot be treated this way
  for $10^{-3} \leq \beta \leq \alpha \cdot z$: $\quad -\frac{dE}{dx} \propto \beta \quad$ non-ionizing, recoil of atomic nuclei
  for $\beta \cdot c \cong v_e$ also capture processes important (shell correction)

Range

Integration over changing energy loss from initial kinetic energy E down to zero

$$R = \int_E^0 \frac{\mathrm{d}E}{\mathrm{d}E/\mathrm{d}x}$$

concept only useful for low energy hadrons (such that R $\leq \lambda_i$) and for muons

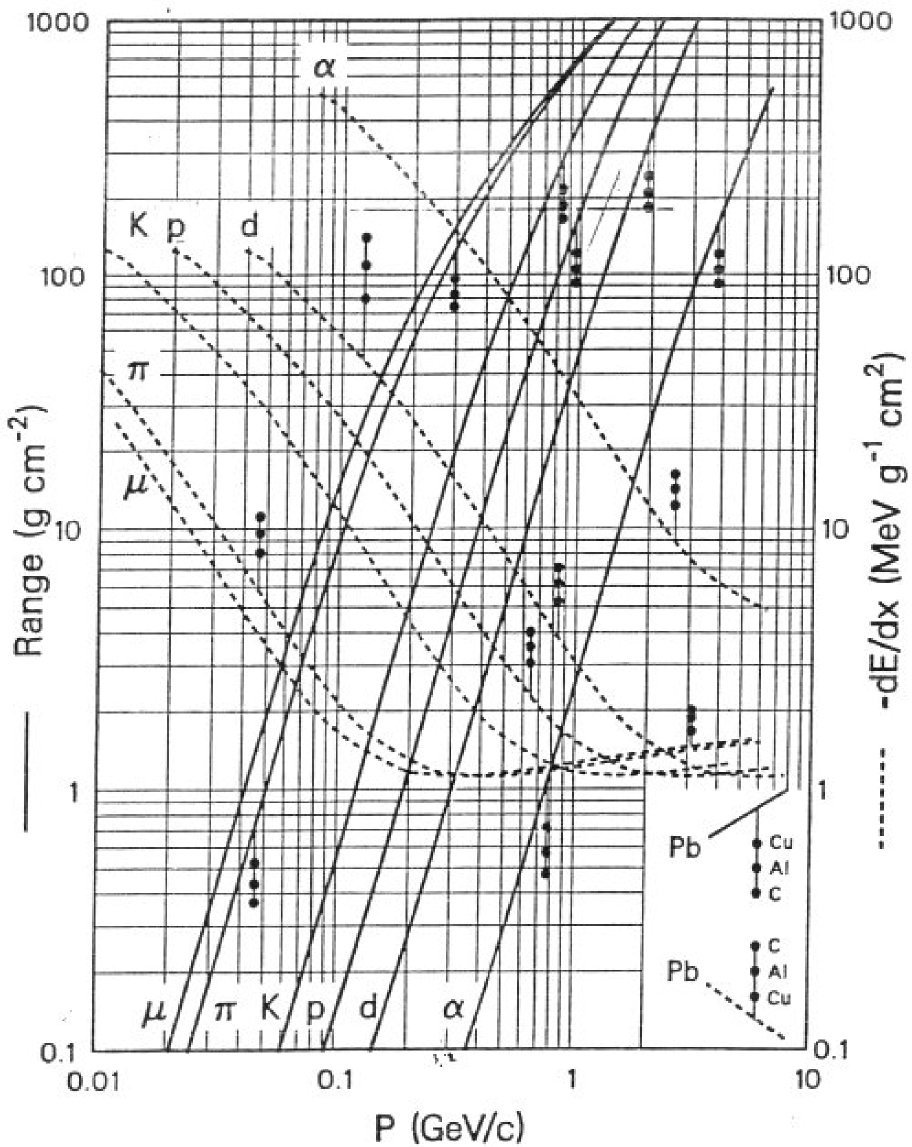

Mean range and energy loss due to ionization in lead, copper, aluminum and carbon

Energy deposition of particles stopped in medium

for $\beta\gamma \simeq 3.5$ $\qquad \langle \frac{dE}{dx} \rangle \simeq \frac{dE}{dx}_{\text{min}}$

for $\beta\gamma \leq 3.5$ $\qquad$ steep rise $\langle \frac{dE}{dx} \rangle \gg \frac{dE}{dx}_{\text{min}}$ down to very small energies,

then decrease again

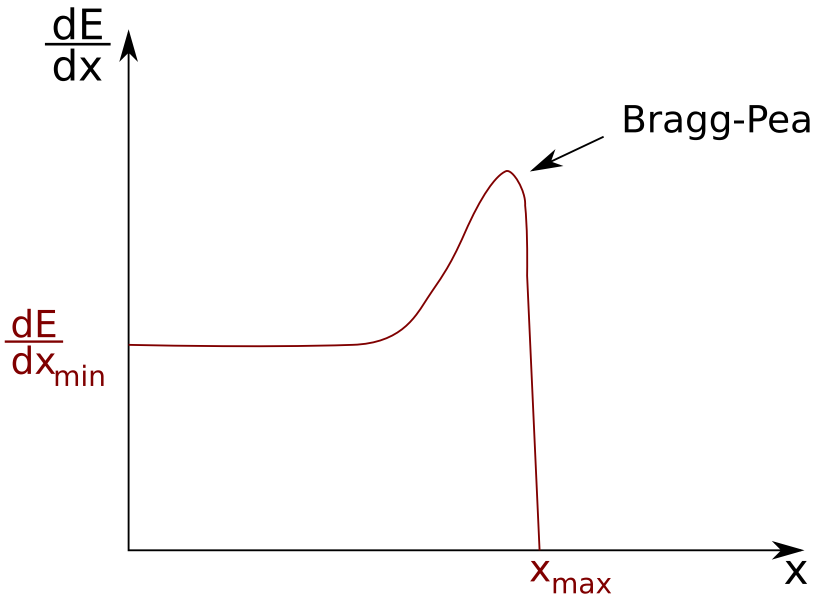

Energy loss curve vs depth showing Bragg peak

Application: tumor therapy - one can deposit precise dose in well defined depth of material (body), determined by initial beam energy, proton therapy
lately also with heavy ions as ^{12}C; HIT tumor center has started operation in Heidelberg (collaboration DKFZ & GSI)
precise 3D irradiation profile by suitably shaped absorber (custom made for each patient)

Delta-Electrons

Electrons liberated by ionization having an energy in excess of some value (e.g. T_{cut}) are called δ-electrons (initial observation in emulsions, hard scattering $\rightarrow$ energetic electrons)

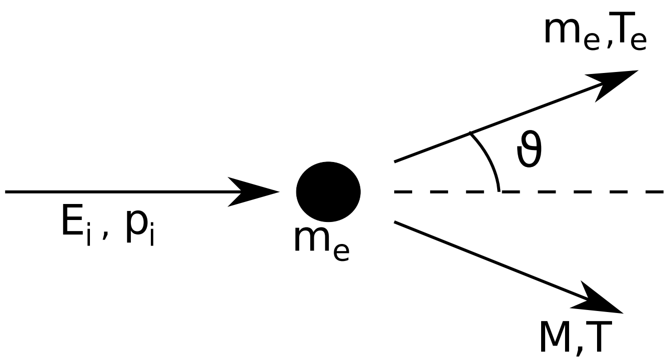

$$T_e = 2m_e \frac{\vec{p}_i^2 \cos^2\theta}{(E_i + m_e)^2 - \vec{p}_i^2 \cos^2\theta}$$

$$\Rightarrow \quad T_e^{\text{max}} = \frac{2m_e \vec{p}_i^2}{(E_i + m_e)^2 - \vec{p}_i^2}$$

$$\approx \frac{2m_e c^2 \beta^2 \gamma^2}{1 + 2\frac{m_e \gamma}{M} + \left(\frac{m_e}{M}\right)^2} \quad \text{for} |\vec{p}_i| \gg M, m_e$$

Massive highly relativistic particle can transfer practically all its energy to a single electron!
Probability distribution for energy transfer to a single electron:

$$\frac{d^2W}{\text{dx d}E} = 2m_e c^2 \pi r_e^2 \frac{z^2}{\beta^2} \cdot \frac{Z}{A} N_A \cdot \rho \cdot \frac{1}{E^2}$$

unpleasant: often this electron is not detected as part of the ionization trail
$\rightarrow$ broadening of track and of energy loss distribution

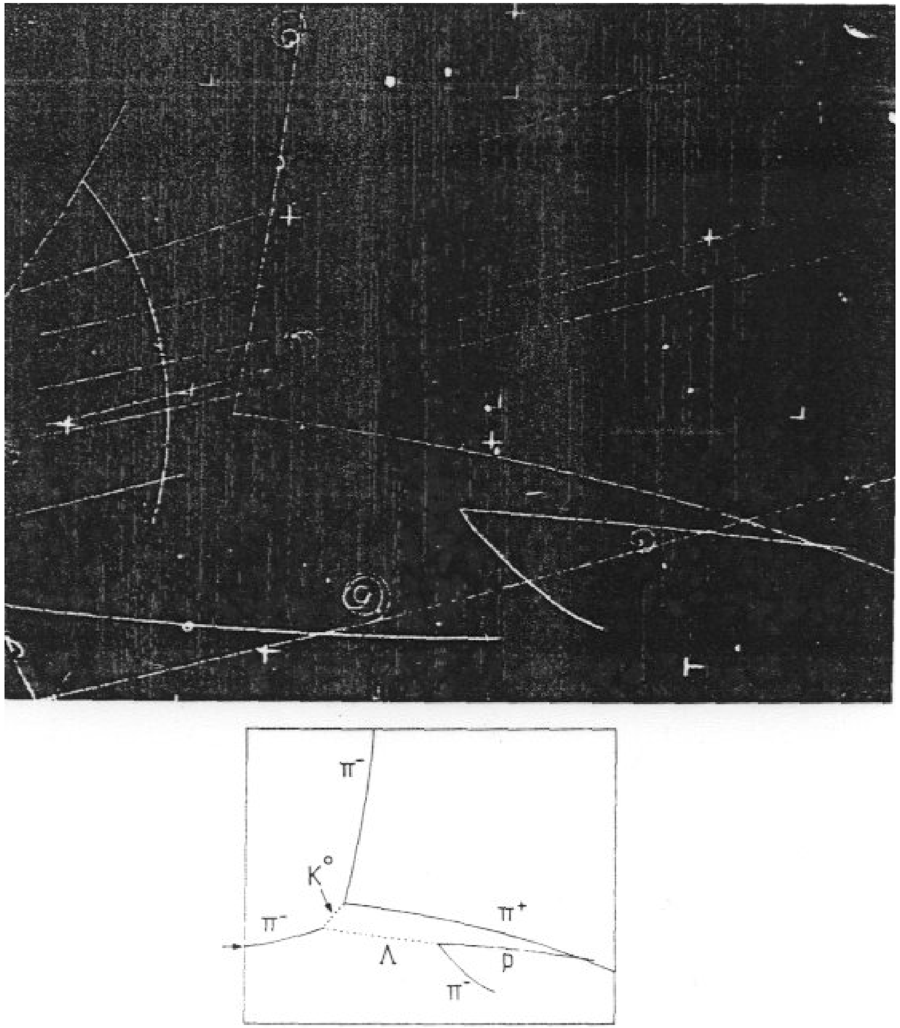

A bubble chamber picture of the associated production reaction $\pi^- + \text{p} \rightarrow \text{K}^0 + \Lambda$. The incoming pion is indicated by the arrow, and the unseen neutrals are detected by their decays $\text{K}^0 \rightarrow \pi^+ + \pi^-$ and $\Lambda \rightarrow \pi^- + \text{p}$. This picture was taken in the 10-inch (25 cm) bubble chamber at the Lawrence Berkeley Radiation Laboratory. The spirals are δ electrons.

Energy loss distribution for finite absorber thickness

Energy loss by ionization is distributed statistically: 'energy loss straggling'
Bethe-Bloch formula describes the *mean energy loss*
strong fluctuations about mean: first considered by *Bohr 1915*

$$\sigma^2 = \langle E^2 \rangle - E_0^2 \cong 4\pi n z^2 e^4 \Delta x$$

σ: standard deviation of Gaussian distribution with mean deposited energy E_0 and tail towards high energies due to δ-electrons (actual solution complicated problem)

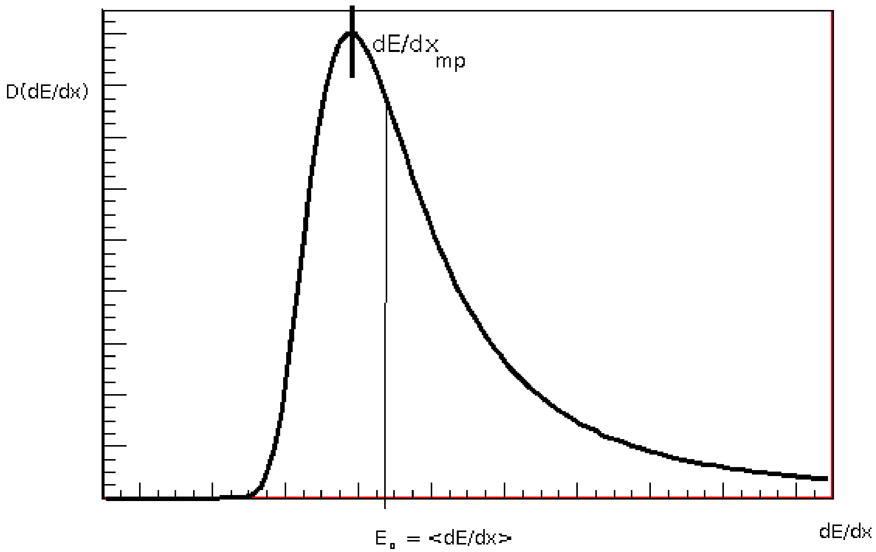

'Landau distribution' for thin absorber
Vavilov (1957): correction for thicker absorber
approximation:

$$D\left(\frac{\mathrm{d}E}{\mathrm{d}x}\right) = \frac{1}{\sqrt{2\pi}} \exp\left(-\frac{1}{2}\left(\underbrace{\frac{\frac{\mathrm{d}E}{\mathrm{d}x} - \frac{\mathrm{d}E}{\mathrm{d}x}_{\mathrm{mp}}}{\xi}}_{\lambda} + e^{-\lambda}\right)\right)$$

ξ is a material constant

more precise: Allison & Cobb (using measurements and numerical solution)
Ann. Rev. Nuclear Sci. 30 (1980) 253

Energy loss distribution normalized to thickness x
with increasing thickness:

- most probable $\mathrm{d}E/\mathrm{d}x$ shifts to large values
- relative width shrinks
- asymmetry of distribution decreases

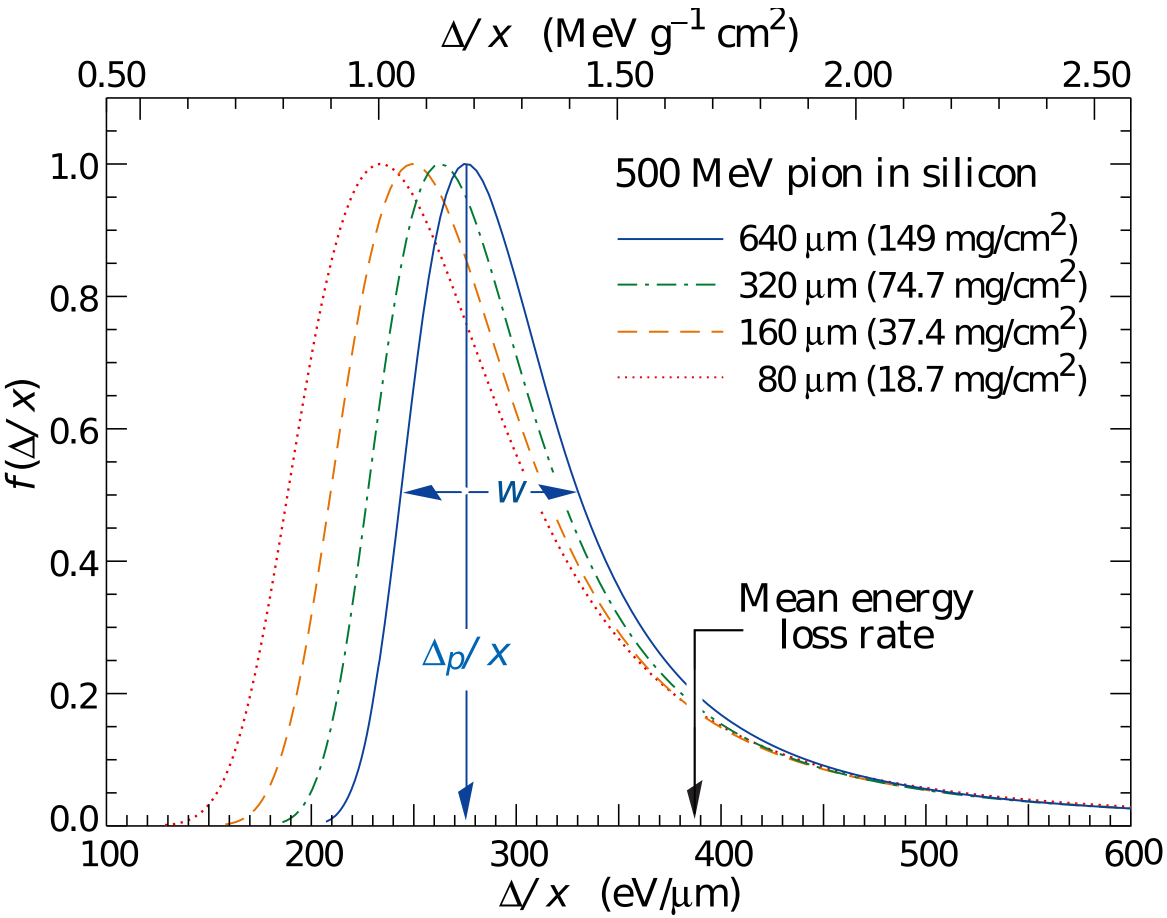

Straggling functions in silicon for 500 MeV pions, normalized to unity at the most probable value Δ_p/x. The width w is the full width at half maximum.

Multiple (Coulomb) scattering

In deriving energy loss by ionization we had considered the

transverse momentum transfer to electron $\Delta p_{\perp} \simeq \dfrac{2ze^2}{bv}$

there is a corresponding momentum transfer to primary particle that is losing energy. But here, most visible: deflection by target nuclei due to factor Z

$$\theta \simeq \frac{\Delta p_{\perp}}{p_{||}} \simeq \frac{\Delta p_{\perp}}{p}$$

$$= \frac{2Zze^2}{b} \frac{1}{pv}$$

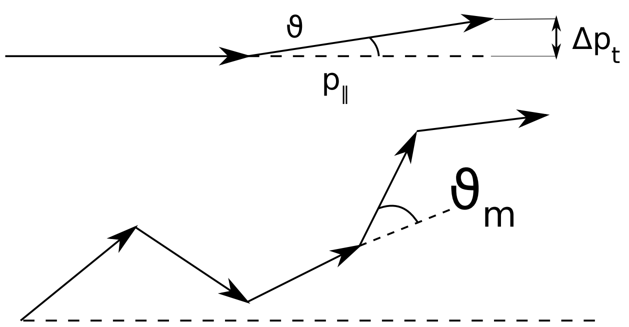

after k collisions

$$\langle \theta_k^2 \rangle = \sum_{m=1}^{k} \theta_m^2 = k \langle \theta^2 \rangle$$

for very thin absorber: single collision dominates, Rutherford scattering $d\sigma/d\Omega \propto \sin^{-4}\theta/2$
for a few collisions: difficult
for many collisions (> 20): statistical treatment 'Molière theory' *(G.Z. Molière 1947, 1948)*

Molière theory: averaging over many collisions and integration over b, angular distribution roughly Guassian
the rms deflection angle projected to a plane is

$$\sqrt{\langle\theta^2(x)\rangle} = \theta_{\text{rms}}^{\text{plane}} = \frac{13.6\ \text{MeV}}{\beta pc} z \sqrt{\frac{x}{X_0}}(1 + 0.038 \ln \frac{x}{X_0})$$

X_0: ‘radiation length’, material constant

$$\text{in 3D:} \qquad \theta_{\text{rms}}^{\text{space}} = \sqrt{2}\ \theta_{\text{rms}}^{\text{plane}} \qquad 13.6 \rightarrow 19.2$$

at small momenta this multiple scattering effect limits the momentum and vertex resolution

2.2 Interaction of photons with matter

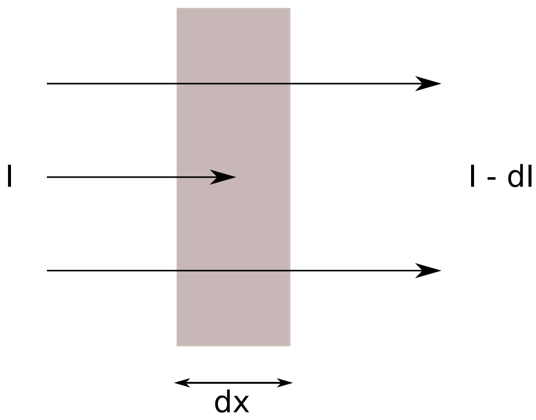

characteristic for photons: in a single interaction a photon can be removed out of beam with intensity I

$$\begin{aligned} \mathrm{d}I &= -I\mu \, \mathrm{d}x \\ \mu(E, Z, \rho) &\rightarrow \text{absorption coefficient} \end{aligned}$$

Lambert-Beer law of attenuation:

$$I = I_0 \exp -\mu x$$

- mean free path of photon in matter: $\lambda = 1/n\sigma = 1/\mu$

to become independent of state (gaseous, liquid) and reduce variations $\rightarrow$ introduce

$$\text{mass absorption coefficient} \quad \tau = \frac{\mu}{\rho} = N_A \frac{\sigma}{A}$$

example: $E_\gamma = 100$ keV, in iron $Z = 26$, $\lambda = 3$ g/cm^2 or 0.4 cm

3 processes, in order of growing importance with increasing photon energy E

- photo effect
- Compton scattering (incoherent off an electron)
- pair production (in nuclear field)

also present, but for energy loss not as important

- Rayleigh scattering (coherent, atom neither ionized nor excited) $\gamma + e_b \rightarrow \gamma + e_b$
- photo nuclear absorption $\gamma +$ nucleus $\rightarrow (p \text{ or } n) +$ nucleus
- pair production (in electron field)

Photo effect I

$$\gamma + \text{atom} \quad \rightarrow \quad \text{atom}^+ + e^-$$

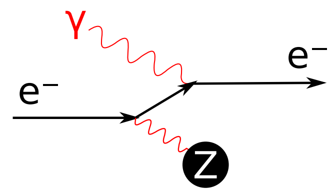

$E_e = h\nu - I_b$
$h\nu$: γ energy
I_b: binding energy of electron; K, L, M absorption edges
since binding energy strongly Z-dependent, strong Z-dependence of cross sections

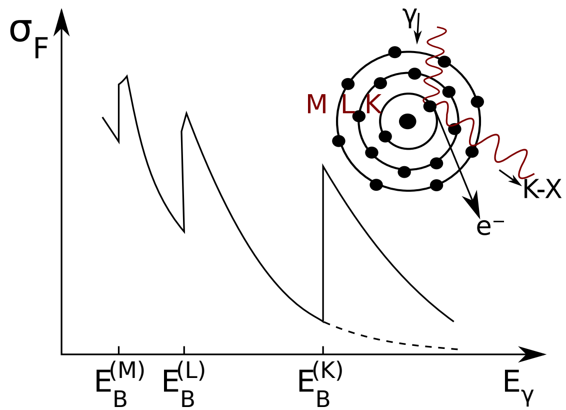

$$I \ll E_\gamma \ll mc^2 \qquad \sigma_{Ph} = \alpha\pi a_b Z^5 \left(\frac{I_0}{E_\gamma}\right)^{\frac{7}{2}}$$

$$a_b = 0.53 \cdot 10^{-10}\text{m} \qquad I_0 = 13.6 \text{ eV}$$

$$\text{for} \quad E_\gamma = 0.1 \text{ MeV}$$

$$\sigma_{\text{Ph}}(Fe) = 29 \text{ b}$$

$$\sigma_{\text{Ph}}(Pb) = 5 \text{ kb}$$

$$\text{for } E_\gamma \gg mc^2 \quad \sigma_{\text{Ph}} \propto \frac{Z^5}{E_\gamma}$$

Photo effect II

The excited atom emits either

$$\begin{aligned} \text{char. X-rays} \quad & \text{atom}_{\text{K}}^{+*} \rightarrow \text{atom}_{\text{LM}}^{+*} + \gamma \\ \text{or Auger electrons} \quad & \text{atom}_{\text{K}}^{+*} \rightarrow \text{atom}_{\text{LM}}^{++*} + e^{-} \end{aligned}$$

Auger electrons have small energy that is deposited locally
X-ray $\rightarrow$ photo effect again, range may be significant
this ‘fluorescence yield’ increases with Z.

Compton scattering

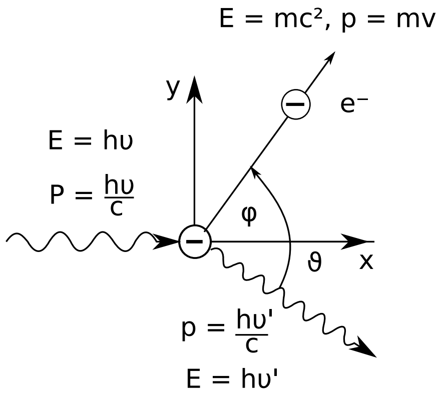

$$\frac{1}{E_{\gamma'}} - \frac{1}{E_\gamma} = \frac{1}{m_e c^2}(1-\cos\theta) \leq \frac{2}{m_e c^2}$$

recoil of electrons

$$T_e = \frac{\frac{E_\gamma}{m_e c^2}(1-\cos\theta)}{\frac{E_\gamma}{m_e c^2}(1-\cos\theta)+1} E_\gamma$$

$$\left(\frac{T_e}{E_\gamma}\right)_{\max} = \frac{E_\gamma}{m_e c^2}\frac{2}{1+\frac{2E_\gamma}{m_e c^2}}$$

$$\text{and} \quad \Delta E = E_\gamma - T_{e,max} = \frac{E_\gamma}{1+\frac{2E_\gamma}{m_e c^2}} \to \frac{m_e c^2}{2} \qquad \text{for } E_\gamma \gg m_e c^2$$

gives rise to 'Compton edge' in measured γ spectrum

Compton edge: in case scattered photon is not absorbed in detector, a minimal amount of energy is missing from the 'full energy peak' (asymptotically half electron rest mass)

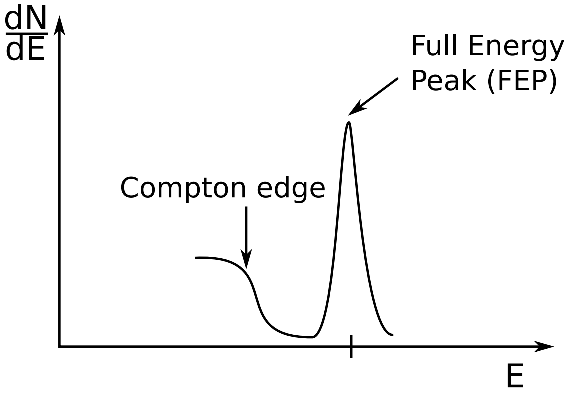

FEP = 'full energy peak':
photo effect and Compton effect with scattered photon absorbed
intensity depends on detector volume

Cross section: calculation in QED - *1929 O. Klein and Y. Nishina*

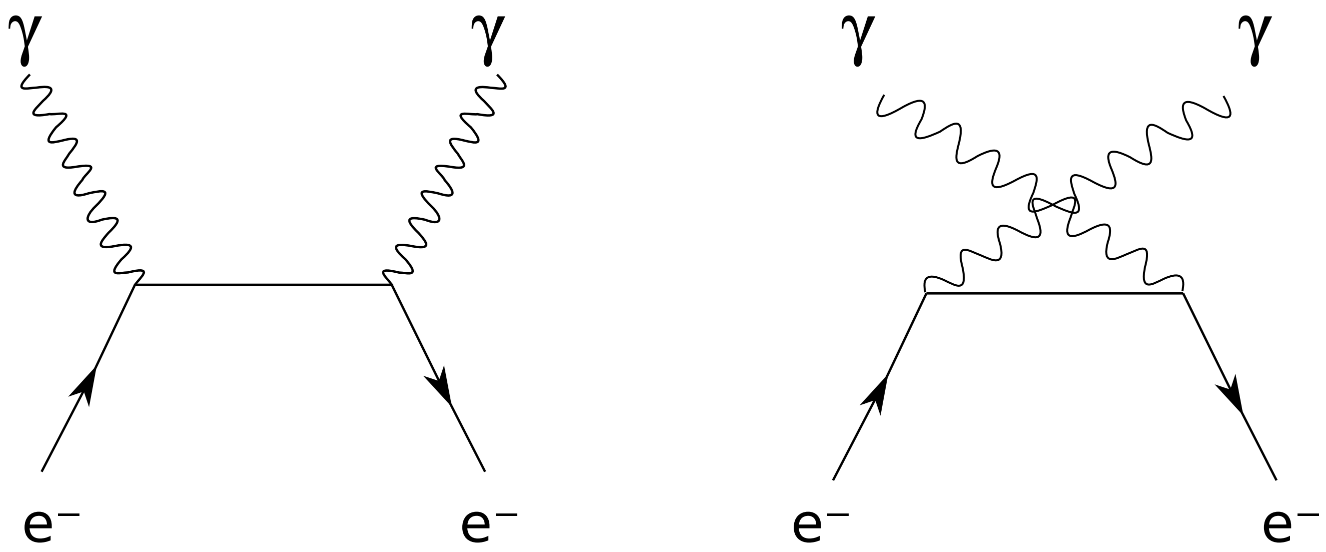

Klein-Nishina diagrams

- order of magnitude given by Thomson cross section

$$\sigma_{\mathrm{Th}} = \frac{8\pi}{3} r_e^2 = 0.66 \text{ b}$$

$$\gamma + e^- \to \gamma + e^- \qquad E_\gamma \to 0$$

Compton cross section

$$E_\gamma \ll m_e c^2 \qquad \sigma_c = \sigma_{\mathrm{Th}} \left(1 - 2\mathcal{E}\right)$$

$$E_\gamma \gg m_e c^2 \qquad \sigma_c = \frac{3}{8} \sigma_{\mathrm{Th}} \frac{1}{\mathcal{E}} \left(\ln 2\mathcal{E} + \frac{1}{2}\right)$$

with $\quad \mathcal{E} = \dfrac{E_\gamma}{m_e c^2}$

angular distribution from QED: Klein-Nishina formula

$$\frac{d\sigma_c}{d\Omega} = \frac{r_e^2}{2} \frac{1}{(1+\mathcal{E}(1-\cos\theta))^2} \left[1 + \cos\theta + \frac{\mathcal{E}^2(1-\cos\theta)^2}{1+\mathcal{E}(1-\cos\theta)}\right] \qquad \mathcal{E} = \frac{E_\gamma}{m_e c^2}$$

angular distribution of scattered photon for high γ-energies forward peaked

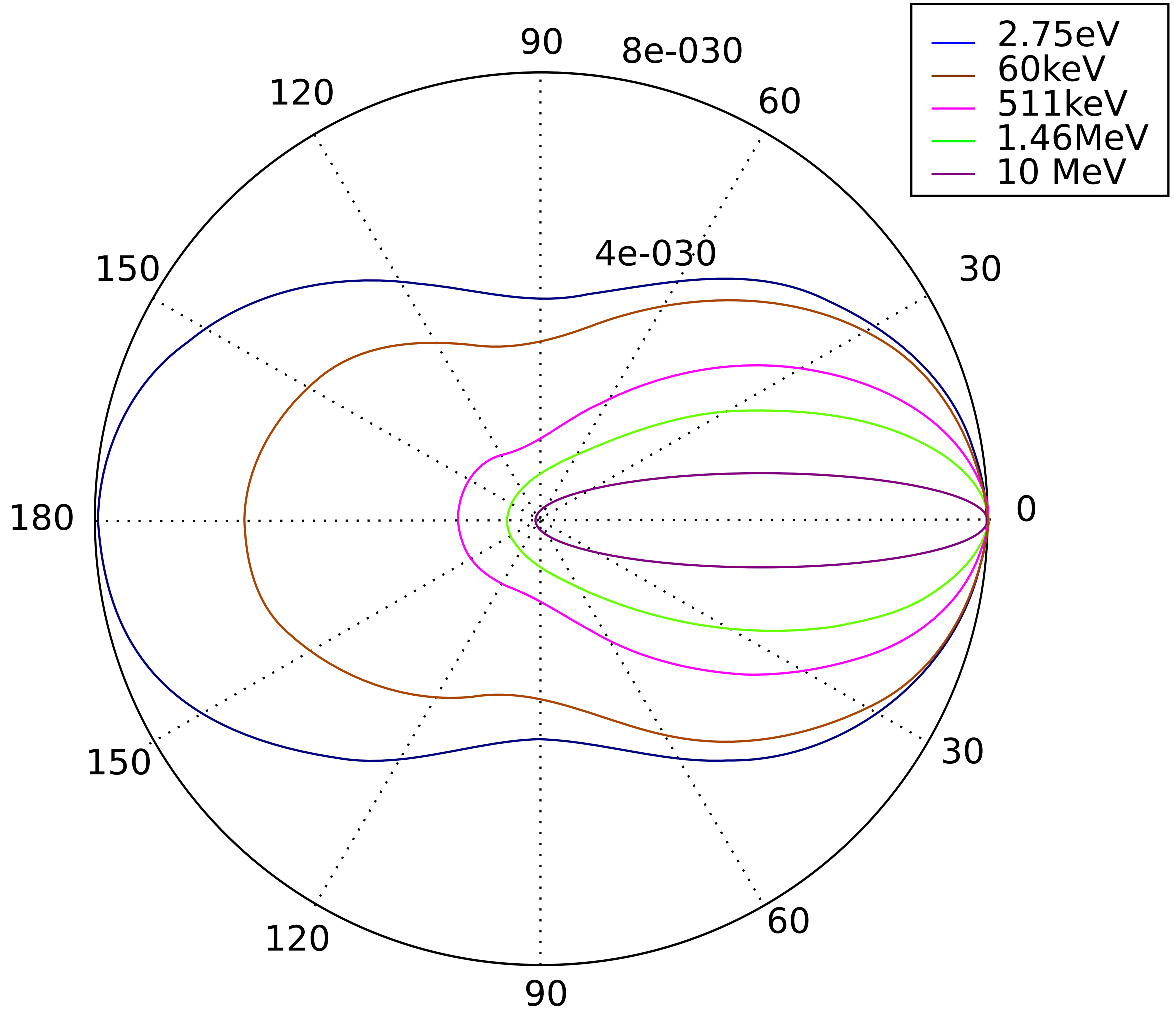

Spectrum of recoil electrons from Klein-Nishina formula after angular integration

$$\frac{d\sigma_c}{dT_e} = \frac{\pi r_e^2}{m_e c^2 \mathcal{E}^2}\left[2 + \frac{s^2}{\mathcal{E}(1-s)^2} + \frac{s}{1-s}\left(s - \frac{2}{\mathcal{E}}\right)\right]$$

$$\mathcal{E} = \frac{E_\gamma}{m_e c^2}$$

$$s = \frac{T_e}{E_\gamma}$$

$$T_e^{max} = E_\gamma\left(1 - \frac{m_e c^2}{2E_\gamma}\right) \qquad \text{for large } E_\gamma$$

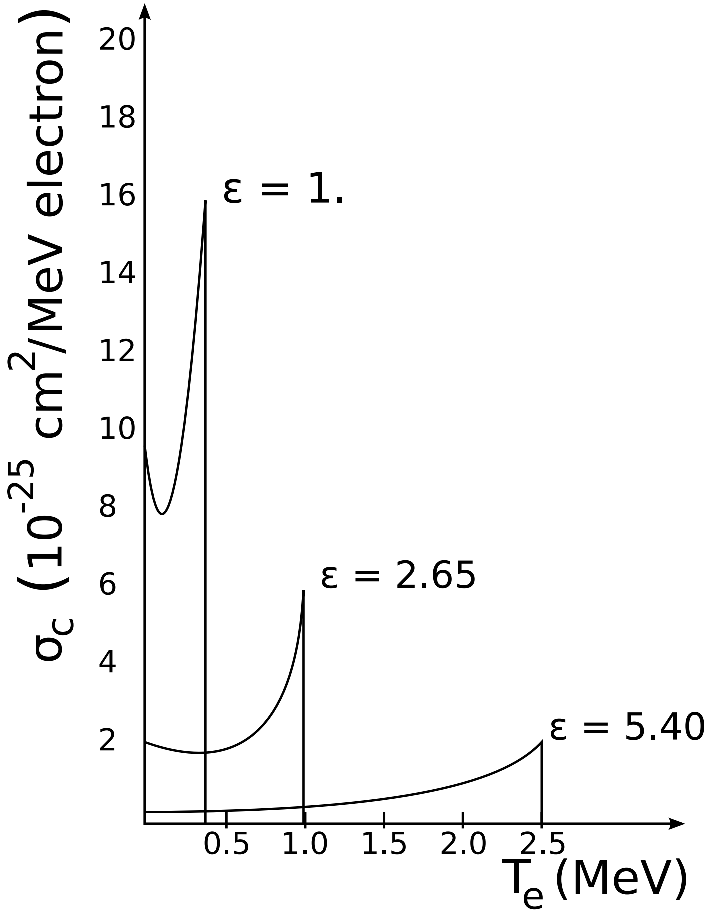

mass absorption coefficient $\frac{\mu_c}{\rho} = \frac{N_A}{A} Z\sigma_c \propto \frac{Z \ln E_\gamma}{E_\gamma}$

Pair production (Bethe-Heitler process) I

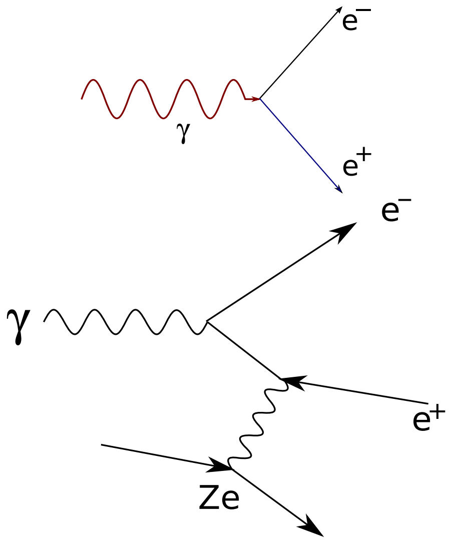

not possible in free space but in Coulomb field of atomic nucleus to absorb recoil

energy threshold

$$E_\gamma \geq 2m_e c^2 + 2\frac{m_e^2 c^4}{m_K c^2}$$

Cross section: for low energies, impact parameters small, photon sees 'naked' nucleus
with increasing E_γ, range of impact parameter b is growing up to $b \geq a_{\text{atom}}$, complete screening $\rightarrow$
saturation of cross section for $E_\gamma \gg m_e c^2$

$$\sigma_{\text{pair}} = 4Z^2\alpha r_e^2 \left(\frac{7}{9}\ln\frac{183}{Z^{1/3}} - \frac{1}{54}\right) \simeq \frac{7}{9}\underbrace{4\alpha r_e^2 Z^2 \ln\frac{183}{Z^{1/3}}}_{(A/N_A)X_0}$$

X_0: 'radiation length' (g/cm^2), to obtain length (cm): $\rho\, X_0$

mass absorption coeff. $\quad \frac{\mu_\text{p}}{\rho} = \frac{N_A}{A}\sigma_p \simeq \frac{7}{9}\frac{1}{X_0}$

Pair production (Bethe-Heitler process) II

	ρ (g/cm^3)	X_0 (cm)
liq H_2	0.071	865
C	2.27	18.8
Fe	7.87	1.76
Pb	11.35	0.56
air	0.0012	30 420

the angular distribution of produced electrons is narrow in forward cone with opening angle of $\theta = m_e/E_\gamma$

definition of radiation length X_0 in terms of energy loss of electron by bremsstrahlung see below

Fractional electron (or positron) energy x

$x = E/k =$ electron energy/photon energy
cross section necessarily symmetric between x and $(1-x)$

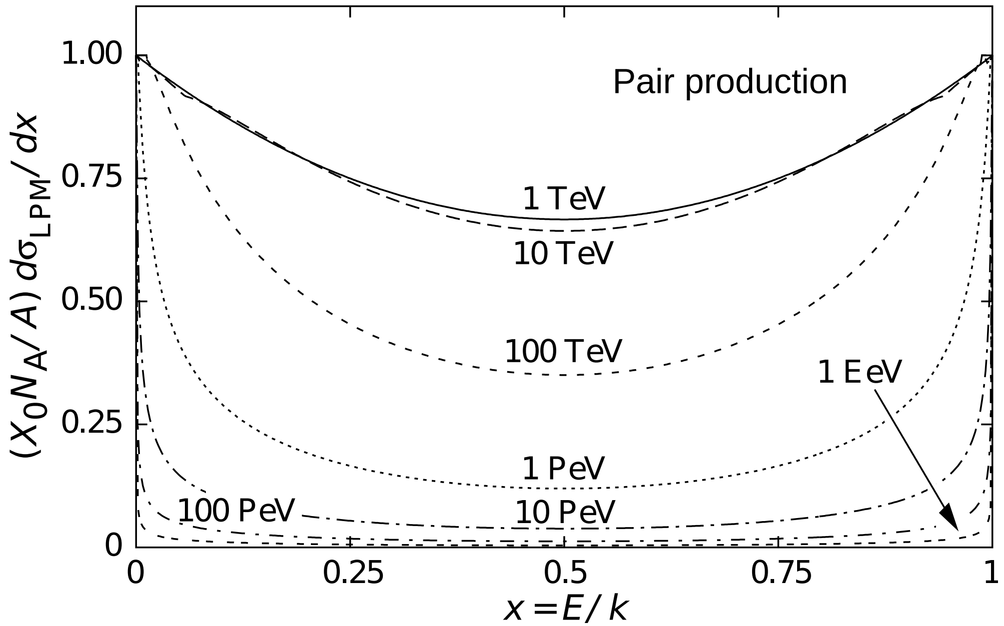

at ultrahigh energies new effect - **Landau Pomeranchuk Migdal effect**: quantum mechanical interference between amplitudes from different scattering centers; relevant scale **formation length** - length over which highly relativistic electron and photon split apart.

interference (generally) destructive $\rightarrow$ reduced cross section for a given, very high photon energy k: if electron (or positron) energy are above some value given by

$E(k-E) > kE_{\text{LPM}} \Rightarrow$ effect visible, cross section reduced

$E_{\text{LPM}} = 7.7\, X_0$ TeV/cm

e.g. for Pb $E_{\text{LPM}} = 4.3$ TeV
take $k = 100$ TeV, suppression for $E > 4.5$ TeV or $x = 0.045$
(see also bremsstrahlung below)

Total absorption coefficient

$$\sigma_{tot} = \sigma_{Ph} + \sigma_c + \sigma_p$$
$$\mu = \mu_{Ph} + \mu_c + \mu_p$$
$$\mu_i = n\sigma_i = \frac{N_A\rho}{A}\sigma_i$$

photon total cross sections as a function of energy in carbon and lead

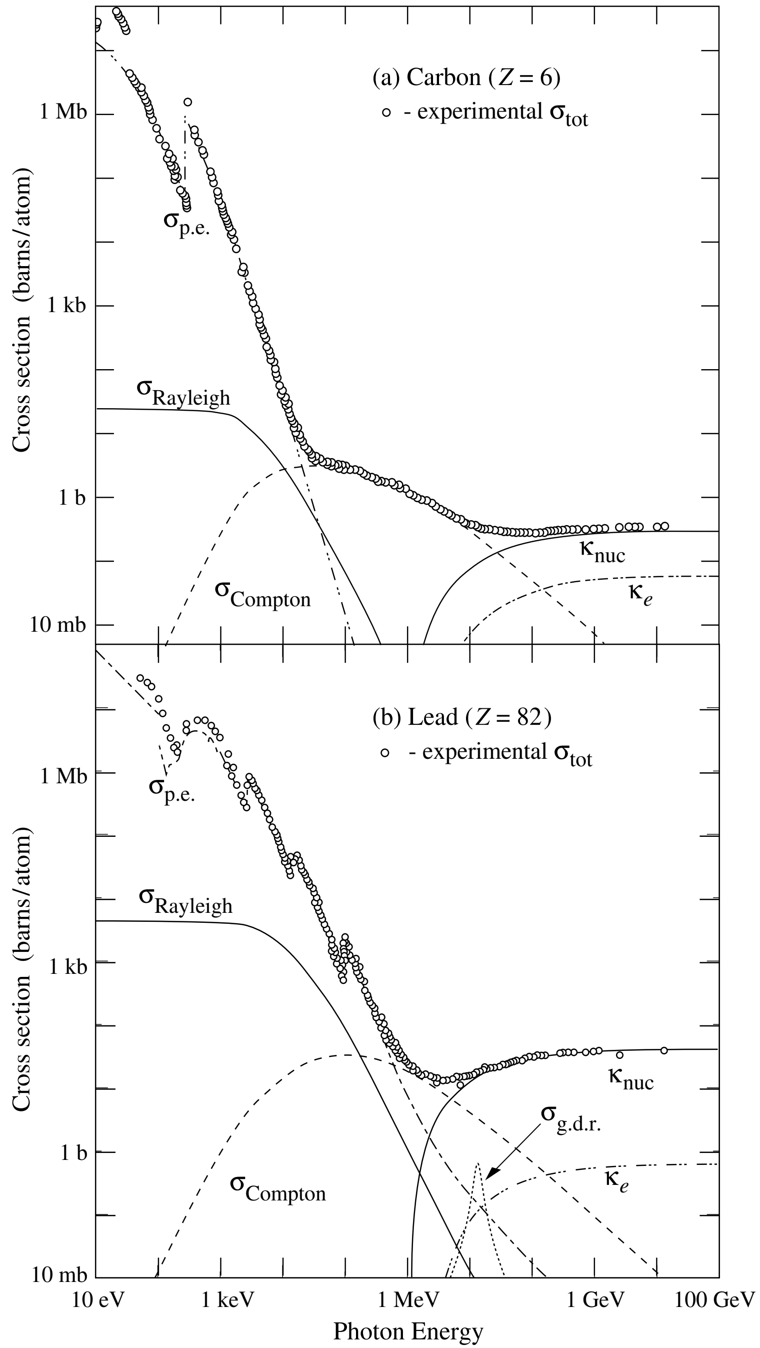

The photon mass attenuation length λ

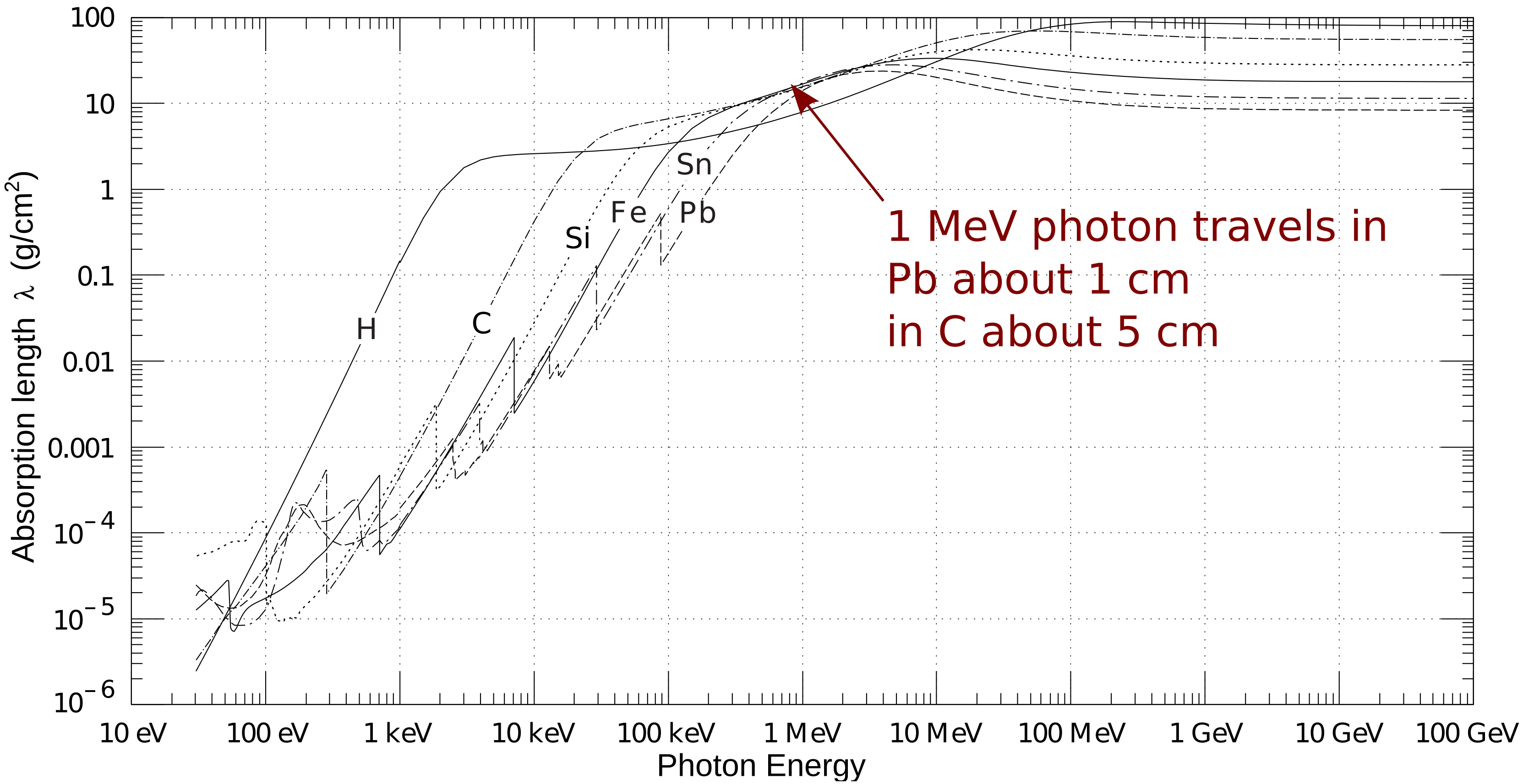

The photon mass attenuation length (or mean free path) $\lambda = \rho/\mu$ for various elemental absorbers as a function of photon energy. The mass attenuation coefficient is μ/ρ, where ρ is the density. The intensity I remaining after traversal of thickness t (in mass/unit area) is given by $I = I_0 \exp -t/\lambda$. The accuracy is a few percent. For a chemical compound or mixture, $1/\lambda_{\text{eff}} \approx \sum_{\text{elements}} w_Z/\lambda_Z$, where w_Z is the proportion by weight of the element with atomic number Z. Since coherent processes are included, not all processes result in energy deposition.

with increasing photon energy pair creation becomes dominant

for Pb beyond 4 MeV
for H beyond 70 MeV

Probability P that a photon interaction will result in conversion to an e^+e^- pair. Except for a few-percent contribution from photonuclear absorption around 10 or 20 MeV, essentially all other interactions in this energy range result from Compton scattering off an atomic electron. For a photon attenuation length λ, the probability that a given photon will produce an electron pair (without first Compton scattering) in thickness t of absorber is $P[1 - \exp(-t/\lambda)]$

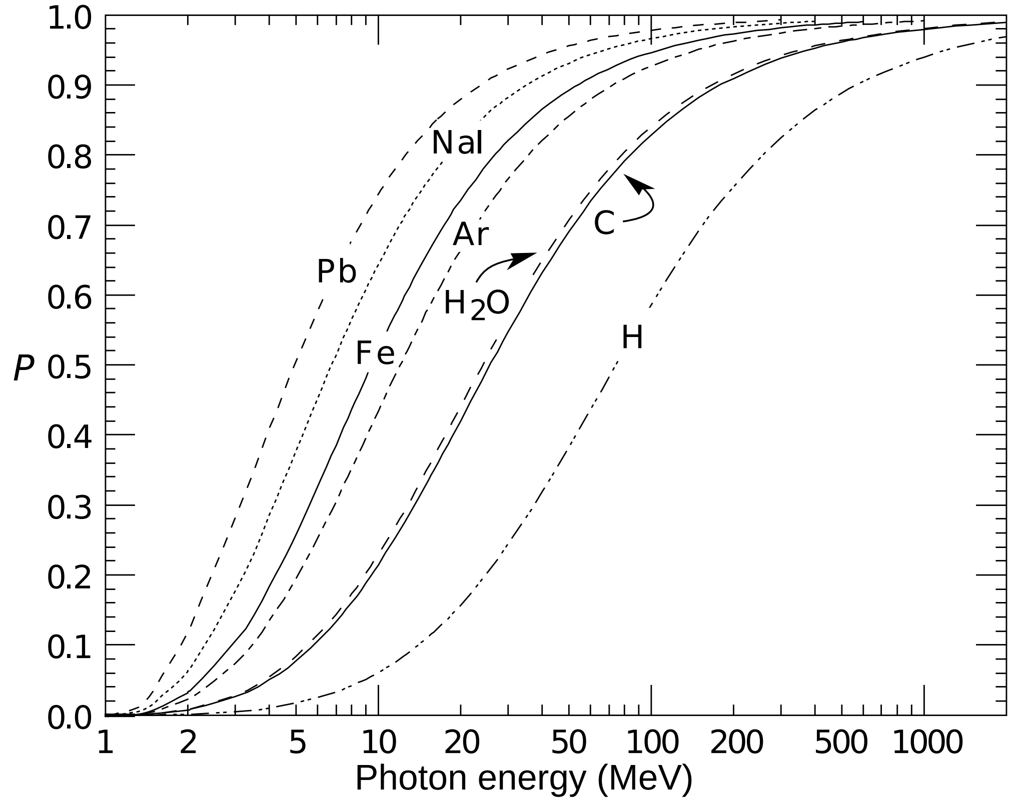

2.3 Interaction of electrons
Energy loss by ionization

Modification of **Bethe-Bloch equation**

m_e small $\rightarrow$ deflection important

identical particles $\rightarrow W_{max} = T/2$

quantum mechanics: after scattering, no way to distinguish between incident electron and electron from ionization.

$\rightarrow$ for relativistic electrons

$$-\frac{\mathrm{d}E}{\mathrm{d}x} = 4\pi N_A r_e^2 m_e c^2 \frac{Z}{A}\frac{1}{\beta^2}\left[\ln \frac{\gamma m_e c^2 \beta \sqrt{\gamma - 1}}{\sqrt{2}I} + F(\gamma)\right]$$

considers kinematics of $e^- + e^-$ collision and screening

positrons: for small energies energy loss a bit larger (annihilation)

also: they are not identical particles

remark: for same β the energy loss by ionization for e^- and p equal within 10%

Ionization yield (also valid for heavy particles)

Mean energy loss by ionization and excitation can be transformed into mean number of electron-ion pairs produced along track of ionizing particle
total ionization = primary ionization + secondary ionization due to energetic primary electron

$$n_t = n_p + n_s$$

mean energy W to produce an electron-ion pair

$$n_t = \frac{\Delta E}{W}$$

$W >$ ionization potential I_0 since

- also ionization of inner shells
- excitation that may not lead to ionization

$$n_t \approx (2-6)n_p$$

typical values

	I_0 (eV)	W (eV)	n_p (cm^{-1})	n_t (cm^{-1})
H_2	15.4	37	5.2	9.2
N_2	15.5	35	10	56
0_2	12.2	31	22	73
Ne	21.6	36	12	39
Ar	15.8	26	29	94
Kr	14.0	24	22	192
Xe	12.1	22	44	307
CO_2	13.7	33	34	91
CH_4	13.1	28	16	53
		in gases $\approx$ 30 eV	diff. due to ρ and Z	diff. due to electronic struct.

Solid state detectors:

	W (eV)	
Si	3.6	additional factor 10^3 due to density
Ge	2.85	$\rightarrow$ many more electron ion pairs!

Lateral straggeling

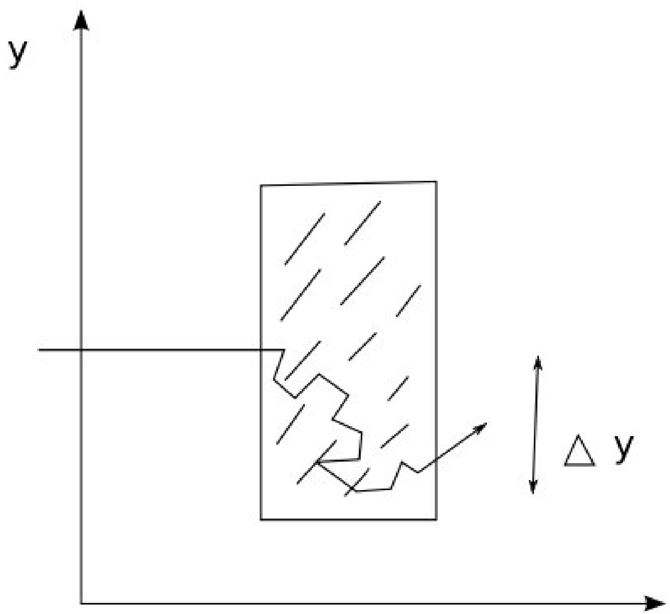

Important difference: electron - heavy particle
heavy particle: track more or less straight
electron: can be scattered into large angles
pathlength $\gg$ range

transverse deflection of an electron of energy $E = E_c$ (see below) after traversing distance X_0 (one radiation length)

$$\Delta y = R_M = \frac{21\ \text{MeV}}{E_c} X_0 \qquad \text{'Molière radius'}$$

	E_c (MeV)	R_M (cm)	X_0 (cm)
Pb	7.2	1.6	0.56
scint.	80	9.1	42
NaI	12.5	4.4	2.6

Consequence of lateral straggeling:
range of electrons much more diffuse in comparison to protons

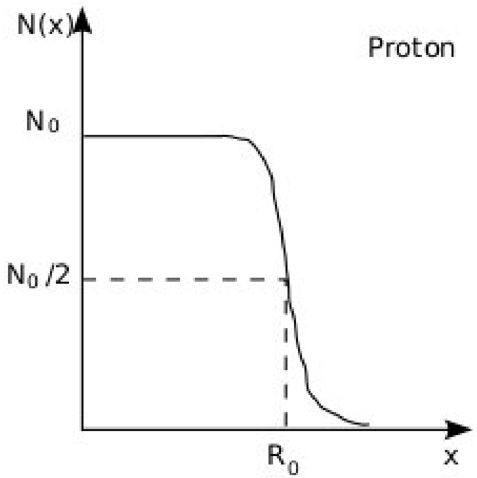

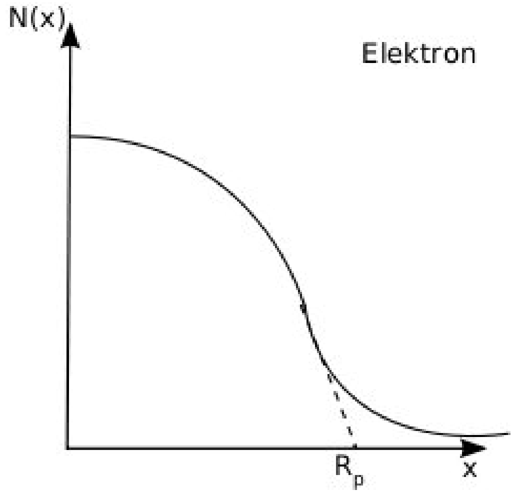

R_p: extrapolated range
rule of thumb: $R_p\left(\frac{\mathrm{g}}{\mathrm{cm}^2}\right) = 0.52\ T - 0.09 \quad$ for $\quad T = 0.5 - 3$ MeV

2.4 Bremsstrahlung

QED process (Fermi 1924, Weizsäcker-Williams 1938)

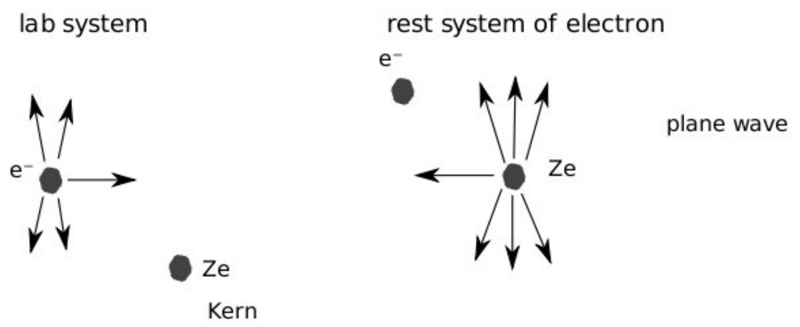

electron is hit by plane electromagnetic wave (for large v)
$E \perp B$ and both $\perp v$; quanta are scattered by electron and appear as real photons

note: graph closely related to pair creation

in Coulomb field of nucleus electron is accelerated
amplitude of electromagnetic radiation $\propto$ acceleration $\propto 1/m_e c^2$

$$\sigma_{\text{brems}} \propto \frac{Z^2\alpha^3}{(m_e c^2)^2}$$

spectrum of photons $\propto \frac{1}{k}$, approximately

$$\frac{d\sigma}{dk} \simeq \frac{A}{X_0 N_A}\frac{1}{k}\left(\frac{4}{3} - \frac{4}{3}y + y^2\right)$$

with $y = k/E$ (corrections later)
$\rightarrow$ normalized bremsstrahlung cross section (in number of photons per radiation length)

$$N_k = \frac{X_0 N_A}{A} k \frac{d\sigma}{dk} = \left(\frac{4}{3} - \frac{4}{3}y + y^2\right)$$

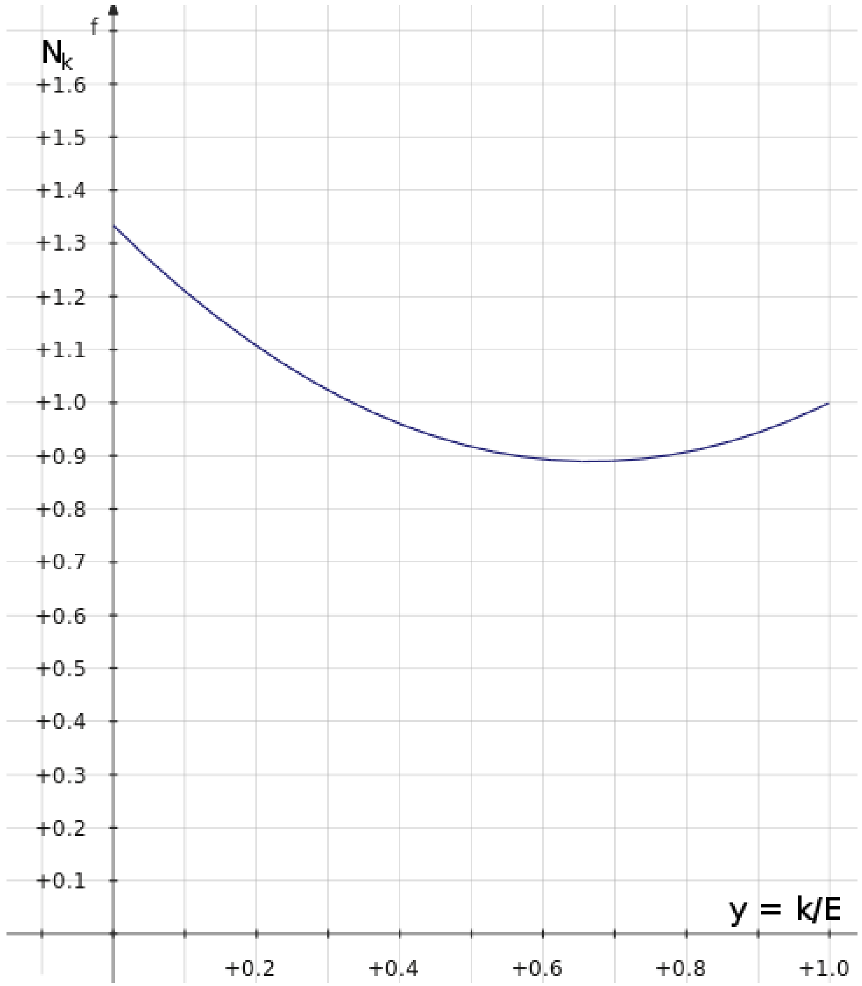

from this compute N_γ in interval $\mathrm{d}k$ and from this energy loss

$$-\frac{\mathrm{d}E}{\mathrm{d}x} = 4\alpha N_A \frac{Z^2}{A} r_e^2 E \ln \frac{183}{Z^{\frac{1}{3}}}$$

remark:

$$r_e^2 = \frac{e^4}{(m_e c^2)^2} = \alpha^2 \left(\frac{\hbar c}{m_e c^2}\right)^2 \leftrightarrow -\frac{\mathrm{d}E}{\mathrm{d}x} \propto \frac{\alpha^3}{(m_e c^2)^2}$$

considering also interaction with electrons in atom

$$-\frac{\mathrm{d}E}{\mathrm{d}x} = 4\alpha N_A \frac{Z(Z+1)}{A} r_e^2 E \ln \frac{287}{Z^{\frac{1}{2}}} = \frac{E}{X_0}$$

so $E(x) = E_0 \exp(-x/X_0)$

$\Rightarrow$ X_0 **is distance over which energy decreases to** $1/e$ **of initial value**

for mixtures:

$$\frac{1}{X_0} = \sum_i \frac{w_i}{X_{0i}} \qquad w_i \text{ weight fraction of substance } i$$

Critical energy

$$-\frac{\mathrm{d}E}{\mathrm{d}x} \quad \text{by ionization} \quad \propto \ln E$$

$$-\frac{\mathrm{d}E}{\mathrm{d}x} \quad \text{by bremsstrahlung} \quad \propto E$$

$\rightarrow$ existence of crossing point beyond which bremsstrahlung dominates

at critical energy E_c $\quad \left(\frac{\mathrm{d}E}{\mathrm{d}x}\right)_{\text{ion}} = \left(\frac{\mathrm{d}E}{\mathrm{d}x}\right)_{\text{brems}}$

for electrons and $Z > 13$ $\quad E_c = \frac{580}{Z}$ MeV

for muons negligible $\quad E_c = \frac{24}{Z}$ TeV $\quad$ due to $\left(\frac{m_\mu}{m_e}\right)^2 = 4.3 \cdot 10^4$

Critical energy for electrons in Cu

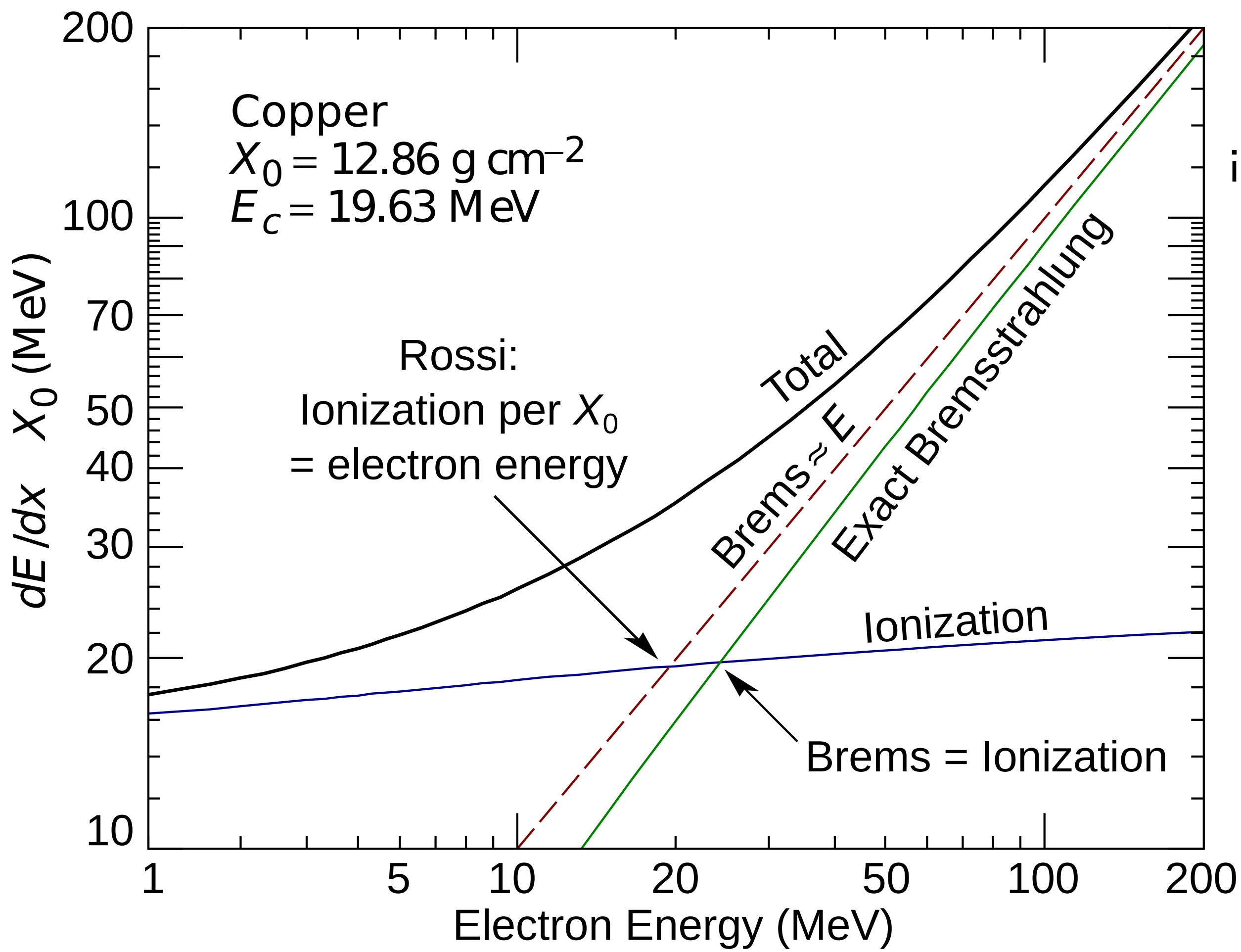

in the literature alternative definitions

- energy at which loss rates of ionization and bremsstrahlung equal
- energy at which ionization energy loss per rad. length is equal to electron energy (Rossi) (equivalent for approximation $\left.\frac{dE}{dx}\right|_{\text{brems}} = \frac{E}{X_0}$) good for transverse em shower description

Total energy loss of electrons and positrons

at small energies also

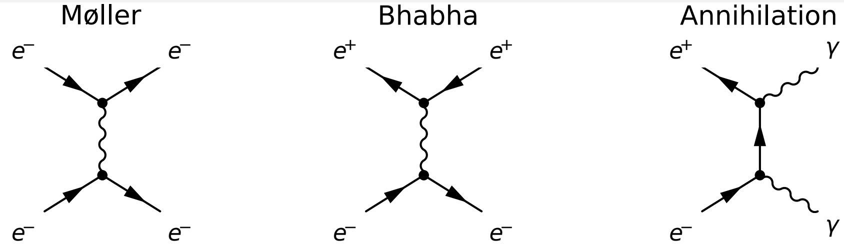

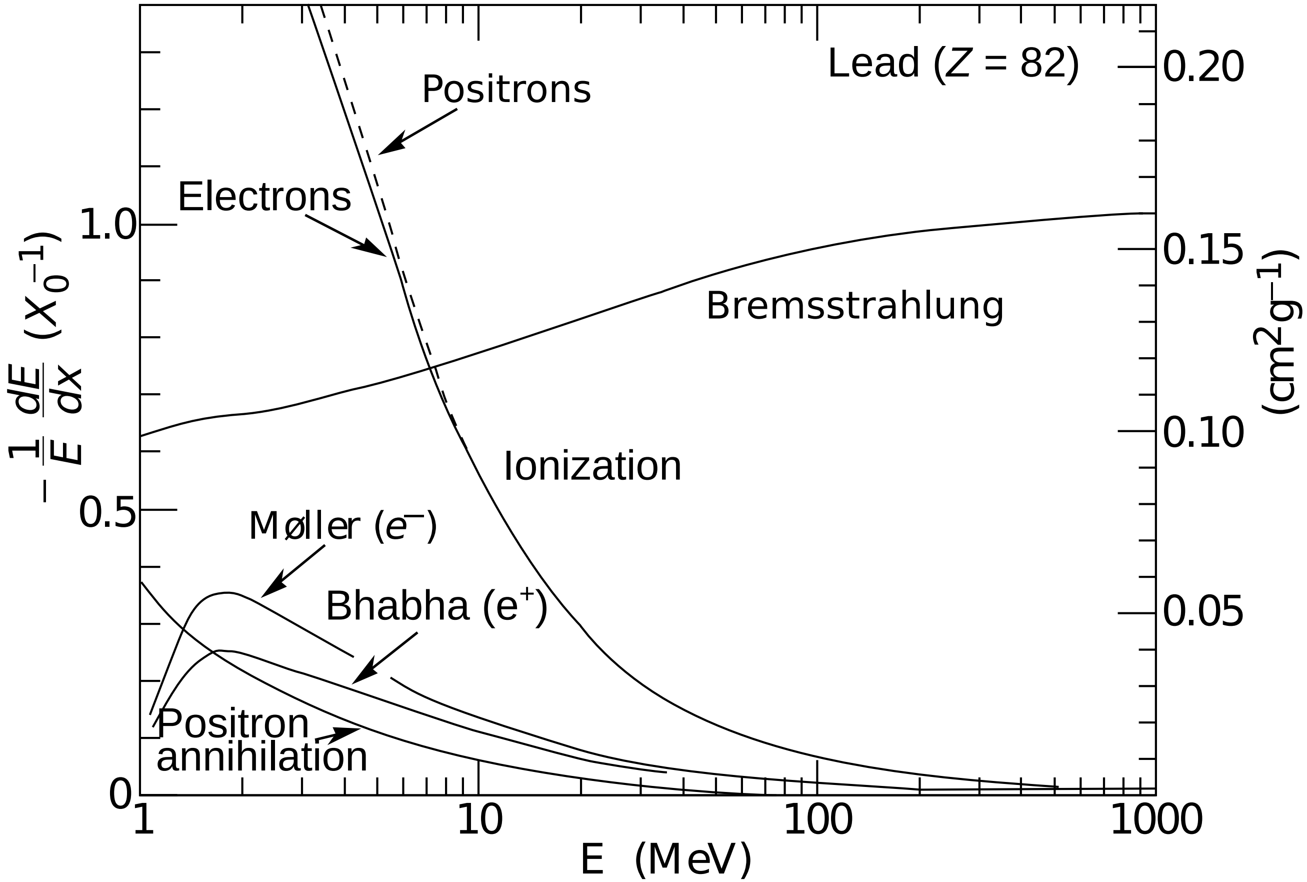

fractional energy loss per radiation length in lead as a function of electron or positron energy; electron (positron) scattering is considered as ionization, when the energy loss per collision is below 0.255 MeV, and as Møller (Bhabha) scattering, when it is above.

Quantum-mechanical suppression of bremsstrahlung I

normalized bremsstrahlung cross section:

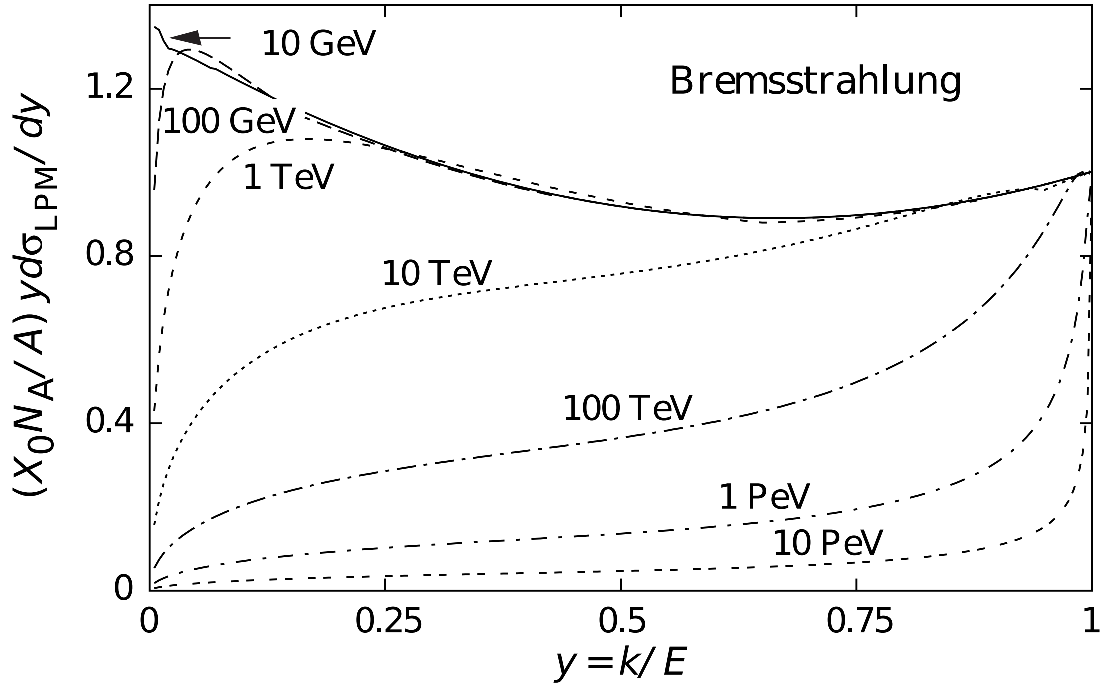

normalized bremsstrahlung cross section $k\,\mathrm{d}\sigma_{\mathrm{LPM}}/\mathrm{d}k$ in lead versus the fractional photon energy $y = k/E$. The vertical axis has units of photons per radiation length.

for small photon energies: again LPM effect important, successive radiations interfere.
radiation spread over formation length and if distance between successive radiations comparable to formation length $\rightarrow$ destructive interference

for Pb and electron of 10 GeV suppression for $k < 23$ MeV
for Pb and electron of 100 GeV suppression for $k < 2.3$ GeV Important for very high energies,

Quantum-mechanical suppression of bremsstrahlung II

e.g. air showers of cosmic ray interactions

- in bremsstrahlung process nucleus absorbs longitudinal momentum

$$c|\vec{q}_{||}| \simeq c|\vec{p}_e| - c|\vec{p}_e{}'| - c|\vec{p}_\gamma| \simeq \frac{E_\gamma}{2\gamma^2}$$

- corresponding to uncertainty principle momentum transferred over finite length scale (formation length)

$$L_F = \frac{\hbar c}{q_{||}c} = \frac{2\gamma^2 \hbar c}{E_\gamma}$$

$$\text{e.g. } E = 25\text{ GeV} \quad E_\gamma = 100\text{ MeV} \quad q_{||} = 20\,\frac{\text{meV}}{\text{c}} \rightarrow L_F = 10\ \mu\text{m}$$

Semi-classically: photon emission and exchange of photon with nucleus take place over length L_F
Alternative: quantum transport approach

Quantum-mechanical suppression of bremsstrahlung III

Semi-classically: photon emission and exchange of photon with nucleus take place over length L_F *but only* if electron and photon remain coherent over this length.
Destruction of coherence via

a) Landau-Pomeranchuk-Migdal effect: decoherence by multiple scattering when

$$\sqrt{\theta_{ms}^2} = \frac{21\text{MeV}}{E}\sqrt{\frac{L_F}{X_0}} \geq \theta_\gamma = \frac{m}{E} = \frac{1}{\gamma}$$

for $E = 25$ GeV and Au target, suppression for $E_\gamma \leq 10$ MeV

b) dielectric effect
phase shift of photons by coherent forward scattering off the electrons in material; strong suppression for

$$E_\gamma \leq \gamma\hbar\omega_p \quad \text{or} \quad \frac{E_\gamma}{E} \leq 10^{-4}$$

c) at large y screening may be incomplete

consequence of a-b: at very high photon and electron energies: strong suppression of bremsstrahlung and pair production
dominance of photonuclear and electronuclear interactions of em interactions

2.5 Cherenkov effect

Particle of mass M and velocity $\beta = v/c$ propagates through medium with real part of dielectric constant

$$\epsilon_1 = n^2 = \frac{c^2}{c_m^2}$$

in case

$$\beta > \beta_{\text{thr}} = \frac{1}{n} \text{ or } v > c_m$$

real photons can be emitted with

$$\begin{aligned} |p| &\simeq |p'| \\ \omega &\ll \gamma M c^2 \end{aligned}$$

emission under angle

$$\cos\theta_c = \frac{\omega}{k \cdot v} = \frac{1}{n\beta}$$

Cherenkov 1934

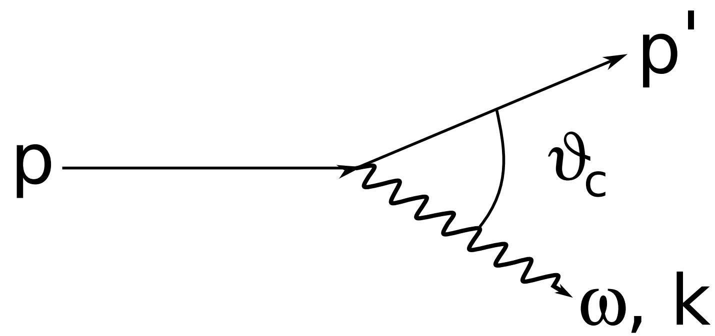

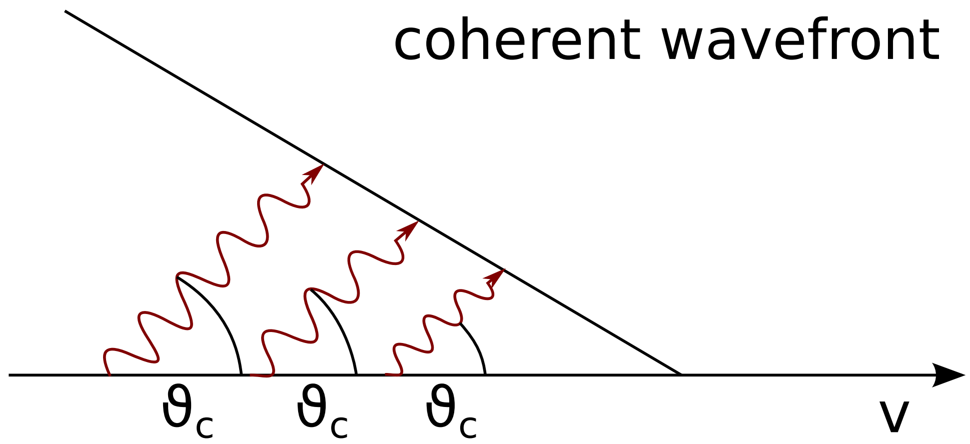

Applications

a) threshold detector: principle - if Cherenkov radiation observed $\Rightarrow \beta > \beta_{\text{thr}}$
e.g. separation of $\pi/\text{K}/\text{p}$ of given momentum p

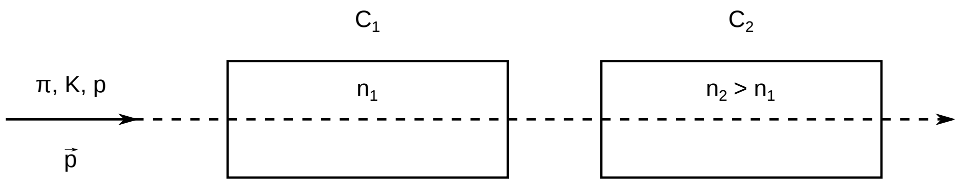

choose $\begin{matrix} n_2 \\ n_1 \end{matrix}$ such that $\begin{matrix} \beta_\pi, \beta_K > \frac{1}{n_2} & \beta_p < \frac{1}{n_2} \\ \beta_\pi > \frac{1}{n_1} & \beta_k, \beta_p < \frac{1}{n_1} \end{matrix}$

light in C_1 and C_2: π
light in C_1 and not in C_2: K
no light in C_1 and C_2: p

b) measurement of θ_c in medium with known $n \Rightarrow \beta$
(RICH, DIRC, DISC detectors)

Spectrum and number of radiated photons

over range in ω where $\epsilon_1 > \frac{1}{\beta^2}$

$$dN_\gamma \propto d\nu = \frac{d\lambda}{\lambda^2}$$ blue dominated

for distance x and frequency interval $d\nu$:

$$N_\gamma = x \underbrace{\frac{\alpha}{\hbar c}}_{370/\text{eV}\cdot\text{cm}} \int_{\omega_1}^{\omega_2} \underbrace{(1 - \frac{1}{\beta^2 n^2(\omega)})}_{\sin^2\theta_c} \hbar d\omega$$

for interval $d\omega$, where $n(\omega)$ varies not much, e.g. gases around visible wavelengths:

300 nm $< \lambda <$ 600 nm: $N_\gamma = 750 \sin^2\theta_c$ /cm

	$(n-1)$	$(\beta\gamma)_{thr}$	θ_c^∞(deg)	$N_\gamma^\infty(cm^{-1})$
H_2	$0.14 \cdot 10^{-3}$	59.8	0.96	0.21
N_2	$0.3 \cdot 10^{-3}$	40.8	1.4	0.45
Freon 13	$0.72 \cdot 10^{-3}$	26.3	2.2	1.1
H_2O	0.33	1.13	41.2	165
lucite	0.49	0.91	47.8	412

typical photon energy: $\simeq 3$ eV

in water $\left.\frac{dE}{dx}\right|_{\text{cher}} = 0.5$ keV/cm $= 0.5$ keV/g/cm^2

cf. ionization $\left.\frac{dE}{dx}\right|_{\text{ion}} \geq 2$ MeV/g/cm^2

$\rightarrow$ energy loss by Cherenkov radiation negligible

danger: emission of scintillation light by excited atoms can fake Cherenkov radiation!

measurement of β via ring radius requires minimum number of detected photo electrons

$$n_e = N_\gamma \cdot \epsilon_{\text{lightcoll}} \cdot \eta \simeq N_\gamma \cdot 0.8 \cdot \text{ quantum efficiency } \simeq 20\%\, N_\gamma$$

example: require for reconstruction of ring in RICH $n_e \geq 4$ and efficiency should be 90%
n_e follows Poisson distribution
for a given $\langle n_e \rangle$ P(4) + P(5) + P(6) + ... ≥ 0.9

$$\begin{aligned} P_n &= \frac{\langle n_e \rangle^n \exp - \langle n_e \rangle}{n!} \qquad \text{Poisson} \\ \text{with} \langle n_e \rangle &= 7 \\ \sum_0^3 P_n &= 7.9\% \qquad \text{efficiency for } n \geq 4: \; 92.1\% \end{aligned}$$

need about 35-45 Cherenkov photons $\rightarrow$ about 0.5 m freon

Asymptotic Cherenkov angle and number of photons as function of momentum

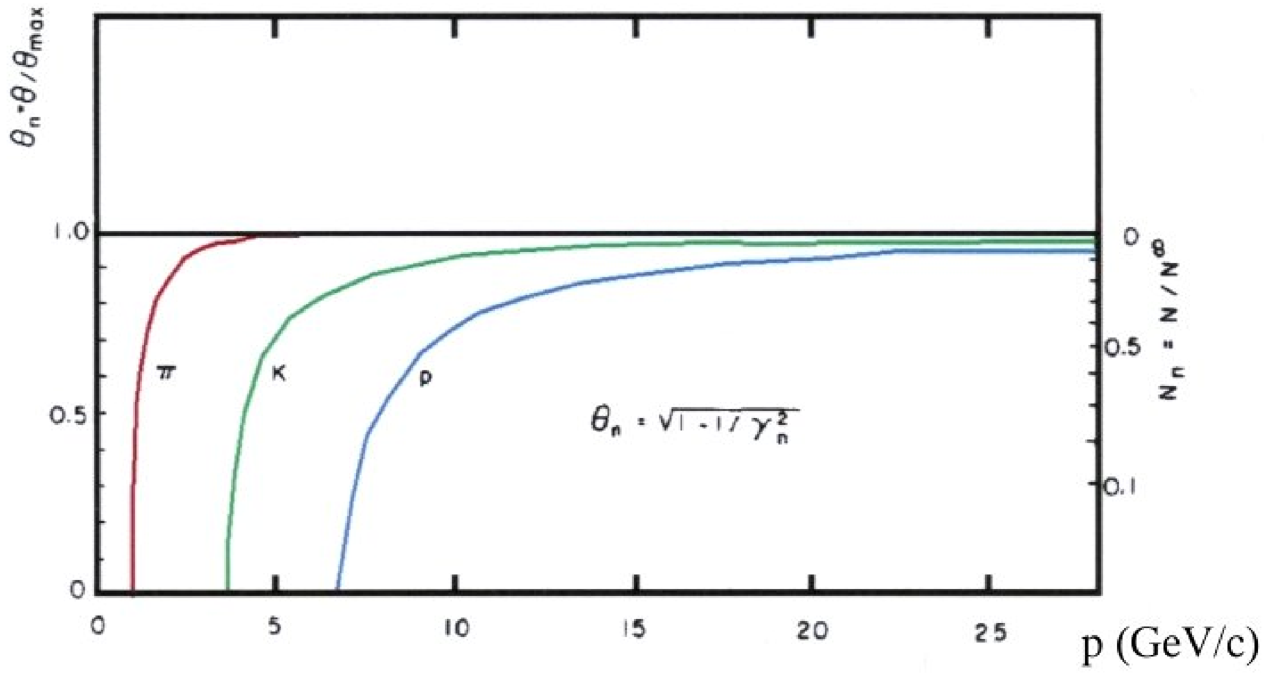

number of photons grows with β and reaches asymptotic value for $\beta \to 1$

$$\cos\theta_c^\infty = \frac{1}{n} \quad \text{or} \quad \theta_c^\infty = \arccos\frac{1}{n}$$

$$N_\gamma = x \cdot 370/\text{cm}\left(1 - \frac{1}{\beta^2 n^2}\right) \qquad \text{for a photon energy interval of 1 eV}$$

$$N_\gamma^\infty = x \cdot 370/\text{cm}\left(1 - \frac{1}{n^2}\right) \qquad \text{"}$$

Use of Cherenkov light for neutrino detection

electron neutrinos: charged current events
all neutrinos: neutral current
leading to final state neutrino and energetic electron detected by Cherenkov radiation (typically $E > 5$ MeV to be above background from natural radioactivity)

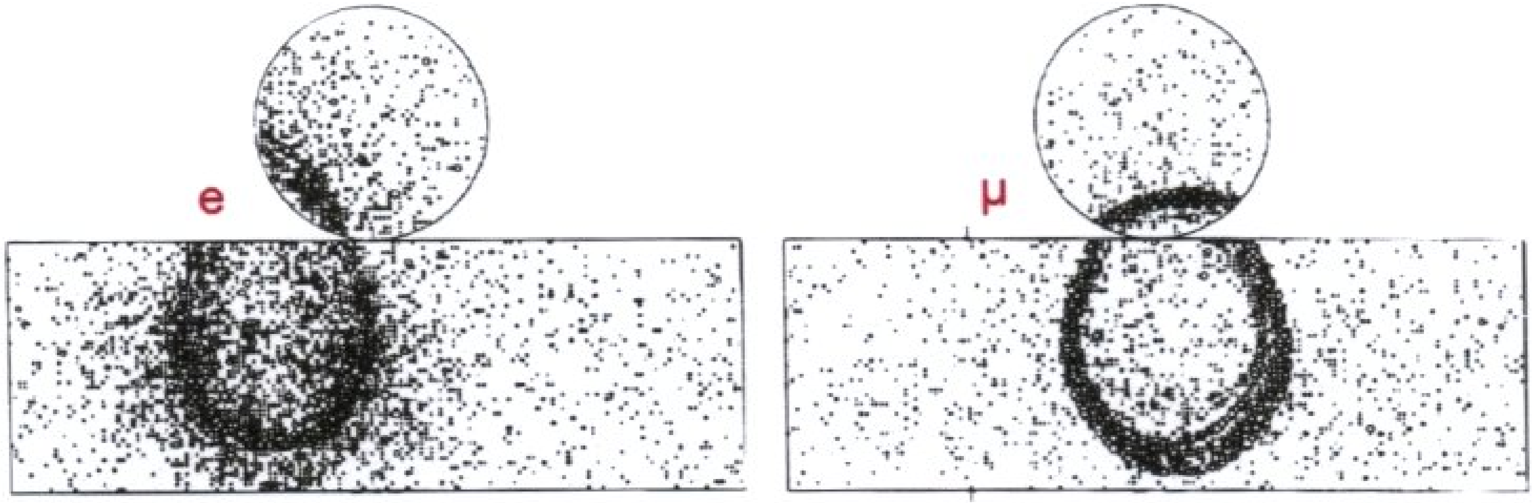

electron and muon Cherenkov rings

electron ring becomes diffuse due to multiple scattering of electron
allows to distinguish electron from muon, important for neutrino detectors (Superkamiokande, SNO)

2.6 Transition radiation

a relativistic particle can emit a real photon when traversing the boundary between 2 different dielectrics
predicted: Ginzburg and Frank 1946; confirmed in 1970ies

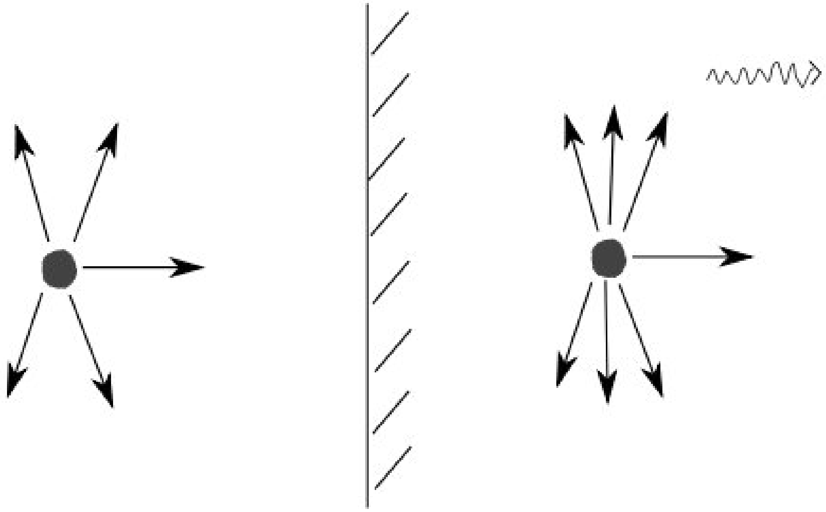

electric field needs to rearrange

simple model: electron moves in vacuum towards a conducting plate, the E-field can be described by method of mirror charges

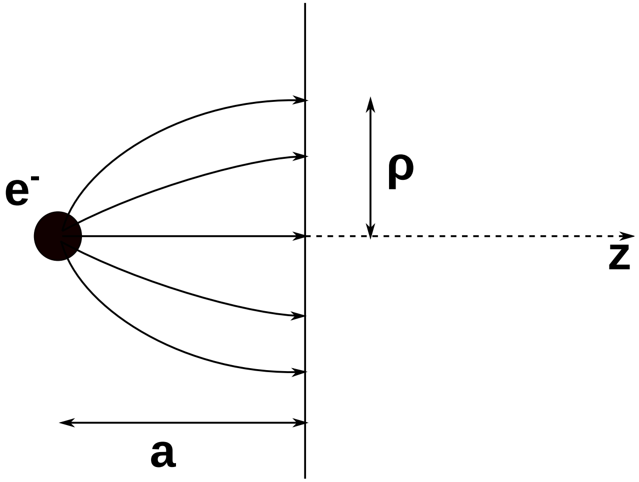

normal component at metal surface

$$|\vec{E}_n| = \frac{a \cdot e}{(a^2 + \varrho^2)^{\frac{3}{2}}}$$

can be generated (Gedankenexperiment) by a dipole $\vec{p} = 2e\vec{a}$

Radiation:
annihilation of dipole as particle enters the metal

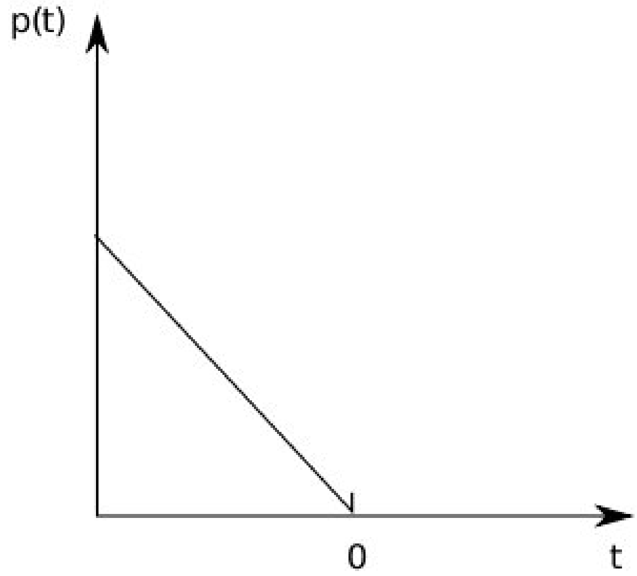

within classical electrodynamics one can show how E-field varies in point $\vec{r}' = (\varrho', z')$
leading to time dependent polarization

at $t = 0$ particle is at origin, it propagates in z-direction, consider radiation in k-direction.

$$E_z = \frac{e\gamma(z' - vt)}{(\varrho'^2 + \gamma^2(z' - vt)^2)^{\frac{3}{2}}}$$

$$E_\perp = \frac{e\gamma\varrho'}{(\varrho'^2 + \gamma^2(z' - vt)^2)^{\frac{3}{2}}}$$

$\rightarrow$ time-dependent polarization $\vec{P}(\vec{r}', t)$

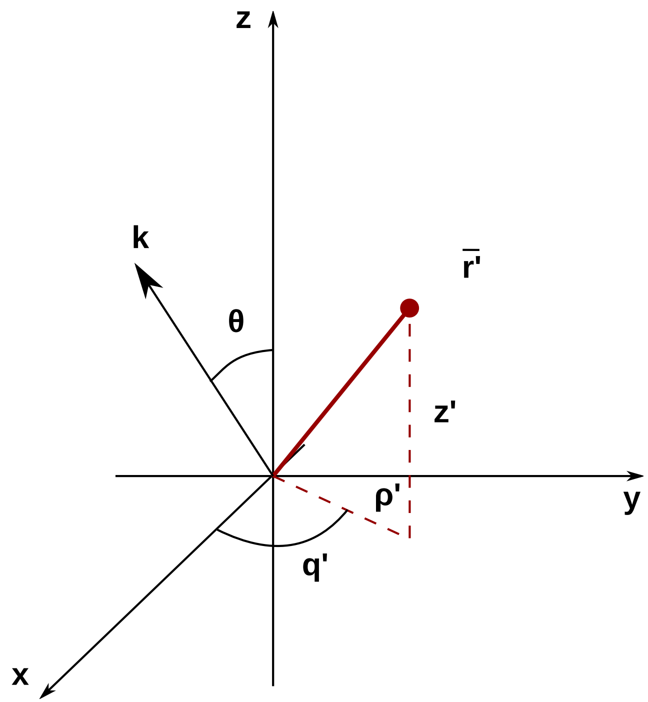

variation of induced dipoles with time leads to radiation of photons

coherent superposition of radiation from neighboring points in vicinity of track
$\rightarrow$ angular range of radiation

θ: large Fourier component of $\vec{P}$ at

$$\varrho^i \leq \frac{\gamma v}{\omega} \simeq \varrho_{\text{max}} \quad \rightarrow \quad \theta \simeq \frac{1}{\gamma}$$

$\rightarrow$ depth from surface up to which contributions add coherently: formation length $D \simeq \gamma \cdot \dfrac{c}{\omega_p}$

$\rightarrow$ volume element producing coherent radiation $V = \pi \varrho_{\text{max}}^2 D$
characterized by plasma frequency ω_p

$$\sqrt{\epsilon_1} = n(\omega) \simeq 1 - \frac{\omega_p^2}{\omega^2} \quad \text{with} \quad \omega_p = \sqrt{\frac{4\pi\alpha n_e}{m_e c^2}} = 28.8\sqrt{\varrho \frac{Z}{A}}\ \text{eV}$$

typical values: $\omega_p^{CH_2}$=20 eV   polyethylene ($\varrho \approx 1$ g/cm^3); for $\gamma = 10^3 \rightarrow D \approx 10\mu$m
$\omega_p^{\text{air}} = 0.7$ eV

$\rightarrow$ radiator made out of foils of this typical thickness; for $d > D$ absorption dominates

typical photon energy: $E_\gamma^{\text{max}} \simeq \gamma \hbar \omega_p$ X-Rays for $\gamma \gg 1$ $$\frac{\mathrm{d}^2 W}{\mathrm{d}\omega \mathrm{d}\Omega} = \frac{\alpha}{\pi^2} \left(\frac{\theta}{\gamma^{-2} + \theta^2 + \xi_1^2} - \frac{\theta}{\gamma^{-2} + \theta^2 + \xi_2^2} \right)^2$$

with $\xi_i = \frac{\omega_{p_i}^2}{\omega^2} = 1 - \epsilon_{1i}(\omega) \ll 1$

$\rightarrow$ per boundary

$$\frac{dW}{d\omega} = \frac{\alpha}{\pi} \left(\frac{\xi_1^2 + \xi_2^2 + 2\gamma^{-2}}{\xi_1^2 - \xi_2^2} \ln \frac{\gamma^{-2} + \xi_1^2}{\gamma^{-2} + \xi_2^2} - 2 \right)$$

foil: contribution from both surfaces, depending on photon interference

typical number of photons per foil $\simeq \alpha$
$\rightarrow$ need many (!) foils
O(100) $\rightarrow \langle n_\gamma \rangle = 1 - 2$

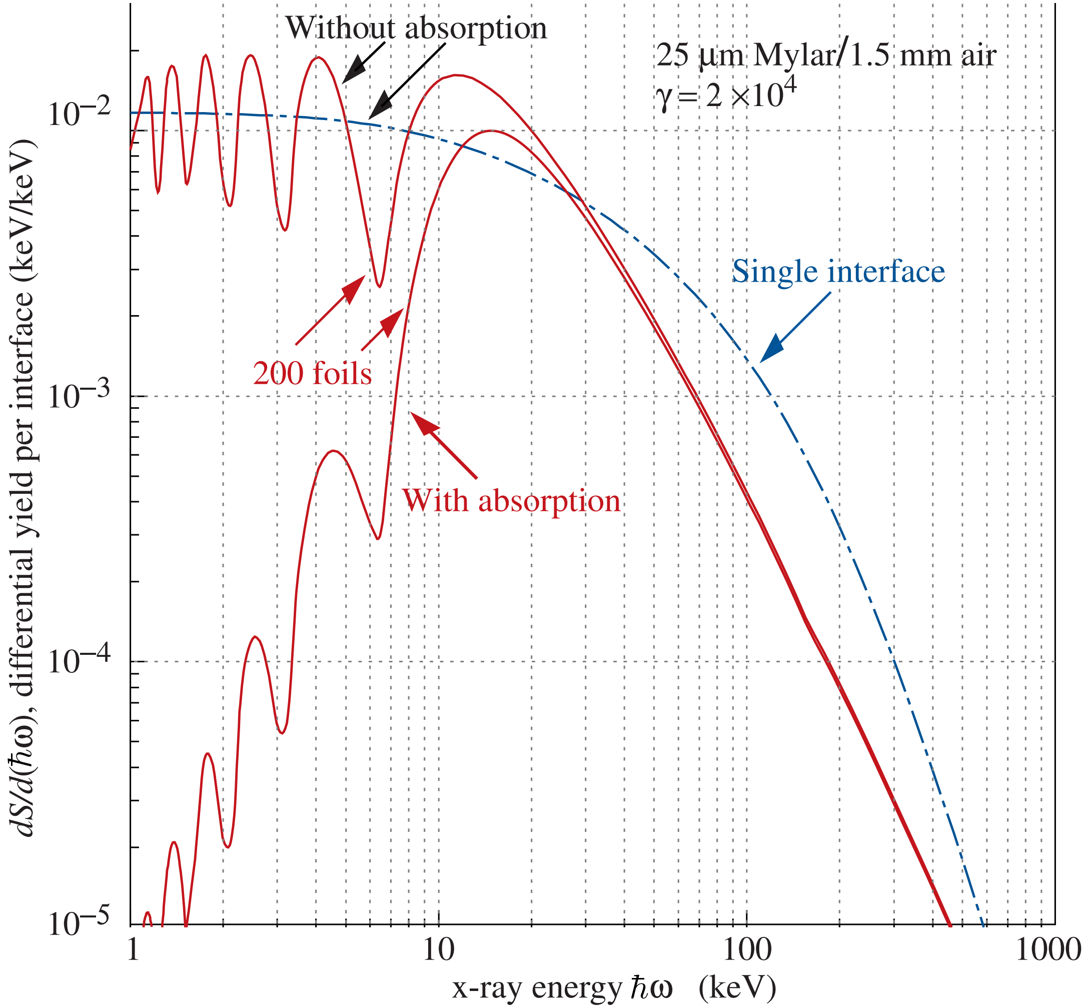

TR spectrum for single interface and multiple foil configurations.

photons generated in e.g. mylar foils and absorbed in gas with high Z (xenon)

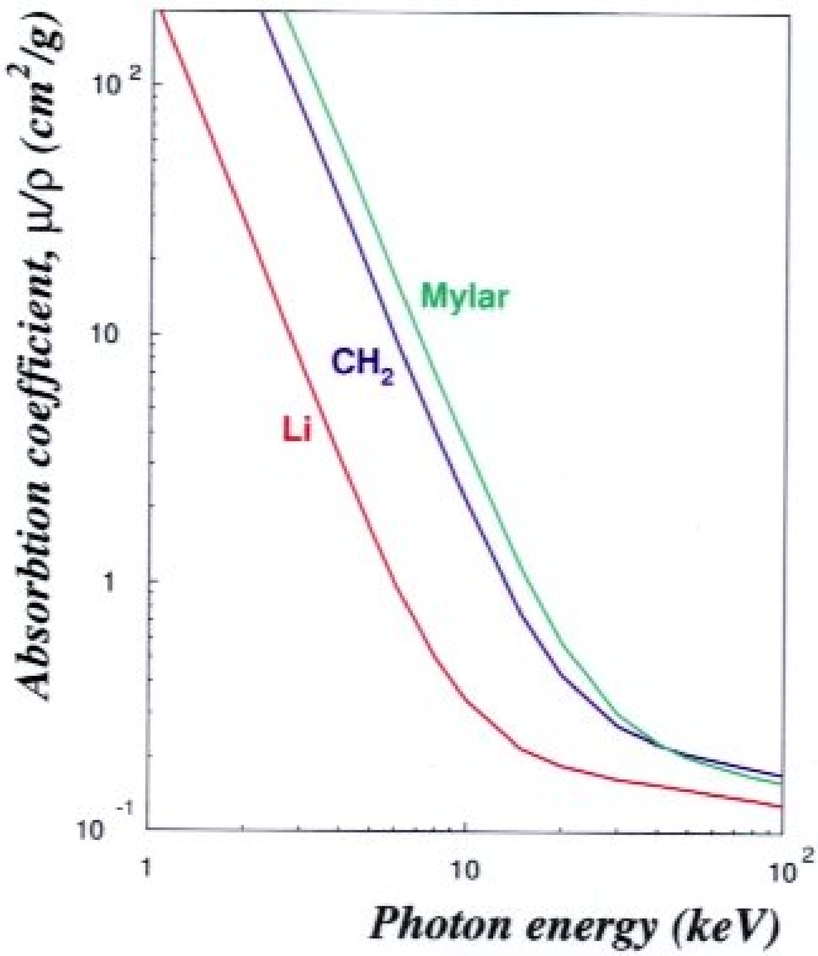

X-Rays absorption coefficient for Li, CH_2 and mylar

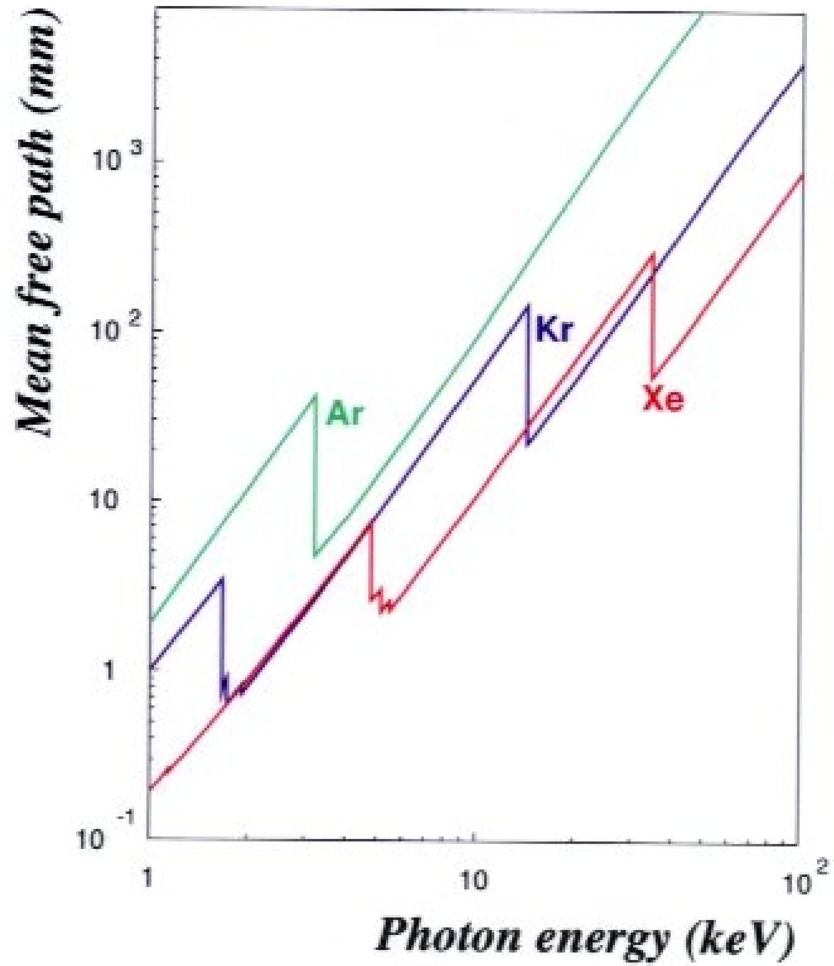

mean free path of X-rays in different gases

Principle of a transition radiation detector

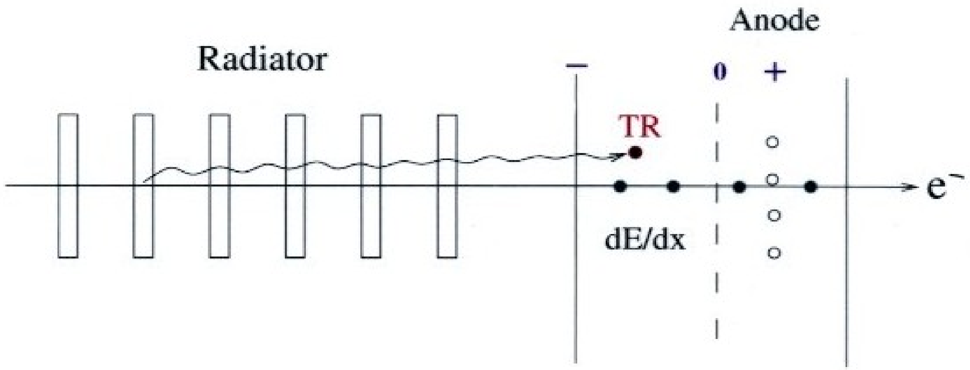

photons generated in e.g. mylar foils and absorbed in gas with high Z (xenon)

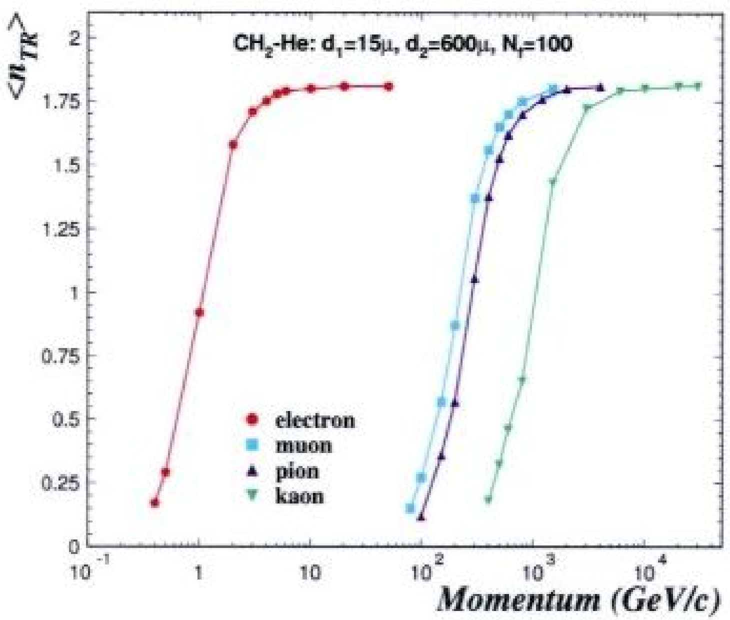

onset of TR production for electrons, muons, pions and kaons. Radiator of 100 foils, thickness d1, spacing d2

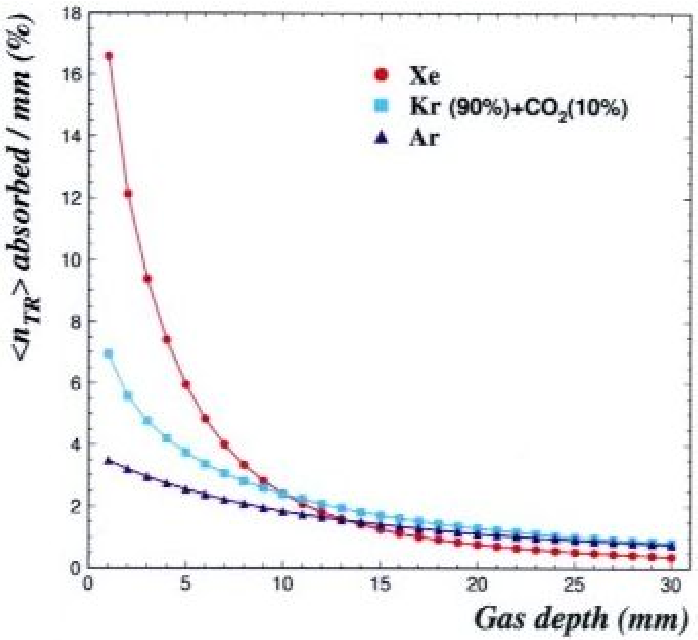

fraction of absorbed TR photons as a function of detector depth. For good absorption probability preferential use of Xe gas, typical dimension cm

the ALICE transition radiation detector TRD

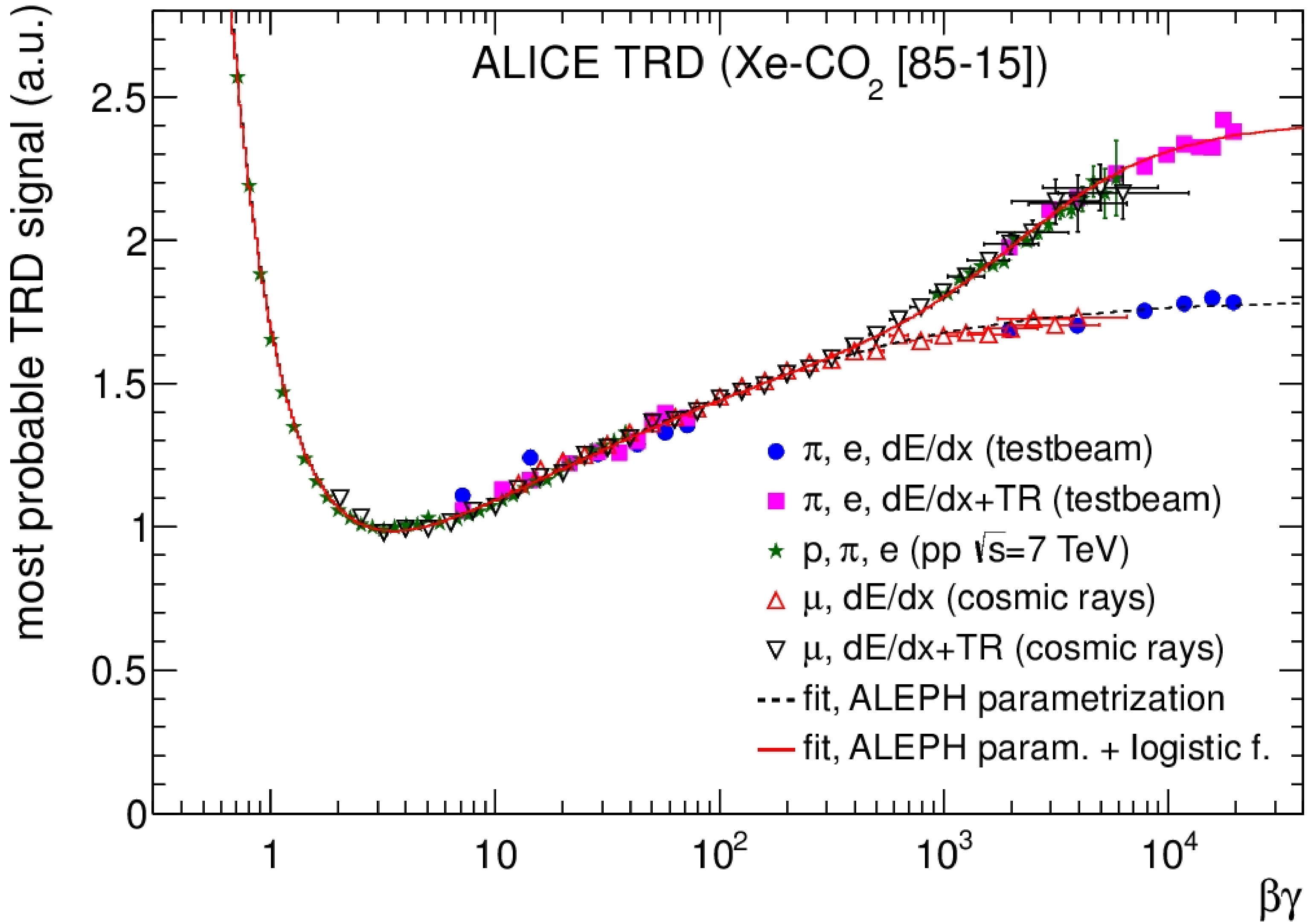

demonstration of the onset of TR at $\beta\gamma \approx 500$
(doctoral thesis Xian-Guo Lu, U. Heidelberg, Oct. 2013)

3. Gas Detectors

3.1 General introduction

Principle

- ionizing particle creates primary and secondary charges via energy loss by ionization (Bethe-Bloch, chapter 2) N_0 electrons and ions
- charges drift in electric field
- generally gas amplification in the vicinity of an anode wire
- signal generation

different operation modes depending on electric field strength

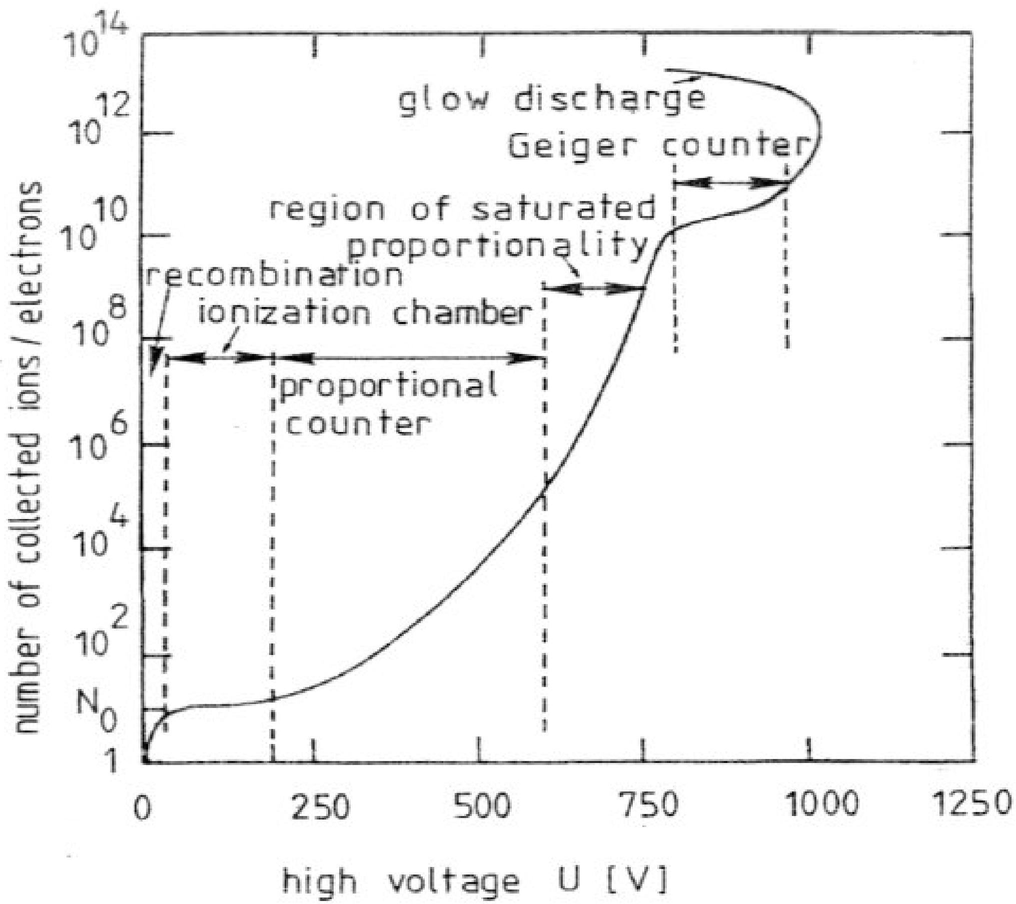

modes of operation of gas detectors (after F. Sauli 1977, lecture notes)

Charge carriers in layer of thickness L for a mean energy W to produce electron-ion pair

- mean number:
$$\langle n_t \rangle = \frac{L \langle \frac{dE}{dx} \rangle_{\text{ion}}}{W}$$
about $2-6$ times the primary number (see chapter 2)
important for spatial resolution: secondary ionization by δ-electrons happens on length scale 10 μm
e.g. $T_e = 1$ keV in iso-butane $\rightarrow R = 20\ \mu m$

- ionization statistics:
$\lambda = 1/\sigma_I \rho$ mean distance between ionization events with cross section σ_I
mean number of ionization events $\langle n \rangle = L/\lambda$

Poisson distribution about mean $\langle n \rangle$

$$P(n, \langle n \rangle) = \frac{\langle n \rangle^n \exp(-\langle n \rangle)}{n!}$$

and specifically probability for **no** ionization

$$P(0, \langle n \rangle) = \exp(-\langle n \rangle) = \exp(-L/\lambda)$$

efficiency of gas detectors allows determination of λ and hence σ_I
typical values:

	λ (cm)
He	0.25
air	0.053
Xe	0.023

$\rightarrow \sigma_I = 10^{-22}$ cm^2 or 100 b

3.2 Charge Transport
- Ion mobility

Ions drift along field lines in external E-field with superimposed random thermal motion
ion transfers in collisions with gas atoms typically half of its energy $\rightarrow$ kinetic energy of ion is approximately thermal energy

$$\langle T_{\text{ion}}(\vec{E})\rangle \simeq \langle T_{\text{ion}}(\text{therm})\rangle = \frac{3}{2}kT$$

drift velocity in direction of $\vec{E}$: develops from one collision to the next (thermal velocity has random orientation relative to $\vec{E}$)
assume instantaneous ion velocity due to electric field $u_e = 0$ at $t = 0$ and typical collision time τ

$\rightarrow$ directly prior to collision $\quad \vec{u}_e = \vec{a} \cdot \tau = \frac{e\vec{E}}{M} \cdot \tau$

$\rightarrow$ drift velocity of ion $\quad \vec{v}_{D^+} = \langle \vec{u}_e \rangle = \frac{1}{2} u_e = \frac{e\vec{E}}{2M}\tau = \mu_+ \vec{E}$ $\quad \boxed{\mu_+ \equiv \text{ion mobility}}$
where $\tau \propto \lambda \propto 1/\sigma_+ \simeq$ constant since $\langle T_{\text{ion}}\rangle$ essentially thermal.

e.g. $C_4H_{10}^+$ in C_4H_{10} $\quad \mu_+ = 0.61 \, \frac{\text{cm/s}}{\text{V/cm}}$ at $E = 1$ kV/cm $\rightarrow v_{D^+} = 0.6$ cm/ms
typical drift distances cm $\rightarrow$ typical ion drift times ms

Electron mobility I

In a constant E-field, electrons drift towards anode of a gas detector with a constant velocity, measurement of drift time allows to determine point of ionization.

$$\Delta t = \frac{L}{v_D}$$

equation of motion of electron in superimposed $\vec{E}$ and $\vec{B}$-fields (Langevin):

$$m\frac{\mathrm{d}\vec{v}}{\mathrm{d}t} = e\vec{E} + e(\vec{v} \times \vec{B}) + \vec{Q}(t)$$

with instantaneous velocity $\vec{v}$ and a stochastic, time dependent term $Q(t)$ due to collisions with gas atoms

assume: collision time τ
$\vec{E}$ and $\vec{B}$ constant between collisions
consider $\Delta t \gg \tau$ (averaging) $\rightarrow Q(t)$ is friction

steady state is reached when net force is zero, defines drift velocity v_D

$$\langle m\frac{d\vec{v}}{dt}\rangle = e(\vec{E} + \vec{v}_D \times \vec{B}) - \underbrace{\frac{m}{\tau}\vec{v}_D}_{\text{Stokes-type}} = 0$$

Electron mobility II

$B = 0$: $\quad \vec{v}_D = \mu_- \vec{E}$ with $\mu_- = \dfrac{e\tau}{m} \equiv \mu$

$B \neq 0$: $\quad \vec{v}_D = \mu_- \vec{E} + \omega\tau(\vec{v}_D \times \vec{B})$ with Larmor frequency $\omega = \dfrac{eB}{m}$ (see below)

Compared to ions, $\mu_+ \ll \mu_-$ since $M \gg m$

2 types of gases

a) hot gases: atoms with few low-lying levels, electron loses little energy in a collision with atom $\rightarrow T_e \gg kT$
acceleration in E-field and friction lead to constant v_D for a given $\vec{E}$
'free fall with friction'
but $\lambda(T_e) \simeq \lambda(|\vec{E}|)$ and
$\mu \propto \tau \propto 1/\sigma(|\vec{E}|)$ not constant.

typical drift velocity: $v_D = 3 - 5$ cm$/\mu$s for 90% Ar/10% CH_4 (typically saturating with E)

b) cold gases: many low-lying degrees of freedom
$\rightarrow$ electrons lose kinetic energy they gain in between collisions (similar to ions)

$$T_e \simeq kT \qquad \mu \simeq \text{constant} \qquad v_D \propto |E|$$

examples: Ar/CO_2 or Ne/CO_2

in latter: $\mu \simeq 7.0 \cdot 10^{-3}$ cm$^2/\mu$s V at 10% CO_2 or $v_D = 2$ cm$/\mu$s at 300 V/cm
$3.5 \cdot 10^{-3}$ cm$^2/\mu$s V at 20% $\quad v_D = 1$ cm$/\mu$s

Electron mobility III

Drift in combined $\vec{E}$ and $\vec{B}$-fields

$$\vec{v}_D = \frac{\mu|\vec{E}|}{1+\omega^2\tau^2}[\hat{E} + \underbrace{\omega\tau\hat{E}\times\hat{B}}_{\substack{\text{component}\\ \text{in direction}\\ \vec{E}\times\vec{B}\\ \propto\,\omega\tau}} + \underbrace{\omega^2\tau^2(\hat{E}\cdot\hat{B})\hat{B}}_{\substack{\text{component}\\ \text{in direction}\\ \vec{B}\\ \propto\,(\omega\tau)^2}}]$$

$\hat{E}$, $\hat{B}$: unit vectors in direction of E- and B-field

Electron loss

with some probability a free electron is lost during drift

a) recombination $\quad \text{ion}^+ + e^-$
decrease in number of negative (and positive) charge carriers

$$-\frac{dN^-}{dt} = p_r \cdot \rho^+ \rho^- \qquad p_r : \text{coefficient of recombination} \simeq 10^{-7}\ \text{cm}^3/\text{s}$$

generally not important

b) electron attachment
on electro-negative molecules, probability can be large

$$e^- + M \rightarrow M^- \qquad \text{for } T_e \simeq 1\ eV$$

otherwise dissociative attachment

$$e^- + XY \rightarrow X + Y^-$$

for gases like O_2, Cl_2, freon, SF_6 probability per collision is of order 10^{-4}
capture coefficient p_c is strongly energy dependent (in many gases there is a minimum around 1 eV, large transparency for slow electrons 'Ramsauer effect')
electron undergoes order of 10^{11} collisions/s $\rightarrow$ for drift time of 10^{-6} s fraction lost x_{loss}
depends on partial oxygen pressure

$$x_{\text{loss}} = 10^{-4} \cdot (10^{11}/\text{s}) \cdot (10^{-6}\ \text{s}) \cdot P_{O_2}/P_{\text{atm}}$$

$\rightarrow$ less than 1% lost for $P_{O_2}/P_{\text{atm}} \leq 10^{-3}$

Remark: in presence of certain quencher gases such as CO_2 the effect of O_2 is enhanced by multistep catalytic reaction
- 10 ppm O_2 can lead to 10% loss within 10 μs $\rightarrow$ need to keep oxygen level low in gas.

Diffusion I

Original ionization trail diffuses (spreads apart) with drift time
$\rightarrow$ effect on space point and momentum resolution, ultimate limit

a) only thermal motion ($|\vec{E}| = |\vec{B}| = 0$)
mean thermal velocity

$$\begin{aligned} \langle v \rangle &= \frac{\lambda}{\tau} \\ \langle T_e \rangle &= \frac{1}{2} m \langle v \rangle^2 \end{aligned}$$

λ mean free path
τ time between collisions

for a point-like source at time $t = 0$, collisions between electrons and gas atoms (molecules)
$\rightarrow$ smearing: spread of charge cloud at time of first collision

$$R^2 = 2\lambda^2$$

and after $n = t/\tau$ collisions

$$\sigma^2(t) = 2\lambda^2 t/\tau$$

define diffusion coefficient $\quad D = \dfrac{\sigma^2(t)}{2t}$

for $|\vec{E}| = |\vec{B}| = 0 \quad D = D_0 = \dfrac{\lambda_0^2}{\tau} = \dfrac{2\langle T_e \rangle}{m} \tau$

Diffusion II

diffusion is isotropic

longitudinal diffusion coefficient $D_{0L} = \frac{1}{3}\frac{\lambda_0^2}{\tau}$

transverse diffusion coefficient $D_{0T} = \frac{2}{3}\frac{\lambda_0^2}{\tau}$

$\rightarrow$ after time t charge cloud has width $\sigma(t) = \sqrt{D2t}$

respectively, in each dimension $\sigma_x(t) = \sigma_y(t) = \sigma_z(t) = \sqrt{\frac{1}{3}D2t}$

charge distribution Gaussian $N(x) = c \cdot \exp(-\frac{x^2}{2\sigma_x^2})$

diffusion equation: charge density $\rho(\vec{r}, t)$ for conserved electron current $\vec{j}$ defined by

$$\frac{\partial \rho}{\partial t} + \nabla \cdot \vec{j} = 0$$

without field, $\vec{j} = -D\nabla\rho \Rightarrow \frac{\partial \rho}{\partial t} = D\Delta\rho$

solved by $\rho(\vec{r}, t) = c \cdot \exp(-\frac{\vec{r}^2}{4Dt})$

Diffusion III

hot gases: $\langle T_e \rangle \gg \frac{3}{2} kT \qquad D$ large

cold gases: $\langle T_e \rangle \simeq \frac{3}{2} kT \qquad D$ small

with 1-dim diffusion coeff. $\quad D = \dfrac{2\langle T_e \rangle}{3m}\tau$

and $\qquad \mu = \dfrac{e}{m}\tau \qquad$ (B=0)

$$\langle T_e \rangle \quad = \quad \frac{3}{2} e \frac{D}{\mu}$$

can define a characteristic energy

$$\epsilon_k = \frac{2}{3}\langle T_e \rangle = e\frac{D}{\mu}$$

diffusion of cloud after distance L

$$\sigma_x^2 = 2Dt = 2D\frac{L}{\mu E} = \frac{2\epsilon_k}{eE}L \qquad (1)$$

for hot gas the same characteristic energy is reached at much lower T

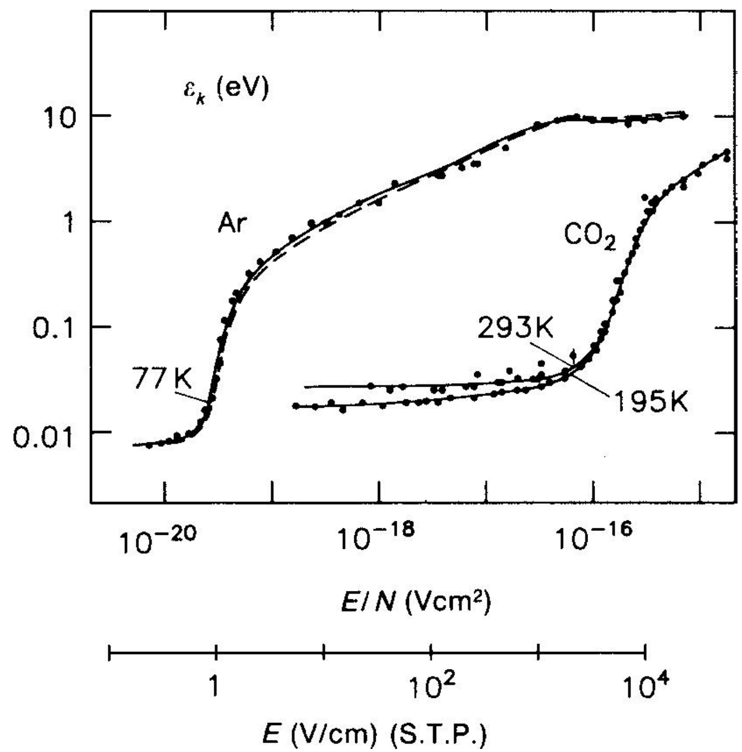

characteristic energy of electrons in Ar and CO_2 as a function of the reduced E. The electric field under normal conditions is also indicated. The parameters refer to temperatures at which the measurements were made.

Diffusion IV

b) diffusion in B-field

$$\vec{B} = B\vec{e}_z$$

along B no Lorentz force

$D_L(B) = D_{0L} = \frac{1}{3} D_0$

in transverse direction Lorentz force helps to keep charge cloud together, i.e. it counteracts diffusion

$$D_T(B) = \frac{D_{0T}}{1 + \omega^2\tau^2}$$

for $\vec{B}$ large

$\rightarrow \omega\tau \gg 1 \qquad D_T(B) \ll D_{0T}$

e.g. Ar/CH_4 at $B = 1.5\ T$

$$D_T(1.5\ T) \simeq \frac{1}{50} D_{0T}$$

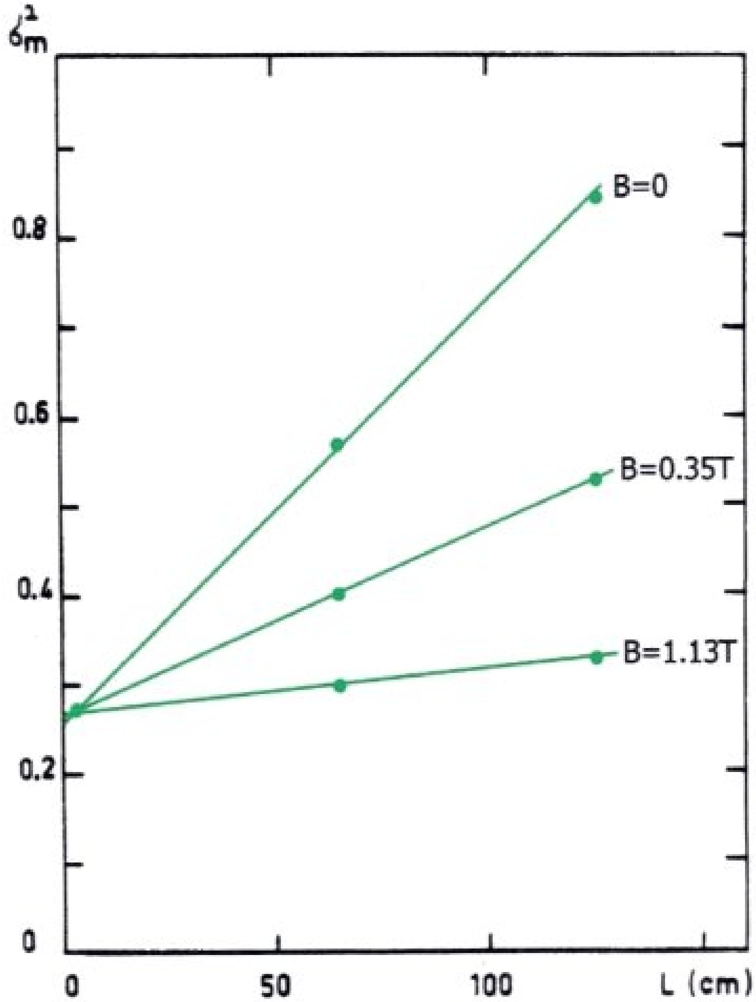

transverse σ^2 as function of L

Diffusion V

c) diffusion in E-field:
ordered drift along field superimposed to statistical diffusion
mobility μ is function of $\langle T_e \rangle$

$$\vec{v}_D = \mu(\langle T_e \rangle) \cdot \vec{E}$$

$\rightarrow$ energy spread leads to longitudinal spreading of electron cloud $D_L \neq \frac{1}{2} D_T$

statistical transverse diffusion not affected by E-field

in hot gases:
for large E, $D_L > D_T$ and values are large

in cold gases: $D_L \simeq D_T$ small

$$\sigma^2(t) = 2Dt = 2D\frac{L_D}{v_D} = \frac{2kT}{e|\vec{E}|} L_D$$

$$\frac{\sigma^2(t)}{L_D} = \frac{2kT}{e|\vec{E}|}$$

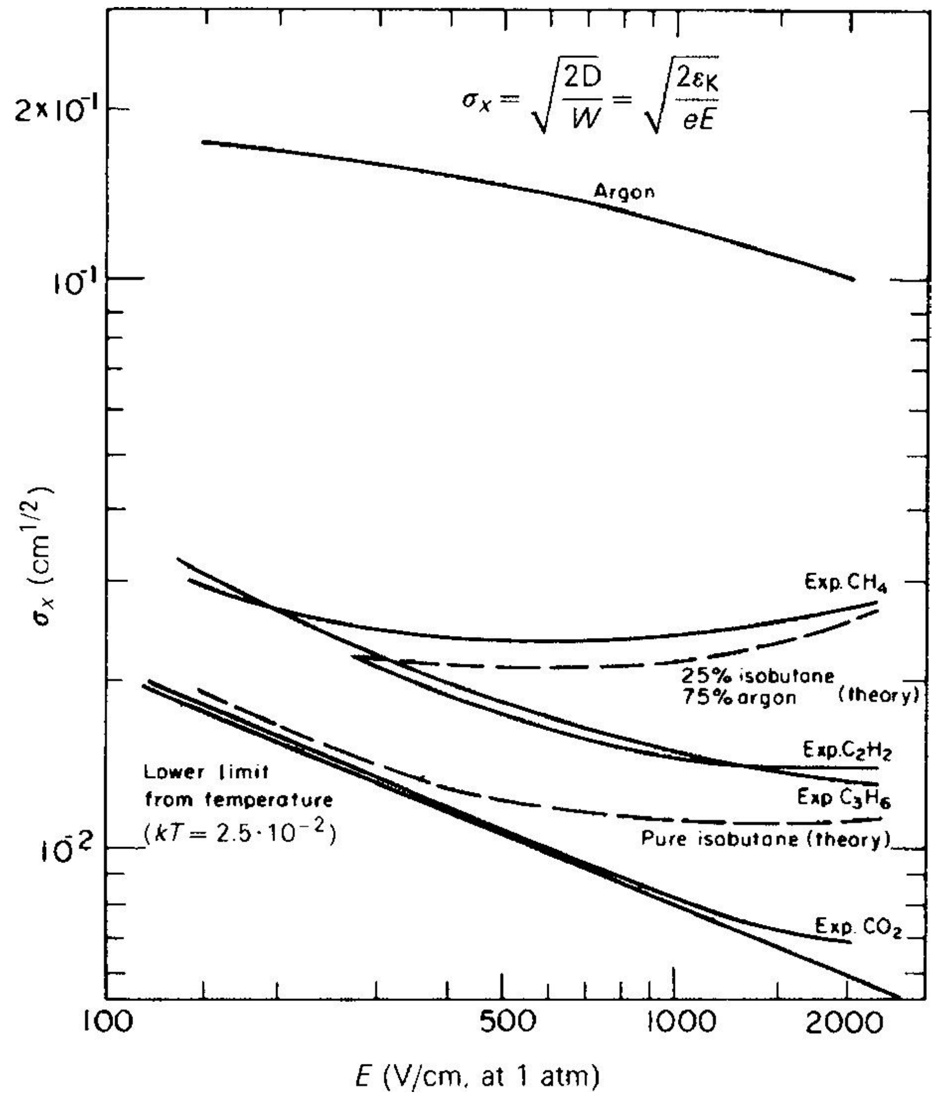

longitudinal diffusion width $\sigma_x/\sqrt{L_D}$ after 1 cm of drift

Exact solution

of drift and diffusion by solving a 'transport equation' for electron density distribution $f(t, \vec{r}, \vec{v})$

Boltzmann-equation:

$$\frac{\partial f}{\partial t} + \underbrace{\vec{v}\frac{\partial}{\partial \vec{r}} f}_{\text{flow term}} + \underbrace{\frac{\partial}{\partial \vec{v}} \vec{g}}_{\text{external forces}} = \underbrace{Q(t)}_{\text{collision term (stochastic)}}$$

$$\vec{g} = \left(\frac{e\vec{E}}{m} + \vec{\omega} \times \vec{v}\right) f$$

numerical solution with codes such as Magboltz & Garfield

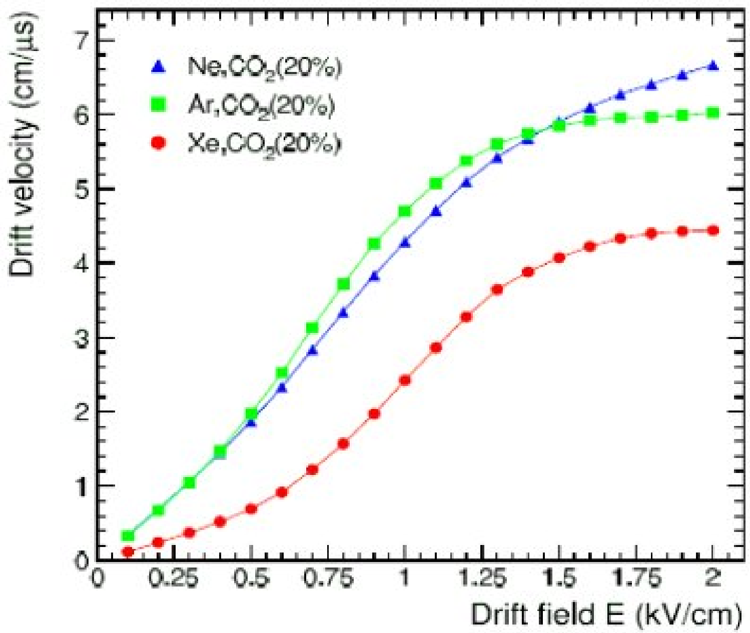

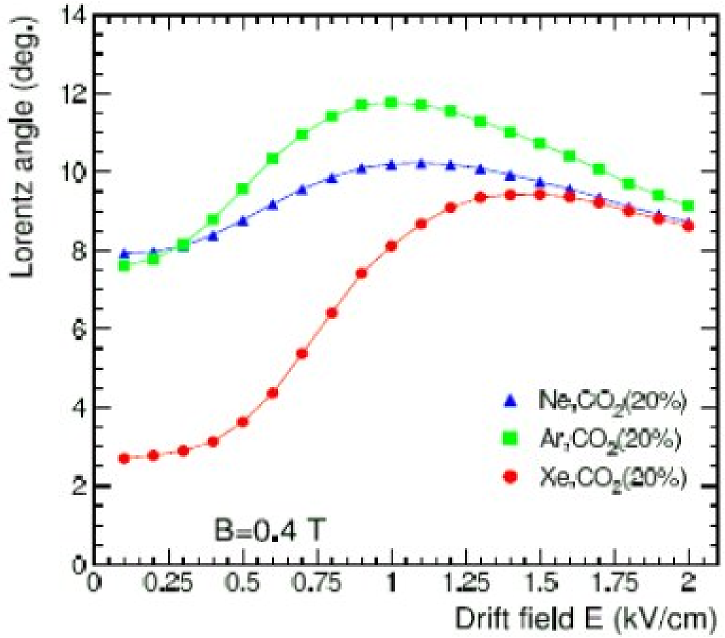

Lorentz angle: angle between E-field and drift velocity of electrons in presence of B not $\perp$ to E

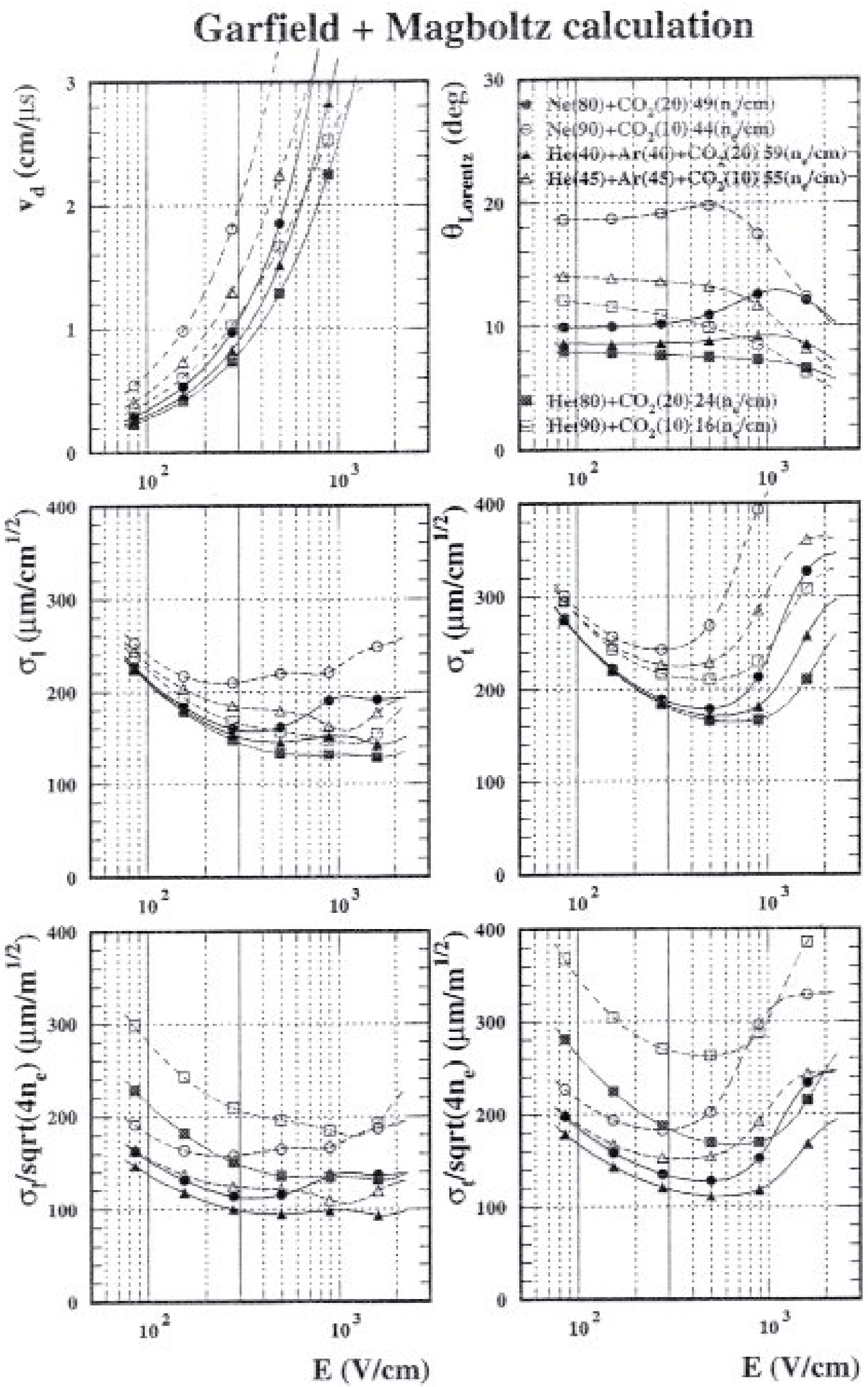

Drift velocity (top left), Lorentz angle (top right), longitudinal and transverse diffusion constants (middle) and longitudinal and transverse diffusion constants normalized to the square root of the number of charge carriers (bottom) for different mixtures of noble gas and CO_2.

Lorentz angle: angle between E-field and drift velocity of electrons in presence of B not $\perp$ to E

3.3 Gas amplification

in case the anode is a (thin) wire, E-field in vicinity of wire very large $E \propto 1/r$
and the electron gains large kinetic energy.

$$\begin{aligned}
\Delta T_e &= e\Delta U \\
&= e\int_{r_1}^{r_2} E(r)\mathrm{d}r \\
&= \frac{eU_o}{\ln r_o/r_i}\int_{r_1}^{r_2}\frac{1}{r}\mathrm{d}r \\
&= eU_o\frac{\ln r_2/r_1}{\ln r_o/r_i}
\end{aligned}$$

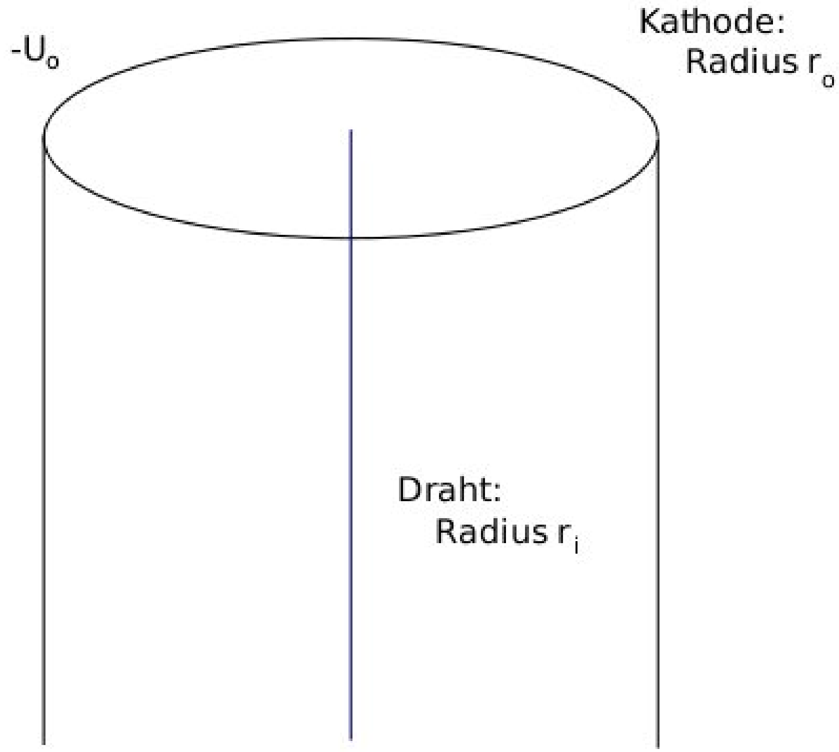

in order to obtain large E and hence large ΔT_e, use very thin wires ($r_i \simeq 10 - 50\ \mu m$)
within few wire radii, ΔT_e becomes large enough for secondary ionization
strong increase of $E \rightarrow$ avalanche formation for $r \rightarrow r_i$.

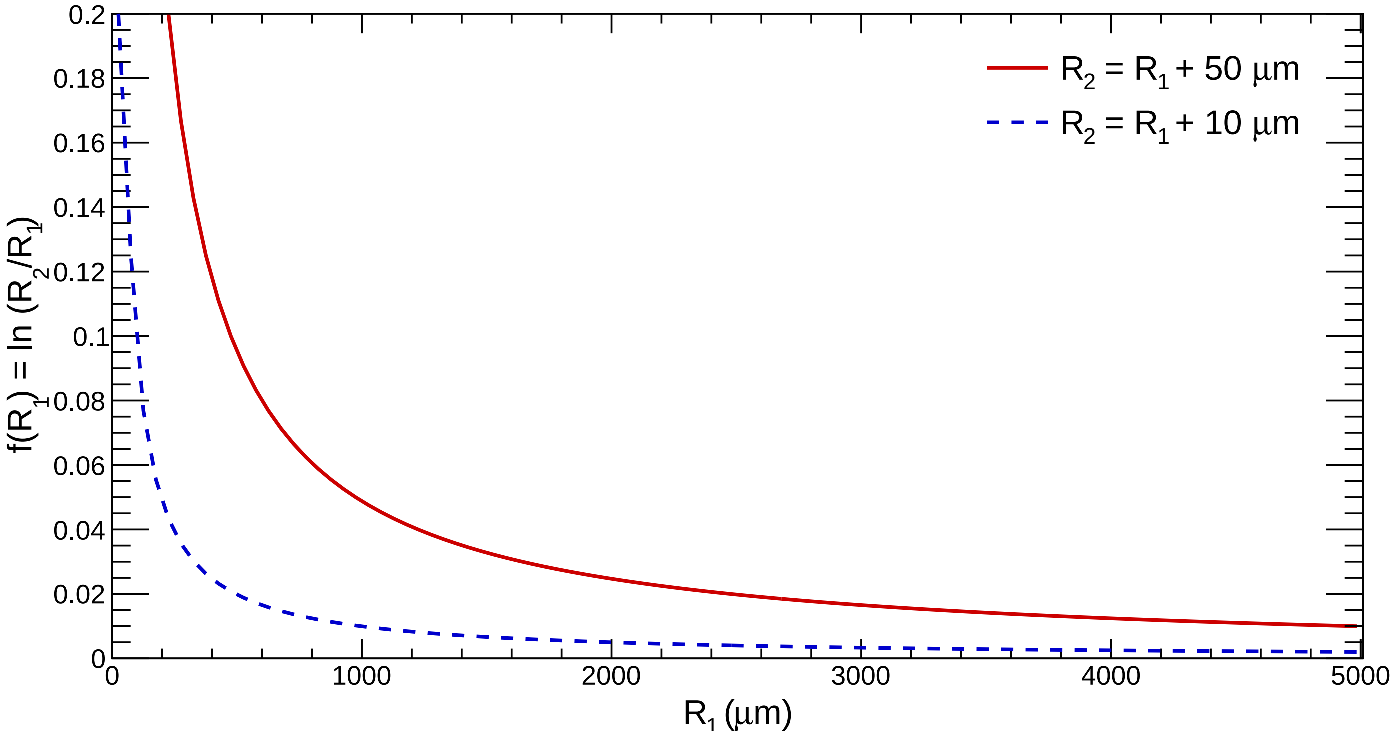

Avalanche formation in vicinity of a thin wire

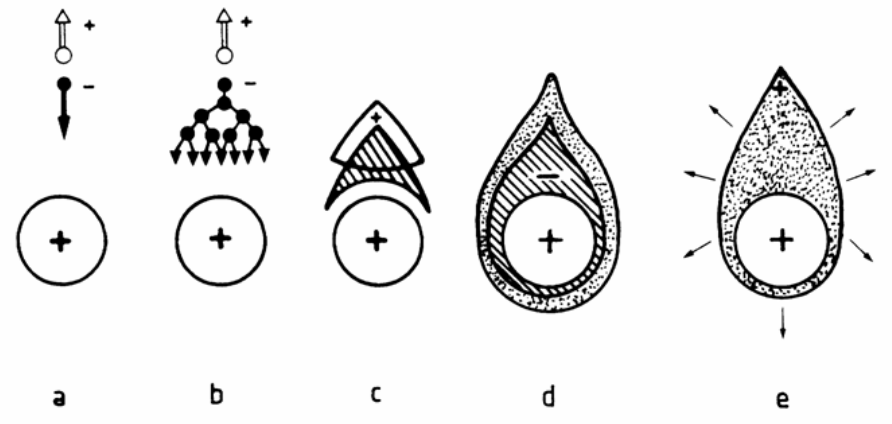

Temporal and spatial development of an electron avalanche

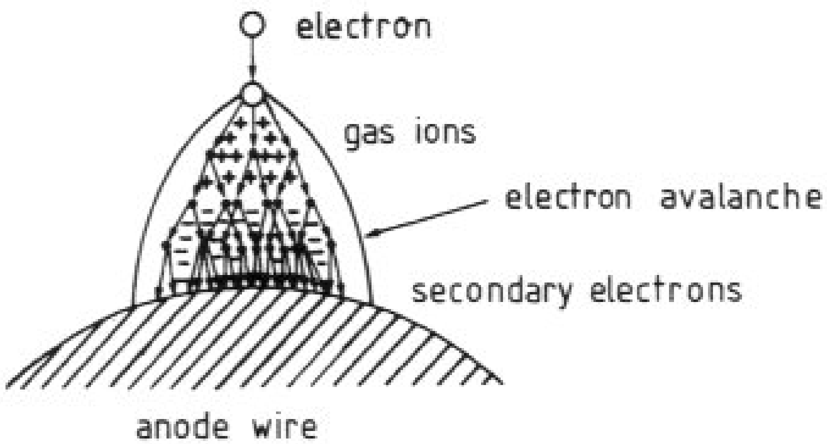

Illustration of the avalanche formation on an anode wire in a proportional counter. By lateral diffusion a drop-shaped avalanche develops.

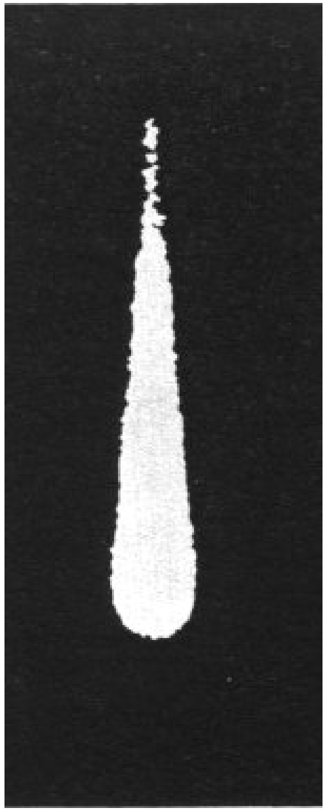

Photographic reproduction of an electron avalanche. The photo shows the form of the avalanche. It was made visible in a cloud chamber by droplets which have condensed on the positive ions.

First Townsend coefficient α

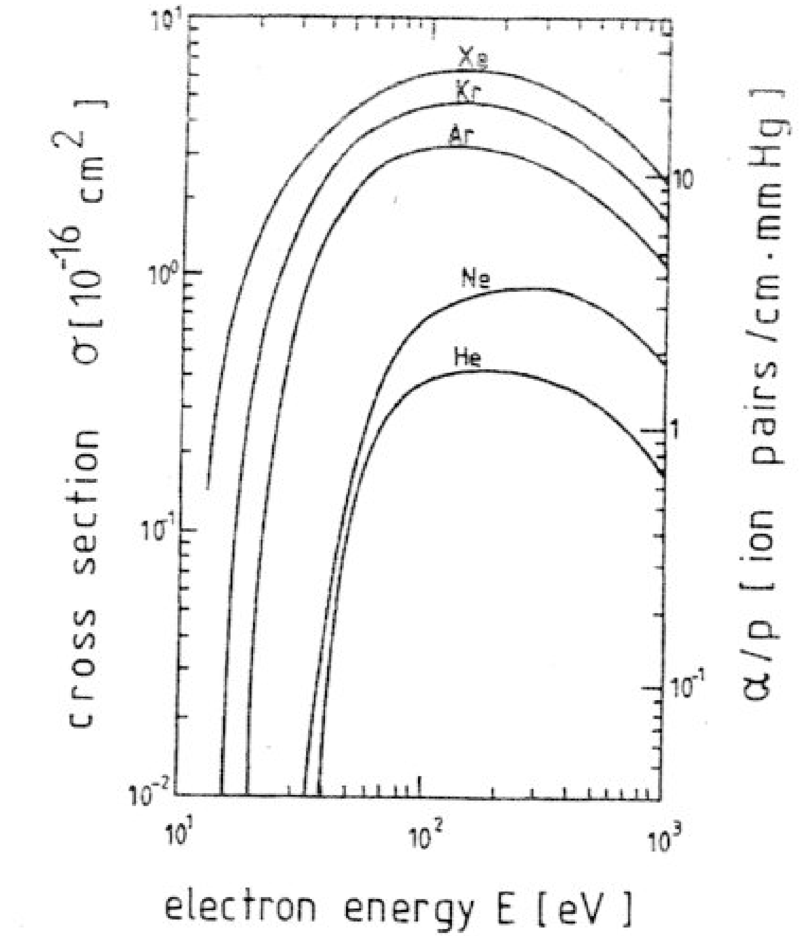

Energy dependence of the cross section for ionization by collision.

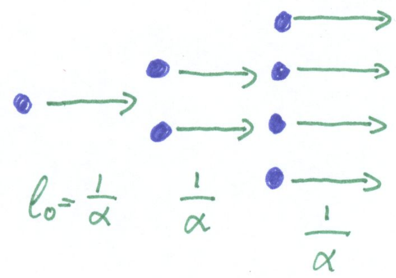

number of electrons $N(x) = N_0 \underbrace{\exp \alpha x}_{\text{gas gain}}$

mean free path $l_0 = 1/\alpha = 1/(N\sigma(T_e))$

$T_e = T_e(E(x))$

$\Rightarrow \alpha = \alpha(x)$

gas gain $G = \exp\left(\int_{r_1}^{r_2} \alpha(x)\, dx\right)$

typically $10^4 - 10^5$, up to 10^6 possible in proportional mode.
limit: discharge (spark) at $\alpha x \simeq 20$
or $G = 10^8$ 'Raether-limit'

Second Townsend coefficient

excitation of gas generates UV-photons which in turn can lead to photo effect in gas and on cathode wire, contributing thus to avalanche.

$$\gamma = \frac{\#\text{ photo effect events}}{\#\text{ avalanche electrons}}$$

gas gain including photo effect

$$G_\gamma \quad = \quad \underbrace{G}_{\text{no}} + \underbrace{G(G\gamma)}_{\text{one}} + \underbrace{G(G\gamma)^2}_{\text{two}} + \ldots = \frac{G}{1-\gamma G}$$

photo effect events

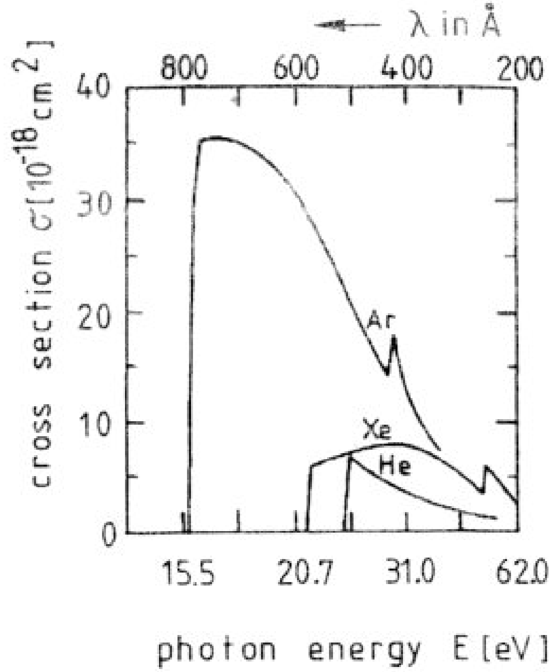

Energy dependence of the cross section for photoionization

limit: $\gamma G \to 1$ continuous discharge independent of primary ionization

to prevent this, add to gas so-called quench-gas which absorbs UV photons strongly, leading to excitation and radiationless transitions

examples: CH_4, C_4H_{10}, CO_2

3.4 Ionization chamber

no gas gain, charges move in electric field and induce signal in electrodes.

2 electrodes form parallel plate capacitor.

consider motion of a free charge q: electric field does work, capacitor is charged (lowering in energy of capacitor).

$$q\vec{\nabla}\Phi \cdot \; d\vec{x} \quad = \quad dq_i \cdot U_0$$

leads to induced current

$$\begin{aligned} I_{\text{ind}} &= \frac{q}{U_0}\vec{\nabla}\Phi \cdot \vec{v_D} \\ \text{with } \vec{E} &= -\vec{\nabla}\Phi \text{ and } U_0 = \Phi_1 - \Phi_2 \end{aligned}$$

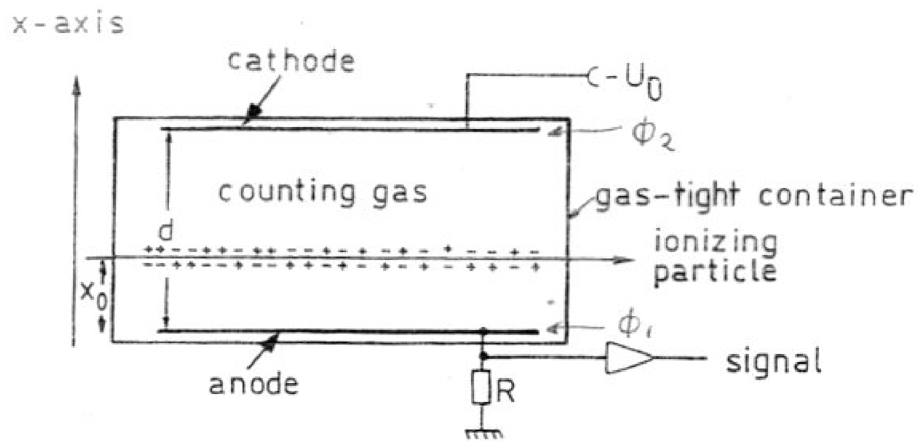

Principle of operation of a planar ionization chamber

- current is constant **while** charge is drifting
- total induced signal (charge) independent of x_0
- signal induced by electrons $$\Delta q_- = \frac{N_e}{U_0}(\Phi(x_0) - \Phi_1)$$
- signal induced by ions $$\Delta q_+ = -\frac{N_e}{U_0}(\Phi(x_0) - \Phi_2)$$
- $|N_{ion}| = |N_e|$, but opposite charge $\rightarrow$ total $\Delta q = \Delta q_- + \Delta q_+ = N_e$

practical problem: ion comparatively slow $w_+ = 10^{-3} \dots 10^{-2} w_-$ (see mobilities above)
(except for semiconductors: typ. $w_+ \approx 0.5\ w_-$)

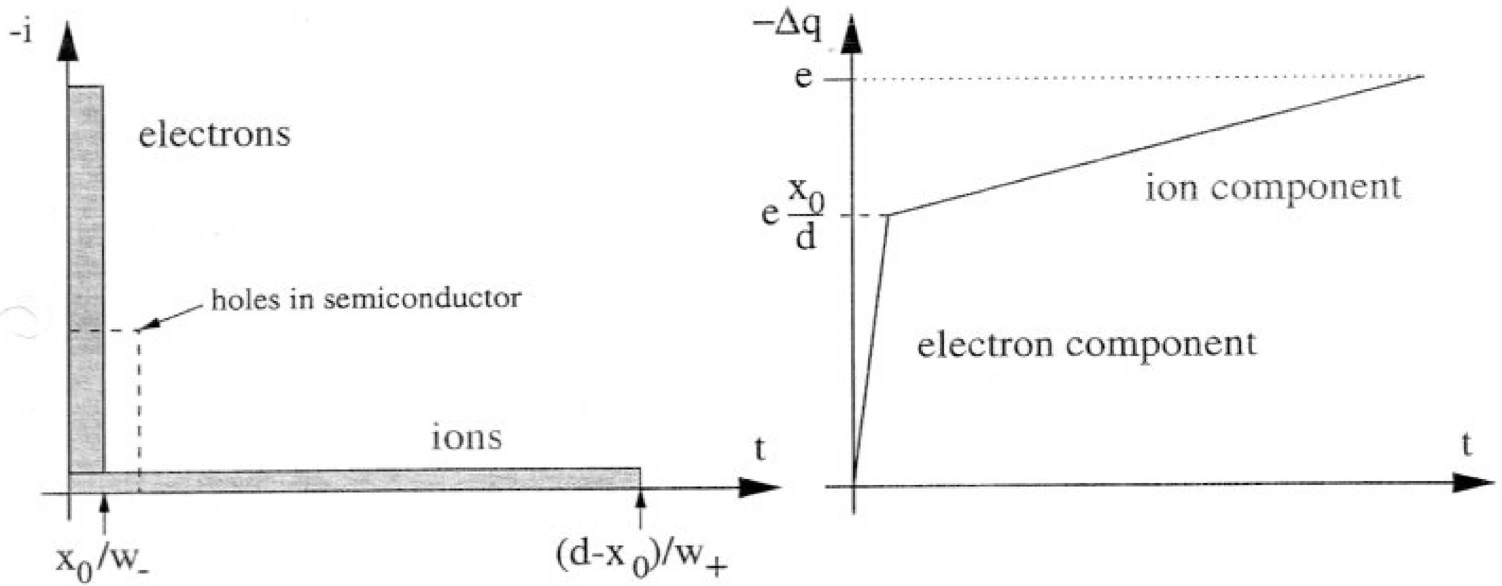

Induced current and charge for parallel plate case, ratio w_-/w_+ decreased for purpose of illustration.

signal generated during drift of charges

- induced current ends when charges reach electrodes
- induced charge becomes constant (total number N_e)
- signal shaping by differentiation (speed of read-out) $\rightarrow$ suppresses slow ion component

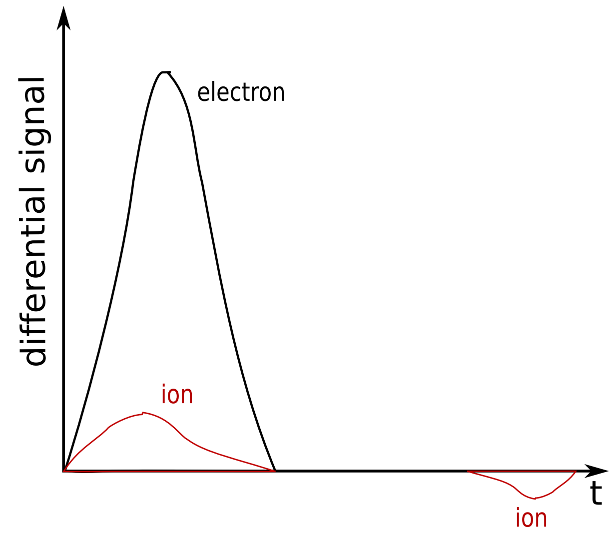

change in potential $dU = \frac{\mathrm{d}Q}{C}$
U_0 = external voltage
typical time constant of power supply (+ cables ...)
$RC \gg \Delta t^-, \Delta t^+$
usually electronic signal shaping needed

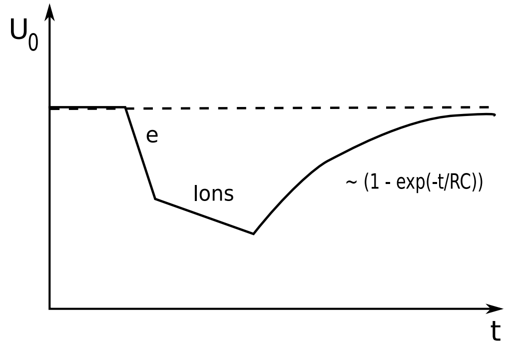

Signal shaping by RC-filter
choose e.g. $\Delta t^- \ll RC \ll \Delta t^+$
damps ion component

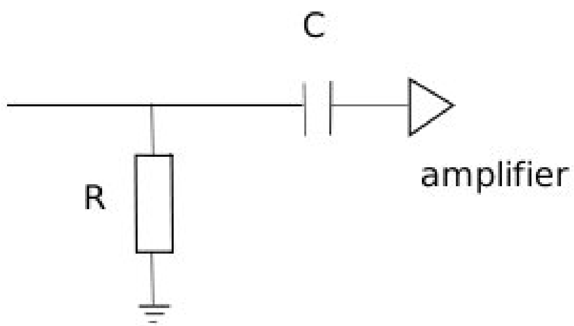

$$\begin{aligned} \Delta U &= \Delta U^- + \Delta U^+ \\ &= \frac{\Delta Q^-}{C} + \frac{\Delta Q^+}{C} \end{aligned}$$

where ΔQ^{+-} is the charge induced in the anode by motion of ions and electrons for total number of ionization events in gas N_e

$$
\begin{aligned}
\Delta Q^- &= N_e \frac{\Phi(x_0) - \Phi_1}{U_0} \\
&= N_e \frac{x_0}{d} \\
\Delta Q^+ &= -N_e \frac{\Phi(x_0) - \Phi_2}{U_0} \\
&= N_e \frac{d - x_0}{d} \\
\text{without filter} \quad \Delta Q &= N_e, \qquad \Delta U = \frac{N_e}{C} \\
\text{with filter} \quad d - x_0 &= v^+ \Delta t^+ \\
&\rightarrow \underbrace{v^+ RC \left(1 - \exp(-\frac{\Delta t^+}{RC})\right)}_{\text{damping of ion component}}
\end{aligned}
$$

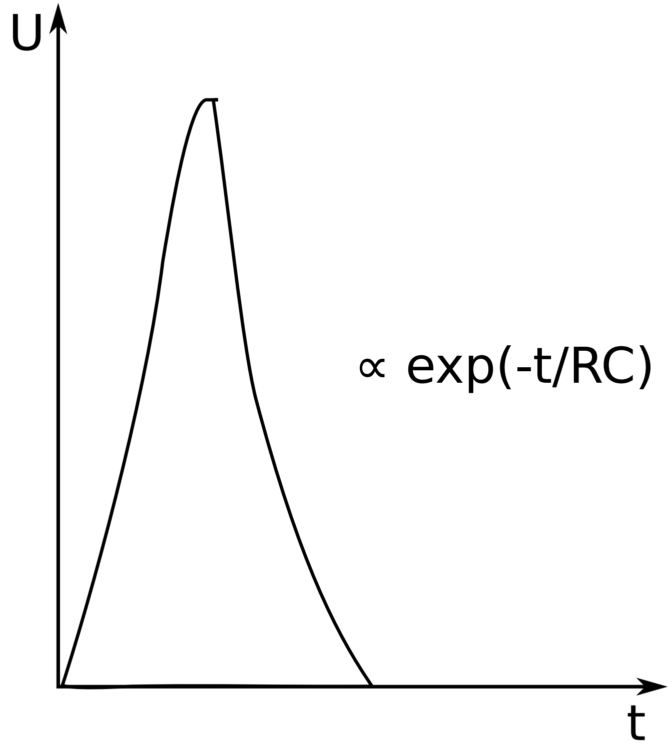

fast rise and decrease of signal but now pulse height depends on x_0

trick: introduce additional grid, the "Frisch grid"
while electrons drift towards Frisch grid, no induced signal on anode, only on Frisch Grid
as soon as electrons pass Frisch grid, signal induced on anode
choose U_g such that the E-field is unchanged

$$\Delta Q = \Delta Q^- = N_e$$
$$\Delta t^- = \frac{d_g}{v^-}$$

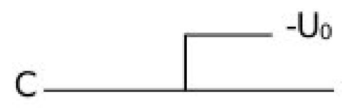

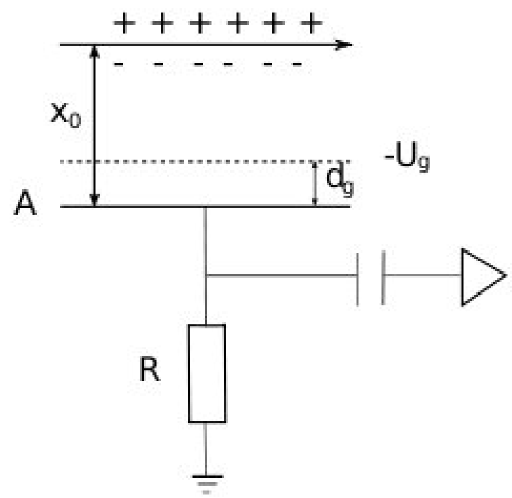

general difficulty for ionization chambers: small signals
example: 1 MeV particle stops in gas

$$\begin{aligned} N_e &\simeq \frac{10^6 \text{ eV}}{35 \text{ eV}} \simeq 3 \cdot 10^4 \\ C &\simeq 100 \text{ pF} \\ \Rightarrow \Delta U_{max} &= \frac{3 \cdot 10^4 \cdot 1.6 \cdot 10^{-19} \text{ C}}{10^{-10} \text{ F}} \\ &= 4.6 \cdot 10^{-5} \text{ V} \end{aligned}$$

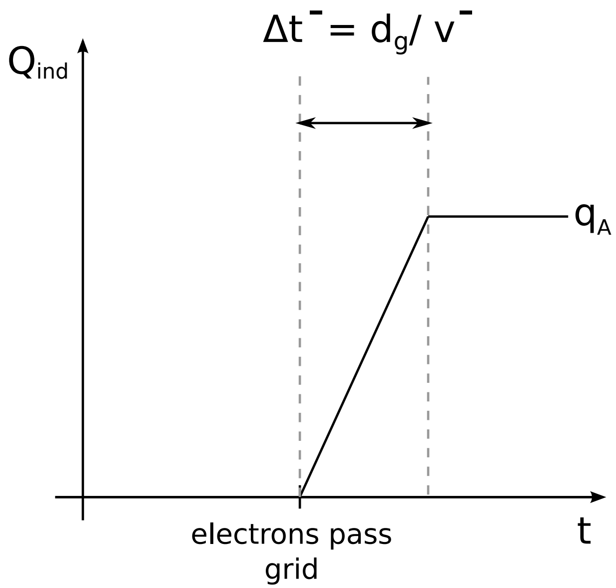

need sensitive, low-noise preamplifier

application: e.g. cylindrical ionization chamber for radiation dosimetry

$$\vec{E}(r) = -\frac{U_0}{r \ln r_a/r_i}\hat{e}_r$$

ionization at radius r_0:

$$\begin{aligned}\Delta t^- &= \int_{r_0}^{r_i} \frac{\mathrm{d}r}{v^-(r)} = -\int \frac{\mathrm{d}r}{\mu^- E} \\ &= -\int_{r_0}^{r_i} \frac{dr}{\mu^- U_0} r \ln\frac{r_a}{r_i} \\ &= \frac{\ln(r_a/r_i)}{2\mu^- U_0}(r_0^2 - r_i^2)\end{aligned}$$

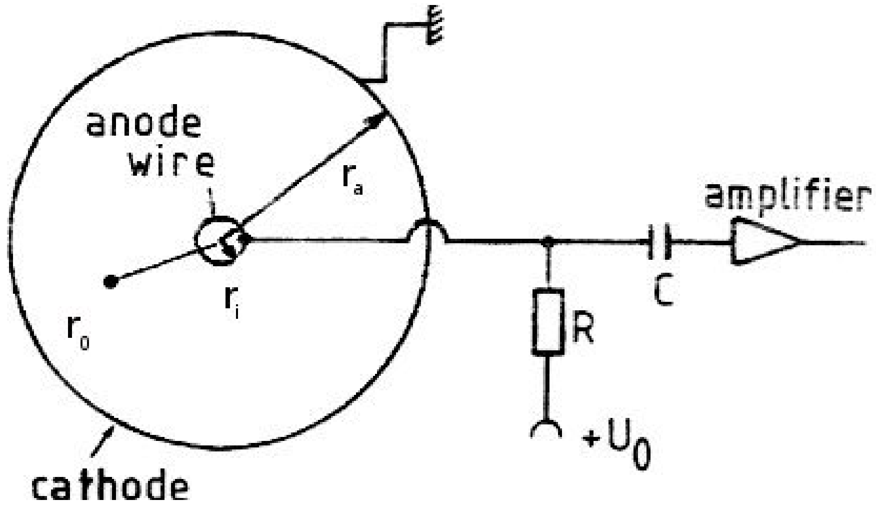

Principle of operation of a cylindrical ionization chamber

l_0: typical ionization length, the centroid of the avalanche is this amount away from the wire

$$\Delta Q^- = \frac{N_e}{U_0}\int E(r)\,\mathrm{d}r = \frac{N_e}{\ln(r_a/r_i)}\ln\frac{r_i}{l_0} \qquad \Delta U^- = \Delta Q^-/C$$

$$\frac{\Delta U^+}{\Delta U^-} = \frac{\ln(r_a/l_0)}{\ln(r_i/l_0)} \qquad r_a \gg r_i \quad \rightarrow \quad \Delta U^+ \gg \Delta U^-$$

in cylindrical geometry, ion signal dominates by typically factor 10 - 100.

Dosimeter for Ionization

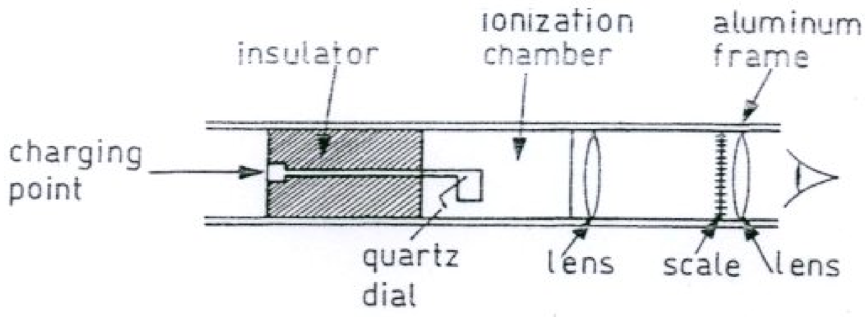

Construction of an ionization pocket dosimeter

- cylindrical capacitor filled with air
- initially charged to potential U_0
- ionization continuously discharges capacitor
- reduction of potential ΔU is measure for integrated absorbed dose
(view e.g. via electrometer)

other applications: measure energy deposit of charged particle, should be highly ionizing (low energy) or even stop (then measure total kinetic energy)
nuclear physics experiments with energies of 10 to 100 MeV
combination of ΔE and E measurements $\rightarrow$ particle identification (nuclei)

3.5 Proportional Counter

gas amplification as described above

$$N = A \cdot N_e$$

with a gas gain in vicinity of wire

$$A = \exp \int_{r_k}^{r_i} \alpha(x) \mathrm{d}x$$

charge avalanche typically builds up within 20 μm
effectively it starts at $r_0 = r_i + k\lambda$
k: number of mean free paths needed for avalanche formation
λ: mean free paths of electrons (order μm)

($2^{10} \cong 1000 \quad 2^{17} \cong 10^5$)

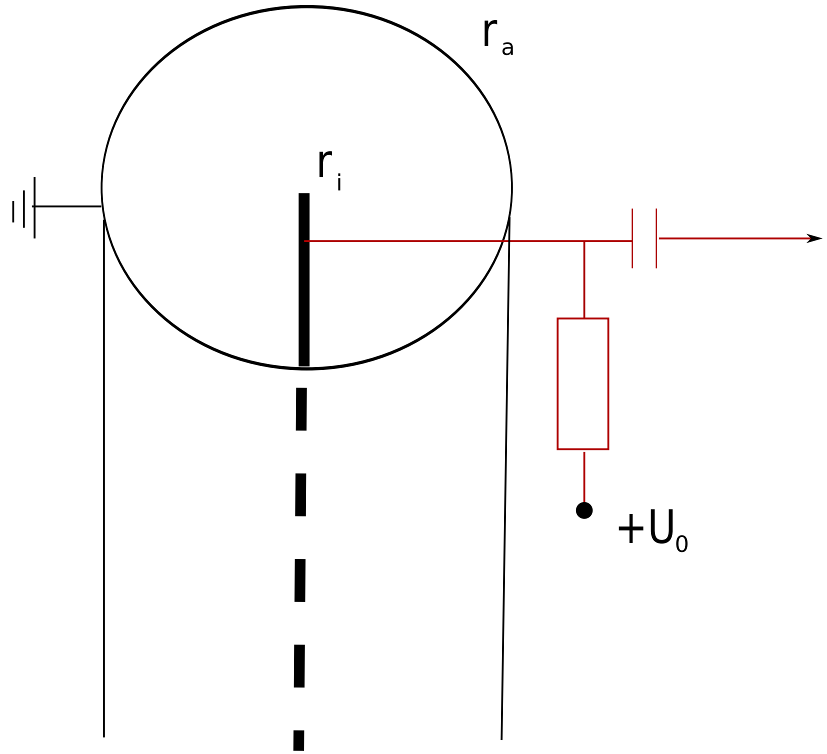

$$\Delta U^- = -\frac{N_e A}{C} \frac{\ln r_0/r_i}{\ln r_a/r_i}$$

$$\Delta U^+ = -\frac{N_e A}{C} \frac{\ln r_a/r_0}{\ln r_a/r_i}$$

$$\frac{\Delta U^+}{\Delta U^-} = \frac{\ln r_a/r_0}{\ln r_0/r_i} = R$$

$r_a = 1$ cm, $r_i = 30\ \mu$m, $k\lambda = 20\ \mu$m for Ar at P_{atm} $\quad \rightarrow R \simeq 10$

In a proportional counter the signal at the anode wire is mostly due to ion drift!

rise time for electron signal as discussed above

$\Delta t^- = \frac{\ln(r_a/r_i)}{2\mu^- U_0}(r_0^2 - r_i^2)$ order of ns for $\mu^- = 100 - 1000$ cm^2/Vs and $U_0 \cong$ several 100 V

ion signal Δt^+ slow, order of 10 ms $\rightarrow$ differentiate with $R_{\text{diff}} \cdot C$

in case $R_{\text{diff}} \cdot C = 1$ ns $\rightarrow$ time structure of individual ionization clusters can be resolved

Typical set-up

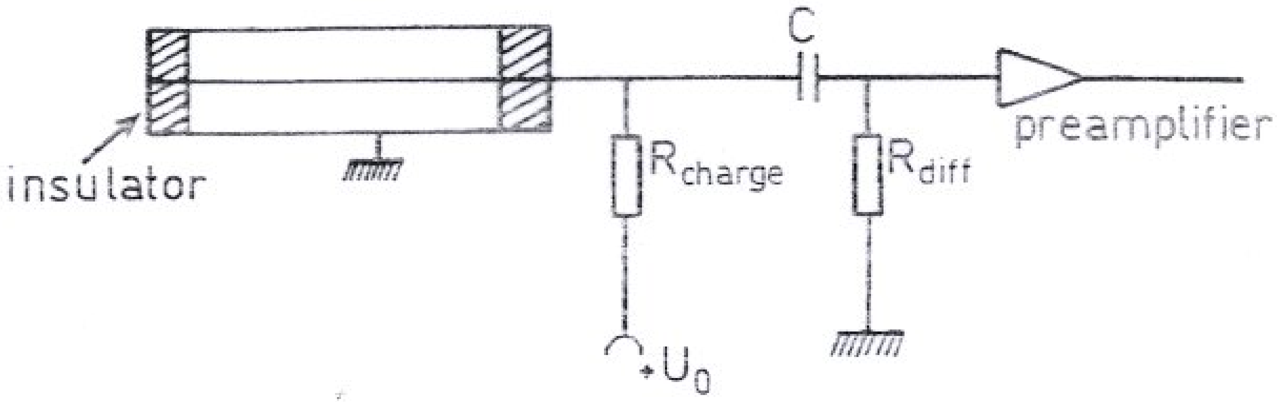

Readout of a proportional counter

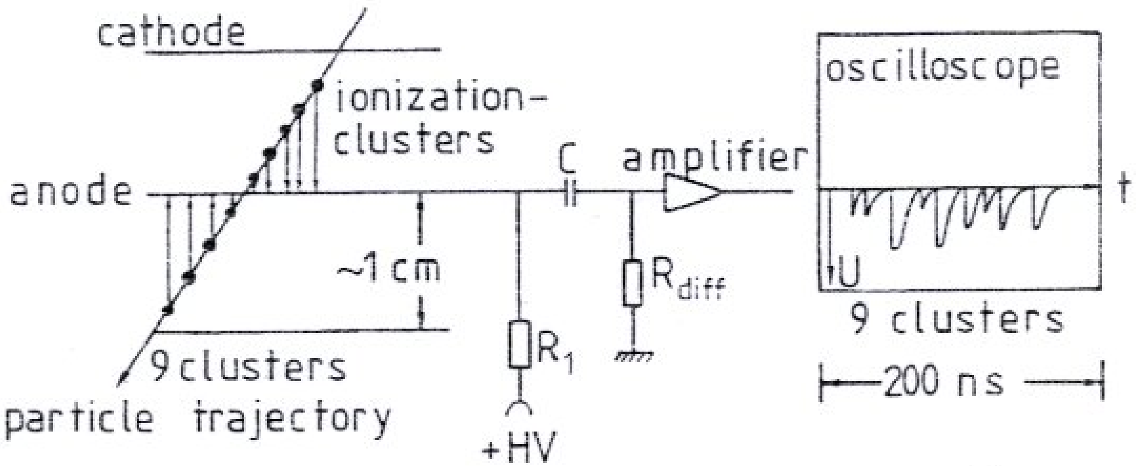

Illustration of the time structure of a signal in the proportional counter

Application outside particle physics: particularly suited to measure X-rays, e.g. 'X-ray imaging' with special electrode geometries for experiments involving synchrotron radiation (high rates!)

Multi-wire proportional chamber

most important application:
Multi-wire proportional chamber MWPC
planar arrangement of proportional counters without separating walls
G. Charpak et al. NIM 62 (1968) 202
Nobel prize 1992, Rev. Mod. Phys. 65 (1993) 591

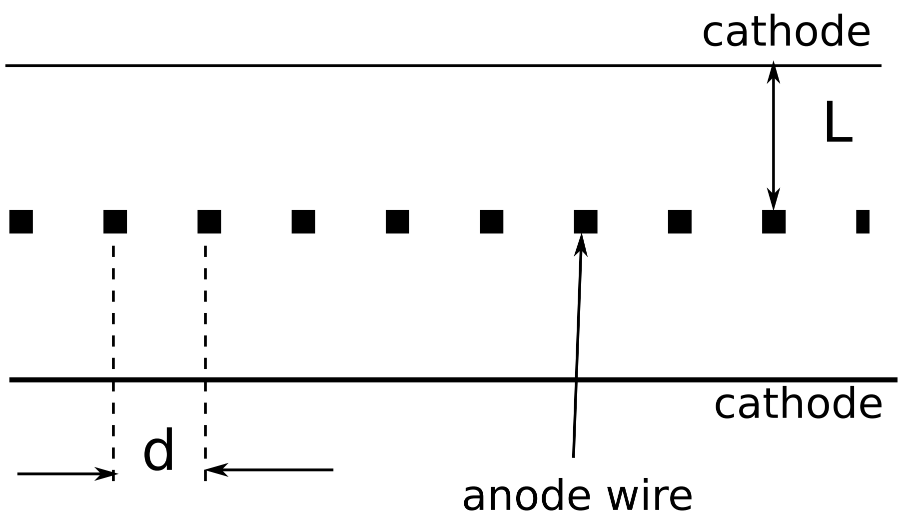

allows: tracking of charged particles, some PID capabilities via dE/dx
large area coverage, high rate capability

as compared to cylindrical arrangement field geometry somewhat different

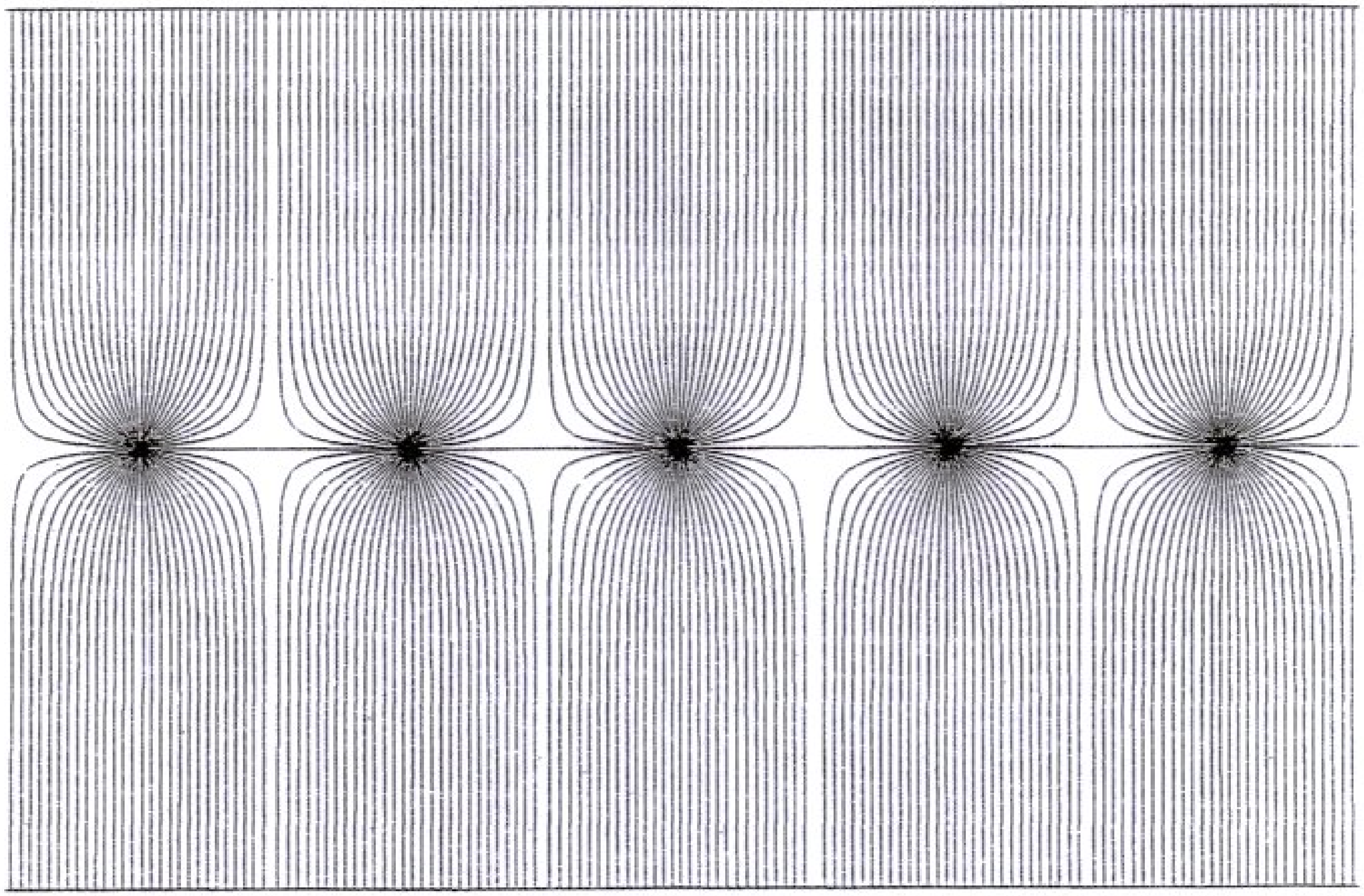

typical parameters:

$$d = 2 - 4 \text{ mm}$$
$$r_i = 15 - 25\ \mu\text{m}$$
$$L = 3 - 6 \text{ mm}$$
$$U_0 = \text{several kV}$$

total area: many m^2

typical geometry of electric field lines in multi-wire proportional chamber

in vicinity of anode wire: radial field
far away homogeneous (parallel-plate capacitor)

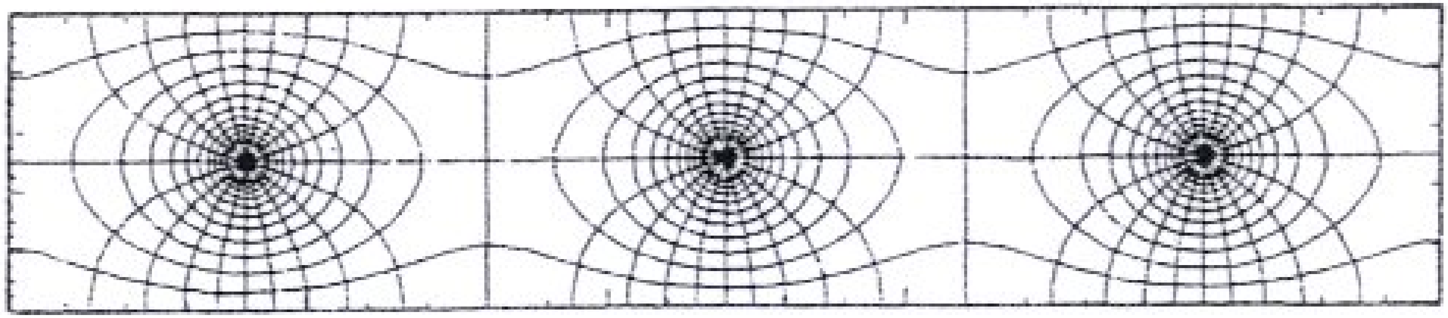

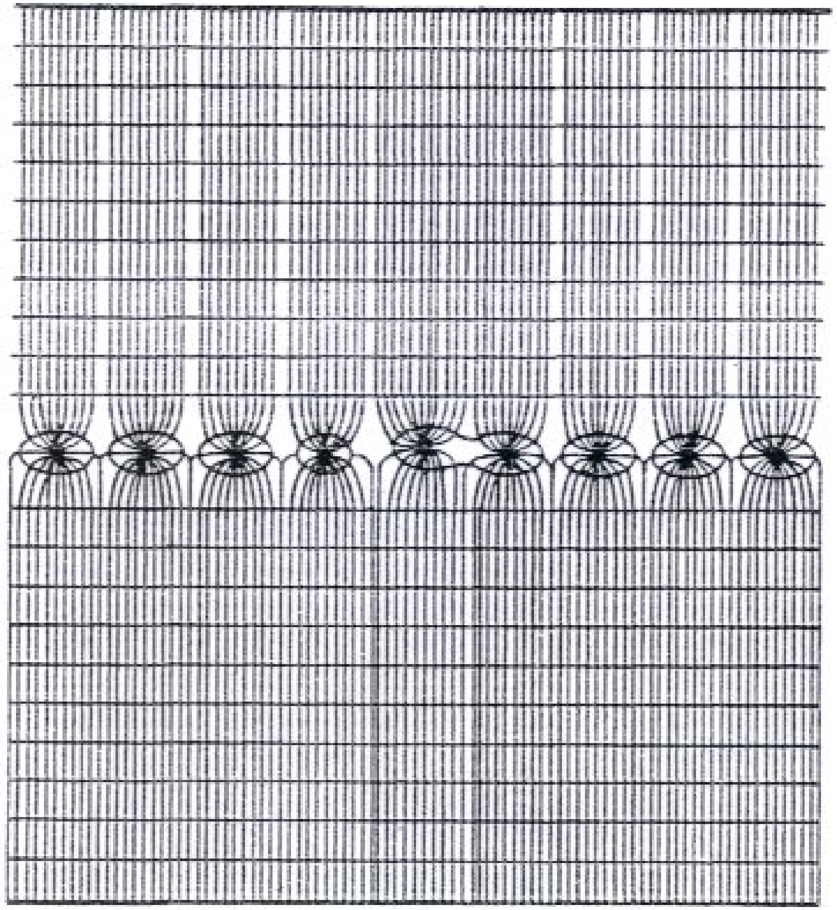

Field lines and equipotential lines

Difficulty:
even small geometric displacement of an individual wire will lead to effect on field quality.

need of high mechanical precision, both for geometry and wire tension (electrostatic effects and gravitational wire sag, see below)

- electrons from primary and secondary ionization drift to closest anode wire
- in vicinity of wire gas amplification $\rightarrow$ formation of avalanche
  ends when electrons reach wire or when space charge of positive ions screens electric field below critical value
- signal generation due to electron- and (mostly) slow ion-drift

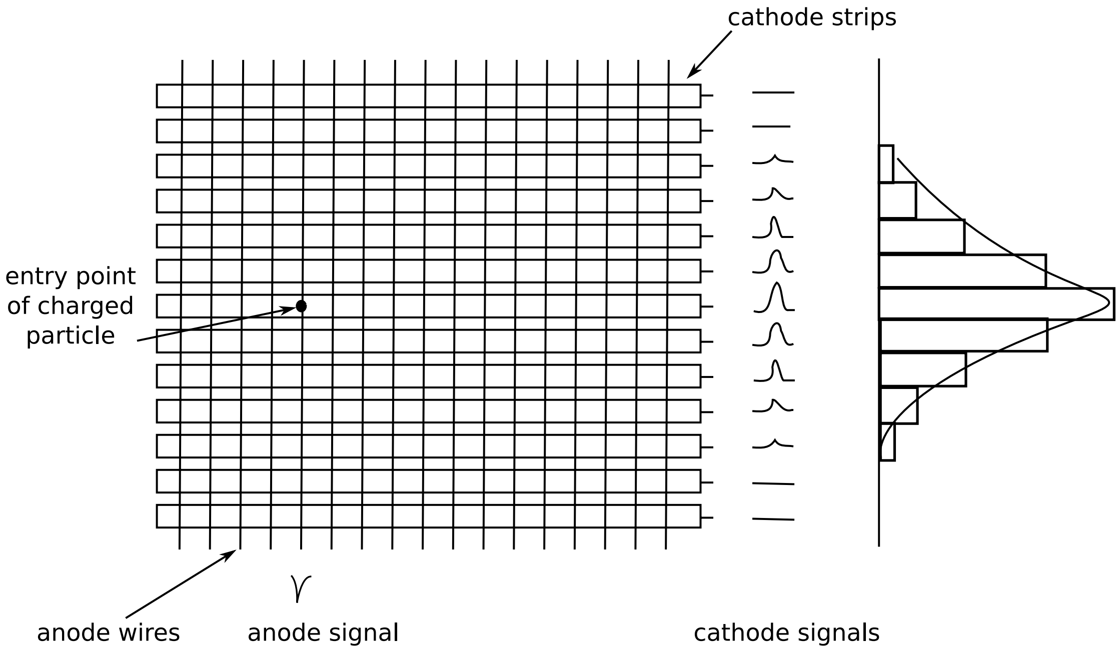

typical space point resolution:
since only information about closest wire $\rightarrow$
$\delta_x = d/\sqrt{12} = 577\ \mu$m for $d = 2$ mm

not very precise and only 1-dimensional

can be improved by segmenting cathode and reading out of signal induced on cathode spread-out over more than 1 strip

the center of gravity of signals on cathode strips can be determined with precision of $50 \ldots 300\ \mu$m! use charge sharing between adjacent strips

Note: The dimension with good resolution is along the wire, perpendicular always $d/\sqrt{12}$.

Resolving ambiguities in case of 2 or more hits in one event:
different orientation of segmentation in several cathode planes

two particles traversing MWPC: with only one orientation of segmentation (strips) possibilities ●● and ○○ cannot be distinguished and one obtains 4 possible coordinates for tracks: 2 real and 2 'ghosts', resolved by second induced strip pattern

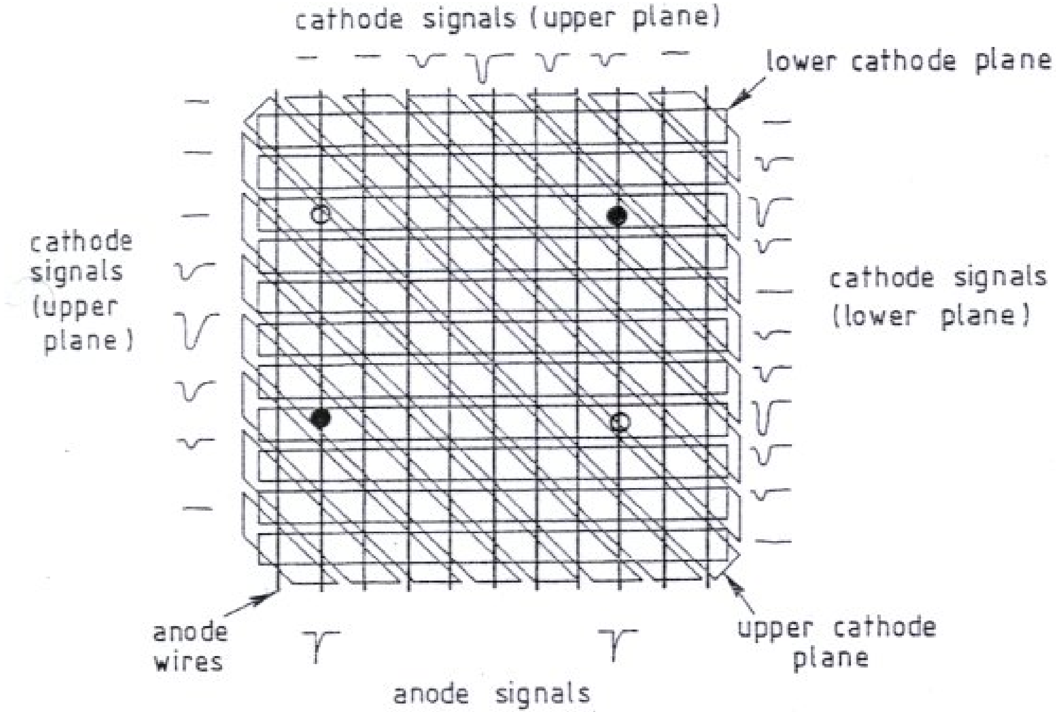

Illustration of the resolution of ambiguities for two particles registered in a multi-wire proportional chamber

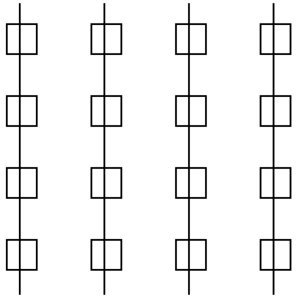

for high hit density environment segmentation of cathode into pads truly 2-d measurement.
but: number of read-out channels grows quadratically with area ($$)

Stability of wire geometry I

Can we make resolution better and better by putting wires closer and closer?
practical difficulty in stringing wires precisely closer than 1 mm
fundamental limitations: stability of wire geometry

- electrostatic repulsion between anode wires, in particular for long wires
  $\rightarrow$ can lead to 'staggering'
  to avoid this, the wire tension T has to be larger than a critical value T_0 given by

$$U_0 \leq \frac{d}{lC}\sqrt{4\pi\epsilon_0 T_0}$$

with

wire length l
wire distance d
capacity per unit length for cylinder $C = \dfrac{4\pi\epsilon_0}{2\ln\left(r_a/r_i\right)}$

approximation for MWPC with distance anode-cathode $L \gg d \gg r_i$

$$C = \frac{4\pi\epsilon_0}{2\left(\frac{\pi L}{d} - \ln\frac{2\pi r_i}{d}\right)}$$

leading to

$$T_0 \geq \left(\frac{U_0 l}{d}\right)^2 4\pi\epsilon_0 \left[\frac{1}{2\left(\frac{\pi L}{d} - \ln\frac{2\pi r_i}{d}\right)}\right]^2$$

with $l = 1$ m, $U_0 = 5$ kV, $L = 10$ mm, $d = 2$ mm, $r_i = 15$ μm $\rightarrow T_0 = 0.49$ N ($\simeq 50$ g)

Stability of wire geometry II

- for horizontal wires also gravity $\rightarrow$ sag

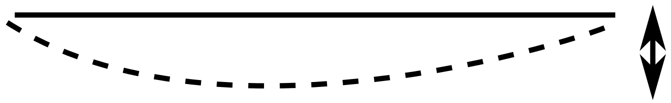

$$f = \frac{\pi r_i^2}{8} \rho g \frac{l^2}{T} = \frac{mlg}{8T}$$

gold-plated W-wire $r_i = 15\ \mu$m, T as above $\rightarrow f = 34\ \mu$m $\quad\rightarrow$ visible difference in gain

some of these problems avoided by 'straw tube chambers' (assembly of single-wire proportional counters):

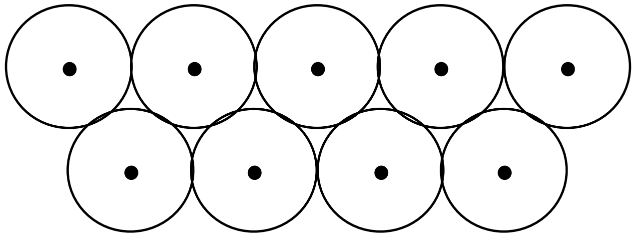

cylindrical wall = cathode
aluminized mylar foil
introduced in 1990ies

further big (!) advantage: a broken wire affects only 1 cell, not entire chamber
straw diameter: $5 - 10$ mm, can be operated at over-pressure,
space point resolution down to 160 μm (e.g. LHCb Outer Tracker)
short drift lengths: enable high rates
operation in magnetic field without degradation of resolution
concept employed in several LHC detectors

- can wires be avoided entirely?

ease of construction
stability
. . .
anode can actually be realized by microstructures on dielectrics

example: microstrip gas detector (developed in 1990ies)

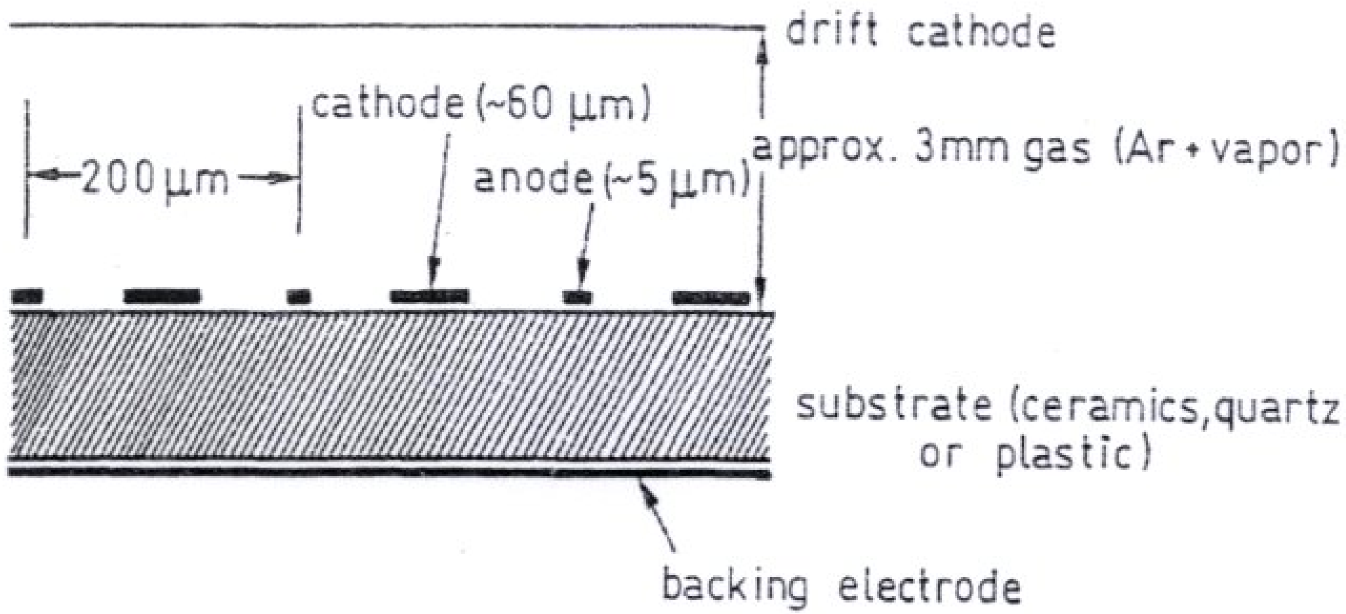

Schematic arrangement of a microstrip gas detector schematics of a **microstrip gas chamber**

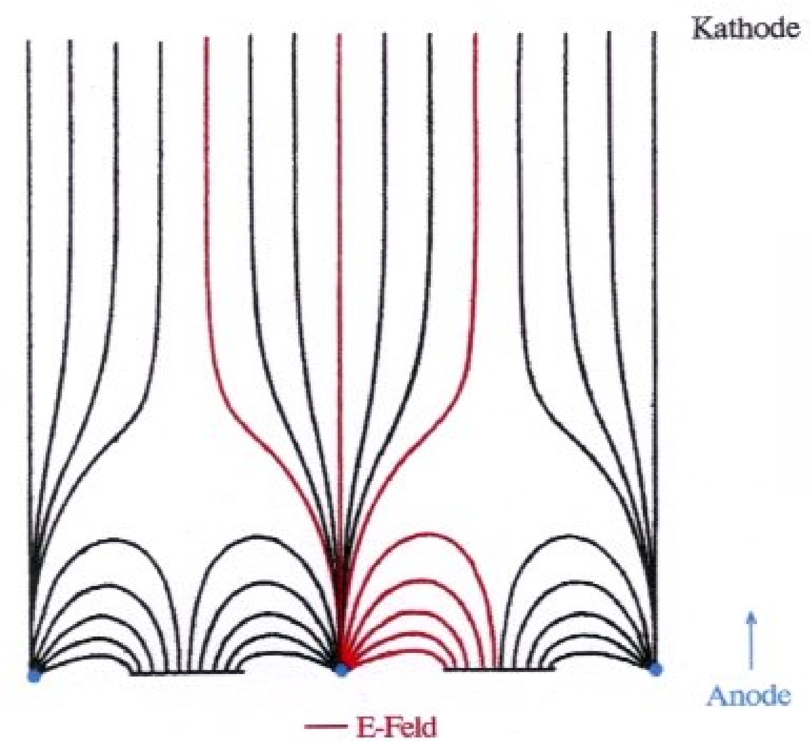

directly above anode strip high density of field lines

advantages

- ions drift only 100 μm
- high rate capability without build-up of space charge
- resolution

fine structures can be fabricated by electron lithography on ceramics, glass or plastic foil on which a metal film was previously evaporated.

problems

charging of isolation structure

$\rightarrow$ time-dependence of gas gain

$\rightarrow$ sparks, destruction of anode structure, corrosion of insulator

basically not a succeessful concept - lifetime of detector too limited

Gas electron multiplier

a possible solution:
pre-amplification with GEM foil

GEM: gas electron multiplier
invented by F. Sauli (CERN) ($\sim$1997)

allows reduced electric field
in vicinity of anode structures.

but: ease of construction again partly
eliminated and danger of discharge
on foil (huge capacitance)

upgrade of Alice TPC for 50 kHz PbPb
collisions based on quadruple GEM layers
challenge: to keep ion feedback below 1 %

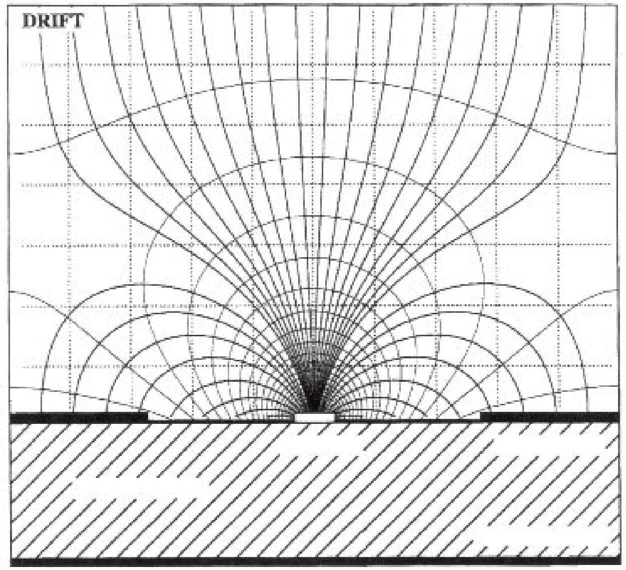

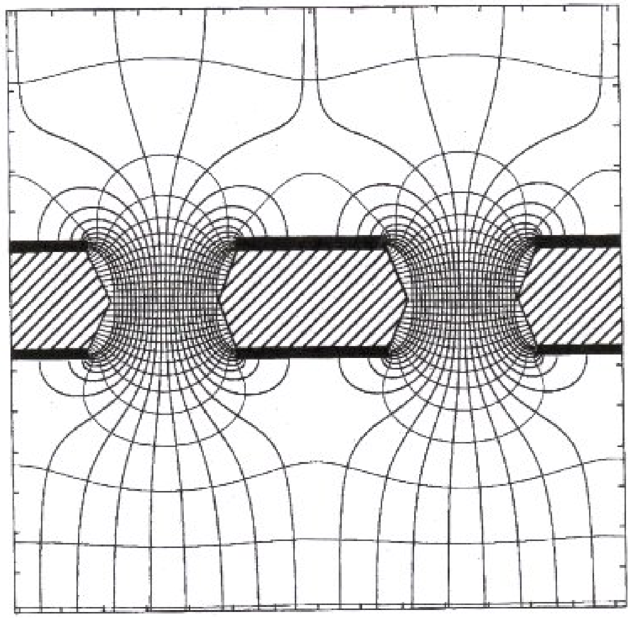

3.6 Drift chambers

invented by A. Walenta, J. Heintze in 1970 at Phys. Inst. U.Heidelberg (NIM 92 (1971) 373)

Principle

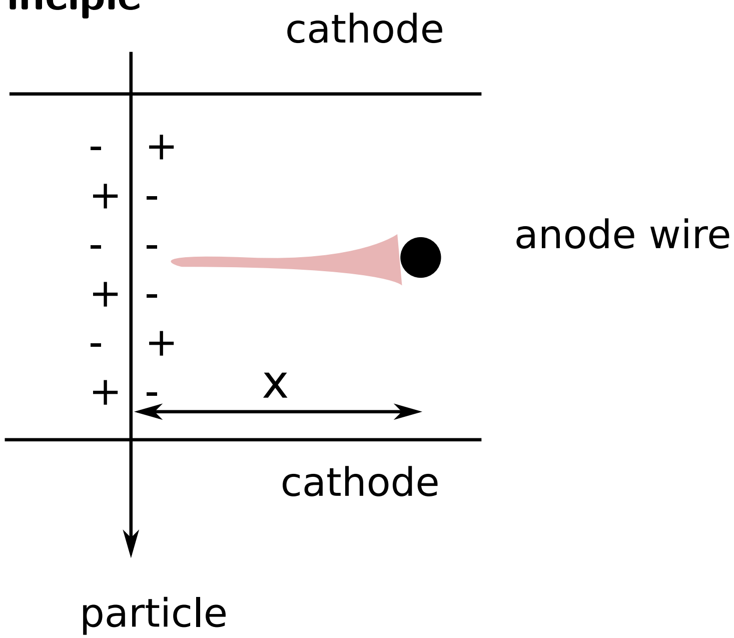

time measurement:

$$x = v_D^- \cdot \Delta t$$

v_D^-: drift velocity of electrons

or, in case drift velocity changes along path

$$x = \int v_D^-(t)\mathrm{d}t$$

needs well defined drift field $\rightarrow$ introduce additional field wires in between anode wires.
but: In that case number of anode wires can be reduced in comparison to MWPC at improved spatial resolution

$$\left.\begin{array}{l} v_D^- \simeq 5 \text{ cm}/\mu\text{s} \\ \text{time resolution of front end electronics } \sigma_t \simeq 1 \text{ ns} \end{array}\right\} \quad \sigma_x \simeq 50\ \mu\text{m is possible}$$

but the resolution is affected by diffusion of drifting electrons and statistical fluctuations in primary ionization (in particular in vicinity of wire).

factors affecting spatial resolution in a drift chamber:

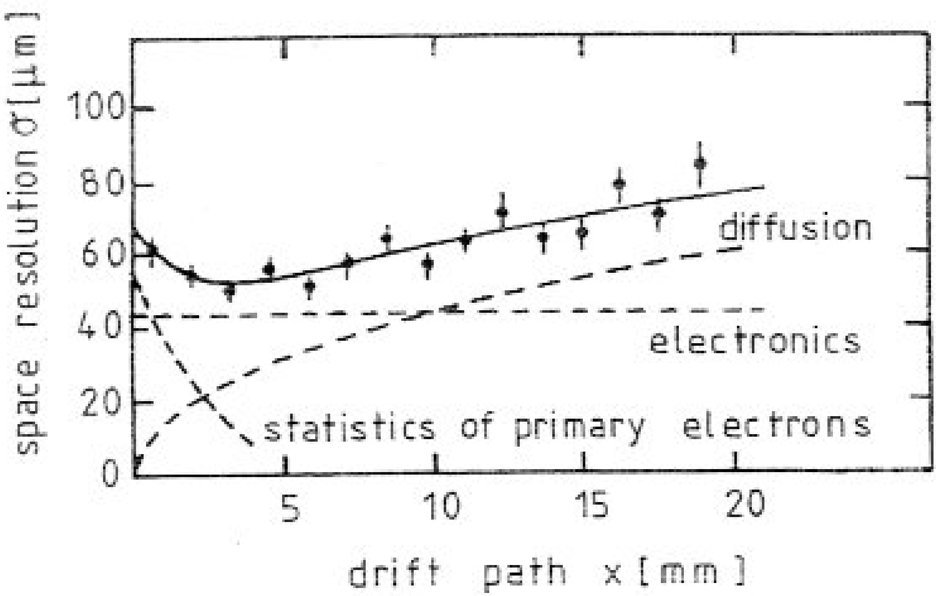

spatial resolution in a drift chamber as a function of the drift path

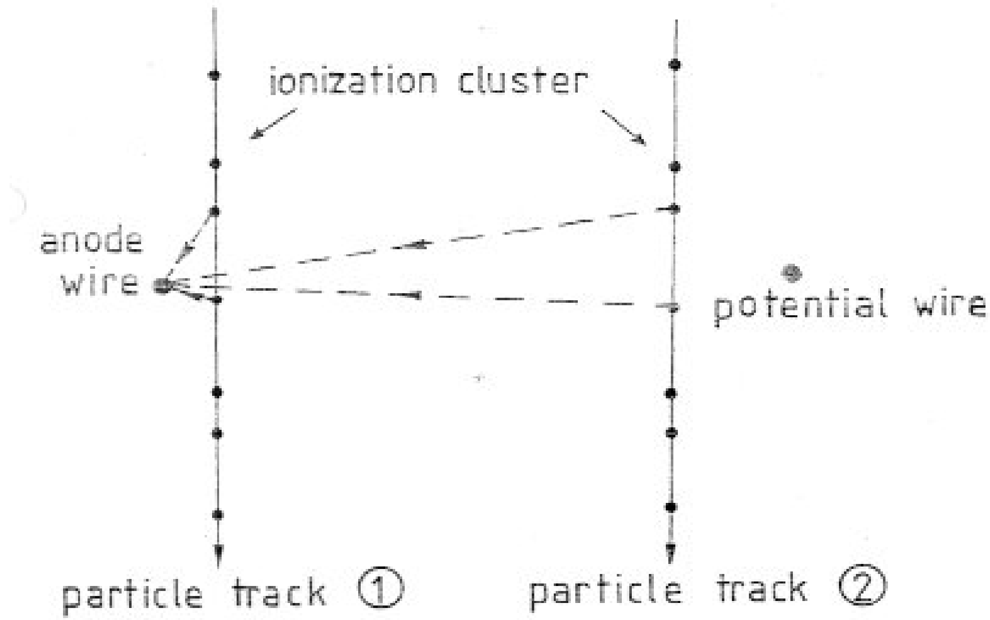

illustration of different drift paths for 'near' and 'distant' particle tracks to explain the dependence of the spatial resolution on the primary ionization statistics

Difficulty: time measurement cannot distinguish between particle passing to the left or to the right of the anode wire $\rightarrow$ 'left-right ambiguity'

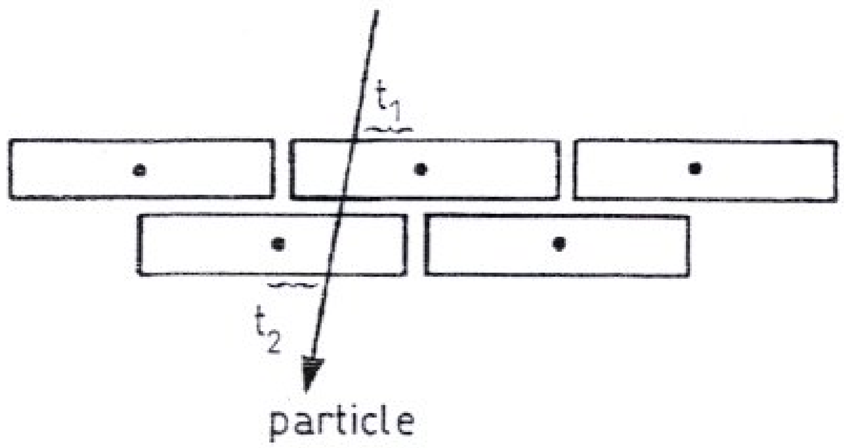

resolution of the left-right ambiguity in a drift chamber

need 2 layers displaced relative to each other by half the wire distance: 'staggered wires'

How to achieve field quality good enough for drift chamber?

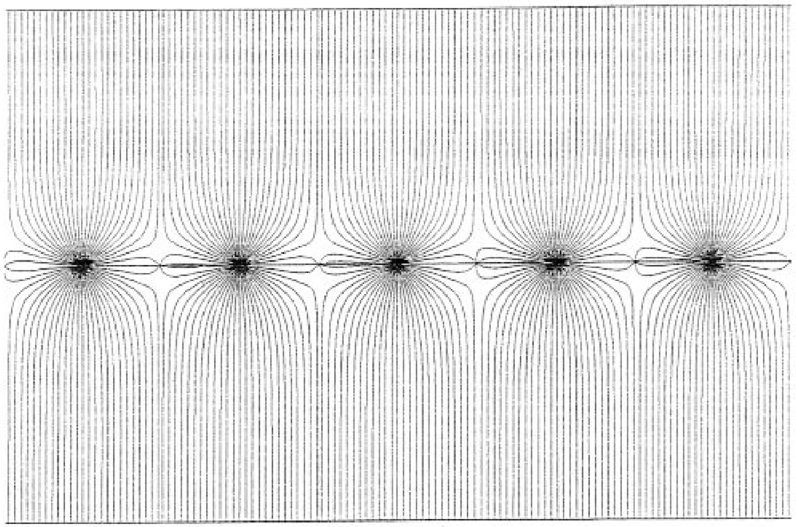

in a MWPC in between anode wires there are regions of very low electric field (see above)

the introduction of additional **'field wires'** at negative potential relative to anode wires strongly improves the field quality

essential for drift chamber where spatial resolution is determined by drift time variations and not by segmented electrode structure

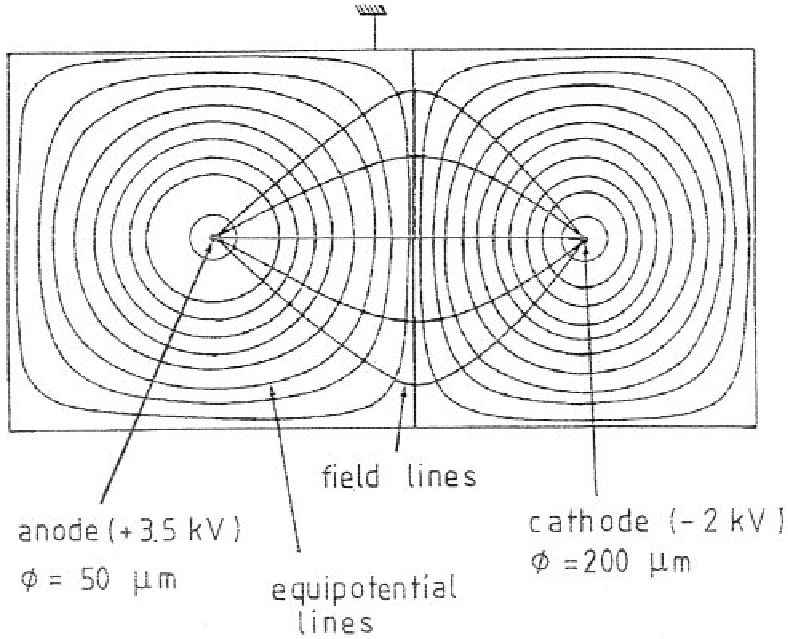

one can build **very large** drift chambers; in this case one introduces a voltage divider by cathode strips connected via resistors, very few or even only one wire.

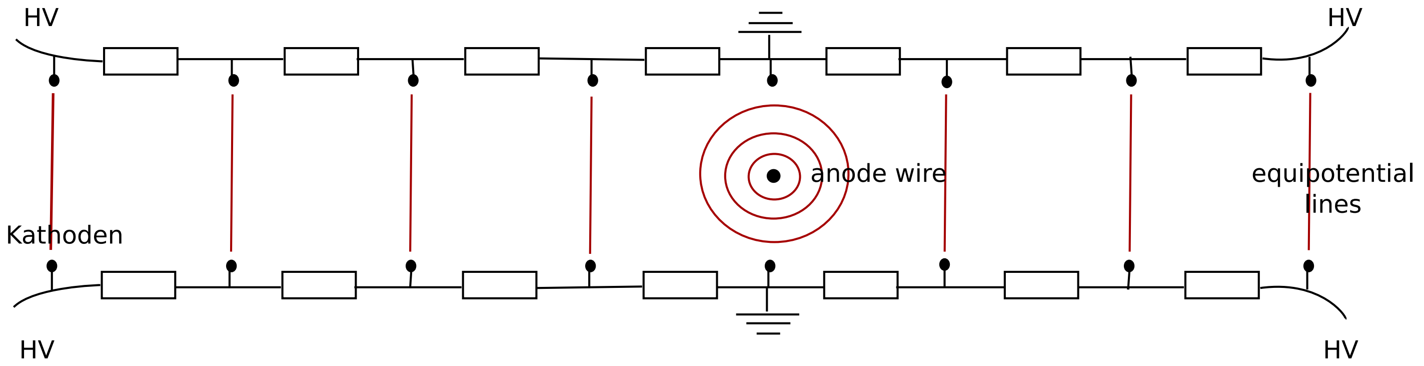

space point resolution limited by mechanical tolerance

for very large chambers
$(100 \times 100\ \text{cm}^2)$ $\simeq 200\ \mu$m

for very small chambers
$(10 \times 10\ \text{cm}^2)$ even $\simeq 20\ \mu$m

but: hit density has to be low!

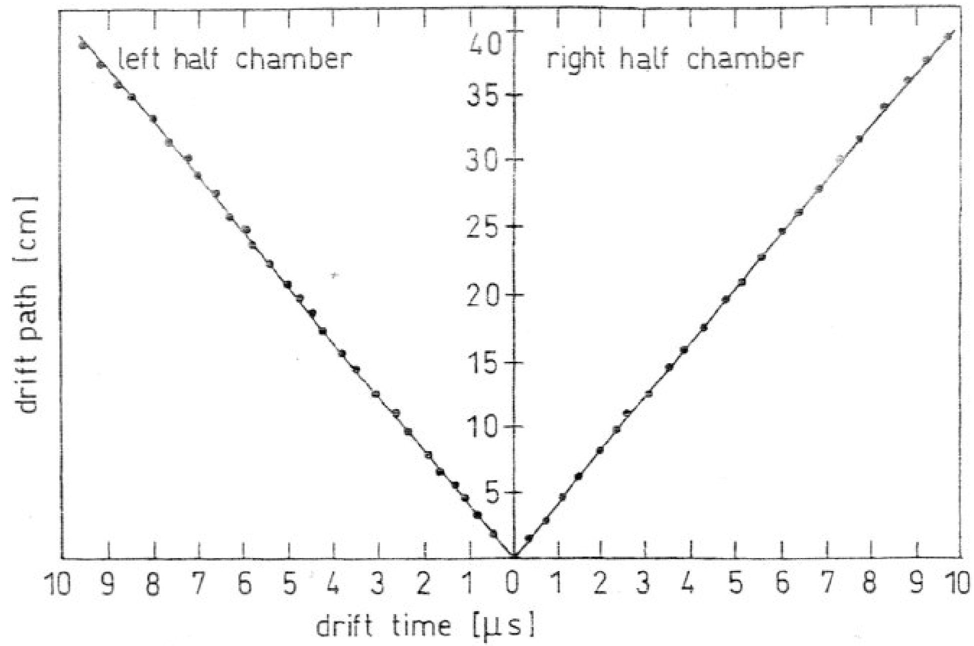

drift time - space relation in a large drift chamber $(80 \times 80\ \text{cm}^2)$ with only one anode wire (Ar + iso-butane 93/7)

field can even be formed by charging up of insulating chamber wall with ions
after some charging time ions cover insulating layer, no field line end there

Resistive plate counter:

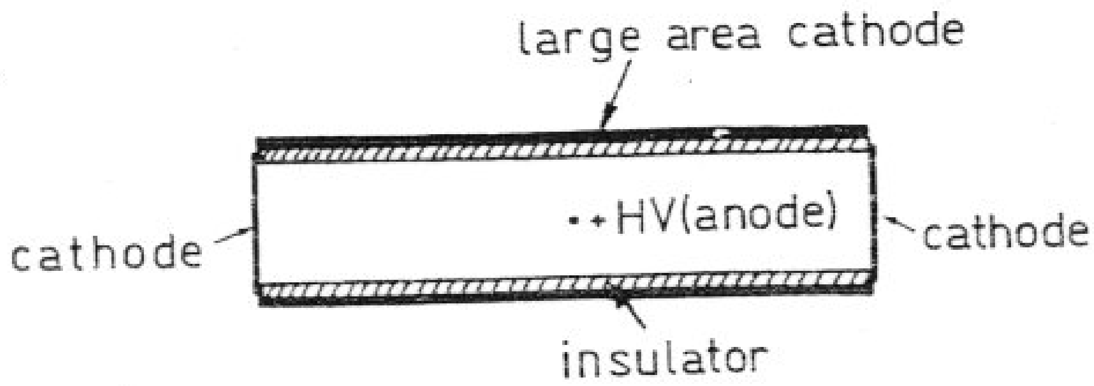

Principle of construction of an electrodeless drift chamber

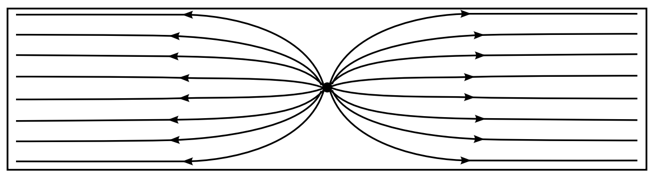

After charging the insulating layer with ions

3.7 Cylindrical wire chambers

in particular for experiments at storage rings (colliders) to cover maximum solid angle

- initially multi-gap spark chambers, MWPC's
- later cylindrical drift chambers, jet chambers
- today time projection chambers (TPC)

generally these cylindrical chambers are operated in a magnetic field $\rightarrow$ measurement of radius of curvature of a track $\rightarrow$ momentum (internally within one detector)

$$p\ (\mathrm{GeV/c}) = 0.3 \cdot B\ (\mathrm{T}) \cdot \rho\ (\mathrm{m})$$

Principle of a cylindrical drift chamber I

principle of a cylindrical drift chamber: wires in axial direction (parallel to colliding beams **and** magnetic field)

alternating anode and field wires

- one field wire between 2 anode wires
- cylindrical layers of field wires between layers of anode wires → nice drift cells

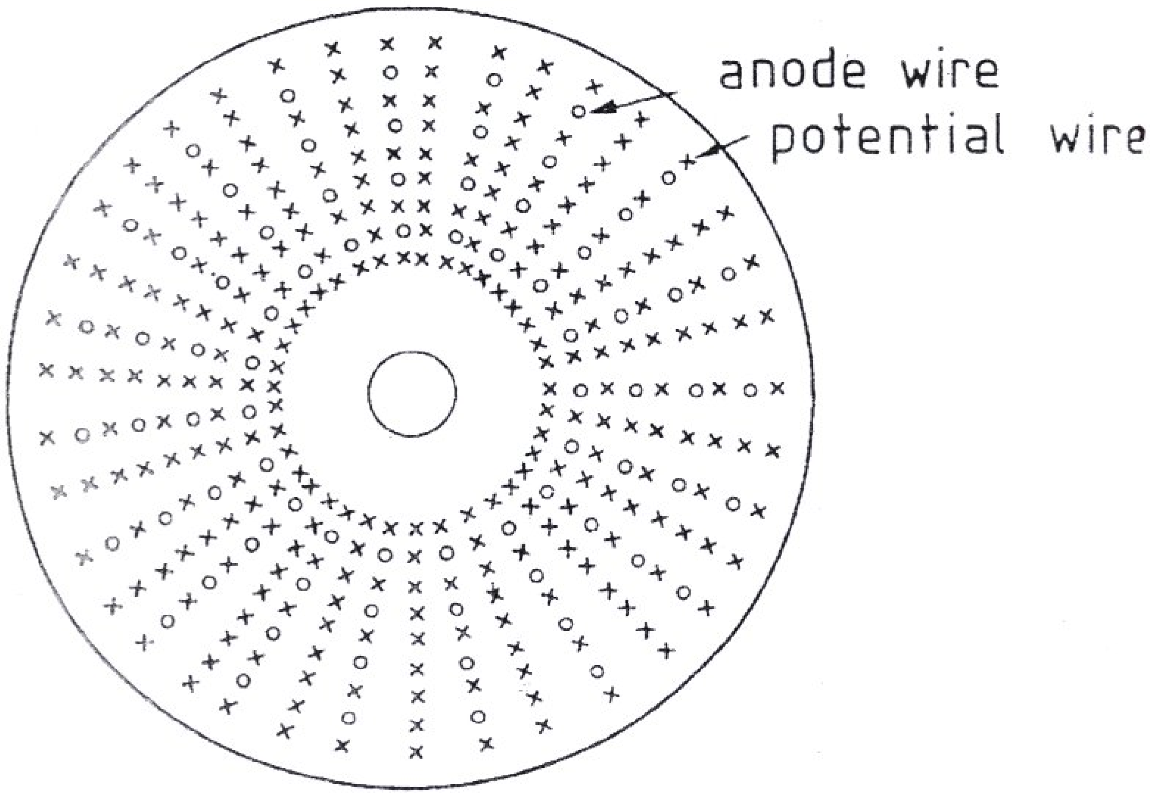

Principle of a cylindrical drift chamber II

different drift cell geometries:

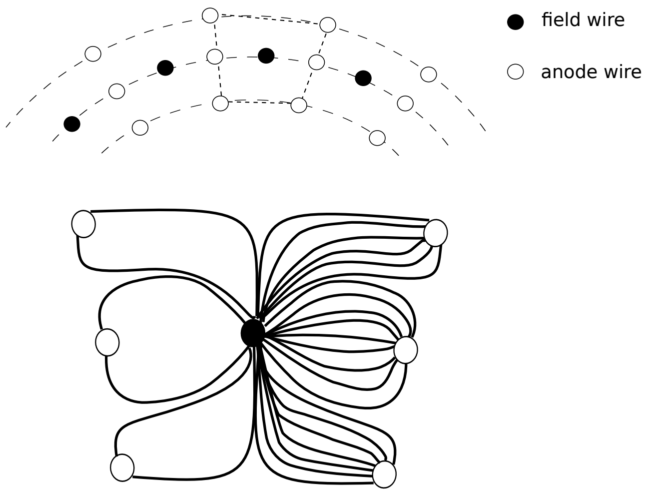

open drift cell

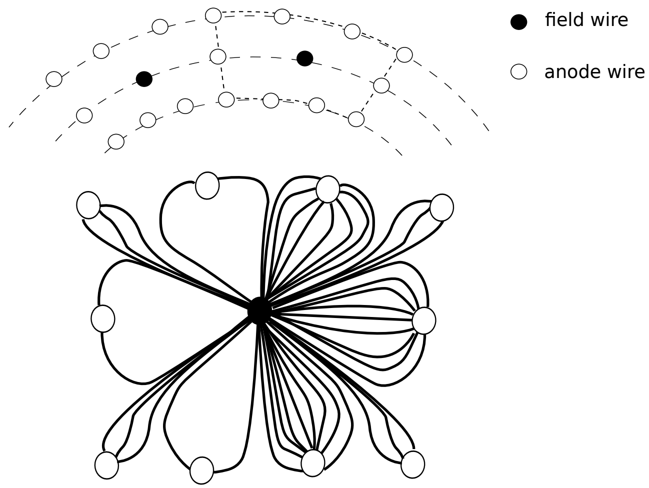

closed drift cell

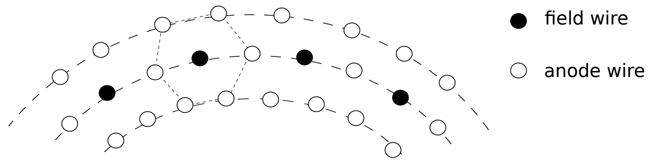

also hexagonal drift cell

always thin anode wires ($\varnothing \simeq 30\ \mu$m) and thicker field wires ($\varnothing \simeq 100\ \mu$m), generally field quality better for more wires per drift cell, but:

- more labor-intensive construction
- wire tension enormous stress on end plates, e.g. for chamber with 5000 anode and 15000 field wires $\rightarrow$ 2.5 t on each endplate

Determination of coordinate along the wire

- current measurement on both ends of anode wire
  charge division, precision about 1% of wire length

$$z \propto \frac{I_1 - I_2}{I_1 + I_2}$$

- time measurement on both ends of wire
- 'stereo wires': layer of anode wires inclined by small angle γ ('stereo angle')
  $\rightarrow \sigma_z = \sigma_x / \sin\gamma$

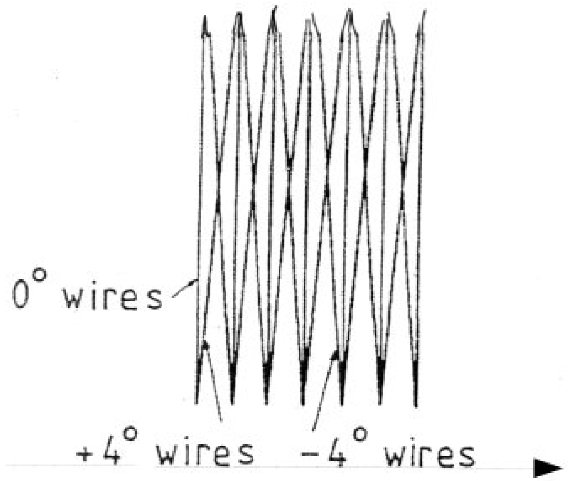

illustration of the determination of the coordinate along the anode stereo wires in general drift field E perpendicular to magnetic field $B \rightarrow$ Lorentz angle for drifting charges

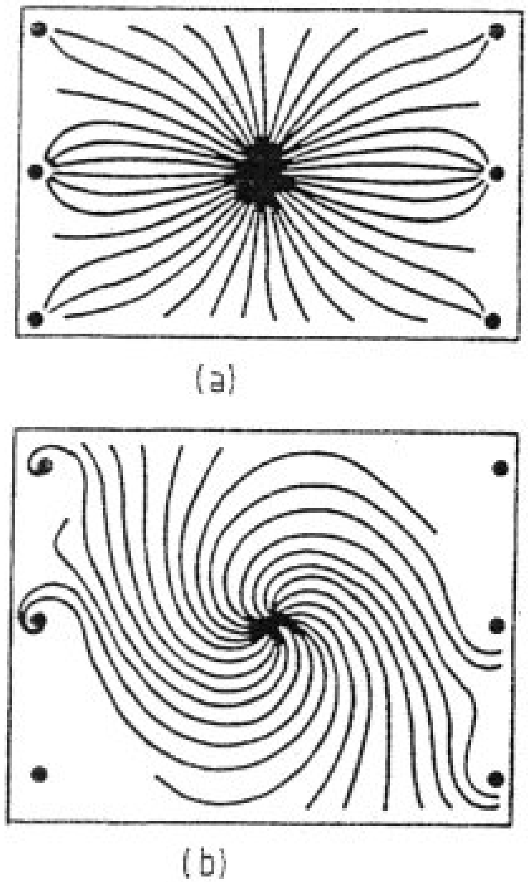

drift trajectories in an open rectangular drift cell a) without and b) with magnetic field

3.8 Jet drift chambers

large drift cells

optimize number of measurements per track

(typically 1/cm)

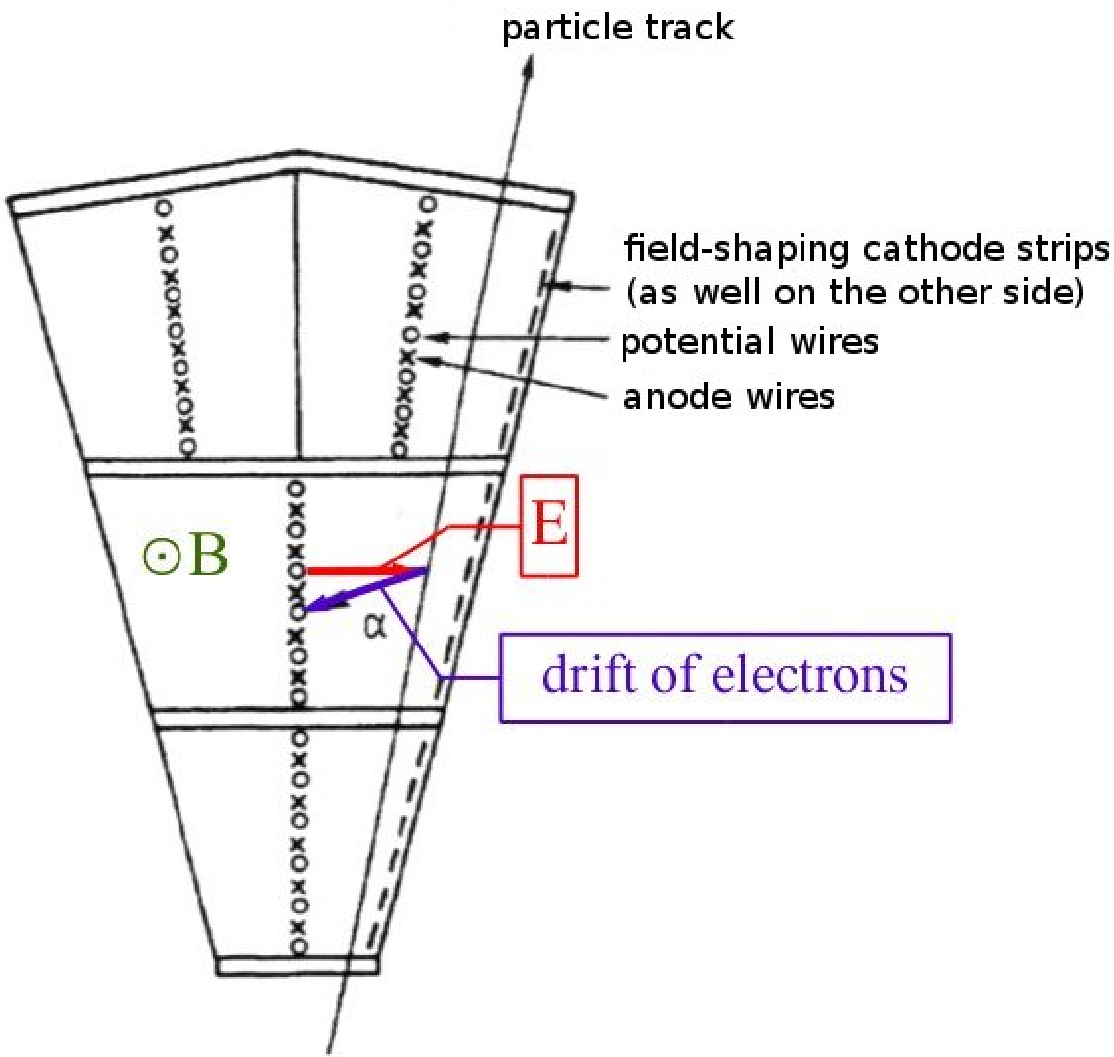

example: JADE jet chamber for PETRA, built by J.Heintze et al. Phys. Inst. U. Heidelberg
length: 2.34 m, radial track length: 57 cm, 47 measurements per track
$\sigma_{r\phi} = 180\ \mu$m, $\sigma_z = 16$ mm

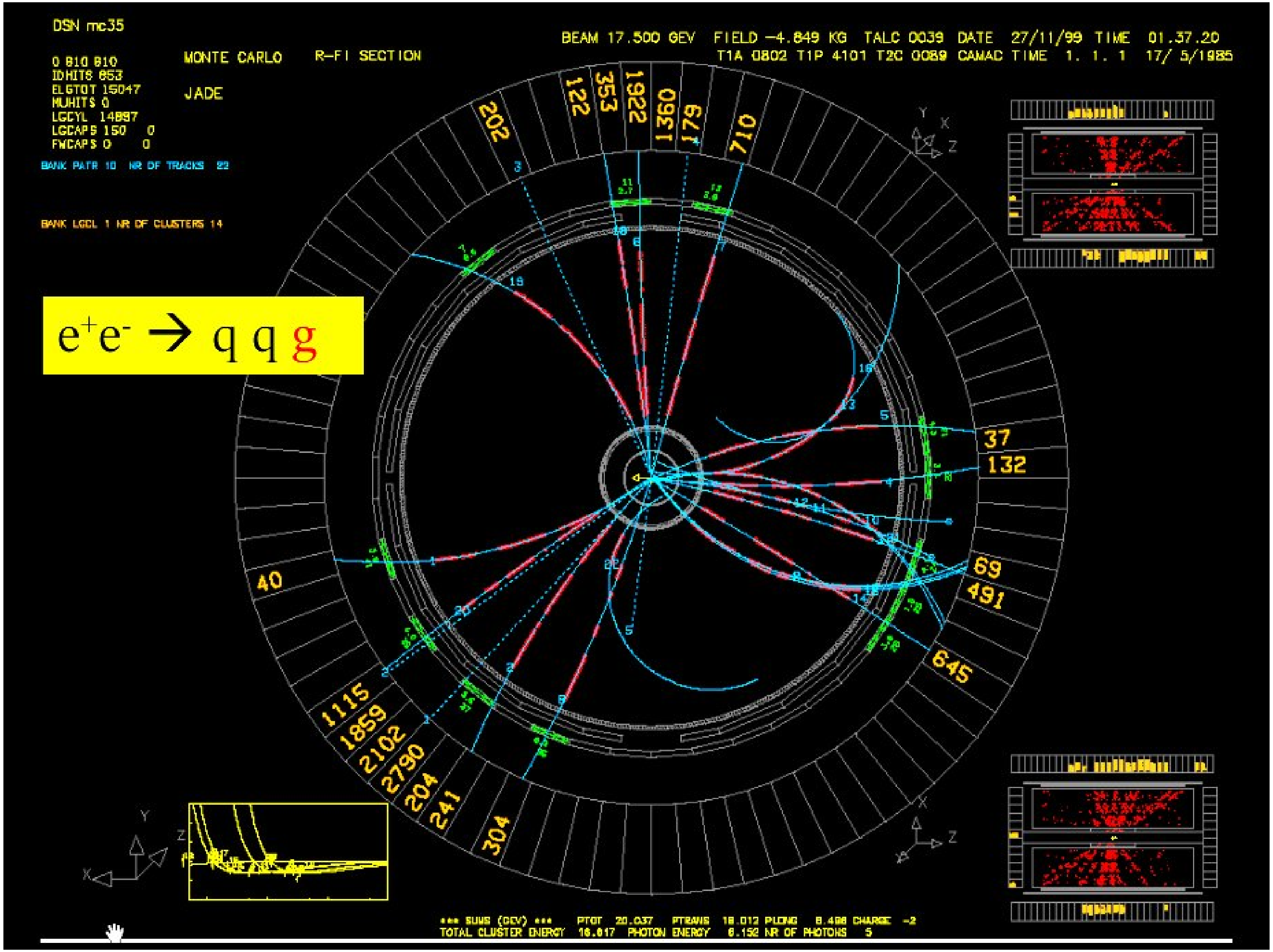

3-jet event by JADE – measurements taken at PETRA $\rightarrow$ discovery of gluon

another example: OPAL at CERN LEP: central tracking chamber built by team from Phys. Inst. Heidelberg – Heintze, Wagner, Heuer, . . .
length: 4 m, radius: 1.85 m, 159 measurements per track, gas: $Ar/CH_4/C_4H_{10}$ at 4 bar
$\sigma_{r\phi} = 135\ \mu$m, $\sigma_z = 60$ mm

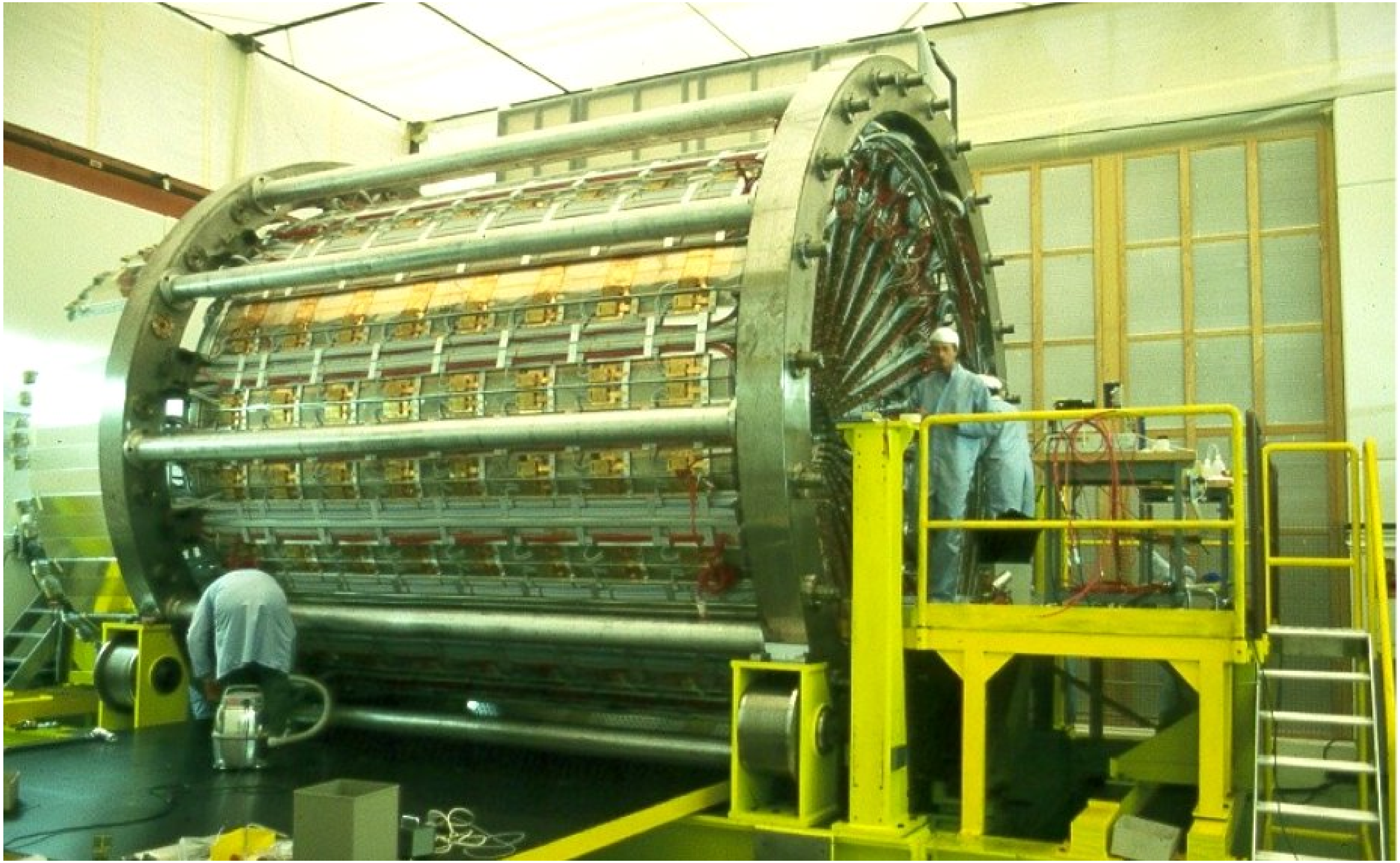

interior of jet chamber of OPAL

application for heavy ion collisions: FOPI (experiment at SIS at GSI):
central drift chamber (CDC), D. Pelte and N. Herrmann Phys. Inst. U.Heidelberg

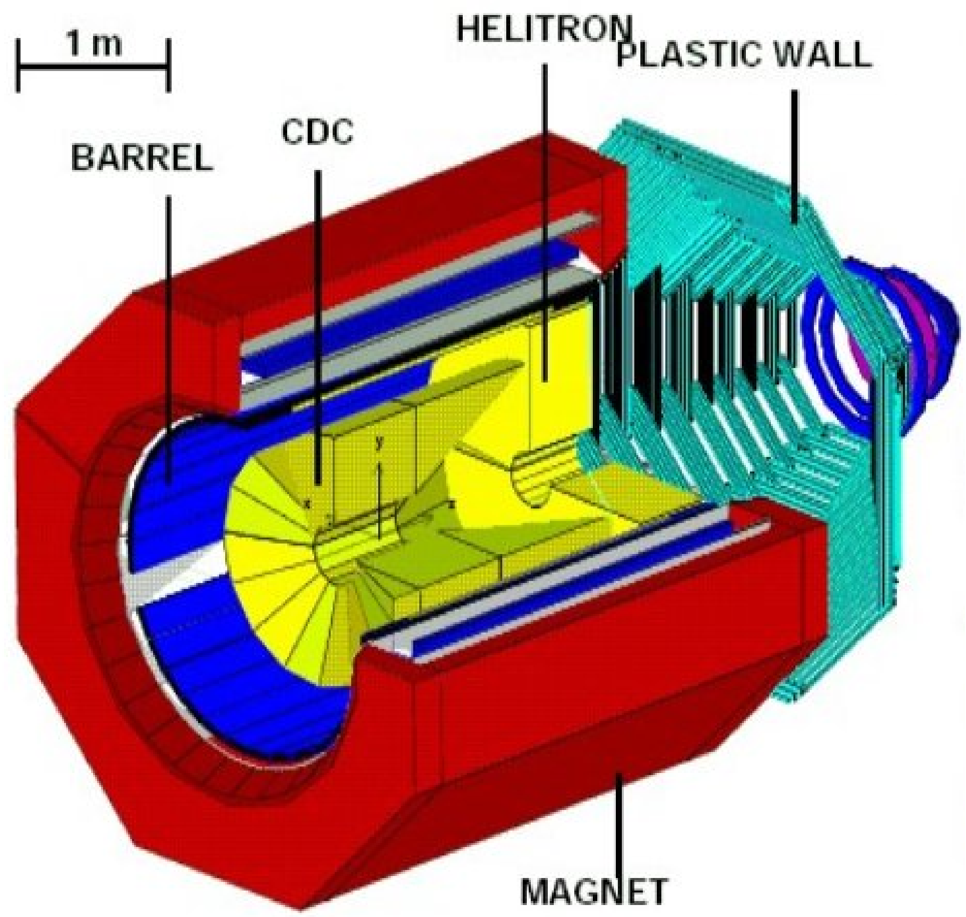

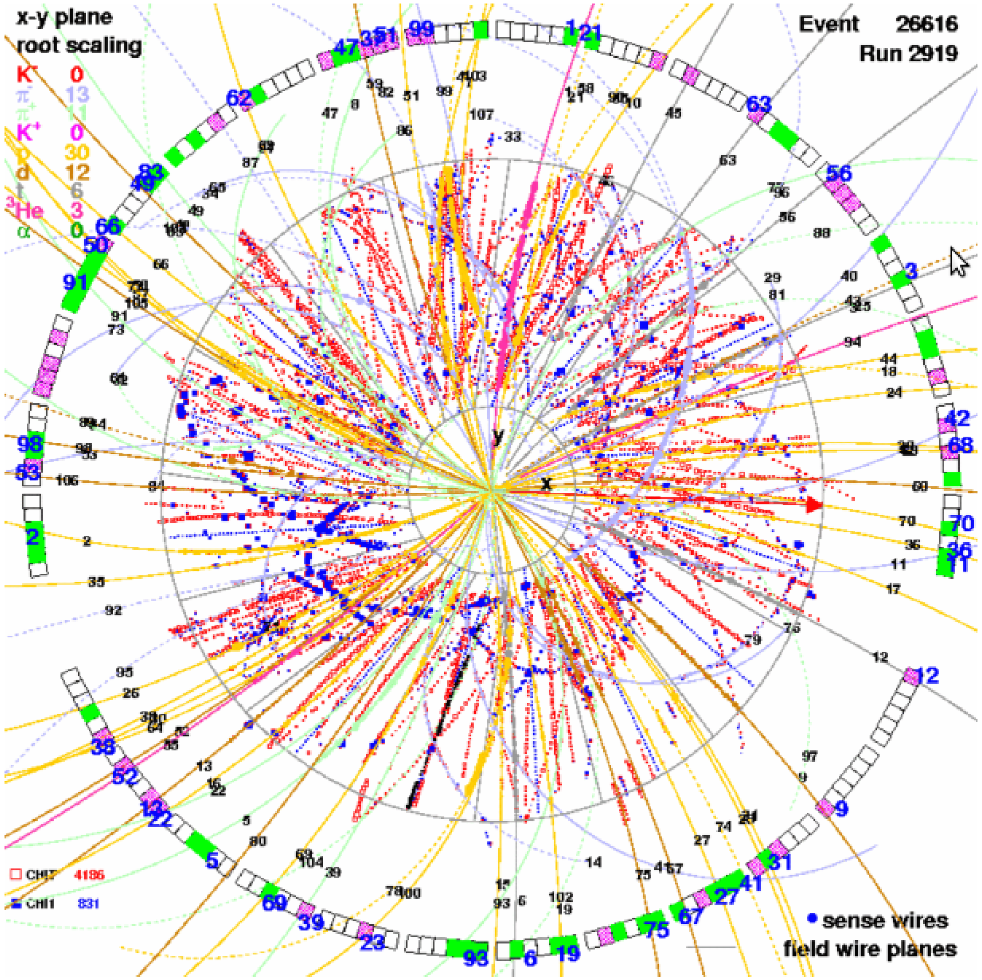

3.9 Time Projection Chamber TPC

3-dimensional measurement of a track – 'electronic bubble chamber'
invented by D. Nygren in 1974 at Berkeley

(mostly) cylindrical detector
central HV cathode
MWPCs at the endcaps of the cylinder
electrons drift in homogenous electric fields towards MWPC, where arrival time and point and amount of charge are continuously sampled (flash ADC)
generally with $B \parallel E \rightarrow$ Lorentz angle $= 0$

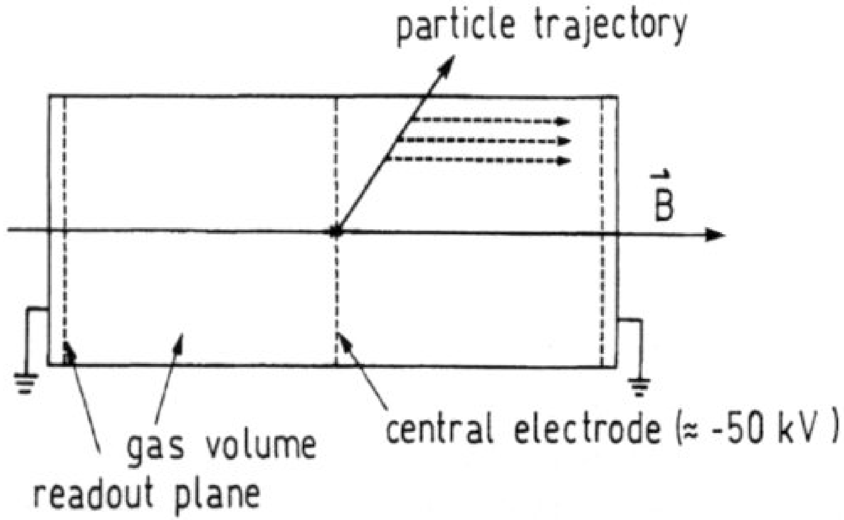

Working principle of a TPC

advantages:

- complete track determination within one detector → good momentum measurement
- relatively few wires (mechanical advantage)
- since also charge is measured: particle identification via dE/dx
- drift parallel to B → transverse diffusion suppressed by factors $10 - 100$ (see above)

disadvantages

- drift time: relatively long - tens of microseconds → not a high rate detector
- large data volume

principle of operation of a TPC

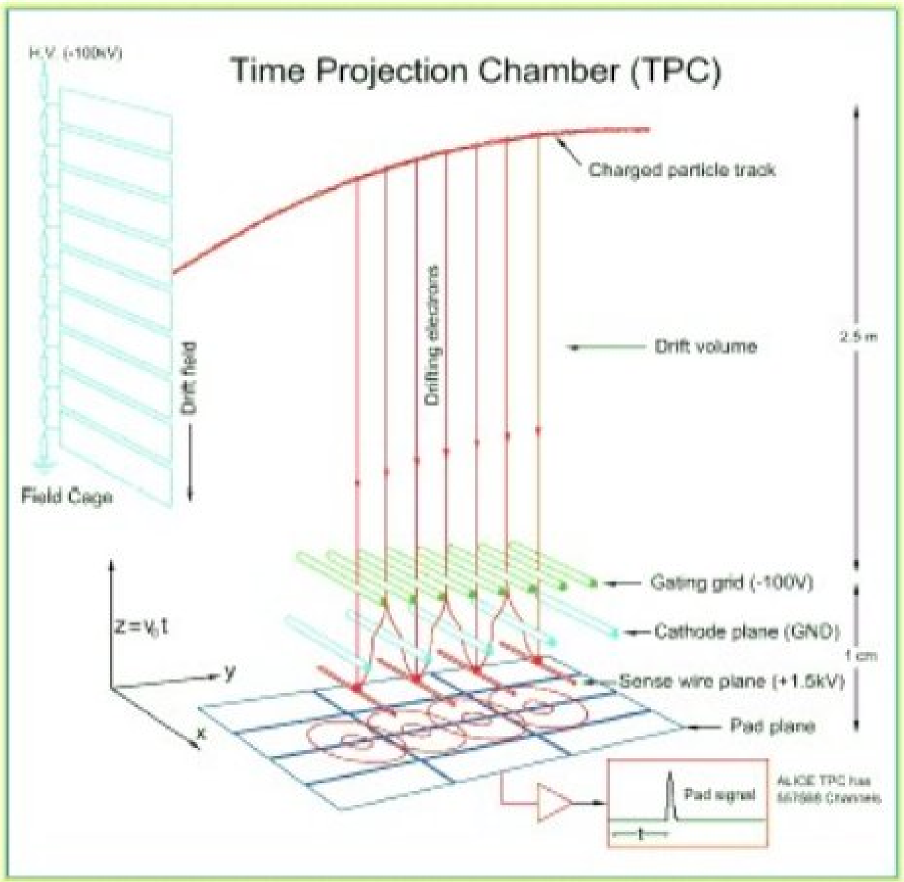

continuously sample induced charge or current signals in a MWPC at end of long drift path

z-dim given by drift time
x-dim given by charge sharing of cathode pads
y-dim given by wire/pad number

truly 3-dimensional measurement of ionization points of entire track and in fact of many tracks simultaneously

typical resolution:
z: mm
$r\phi$ or x: 150–300 μm
y: mm
d$E/$dx: $5 - 10\%$, trick:
kill Landau tail by evaluating truncated mean

challenges:

- long drift path (attachment, diffusion, baseline)
- large volume (precision)
- large voltages (discharges)
- extreme load in Pb+Pb collisions
  space charge in drift volume
  leads to distortion of $\vec{E}$
  gating grid opened (fast ~ 1 μs) for triggered events only, otherwise opaque ($\pm\Delta V$)

serious difficulty:
space charge effects since also ions have long drift path and move factor 1000 more slowly, positive ions change effective E-field in drift region, most (5000:1) come from amplification region

trick: invention of gating grid

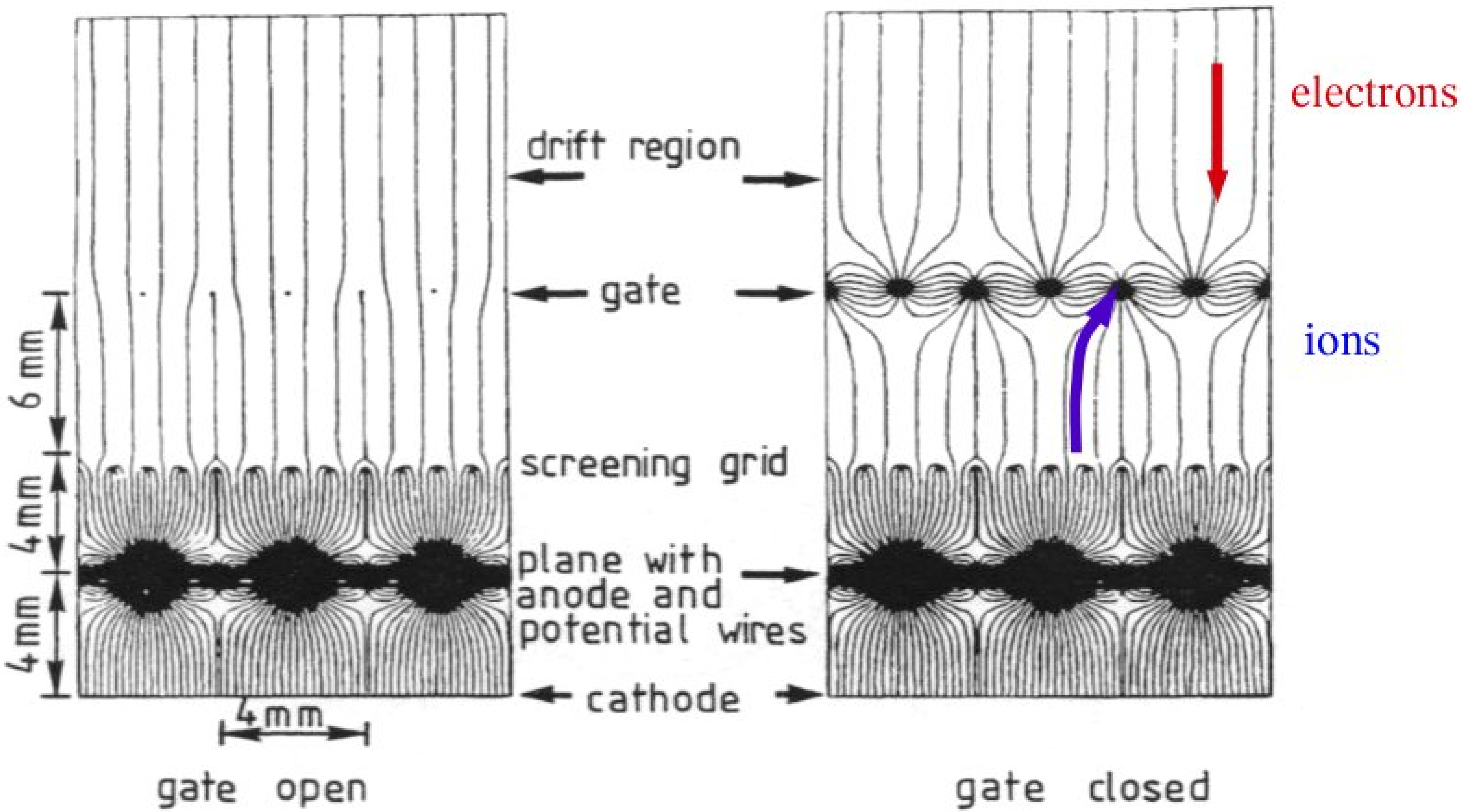

upon interaction trigger switch gating grid to ‘open’ for max drift time, then close again
→ all ions from amplification drift toward gating grid and do not enter drift region.

example: the ALICE TPC for LHC Pb + Pb collisions

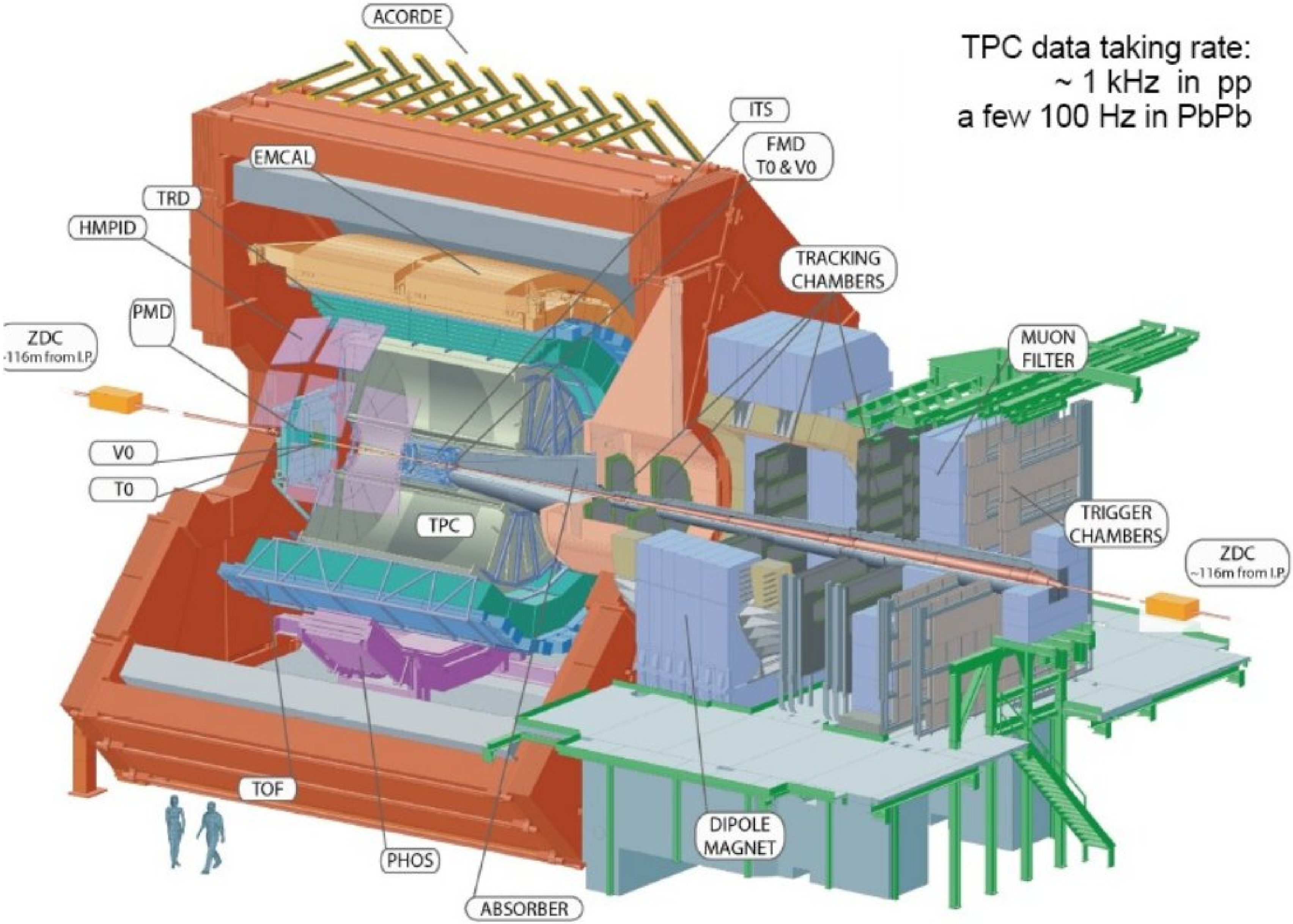

TPC data taking rate:
~ 1 kHz in pp
a few 100 Hz in PbPb

example: the ALICE TPC for LHC Pb + Pb collisions

the challenge:
identification and reconstruction of 5000 (up to 15000) tracks of charged particle in one event

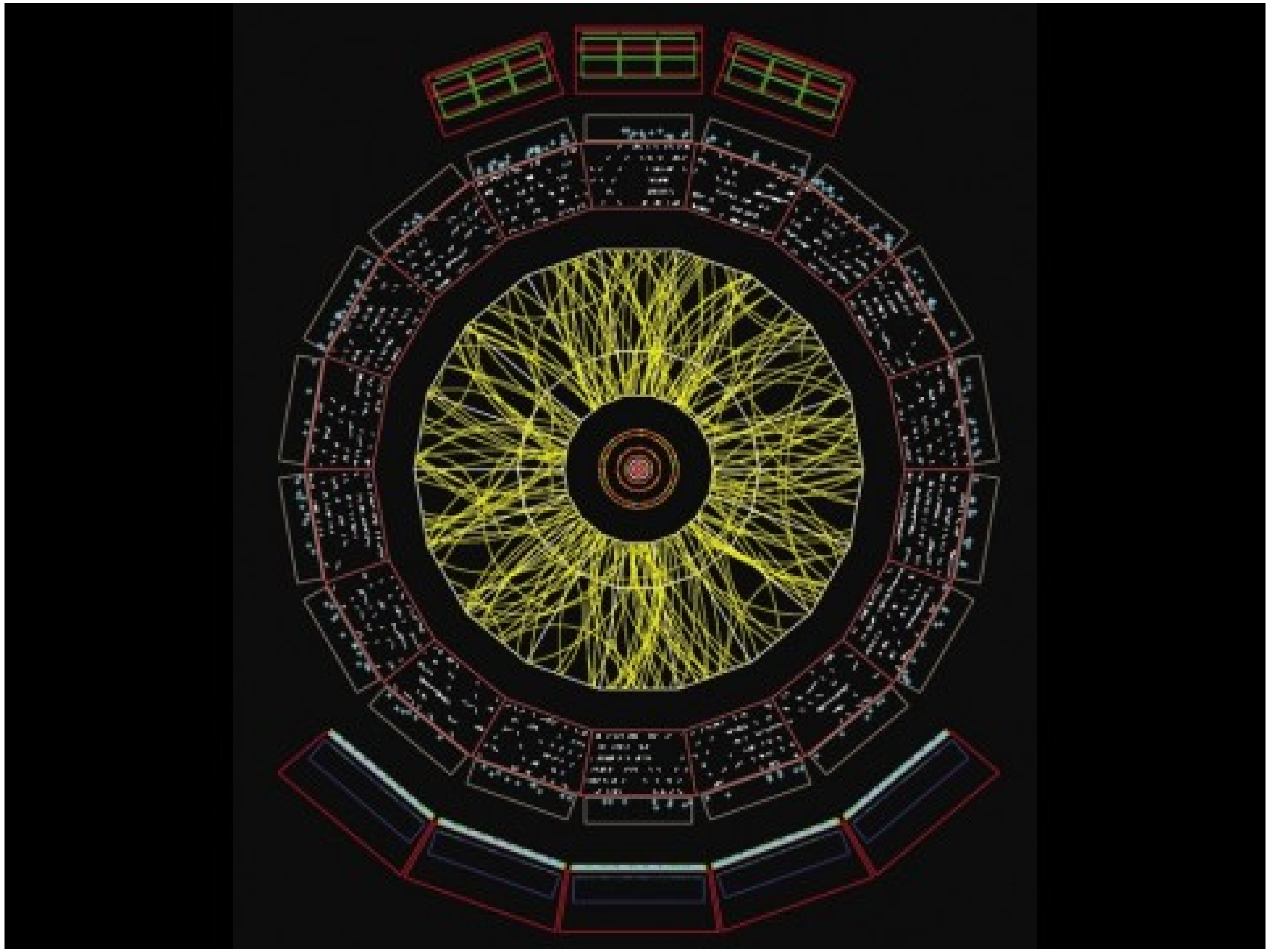

cut through central barrel of ALICE:
tracks of charged particles in a 1 degree segment in θ (1% of all tracks)

example: the ALICE TPC for LHC Pb + Pb collisions

challenges:

- very high multiplicity and desire for very good resolution
  - space charge
    - $\rightarrow$ optimize gating grid (even 1% leakage would be deadly)
    - $\rightarrow$ rate limitation, good luminosity monitoring
  - occupancy, want to keep it at inner radius below 40%
    - $\rightarrow$ optimize pad sizes and shapes (4 x 7.5 mm, total 558 000)
    - $\rightarrow$ 1000 time samples, 159 samples radially
- momentum resolution
  - low multiple scattering, small diffusion
    - $\rightarrow$ low Z cold gas Ne/CO_2 coupled with small drift cells (occupancy)
      temperature control to 0.1 K (even resistors need to be cooled)
      need to know electric field to 10^{-4} precision
    - $\rightarrow$ small amount of electron-ion pairs
    - $\rightarrow$ high gas gain of 10000
- event rate
  - limited by drift time (cold gas and not more than 100 kV, 90 μs)
  - data volume (1 central collision 60 MByte, can't store much more than a few GByte/s)

technical specs:

$r = 0.85 - 2.47$ m, length 2 x 2.5 m, material budget 3.5% X_0

approximate performance:

$\sigma(p)/p = 1\%\ p$, efficiency 97%, $\sigma_{\mathrm{d}E/\mathrm{d}x}/(\mathrm{d}E/\mathrm{d}x) \leq 6\%$, 100-200 Hz event rate inside the field cage:

The TPC (Time Projection Chamber) – 3D reconstruction of up to 15 000 charged particle tracks per event

with 95 m^3 largest TPC ever built

central HV electrode 100 kV

field cage: voltage divider with E-field homogeneity of 10^{-4}

in the end caps: 72 multi-wire proportional chambers with cathode pad read-outs

560 million pixels!
precision better than 500 μm in all 3 dimensions, 159 points per track

Construction of multi-wire proportional chambers, 3 wire planes plus cathode pad read-out

at GSI, Phys. Inst. U. Heidelberg. U. Bratislava

challenge: small spacings, high gas gain, high geometrical precision

Pad Plane: 5504 pads (4 x 7.5 mm)

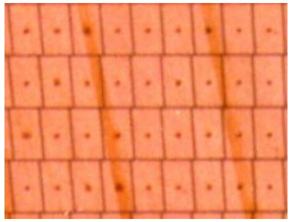

Close-up on the pads

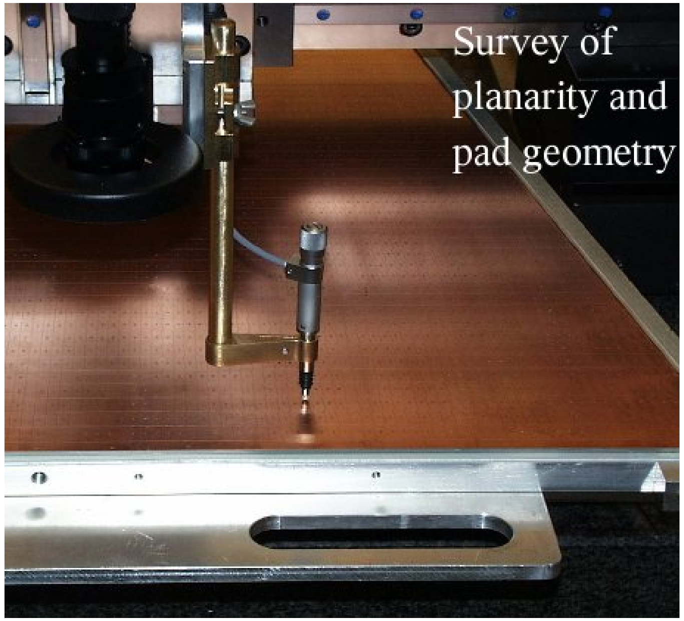

TPC Front End Electronics – 2 ASICS developed at Phys. Inst. U.Heidelberg and CERN, cooperation with ST Microelectronics

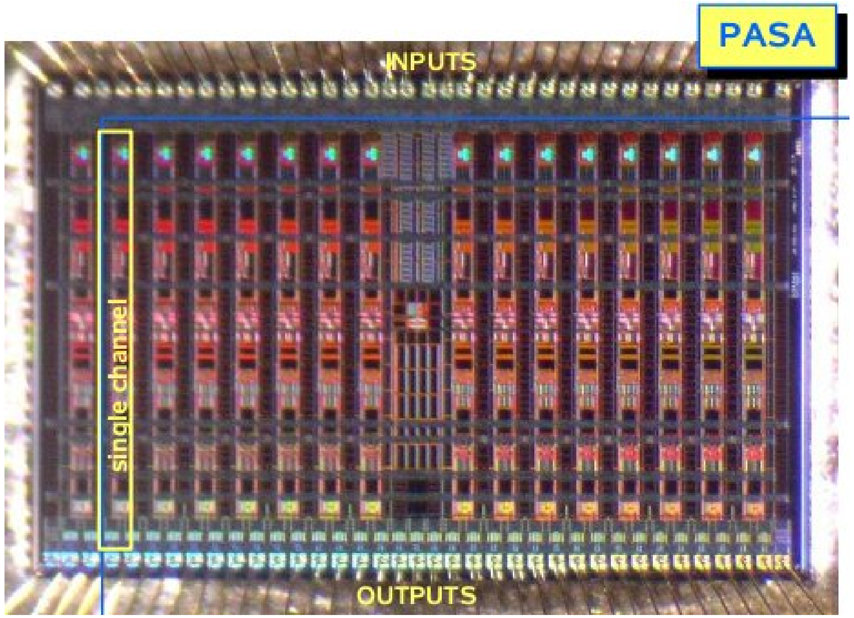

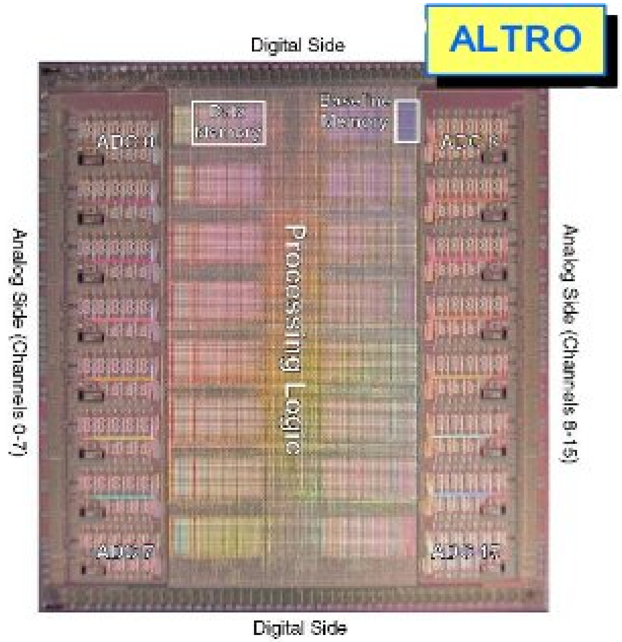

excellent performance (now also used by STAR at RHIC)

PASA: low noise preamplifier/shaper

ALTRO: commercial ADC (ST) **in same custom chip** with digital signal processing

electronics needs to be clever:

- zero suppression
- base line restoration
- etc. $\rightarrow$ put a lot of intelligence into digital chip after ADC, the ALTRO

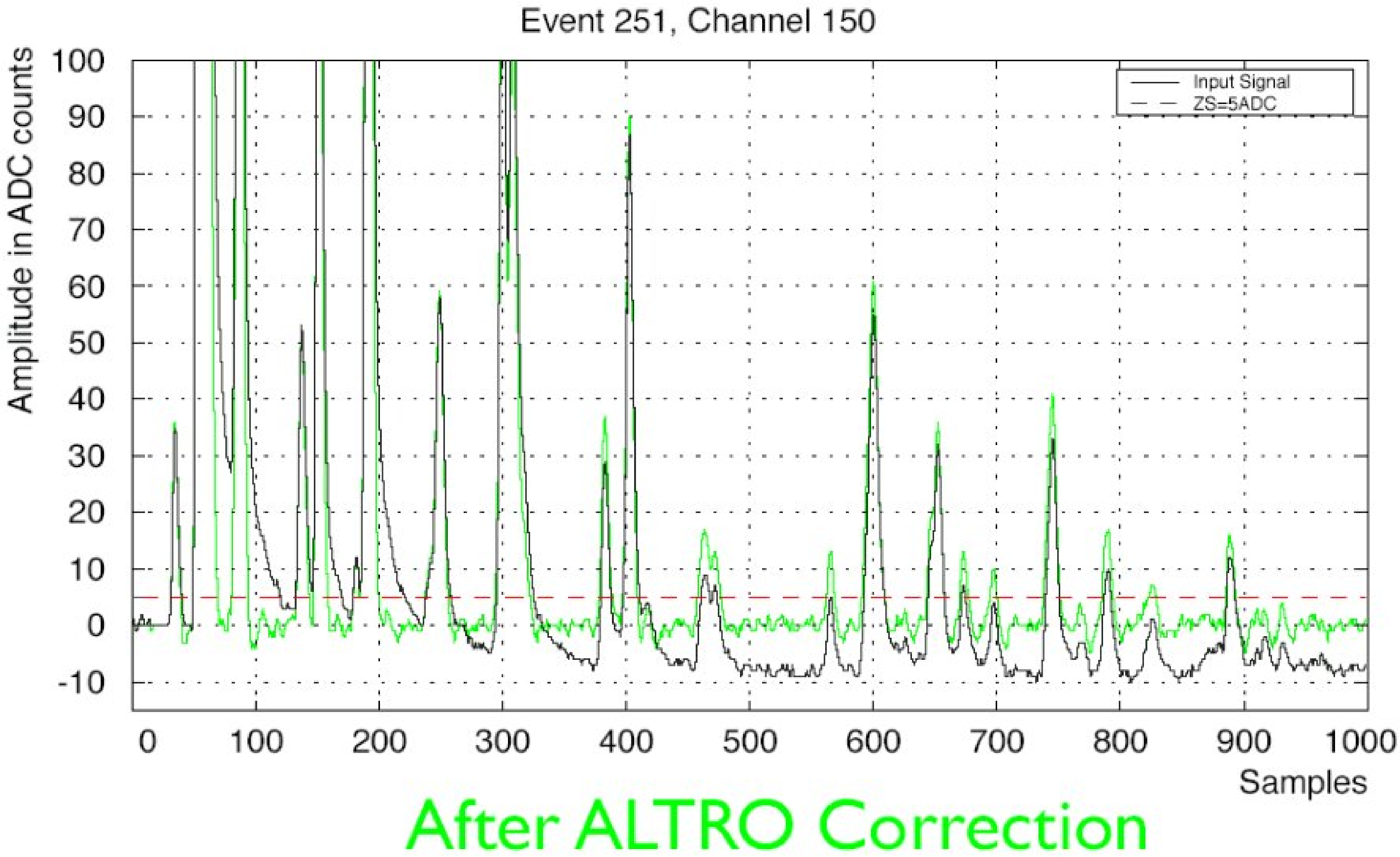

ALICE TPC: drift velocity

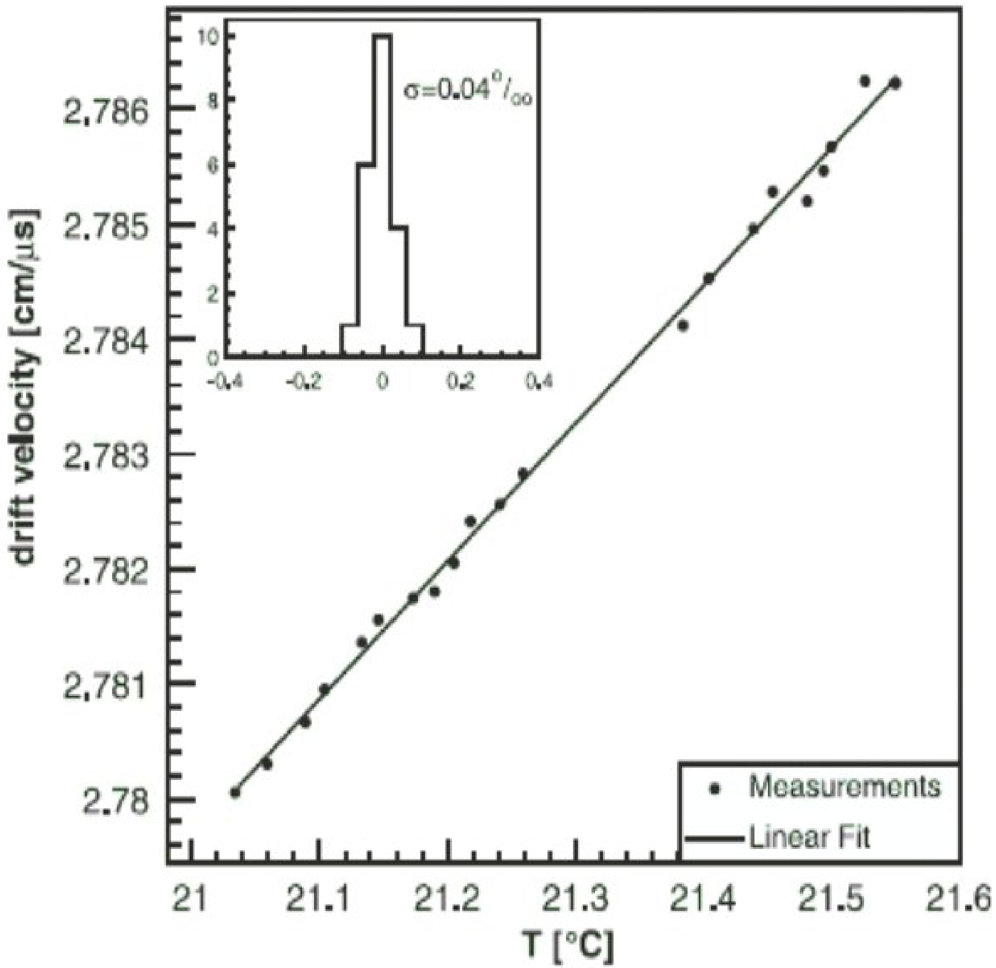

converts time into z coordinate
extreme precision needed . . .
measured with a small TPC
(using laser for gas ionization)

J. Wiechula et al., NIM A 548 (2005) 582

requires temperature stability of 0.1 K
TPC FEE dissipates 27 kW
TRD as direct neighbor 60 kW
60 independent cooling circuits
500 temperature sensors

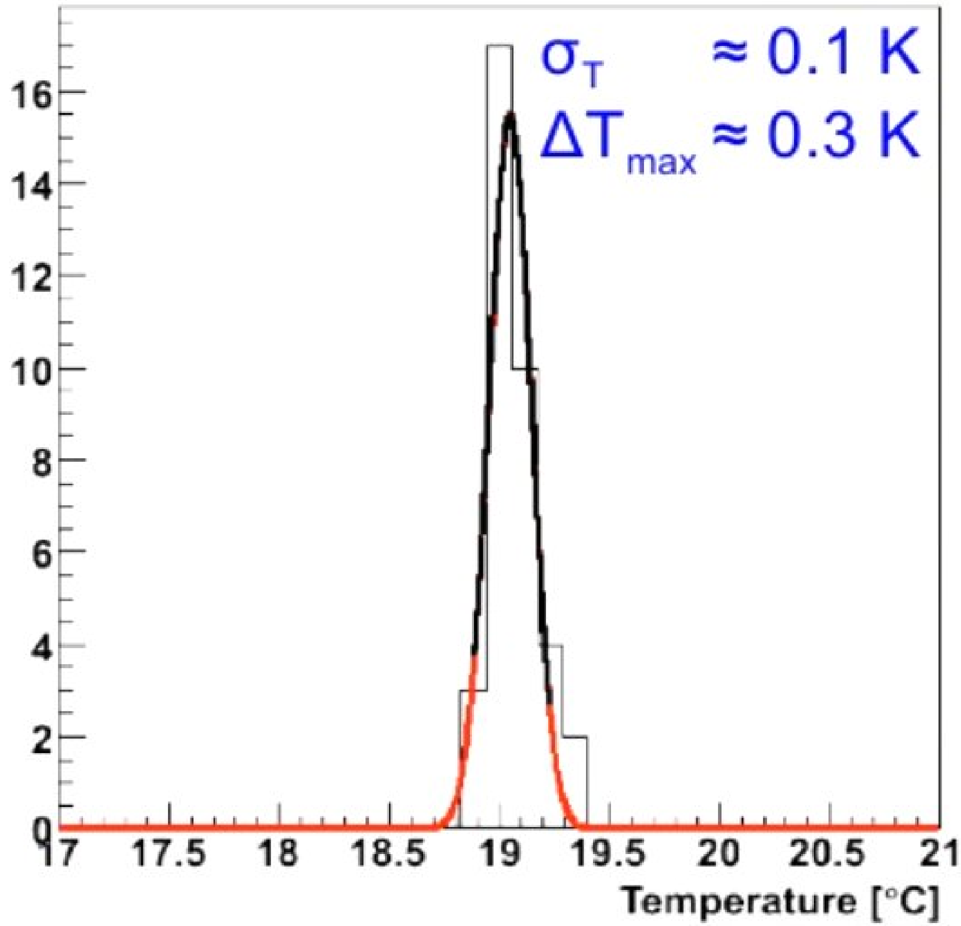

Performance of the ALICE TPC: particle identification

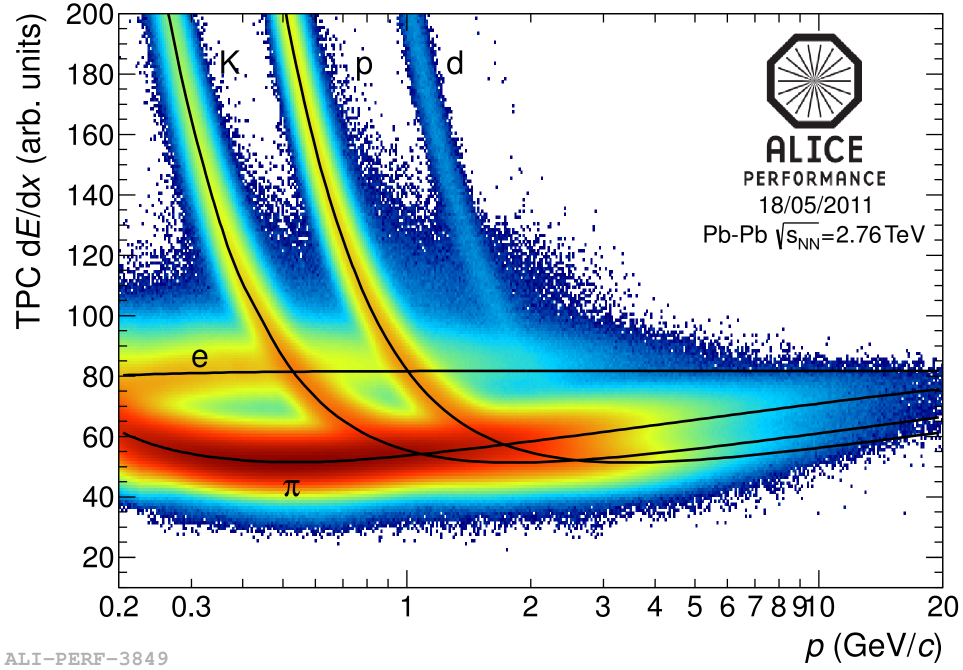

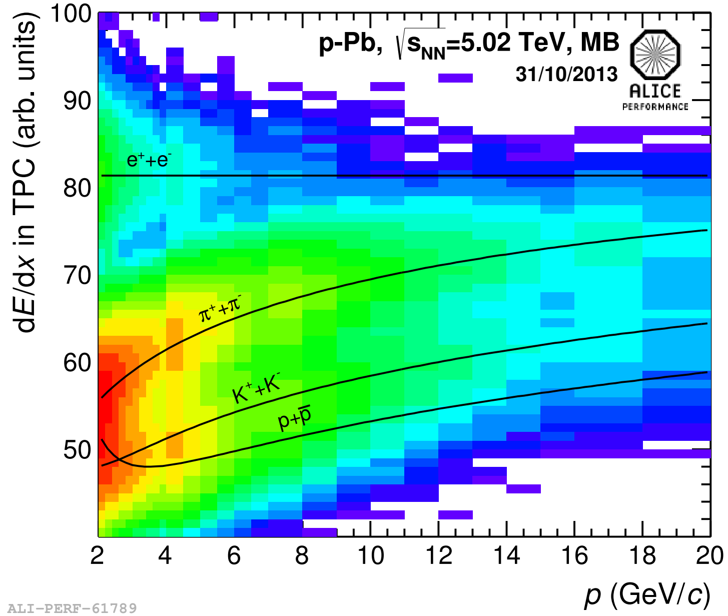

$$\frac{\sigma(\mathrm{d}E/\mathrm{d}x)}{\mathrm{d}E/\mathrm{d}x} = 5.2\% \text{ to } 6.5\%$$

(pp to central Pb-Pb)

crossings: use of TOF to resolve ambiguity

statistical separation possible even in relativistic rise region

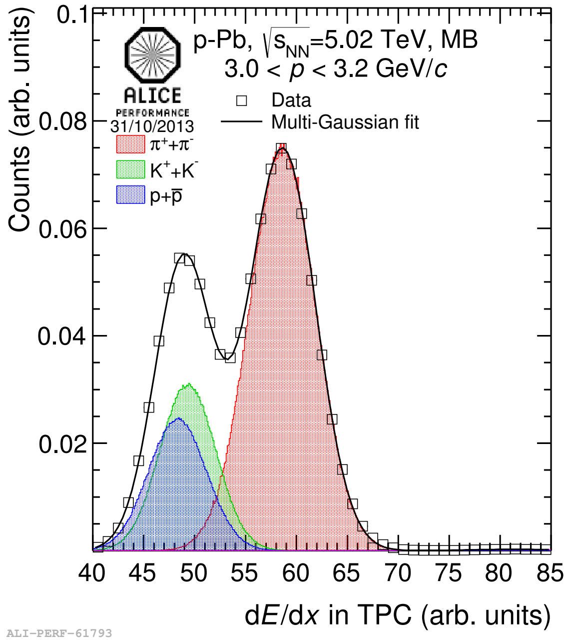

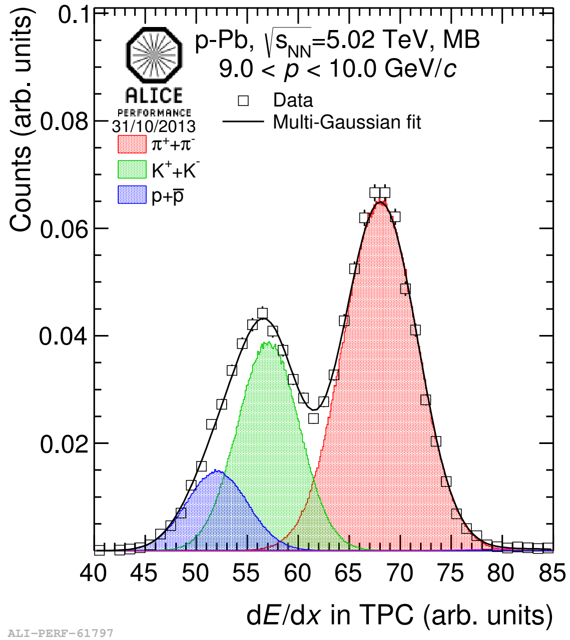

Performance of the ALICE TPC: momentum resolution

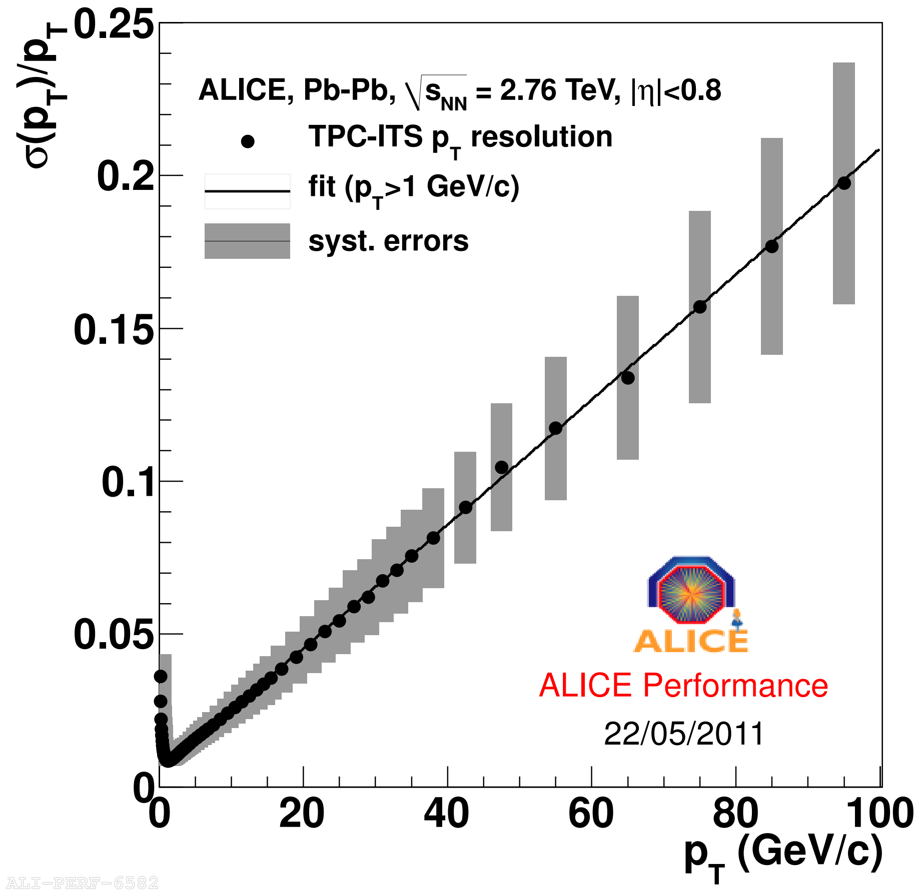

TPC standalone $p_\perp$-resolution

resolution at large $p_\perp$ is improved by a factor of about 3 if vertex is included in fit

further improvement by inclusion of track segments of Inner Tracker System and Transition Radiation Detector

TPC fully instrumented and installed in ALICE on Jan. 6, 2007

laser tracks

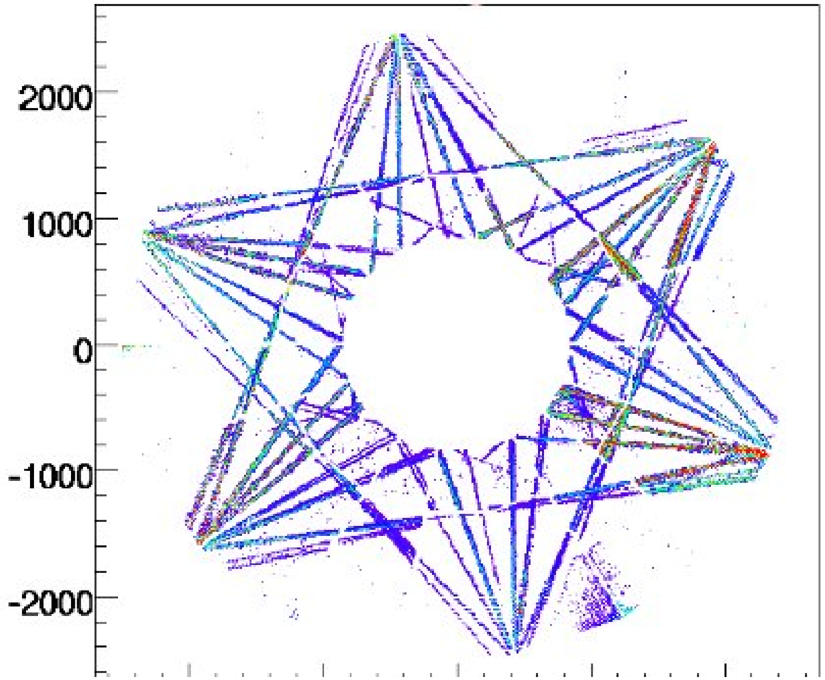

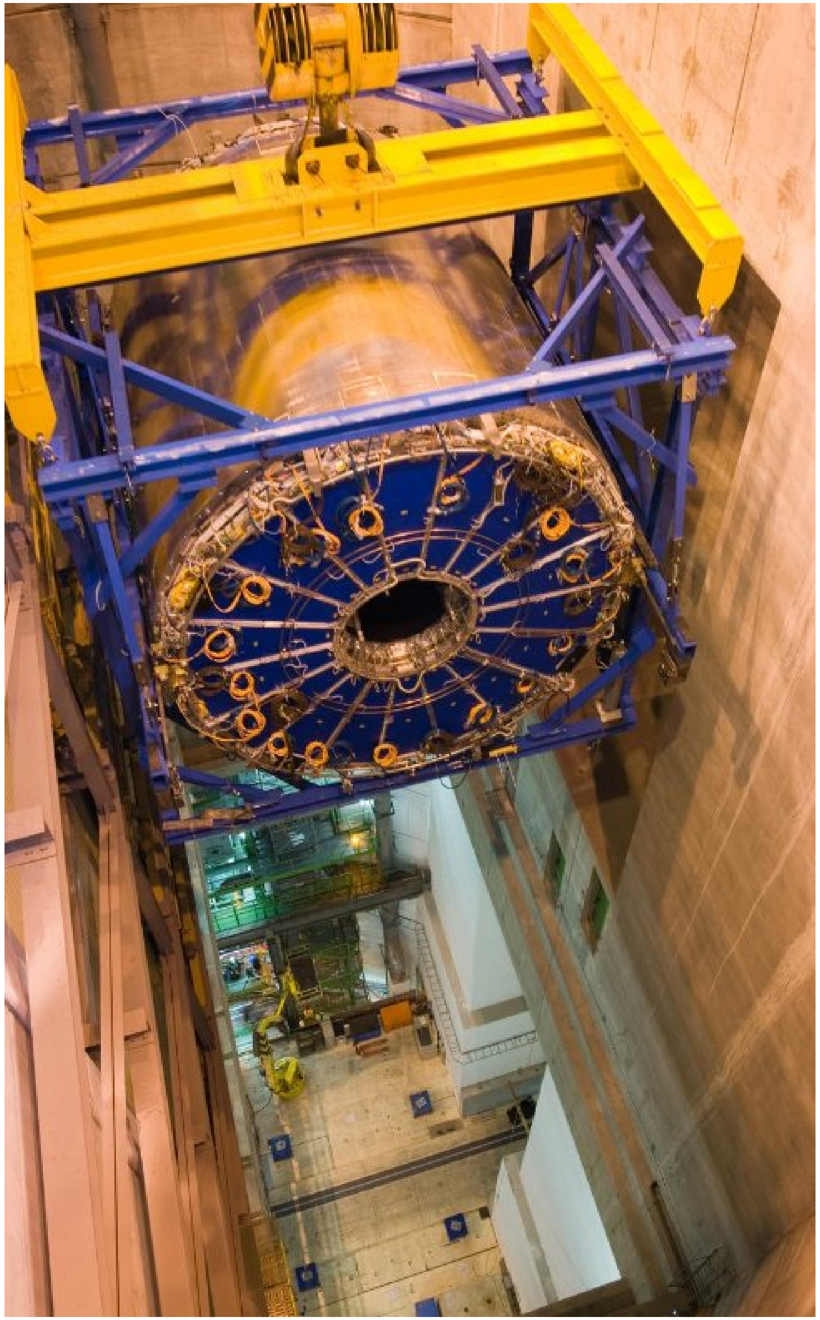

ALICE TPC up and running

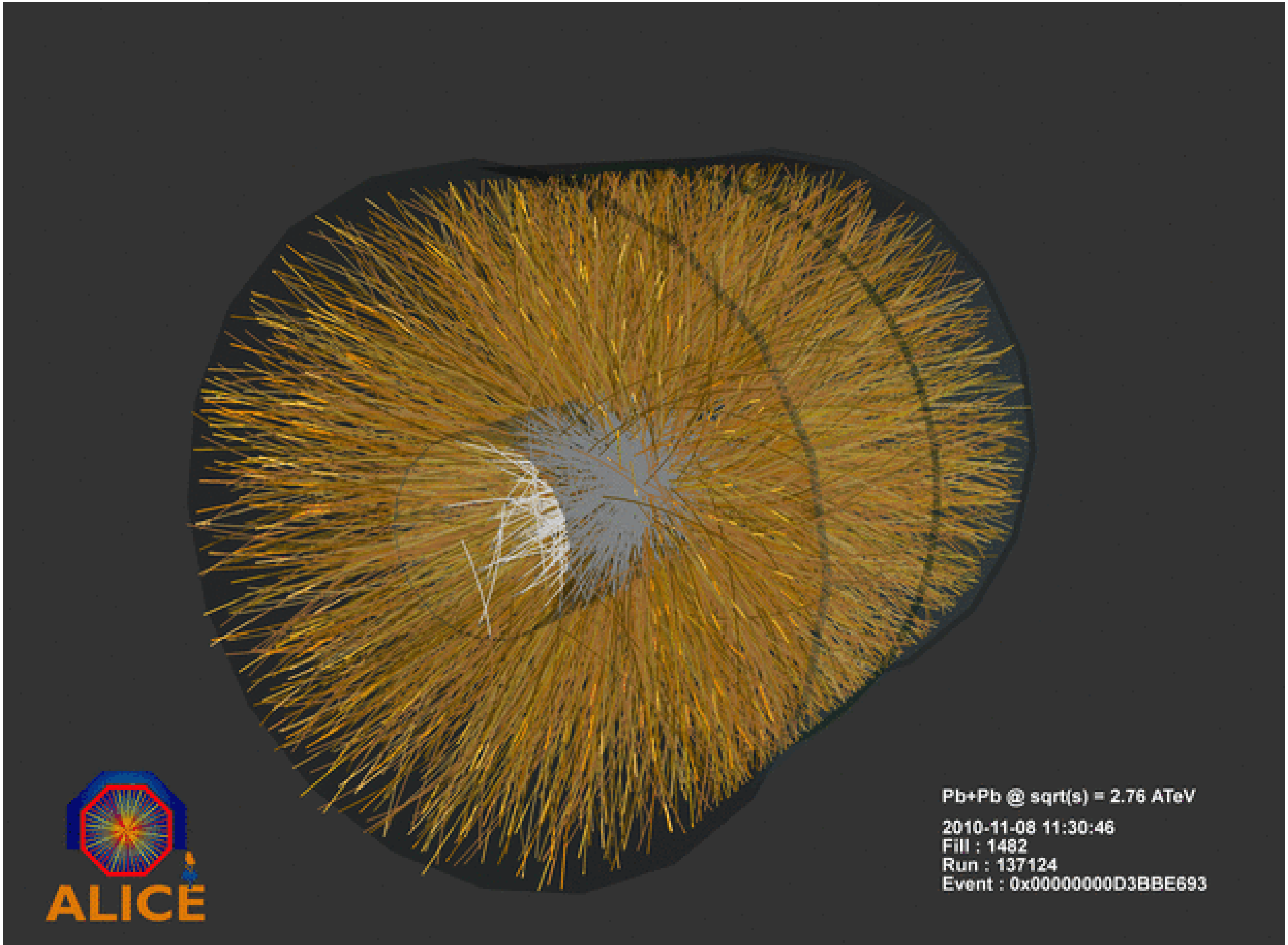

4 Semiconductor Detectors
- Principle of operation
- p-n junction
- Signal generation in semiconductor detectors
- Ionization yield and Fano factor
- Energy measurement with semiconductor detectors
  - Ion implanted or diffusion barrier detectors
  - Surface barrier detectors
  - p-i-n detectors Ge(Li), Si(Li)
  - High purity or intrinsic Ge detectors
  - Bolometers
- Position measurement with semiconductor detectors
  - Principle
  - Micro-strip detectors (about 1983)
  - Double-sided micro-strip detectors
  - Silicon drift detectors
  - Pixel detectors (Si)
  - putting it all together: the LHC experiments use Si pixels, strips, and drift
  - CCD, charge-coupled device
- Radiation damage

Main applications:

- γ spectroscopy with high energy resolution (10 keV - few MeV range)
- vertex and tracking detectors with high spatial resolution
- energy measurement of charged particles (few MeV) and PID via dE/dx (multiple layers)

- use microchip technology; structures with sub μm precision can be produced at low cost; read-out electronics can be directly bonded to detector
- only a few eV per electron-hole pair
- high density compared to gases - need only thin layers

4.1 Principle of operation

in semiconductors like Si, Ge, GaAs
lower edge of conduction band E_C only a few eV above upper edge of valence band E_V.

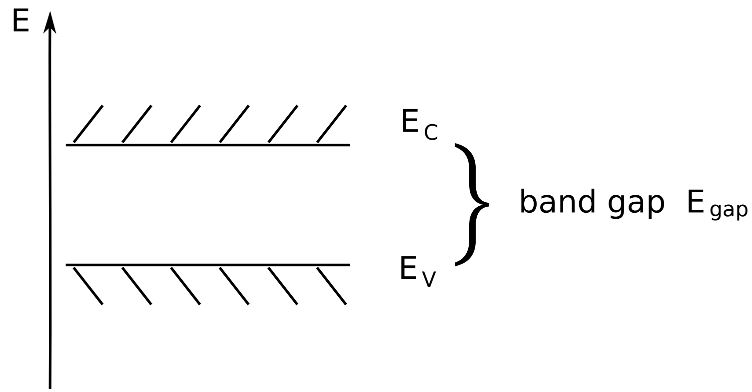

detector operates like solid state ionization chamber:

- charged particle creates electron-hole pairs
- crystal between two electrodes that set up electric field in which charge carriers drift and induce signal
- primary ionization electron has high energy, up to 20 keV $\rightarrow$ many secondary electron-hole pairs and lattice excitations (phonons)
- effect: along track of primary ionizing particle plasma tube of electrons and holes with very high concentration ($10^{15} - 10^{17}$ cm^{-3})
- challenge: need to collect charge carriers before they recombine $\rightarrow$ very high purity semiconductor needed

Primer Semiconductors - only what is needed here

Introduction to band structure:
in a metal an electron interacts with a large number of atoms (order N_A)
$\rightarrow$ discrete atomic levels form a group of N very closely spaced levels, 'band'
electrons in a band similar to particles in a box or potential well $\rightarrow$ Fermi gas model

$$E \propto k^2, \text{ density of states} \qquad g(E) = \frac{g(\lambda)}{dE/d\lambda} = \frac{2m}{\hbar^2 \lambda} = \frac{(2m)^{3/2}}{2\pi^2 \hbar^3} \sqrt{E}$$

number of electrons as function of energy E is determined by a distribution function, the Fermi-Dirac distribution function

$$f(E) = \frac{1}{1 + \exp((E - E_F)/kT)}$$

and the number of electrons per energy interval

$$n(E)\mathrm{d}E = g(E) f(E) \mathrm{d}E$$

characteristics of solid determined by location of Fermi energy relative to energy bands

- metal: E_F below top of an energy band
- insulator: E_F at top of valence band and gap to next allowed band too large to be bridged by optical or thermal excitation or electric force at normal E-field
- semiconductor: gap smaller so that electrons can be excited across thermally or optically, E_F between valence and conduction band

Distribution of electrons and energy levels in semiconductors

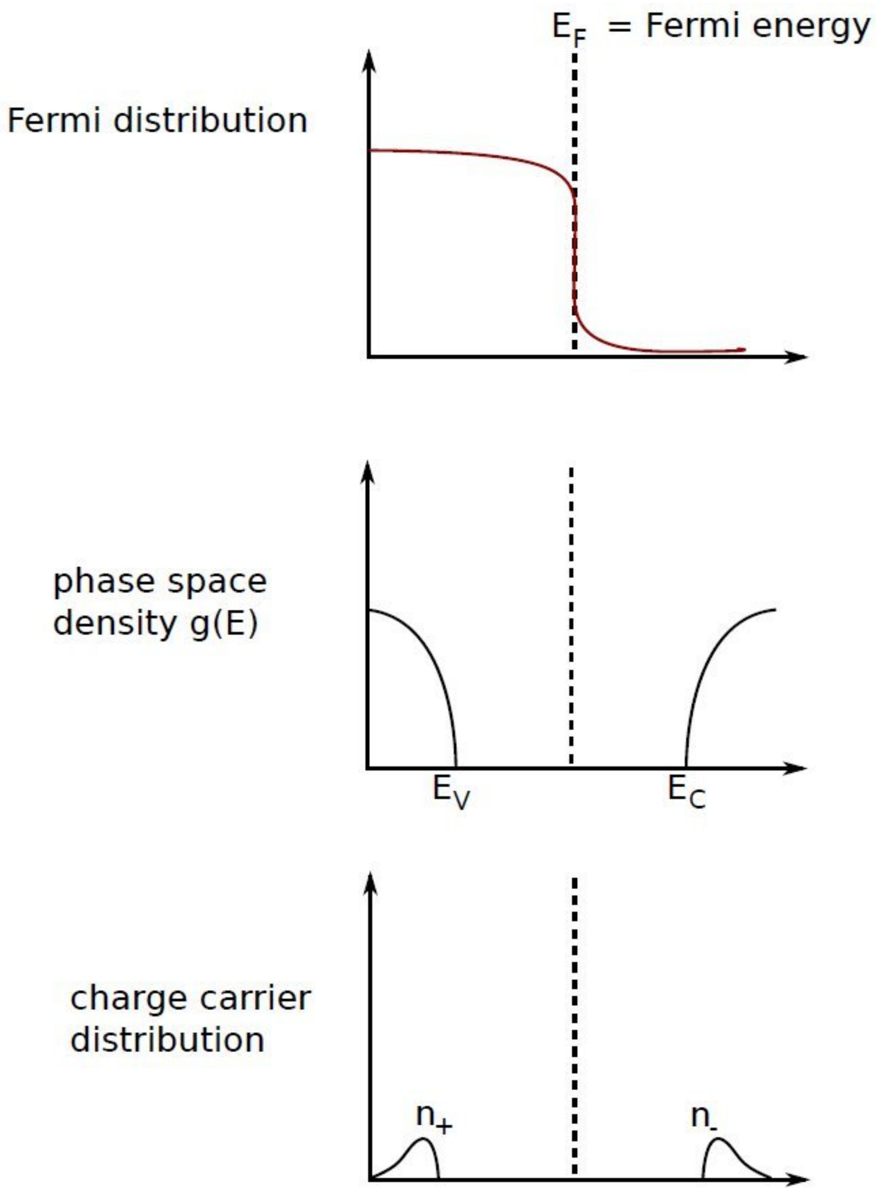

$$f(E) \approx \exp[-(E - E_F)/kT] \qquad E > E_F$$
$$1 - f(E) \approx \exp[-(E_F - E)/kT] \qquad E < E_F$$

Fermi gas model

$$g_C(E) = \frac{(2m_n^*)^{3/2}}{2\pi^2\hbar^3}\sqrt{E - E_C} \qquad E > E_C$$
$$g_V(E) = \frac{(2m_p^*)^{3/2}}{2\pi^2\hbar^3}\sqrt{E_V - E} \qquad E < E_V$$

$$n_-(E) = f \cdot g_C$$
$$n_+(E) = (1 - f) \cdot g_V$$

Intrinsic and extrinsic semiconductors

intrinsic semiconductor:

- very pure material, charge carriers are created by thermal or optical excitation of electrons to conduction band $N_- = N_+$

impurity or extrinsic semiconductor:

- majority of charge carriers provided by impurity atoms at lattice sites of crystal
- impurity atom provides either an extra electron above number required for covalent bonds $\rightarrow$ majority charge carriers are electrons **'n-type semiconductor'**
  or
- impurity atom has insufficient number of electrons for covalent bonds, free hole at impurity site $\rightarrow$ majority charge carriers are holes **'p-type semiconductor'**

most common:

- crystal of element of group IV such as Si or Ge
- impurities of group V (P, As, Sb) or of group III (Al, Ga, In)
- but also GaAs or CdS

in semiconductors like Si, Ge, GaAs, lower edge of conduction band E_c only a few eV above upper edge of valence band E_v.

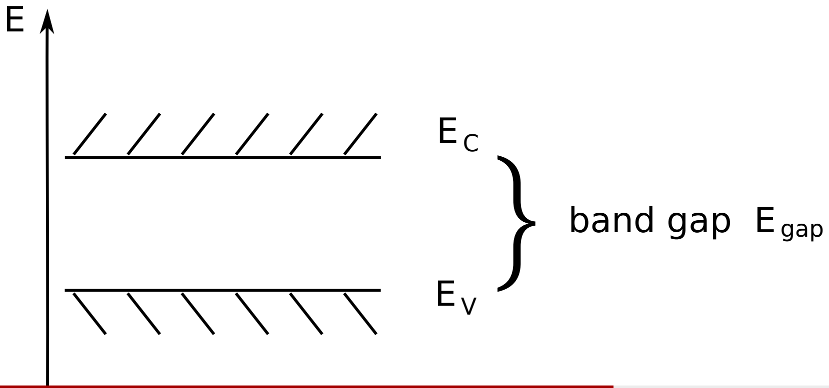

	E_{gap}
Si	1.12 eV
Ge	0.66 eV
GaAs	1.43 eV

acceptor and donor levels very close to valence and conduction bands (drawing not to scale!)

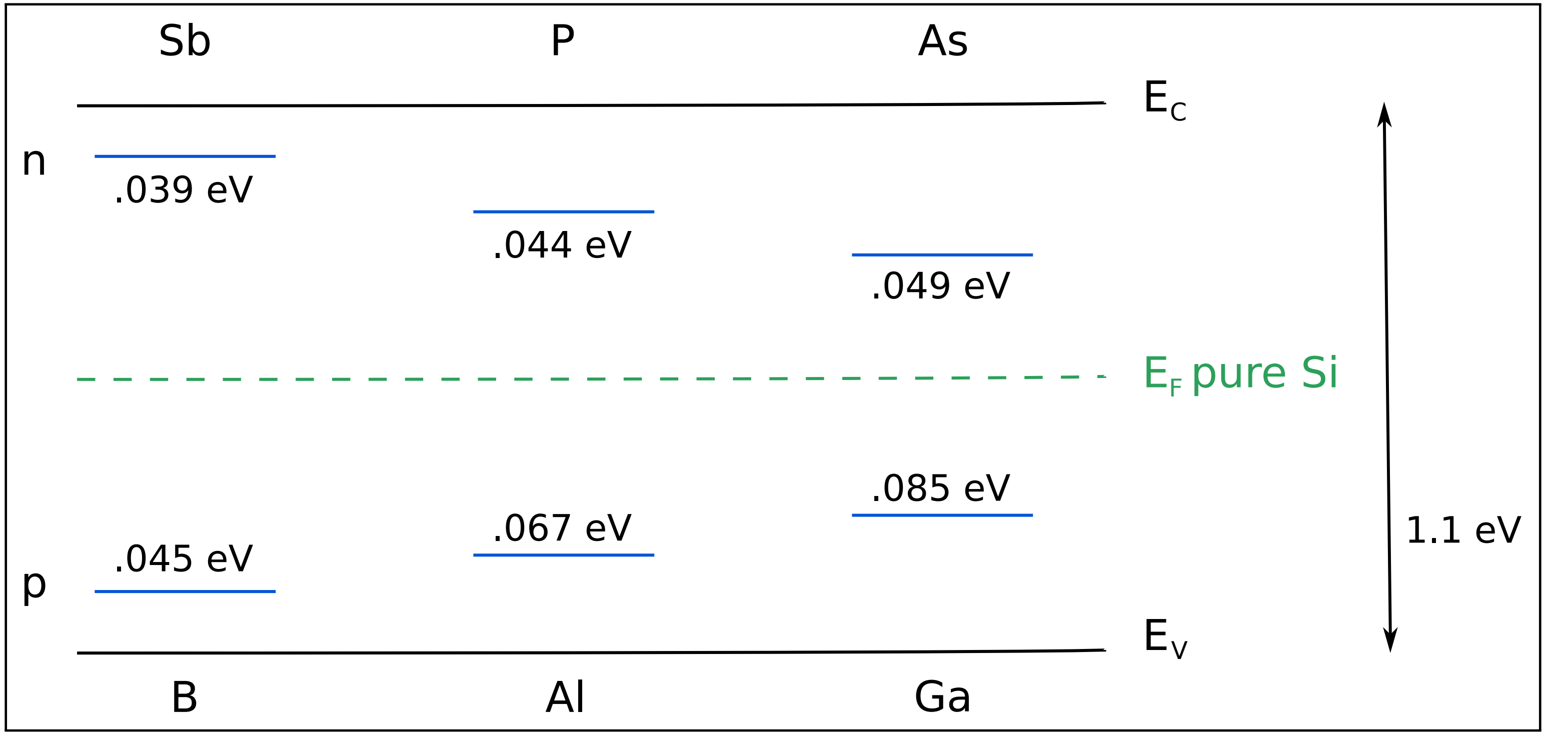

electron donors (P, Sb, . . .): 5^{th} electron bound only weakly in Si-crystal
can easily be promoted into conduction band (Li-like)

electron acceptors (B, Al, . . .): only valence electrons, one unsaturated binding in Si-crystal
tendency to 'accept' an electron from Si leaving behind
a 'hole' in valence band

Intrinsic and extrinsic semiconductors

intrinsic semiconductor:

the smaller the band gap, the larger the number of charge carriers

$n = \int n_{-}(E)\mathrm{d}E$

$p = \int n_{+}(E)\mathrm{d}E$

$n = p$

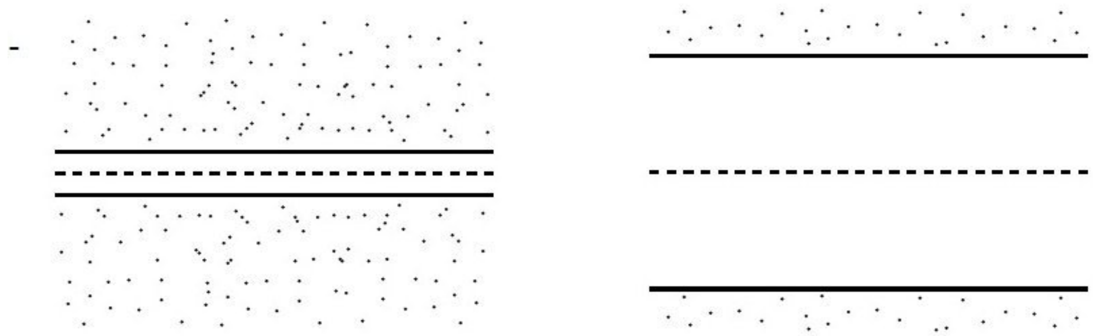

doped semiconductor:

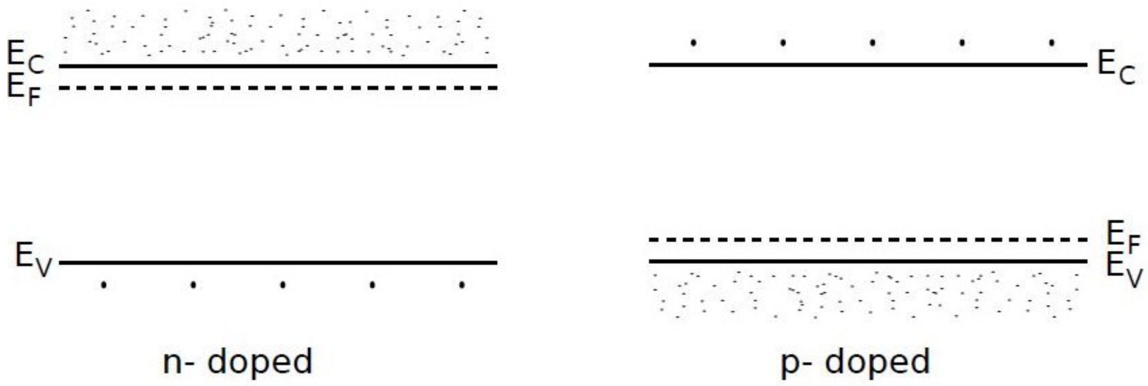

$T = 0$	Si + P	Si + B	not conducting
$T \neq 0$	Si + P^+ + e^-	Si + B^- + $\oplus$	
	n conducting	p conducting	

Intrinsic and extrinsic semiconductors

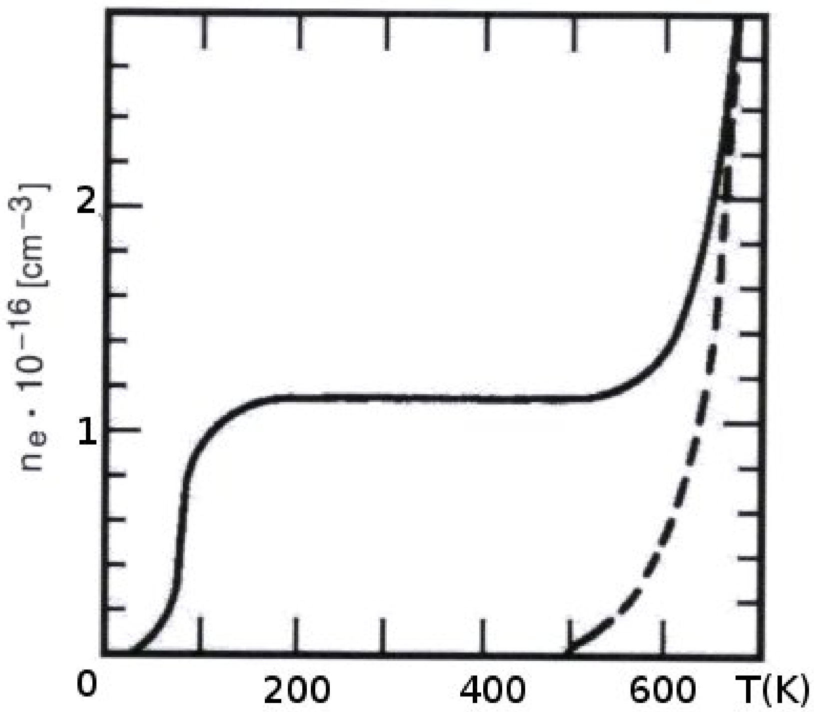

electron density in conduction band in pure Si (dashed) and in Si doped with As ($10^{16}/\mathrm{cm}^3$)

electrical behavior determined by mobility of charge carriers μ (m^2/Vs)

- drift velocity $v_D = \mu E$
- specific resistance ρ (Ωm)
- resistance $R = \rho\, l/A$ with length l and area A transverse to E

Intrinsic semiconductors I

- density of electrons in conduction band

$$n = \int n_- dE = \int_{E_c}^{\infty} f\, g_c\, dE = N_c \exp[-(E_c - E_F)/kT]$$

  and correspondingly density of holes in valence band

$$p = \int n_+ dE = \int_{-\infty}^{E_v} (1-f)\, g_v\, dE = N_v \exp[-(E_F - E_v)/kT]$$

  N_c, N_v: effective density of states at edges of conduction and valence bands with
  $N_{c,v} = 2\left(\frac{m^*_{n,p} kT}{2\pi\hbar^2}\right)^{\frac{3}{2}}$ with effective masses m^* of electrons and holes
  i.e. much weaker T-dependence compared to exponential,
  looks like only levels at E_c and E_v present, not broad bands

- for pure or intrinsic semiconductors

$$\begin{aligned} E_c - E_F &= E_F - E_v \quad \Rightarrow \quad n_i = p_i \\ np &= N_c N_v \exp\left(-\frac{(E_c - E_v)}{kT}\right) = n_i^2 \end{aligned}$$

note: product of n and p at a given T has fixed value, characterized by effective masses and band gap (often called 'law of mass action') typical values at 300 K :

Si $n_i = 1.5 \cdot 10^{10}$ cm^{-3} raise T by 8 K $\rightarrow n_i$ doubles
Ge $n_i = 2.4 \cdot 10^{13}$ cm^{-3}

- drift of charge carriers: as in gases, random thermal motion plus drift in electric field

$$
\begin{aligned}
\text{mobility} \quad \mu &\cong \text{const. for } E < 10^3 \text{ V/cm} \\
\mu &\propto \frac{1}{\sqrt{E}} \text{ for } 10^3 \text{ V/cm} < E < 10^4 \text{ V/cm} \\
\mu &\propto \frac{1}{E} \text{ for } E > 10^4 \text{ V/cm} \quad \Rightarrow \quad \boxed{v_D = \mu \cdot E \rightarrow \text{const.}}
\end{aligned}
$$

  saturates at about 10 cm/μs (similar to gases)
  $\rightarrow$ fast collection of charges (10 ns for 100 μm)
  but: $v_h \cong 0.3 - 0.5\, v_e$ (very different from gases!)

- conductivity σ given by: $I = \underbrace{e \cdot n_i(\mu_e + \mu_h)}_{\sigma = 1/\rho} E$

Properties of Intrinsic Silicon and Germanium

		Si	Ge
Atomic number		14	32
Atomic weight	u	28.09	72.60
Stable isotope mass numbers		28-29-30	70-72-73-74-76
Density (300 K)	g/cm^3	2.33	5.32
Atoms/cm^3	cm^{-3}	$4.96 \cdot 10^{22}$	$4.41 \cdot 10^{22}$
Dielectric constant		12	16
Energy gap (300 K)	eV	1.115	0.665
Energy gap (0 K)	eV	1.165	0.746
Intrinsic carrier density (300 K)	cm^{-3}	$1.5 \cdot 10^{10}$	$2.4 \cdot 10^{13}$
Intrinsic resistivity (300 K)	Ωcm	$2.3 \cdot 10^{5}$	47
Electron mobility (300 K)	cm^2/Vs	1350	3900
Hole mobility (300 K)	cm^2/Vs	480	1900
Electron mobility (77 K)	cm^2/Vs	$2.1 \cdot 10^{4}$	$3.6 \cdot 10^{4}$
Hole mobility (77 K)	cm^2/Vs	$1.1 \cdot 10^{4}$	$4.2 \cdot 10^{4}$
Energy per electron-hole pair (300 K)	eV	3.62	
Energy per electron-hole pair (77 K)	eV	3.76	2.96

Source: G. Bertolini and A. Coche (eds.), Semiconductor Detectors, Elsevier-North Holland, Amsterdam, 1968

Doped semiconductors I

donor atom is either neutral or ionized: $N_D = N_D^0 + N_D^+$
and accordingly $N_A = N_A^0 + N_A^-$ with

$$N_D^+ = N_D\,(1 - f(E_D))$$
$$N_A^- = N_A\,f(E_A)$$

and

$$f(E) = \frac{1}{exp[(E - E_F)/kT + 1}$$

Note: for $T \neq 0$ one should use μ instead of E_F, but follow here solid state textbooks
Fermi energy is temperature dependent and defined by charge neutrality

$$n + N_A^- = p + N_D^+$$

and as above we have

$$n = N_c \exp[-(E_c - E_F)/kT]$$
$$p = N_v \exp[-(E_F - E_v)/kT]$$

$\rightarrow$ location of donor or acceptor levels of doped semiconductor together with $N_{c,v}$ and T determines properties

Doped semiconductors II

for n-type semiconductor: Fermi energy moves with increasing temperature from value between conduction band and donor levels to middle between valence and conduction band
at room temperature E_F is close to E_D
$\rightarrow kT \approx E_c - E_D = E_d$ and $\exp[-E_d/kT] \approx 1$
charge carriers dominantly electrons of the donor and nearly all donors ionized
$n \cong N_D \approx const. \gg n_i$

p-conducting material: analogous for positively charged holes of acceptor

typical dopant concentration: $\geq 10^{13}$ atoms/cm^3 (compare density of Si: $5 \cdot 10^{23}$/cm^3)
strong doping: 'n$^+$' or 'p$^+$' $\cong 10^{20}$ atoms/cm^3

equilibrium between densities of electrons and holes:

increase of one type of carrier concentration $\rightarrow$ reduction of the other due to recombination following the law of mass action

$$n \cdot p = n_i p_i = A \cdot T^3 \exp\left(-\frac{E_{gap}}{kT}\right)$$

so, for n-doped material concentration of holes is decreased

Doped semiconductors III

example: at 300 K in Si

$$n_i = p_i = 10^{10}\ \mathrm{cm}^{-3}$$
$$n = 10^{17}\ \mathrm{cm}^{-3} \quad \rightarrow \quad p = 10^{3}\ \mathrm{cm}^{-3}$$

conductivity determined by majority carriers (electrons in n-doped, holes in p-doped)
role of minority carriers negligible with

$$\begin{aligned} n &\cong N_D \\ p &\cong \frac{n_i p_i}{N_D} = \frac{n_i^2}{N_D} \\ \frac{1}{\rho} &= \sigma = e \cdot N_D \cdot \mu_e \end{aligned}$$

typical values:

pure Si	Si p-type 10^{13} cm^{-3}
$2.3 \cdot 10^5$ Ωcm	500 Ωcm

Doped semiconductors IV

important for fabrication of semiconductor detectors:
on a substrate very thin layers ('epitactic layers') of $< 1\,\mu$m thickness can be grown with density of carriers very different from substrate.

e.g. film with low carrier density (ρ large) on high charge carrier density substrate (ρ small): within $1\,\mu$m density can change by factor $10 - 100$

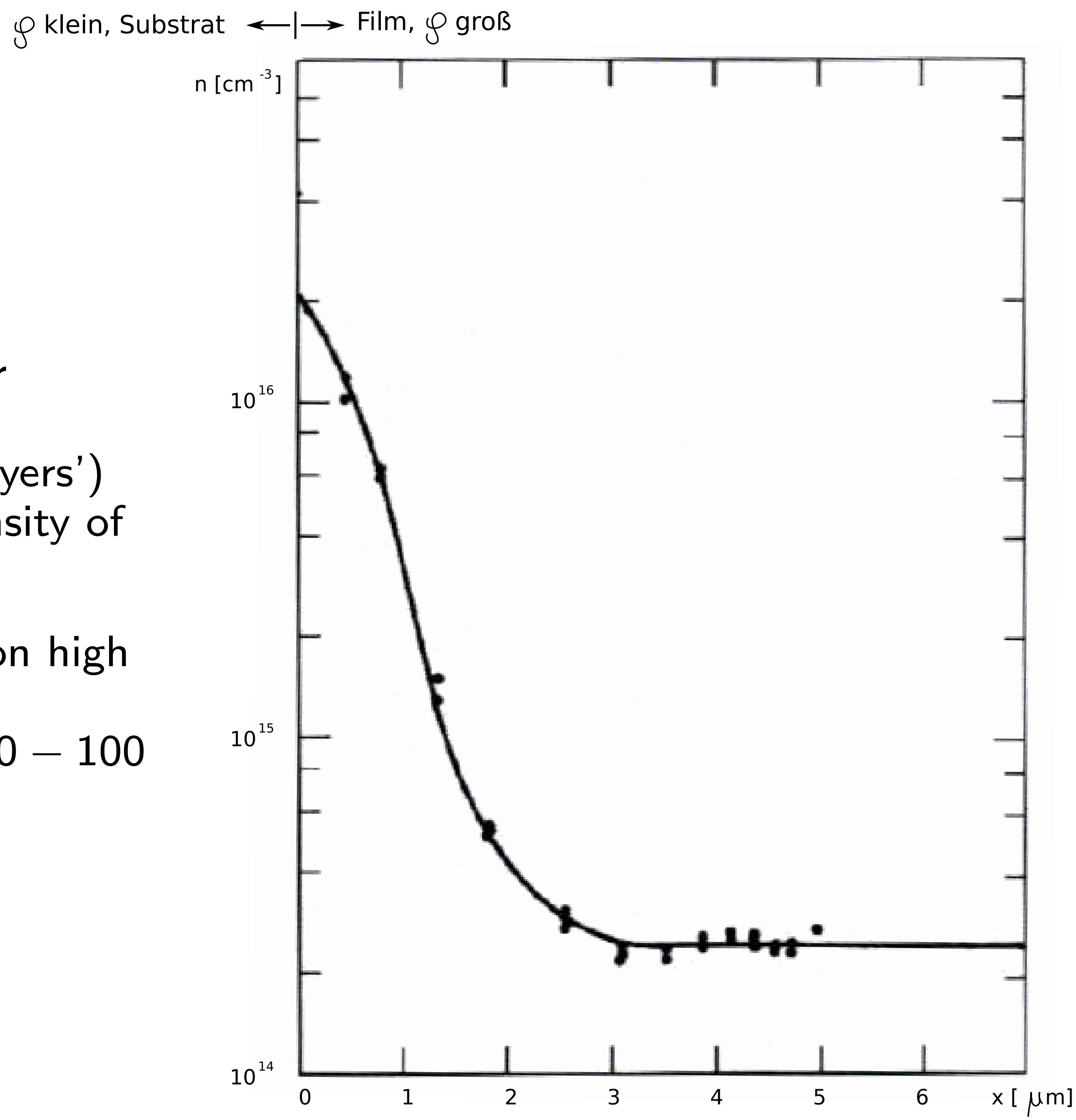

4.2 p-n junction

- bring p- and n-semiconductors into contact; thermodynamic equilibrium → Fermi-energies of both systems become equal

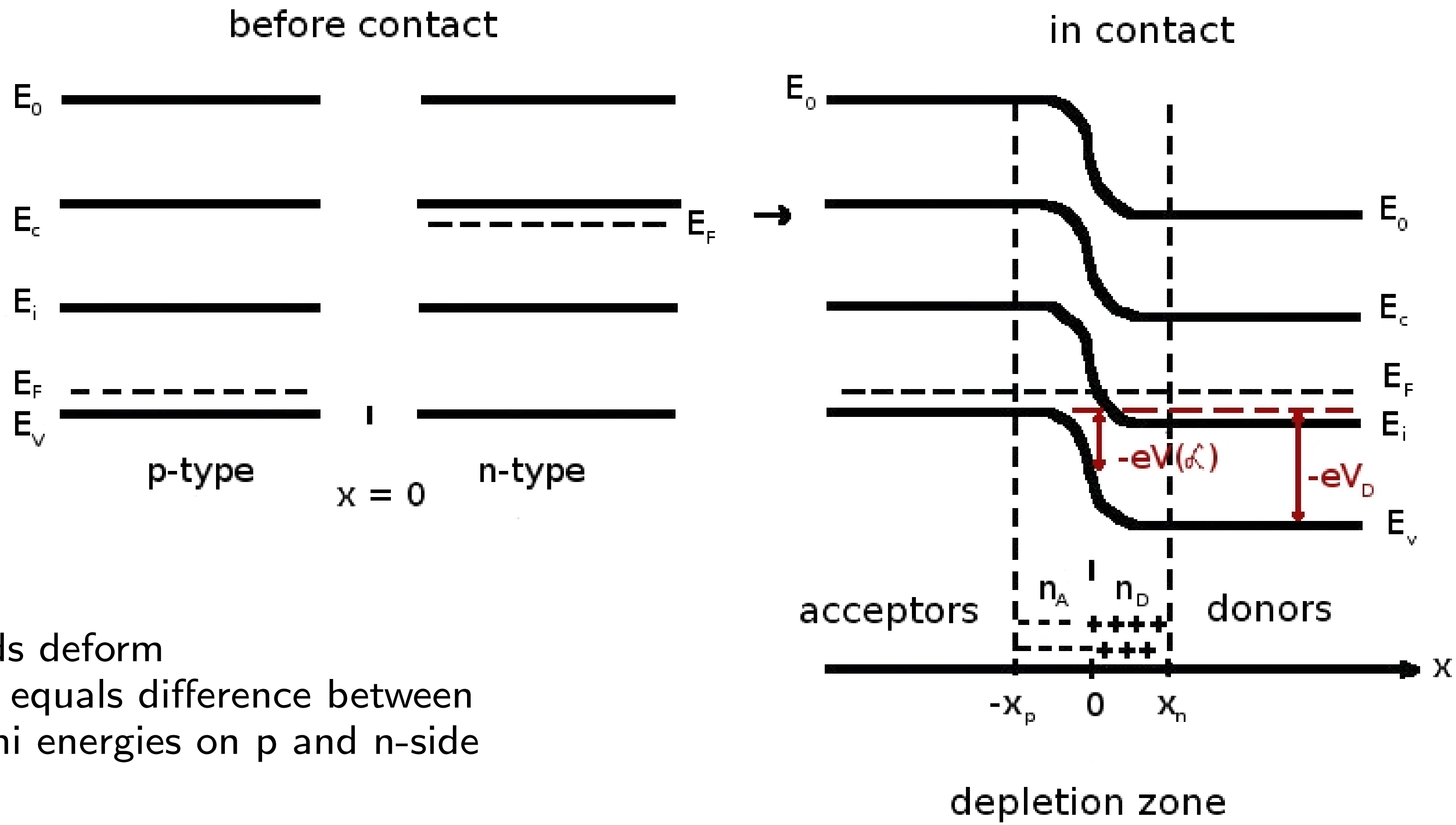

- bands deform
  eV_D equals difference between
  Fermi energies on p and n-side

- equilibration is achieved by electrons diffusing from n to p semiconductor and holes from p to n
- at the boundary, a zone with few free charge carriers (electrons and holes) builds up 'depletion layer
- fixed charges are left behind (ionized donors and acceptors) $\rightarrow$ space charge E-field builds up and counteracts the diffusion which stops eventually (like Hall effect) with $n \approx N_D$ and $p \approx N_A$, difference between Fermi energies on both sides gives

$$
\begin{aligned}
eV_D &= E_c - kT \ln \frac{N_c}{N_D} - E_v - kT \ln \frac{N_v}{N_A} \\
&= E_{gap} - kT \ln \frac{N_c\, N_v}{N_D\, N_A}
\end{aligned}
$$

V_D: diffusion/contact potential

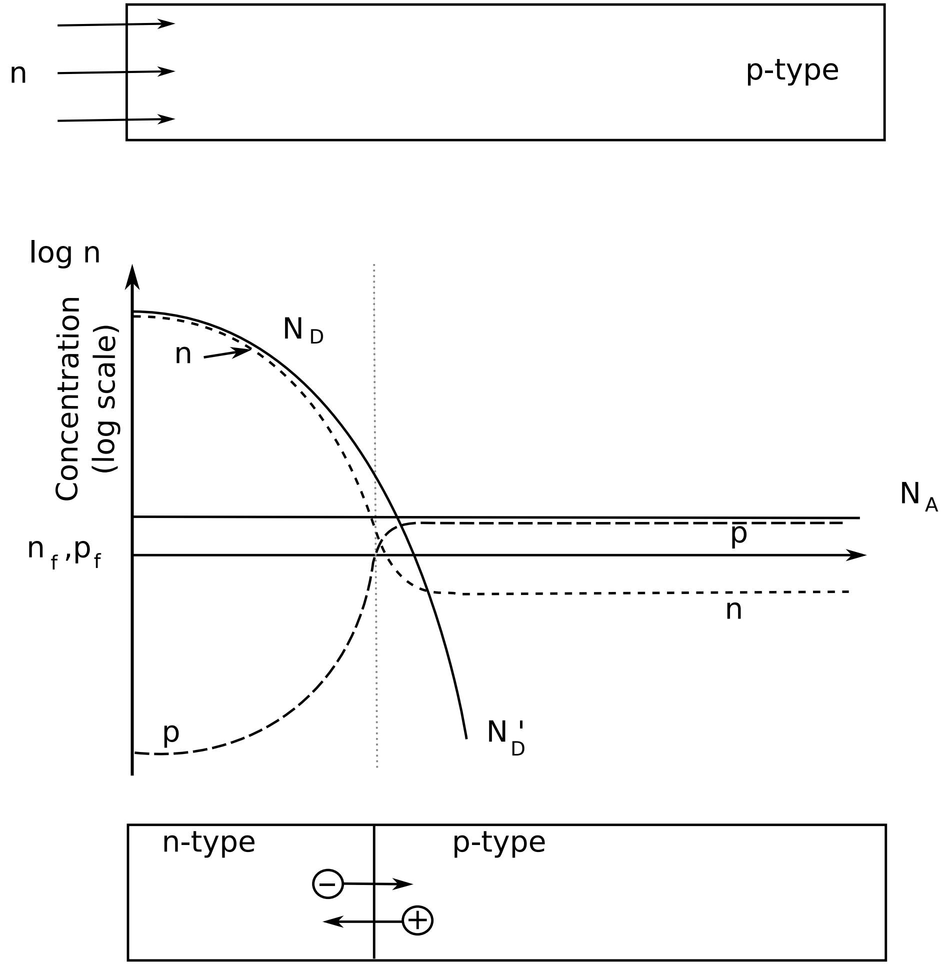

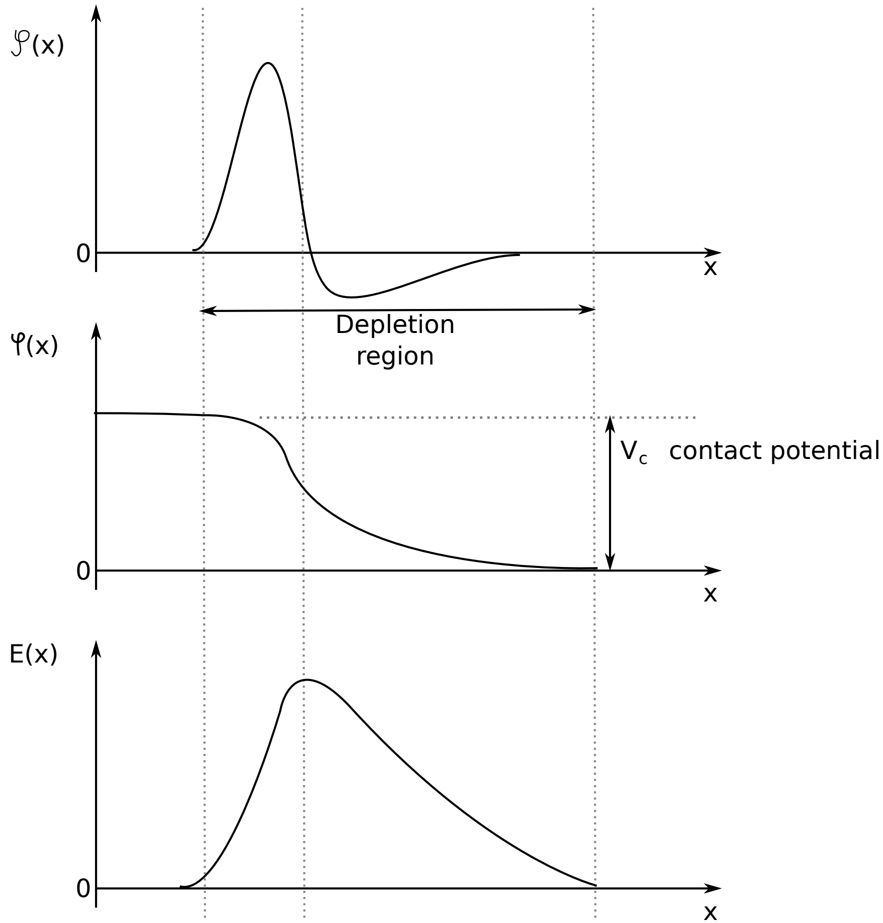

$$\text{n-region} \qquad \rho = \quad e(N_D^+ - n_n(x) + p_n(x))$$

$$\text{p-region} \qquad \rho = -e(N_A^- + n_p(x) - p_p(x))$$

density of majority carriers $n_n, p_p \quad \gg \quad$ density of minority carriers n_p, p_n

potential and space charge related by Poisson equation

$$\frac{\partial^2 V(x)}{\partial x^2} = -\frac{\rho(x)}{\epsilon \cdot \epsilon_0}$$

but $\rho(x)$ depends on the potential, need to solve self-consistently

approximation: concentration of free charge carriers in depletion layer very small (approx. 0), abrupt change
$n > 0 \;\rightarrow\; n = p = 0 \;\rightarrow\; p > 0$
in reality over small length
(Debye length, $0.1 - 1\,\mu$m)

for steps in density: Schottky model
area of rectangles such, that overall region space-charge neutral

$$\rho(x) = \begin{cases} 0 & \text{for} \quad x < -d_p \\ -eN_A & \quad -d_p < x < 0 \\ +eN_D & \quad 0 < x < d_n \\ 0 & \quad d_n < x \end{cases}$$

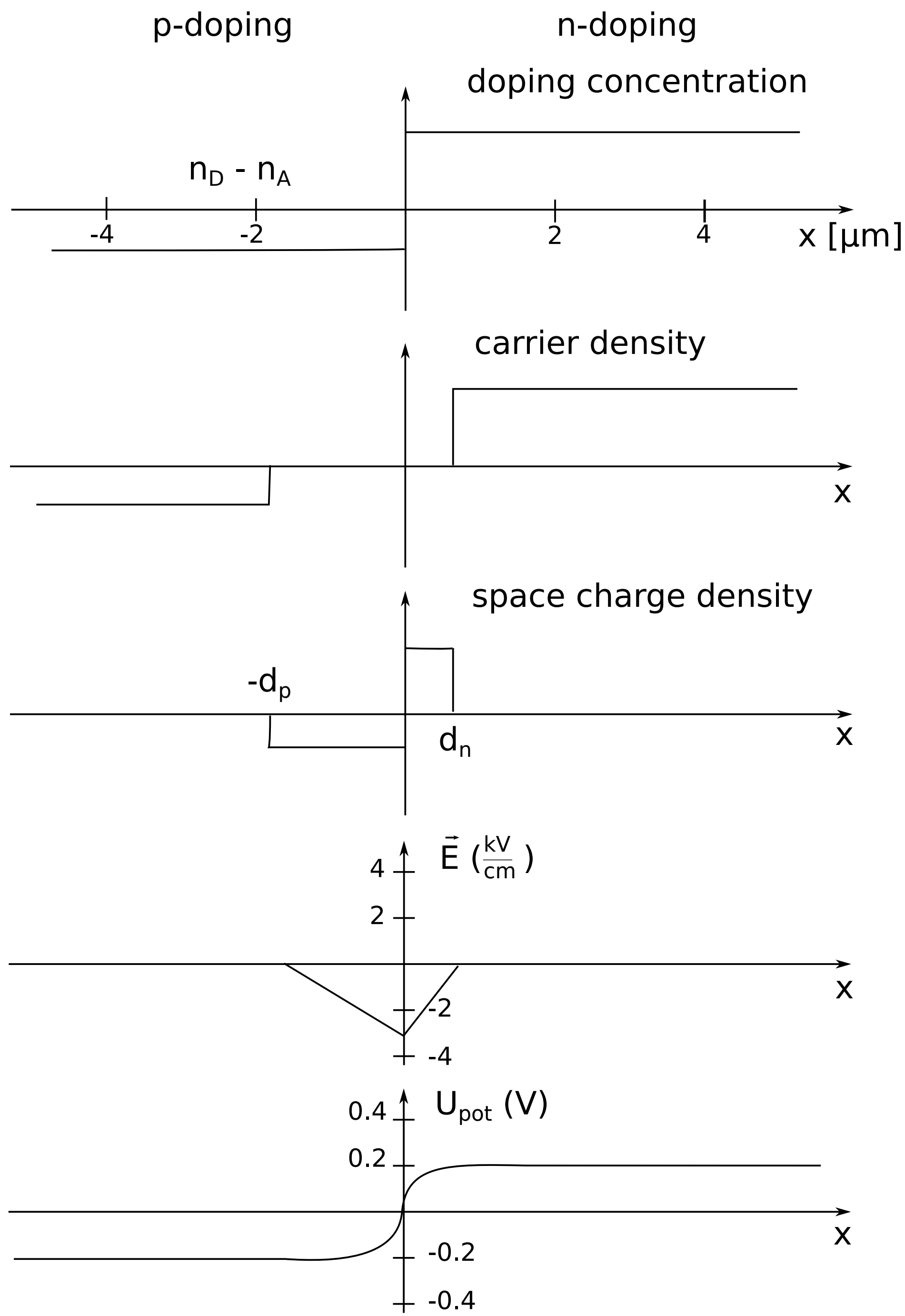

thickness of depletion layer d_p and d_n: integrate Poisson equation in pieces
n-doped region:

$$\begin{aligned}
\frac{\partial^2 V(x)}{\partial x^2} &= -\frac{eN_D}{\epsilon\epsilon_0} \\
E_x &= -\frac{\partial V}{\partial x} = -\frac{e}{\epsilon\epsilon_0} N_D (d_n - x) \\
V(x) &= V_n(\infty) - \frac{e}{2\epsilon\epsilon_0} N_D (d_n - x)^2
\end{aligned}$$

p-doped region equivalently

condition of neutrality: $N_D d_n = N_A d_p$

continuity of potential $V(x)$ at $x = 0$

$$\frac{e}{2\epsilon\epsilon_0}(N_D d_n^2 + N_A d_p^2) = V_n(\infty) - V_p(-\infty) = V_D$$

$$\Rightarrow \quad d_n = \sqrt{\frac{2\epsilon\epsilon_0 V_D}{e} \frac{N_A/N_D}{N_A + N_D}} \quad \text{and} \quad d_p = \sqrt{\frac{2\epsilon\epsilon_0 V_D}{e} \frac{N_D/N_A}{N_A + N_D}}$$

$$\text{e.g.} \quad \left.\begin{array}{lllll} eV_D & \cong & E_{gap} & \cong & 1 \text{ eV} \\ N_A & \cong & N_D & = & 10^{14} \text{ cm}^{-3} \end{array}\right\} \begin{array}{c} d_n \cong d_p \cong 1\,\mu\text{m} \\ E \cong 10^6 \text{ V/m} \end{array}$$

to achieve large width on one side choose asymmetric doping,
e.g. $N_D = 10^{12}/\text{cm}^3$ and $N_A = 10^{16}/\text{cm}^3$ (need very pure material to start with)

in presence of external field
most of the voltage drop U occurs in depletion layer (very few free carriers, large ρ)

$$V_n(\infty) - V_p(\infty) = V_D - U$$

choose sign such that positive U is opposite to diffusion potential (contact potential)
Forward bias, $U > 0$:
holes diffuse in n-direction electrons diffuse in p-direction, potential barrier is lowered

majority carriers recombine in depletion region: 'recombination current',
or penetrate to the other side: 'diffusion current',
depletion zone narrows

$$\begin{aligned} d_n(U) &= d_n(0)\sqrt{1 - \frac{U}{V_D}} \\ d_p(U) &= d_p(0)\sqrt{1 - \frac{U}{V_D}} \end{aligned}$$

Reverse bias, $U < 0$:
electron-hole pairs generated in or near the depletion layer by thermal processes (or in the case of detector by ionization) are separated: 'leakage current'
depletion zone becomes wider (at 300 V order of 1 mm)

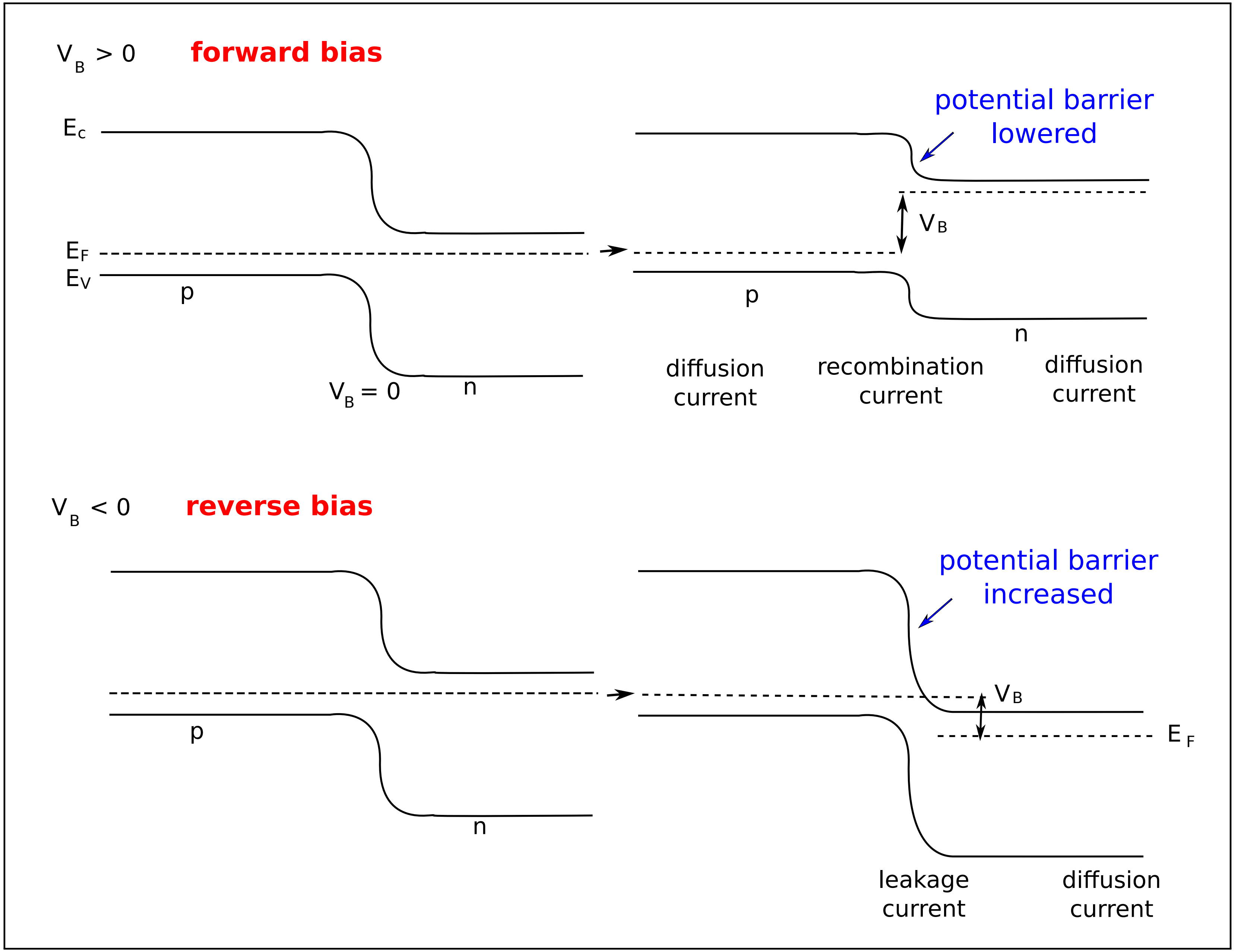

note:
to maximize thickness of depletion layer, need high resistivity (pure material) $\quad d \cong \sqrt{2\epsilon\epsilon_0 U\rho\mu}$

p-n semiconductor detector

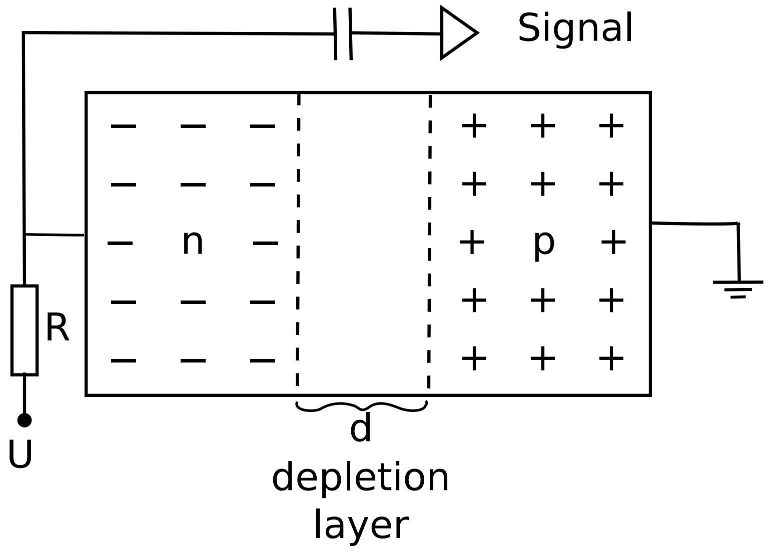

$+++, ---$: free charge carriers

typical realization:

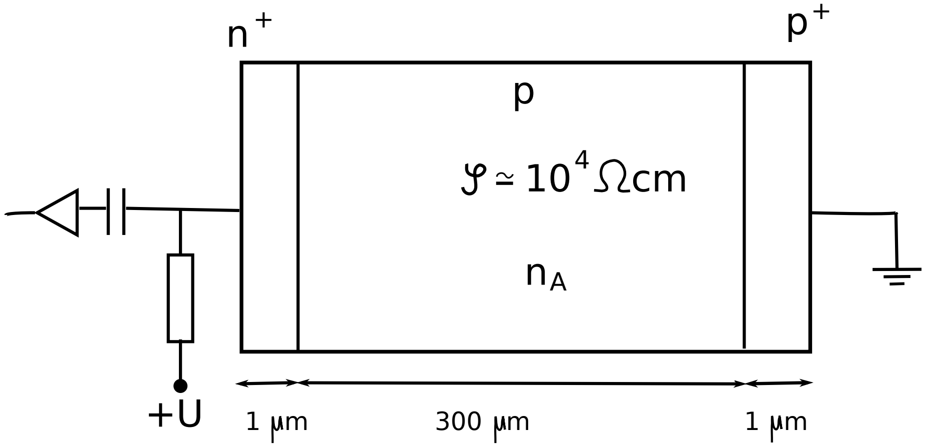

p^+, n^+: very highly doped, conducting

$$d_p + d_n \;\cong\; d_p \cong \sqrt{\frac{2\epsilon\epsilon_0}{e}\,\frac{U}{N_A}}$$

since $N_A \ll N_D, \;\; V_D \ll U$

with $N_A \cong 10^{15}\ \mathrm{cm}^{-3} \Rightarrow$

$$U \;=\; \frac{e}{2\epsilon\epsilon_0} N_A d_p^2 \cong 100\ \mathrm{V}$$

$$|E| \;=\; \frac{100\ \mathrm{V}}{300\cdot 10^{-6}\ \mathrm{m}} = 3\cdot 10^5\ \mathrm{V/m}$$

(safe; spark limit at 10^7 V/m)

4.3 Signal generation in semiconductor detectors

in principle like ionization chambers:
if E const: each drifting electron contributes to signal current while drifting

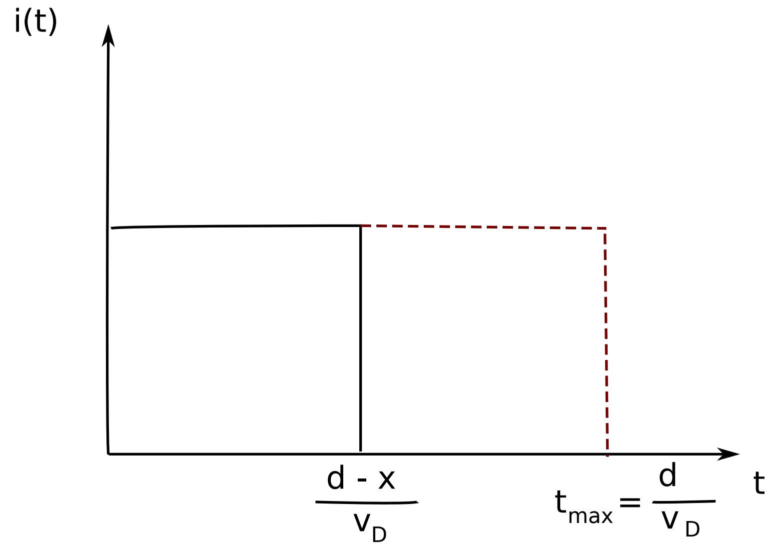

$$i = \frac{\mathrm{d}q}{\mathrm{d}t} = e\frac{\mathrm{d}x}{d}\frac{1}{dx/v_D} = e\frac{v_D}{d}$$

d: width of depletion zone
x: location where electron was generated

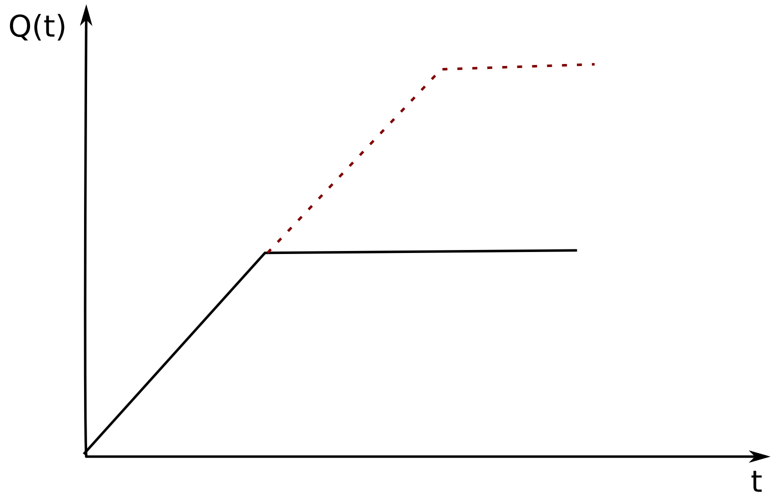

capacitor charges:

$$Q = e\frac{v_D}{d}\cdot t = e\frac{v_D}{d}\frac{d-x}{v_D}$$

line charge of electrons across the depletion layer (constant ionization along track):

$$\begin{aligned} i &= N_0 e \frac{v_D}{d}\left(1 - \frac{t v_D}{d}\right)\Theta\left(1 - \frac{t v_D}{d}\right) \\ Q(t) &= N_0 e \frac{v_D}{d}\left(t - \frac{t^2 v_D}{d}\right)\Theta\left(1 - \frac{t v_D}{d}\right) \end{aligned}$$

integrated:

$$Q\left(t = \frac{d}{v_D}\right) = \frac{N_0 e}{2}$$

same signal for positive carriers (holes), thus in total

$$\boxed{N_0 \cdot e = Q_{tot}}$$

more realistic treatment: E-field depends on x

simple ansatz: $|\vec{E}| = \dfrac{e\,N_A}{\epsilon\epsilon_0} \cdot x$

and with $\sigma = \dfrac{1}{\rho} = e\,N_A\,\mu_+$ and $\tau = \dfrac{\epsilon\epsilon_0}{\sigma}$

$$|\vec{E}| = \frac{x}{\mu_+\tau} \qquad (\tau \cong 1 \text{ ns})$$

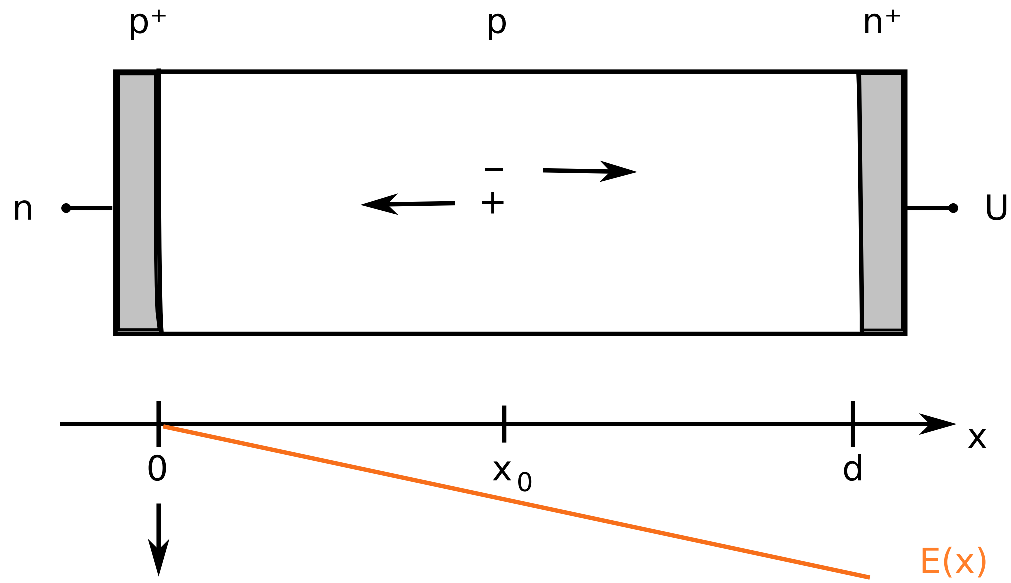

for an electron generated at location x inside depletion zone and mobilities independent of E:

$$v_- = -\mu_- E = \frac{\mu_-}{\mu_+}\frac{x}{\tau} \quad \Rightarrow \quad x = x_0 \exp\left(\frac{\mu_- t}{\mu_+\tau}\right)$$

total drift time of electrons:

$$t_d = \tau\frac{\mu_+}{\mu_-}\ln\left(\frac{d}{x_0}\right)$$

charge signal for $t < t_d$

$$Q_-(t) = -\frac{e}{d}\int\frac{dx}{dt}dt = \frac{e}{d}x_0\left(1 - \exp\left(\frac{\mu_- t}{\mu_+\tau}\right)\right)$$

analogously for hole

$$v_+ = \mu_+ E = -\frac{x}{\tau} \quad \Rightarrow \quad x = x_0\exp\left(-t/\tau\right)$$

$$Q_+(t) = -\tfrac{e}{d}x_0\left(1 - \exp\left(-t/\tau\right)\right)$$

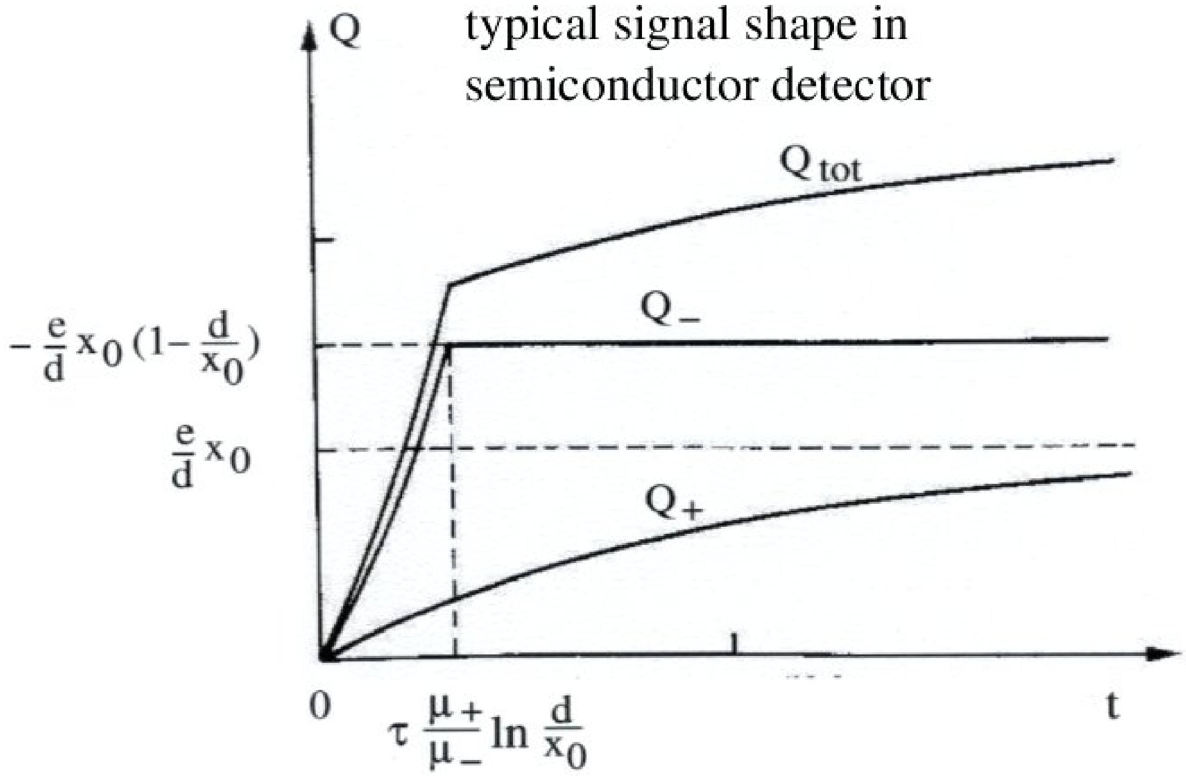

Total charge signal:

$$Q_-(t_d) + Q_+(t \to \infty) = -e$$

signal rise time essentially determined by

$$\tau = \rho \cdot \epsilon \cdot \epsilon_0$$

in reality a bit more complicated:

- track not exactly a line charge (distributed over typically 50 μm width)
- $\mu_\pm \neq$ constant
- some loss of charges due to recombination at impurities

for Si $\tau = \rho \cdot 10^{-12}$ s (ρ in Ωcm), $\rho = 1000\ \Omega$cm $\to \tau = 1$ ns

4.4 Ionization yield and Fano factor

mean energy per electron-hole pair

	$E_0^{300\ \mathrm{K}}$	$E_0^{77\ \mathrm{K}}$	E_{gap}
Si	3.6 eV	3.8 eV	1.1 eV
Ge	-	2.9 eV	0.7 eV

$\sim \frac{2}{3}$ goes into excitation of crystal lattice

Energy loss $\Delta E \quad \Rightarrow$

- lattice vibrations: generation of phonons, typical quantum energy $E_x = 0.037$ eV
- ionization: characteristic energy $E_i = E_{\mathrm{gap}} = 1.1$ eV in Si
- total: $\Delta E = E_i N_i + E_x N_x$

assume Poisson distributions for both processes with $\sigma_i = \sqrt{N_i} \quad \sigma_x = \sqrt{N_x}$

for a fixed energy loss ΔE:
sharing between ionization and lattice excitation varies as $\quad E_x \Delta N_x + E_i \Delta N_i = 0$

on average: $\quad E_i \sigma_i = E_x \sigma_x$

$$\sigma_i = \frac{E_x}{E_i}\sigma_x = \frac{E_x}{E_i}\sqrt{N_x}$$

using $N_x = (\Delta E - E_i N_i)/E_x$

$$\sigma_i = \frac{E_x}{E_i}\sqrt{\frac{\Delta E}{E_x} - \frac{E_i}{E_x}N_i}$$

$$N_i = \frac{\Delta E}{E_0}$$ in case of ideal charge collection without losses

$$\rightarrow \qquad \sigma_i = \frac{E_x}{E_i}\sqrt{\frac{\Delta E}{E_x} - \frac{E_i}{E_x}\frac{\Delta E}{E_0}} = \underbrace{\sqrt{\frac{\Delta E}{E_0}}}_{\sqrt{N_i}} \; \underbrace{\sqrt{\frac{E_x}{E_i}\left(\frac{E_0}{E_i} - 1\right)}}_{\sqrt{F}}$$

F: Fano factor

Si: $E_0 \cong 3.6$ eV $\quad F \cong 0.1$
Ge: $E_0 \cong 2.9$ eV $\quad F \cong 0.1$

$$\boxed{\sigma_i = \sqrt{N_i}\sqrt{F}}$$

smaller than naive expectation

due to energy conservation, fluctuations are reduced for a given energy loss ΔE (the total absorbed energy does not fluctuate)

relative energy resolution

$$\boxed{\frac{\sigma_i}{N_i} = \frac{\sqrt{N_i\, F}}{N_i} = \frac{\sqrt{F}}{\sqrt{N_i}} = \frac{\sqrt{F\, E_0}}{\sqrt{\Delta E}} = \frac{\sigma_{\Delta E}}{\Delta E}}$$

example: photon of 5 keV, $E_\gamma = \Delta E$, $\sigma_{\Delta E} = 40$ eV $\cong 1\%$ instead of 2.7% w/o Fano factor

Energy resolution of semiconductor detector

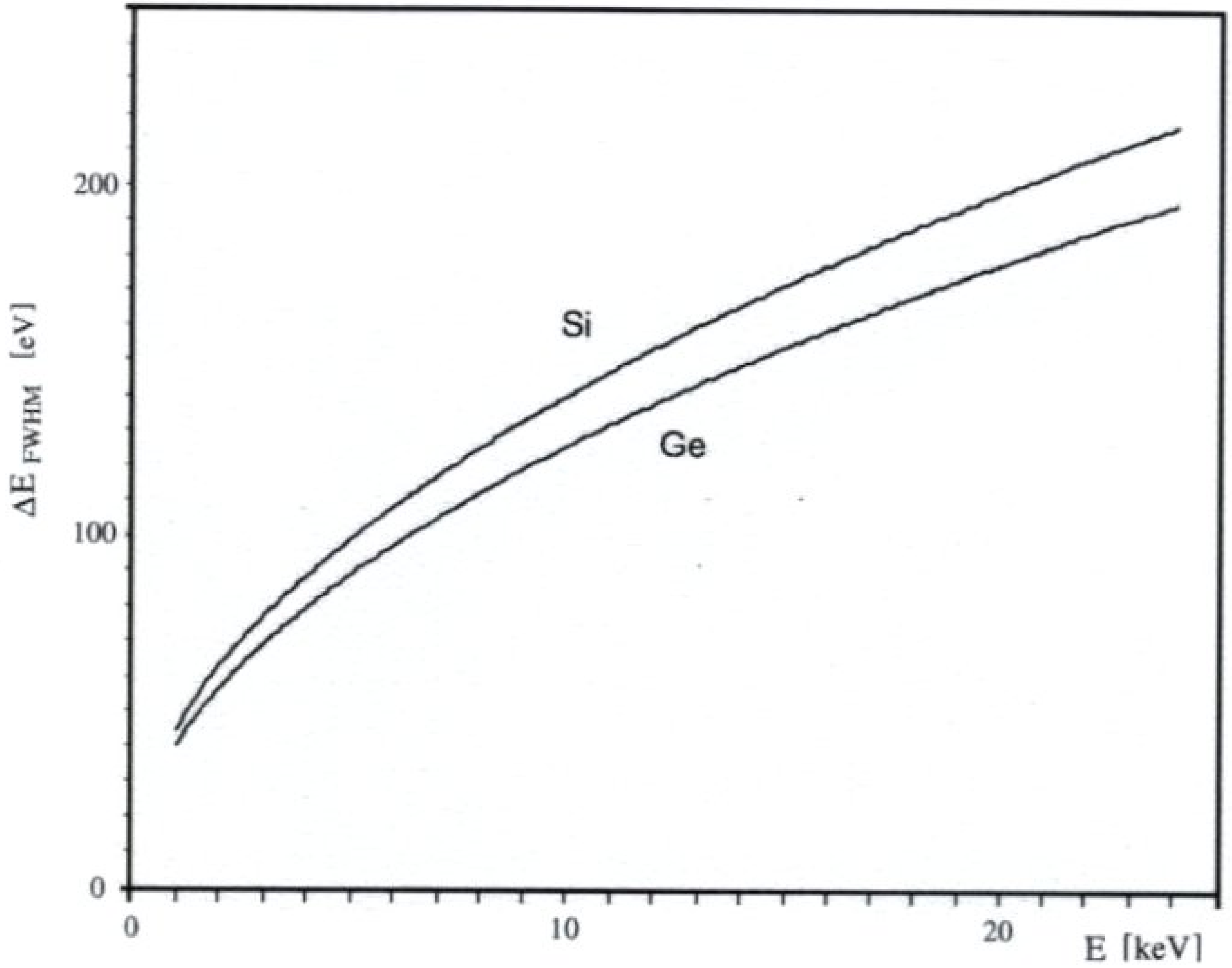

intrinsic resolution due to statistics of charge carriers generated, in addition noise and non-uniformities in charge-collection efficiency

4.5 Energy measurement with semiconductor detectors

for low energies, e.g. α-particles, low energy electrons or X- and γ-rays

4.5.1 Ion implanted or diffusion barrier detectors

as described in previous paragraph:
p-material with n^+ and p^+ surface contacts of
50 nm (ion implantation) or
0.1 – 1 μm (diffusion doping) thickness

$+U$ applied at n^+ side

p-layer typically 300 μm thick, usually
'fully depleted' i.e. depletion layer = p-zone

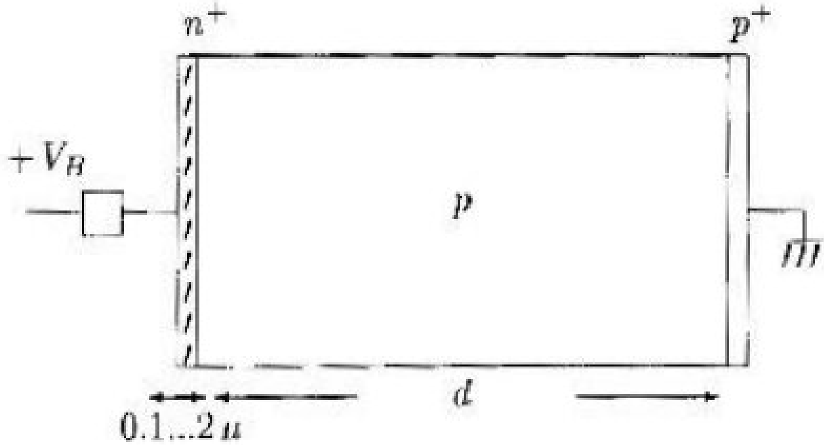

Disadvantage: n^+ contact layer acts as dead material for entering particles

- part of energy loss not measured $\rightarrow$ additional fluctuations
- very soft particles or short range particles like α's may not reach the depletion layer

4.5.2 Surface barrier detectors

contacts are very thin evaporated metal layers, 40 μg/cm^2 $\hat{=}$ 20 nm

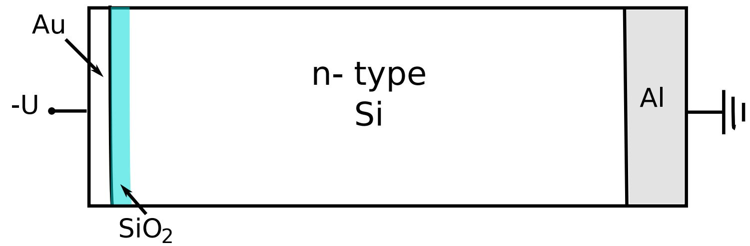

2-band model of Schottky diode

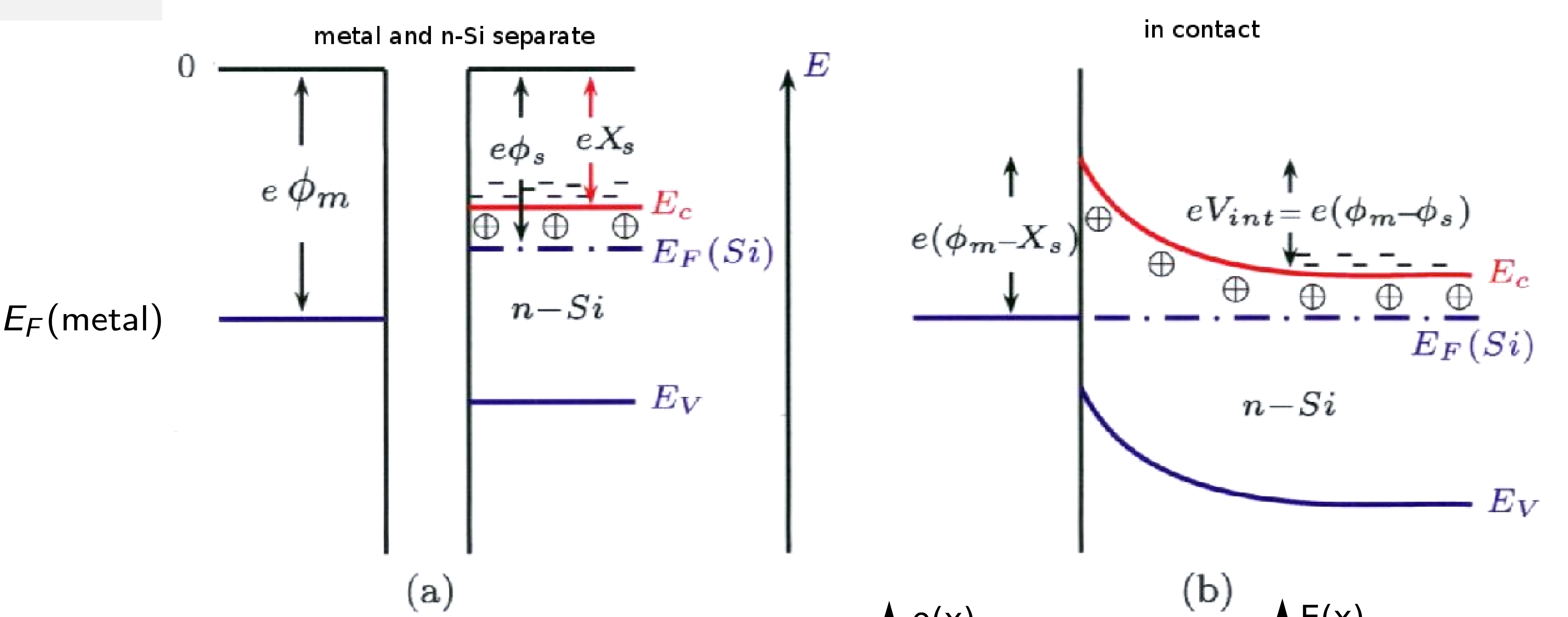

$e\Phi_m$ work function metal
$e\Phi_S$ work function semiconductor $< e\Phi_m$
(otherwise interface would be conducting)
eX_S electron affinity semiconductor

bringing metal in contact with n-Si:
electrons diffuse from Si into metal until
$E_F^{\text{metal}} = E_F^{\text{Si}} \rightarrow$ strong E-field at surface

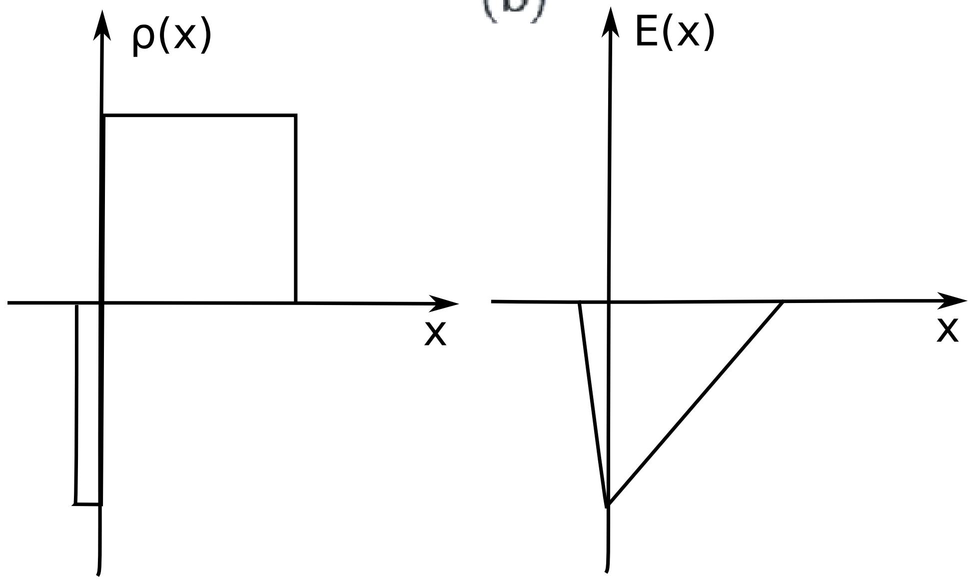

metal – semiconductor junction acts as diode, region with high resistance
$eV_{int} = e(\phi_m - \phi_S)$ potential barrier at surface for electrons in conduction band in Si

applying $-U$ at metal: this barrier is increased $\rightarrow$ no tunneling (dark current)
current only due to ionization

depletion layer in n-Si up to several mm thick
used since the 1960ies for particle detection

advantage of surface barrier detector:
very thin entrance window

- energy loss negligible
- for detection of photons down to eV energy range
  but usually thickness too small for γ-ray detection above 100 keV,
  i.e. good for X-rays

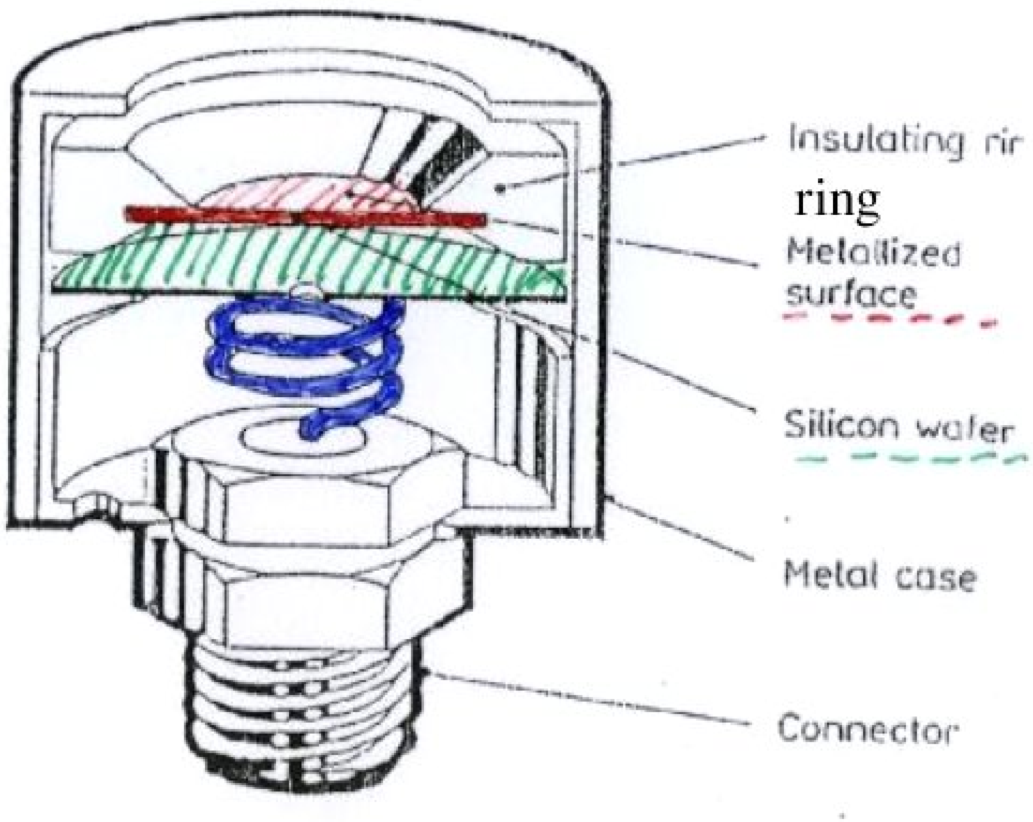

4.5.3. p-i-n detectors Ge(Li), Si(Li)

from 1960ies, trick: create a thick (cm) depletion layer with intrinsic conductivity by compensation

1. start with high-purity p-type Ge or Si, acceptor typically Boron
2. bring in contact with liquid Li bath ($350 - 400^\circ$ C) Li diffuses into Ge/Si
3. apply external field $\rightarrow$ positive Li-ions drift far into crystal and compensate B-ions locally

   typically 10^9 cm^{-3} Li atoms

   p-Si + Li$^+$ $\hat{=}$ neutral
   $\rho = 2 \cdot 10^5$ Ωcm possible
   i.e like true intrinsic material

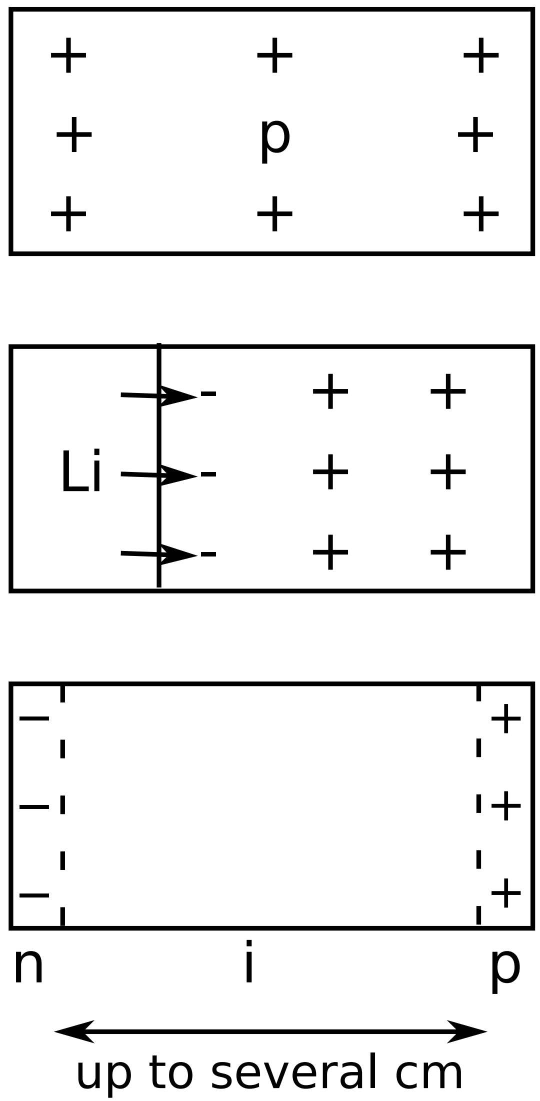

needs to be cooled permanently (liq. N_2) to avoid separation of Li from impurities by diffusion!

application: γ-spectroscopy

larger cross section for photo effect in Ge as compared to Si
$\rightarrow$ Ge(Li) preferred

however: full energy peak contains only order of 10 % of the signal in a 50 cm^3 crystal
(30 % in a 170 cm^3 crystal))

- resolution much better than NaI
- efficiency significantly lower

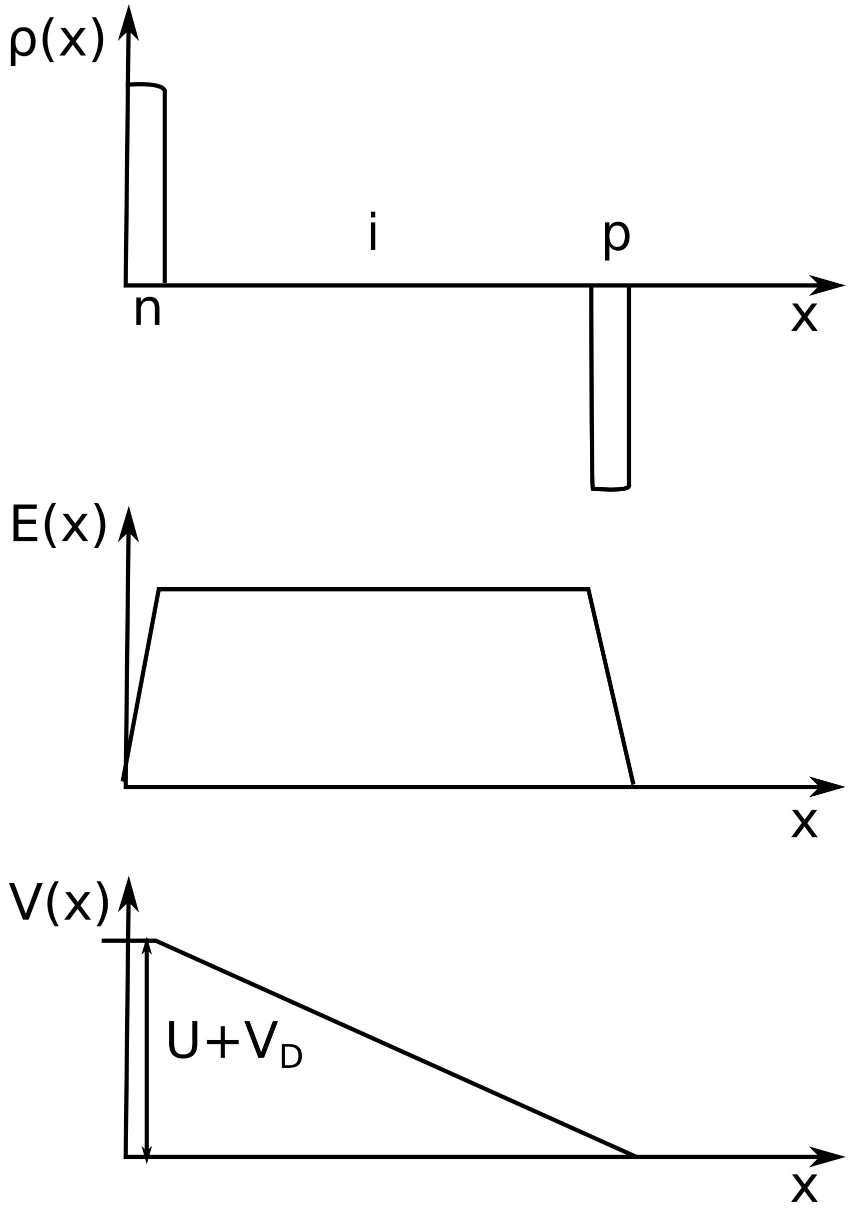

external voltage U and diffusion voltage V_D

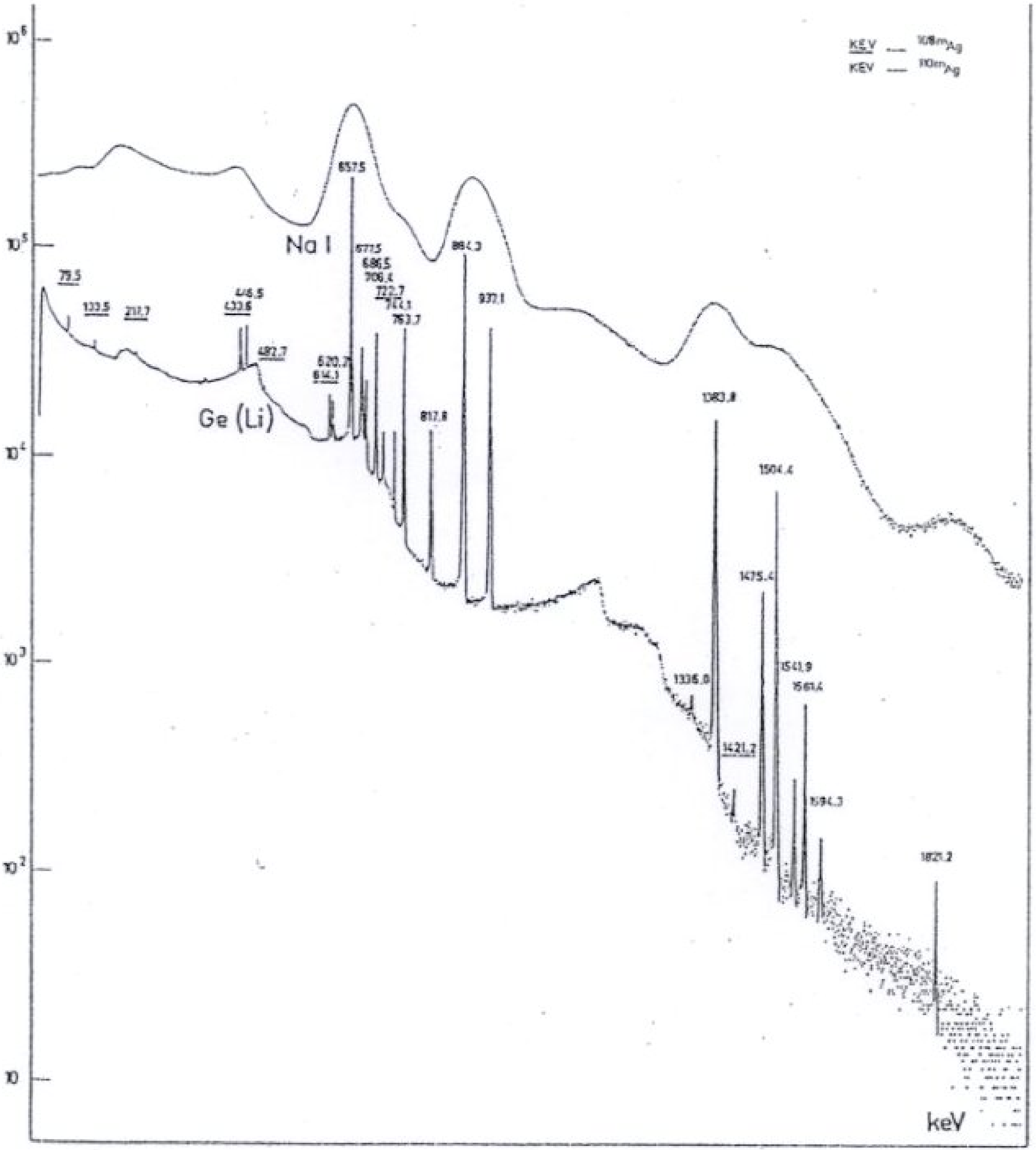

Ge(Li) detectors - a revolution in γ spectroscopy in the mid 1960ies:
comparison of spectra obtained with NaI (state of the art technique until then) and Ge(Li)

comparative pulse height spectra recorded using a sodium iodide scintillator and a Ge(Li) detector source of γ radiation: decay of ^{108m}Ag and ^{110m}Ag, energies of peaks are labeled in keV

4.5.4 High purity or intrinsic Ge detectors

from late 1970ies

similar to Li doped Ge or Si detectors, but dark current is kept low not by compensating impurities, but by making material very clean itself

by repeating the purification process (zone melting), extremely pure Ge can be obtained ($\leq 10^9$ impurity atoms per cm^3)
intrinsic layer like compensated zone in Ge(Li), similar sizes possible
advantage: cooling only needed during use to reduce noise

other applications

- low energy electrons
- strongly ionizing particles
- dE/dx for particle identification

useful energy range determined by range of particle vs. size of detector ranges of electrons, p, d, α, ... in Si

particles stopped in 5 mm Si(Li) detector:

α up to 120 MeV kinetic energy
p up to 30 MeV
e up to 3 MeV

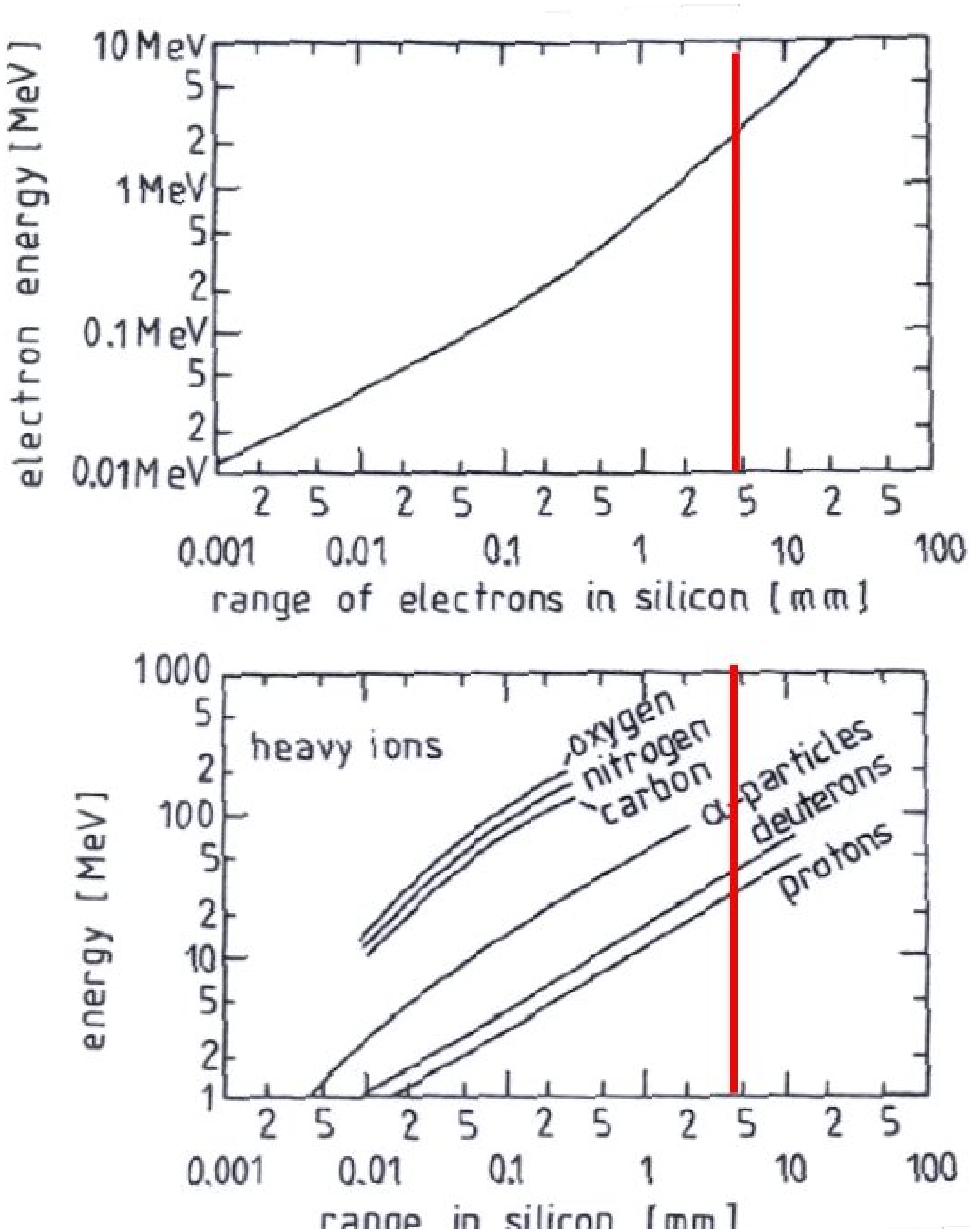

energy-range relation for electrons (top) and more massive particles (bottom)

4.5.5 Bolometers

how to increase resolution further?
use even finer steps for energy absorption, e.g. break-up of Cooper pairs in a semiconductor
operate at cryo-temperatures

instead of current one can measure temperature rise due to absorption of e.g. an X-ray,
couple absorber with extremely low heat capacity (HgCdTe) with semiconductor thermistor
$\rightarrow$ excellent energy resolution: 17 eV for 5.9 keV X-ray, i.e. $\Delta E/E = 2.9\,10^{-3}$
but low rate capability

applications: dark matter searches, astrophysical neutrinos, magnetic monopole searches

4.6 Position measurement with semiconductor detectors

4.6.1 Principle

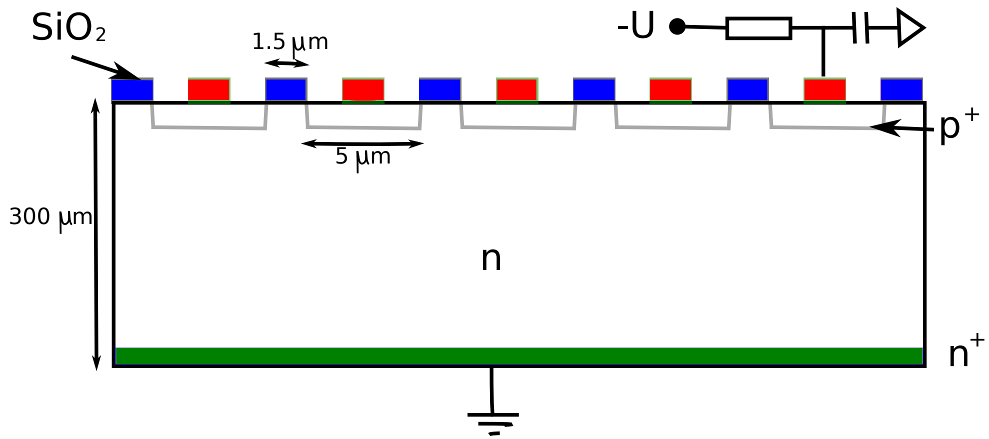

segmentation of readout electrodes into strips, pads, pixels
first usage in 1980ies
standard part of high energy experiments since LEP and Tevatron era

limitations of position resolution

- δ-electrons can shift the center of gravity of the track
  estimate limit in Si for track incidence $\perp$ detector:
  r_δ range of δ-electron
  energy of δ-electron such that N_δ electron-hole pairs generated vs N_p for primary track:
  assume $\delta \perp$ to primary track

$$\Delta x = \frac{N_\delta (r_\delta/2)}{N_\delta + N_p}$$

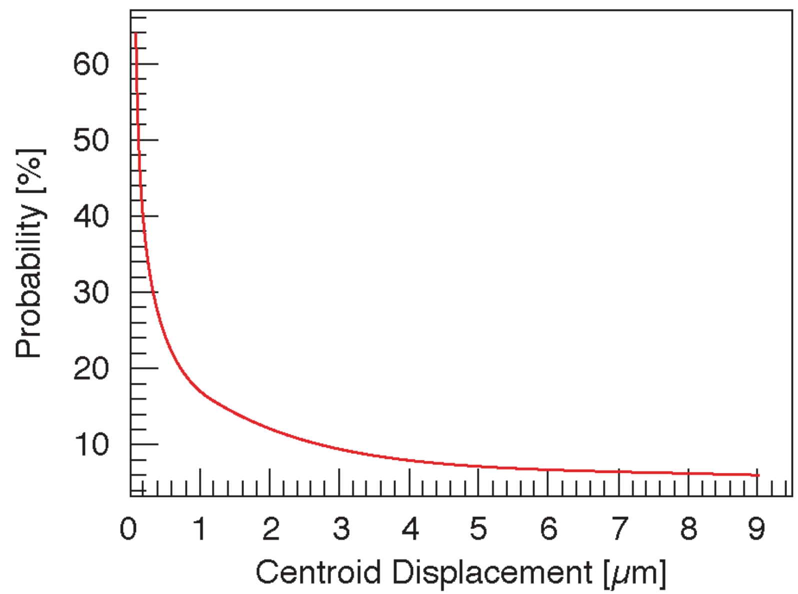

example:
100 μm Si, 5 GeV pion $\rightarrow$ 240 eV/μm $\rightarrow N_p = 6700$
10% probability for δ with $T_\delta > 20$ keV and $r_\delta = 5\ \mu$m
$\rightarrow\ \Delta x \approx 1\ \mu m$
worse for thicker detector: see Fig for 300 μm Si

- energy loss (Landau) fluctuations have influence on position measurement

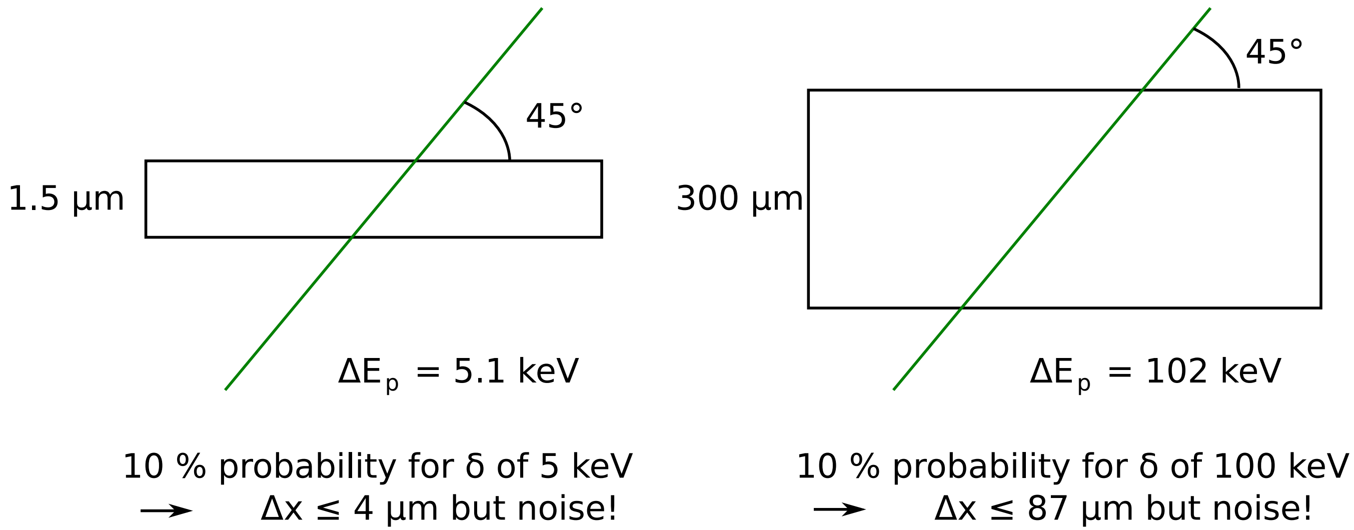

- noise: position measurement requires $S \gg N$
  if signal only on 1 strip (or pad), resolution $\sigma_x = \Delta s/\sqrt{12}$, independent of S/N
  if signal on several strips $\Rightarrow$ more precise position by center-of-gravity method (see below), but influenced by S/N
- diffusion: smearing of charge cloud (see gaseous detectors, transverse diffusion)
  initially helps to distribute signal over more than one strip
  but 2-track resolution and S/N deteriorate with diffusion
- magnetic fields: Lorentz force on drifting electrons and holes: track signal is displaced if E not parallel B, increasing displacement with drift length

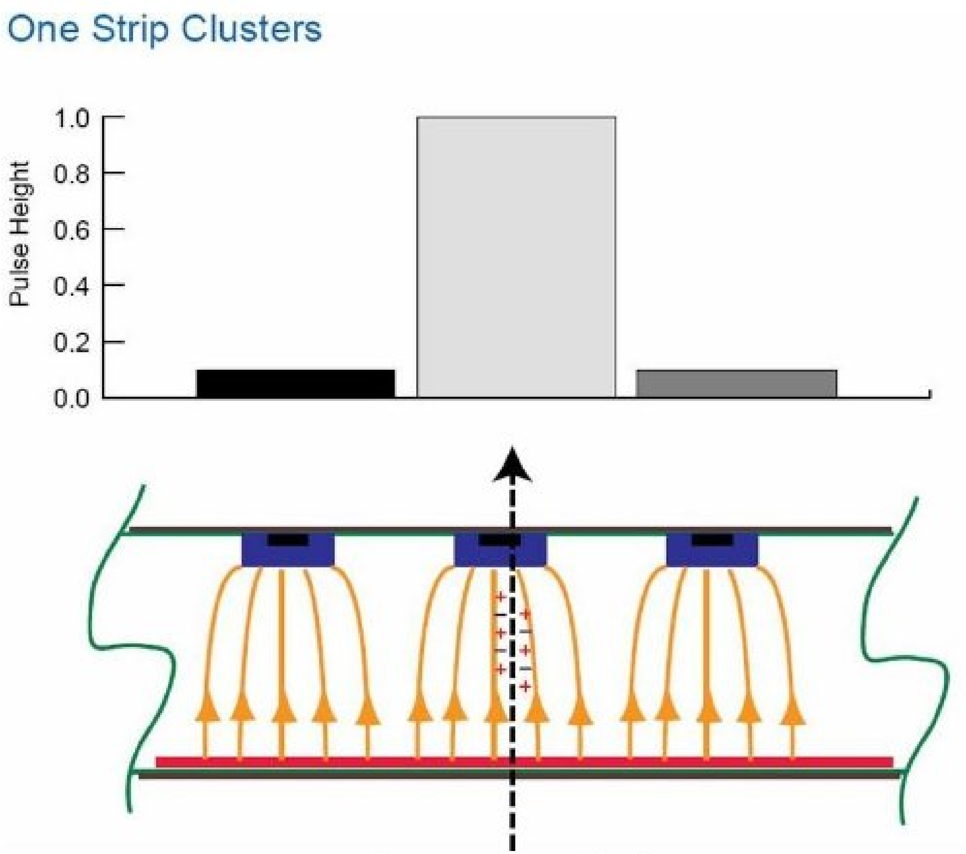

Δs: strip pitch

$$\sigma_x = \Delta s/\sqrt{12}$$

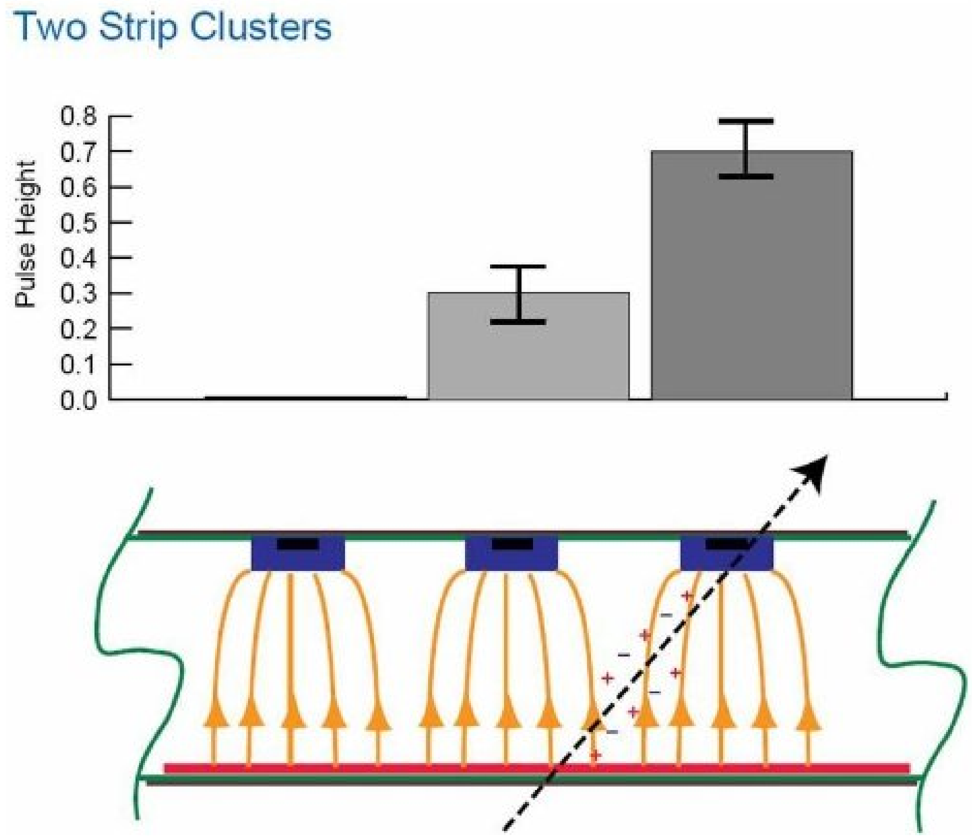

centroid resolution

$$\sigma_x \approx (\Delta s/2)(N/S)$$

charge distribution registered for a semiconductor detector with or without magnetic field

no field

$B = 1.68\ T$

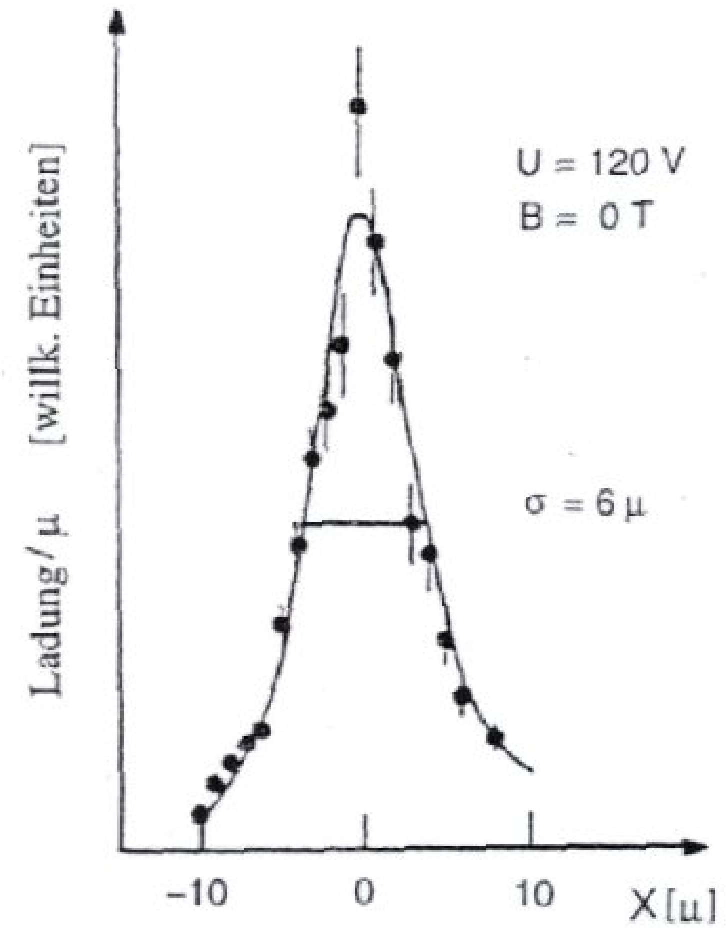

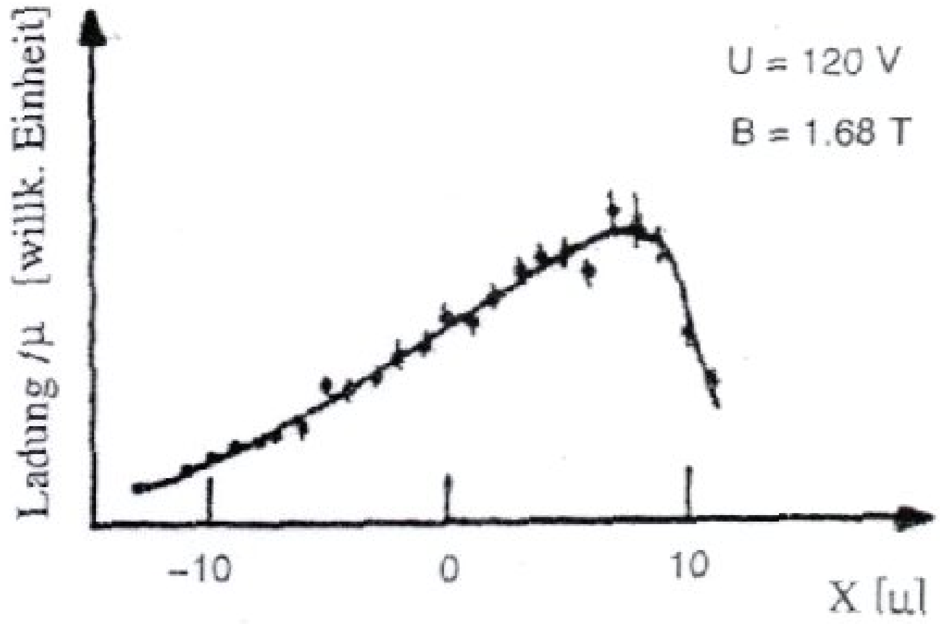

Si vertex detectors

main applications:

- tracking of particles close to primary vertex before multiple scattering
  $\Rightarrow$ good angular resolution
- identification of secondary vertices
  c, b, τ decays $\tau = 10^{-12} \ldots 10^{-13}$ s,
  $\gamma c\tau \cong \gamma \cdot 30\ \mu$m

'b-tagging' for top or Higgs decays

example: 4 layers microstrips of H1 experiment
$\Longrightarrow$

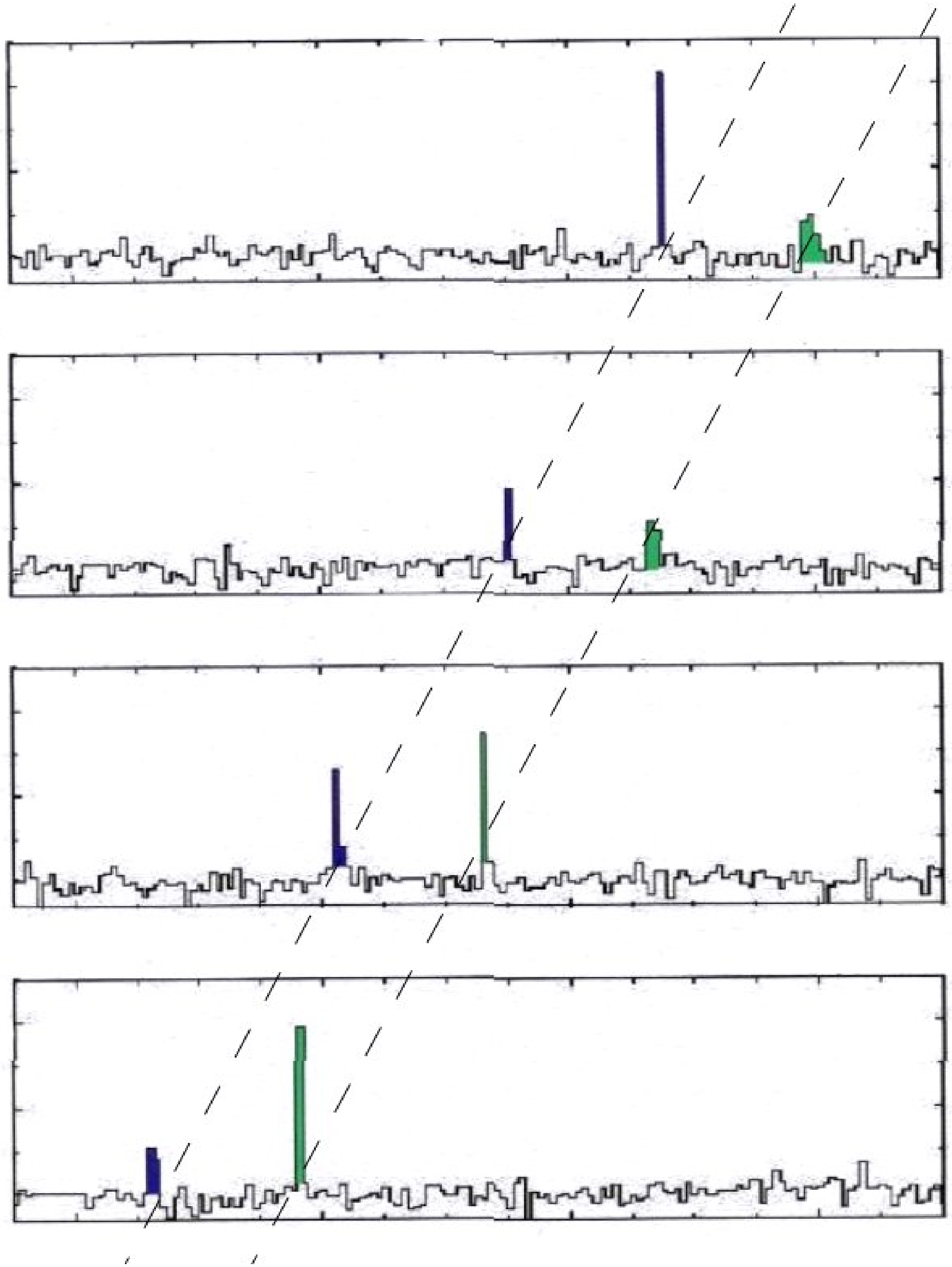

before and after vertex cuts

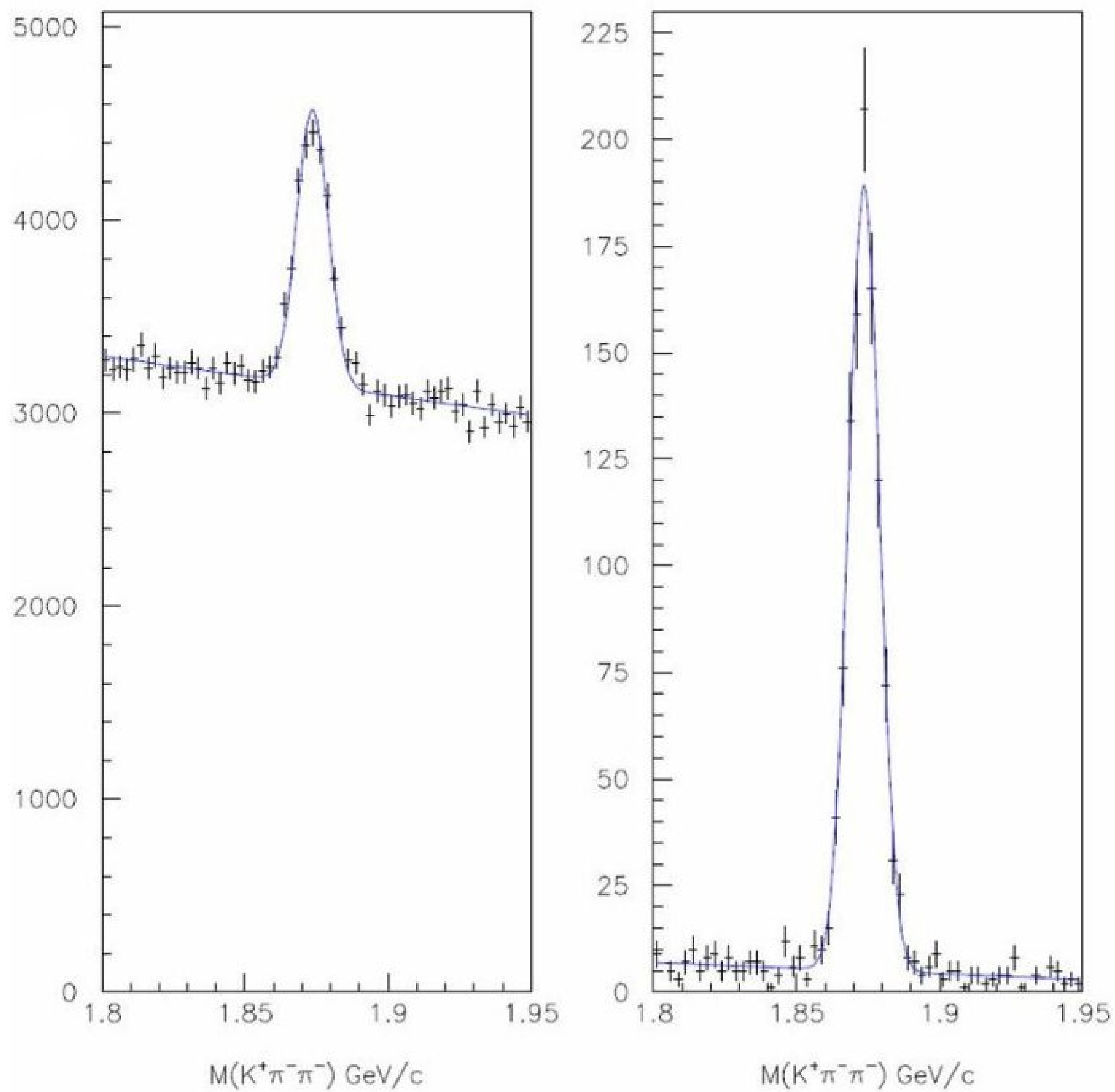

example: CDF

discovery top quark
3 Si-layers at
r = 1.5, 5-10, 20-29 cm
total active area approx. 10 m^2

$D^{\pm} \rightarrow K\pi\pi$ mass peaks
before and after 7σ vertex cut

example (CDF): detection of 2 b-jets from $t\bar{t}$-decay

$$
\begin{aligned}
p + \bar{p} &\rightarrow t\bar{t} + X \\
&\quad \hookrightarrow \bar{b} + W^+ \\
&\qquad\qquad \hookrightarrow e^+ + \nu_e \\
&\quad \hookrightarrow b + W^- \\
&\qquad\qquad \hookrightarrow q\bar{q} \text{ (2 jets)}
\end{aligned}
$$

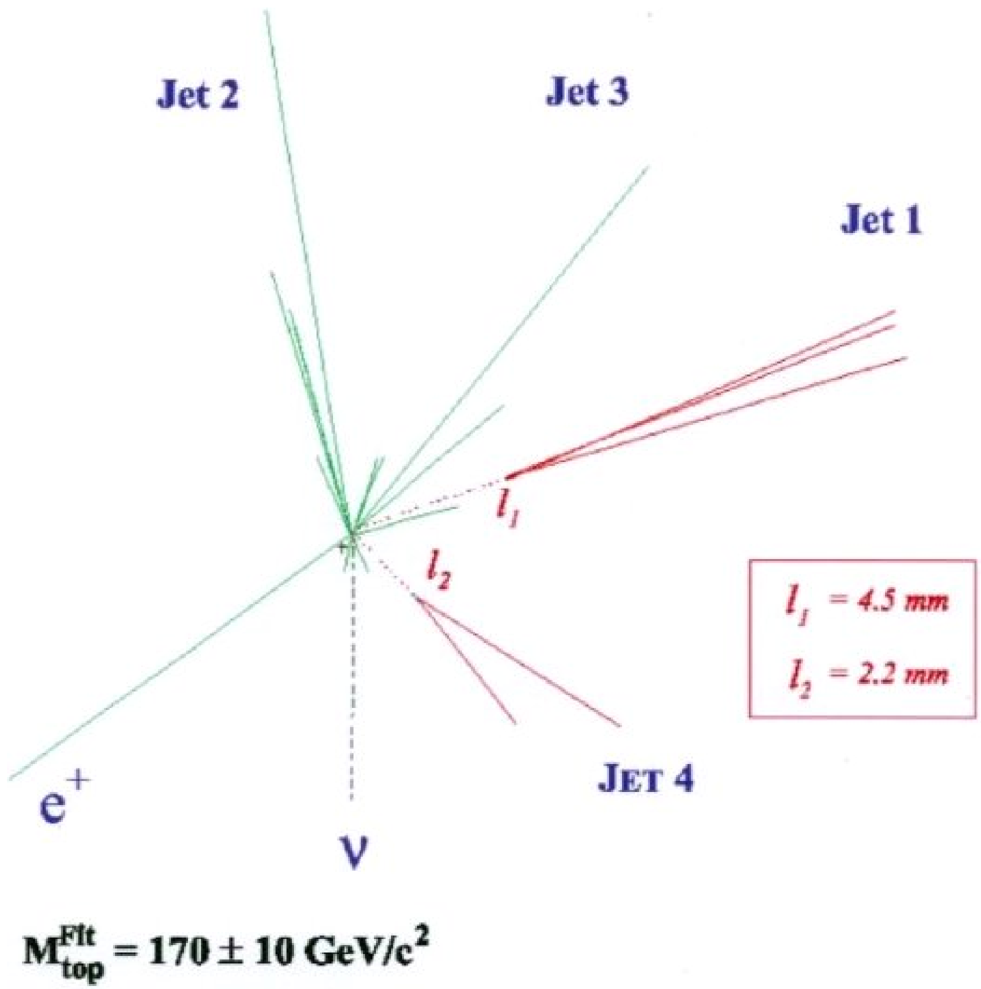

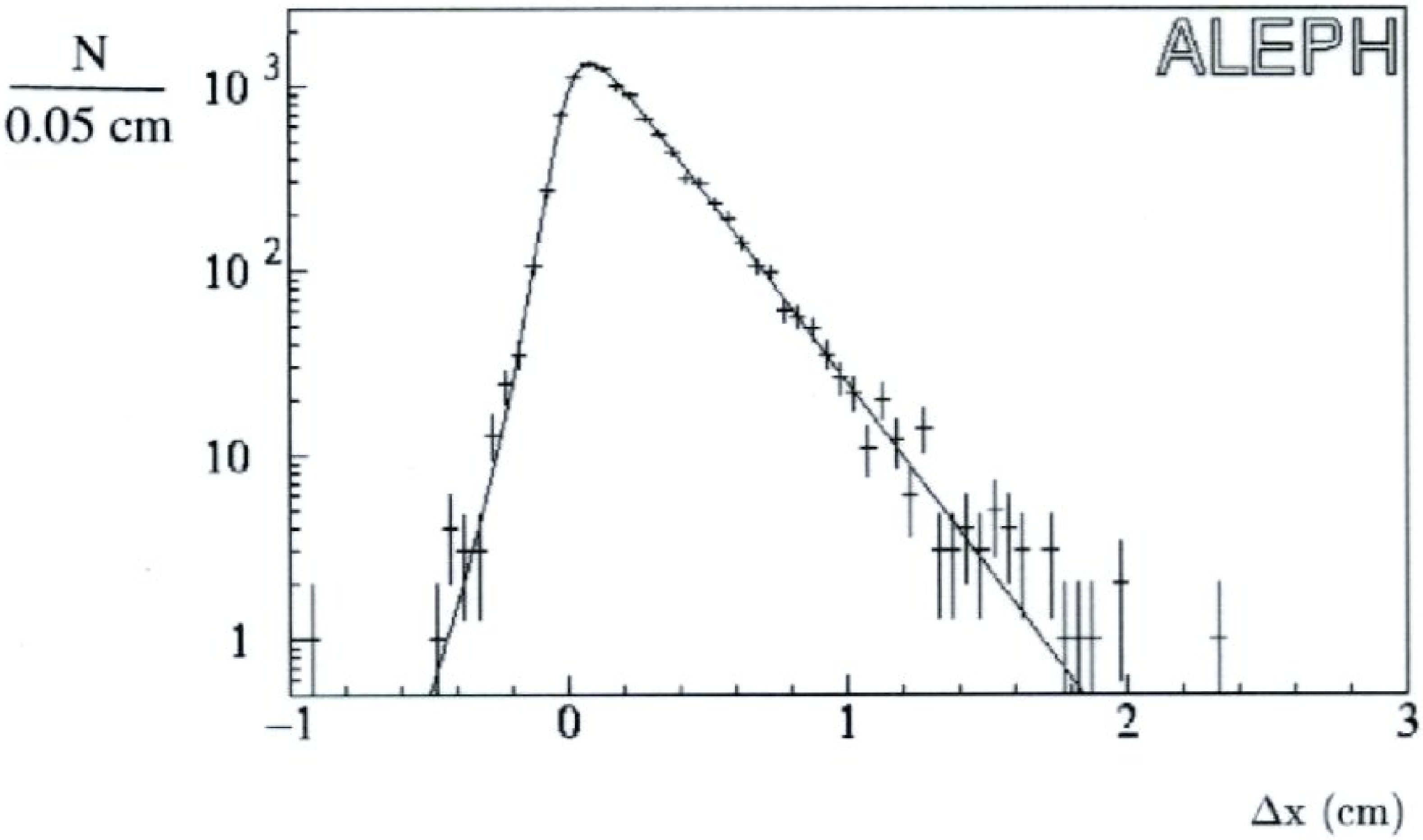

distribution of secondary vertices typical for charm decays in ALEPH.

how to use it: make a cut at e.g. $x > 3\sigma$ of vertex resolution $\rightarrow$ secondary vertex

critical for detection of secondary vertices:
impact parameter resolution

'impact parameter' b: closest distance from (extrapolated) track to primary vertex

$$\frac{\sigma_b}{\sigma_1} = \frac{r_2}{r_2 - r_1}$$

$$\boxed{\sigma^2 = \left(\frac{r_1}{r_2 - r_1}\sigma_2\right)^2 + \left(\frac{r_2}{r_2 - r_1}\sigma_1\right)^2 + \sigma_{MS}^2}$$

$$\frac{\sigma_b}{\sigma_2} = \frac{r_1}{r_2 - r_1}$$

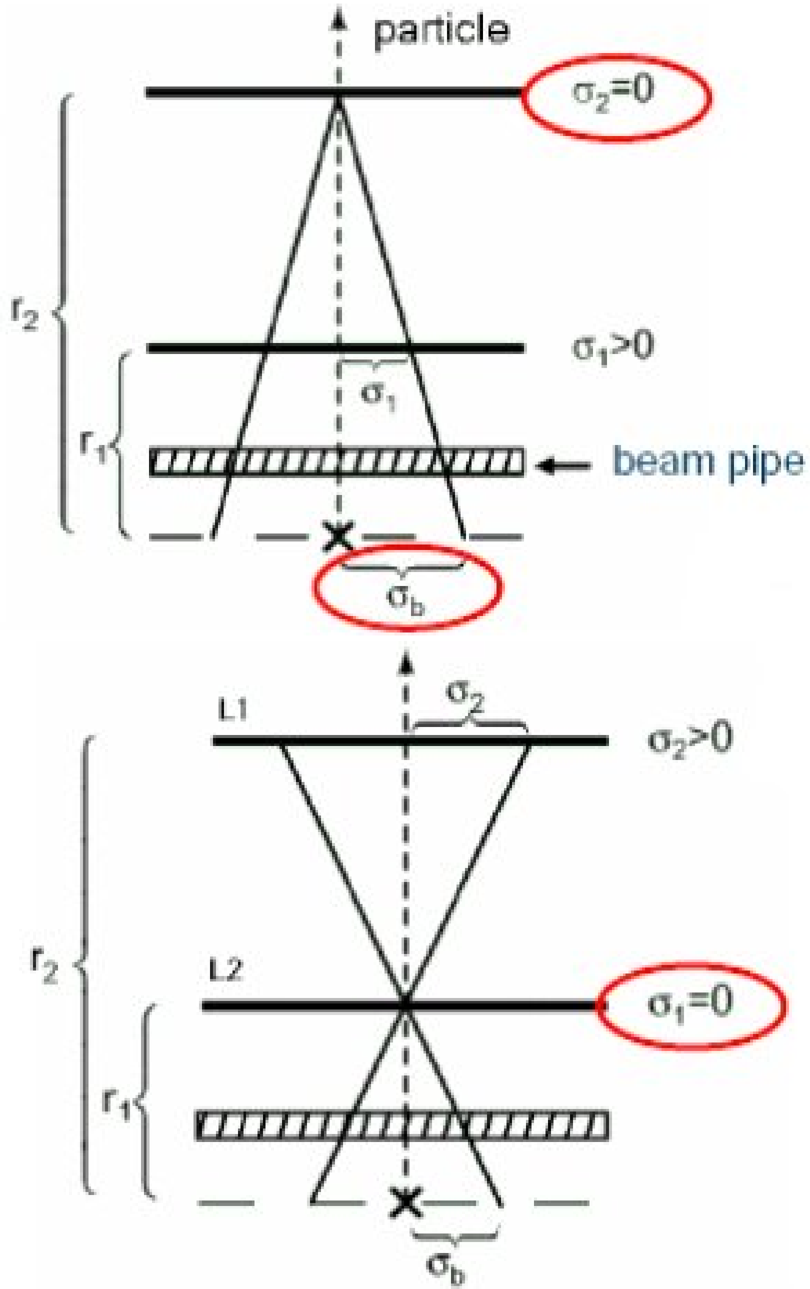

optimum resolution for r_1 small, r_2 large and σ_1, σ_2 small
make contribution of multiple scattering small, as little material as possible $\quad \sigma_{MS} \propto \frac{1}{p}\sqrt{\frac{X}{X_0}}$
practical values $< 100\ \mu$m for $p > 1$ GeV/c

4.6.2 Micro-strip detectors (about 1983)

principle and segmentation see above

- typical pitch $20 - 50\ \mu$m
- width of charge distribution (for $\perp$ incidence) $\cong 10\ \mu$m
- signal in 300 μm Si: $\cong 25\,000\, e$ for minimum ionizing particles
- order 100 channels/cm^2

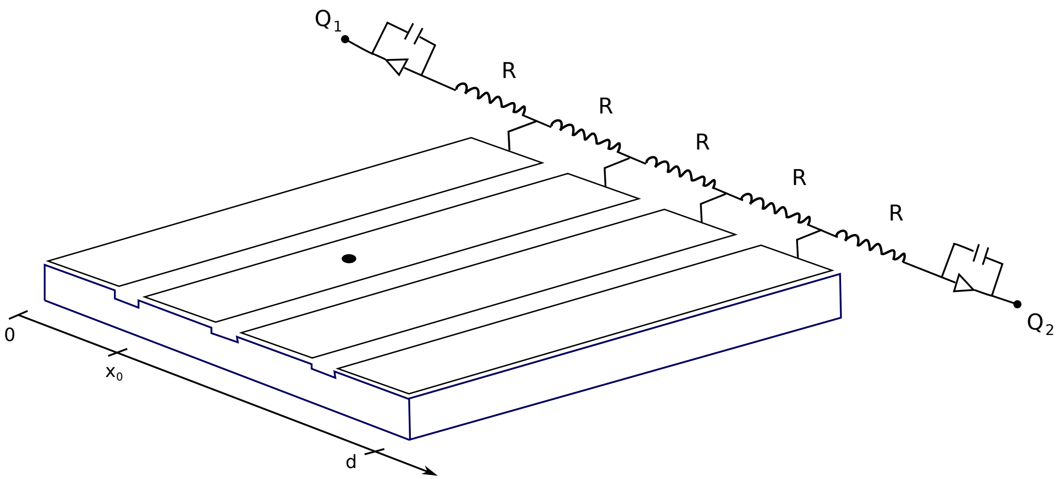

read-out:

- resistor network for charge division

$$\langle x \rangle = \frac{Q_2}{Q_1 + Q_2} d$$

charge sensitive preamplifier

disadvantages:

- only 1 hit per event and detector
- R has to be large enough for good S/N
- slow due to RC of resistor chain

- **individual read-out of all strips:**

  charge-sharing by capacitive coupling between strips $\cong$ 1 pF/cm

  $\Rightarrow$ signal on neighboring strip a few % of central signal

  typical position resolution $\sim 10\ \mu$m

  vertex resolution determined by

  - position resolution
  - lever arm
  - multiple scattering
  - momentum p or $p_\perp$, respectively track curvature in magnetic field
  - effect of Lorentz force on drifting charge

  typical value (H1 detector):

$$\sigma_{vtx} = 27\ \mu\text{m} \oplus \frac{98\ \mu\text{m}}{p_\perp\ (\text{GeV/c})}$$

  $\oplus$: addition in quadrature

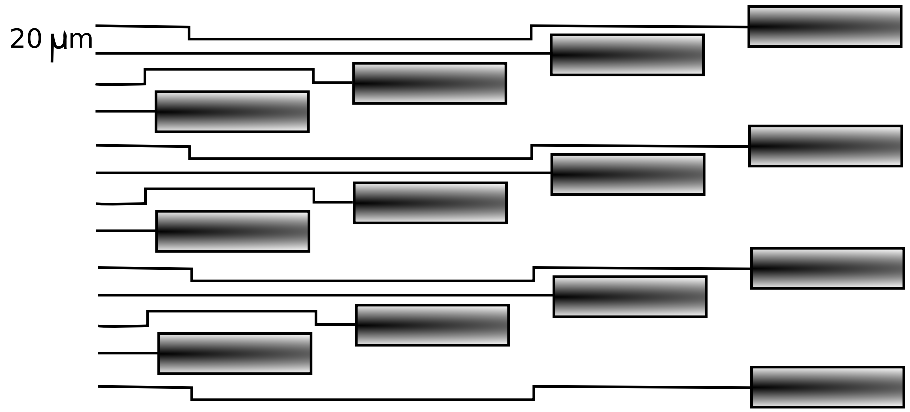

contact pads for readout electronics

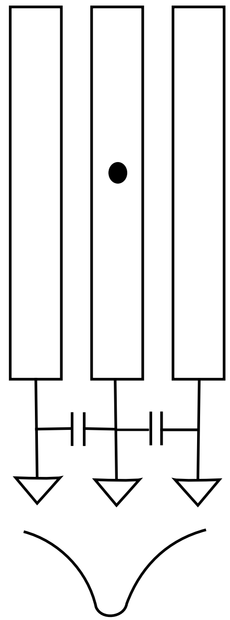

4.6.3 Double-sided micro-strip detectors

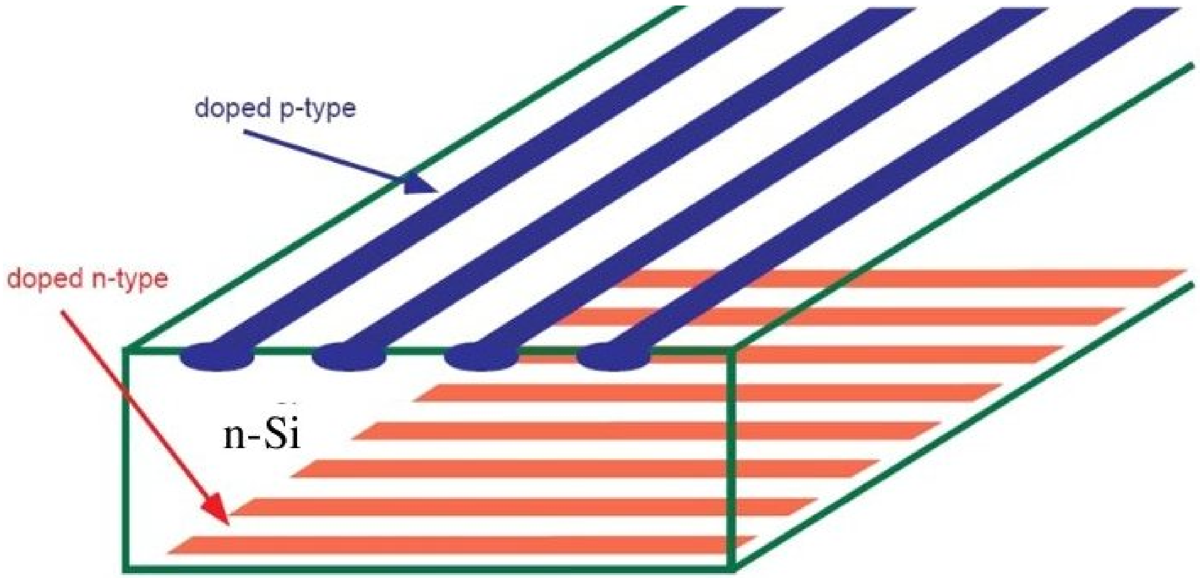

between n^+ side strips, additional strips are needed for insulation:
SiO_2 surface layer: positive space charge $\Rightarrow e^-$ layer in n-material
p^+ blocking electrodes for separation of n^+ strips

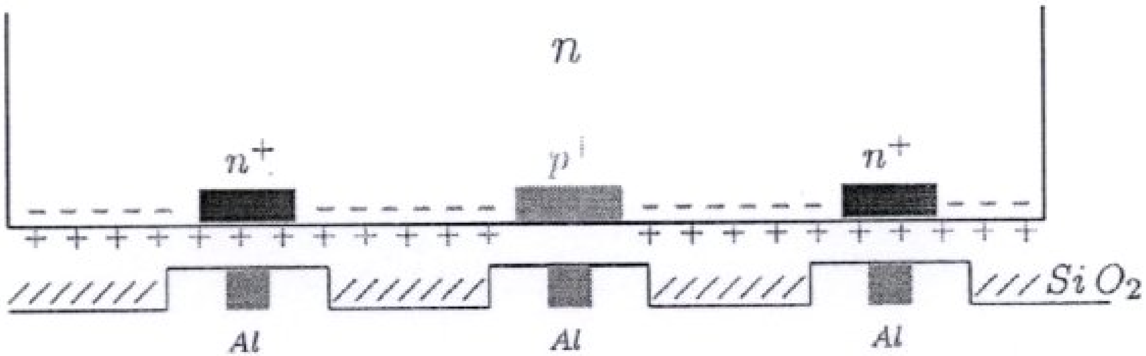

used in:
DELPHI, ALEPH, H1, ZEUS, HERA-B, CDF, D0

Example: Delphi vertex detector

3 coaxial layers of double-sided micro-strips, capacitive coupling, 6.3, 9.0, 10.9 cm from beam axis

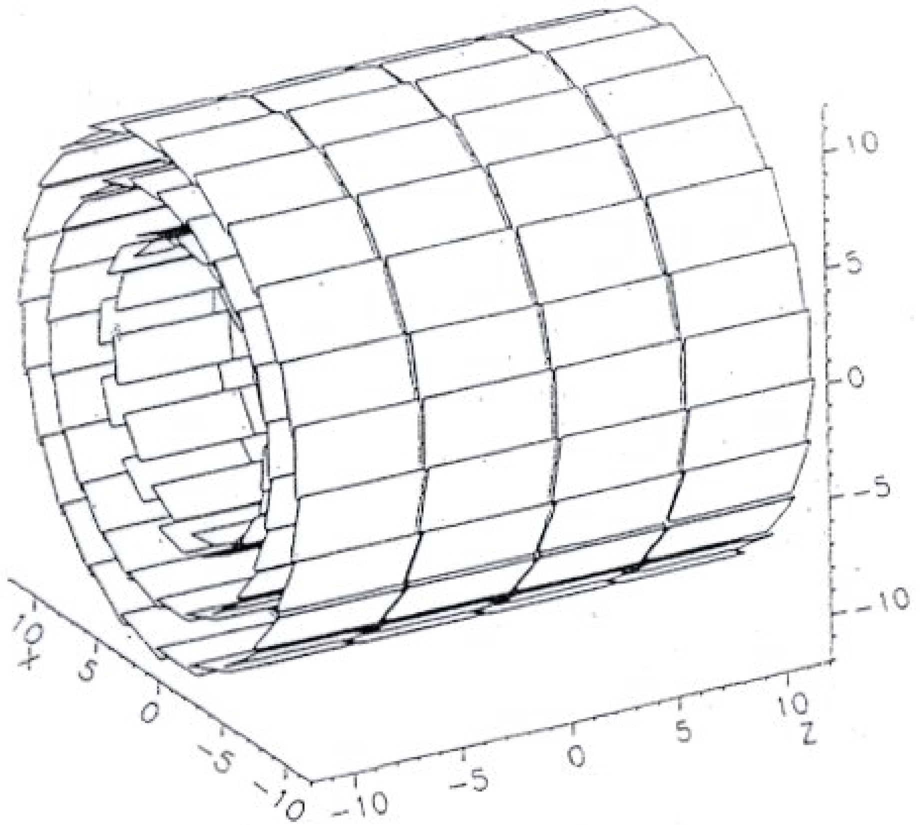

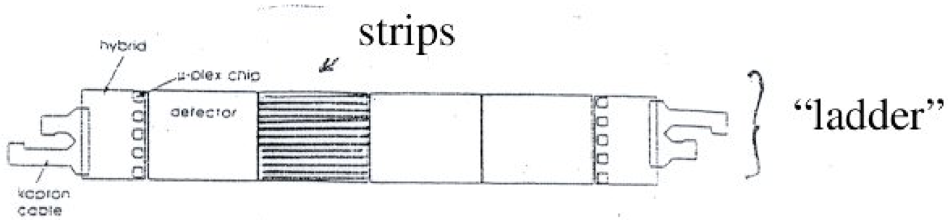

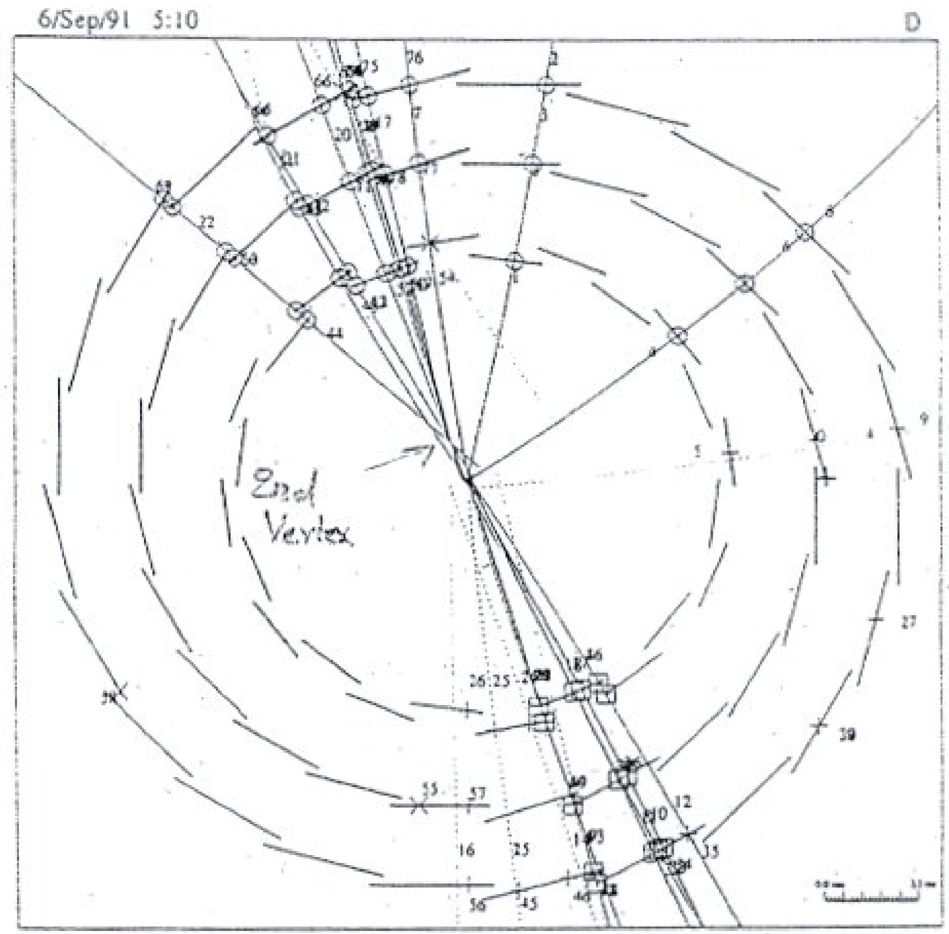

event recorded by the Delphi micro-vertex detector

4.6.4 Silicon drift detectors

proposed by Gatti and Rehak in 1984, first realized in 1990ies

potential inside wafer has parabolic shape (see next page), superimpose linear electric field

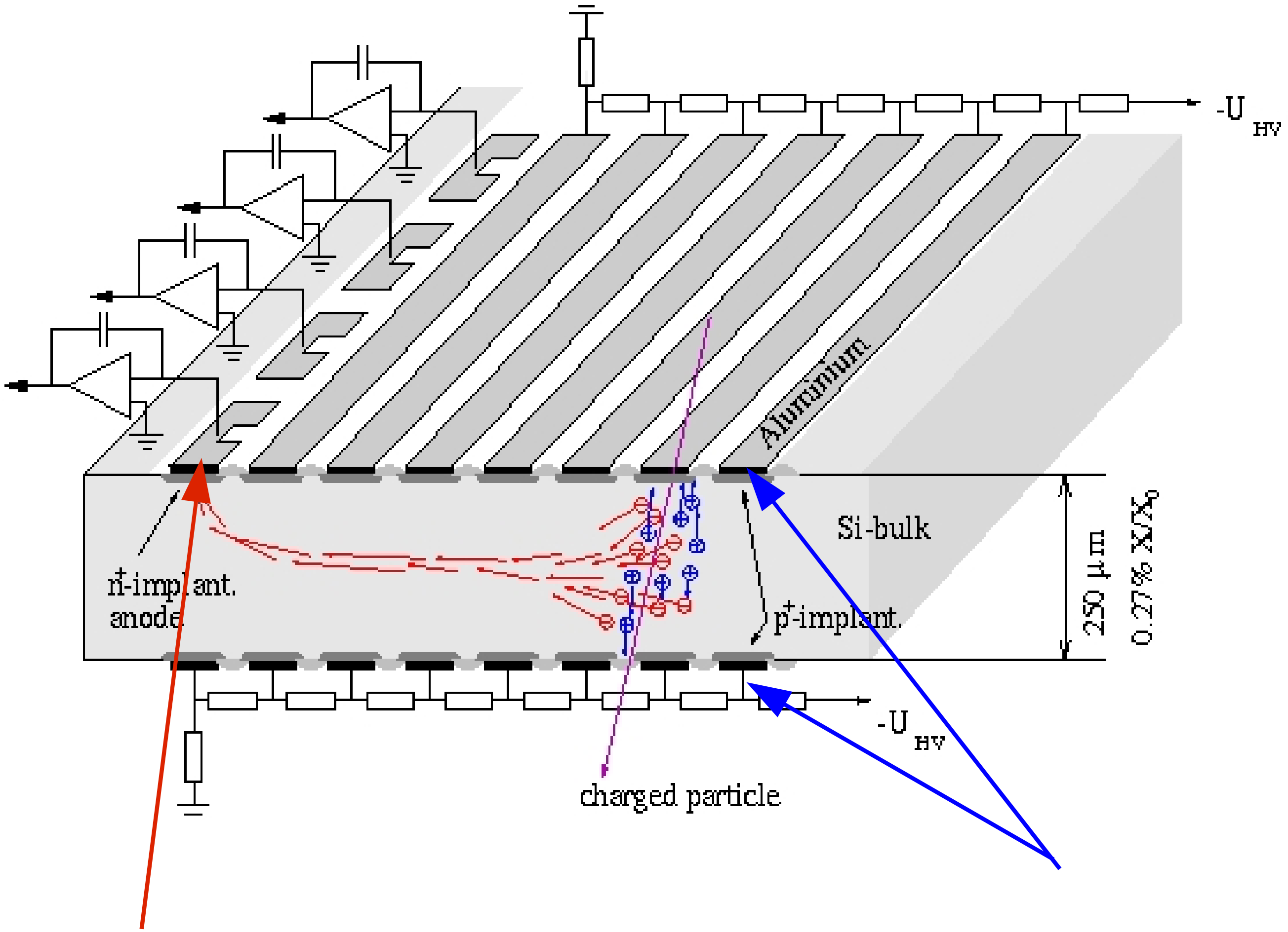

wafer can be fully depleted by reverse bias voltage on a small n+ anode implanted on wafer edge

n-type bulk Si with p+ electrodes on both flat sides analog to gaseous drift chambers: charge carriers drifting in well-defined E-field

measurement of drift time
⇒ position of ionizing track

typical drift time: a few μs for $5 - 10$ cm

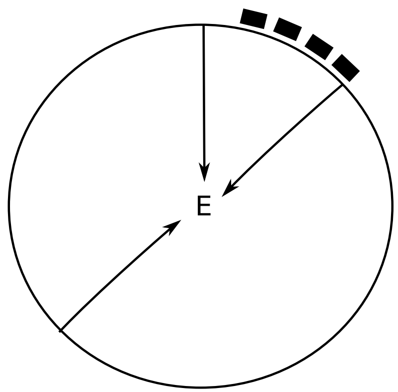

first example CERES at SPS:
radial Si drift-chamber

readout: 1° sectors in φ, 256 time samples (flash ADC) for determination of r, equivalent of 1 plane in a TPC

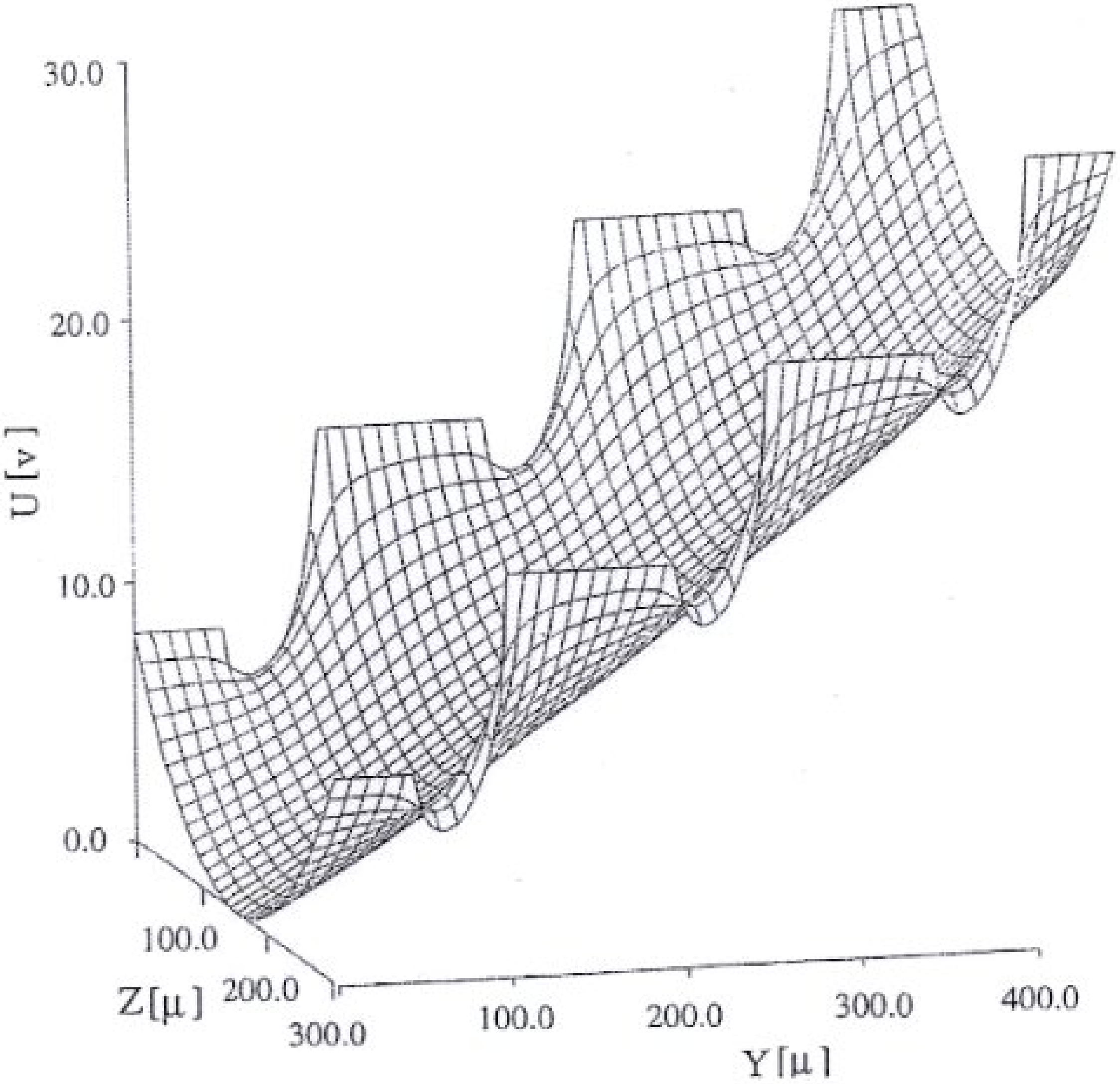

potential shape in Si drift-chamber:
trough-like shape due to positive space charge in depletion area, slope from external voltage divider

CERES 4 inch Si drift detector

event display

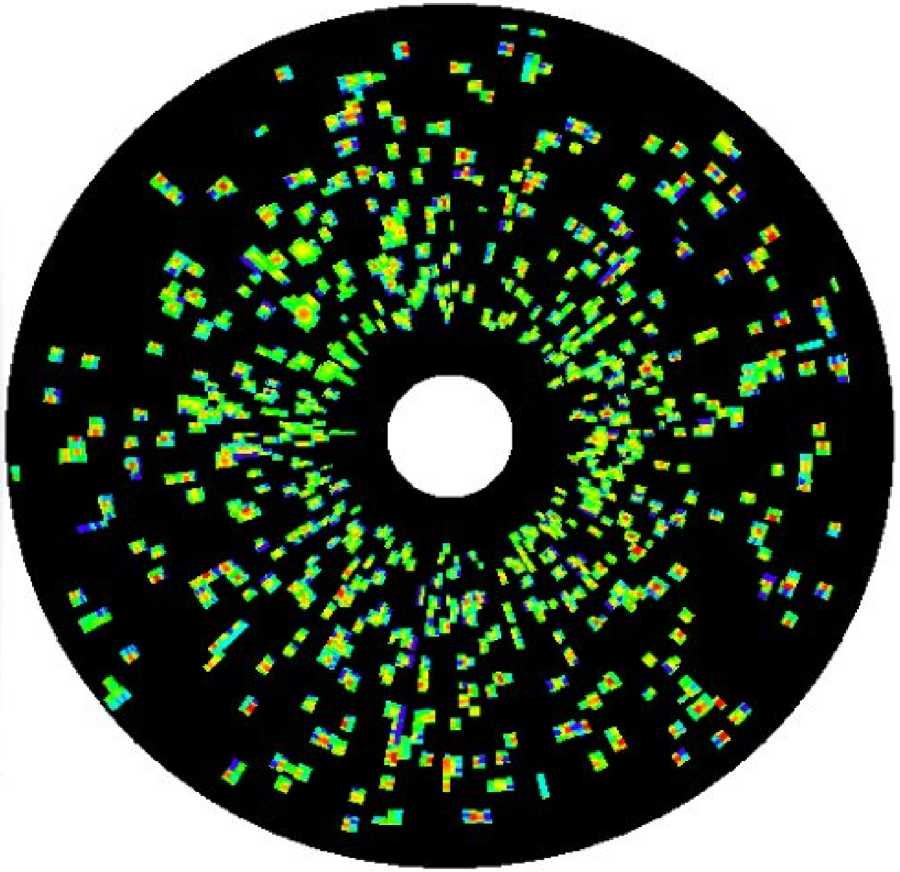

active area	52 cm^2
granularity	360 anodes $\times$ 256 time bins
	$=$ 92 160 pixels
max. number of resolved hits	$2 \cdot 10^4$
wafer thickness	250 μm
radiation length	0.27% of X_0
multiple scattering	$\approx$ 0.54 mrad @ 1 GeV/c

4.6.5 Pixel detectors

- principle: like micro-strips, but 2-dimensional segmentation of p^+ contacts: 'pixel'
  each pixel connected to bias voltage and readout electronics

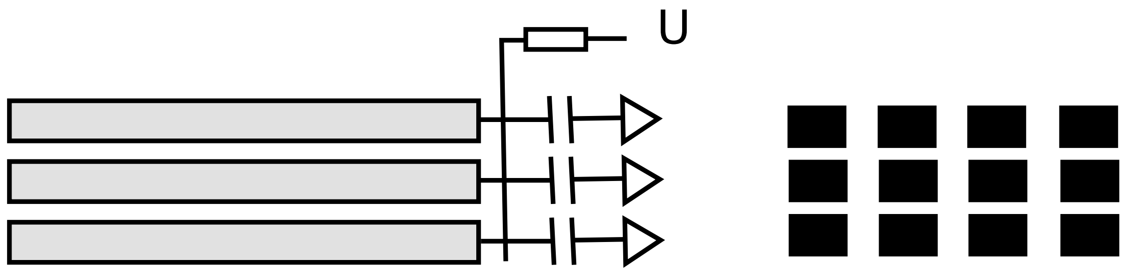

- advantage: 2-dim information like double-sided micro-strip,
  but more simultaneous hits per detector allowed
  low capacity and thus low noise $\Rightarrow$ good S/N
- disadvantage: large number of read-out channels $\Rightarrow$ expensive, large data volume
  pixel contacts are complicated ('bump bonding' or 'flip chip' technologies)
- typical pixel areas $\sim 2000\ \mu\text{m}^2 \rightarrow$ order 5000 channels/cm^2
  square ($150 \times 150\ \mu\text{m}^2$)
  rectangular ($50 \times 300\ \mu\text{m}^2$)
- hit resolution: $\Delta x/\sqrt{12}$ and $\Delta y/\sqrt{12}$

examples: all LHC experiments

bump bonding

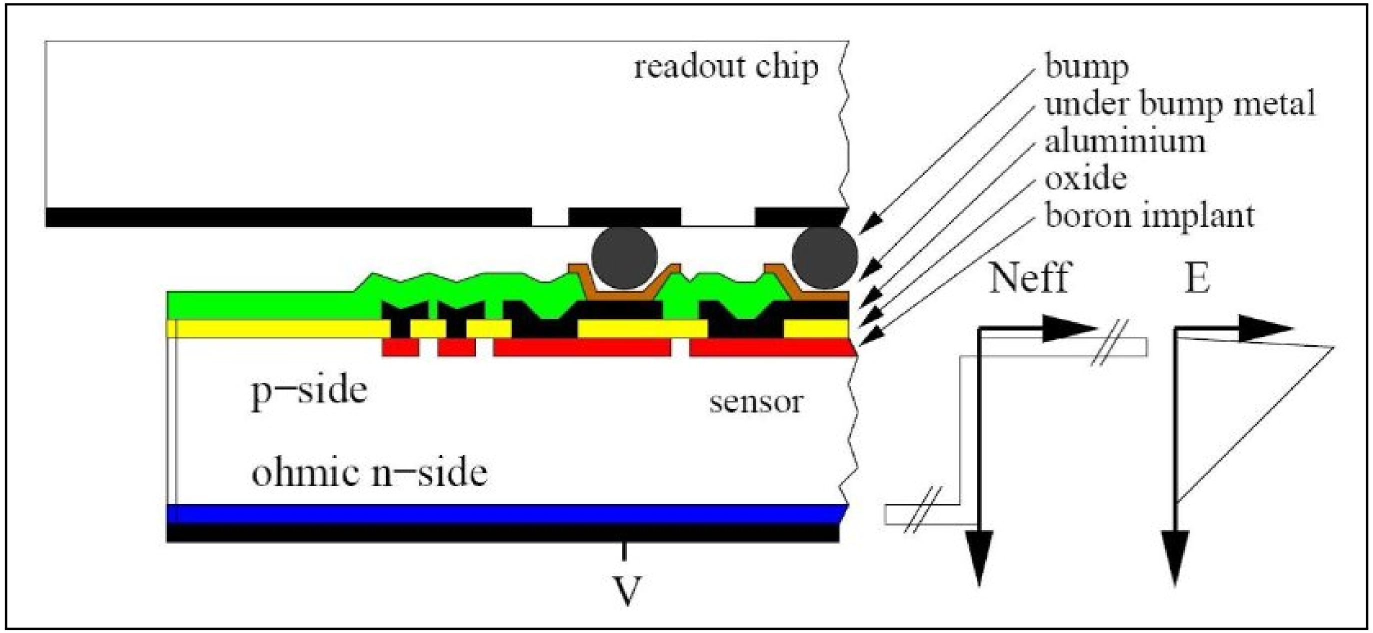

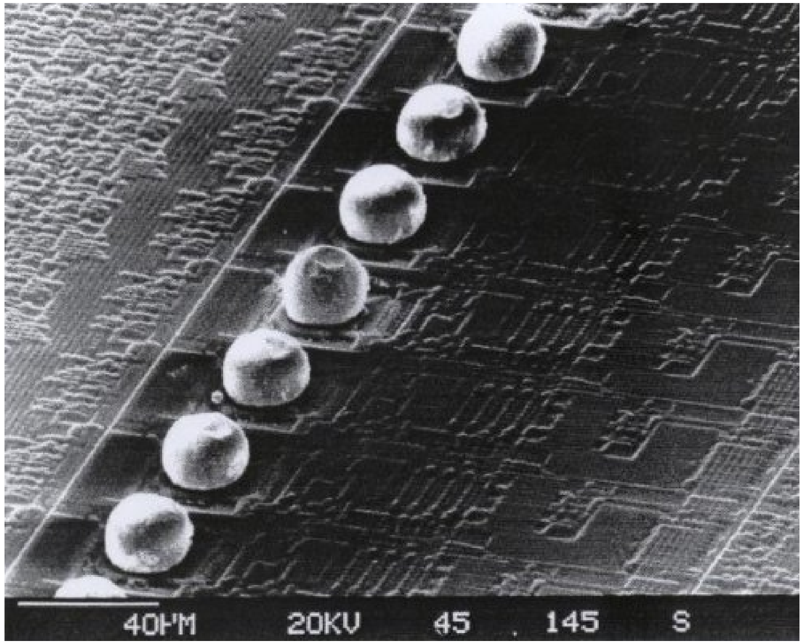

SEM photograph of solder bumps on an Omega3 chip

connection pixel chip ↔ readout chip

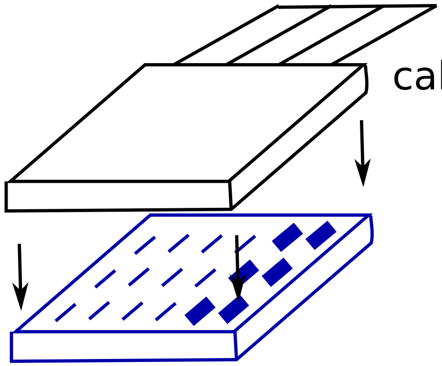

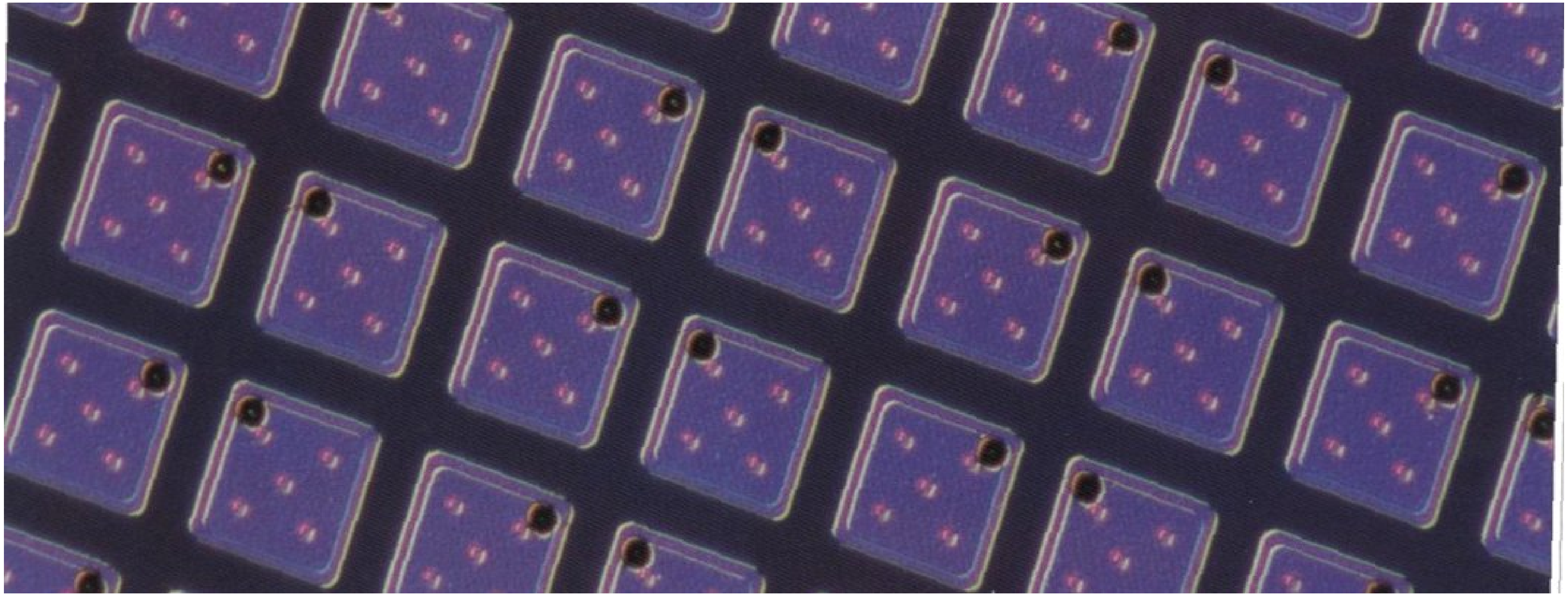

pixel detectors depend on the bump-bonding technique, which PSI adapted and miniaturized
contact between pixel and microchip is a 17 μm solder ball of indium
microscope image shows pixels with the indium balls (dark points).

prototype Si pixel telescope

7(9) Si pixel detectors
0.5 M (0.7 M) channels
+ Si μstrip planes

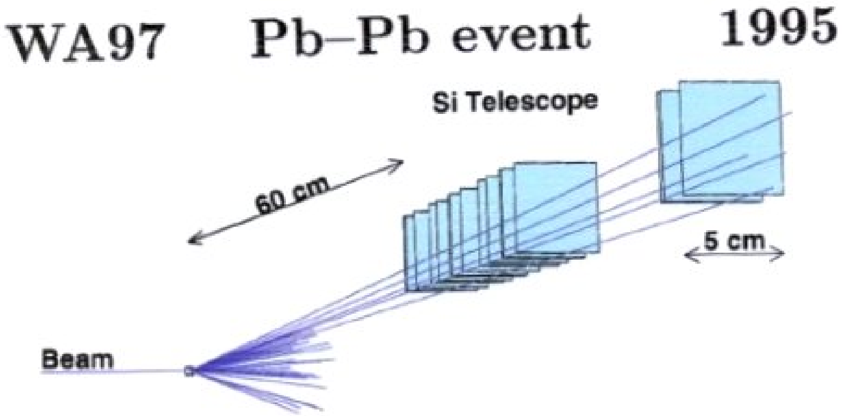

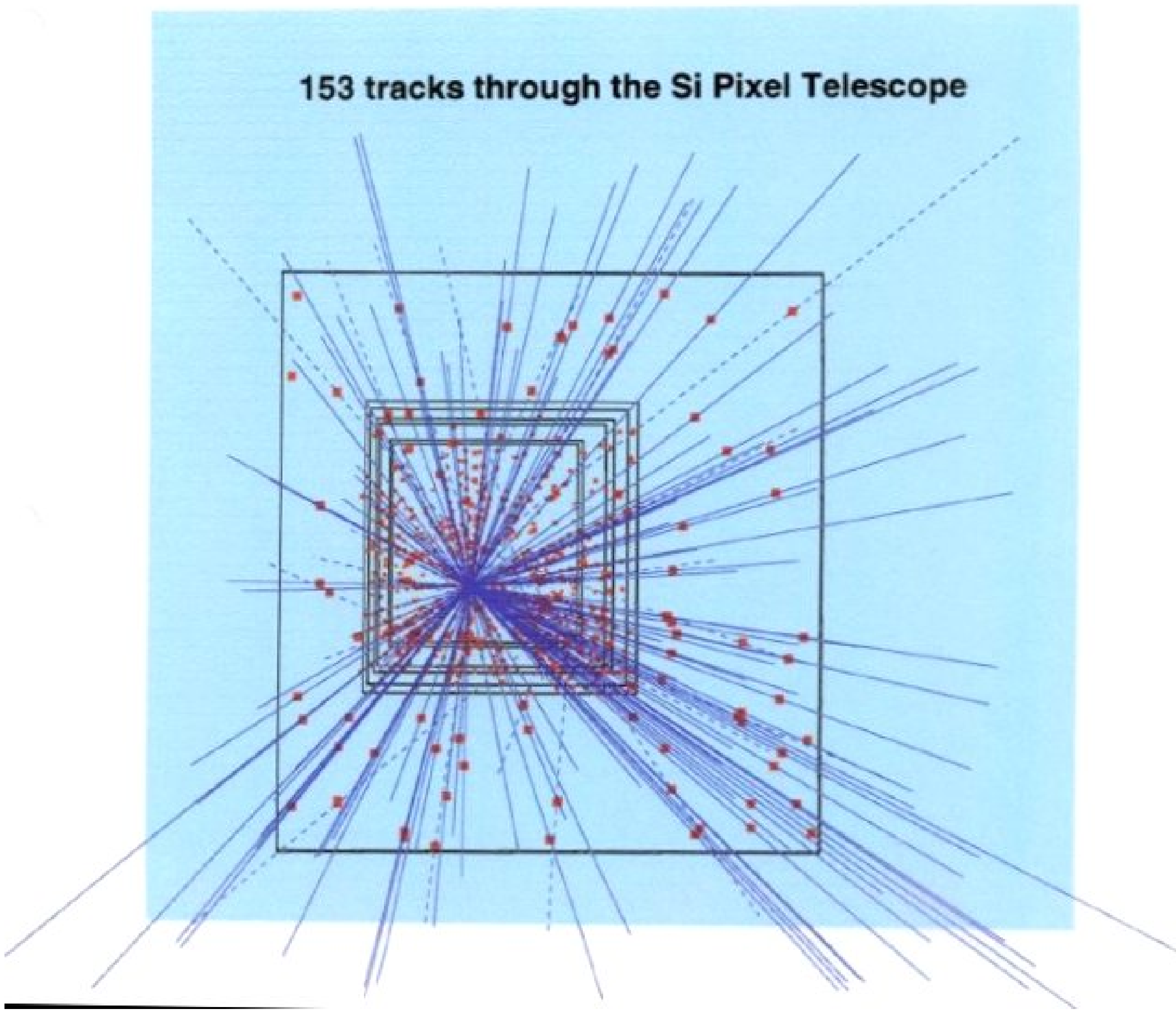

4.6.6 putting it all together: the LHC experiments use Si pixels, strips, and drift

the challenge at LHC:

high rate, high hit density, radiation damage

$\sim$ 1000 tracks every 25 ns or 10^{11}/s

$\Rightarrow$ high radiation dose

$10^{15} \frac{n_{eq}}{\mathrm{cm}^2 \cdot 10\mathrm{a}}$ @ LHC

or

600 kGy (60 Mrad)
1 kGy = 1 J/g

through the ionization of mips
in bulk silicon

LHC $\cong 10^6 \times$ LEP in track rate!
detectors in ATLAS and CMS need to be replaced by 2018

14 TeV pp-collisions seen with the ATLAS pixel detector

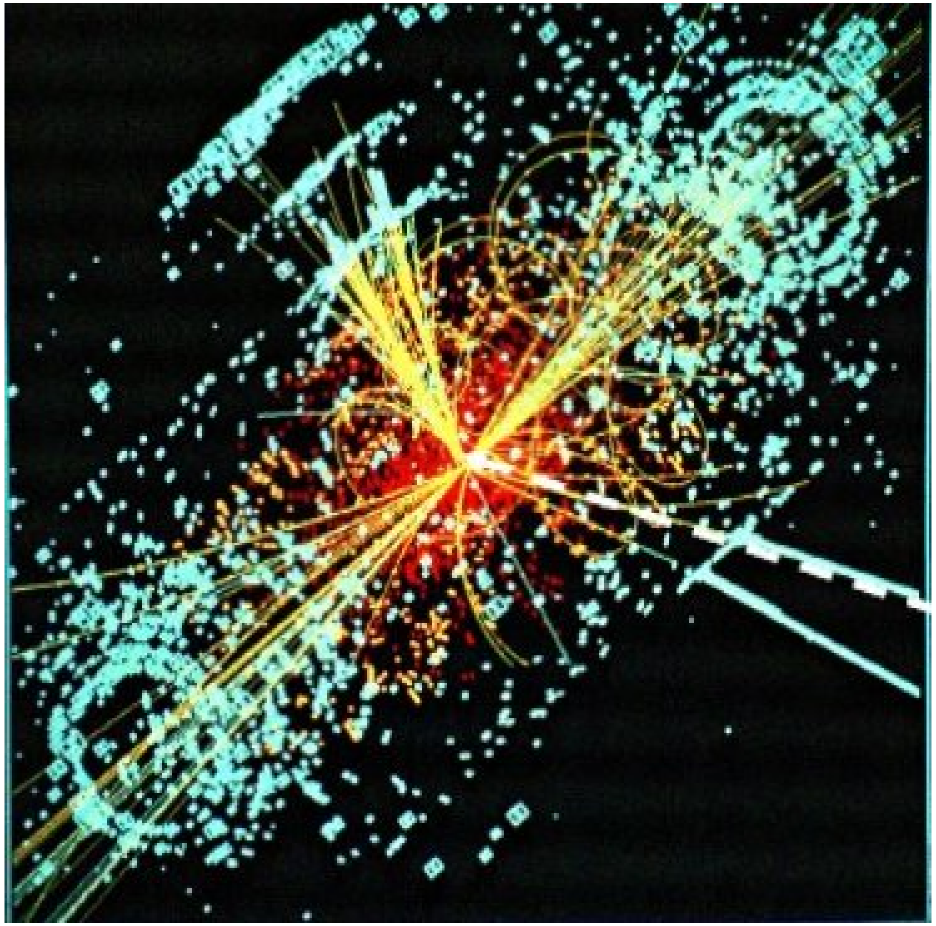

Tasks for pixel detectors in LHC experiments

- pattern recognition and tracking

  precision tracking point (3D); can do in one pixel layer the equivalent of $3-4$ strip layers

  momentum measurement before much material (mult. scattering)
  e.g. ATLAS: $\sigma(p_t)/p_t = 0.03\,\% p_t$ (GeV/c) $\oplus$ 1.2%

- vertexing

  find primary vertex (can use all tracks, get 10 μm precision in x, y and 50 μm in z)

  find secondary vertex (c,b) (few tracks, get 50 μm in x, y and 70 μm in z)

  impact parameter for tracks not from primary vertex (electrons from semileptonic D and B decays

tracking detectors: ATLAS

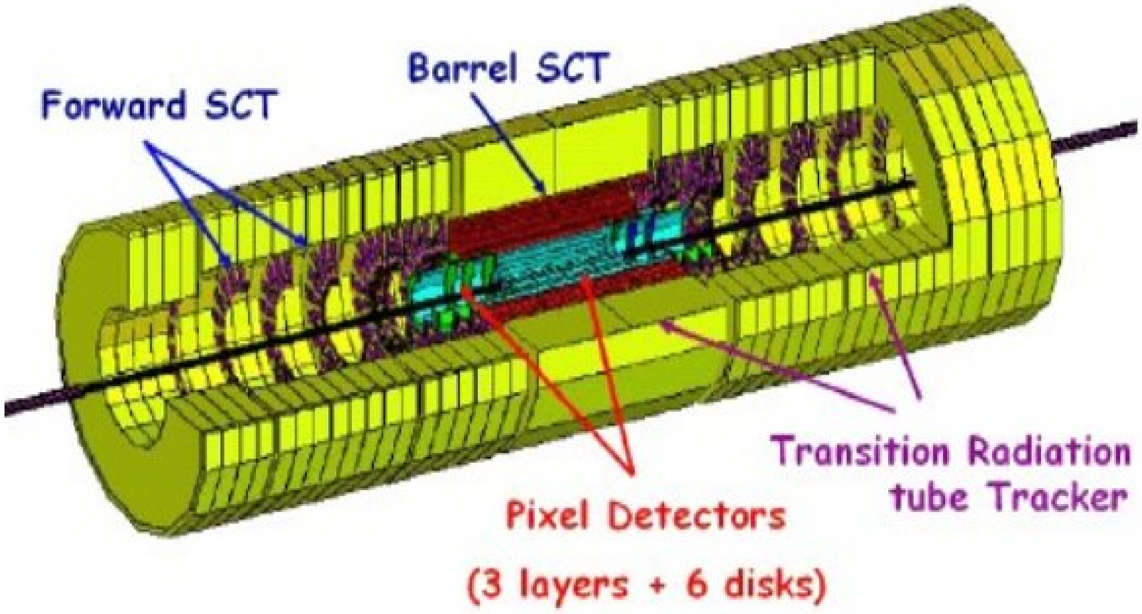

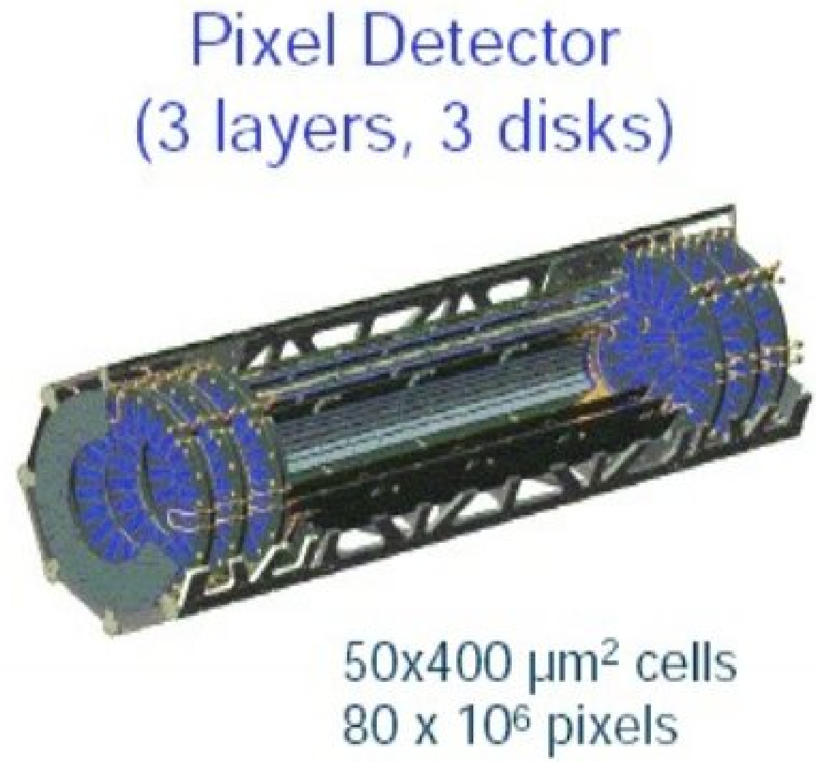

	points	$\sigma(R\phi)$ μm	$\sigma(Rz)$ μm
pixel	3	12	60
SCT	4	17	580
TRT	36	170	-

Silicon Pixel Detector $\sim$ 1.8 m^2
Silicon Strip Detector $\sim$ 60 m^2
Transition Radiation Tracker $\sim$ 300 m^2_{eq}

ATLAS micro strip detector (15 million strips)

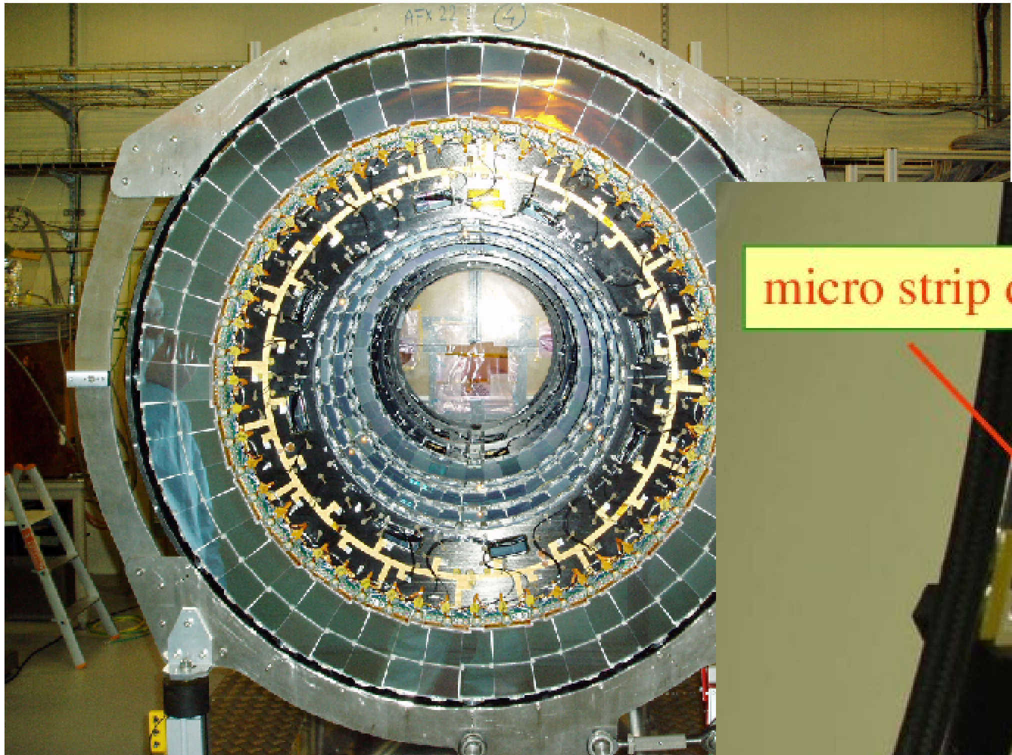

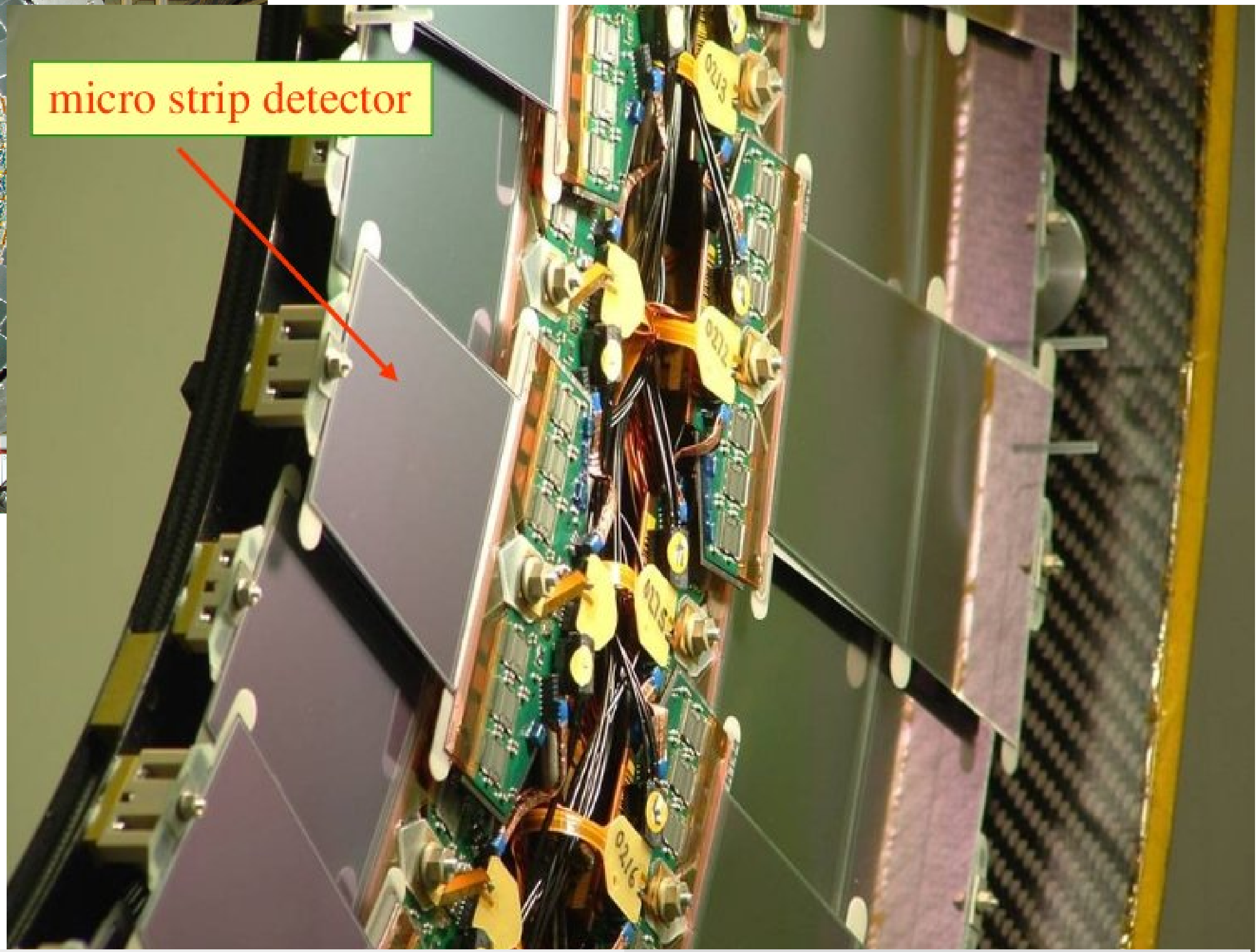

Freiburg, MPP München

ATLAS pixel detector: 5 cm from collision point

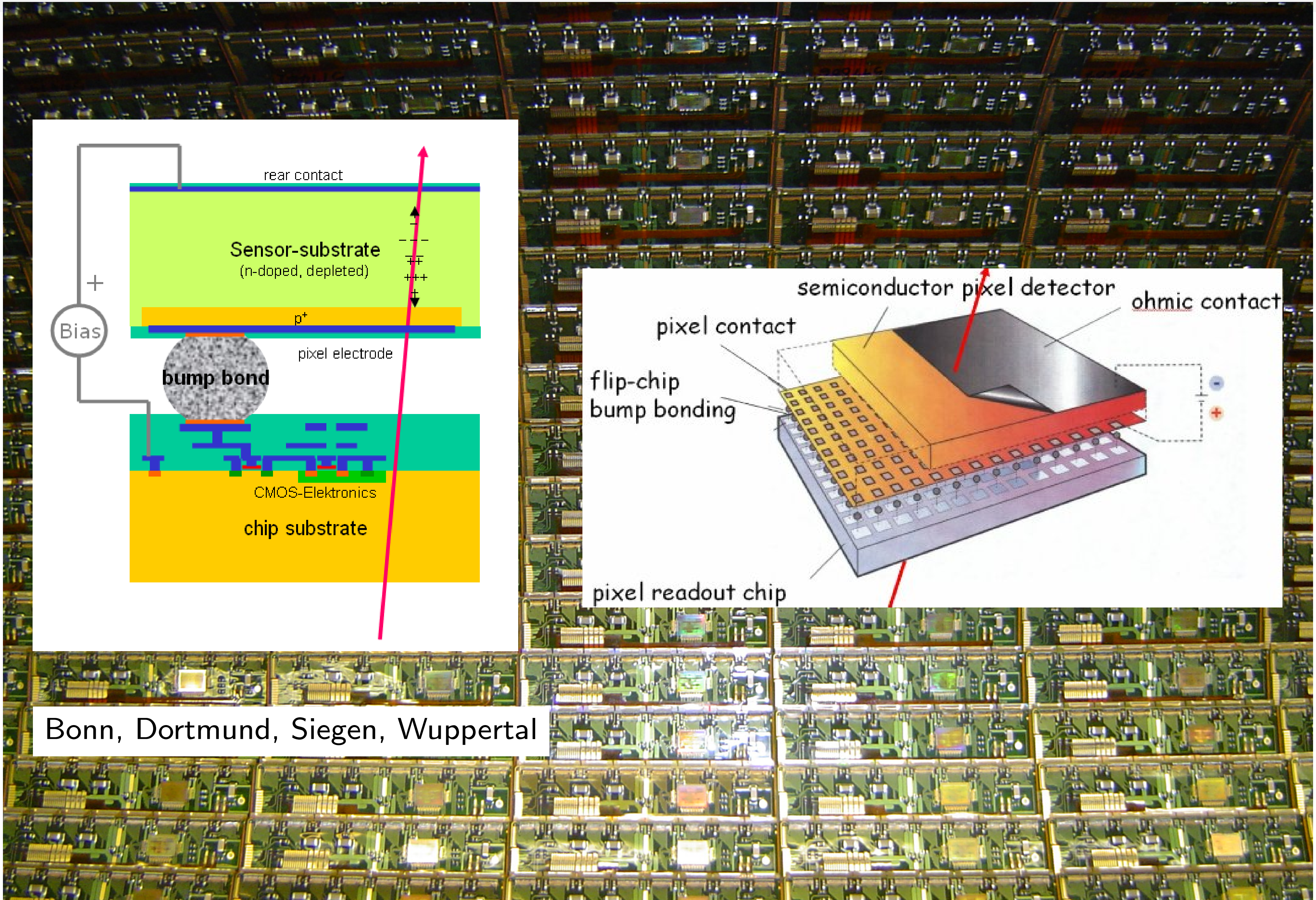

Bonn, Dortmund, Siegen, Wuppertal

ATLAS pixel detector

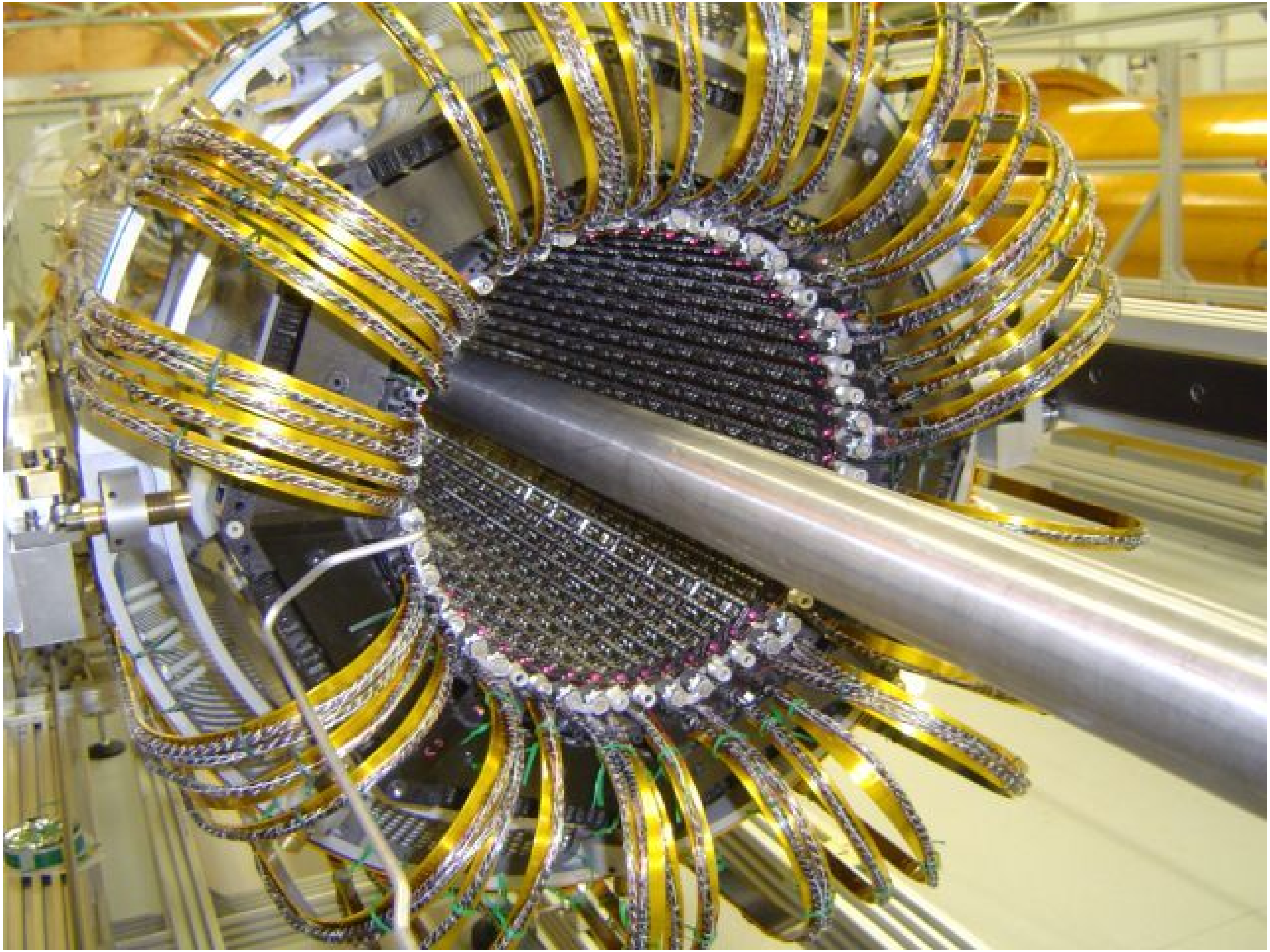

tracking detectors: CMS

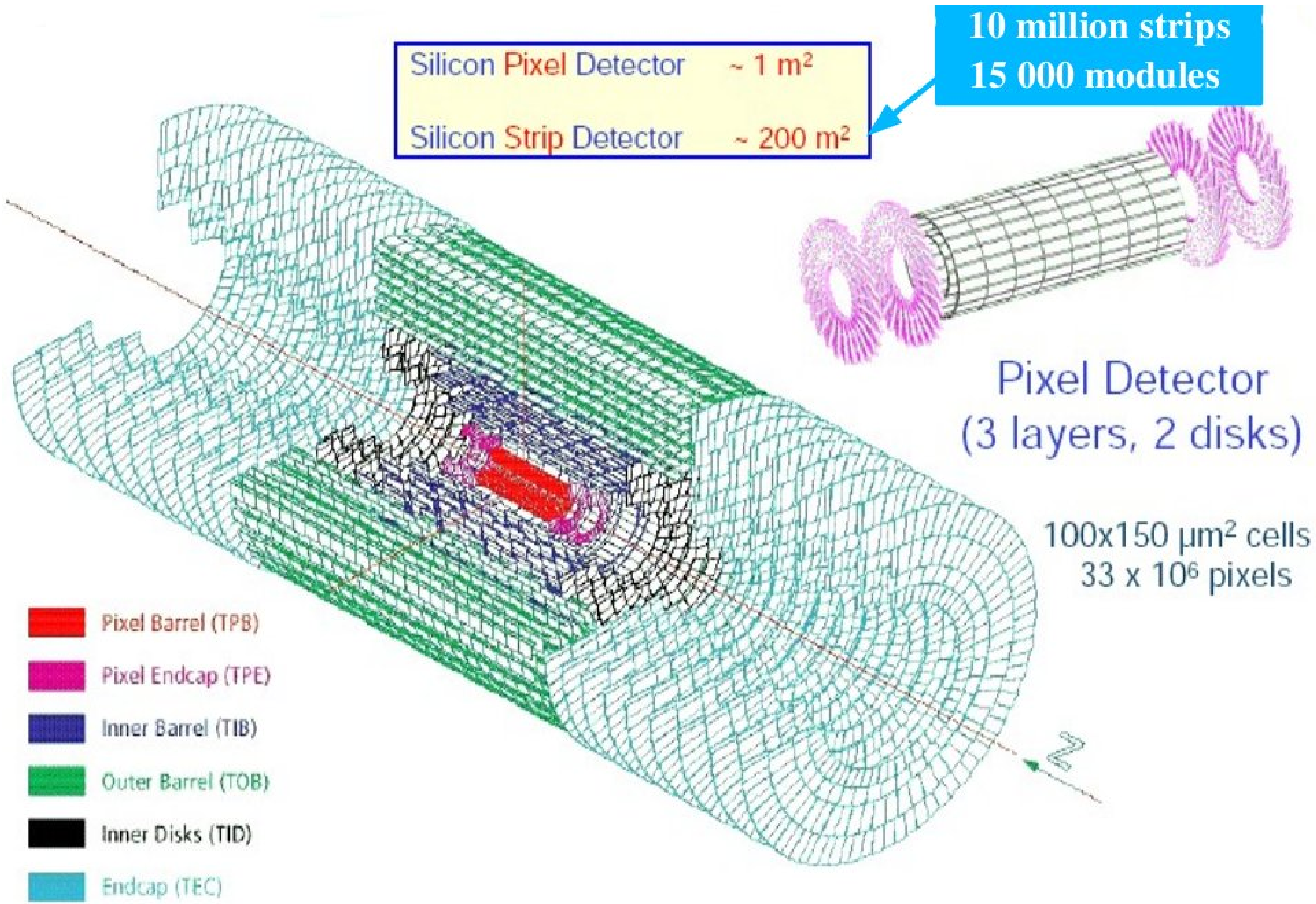

CMS tracker-supermodule and -endcap

assembly and tests of supermodules (petals)
(Aachen, Hamburg, Karlsruhe)

↑ 90 cm ↓

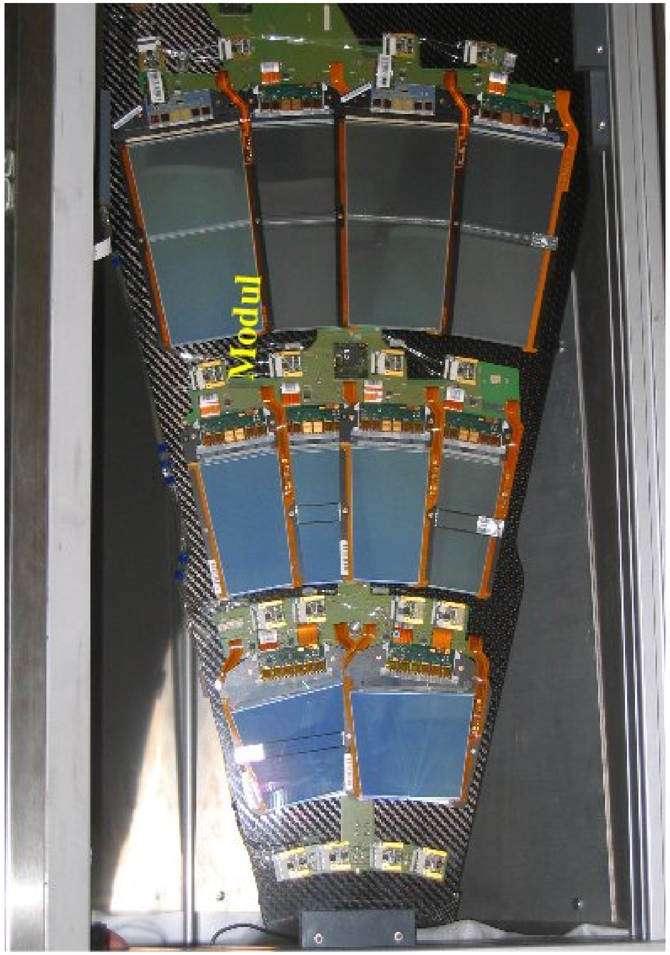

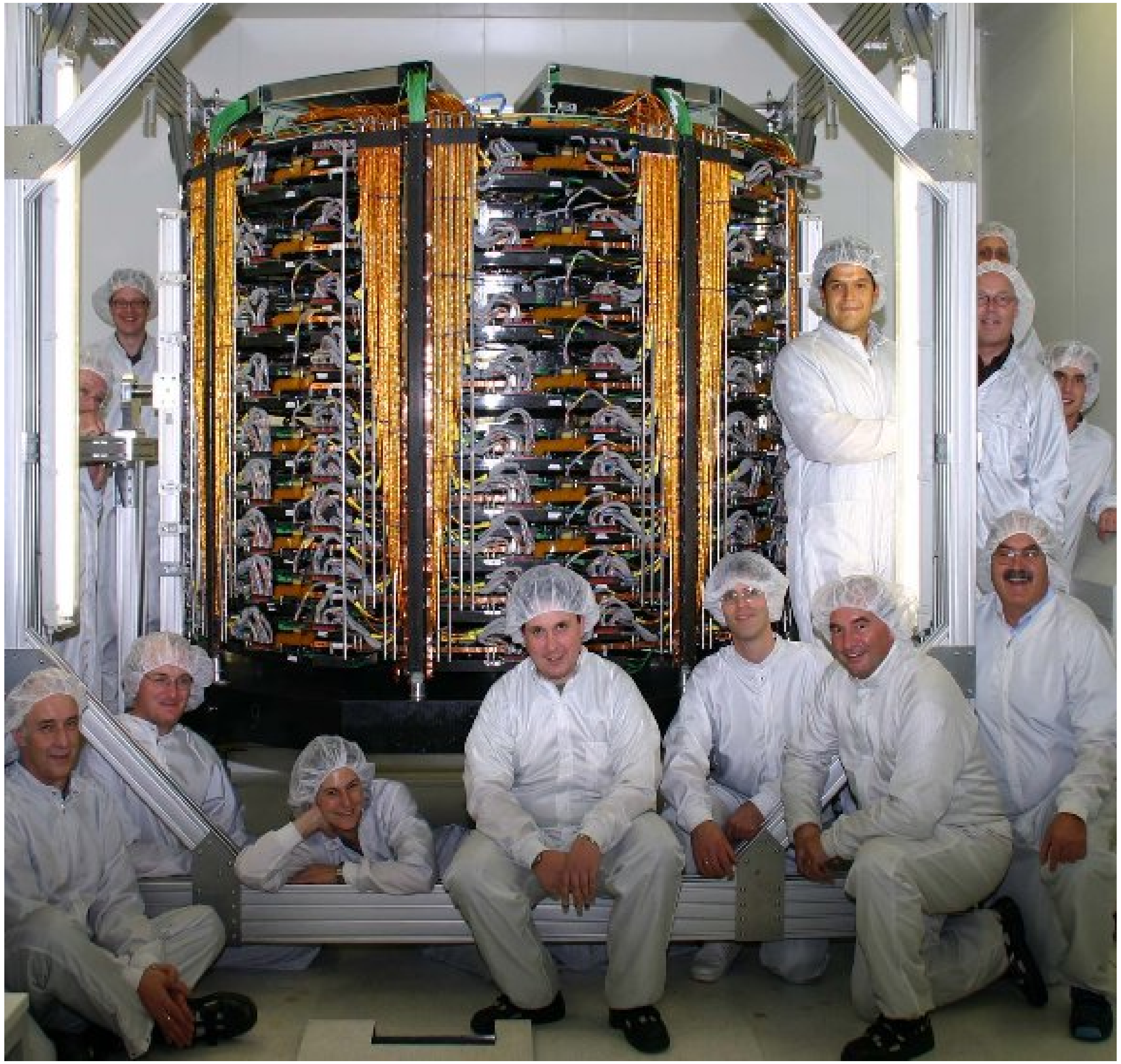

134 petals assembled
(mechanics + electronics + cooling)
288 petals tested

integration of tracker-end cap (Aachen)
end cap (with 144 petals) before transport to CERN

inner tracking detectors: ALICE

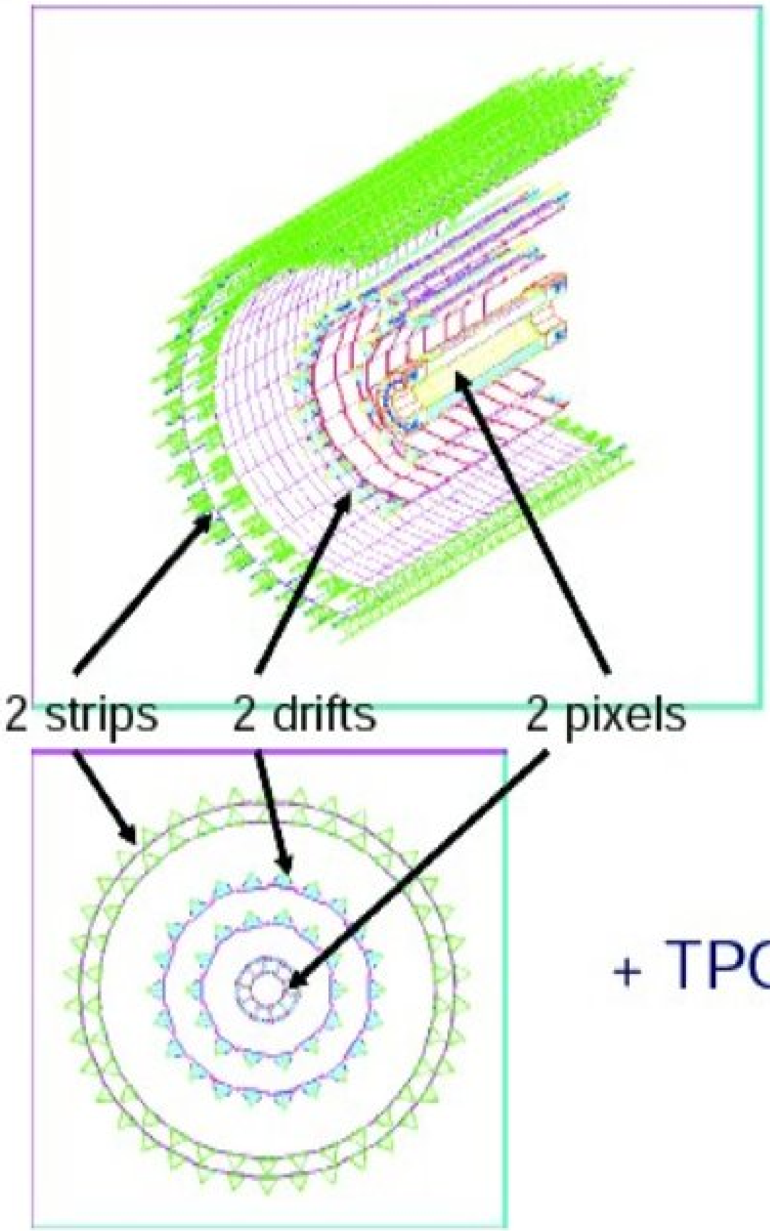

+ TPC

Silicon Pixel Detector	~ 0.2 m^2
Silicon Drift Detector	~ 1.3 m^2
Silicon Strip Detector	~ 4.9 m^2

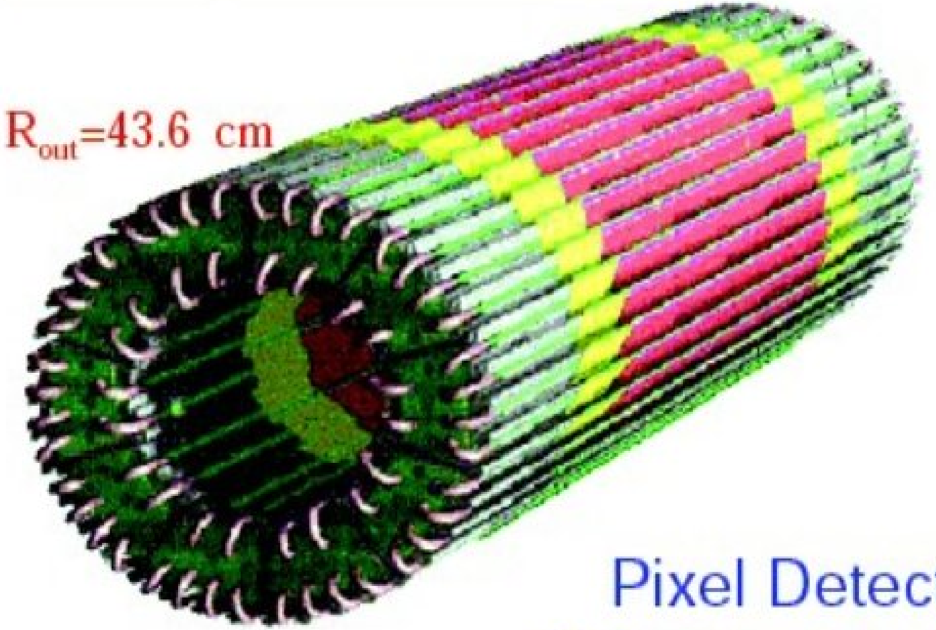

Pixel Detector
(2 layers, no disks)

50x450 μm^2 cells
10 x 10^6 pixels

ALICE ITS

inner tracker system

layer	type	r(cm)	$\pm z$(cm)	area (m^2)	ladders	lad./stave	det./lad.	tot. channels
1	pixel	4	16.5	0.09	80	4	1	5 242 880
2	pixel	7	16.5	0.18	160	4	1	10 485 760
3	drift	14.9	22.2	0.42	14	-	6	43 008
4	drift	23.8	29.7	0.89	22	-	8	90 112
5	strip	39.1	45.1	2.28	34	-	23	1 201 152
6	strip	43.6	50.8	2.88	38	-	26	1 517 568

dimensions of the ITS detectors (active areas)

6 layers
3 technologies:
pixel, drift, strips

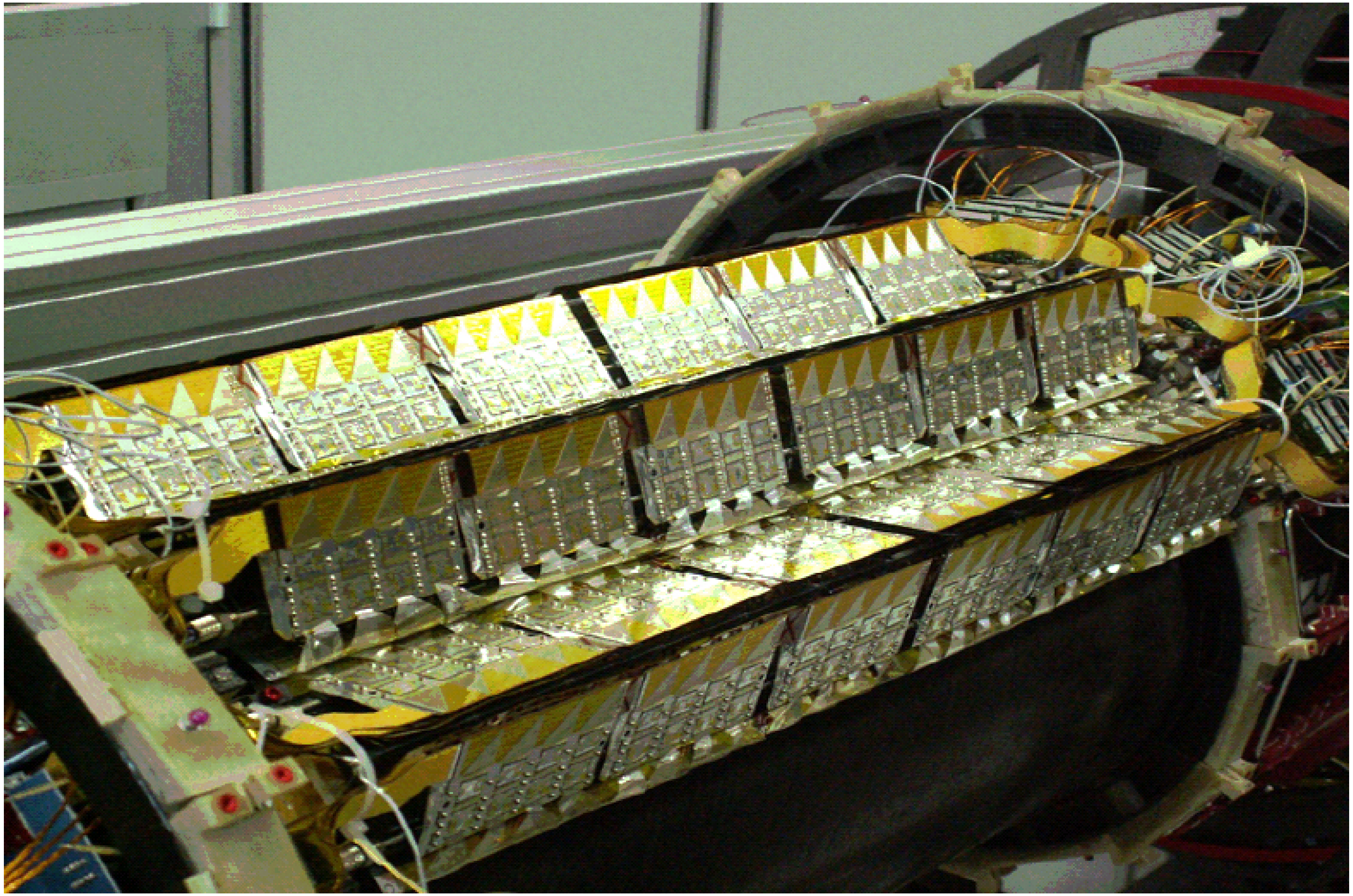

main issue for ALICE: minimal material

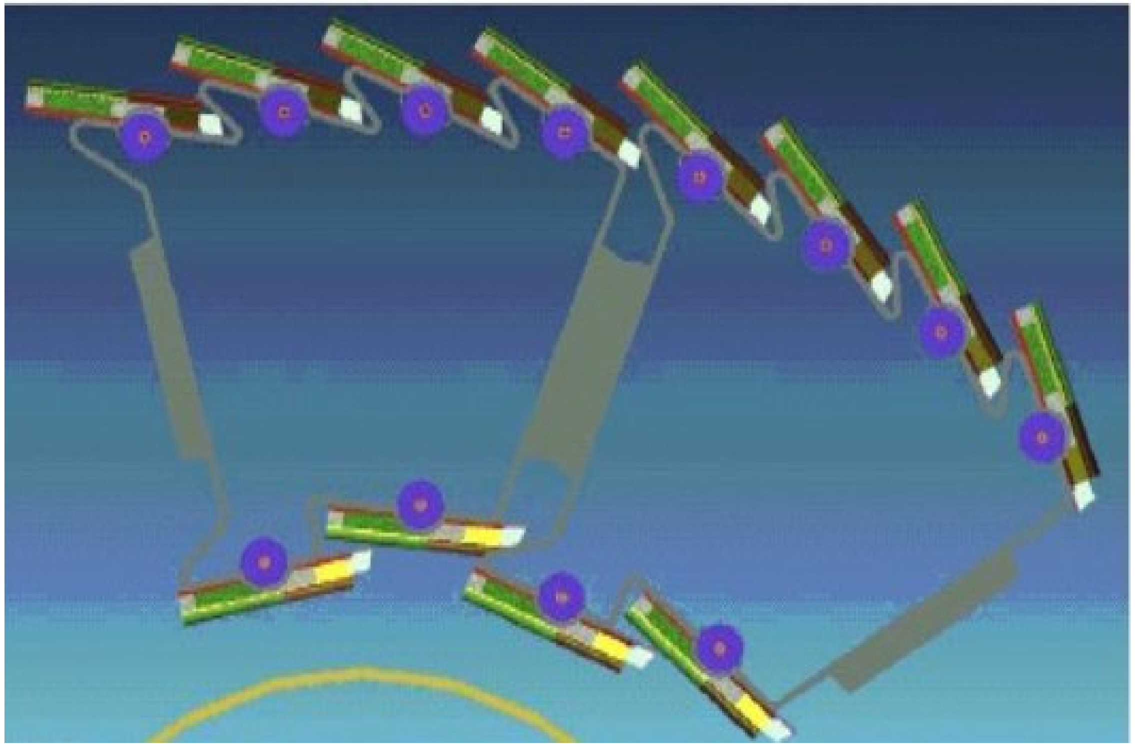

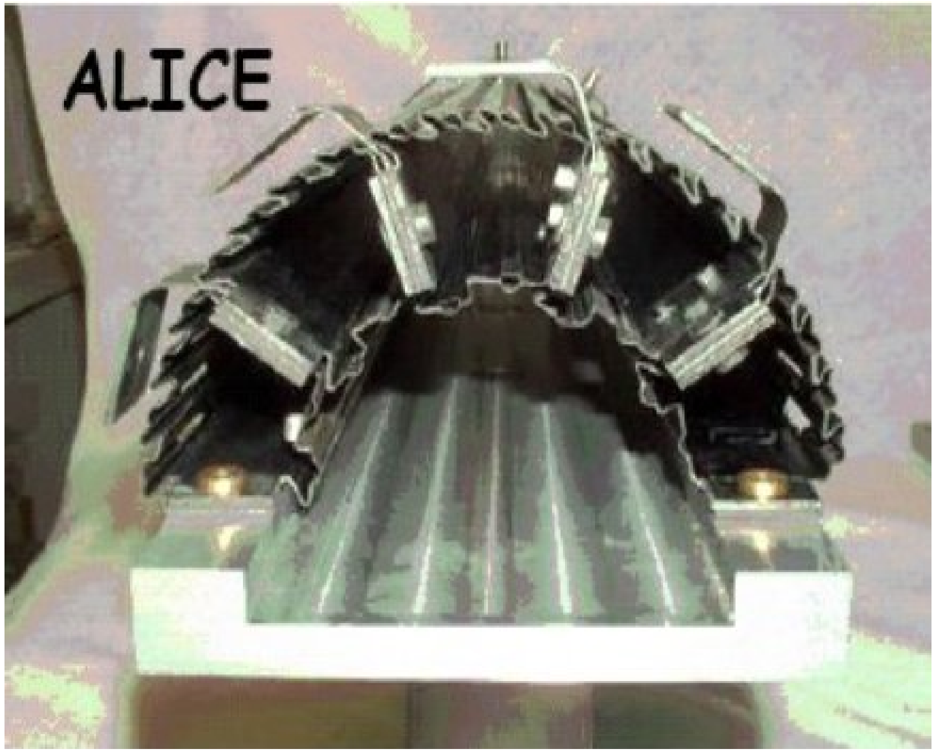

very light-weight carbon fiber support structure
(200 $\mu m, \sim 0.1\%\ X_0$)

sensor	200 μm
IC	150 μm
cooling (C_4F_{10}) @ RT	0.3% X_0

(PHYNOX tubes, wall 40 μm)

total X_0 per layer $\sim$ 0.9%
(ATLAS, CMS $>$ 2%)

the LHCb Vertex Locator (VELO)

cross section
at x=0:

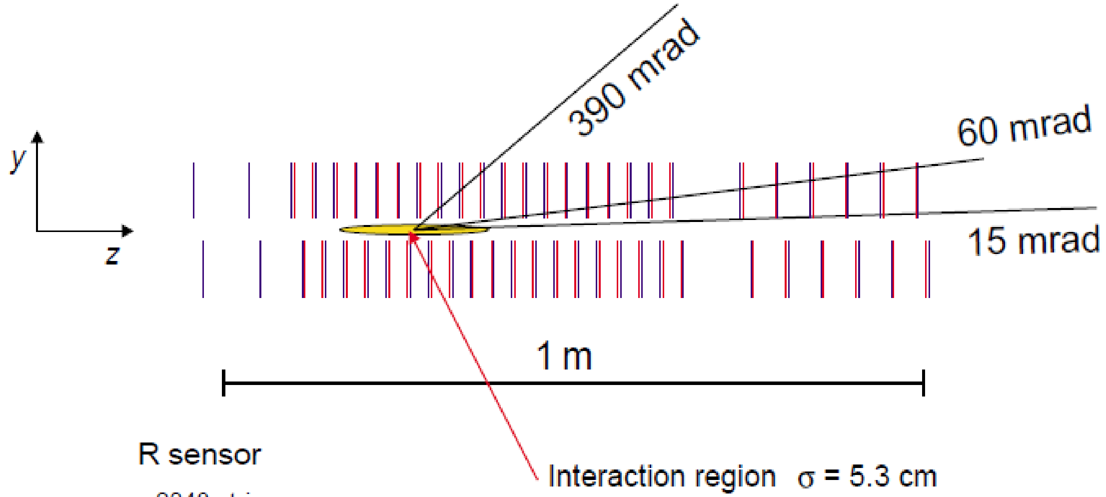

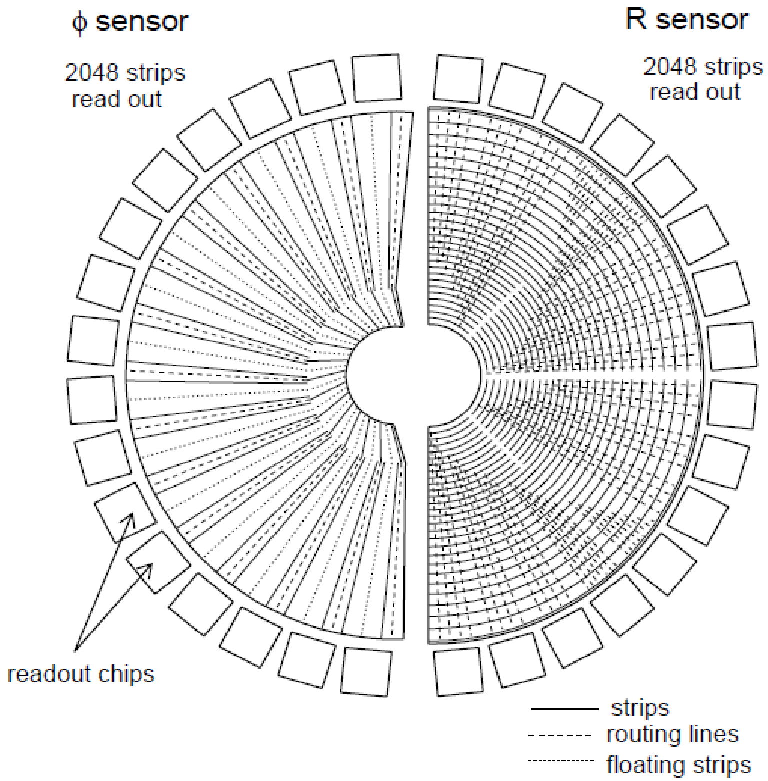

25 stations of R and phi sensors

pitch 40-100 mm

signals routed to outer radius where electronics (chips) sits

innermost active structure 7 mm from the beams!

- smaller than aperture required for LHC beams

during injection → the 2 detector halves opened during injection (29 mm) and closed thereafter (reproducible to 10 µm)

operation in secondary vacuum, shield detector against RF pickup from beams and vice versa

the LHCb Vertex Locator (VELO)

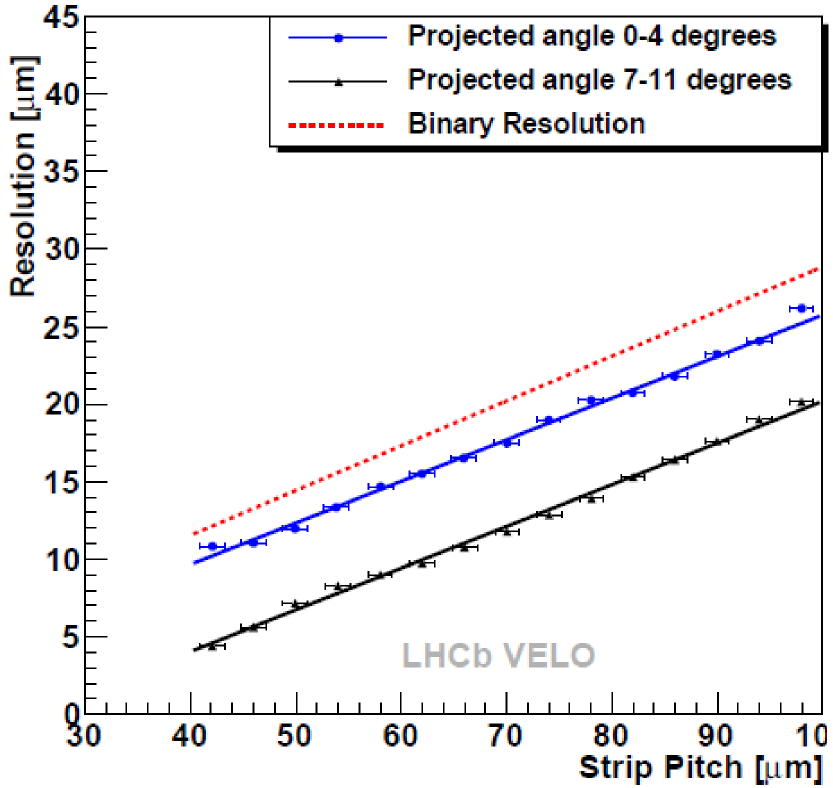

single hit resolution depending on strip pitch

primary vertex resolution as function of number of tracks contributing to vertex

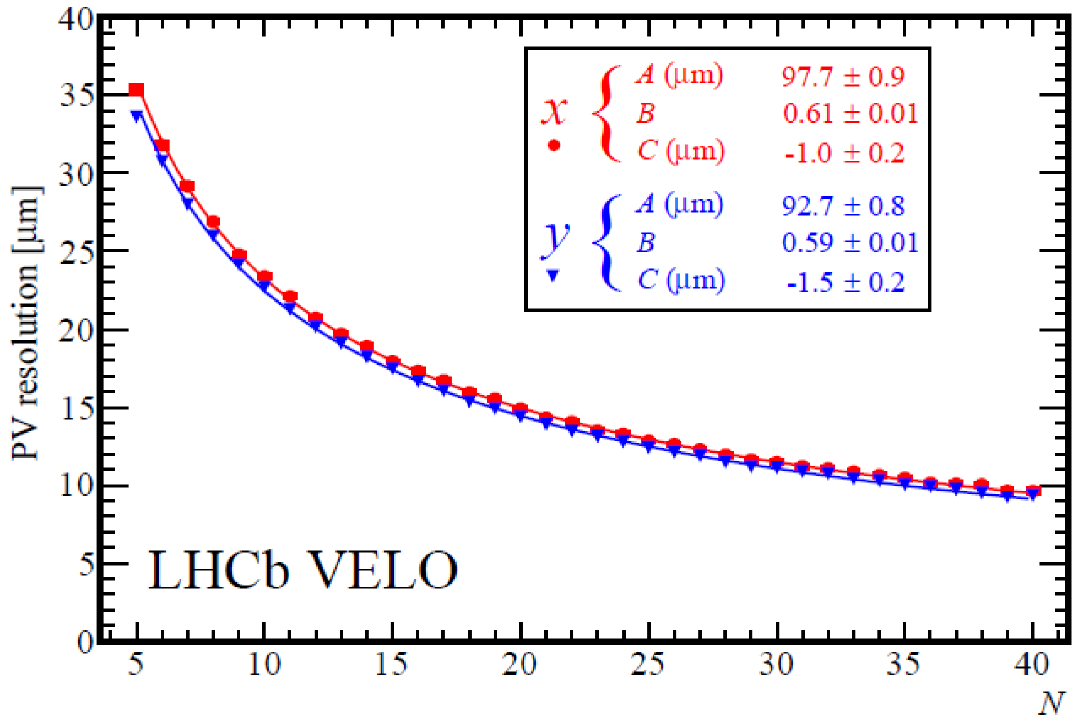

secondary vertices: impact parameter resolution limited by multiple scattering in detector) 3.2% X_0 → better 35 µm

Most recent developments: MAPS (monolithic active pixel sensors)

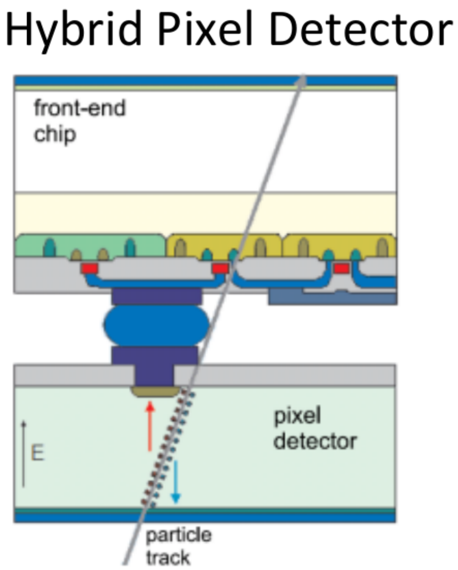

N. Wermes (Univ. of Bonn)

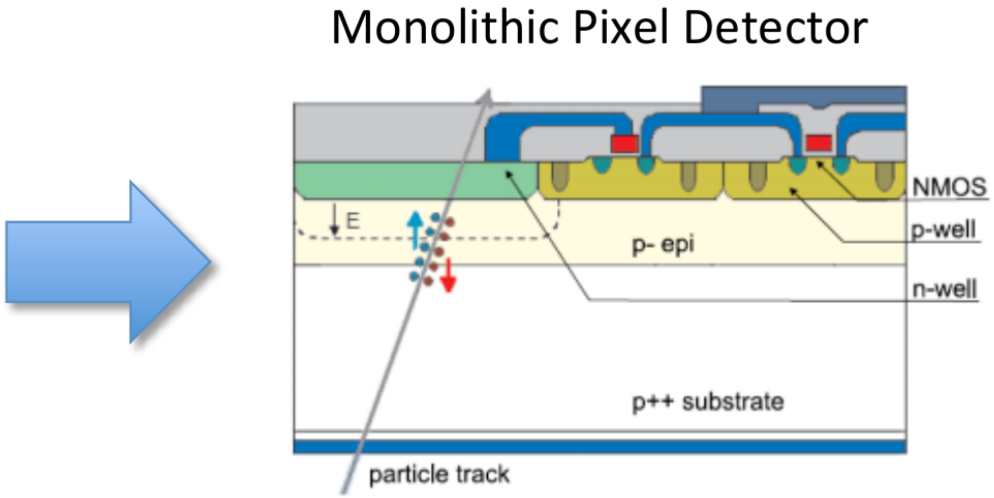

N. Wermes (Univ. of Bonn)

advantages:

- low material budget
- cost
- power
- lower integration complexity $\rightarrow$ easier system assembly

Key technology steps that made MAPS possible:

- CMOS on high-resistivity silicon (needed as bulk material for the sensor)
- full CMOS in pixel area (both types of transistors $\rightarrow$ fast readout)

MAPS (monolithic active pixel sensors)

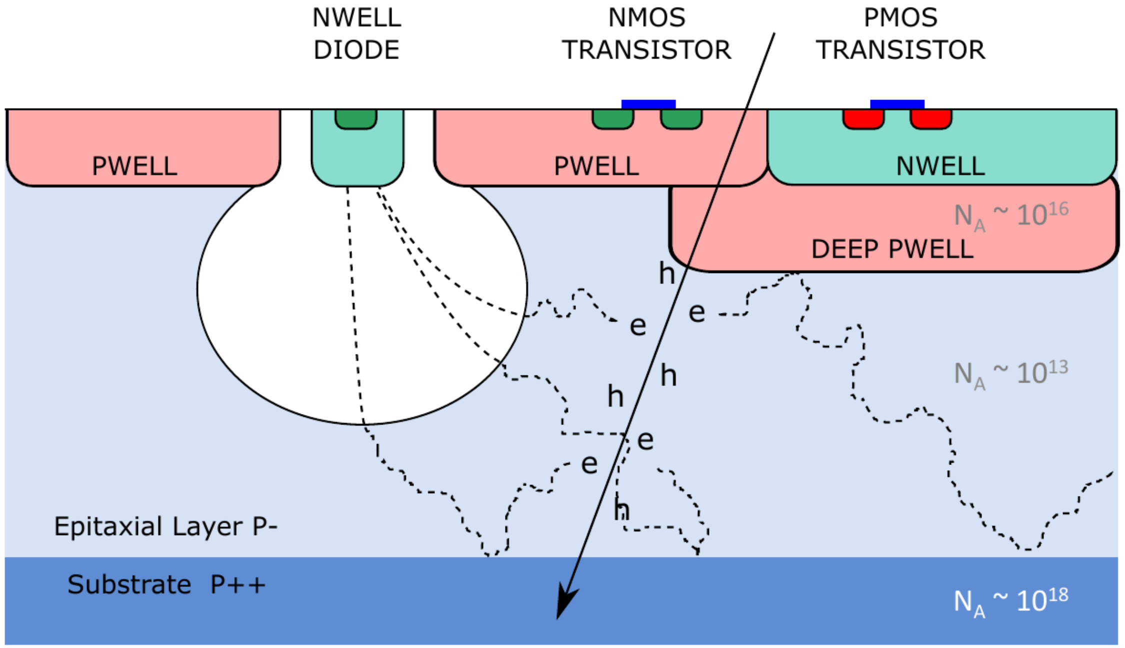

- small n-well collecting diode (2 μm diameter), $\sim$ 100 times smaller than pixel $\rightarrow$ very low capacitance (few fF)
- reverse bias (6 V) to substrate (contact from top) to increase depletion zone around n-well collection diode
- PMOS transistors shielded by deep p-well
- full CMOS amplifier circuit within active area
- fast signal rise-times ($\sim$ 1 ns)

- high resistivity ($<$ 1 kΩcm) p-type epitaxial layer (25 μm) on p-type substrate

Upgrades of LHC detectors, e.g. ALICE ITS Upgrade (ALPIDE = **ALI**CE **P**ixel **De**tector)

Further Reading

- Rossi, Fischer, Rohe, Wermes, **'Pixel Detectors: From Fundamentals to Applications'**
  Springer Berlin-Heidelberg-New York, 2006, (ISBN 3-540-283324)
- G. Lutz, **'Semiconductor Radiation Detectors'**
  Springer Berlin-Heidelberg-New York, 1999
- E. Heijne, **'Semiconductor Micro-pattern Pixel Detectors: A Review of the Beginnings'**
  NIM A465 (2001) 1-26
- N. Wermes, **'Pixel Detectors for Tracking and theirs Spin-off in Imaging Applications'**
  NIM A541 (2005) 150-165, e-Print Archive: physics/0410282
  and
  'Pixel Detectors' in LECC2005 Heidelberg 2005, Electronics for LHC and future experiments
  e-print Archive: physics/0512037

4.6.7 CCD, charge-coupled device

MOS structure (metal-oxide-silicon)

many independent and separately switchable gates (electronically shielded potential wells) on SiO_2 over p-substrate

- pixels $50 \times 50\ \mu m^2$ (or even 20×20), act at low voltage (2 V) as capacitors storing charges produced by ionizing tracks

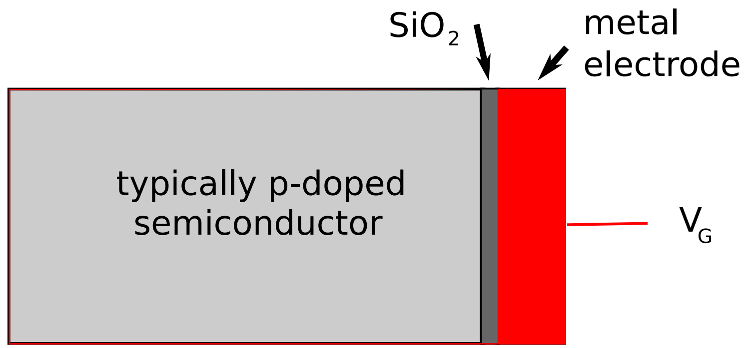

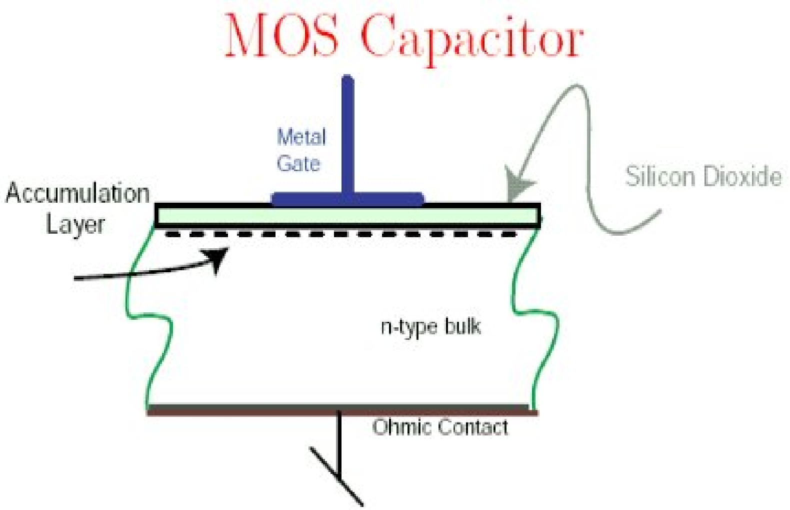

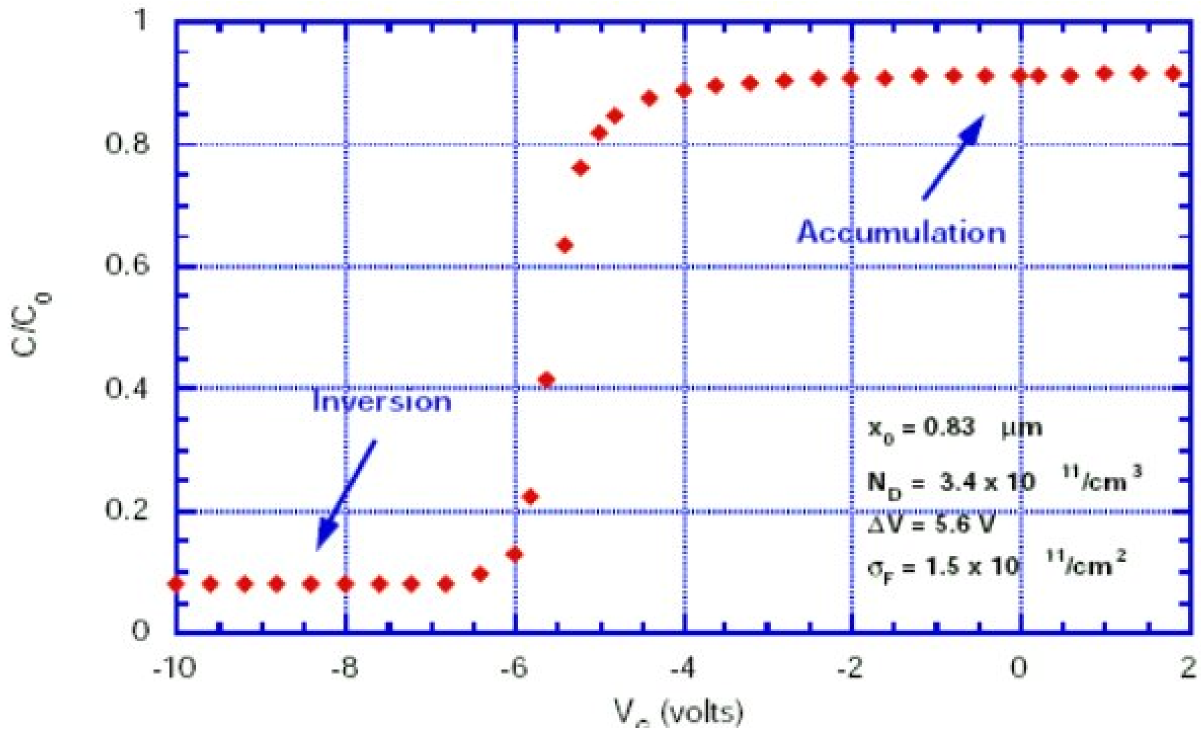

MOS high frequency C-V characteristic curve (n-type bulk)

Band model of MOS contact

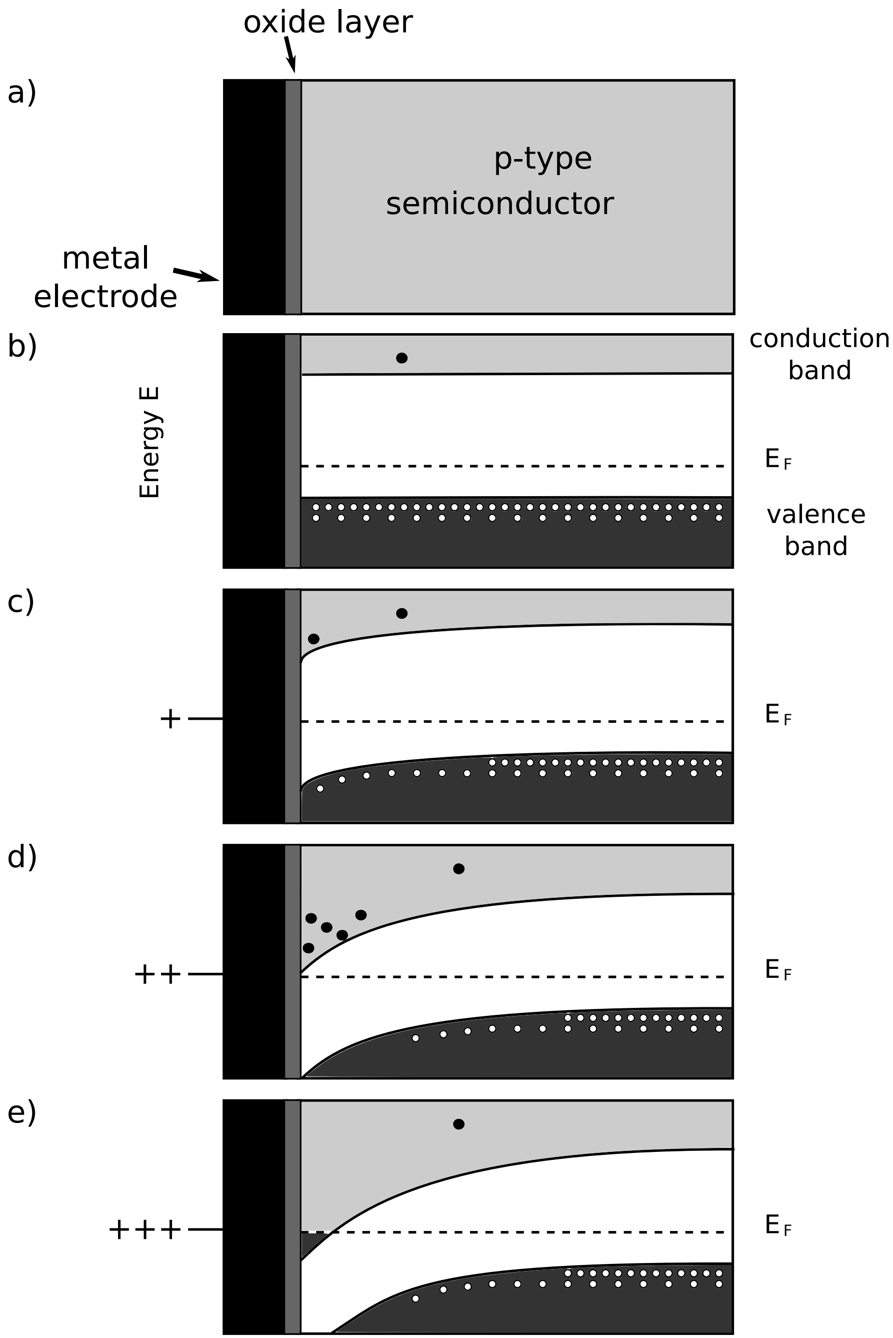

b) energy levels without external field

c) small positive bias: depletion near surface
(like at p-n junction)
high resistance space charge zone, can store charge

d) higher positive bias: band are lowered towards interface, in thin layer conduction goes from p to n separated by depletion layer from p-bulk, "inversion"

e) further increase of potential: conduction band dives below Fermi level → degenerated Fermi gas – conducting

- **serial readout**:

  make use of fact that boundary becomes conducting at higher voltage (5-10 V)

  charge follows a wandering potential well produced by a pulse sequence applied to the gates, until it reaches charge-sensing preamplifier

2 or 3-phase clock
typical frequency 8 MHz

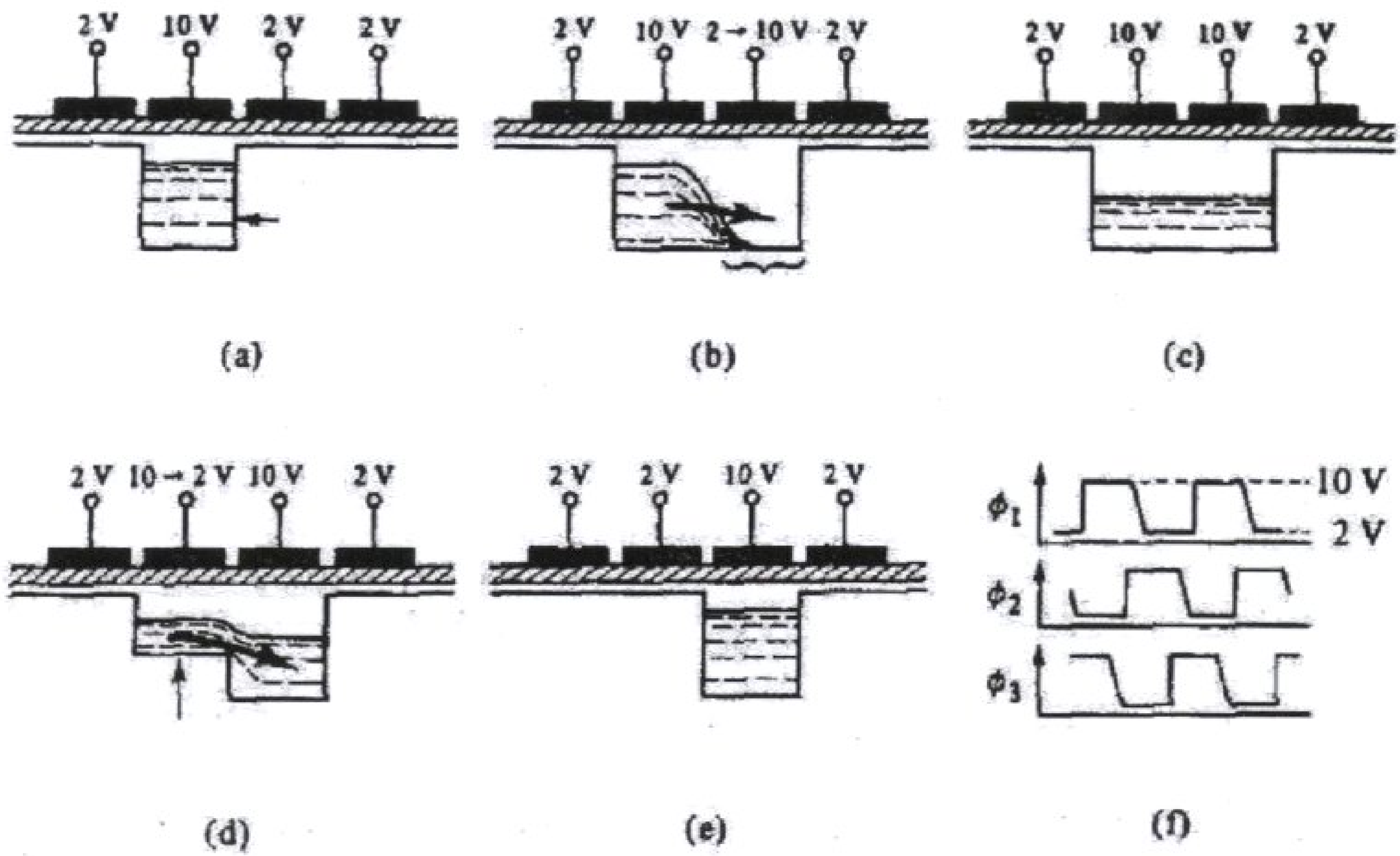

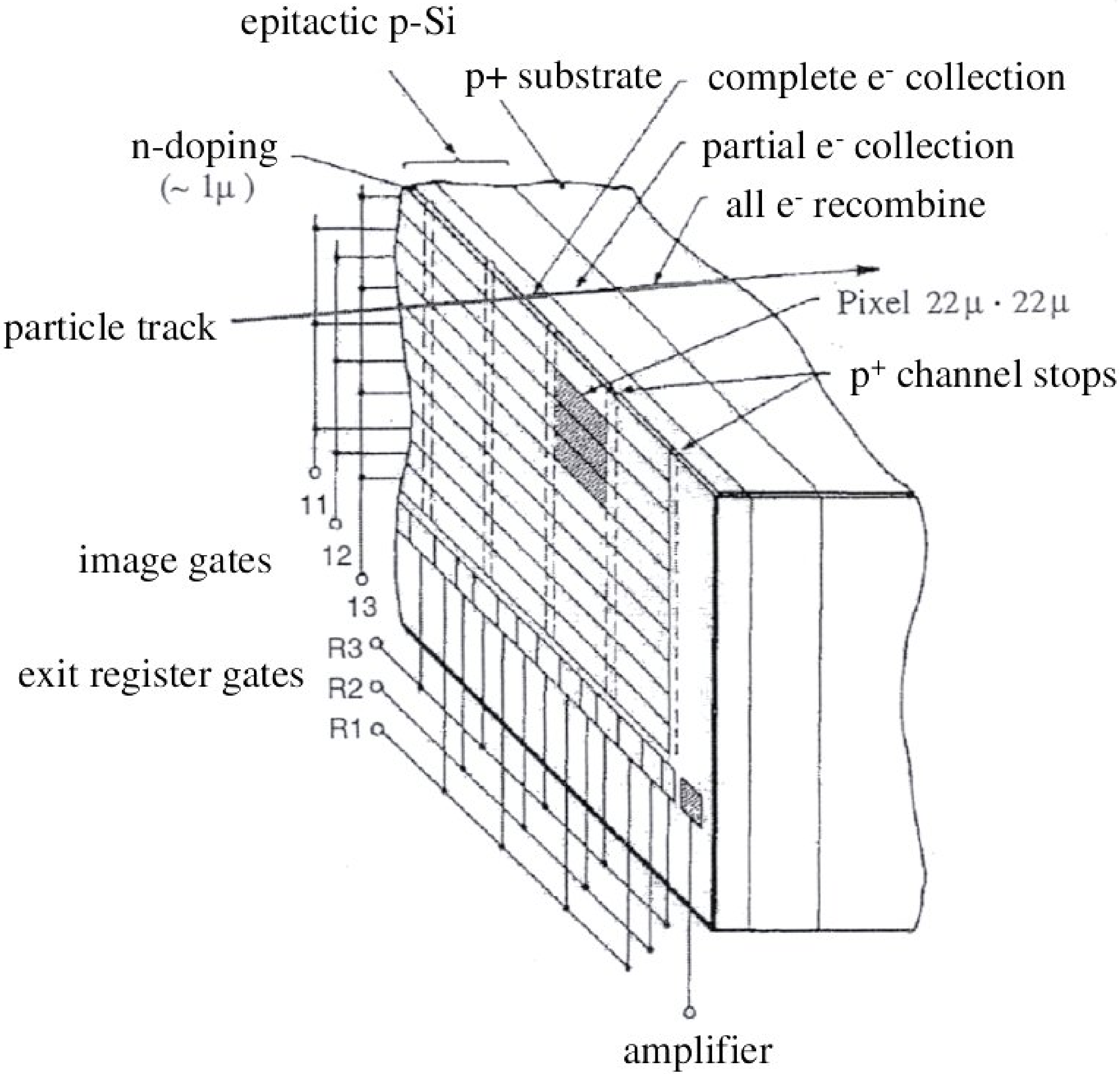
epitactic p-Si
p+ substrate
complete e⁻ collection
partial e⁻ collection
all e⁻ recombine
n-doping
(~ 1µ)
particle track
Pixel 22µ · 22µ
p⁺ channel stops
11
12
13
image gates
R3
R2
R1
exit register gates
amplifier

CCD - principle of operation I

a detailed look at the charge storage and charge transfer process

1. charge storage

incident light generates charge, i.e. electron-hole pairs.
if light is incident on a localized section of p-type silicon, below a positive contact, charge will accumulate.

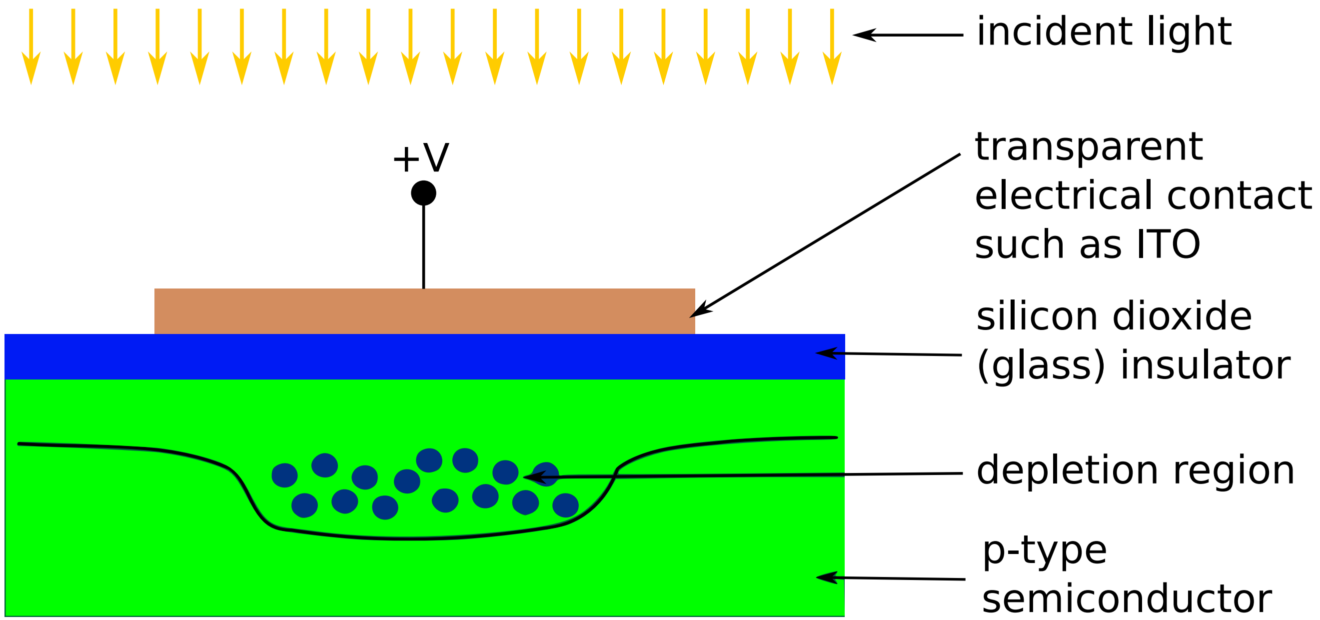

CCD - principle of operation II

2. charge transfer

as voltage on adjacent well is increased, the width of the well increases and the charge becomes shared between the two electrodes

removing voltage from the first well decreases the charge stored below it

the charge packet is therefore transferred to the adjacent electrode

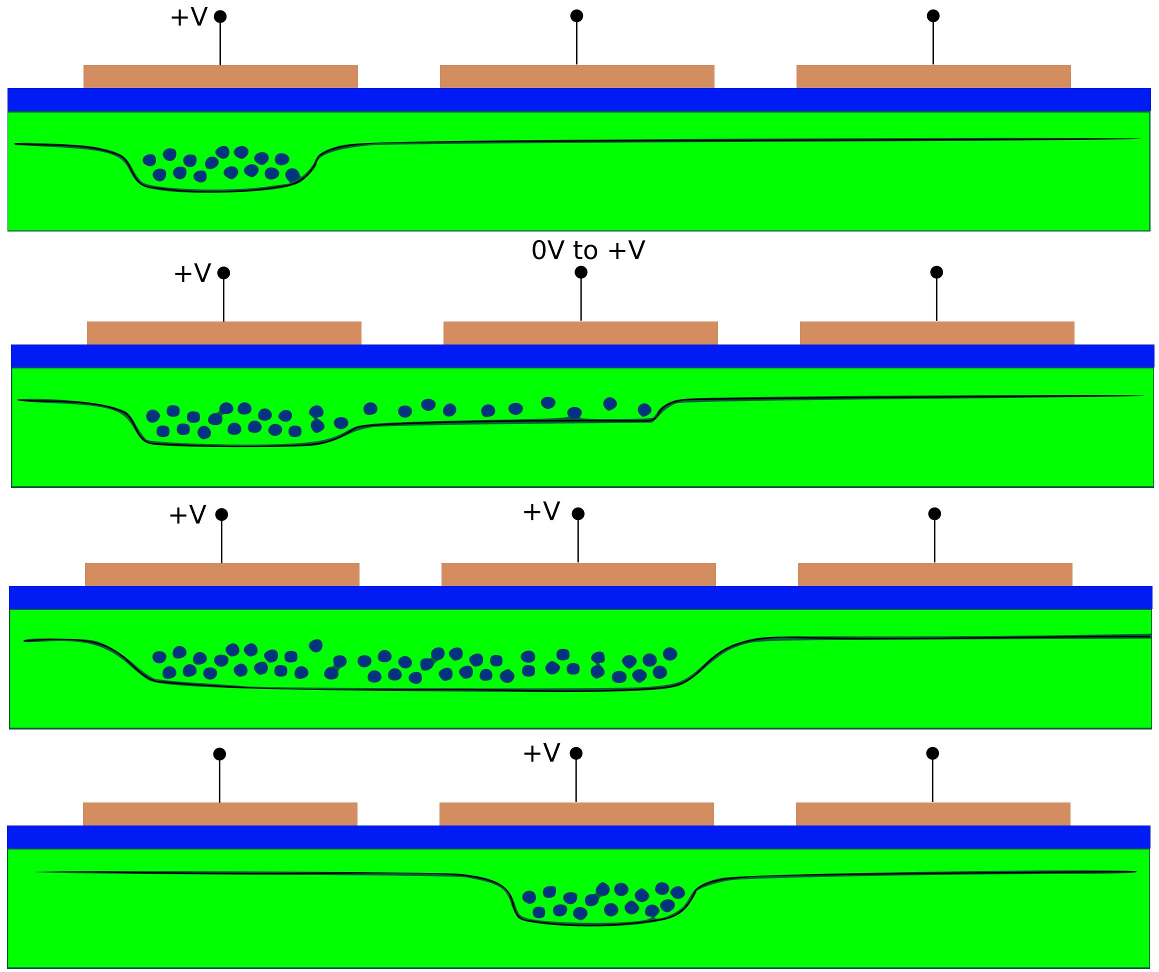

optical imaging with CCD arrays

charge creation by incident light prior to charge transfer, amount of charge represents integration of light.

charge packet transfer: electrodes are grouped into sets of three or four. These 'phases' remove the charge from the detecting part of the device to the digitizing part.

example of a clocking sequence for a three phase arrangement.

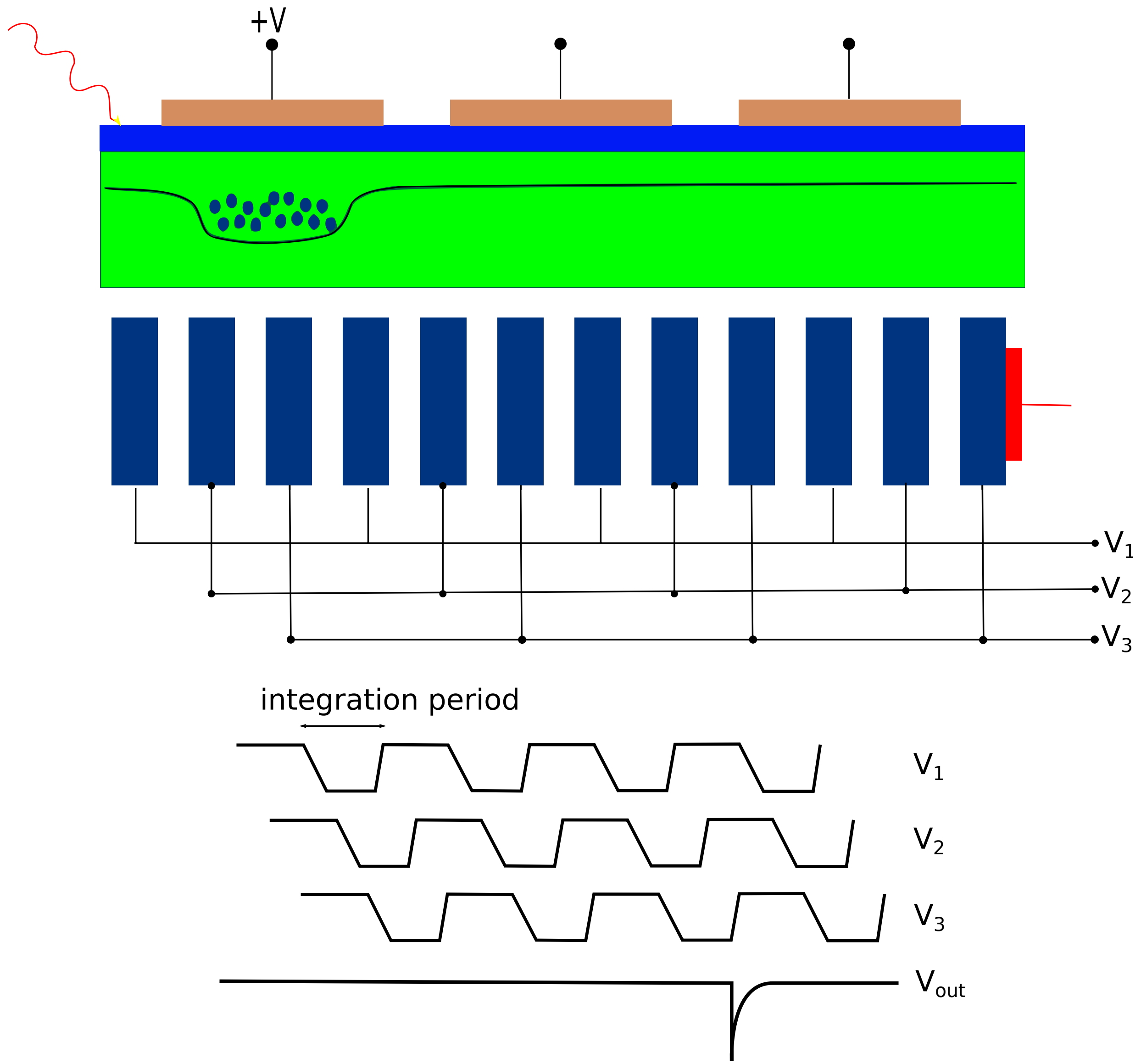

CCD arrays I

2-dimensional images are digitized using a 2-dimensional array of CCD elements. There are 3 different methods of sequentially reading and storing the spatial light patterns that fall onto the array.

1. full frame CCD
accumulated charge shifted vertically row by row to serial read-out register, for each row the read-out register must be shifted horizontally → 'progressive scan'
disadvantage: smearing of image due to light falling on sensor while transferring accumulated charge (could use mechanical shutter in addition)

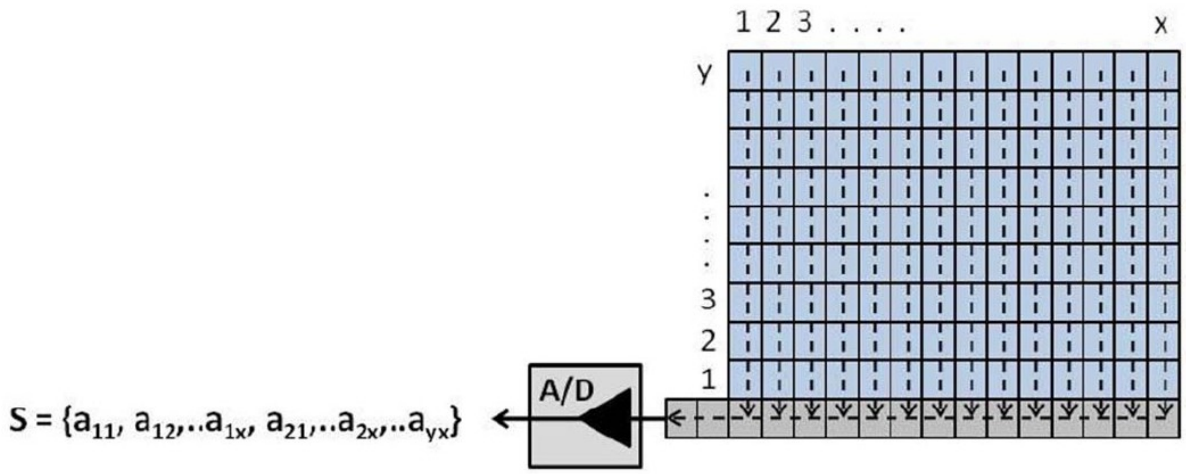

CCD arrays II

2. frame transfer

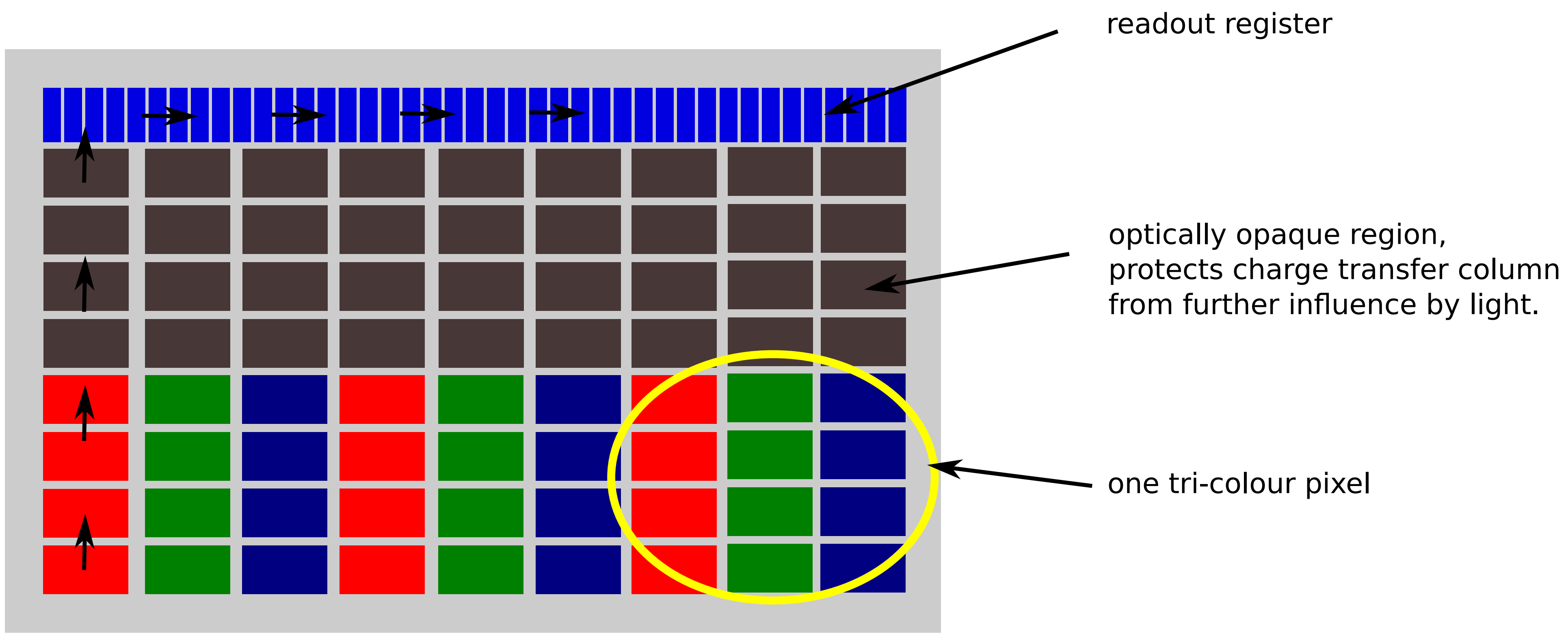

two part sensor, half of the array is used as storage region and protected from light
'up and out' - data are read-out and digitized frame by frame $\rightarrow$ high resolution, slow transfer

CCD arrays III

3. interline transfer

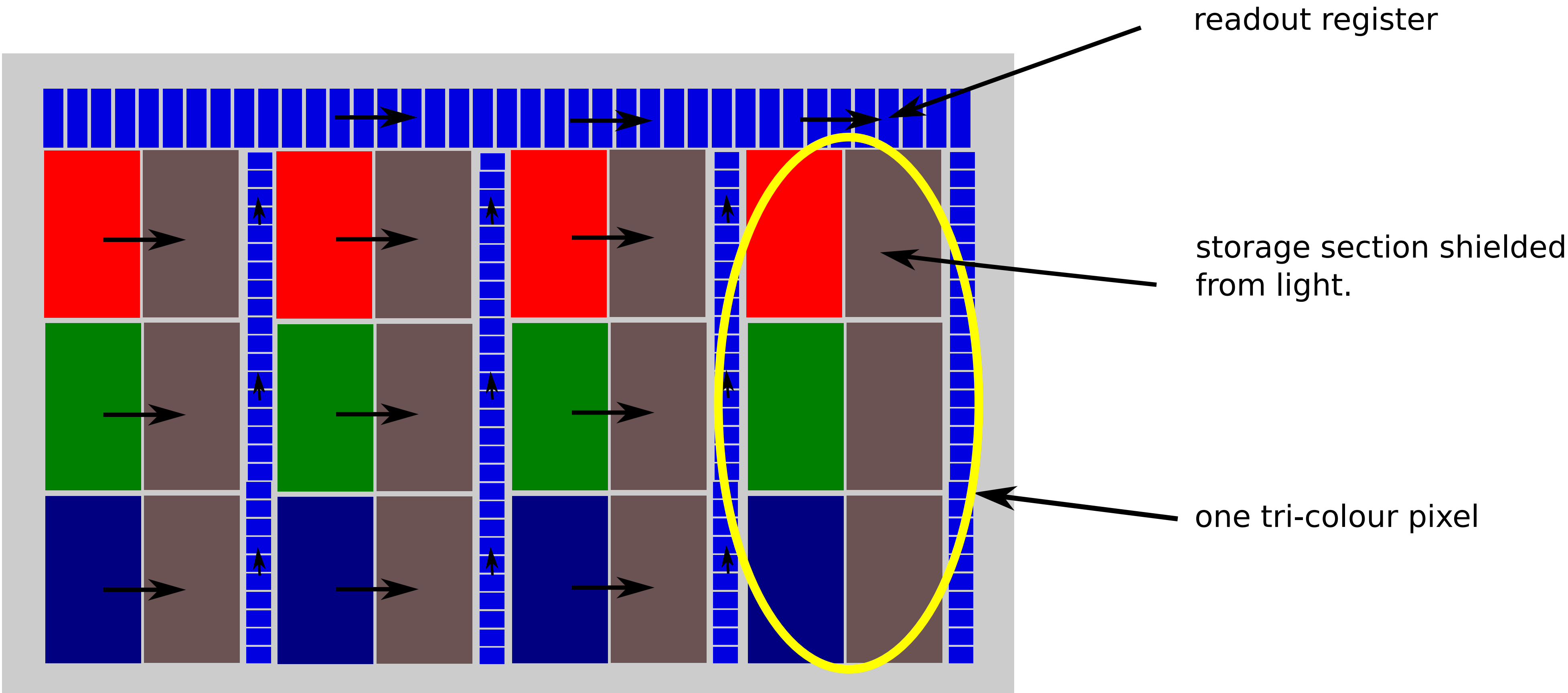

charge transfer channels adjacent to each photodiode, 'over, up and out' - data are read-out and digitized line by line $\rightarrow$ lower resolution (reduced image area), fast transfer reducing image smear

CCD principle conceived by Boyle and Smith at Bell Labs in 1970

The Nobel Prize in Physics 2009

"for groundbreaking achievements concerning the transmission of light in fibers for optical communication"

"for the invention of an imaging semiconductor circuit – the CCD sensor"

Photo: U. Montan

Charles K. Kao

1/2 of the prize

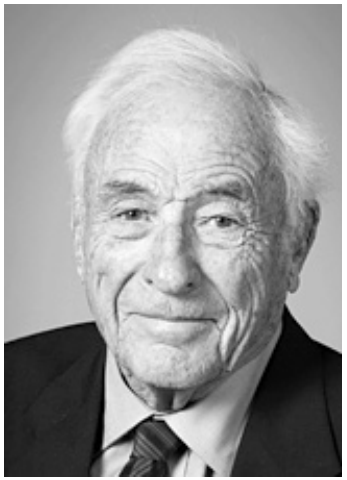

Photo: U. Montan

Willard S. Boyle

1/4 of the prize

Photo: U. Montan

George E. Smith

1/4 of the prize

a large state of the art CCD camera

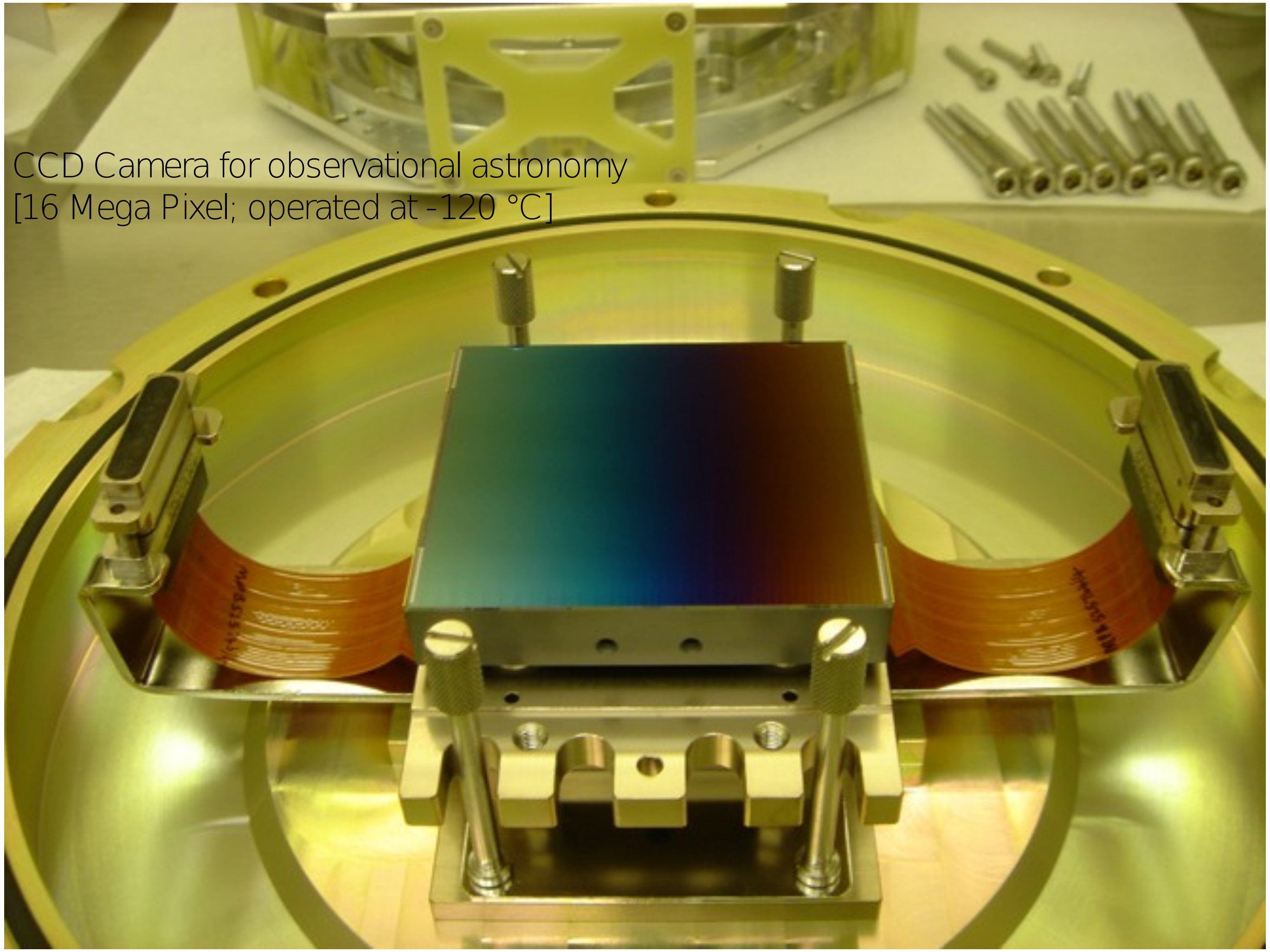

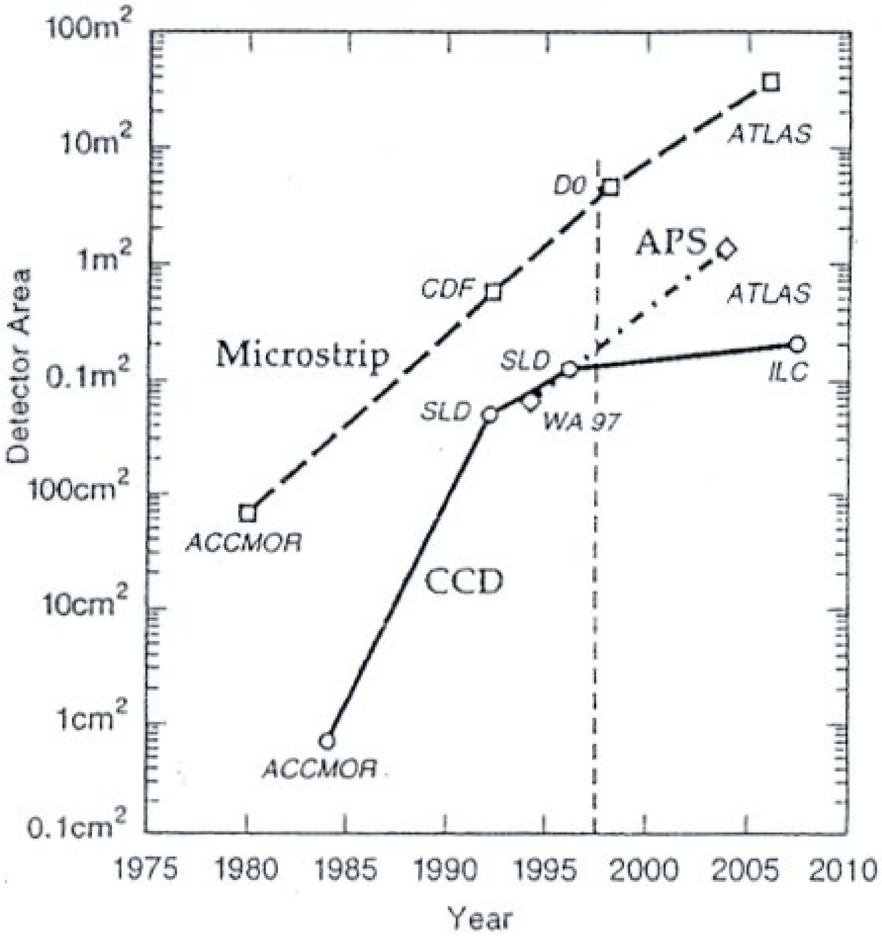

active area of the silicon vertex/tracking detectors as function of time. Micro-strip detectors retain the capability of largest area coverage.

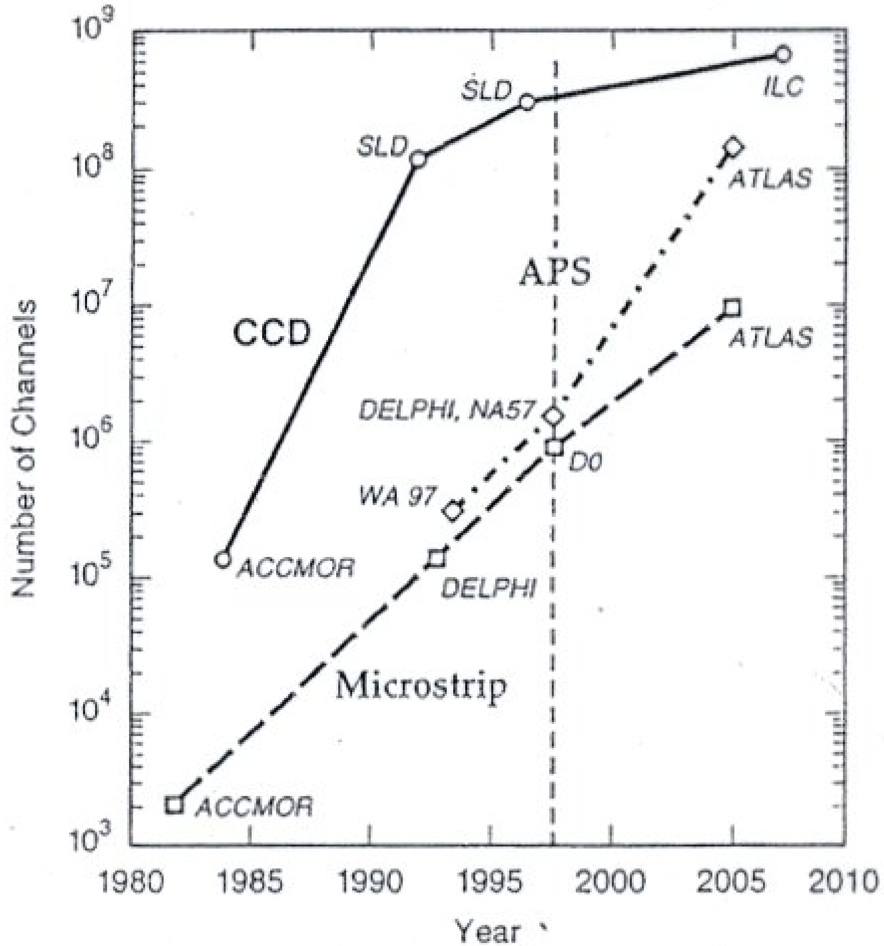

number of channels in the silicon vertex/tracking detectors as function of time. CCD-based pixel detectors retain the capability of finest granularity, but APS ('Active Pixel Sensors') detectors may come close in the long-term future.
2018: now they are! see colloquium L. Musa

Figs from C.J.S. Damerell, Rev. Sci. Instr. 69 (1998)1570

4.7 Radiation damage

major issue at LHC: with design luminosity of $10^{34}/\mathrm{cm}^2\mathrm{s}$ at radius of 10 cm
over 10 years of running accumulated radiation dose $10^{15} n_{eq}/\mathrm{cm}^2$ equal 600 kGy
high luminosity LHC (HL-LHC) starting from 2021: 10 times the dose of LHC

intensive irradiation R&D program over past 20 years to study and minimize effects

- Si sensors
- electronics
- glue and other material

radiation damage in Si sensors:
when e.g. a 1 MeV neutron hits Si nucleus $\rightarrow$ recoil kinetic energy of Si 30 keV

compare to typical binding of Si in crystal lattice of $15 - 25$ eV

similarly, incident pions in few hundred MeV range form Δ resonance when hitting p or n

decay momentum of 200 MeV/c gives recoil to decay p or n of about 2 MeV

NIEL (non-ionizing energy loss) dislocates Si-atoms from their lattice positions

for one 1 MeV neutron about 10^3 atoms in region of about 100 nm are displaced

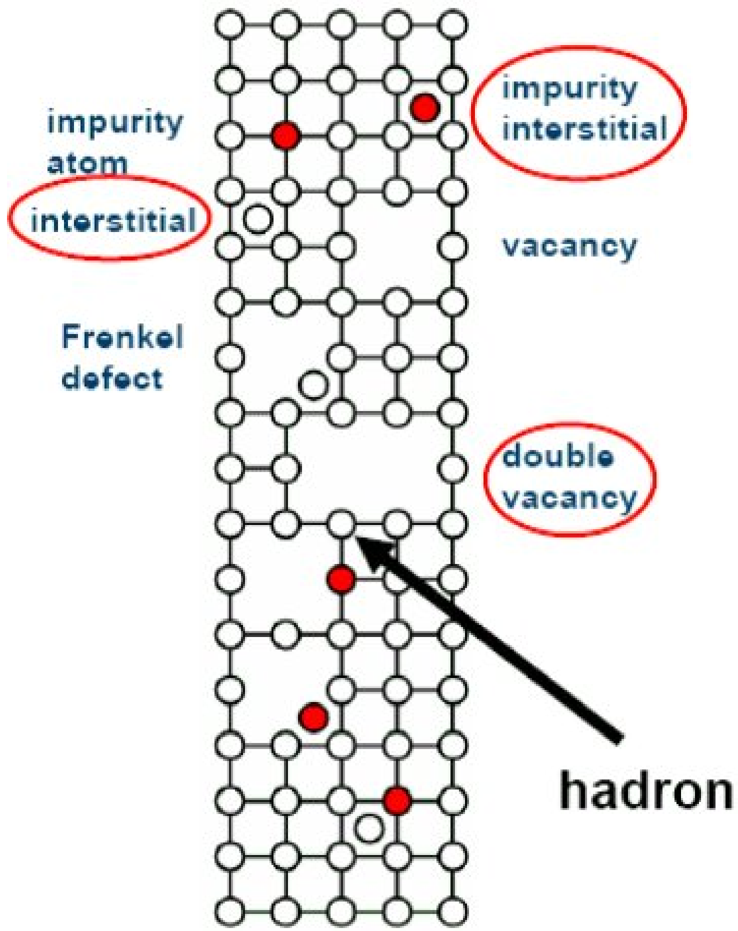

- generation and recombination of levels in band gap → increase of leakage current
  $I = I_0 + \alpha \phi V$ with $\alpha = 2 \cdot 10^{-17}$ A/cm^2 for particle flux ϕ (per cm^2) and volume V
  increased detector noise, worse resolution (S/N)
- creation of trapping centers → trapping of signal charge by recombination
- change of space charge in depleted region → change of effective doping
  most severe effect, increasing generation of acceptor-like defect leads eventually totype inversion, n-type → p-type

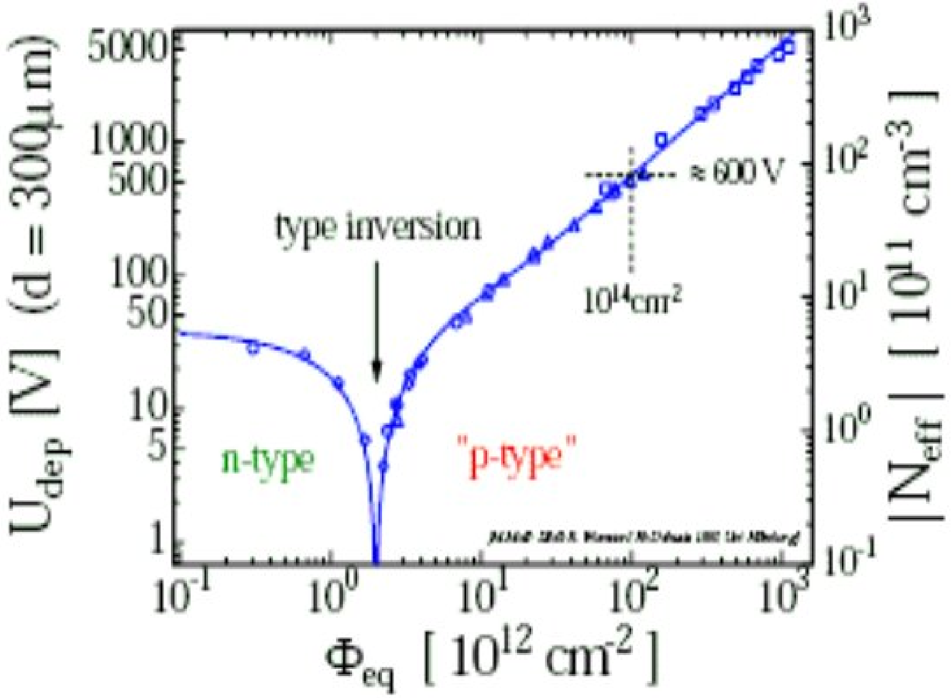

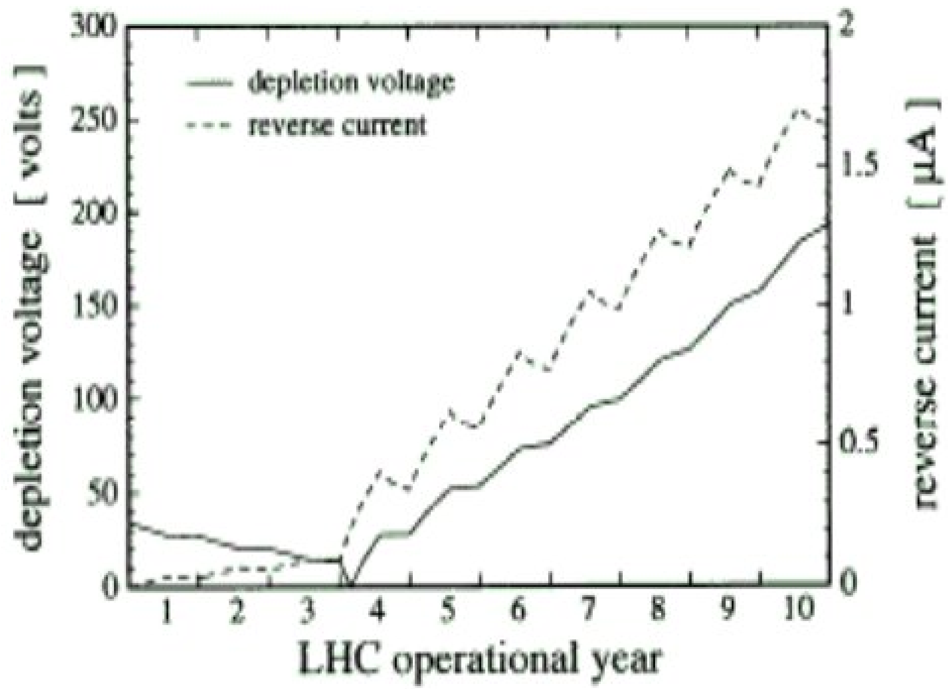

can operate detector up to about $10^{14} n_{eq}/\mathrm{cm}^2$ as for $U > 600$ V discharge
this would be only one year at LHC nominal luminosity → not good enough!

after irradiation complicated time dependence of damage:

- for irradiation without type-inversion slow healing of damages (months)
- after type-inversion:

  - for first week, effective doping concentration decreases at room temperature (beneficial annealing)

  - after that, doping concentration slowly increases (reverse annealing); can be minimized by keeping detector cool in between running periods

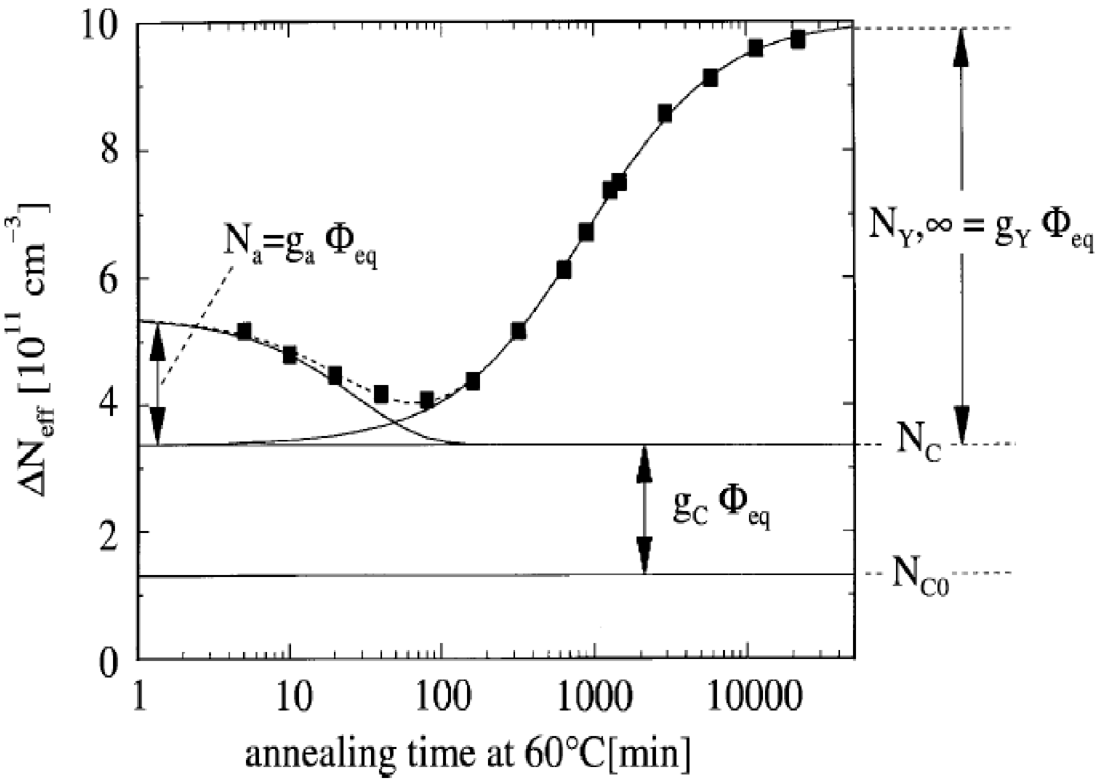

measurements carried out at increased temperature to accelerate effect of long term annealing (compress 10 years LHC running into weeks)

the solutions for LHC:

1. defect engineering: oxygenated Silicon = deliberate addition of impurities to bulk material, i.e. enrichment of Si substrate with oxygen
- electrically active defects capture vacancies in stable and electrically neutral point defects
- increases radiation hardness by factor 3 (slope g_c) for irradiation with charged hadrons (protons, pions)

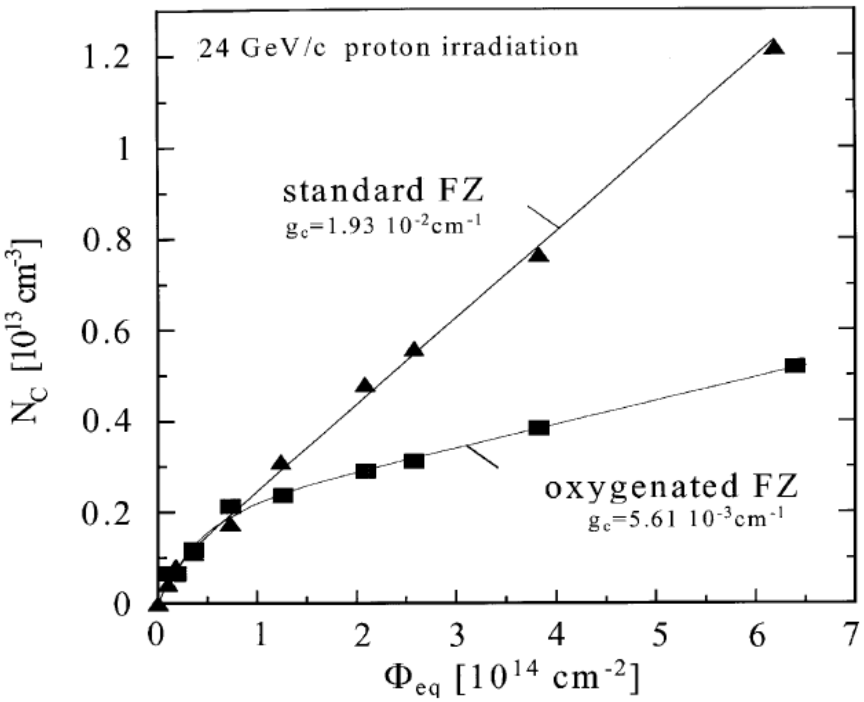

RD48, G. Lindström et al., NIM A465 (2001) 60

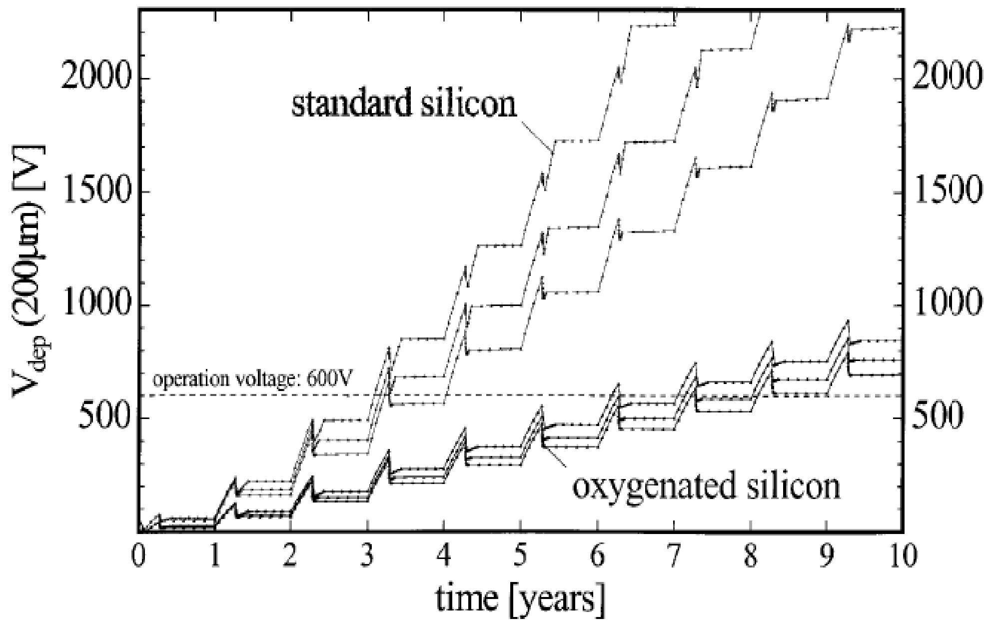

damage projection for ATLAS pixel B-layer for 100 day runs and different temperature scenarios

measuring the effective depletion depth after irradiation

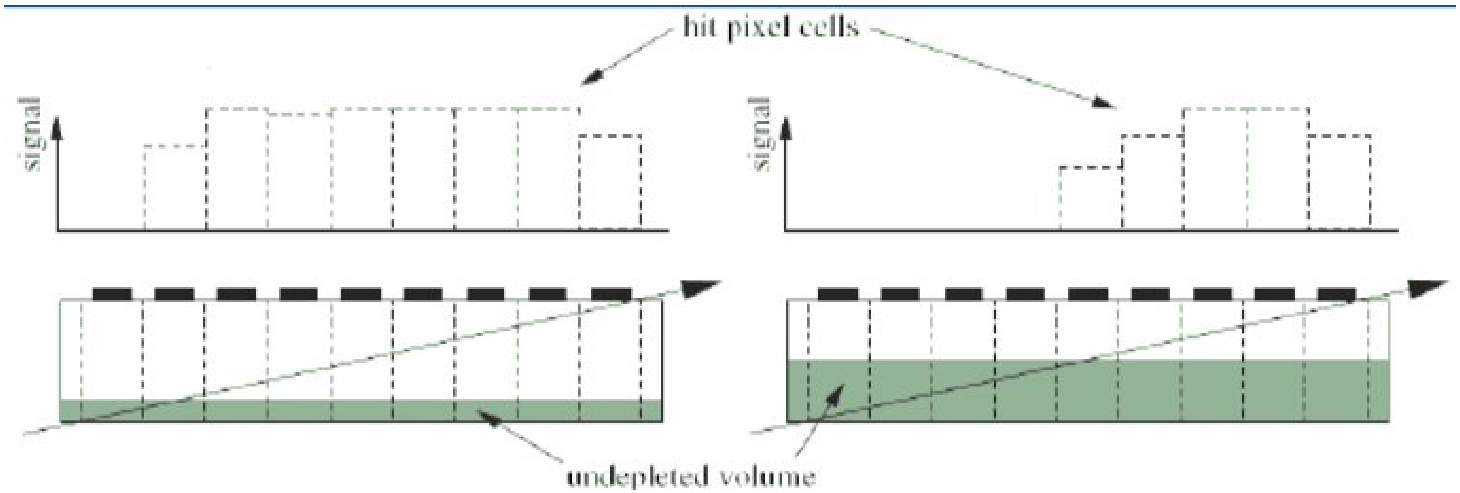

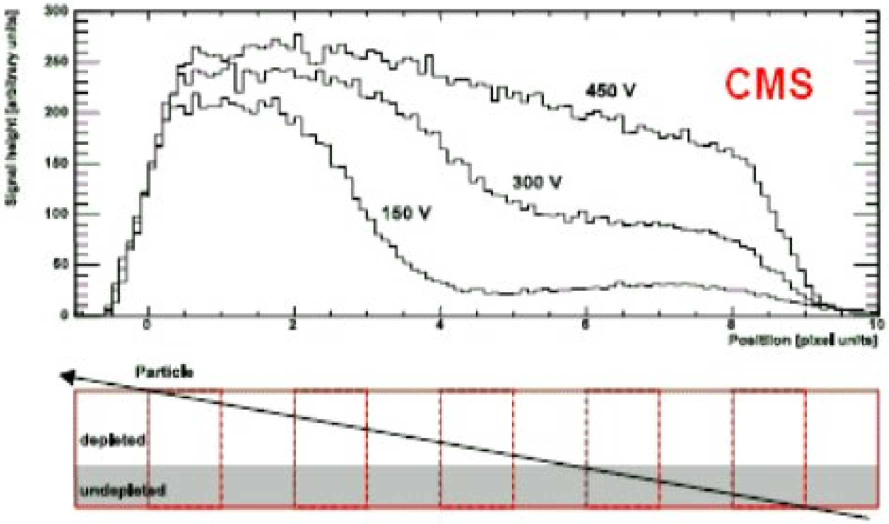

V.Chiochia, M. Swartz et al.
arxiv.org/abs/physics/0409049, IEEE NSS 04 in Rome

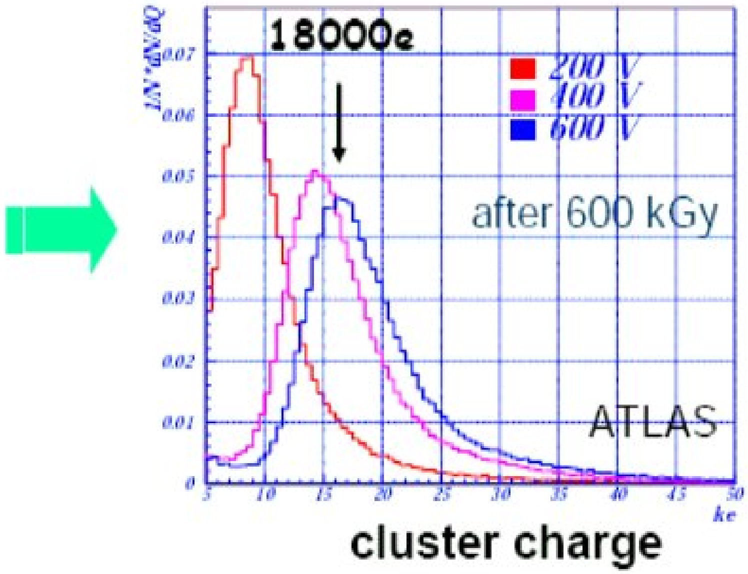

2. use of n+ in n (all LHC pixel detectors):

n+ implants in n-type Si

after type-inversion depletion region grows from n+ side → can operate detector partially depleted when full voltage cannot be applied any longer

plus, usage of guard rings around sensor at ground potential to protect sensitive frontend electronics from discharges

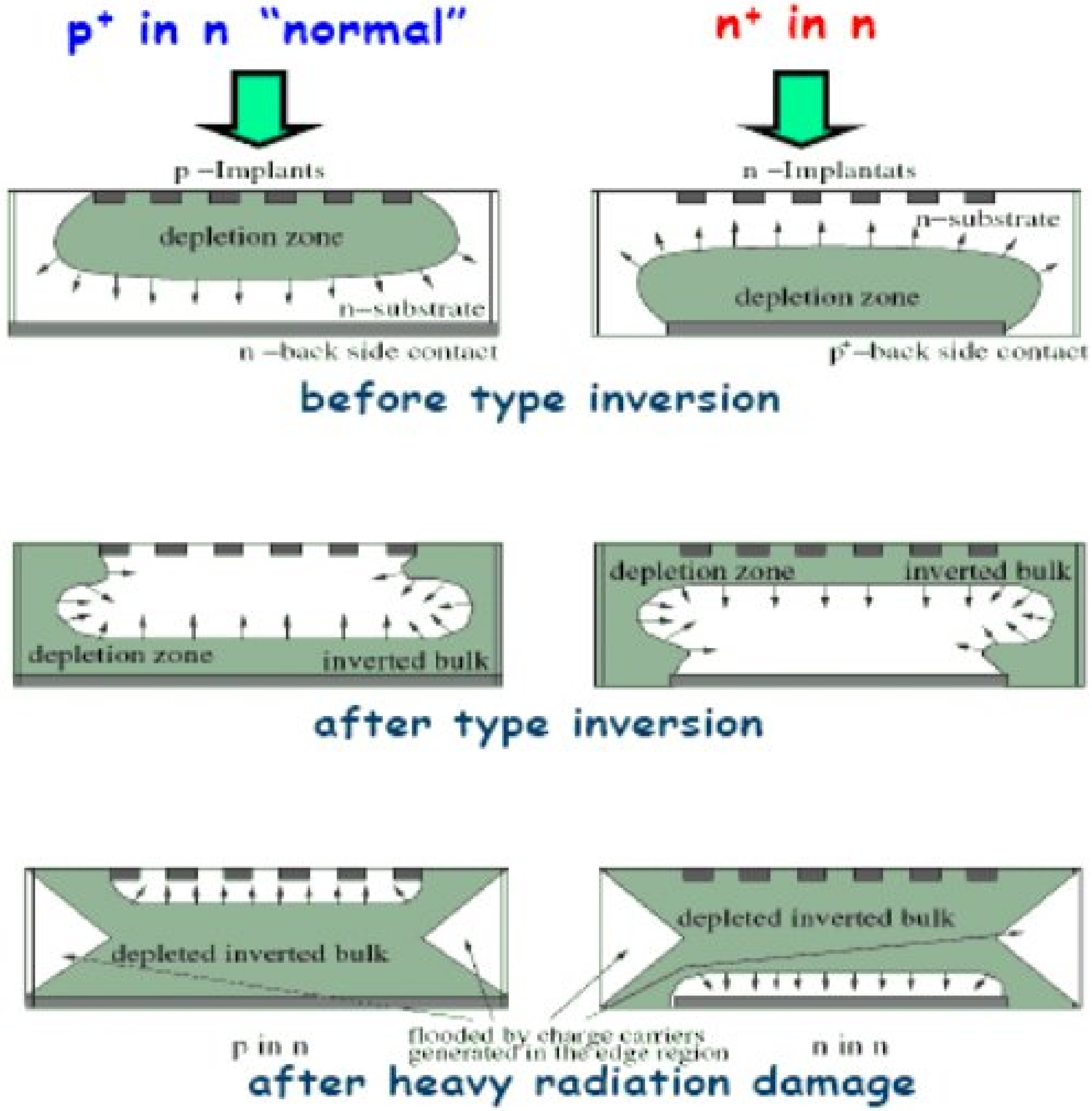

L. Andricek et al., NIM A409 (1998) 184

long-term prospects 1: Diamond detectors

($E_{gap} = 5.45$ eV)

much better behavior after irradiation

- lower leakage current
- increased mean free path for charge carrier trapping
- radiation hard up to $5 \cdot 10^{15}$ cm^2

but: can produce only thin detectors (less than 300 μm)
worse S/N, a lot of R&D needed

can already produce cheap material by evaporation (chemical vapor deposition)

long-term prospects 2: 3D - silicon detectors

(see e.g. C. DaVia, CERN courier Jan/Feb 2003):
proposed by Sherwood Parker in 1995: p+ and n+ electrodes penetrate silicon bulk

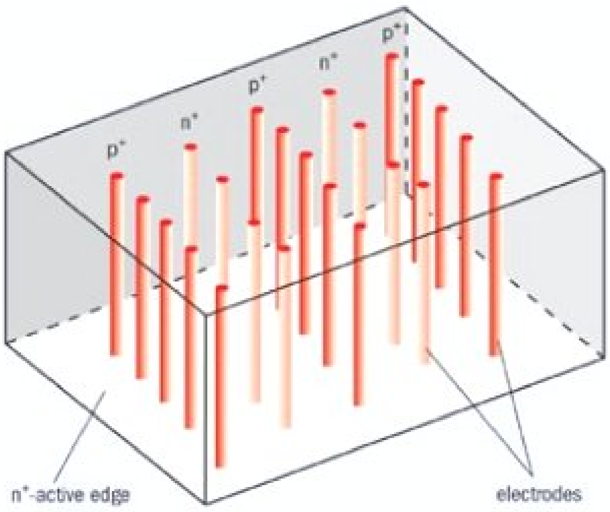

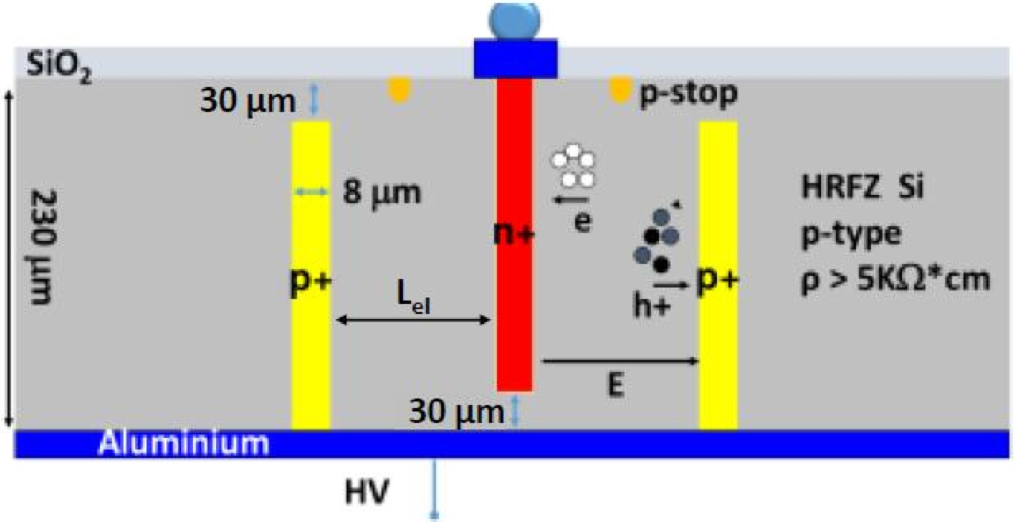

the same charge as in planar detector is collected in shorter time over shorter distance and with 10 times less depletion voltage

design parameter	3D	planar
depletion voltage (V)	< 10	70
collection length (μm)	~ 50	300
charge collection time (ns)	$1-2$	$10-20$
edge sensitivity (μm)	< 10	~ 300

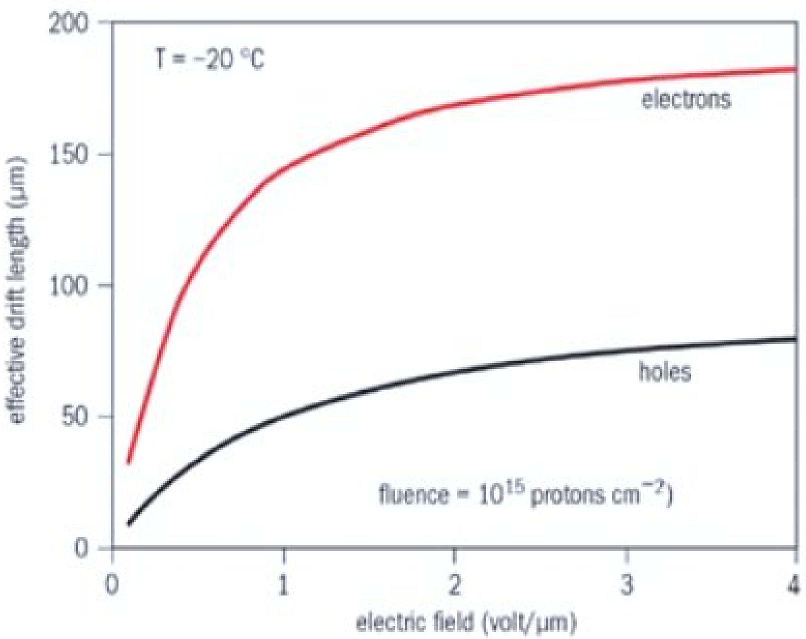

generally, electric field in sensor must be as large as possible → maximizes drift velocity → maximizes effective drift length before charge is trapped by defects $L_{drift} = v_{drift} \cdot \tau_{tr}$ with a trapping time τ_{tr}

drift lengths decrease linearly with fluence, device with larger drift length becomes inefficient at high radiation levels.
in detector with segmented electrode (pixels), larger fraction of signal generated by charge carrier drifting towards it
in irradiated detector, electrons travel farther before being trapped, therefore advantageous to collect signal at n+ electrode

deep reactive ion etching to 'drill' holes in silicon with thickness/diameter = 20 : 1, means holes into 300 μm substrate can be 'drilled' 50 μm apart

fill holes with poly-crystalline Si doped with B or P, which is then diffused into the surrounding pure silicon to make electrodes

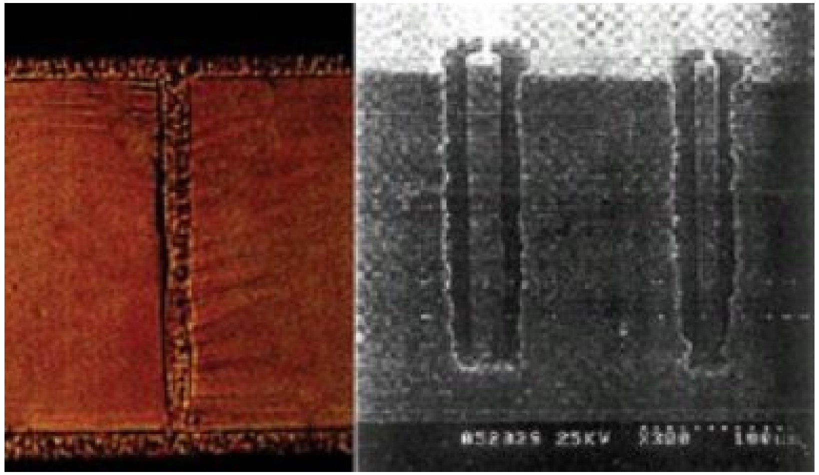

right: 290 μm deep etching followed by deposition of 2 μm poly-crystalline Si
left: broken wafer showing filled electrode holes

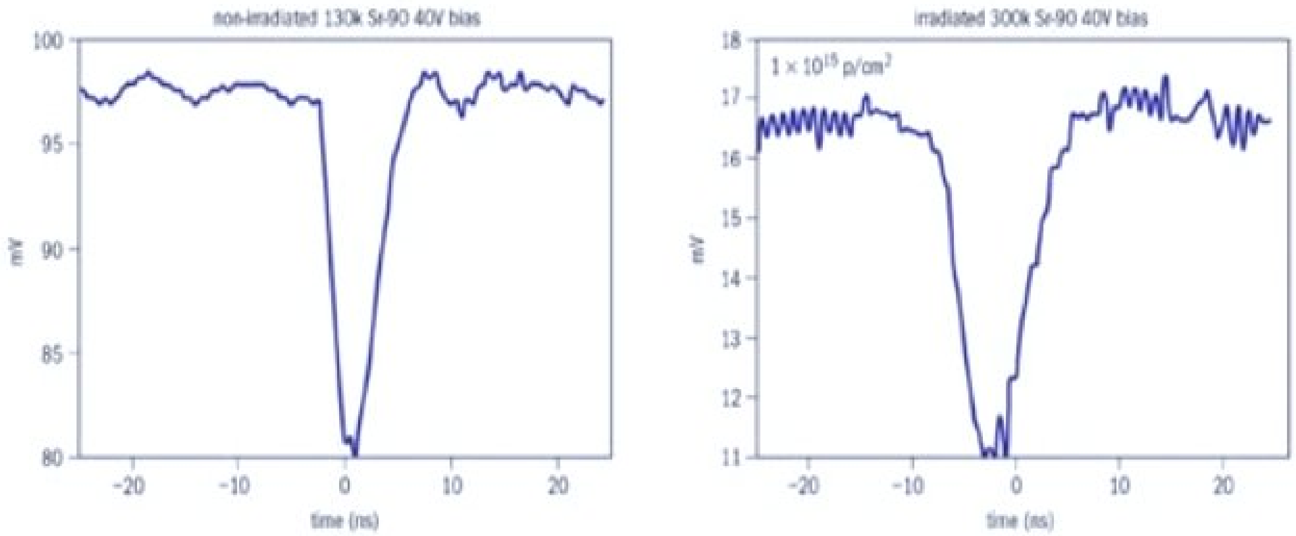

3D silicon sensor before and after irradiation: signal smaller but response still fast

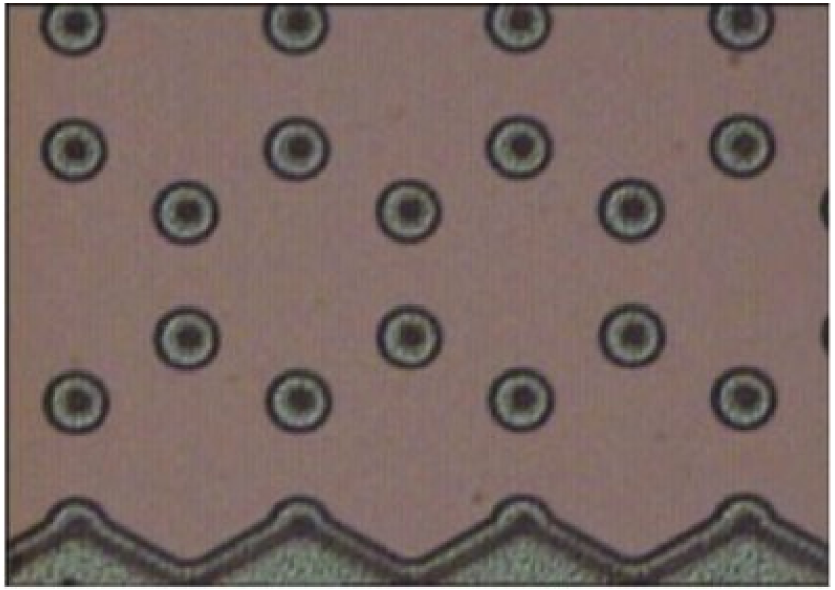

3D sensor in the process of fabrication: 1 set of electrodes completed in hexagonal pattern
bottom: active edge filled with dopant to form electric field inside sensor $\rightarrow$ deplete within a few microns of edge

technology also important for X-ray imaging, e.g., in molecular biology (protein folding)

3D pixel sensors for HL-LHC:

small pitch 3D silicon detectors for ATLAS HL-LHC pixel detector upgrade

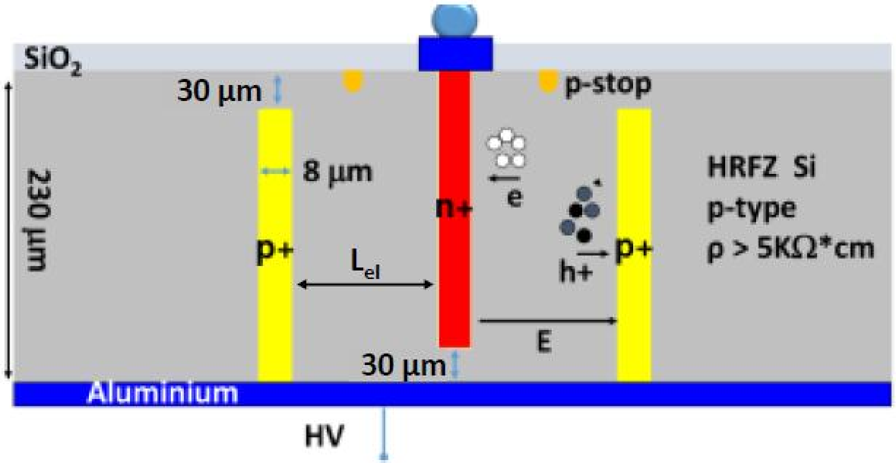

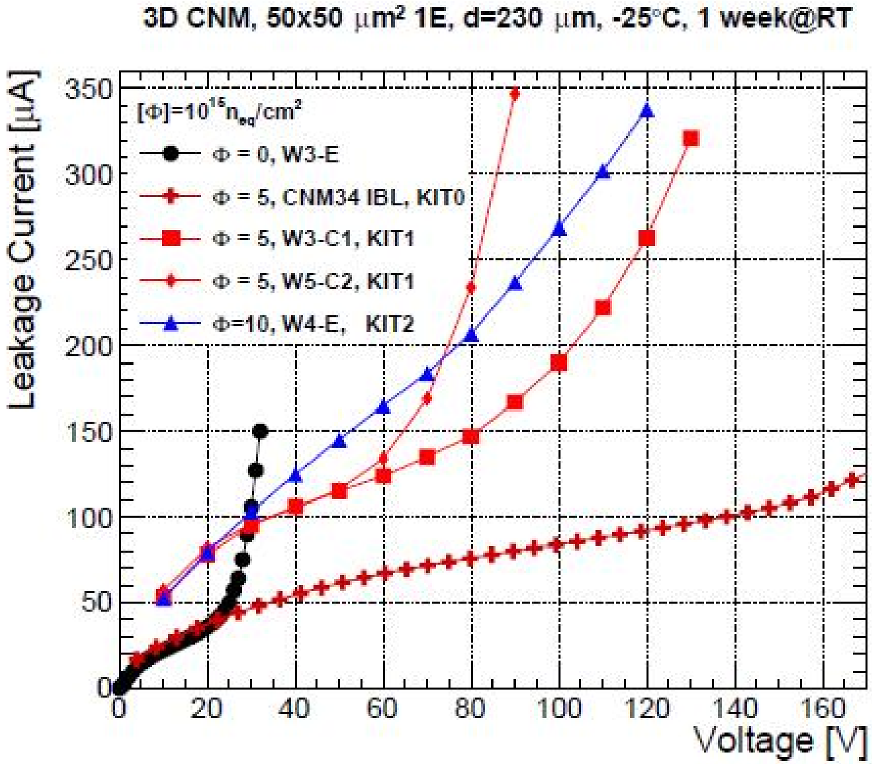

J. Lange et al., arXiv:1805.10208

Irradiations up to particle fluences of $3 \times 10^{16} \mathrm{n_{eq}/cm^2}$, beyond full expected HL-LHC fluences show good performance

5. Scintillation counters

detection of radiation by means of scintillation is among oldest methods of particle detection
historical example: particle impinging on ZnS screen $\rightarrow$ emission of light flash

Principle of scintillation counter:

- dE/dx is converted into visible light and transmitted to an optical receiver
  sensitivity of human eye quite good: 15 photons in the correct wavelength range
  within Δt = 0.1 s noticeable by human

scintillators make **multipurpose detectors**; can be used in calorimetry, time-of-flight measurement, tracking detectors, trigger or veto counters

Scintillating materials:

- inorganic crystals
- organic crystals
- polymers (plastic scintillators)

5.1 Scintillators

Inorganic crystals: crystal (electric insulator) doped with activator (color center) e.g. NaI(Tl)

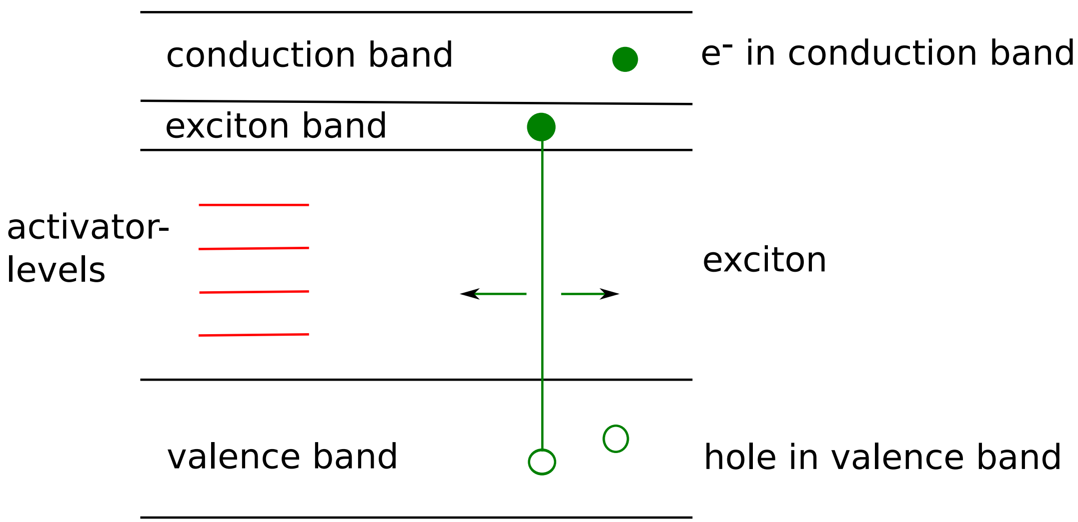

- energy loss can promote electron into conduction band → freely movable in crystal
- also possible: electron remains electrostatically bound to the hole → ≡ 'exciton', hydrogenlike quasiparticle, but much more weakly bound and much bigger, energy levels slightly below conduction band
- exciton moves freely through crystal → transition back into valence band under light emission inefficient process
- doping with activator (energy levels in band gap) to which energy is transferred → photon emission can be much more likely

Inorganic crystals

$$\text{exciton} + \text{activator } A \rightarrow A^* \rightarrow A + \text{photon}$$
$$\text{or } A + \text{lattice vibration}$$

- typical decay time of signal: ns - μs depending on material

  example: NaI(Tl)

$$\begin{aligned} \lambda_{max} &= 410 \text{ nm} \cong 3 \text{ eV} \\ \tau &= 0.23\ \mu\text{s} \\ X_0 &= 2.6 \text{ cm} \end{aligned}$$

- quality of scintillator: light yield ε_{sc} $\equiv$ fraction of energy loss going into photons

  example: for NaI(Tl) 38000 photons with 3 eV per MeV energy loss (deposit in scint.)

$$\varepsilon_{sc} \cong \frac{3.8 \cdot 10^4 \cdot 3 \text{ eV}}{10^6 \text{ eV}} = 11.3\% \quad \leftarrow \text{good}$$

characteristics of different inorganic crystals

type	λ_{max}[nm]	τ[μs]	photons per MeV	X_0[cm]
NaI(Tl)	410	0.23	38000	2.6
CsI(Tl)	565	1.0	52000	1.9
CsI (at 77 K)*	400	0.60	8300	1.85
	310	0.02	74000	1.85
BGO (bismuth germanate)	480	0.35	2800	1.1
BaF_2	310	0.62	6300	2.1
	220	0.0007	2000	2.1
CeF_3	330	0.03	5000	1.7
$PbWO_4$	430	0.01	100	0.9

* at roomtemperature more than factor 100 less light

- advantages of inorganic crystals:
  - high light yield
  - high density $\rightarrow$ good energy resolution for compact detector
- disadvantage:
  - complicated crystal growth $\rightarrow$ $$$ (several US$ per cm^3)

application in large particle physics experiments

- BaBar (SLAC):

  6580 CsI(Tl) crystals
  depth 17 X_0
  total 5.9 m^3
  readout Si photodiode (gain = 1)
  noise 0.15 MeV
  dynamic range 10^4

- CMS (LHC):

  76150 $PbWO_4$ crystals
  26 X_0
  total 11 m^3
  read-out APD (gain = 50)
  noise 30 MeV
  dynamic range 10^5

$PbWO_4$: fast, small radiation length, good radiation hardness compared to other scintillators, but comparatively few photons (order of 10 photoelectrons per MeV)

always need to consider: match of spectral distribution of light emission, absorption and sensitivity of photosensor

typical spectral distributions:

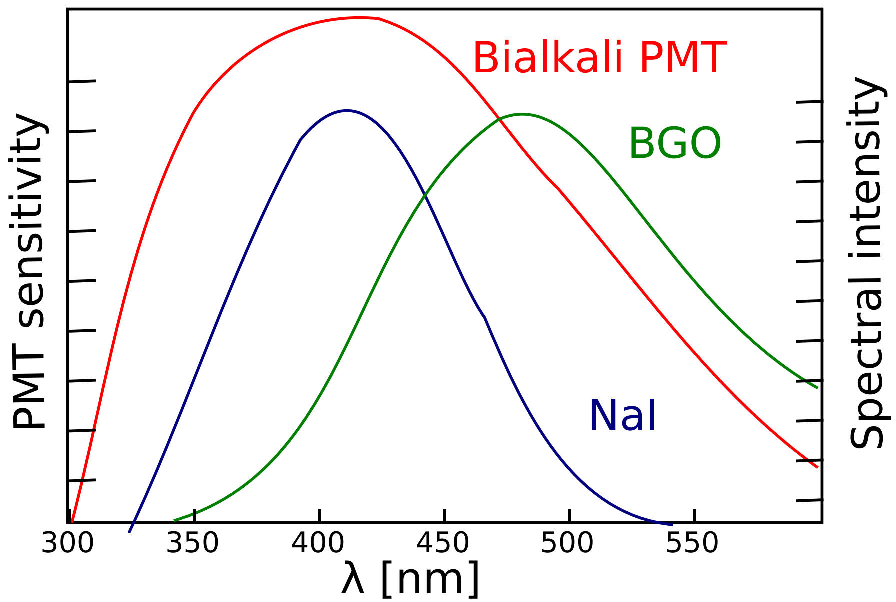

Organic crystals

aromatic hydrocarbon compoints
scintillation is based on the delocalized π electrons of aromatic rings (see below)

	λ_{max}[nm]	τ[ns]	light yield rel. to NaI
naphthalene 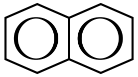	348	96	12%
anthracene 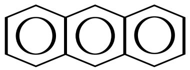	440	30	50%

advantages: relatively fast, cheap, mechanically strong
disadvantages: mechanically difficult to process, light output anisotropic (due to channeling in crystals)

Plastic scintillators

polymer + scintillator + wavelength shifter or liquid + scintillator + wavelength shifter

- **Polymers** (transparent)

  polystyrene

  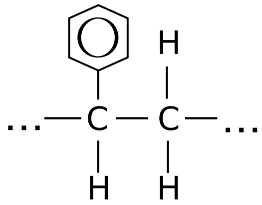

  lucite (plexiglas)

  polyvinyltoluene

- **Liquid** (transparent): benzene, toluene, mineral oil

- **Scintillators**

		λ_{max}[nm]	τ[ns]	ε_{sc}
p-Terphenyl	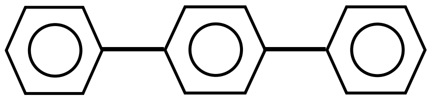	440	5	25%
PBD 2-phenyl-5(4-biphenyl)-1,3,4-oxadiazole	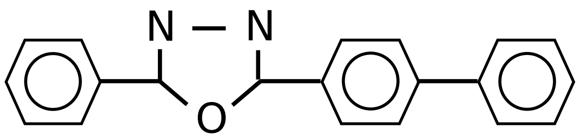	360	1	

disadvantages: low light yield: in plastic scintillator typically 10 photons per 1 MeV energy loss, low radiation length $X_0 = 40 - 50$ cm,
advantages: fast decay time (order of) ns, cheap, easy to shape, typically also high neutron detection efficiency via (n,p) reactions

typical organic scintillators and wavelength shifters:

primary fluorescent agent	structure	λ_{max} emission $[nm]$	decay time $[ns]$	light yield rel. to NaI
naphtalene	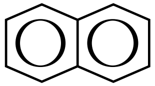	348	96	0.12
anthracene	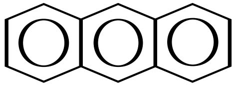	440	30	0.5
p-terphenyl	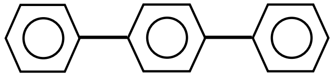	440	5	0.25
PBD	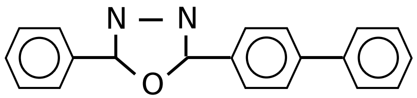	360	1.2	
wavelength shifter				
POPOP	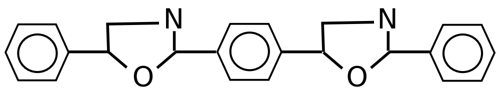	420	1.6	
bis-MSB	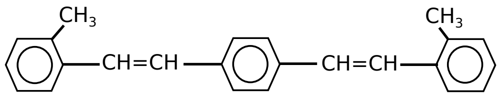	420	1.2	

what does wavelength shifter do?

- it absorbs primary scintillation light and reemits at longer wavelength
  $\rightarrow$ good transparency for emitted light
- adapts wave length to spectral sensitivity of photosensor

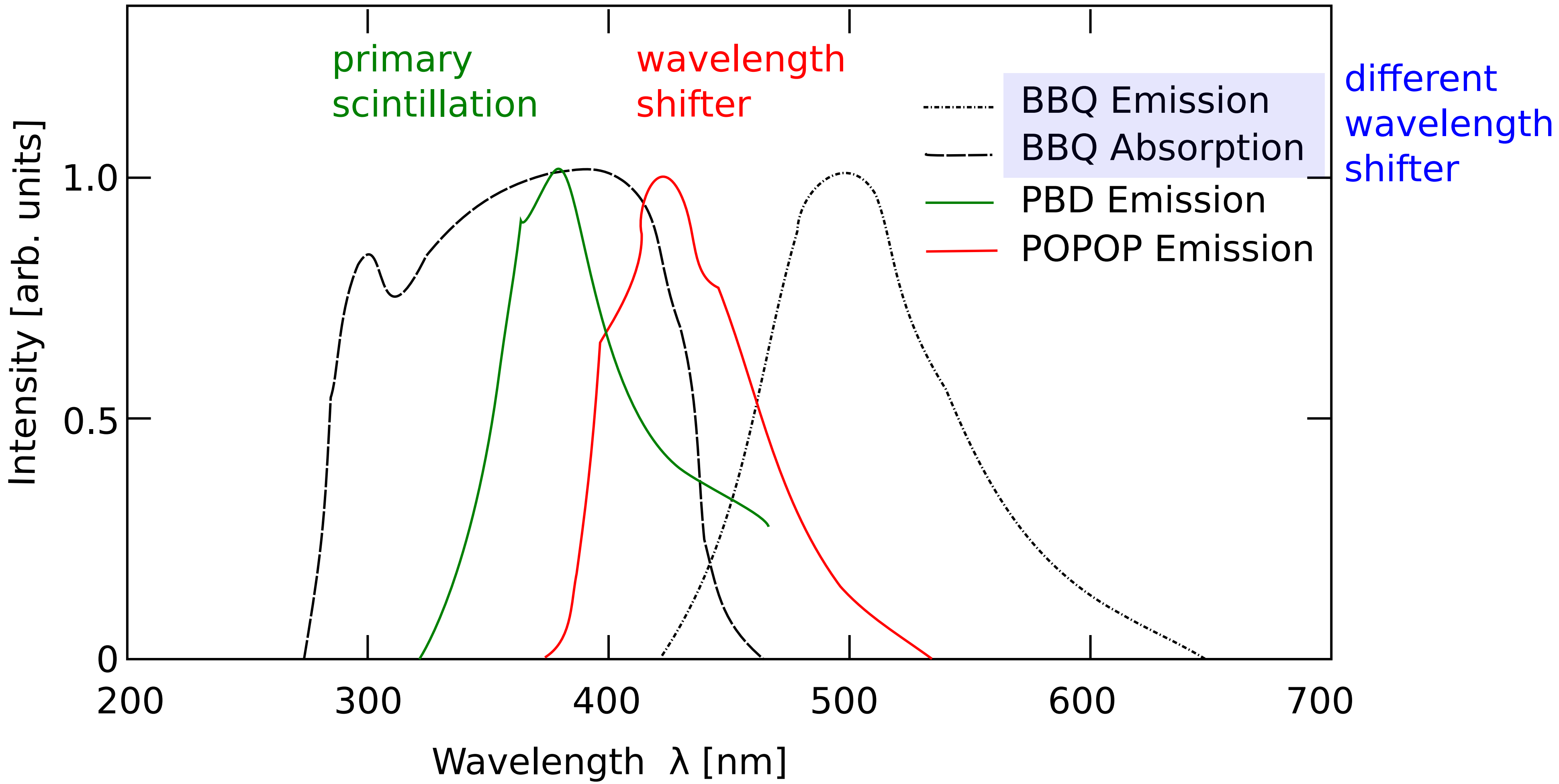

emission spectra of primary fluorescent substance (PBD)
and of two different wavelength shifters, BBQ (benzimidazo-benzisochinolin-7-on) and POPOP (1,4-bis-[2-(5-phenyloxazolyl)]-benzene))
and absorption spectrum of wavelength shifter BBQ

principle of operation of organic scintillator:

aromatic molecules with delocalized π-electrons, valence electrons pairwise in π states, level scheme splits into singlet and triplet states

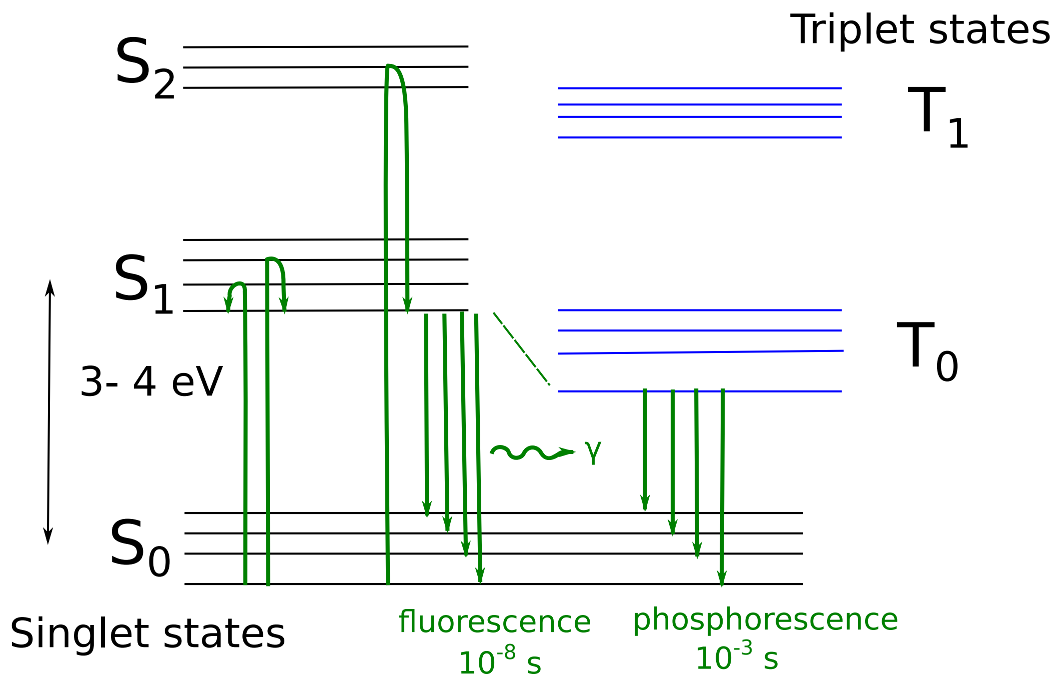

- excitation of π electrons
  energy absorption $\rightarrow S_1^*,\ S_2^* \rightarrow S_1$ radiationless on time scale 10^{-14} s
  fluorescence: $S_1 \rightarrow S_0$
- ionization of π electrons followed by recombination populates T states
  phosphorescence $T_0 \rightarrow S_0$
- excitation of σ-electrons $\rightarrow$ thermal deexcitation, radiationless, collisions and phonons
- other ionization $\rightarrow$ radiation damage

material transparent for radiation with $E_\gamma < S_1^0 - S_0^0$

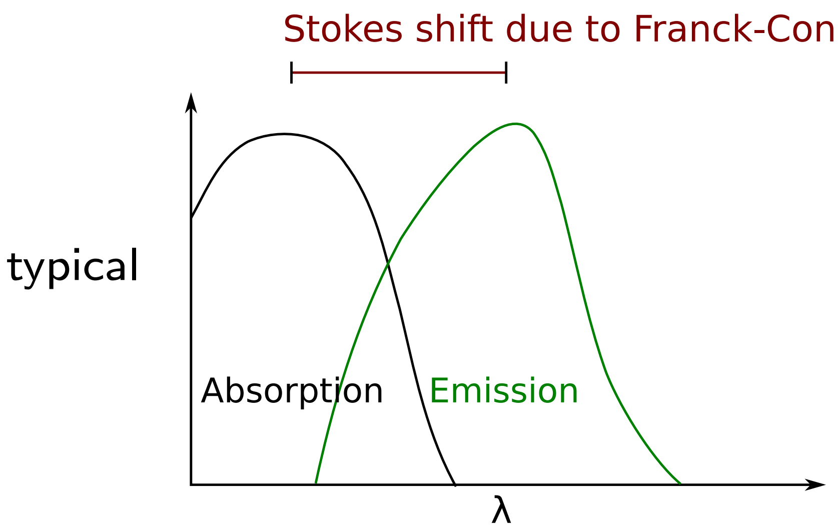

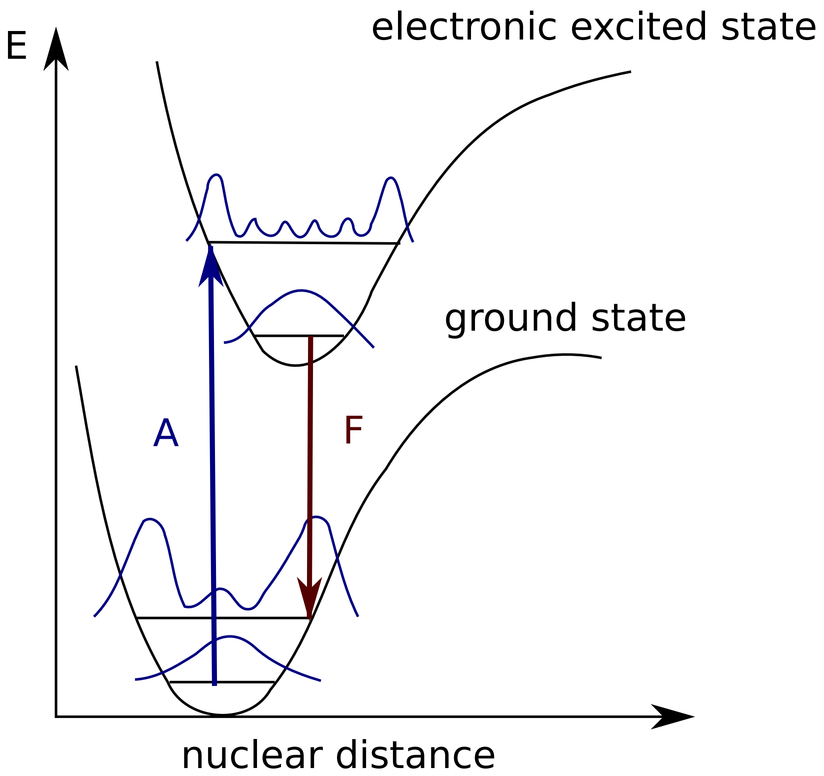

excitation on time scale 10^{-14} s
typical vibration time scale 10^{-12} s
typical S_1 lifetime 10^{-8} s
excitation into higher vibrational state
deexcitation from lowest vibrational state

in base material energy deposit
$\rightarrow$ excitation
generally bad light yield

transfer of excitation to primary fluorescent

primary fluorescent
good light yield

absorption spectrum needs to be matched to excited states in base material

depending on material, a secondary fluorescent (wavelength shifter) is introduced to separate emission and absorption spectrum (transparency)

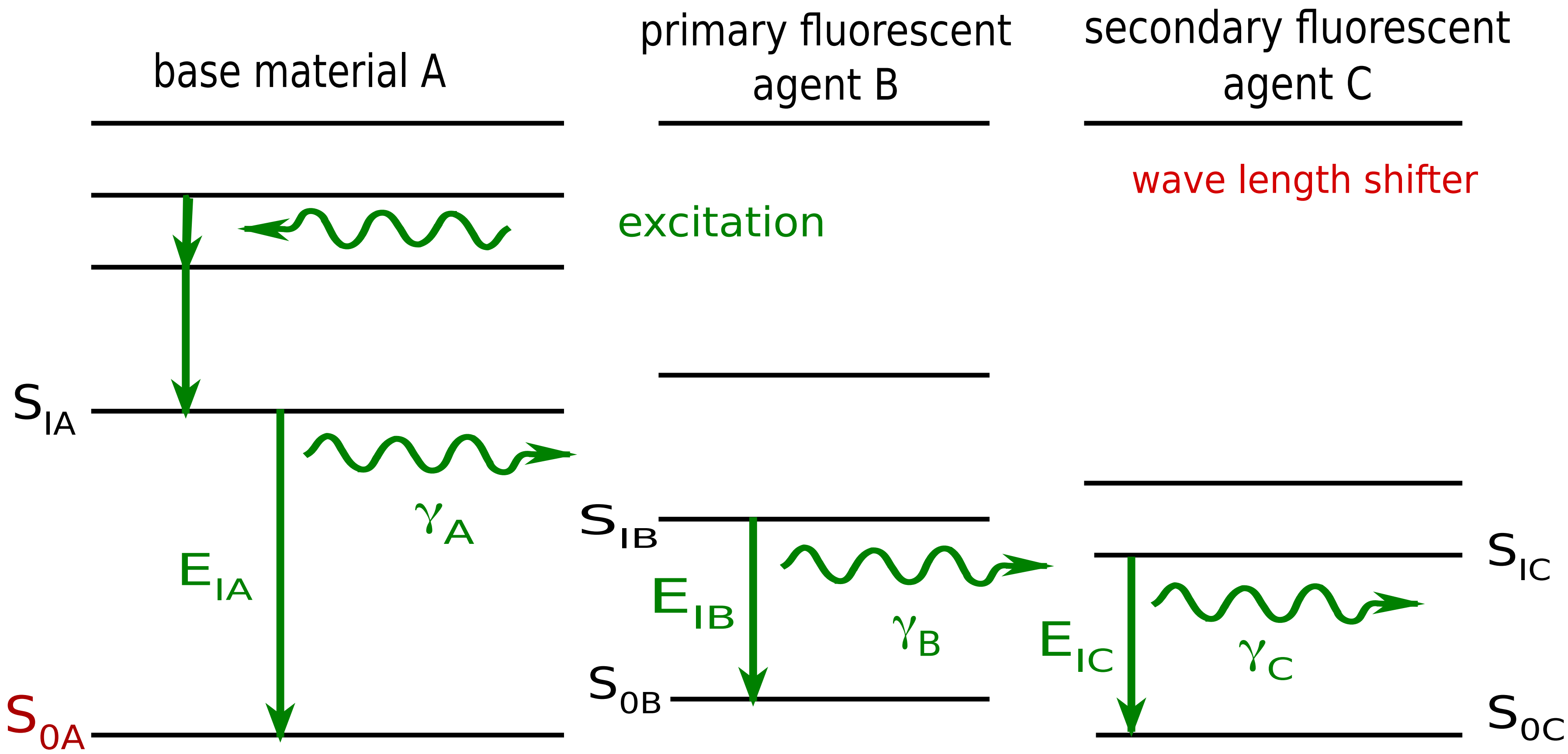

Scintillating gases

- many gases exhibit some degree of scintillation

	λ_{max} [nm]	γ/4.7 MeV α
N_2	390	800
He	390	1100
Ar	250	1100

contributes in gas detector to electric discharge, and be careful in Cherenkov detectors!

Pierre Auger Observatory for cosmic-ray-induced air-showers: employs water Cherenkov detectors and fluorescence detectors to observe UV fluorescence light emitted by atmospheric nitrogen (up to 4 W at maximum of cascade)

- liquid noble gases: lAr, lKr, lXe also scintillate
  in UV (120-170 nm),
  good light yield (40 000 photons per MeV),
  fast (0.003 and 0.022 μs)
  usage in (sampling) calorimeters

5.2 Photon detection

5.2.1 Photomultiplier

i) photo effect in photocathode: $\gamma + \text{atom} \rightarrow \text{atom}^{+} + e^{-}$

$$T_e = h\nu - W$$

W: work function, in metals $3-4$ eV, bad! comparable to energy of scintillation photon

$\Rightarrow$ specially developed alloys (bialkali, multialkali) with $W = 1.5 - 2$ eV

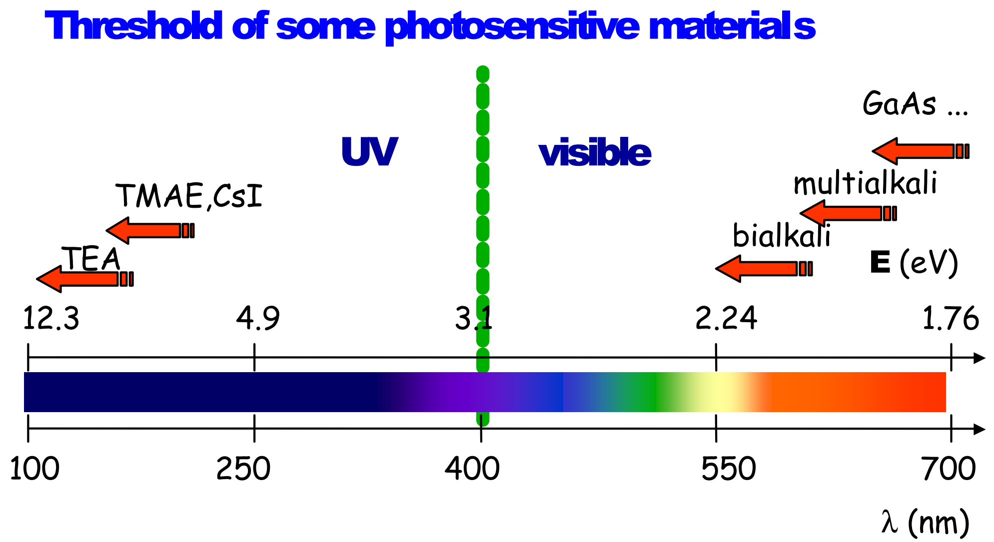

figure of merit: quantum yield

$$Q = \frac{\#\text{photoelectrons}}{\#\text{photons}} \cong 10 - 30\%$$

typical spectral sensitivity

cut-off at small wavelength: glass window can be replaced by quartz, extending range to smaller wavelengths (see e.g. fast component of light of BaF_2)

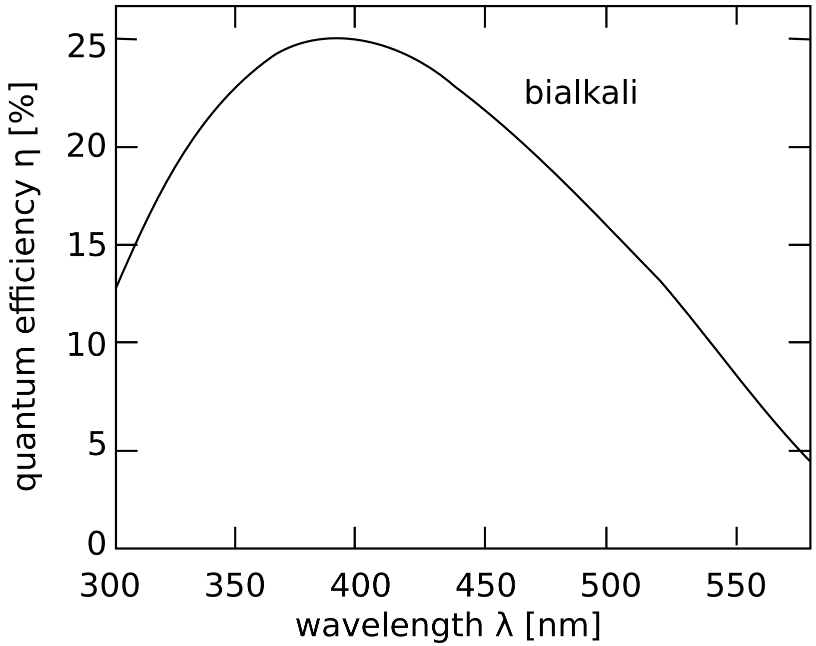

spectral sensitivity (quantum efficiency) of a bialkali (SbKCs) photocathode as a function of the wavelength

also used:

- SbRbCs
- SbCs
- $SbNa_2KCs$ (multialkali)

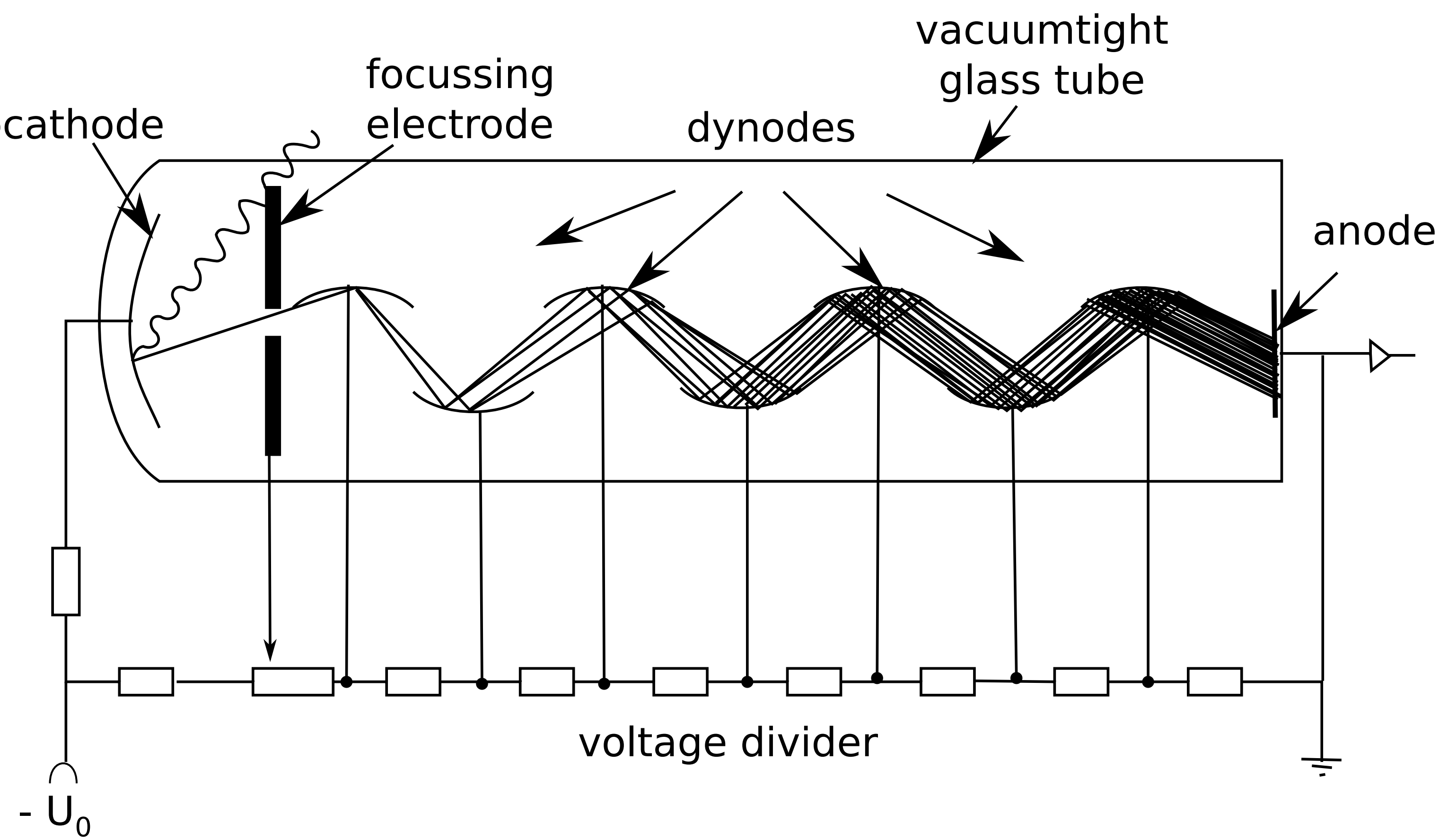

working principle of a photomultiplier   electrode system mounted in an evacuated glass tube

photomultiplier usually surrounded by a μ-metal cylinder (high permeability material) to shield against stray magnetic fields (e.g. the magnetic field of the earth)

ii) multiplication of photoelectrons by dynodes

- electrons are accelerated towards dynode
- knock out further electrons in dynode

secondary emission coefficient $\delta = \dfrac{\#\text{ leaving } e^-}{\#\text{ incident } e^-}$

$$\left.\begin{array}{lll} \text{typically} & & \delta = 2 - 10 \\ \#\ \text{dynodes} & & n = 8 - 15 \end{array}\right\} \quad G \propto \delta^n = 10^6 - 10^8$$

δ dependent on dynode potential difference:

$$\delta = k \cdot U_D$$

$$G = a_0 (kU_D)^n \qquad a_0 : \text{ collection efficiency between cathode and first dynode}$$

operational voltage $U_B = nU_D$ dynodes connected via resistive divider chain

$$\frac{dG}{G} = n\frac{dU_D}{U_D} = n\frac{dU_B}{U_B}$$

Limitations in energy measurement

- linearity of PMT: at high dynode current possibly saturation by space charge effects
  $I_A \propto n_\gamma$ for 3 orders of magnitude possible
- photoelectron statistics for mean number of photoelectrons n_e given by Poisson distribution

$$P_n(n_e) = \frac{n_e^n \exp(-n_e)}{n!}$$

with good PMT, observation of single photoelectrons possible

photoelectron statistics for a given energy loss dE/dx respectively E_γ defined by

$$n_e = \frac{dE}{dx} \times \frac{\text{photons}}{\text{MeV}} \times \text{ light collection efficiency } \times \text{ quantum efficiency}$$

e.g. in NaI(Tl) for 10 MeV incident photon:

$$
\begin{aligned}
n_e &= 10\text{ MeV} \times \frac{38000}{\text{MeV}} \times 0.2 \times 0.25 = 15000 \\
\frac{\sqrt{n_e}}{n_e} &= 0.8\%
\end{aligned}
$$

- fluctuations of secondary electron emission at mean multiplication factor δ (again Poisson)

$$P_n(\delta) = \frac{\delta^n \exp(-\delta)}{(n!)} \qquad \text{for Poisson with mean } \langle n \rangle = \delta$$

$$\text{variance} \quad \sigma_n^2 = \langle n \rangle = \delta$$

contribution to resolution $\quad \dfrac{\sigma_n}{\langle n \rangle} = \dfrac{1}{\sqrt{\delta}}$

N stages of dynodes which each amplify by factor δ:

$$
\begin{aligned}
\left(\frac{\sigma_n}{\langle n \rangle}\right)^2 &= \frac{1}{\delta} + \frac{1}{\delta^2} + \ldots + \frac{1}{\delta^n} = \frac{1-\delta^{-N}}{\delta - 1} \cong \frac{1}{\delta - 1} \\
\frac{\sigma_n}{\langle n \rangle} &= \frac{1}{\sqrt{\delta - 1}}
\end{aligned}
$$

quality of PM dominated by first stage

Pulse shape:

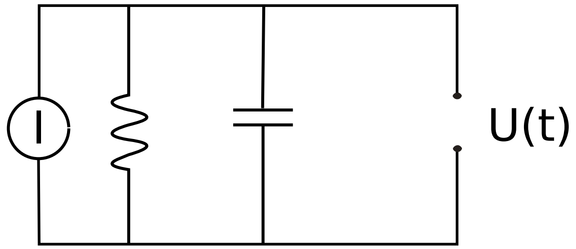

ideal current source with parallel resistance R and capacitance C

light incident with decay time of scintillator τ_{sc}

$$N_\gamma = N_0 \exp\left(-t/\tau_{sc}\right)$$

anode current
$$I(t) = \frac{G n_e e}{\tau_{sc}} \exp\left(-t/\tau_{sc}\right) = I_0 \exp\left(-t/\tau_{sc}\right)$$

$$Q = \int I \mathrm{d}t = I_0 \tau_{sc} = G n_e e$$

$$I(t) = \frac{U(t)}{R} + C \frac{\mathrm{d}U(t)}{\mathrm{d}t}$$

$\rightarrow$ voltage signal (with $U(t = 0) = 0$)

$$\boxed{U(t) = \frac{Q \cdot R}{\tau - \tau_{sc}} \left[\exp\left(-\frac{t}{\tau}\right) - \exp\left(-\frac{t}{\tau_{sc}}\right)\right]} \qquad \tau = RC$$

2 possible realizations (limiting cases) optimized for i) pulse height or ii) timing:

i) $RC = \tau \gg \tau_{sc}$

$$
\begin{aligned}
U(t) &= \frac{Q}{C}\left(\exp\left(-\frac{t}{\tau}\right) - \exp\left(-\frac{t}{\tau_{sc}}\right)\right) \\
&= \begin{cases} \frac{Q}{C}\left(1 - \exp\left(-\frac{t}{\tau_{sc}}\right)\right) & \tau \gg t \\ \frac{Q}{C}\exp\left(-\frac{t}{\tau}\right) & t \gg \tau_{sc} \end{cases}
\end{aligned}
$$

rising edge of pulse characterized by τ_{sc} linear in t
pulse length characterized by $\tau = RC$

$$U_{max} \cong Q/C \propto N_\gamma \quad \rightarrow \quad \boxed{\text{energy measurement}}$$

ii) $RC = \tau \ll \tau_{sc}$

$$
\begin{aligned}
U(t) &= \frac{\tau}{\tau_{sc}}\frac{Q}{C}\left(\exp\left(-\frac{t}{\tau_{sc}}\right) - \exp\left(-\frac{t}{\tau}\right)\right) \\
&= \begin{cases} \frac{\tau}{\tau_{sc}}\frac{Q}{C}\left(1 - \exp\left(-\frac{t}{\tau}\right)\right) & t \ll \tau_{sc} \\ \frac{\tau}{\tau_{sc}}\frac{Q}{C}\exp\left(-\frac{t}{\tau_{sc}}\right) & t \gg \tau \end{cases}
\end{aligned}
$$

rising edge of pulse given by small RC, again linear in t
decay of pulse given by τ_{sc} $\rightarrow$ $\boxed{\text{time measurement}}$
sensitivity to Q/C weakened by small RC

time resolution given by:

- rise time of signal (order $1-2$ ns)
- transit time in photomultiplier (order $30-50$ ns)
  respectively, variations in transit time (order 0.1 ns for good PMT)

transit time variations via

- path length differences cathode - first dynode

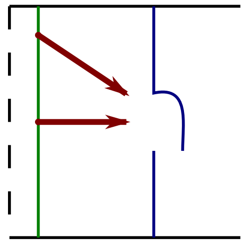

$$\Delta t \cong 1 \text{ ns} \qquad \text{for cathode } \varnothing\ 10 \text{ cm}$$
$$5 \text{ ns} \qquad \varnothing\ 50 \text{ cm}$$

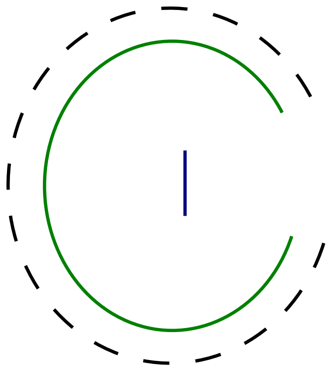

  hence spherical arrangement for very large PMTs
  (e.g. 20" in Superkamiokande)

- energy spread of photoelectrons when they leave the photocathode
  timing difference for photoelectron accelerated from rest
  ($T_e = 0$) relative to one with T_e

$$\Delta t = \frac{\sqrt{2mT_e}}{eE}$$

therefore maximize potential difference between cathode and first dynode, e.g.

$$T_e = 1 \text{ eV} \qquad E = 200 \text{ V/cm} \quad \rightarrow \quad \Delta t = 0.17 \text{ ns}$$

strong reduction of pathlength difference:
"micro channel plate"

arrangement of $10^4 - 10^7$ parallel channels (glass tubes)
of $10 - 50\ \mu$m diameter, $5 - 10$ mm length

electric field inside by applying voltage to one end (~ 1000 V) and coated inside with resistive layer acting as a continuous dynode

realization: holes in lead glass plate

$$G = 10^5 - 10^6 \qquad \Delta t = 0.1 \text{ ns}$$

further advantage: can be operated inside magnetic field

difficulty: positive ions created by collisions with rest gas inside channel must be prevented from reaching photo cathode (otherwise death of MCP)
$\rightarrow$ extremely thin ($5 - 10$ nm) Al window between channel plate and photocathode

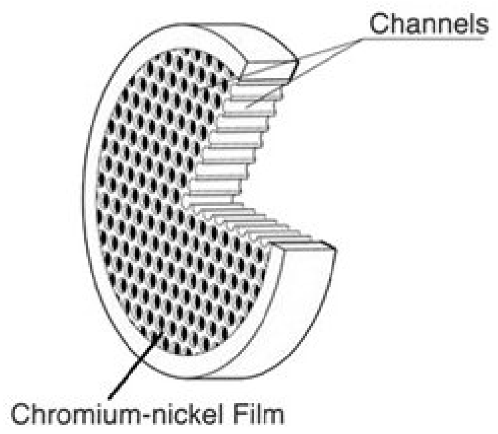

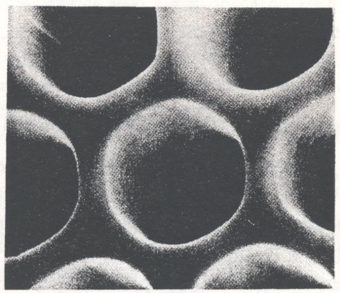

Fig. 5.6. Microphotograph of microchannels [384].

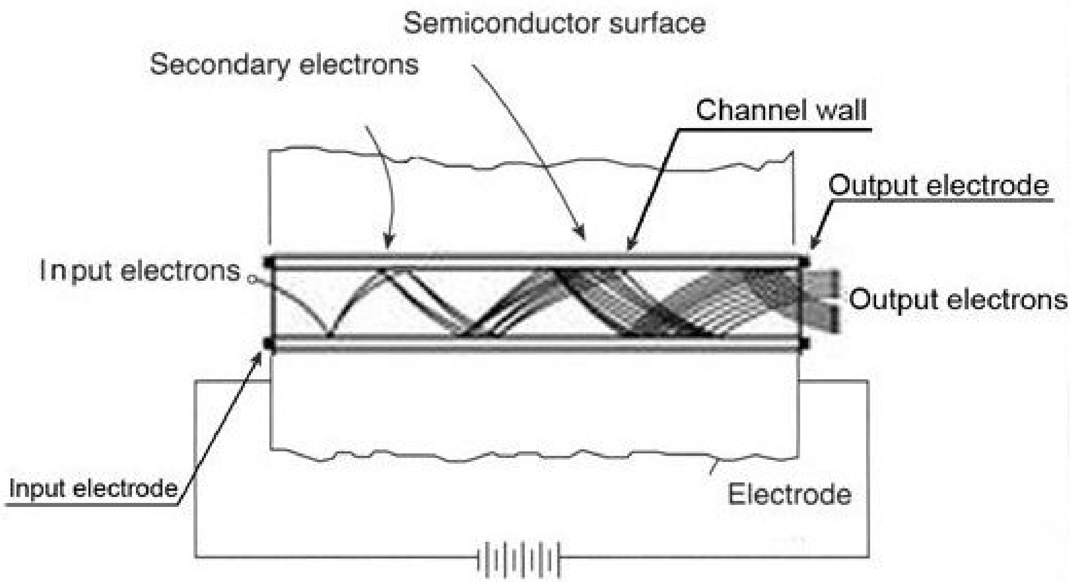

characteristics for several commercially available PMTs and microchannel plates

	Amperex XP 2020	RCA 8854	Hamamatsu R 647-01	ITT F 4129	Hamamatsu R 1564U
amplification	$> 3 \cdot 10^7$	$3.5 \cdot 10^8$	$> 10^6$	$1.6 \cdot 10^6$	$5 \cdot 10^5$
HV anode-cathode (V)	2200	2500	1000		
microchannel voltage (V)				2500	3400
rise time τ_R (ns)	1.5	3.2	2	0.35	0.27
transit time τ_T (ns)	28	70	31.5	2.5	0.58
transit time variation τ_S, one PE	0.51	1.55	1.2	0.20	0.09
transit time variation τ_S', many PEs	0.12		0.40	0.10	
number of PEs for transit time τ_S' meas.	2500		100	800	
quantum yield (%)	26	27	28	20	15
photocathode diameter (mm)	44	114	9	18	18
dynode material	Cu Be	GaP/BeO			

time resolution influenced by transit time variation and dimensions of scintillator (timing variation of light collection):

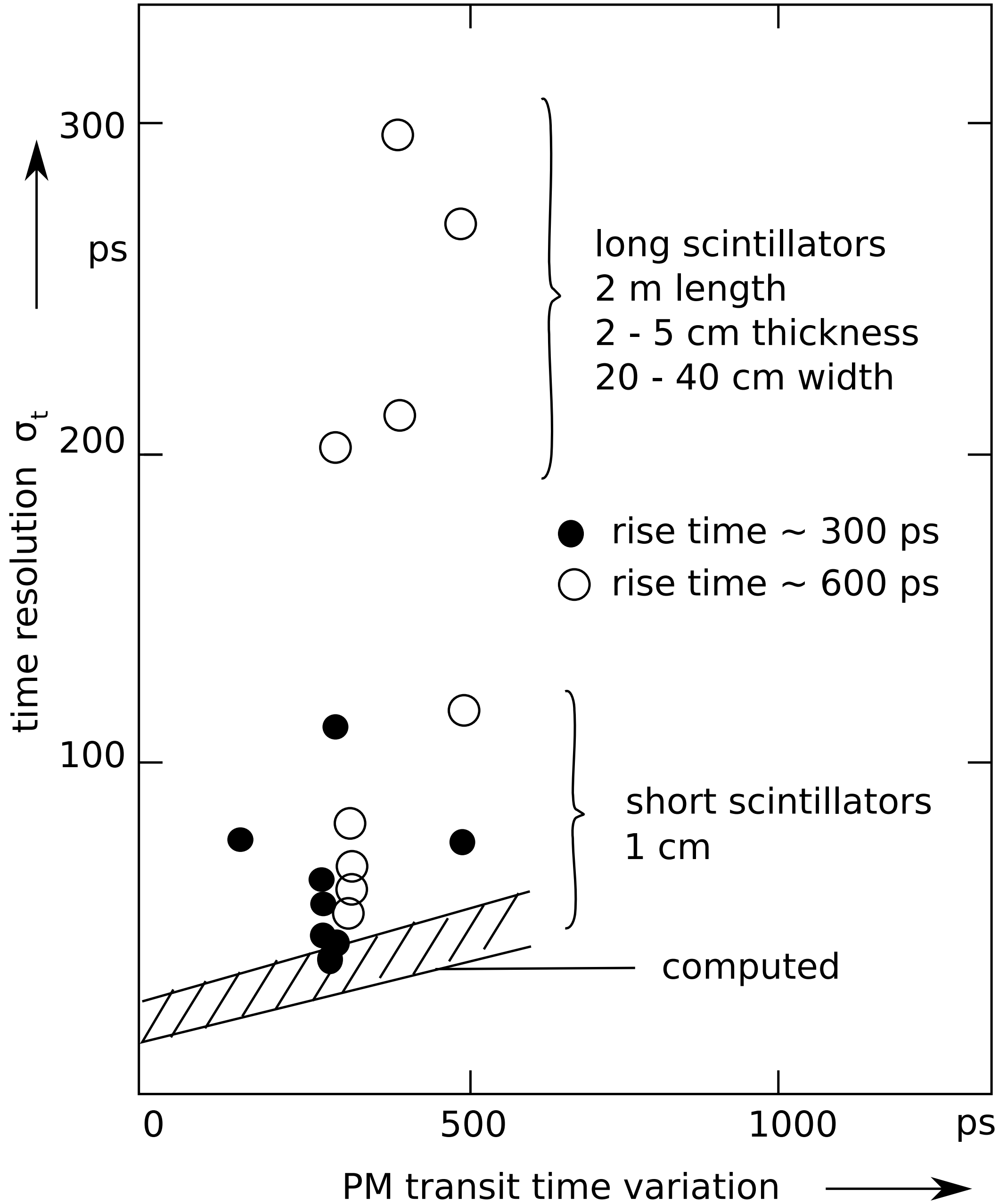

different light paths in scintillator:

affect both time resolution and pulse height
typical attenuation length about 1 m
attenuation mostly at short wavelengths

⇒ use of yellow filter reduces dependency

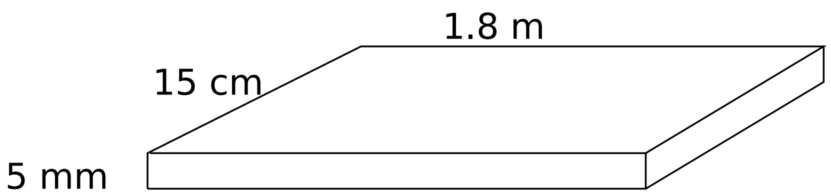

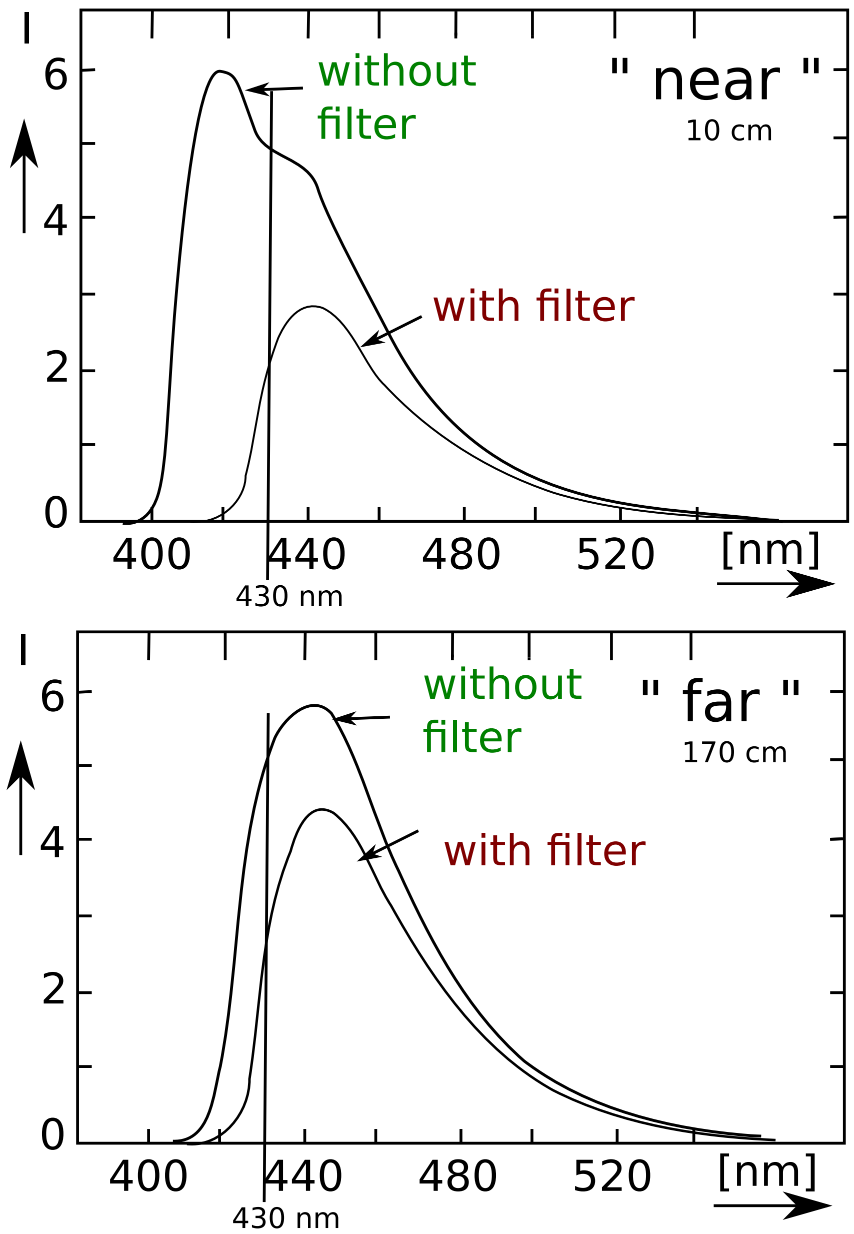

amplitude distribution with and without yellow filter in front of cathode

also: read-out of long scintillator at both ends reduces both timing variations and spatial dependence of pulse height

Photomultipliers in magnetic field

B-field disturbs focusing of photoelectrons and secondary electrons
typical kinetic energies $T \leq 200$ eV
in region of dynodes: $B \leq 10^{-4}$ T needed
typical magnitude of effect: $B = 0 \rightarrow 0.15 \cdot 10^{-4}$ T means $I_A \rightarrow \frac{1}{2} I_A$

solution: small fields can be shielded by so-called μ-metal

use of mesh-type dynodes ($\vec{E}$ and $\vec{B}$ parallel)

use of channel plate, photodiodes, silicon-PM, or hybrid photon-detectors (see journal club for the latter two)

5.2.2 Photodiodes

normal photodiode: PIN type gain $= 1$,
i.e. each photoelectron contributes 1 e to final signal (see chapter 4)

avalanche photodiode (APD): typical gain $= 30 - 50$ (CMS EMCal)
amplification of photocurrent through avalanche multiplication of carriers in the junction region (high reverse bias voltage, 100-200 V)

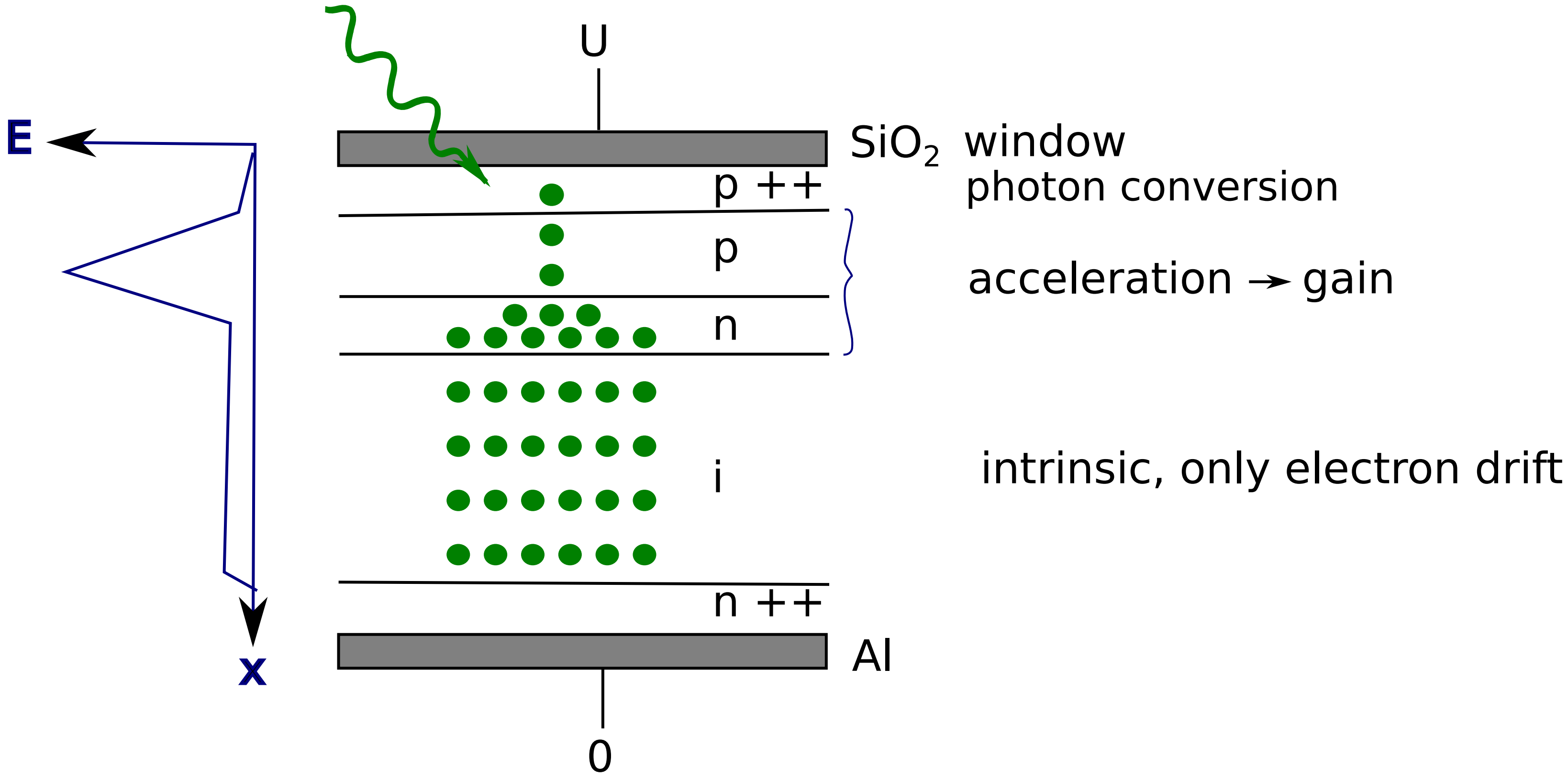

5.3 Propagation of light

- in scintillator itself:
    - absorption $N_\gamma = N_0 \exp(-x/L)$
      with L: absorption length
    - reflection at the edge, total reflection for
      $$\theta > \theta_{tot} = \arcsin(n_0/n_s)$$

  in typical scintillator $n \cong 1.4$, $\theta_{tot} \cong 45^\circ$

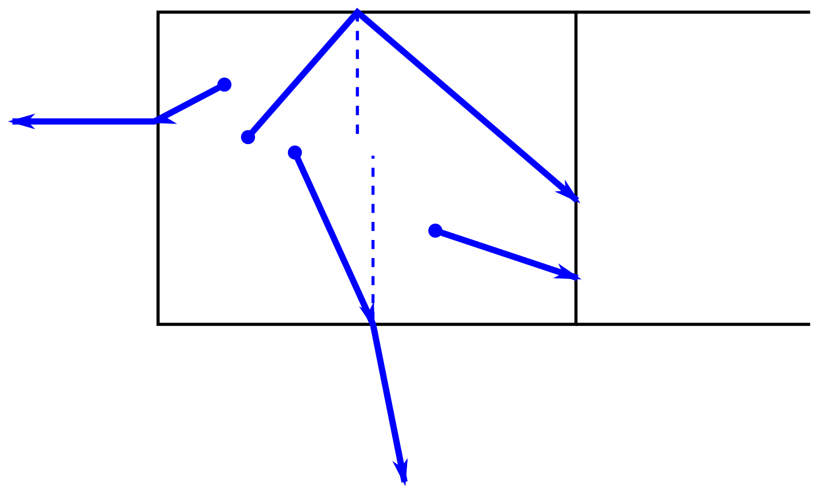

- light guide
    - the light exiting the scintillator on one end (rectangular cross section) needs to be guided to PMT (normally round cross section) $\Rightarrow$ 'fish tail' shape

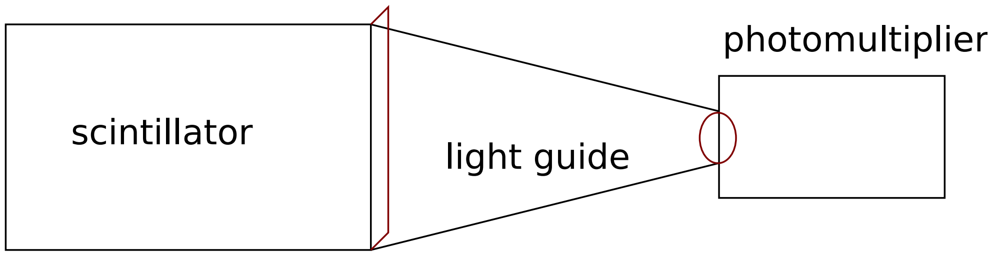

Light guide

Liouville theorem is valid also for guiding light:

$$\Delta x \cdot \Delta\theta_x = \text{const.}$$

i.e. product of width and divergence is constant

for guiding light $\Delta\theta = \text{const}$,
Δx must not decrease, otherwise loss of light,
so keep area constant

curvature should only be weak to maintain
total reflection for photons captured once
(adiabatic light guide)

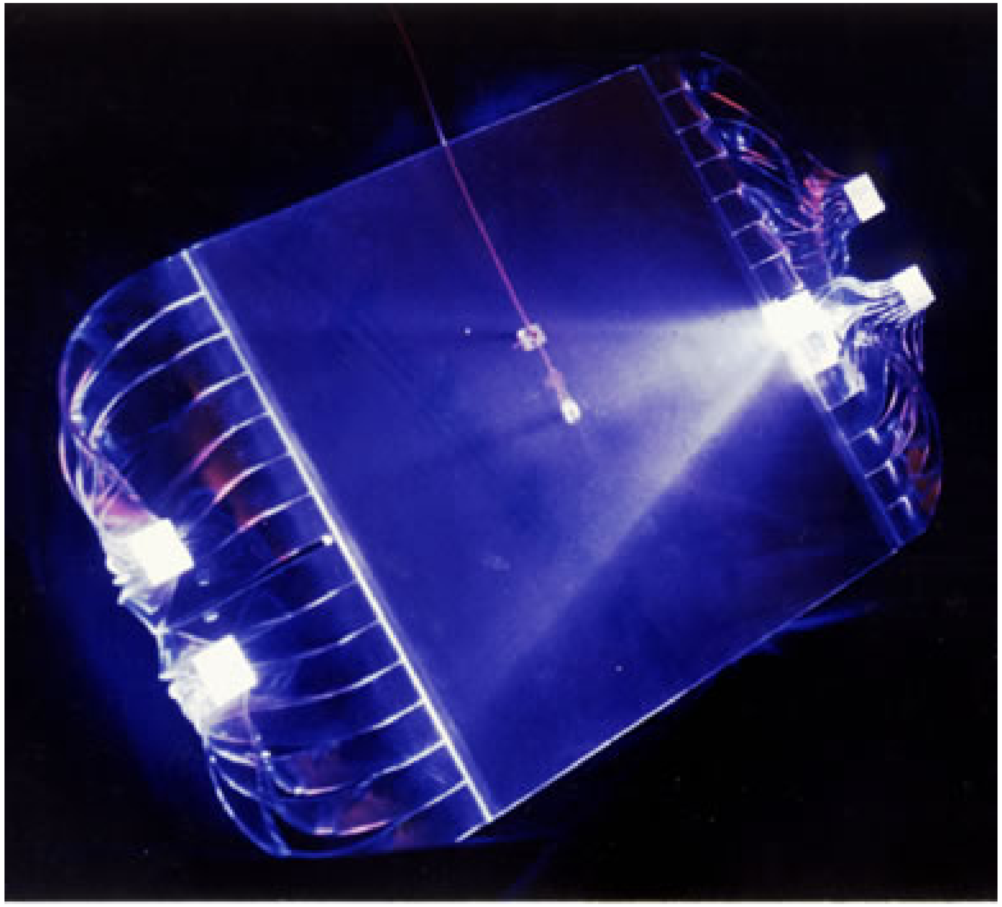

Wavelength shifter

when enough light: can use 2^{nd} wavelength shifter, e.g. along edge of scintillator plate, wavelength shifter rod absorbs light leaving scintillator and reemits isotropically at (typically) green wavelength, small part ($5 - 10\%$) is guided to PMT
advantage: can achieve very long attenuation length this way, correction small

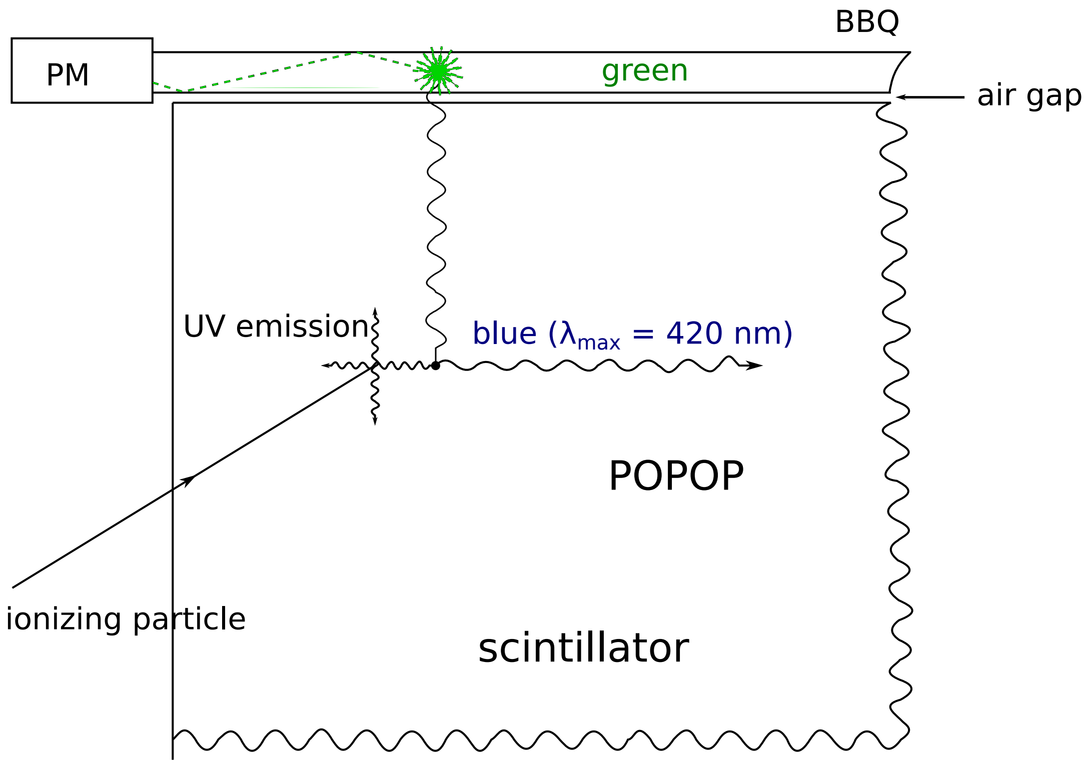

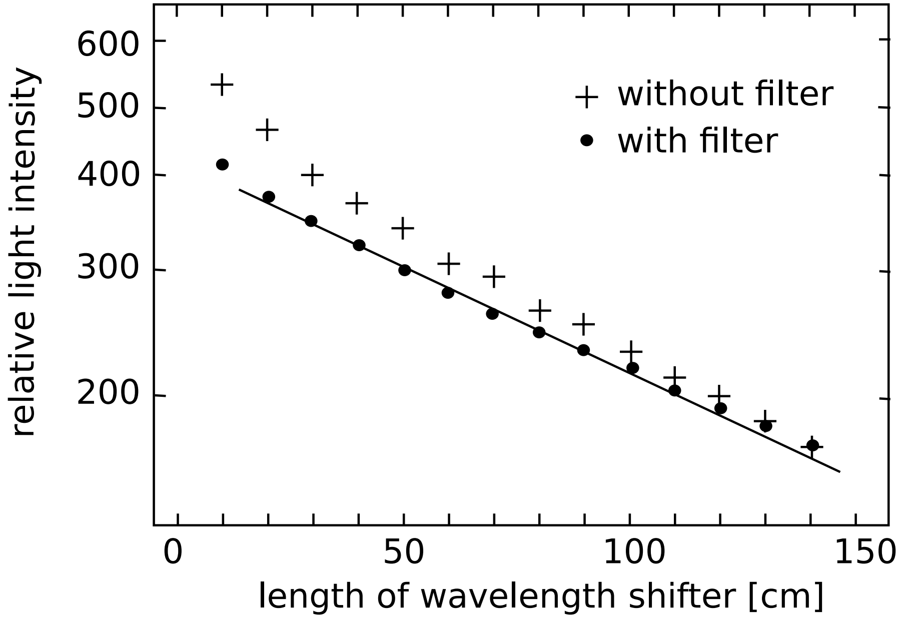

light absorption in 3 mm thick BBQ wavelength shifter rod:
better uniformity of light collection by giving up shorter wavelength component (yellow filter)

5.4 Applications of scintillation detectors

- time-of-flight measurement, 2 scintillation counters (read-out on both ends) at large enough distance
- precise photon energy: crystal calorimeter
- sampling calorimeter for photons and hadrons: alternating layers of absorber (Fe, U, ...) and scintillator with wavelength shifter rods and PMTs
- scintillating fibre hodoscope: layers of fibres, diameter order 1 mm or less, precision tracking, fast vertexing

Sampling calorimeter (see Chapters 8/9)

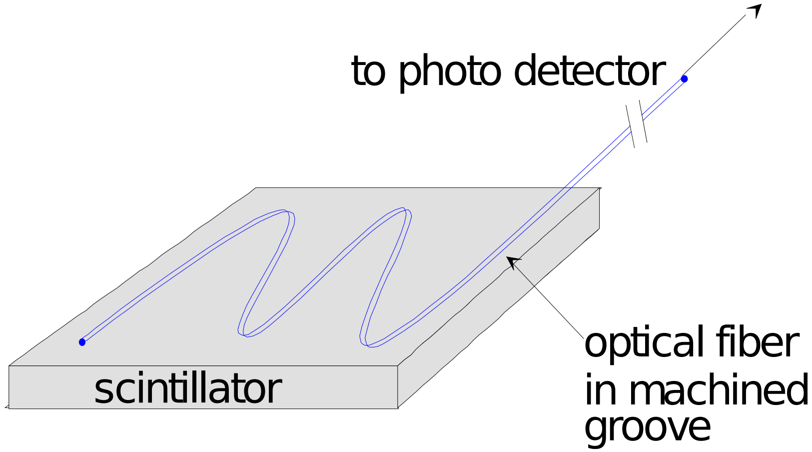

- typically enough light available and uniformity of response and linearity more important
- light emerging from end of scintillator sheet absorbed by external wavelength shifter rod and reemitted isotropically
- air gap essential for total internal reflection
- only a few % of energy loss in light

wavelength shifter rods can be replaced by wavelength shifting scintillating fibers embedded into scintillator sheet or directly into absorber

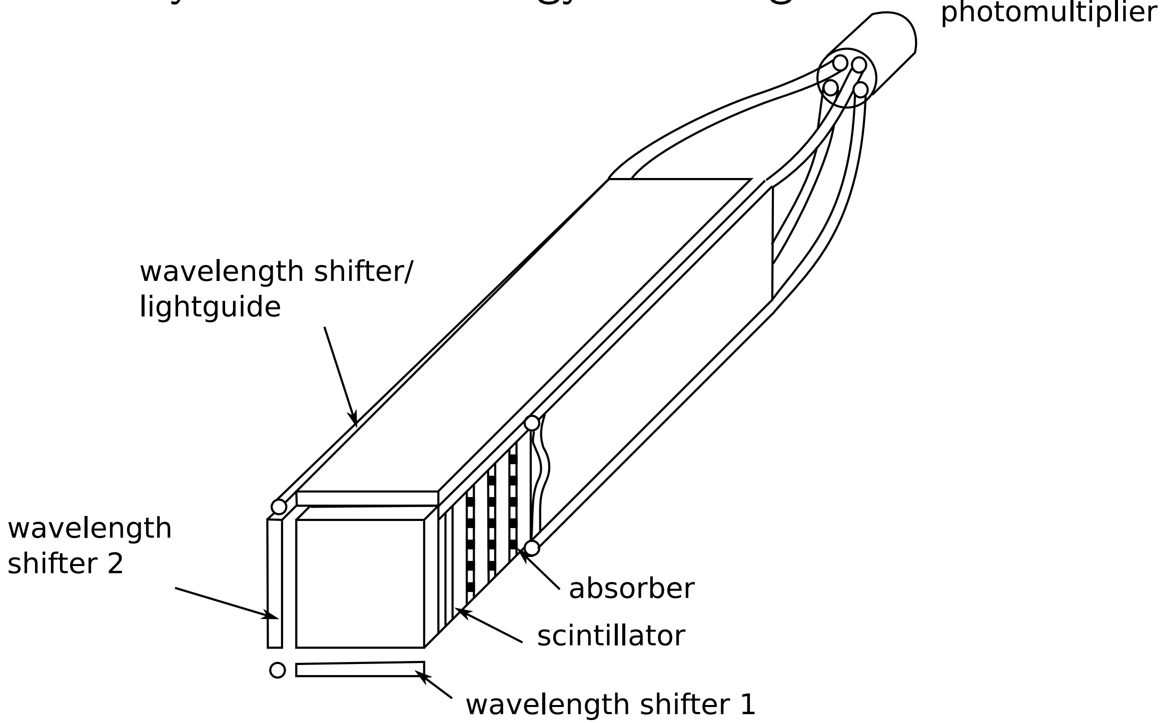

Scintillating fibre hodoscopes

follow track of a charged particle in fine steps but not in gas detector

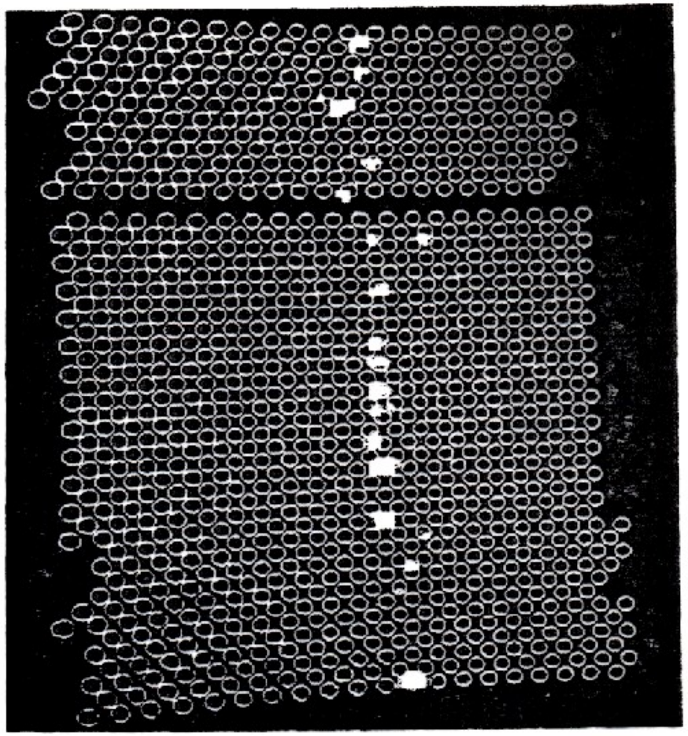

track in scintillating fibre array,
fibre diameter 1 mm

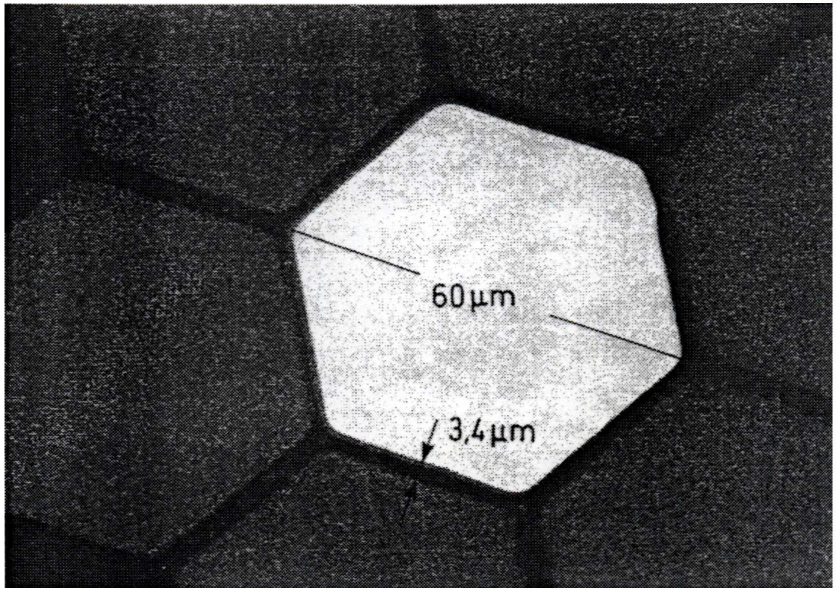

60 μm fibre in a fibre bundle covered with cladding of lower *n*, single track resolution few tens of μm

Example: Scintillation fibre hodoscope COMPASS at CERN SPS

cover beam area of a $100 - 200$ GeV muon beam, 10^8 Hz or 10^6 Hz per fiber channel

J. Bisplinghoff et al., NIM A490 (2002) 101

to provide enough photoelectrons 4 layers of fibres of 1 mm diameter
fibres in each column joined to same PMT pixel of a multianode PMT
$\rightarrow$ 30 photoelectrons per muon

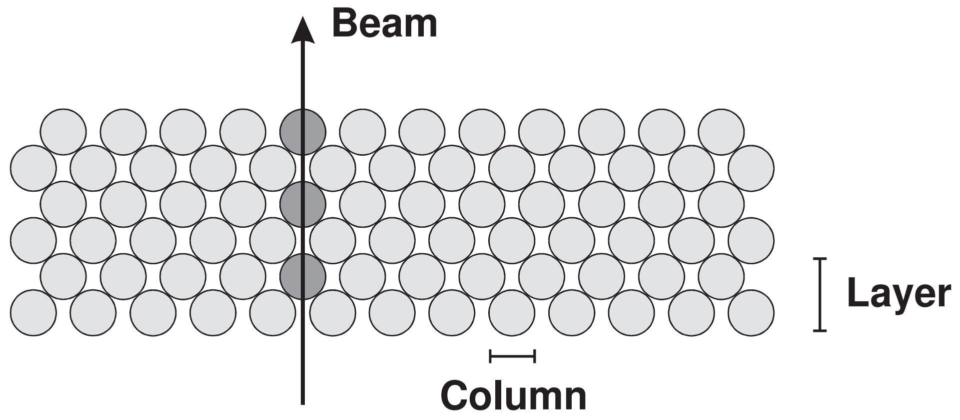

fibre configuration for scintillating fibre hodoscope with 3 layers of fibers

SCSF-78MJ scintillating fibers, 1.5 m attenuation length, active area about 10×10 cm^2, then light guides of clear fibers 1.5 m long (attenuation length 4 m) to PMT

high radiation tolerance (important for beam hodoscope): 100 kGy (10 Mrad) lead to only 15% reduction of signal.

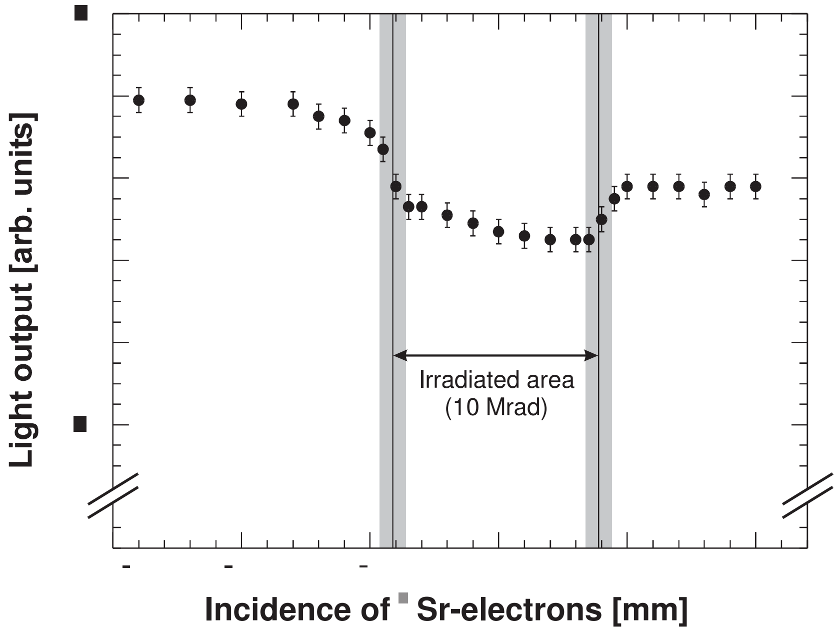

light output of Kuraray SCSF-78MJ scintillating fibers after local irradiation ($\approx$ 100 kGy), as indicated by shaded vertical bars

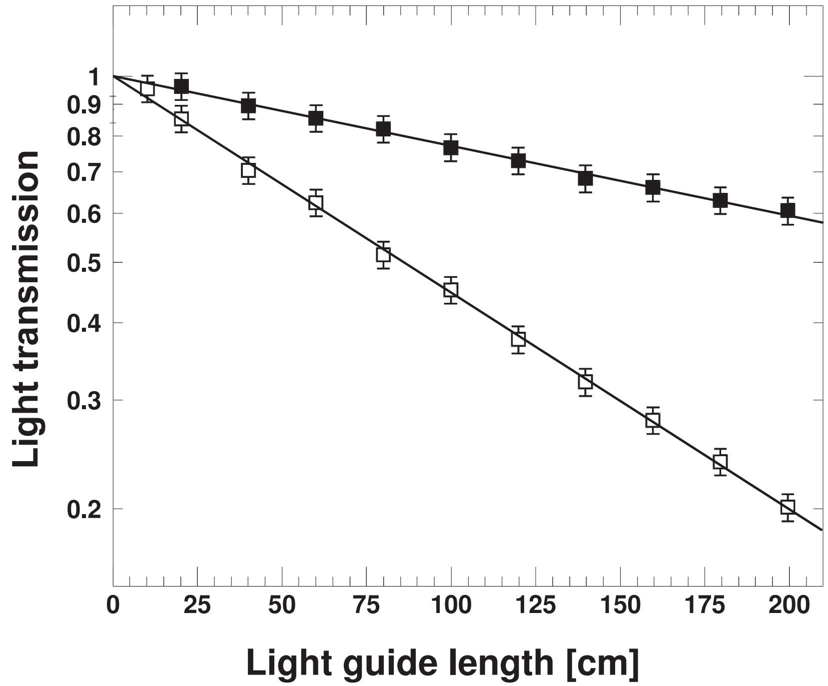

light attenuation of light guides (clear fibers PSMJ, Kuraray Corp.), as measured before (solid squares) and after (open squares) about 10 kGy of irradiation (more than 10 times what is expected for beam halo), homogeneously applied across the entirely of their length.

attentuation length of lightguide drops from 4 m to 1.2 m

'price' for light-saving use of clear fibers:
an additional joint → glue

glue not radiation hard (yellows)
→ needed to learn to 'fuse' fibers

Hamamatsu 16-anode PMT was a breakthrough in gain uniformity and cross talk

H6568 MA-PMT: equipped with a common photocathode followed by 16 metal channel dynodes each with 12 stages of mesh type and a multi-anode read-out. They are arranged as a 4 × 4 block (individual effective photocathode pads with an area of 4 mm × 4 mm each and a pitch distance of 4.5 mm (see figure).

figure: layout and dimensions of the multi-channel photomultiplier tube H6568. The upper part shows the front view of the cathode grid.

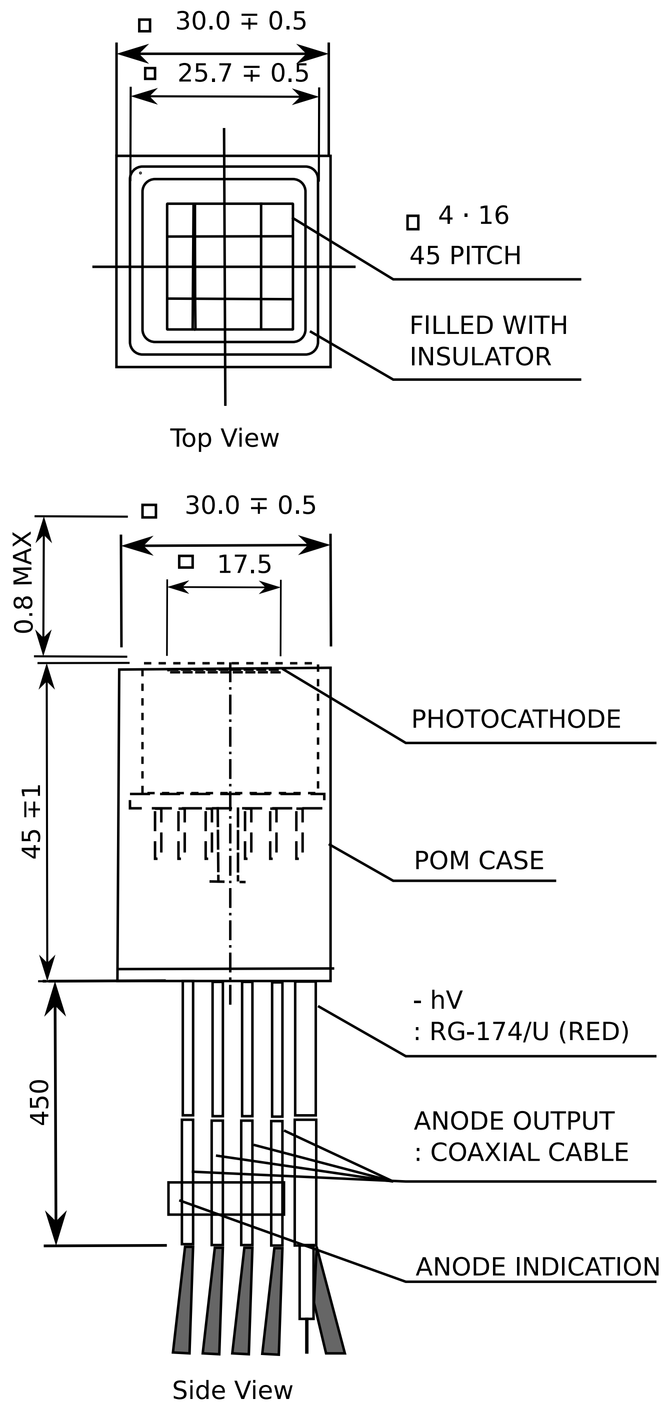

noise only 1/5 of single photoelectron response (SER)

low cross talk (less than 5 %)

good gain uniformity (about 20 %)

voltage divider for dynodes needs to be specifically designed to be stable at rates up to 100 MHz

'active base' (use of transistors instead of resistors for last stages) instead of simple voltage divider, otherwise drop of signal with rate due to large currents through last dynodes leading to drop of interstage voltage

achieved time resolution 330 ps

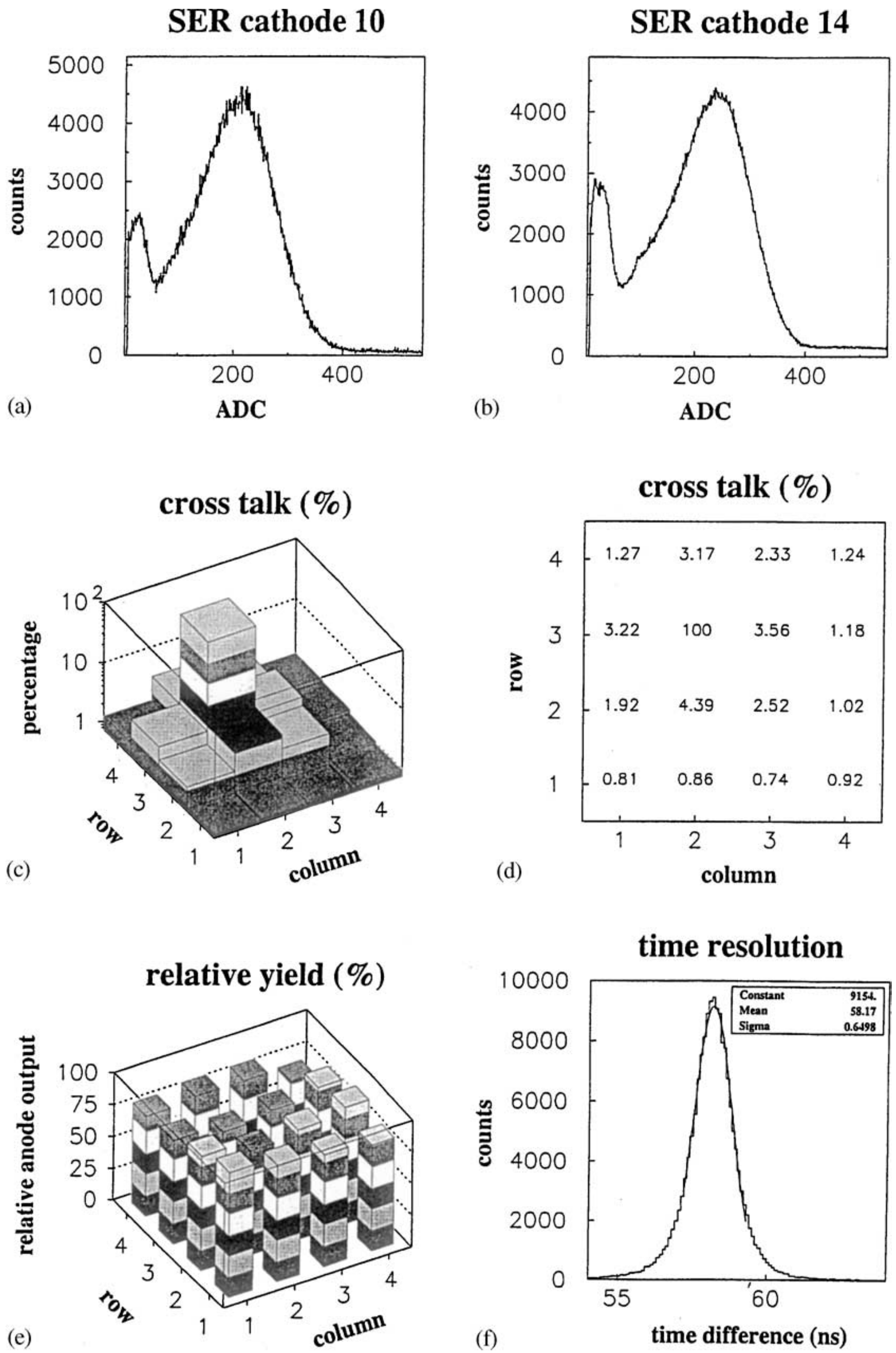

6. Momentum Measurements

Deflection of track of charged particle in magnetic spectrometer
Lorentz force $\rightarrow$ circular orbit of curvature radius ρ in homogeneous magnetic field

$$\frac{mv^2}{\rho} = q\vec{v} \times \vec{B} = qv_\perp \cdot |\vec{B}|$$

$v_\perp$: component of $\vec{v} \perp$ to $\vec{B}$

$$\rho = \frac{p^2}{qp_\perp B}$$

$p_\perp$: analogue

and for $\vec{p} \perp B$

$$\rho = \frac{p}{qB}$$

units: for ρ in m
p in GeV/c
B in T
q in units of e

$$\boxed{\rho = \frac{p}{0.3\, qB} \qquad \text{or} \qquad p = 0.3\, q\rho B}$$

6.1 Forward Spectrometer

Mainly in fixed target experiments, but also LHCb or ALICE forward muon spectrometer

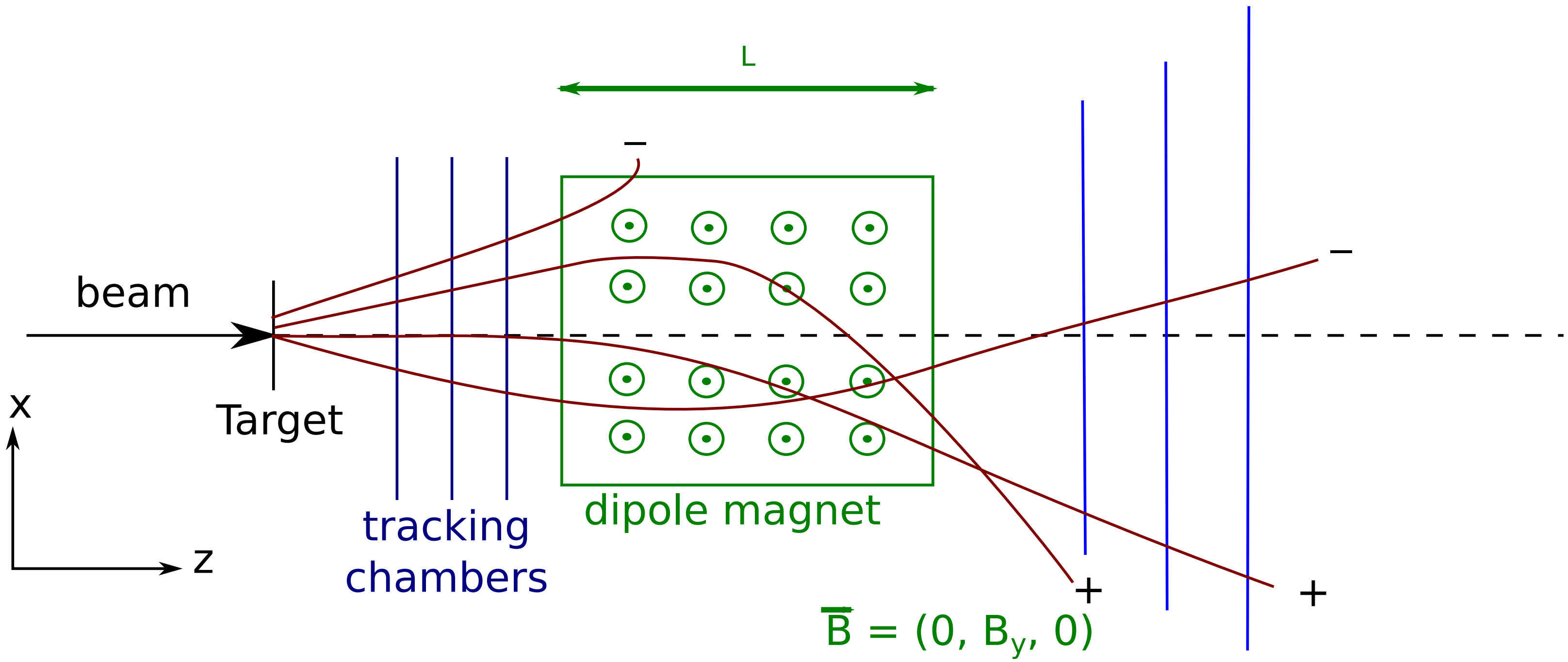

magnetic field gives (additional) $p_\perp$-kick $\Delta p_\perp$
typically $p \gg p_\perp$, $\Delta p_\perp \rightarrow$ Lorentz force always approximately in x-direction and

$$\Delta p_x = 0.3\, L\, q\, B$$

or for magnetic field not constant over entire path

$$\Delta p_x = 0.3\, q \int_L B \mathrm{d}L$$

ALICE (Di)-Muon Spectrometer

$\theta = 171^\circ - 178^\circ \quad -4.0 \leq \eta \leq -2.5$

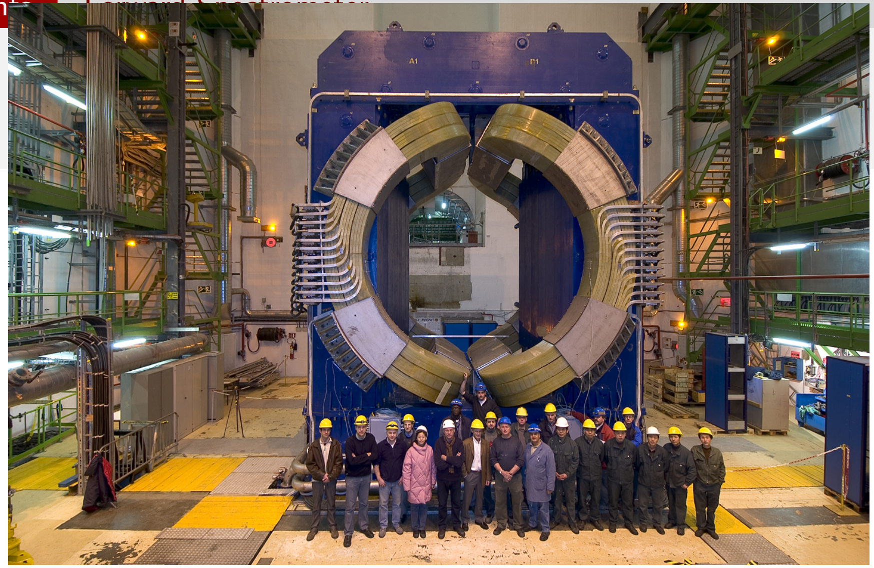

Dipole magnet

Muon chambers

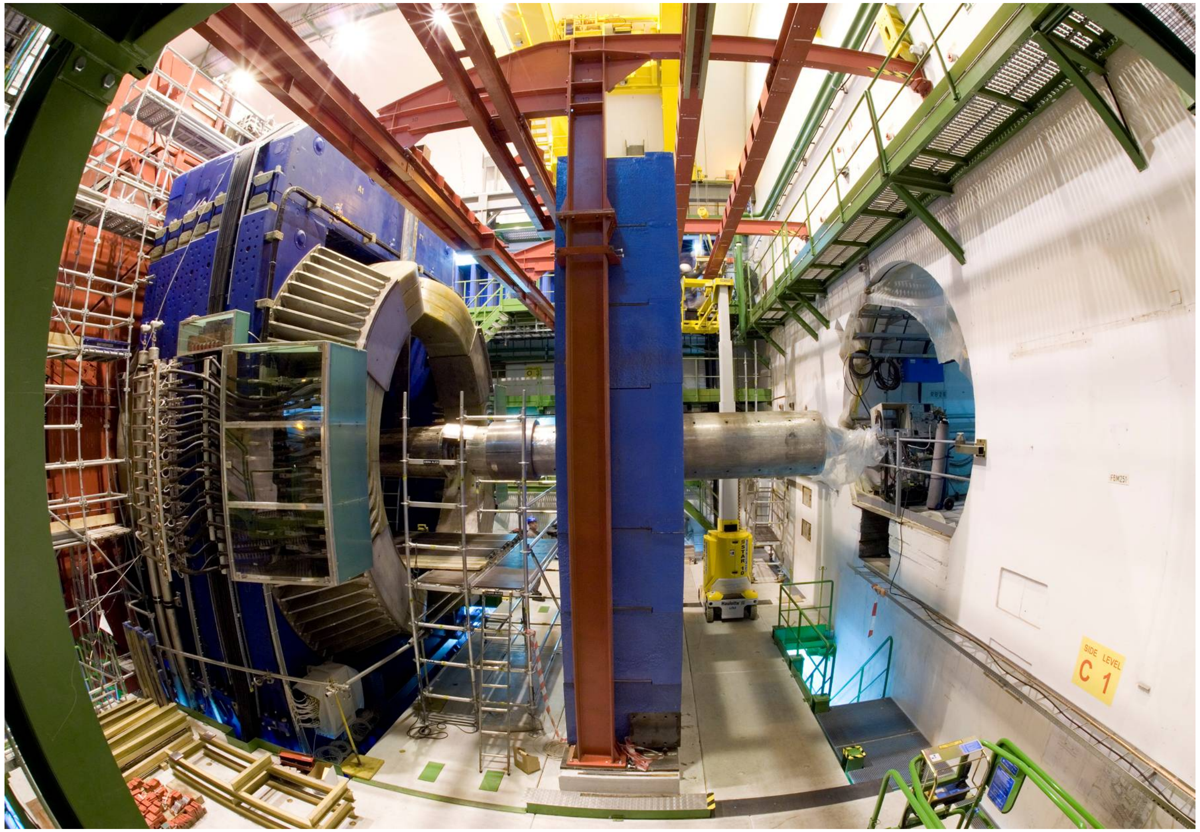

Muon absorber and filter

Example: proton of

$$\begin{aligned} p &= 10 \text{ GeV/c} \simeq p_z \\ \int BdL &= 6 \text{ Tm} \\ \Delta p_x &= 1.8 \text{ GeV/c} \\ \Delta\theta_x &= 10^\circ \end{aligned}$$

about the limit for small angle approximation

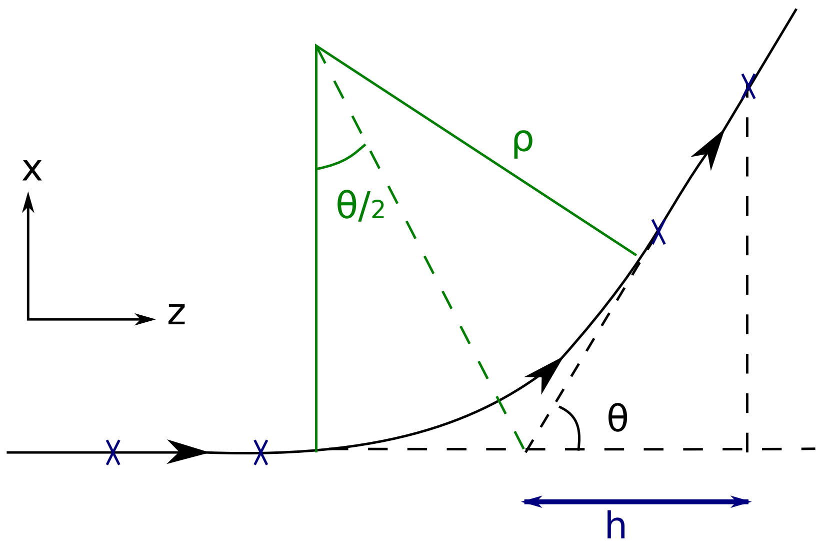

for $\rho \gg L$

$$\theta \approx \frac{L}{\rho} = \frac{LqB_y}{p}$$

$$\Delta p_x = p \sin\theta \approx p\theta = LqB_y$$

or $$\approx q \int_0^L B_y \mathrm{d}L$$

Momentum resolution

$$p = q\rho B_y = q\frac{L}{\theta}B_y$$
$$\frac{dp}{d\theta} = qLB_y\frac{1}{\theta^2} = \frac{p}{\theta}$$

$$\Rightarrow \quad \frac{dp}{p} = \frac{d\theta}{\theta} \qquad \frac{\sigma_p}{p} = \frac{\sigma_\theta}{\theta}$$

accuracy of angular measurement $\equiv$
accuracy of momentum measurement

minimum tracking: two measured points before and two after deflection

in practice always 3 or more measurements, since detectors need to be aligned relative to each other (best done with straight tracks)

in case all measured points have identical resolution σ_x:

$n/2$ points before
$n/2$ points after deflection
lever arm h (see Fig. previous page)

$$\Rightarrow \quad \sigma_\theta = \sqrt{\frac{8}{n}}\frac{\sigma_x}{h}$$

$$\boxed{\frac{\sigma_p}{p} = \frac{\sqrt{8/n}\,\sigma_x}{h}\frac{p}{qLB_y} = \frac{\sqrt{8/n}\,\sigma_x}{h}\frac{p}{\Delta p_x}}$$

contribution of space point resolution
to momentum resolution

typical form $\quad \frac{\sigma_p}{p} = \text{const}\cdot p \quad$ with const $= 10^{-3}\ldots 10^{-5}$ i.e. 0.1% - 0.001%

Example: 6 measurements each with $\sigma_x = 200\ \mu$m, $h = 5$ m, deflection 1° for p $= 10$ GeV/c

$$\theta_x = \frac{\Delta p_x}{p} = 0.017$$
$$\Rightarrow \frac{\sigma_p}{p} = 3\cdot 10^{-3} = 3\cdot 10^{-4}\,p$$

Effect of multiple scattering

(see Chapter 2)
multiple Coulomb scattering along particle trajectory of length L contributes to $p_\perp$-broadening perpendicular to direction of propagation

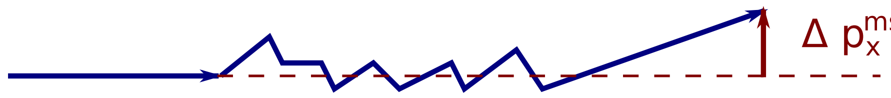

$$\Delta p_\perp^{ms} = p \sin\theta_{rms} \simeq p\theta_{rms} = \frac{q \cdot 19.2 \text{ MeV/c}}{\beta}\sqrt{\frac{L}{X_0}}$$

where X_0 is the radiation length. In the direction of deflection (x) this means:

$$\Delta p_x^{ms} = \frac{q \cdot 19.2 \text{ MeV/c}}{\beta\sqrt{2}}\sqrt{\frac{L}{X_0}} = \frac{q \cdot 13.6 \text{ MeV/c}}{\beta}\sqrt{\frac{L}{X_0}}$$

for sufficiently large momenta independent of p

contribution to momentum resolution:

$$\boxed{\left(\frac{\sigma_p}{p}\right)_{ms} = \frac{\Delta p_x^{ms}}{\Delta p_x} = \frac{13.6 \text{ MeV/c}\sqrt{L/X_0}}{e\int B_y \mathrm{d}L}}$$

where Δp_x is the deflection due to magnetic field (see above).

total momentum resolution

Example: as 2 pages above

$$e \int BdL = \; 0.57 \text{ Tm} \qquad \Delta p_x = 0.17 \text{ GeV/c}$$

$$L = 15 \text{ m}$$

$$\text{material: air,} \quad X_0 = 304 \text{ m}$$

$$\left(\frac{\sigma_p}{p}\right)_{ms} = 1.8\%$$

$$vs. \left(\frac{\sigma_p}{p}\right)_{defl} = 0.03\% \, p \quad \Rightarrow$$

multiple scattering dominates at small momenta

$$\boxed{\left(\frac{\sigma_p}{p}\right)^2 = \left(\frac{\sigma_p}{p}\right)^2_{ms} + \left(\frac{\sigma_p}{p}\right)^2_{defl}}$$

momentum resolution in magnetic spectrometer

Example:

$$\left(\frac{\sigma_p}{p}\right)^2 = (1.8\%)^2 + (0.06\% \cdot p)^2$$

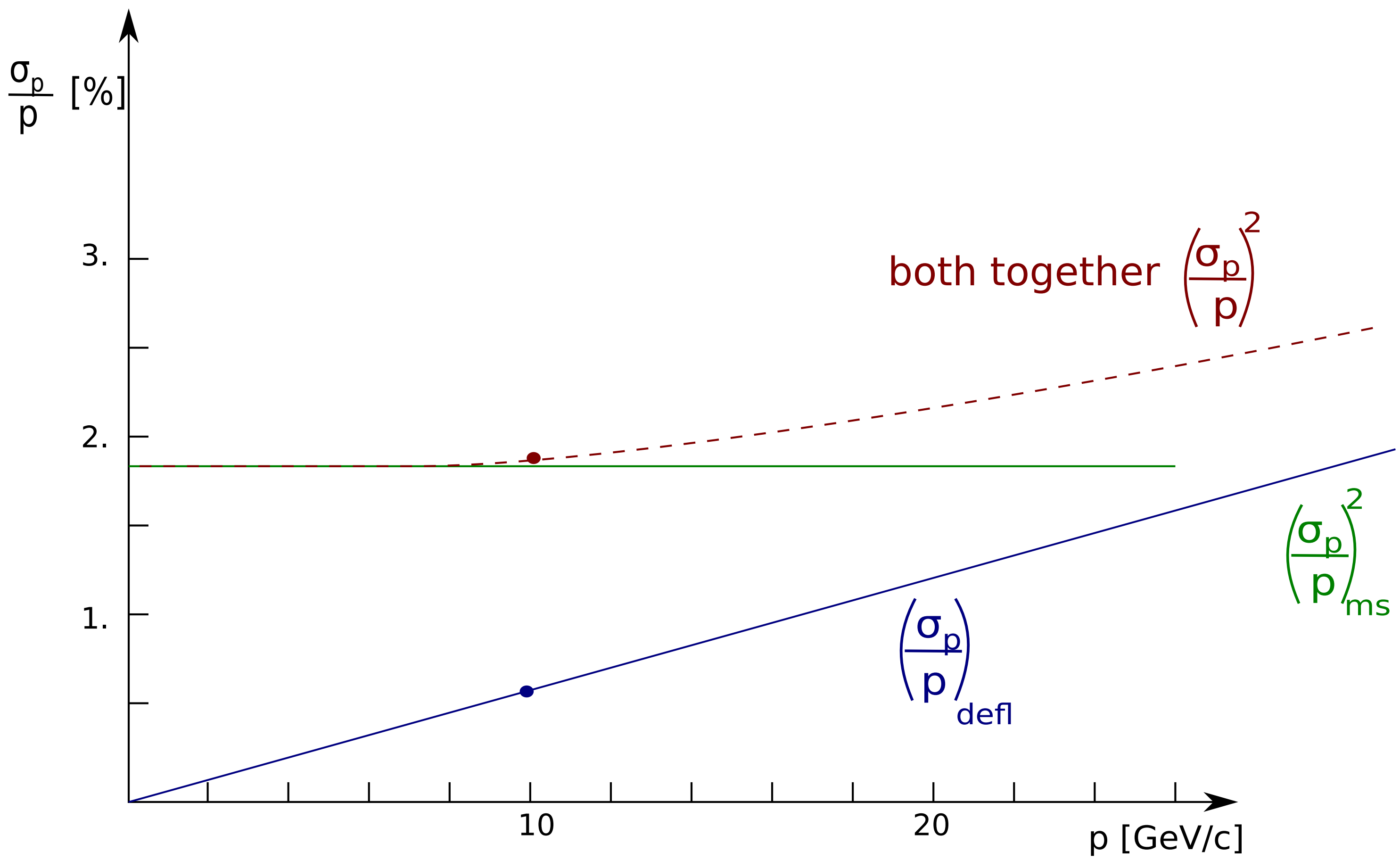

Multiple scattering particularly relevant if **magnetized iron** is used, as frequently done for measurements of muon momentum

- advantage: high B-field, stops π, K before they decay into μ
- disadvantage: worsens momentum resolution by multiple scattering

$$X_0^{Fe} = 1.76 \text{ cm}, \qquad B = 1.8 \text{ T}, \qquad L = 3 \text{ m}, \qquad \Delta p_x = 1.6 \text{ GeV/c}$$

$$\Rightarrow \qquad \left(\frac{\sigma_p}{p}\right)_{ms} = 11\%$$

depending on desired momentum range, accuracy of deflection measurement can be chosen accordingly

6.2 Solenoidal and Toroidal Fields - mostly at Colliders

Normally 4π coverage desired, leading to special spectrometer configuration

dipole disfavored

- deflects beam which must be compensated
- not nice symmetry for 4π experiment

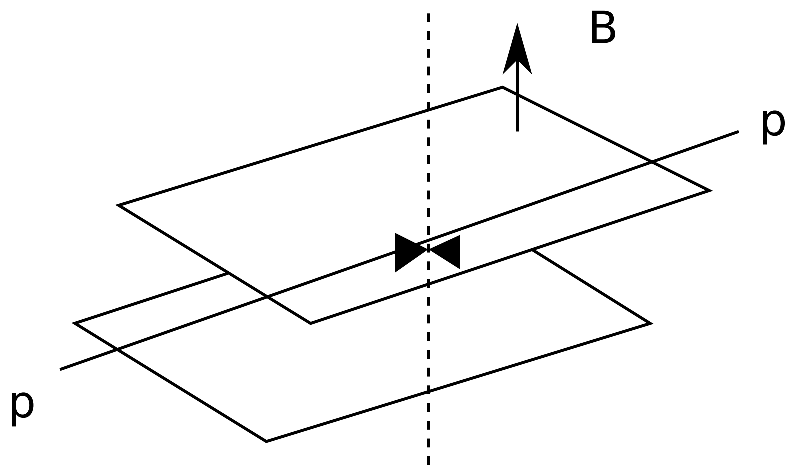

Solenoid

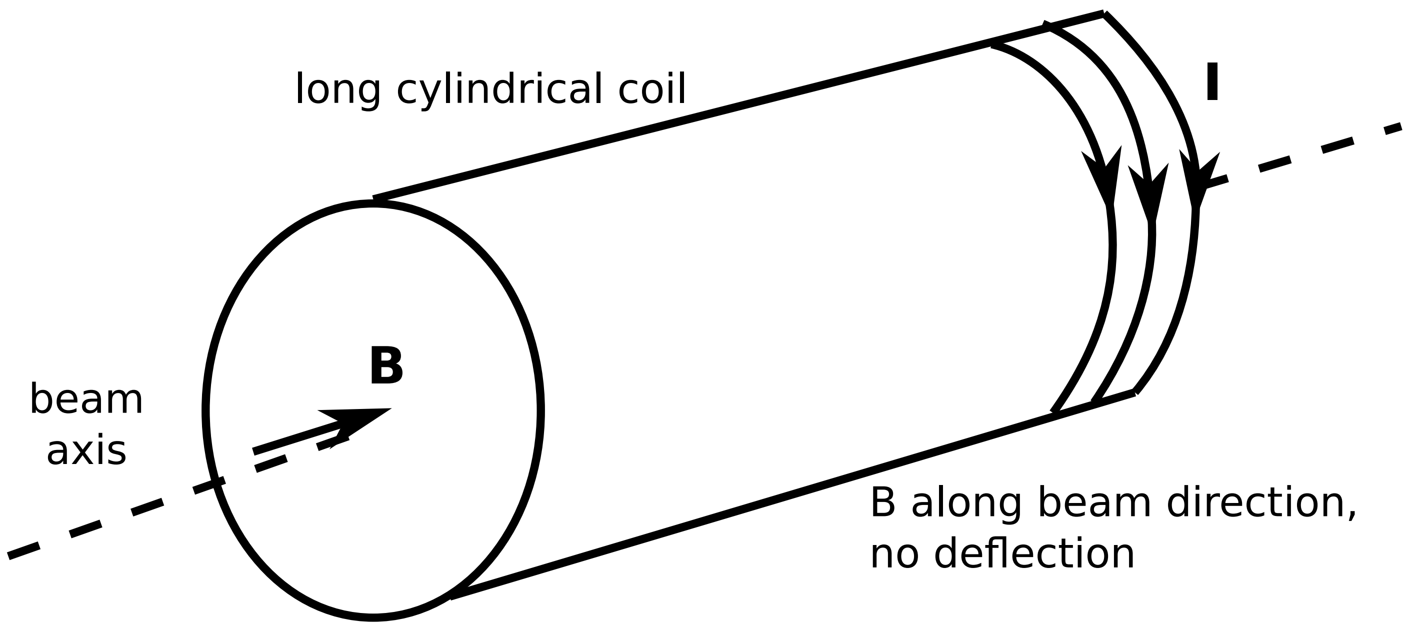

measure momentum component $p_\perp$ perpendicular to beam

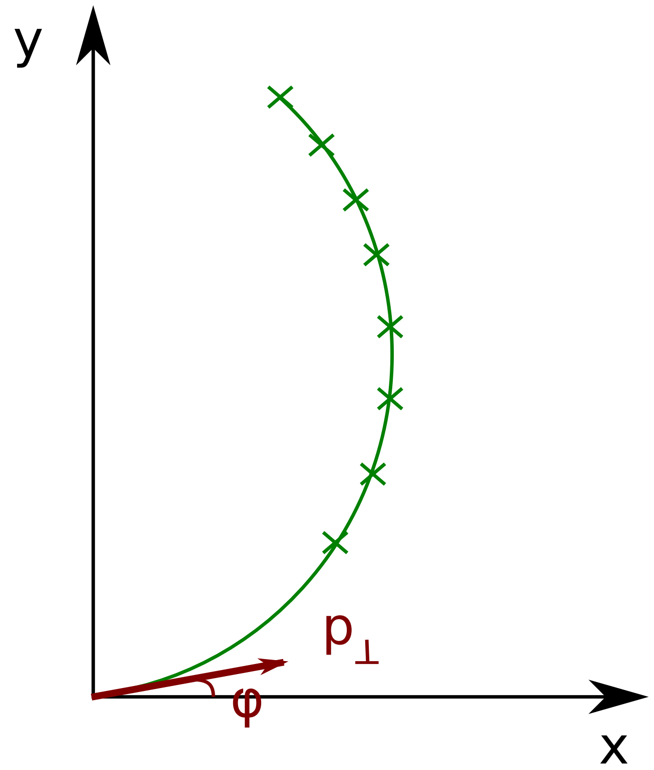

beam and B-field along z-axis

particle produced with momentum $\vec{p}$

completely characterized by p_x, p_y, p_z, where p_x and p_y can be written in terms of $(|p_\perp|, \varphi)$:

$$p_x = |p_\perp| \cos\varphi$$
$$p_y = |p_\perp| \sin\varphi$$

need to measure at least 3 points of track

circular in xy-plane

$\Rightarrow$ ρ (radius of curvature) or $p_\perp$ and φ

measurement of θ:

$$p_{||} = \frac{p_\perp}{\tan\theta}$$
$$p = \frac{p_\perp}{\sin\theta}$$

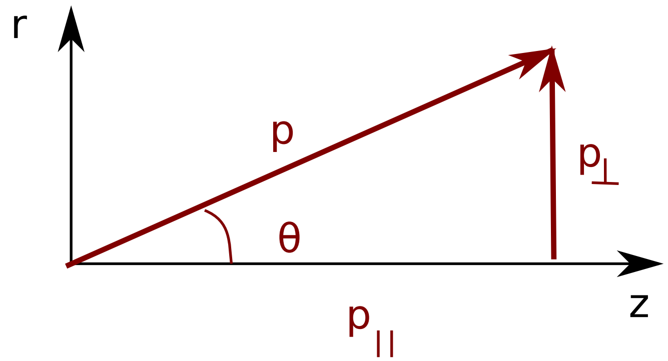

$\boxed{\text{complete measurement of particle momentum}}$

Sagitta Method

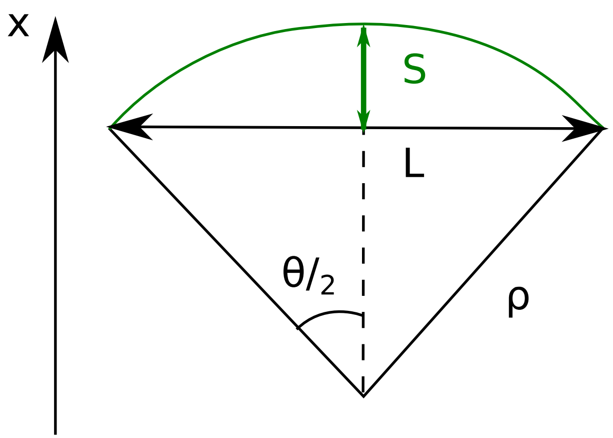

$$\text{Sagitta} \qquad S = \rho - \rho\cos\frac{\theta}{2} = \rho\left(1-\cos\frac{\theta}{2}\right)$$
$$= 2\rho\,\sin^2\frac{\theta}{4}$$
$$\text{for small } \theta \qquad S \simeq \frac{\rho\,\theta^2}{8}$$

$$\text{with } \rho = \frac{p_\perp}{qB} \quad \text{and} \quad \sin\theta/2 \simeq \theta/2 = \frac{L/2}{\rho}$$

$$\boxed{S = \frac{qL^2B}{8p_\perp}}$$

B in T, L in m, $p_\perp$ in GeV/c, q in e

$$S(\mathrm{m}) = \frac{0.3\,qL^2B}{8p_\perp}$$

Measurement of at least 3 points with coordinates $x_1,\ x_2,\ x_3$

$$S = x_2 - \frac{x_1 + x_3}{2}$$

$$\sigma_S = \sqrt{\frac{3}{2}}\sigma_x$$

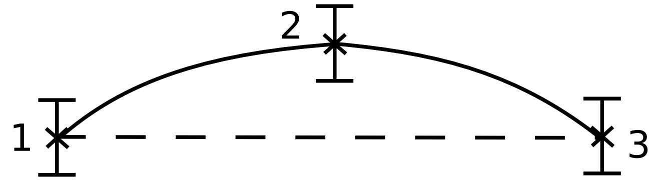

$$\boxed{\Rightarrow \frac{\sigma_p}{p} = \frac{\sigma_S}{S} = \frac{\sqrt{3/2}\,\sigma_x 8p}{qBL^2}}$$

Measurement of N equally spaced points:

$$\boxed{\frac{\sigma_p}{p} = \frac{\sigma_x}{qBL^2}\sqrt{\frac{720}{(N+4)}}p}$$

NIM 24 (1963) 381

- example: (remember factor 0.3 as soon as you put dimensioned quantities)

$$\left.\begin{array}{lcl} B & = & 0.5\ \mathrm{T} \\ L & = & 2\ \mathrm{m} \\ \sigma_x & = & 400\ \mu\mathrm{m} \\ N & = & 150 \end{array}\right\} \frac{\sigma_p}{p} \simeq 1.4 \cdot 10^{-3} p$$

similar to ALICE TPC, usage of former L3 Magnet

L3

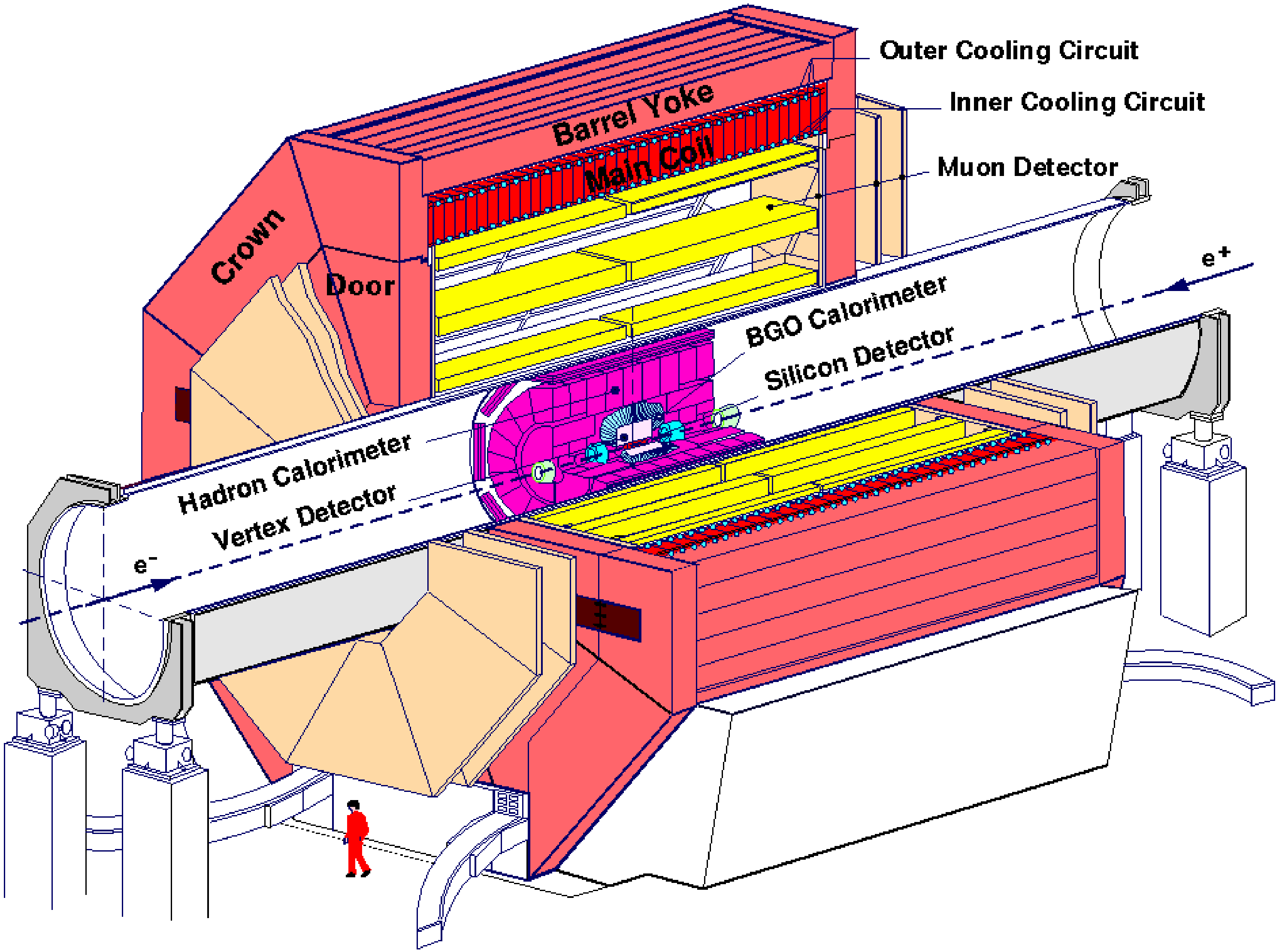

$$\sigma_S = 90\ \mu\text{m} \qquad \frac{\sigma_{p_\perp}}{p_\perp} = 2.5\% \text{ at } 45 \text{ GeV} \quad (\text{typical } Z^0 \text{ decay product})$$

Construction site ALICE 2004 - the solenoid and the iron return yoke

Largest warm magnet, about 7000 t iron
current in magnet 30 kA $\leftarrow$ average lightning
energy stored in magnetic field 150 MJ
dissipated power 4.2 MW

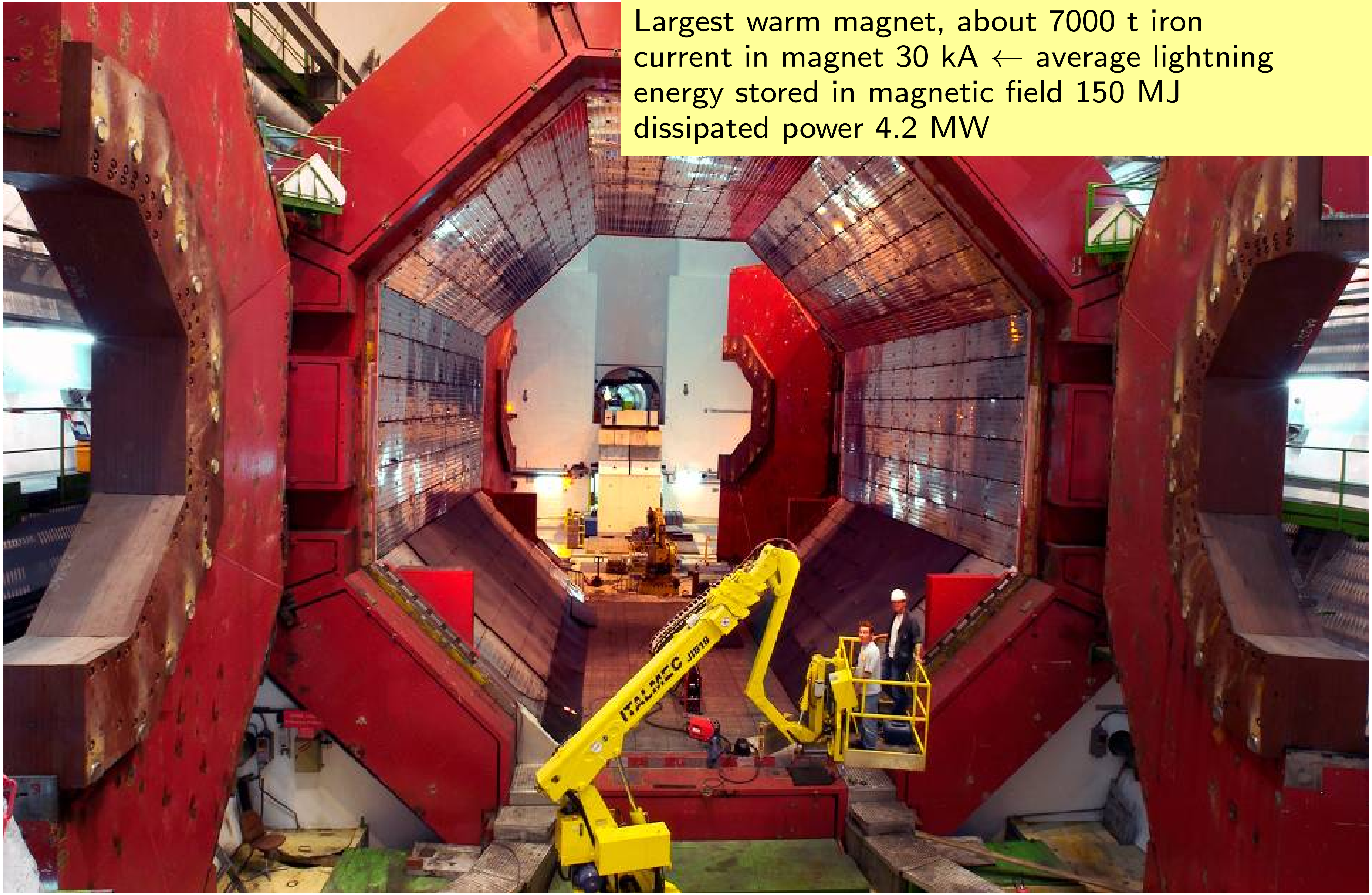

ALICE first 13 TeV pp collisions

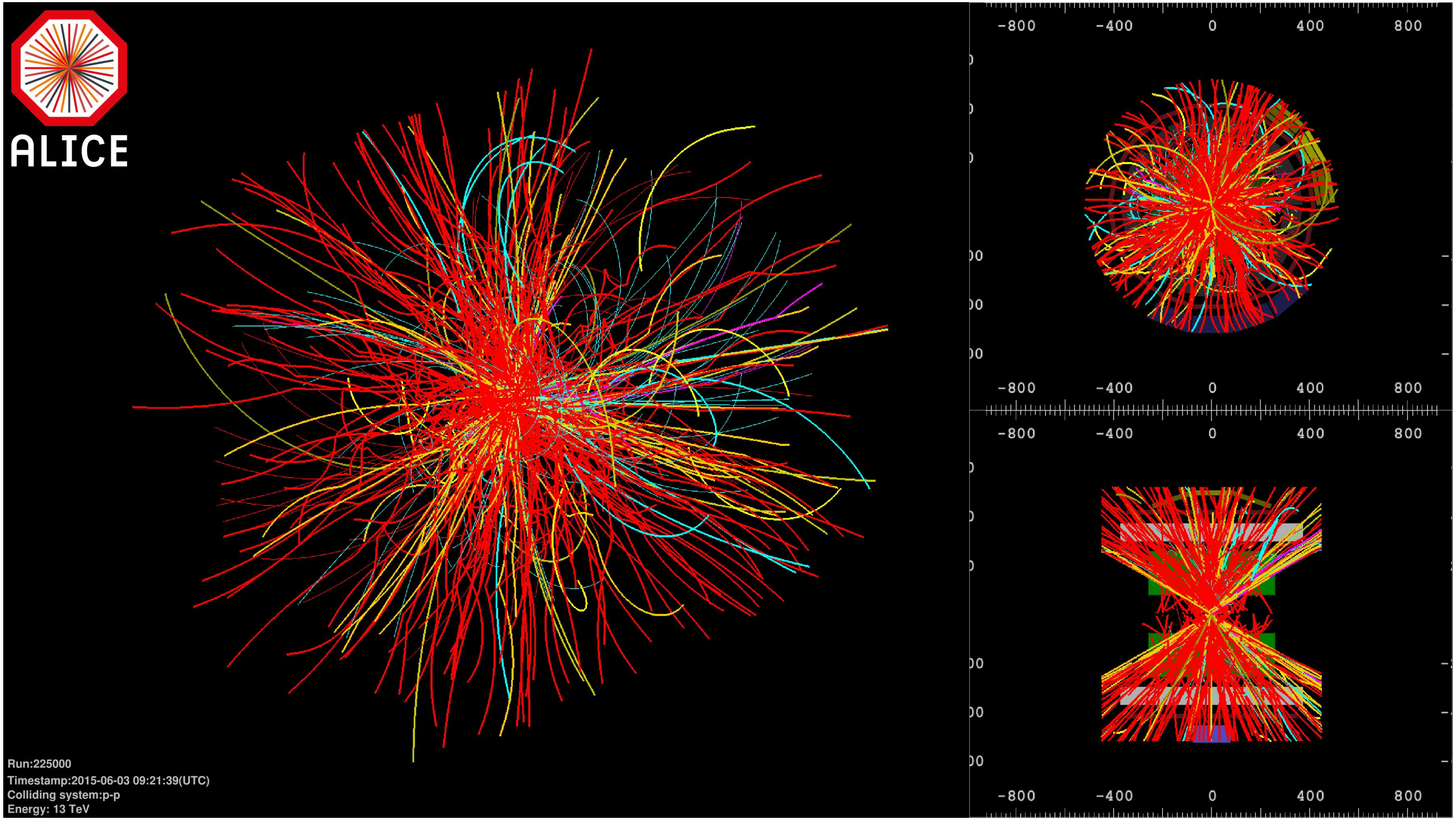

Toroid

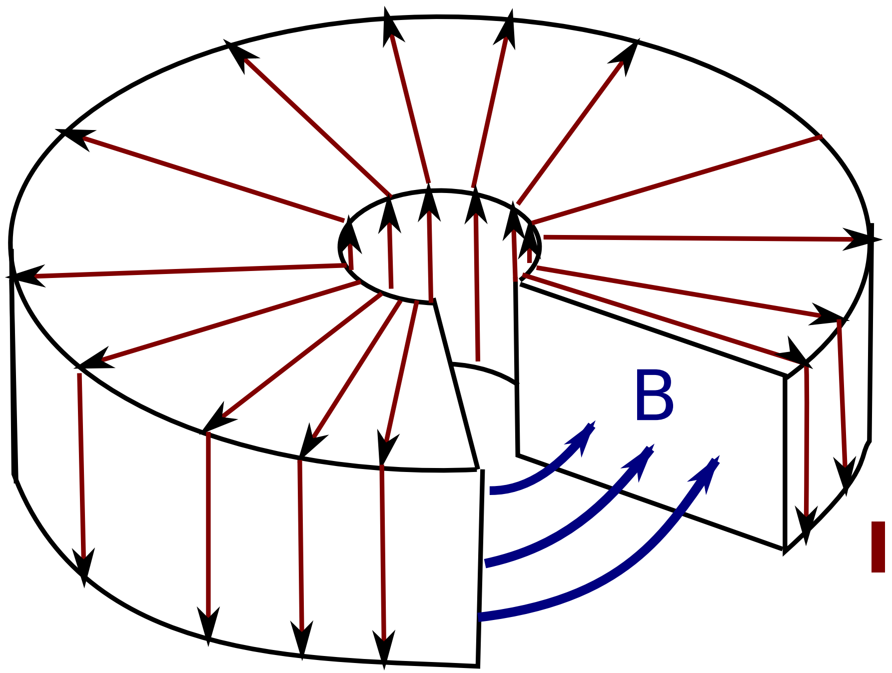

- on axis vanishing B-field
- no deflection of beam
- fill with iron-core e.g. for muon measurement in end caps

Example: H1 forward muon spectrometer

H1 experiment at HERA

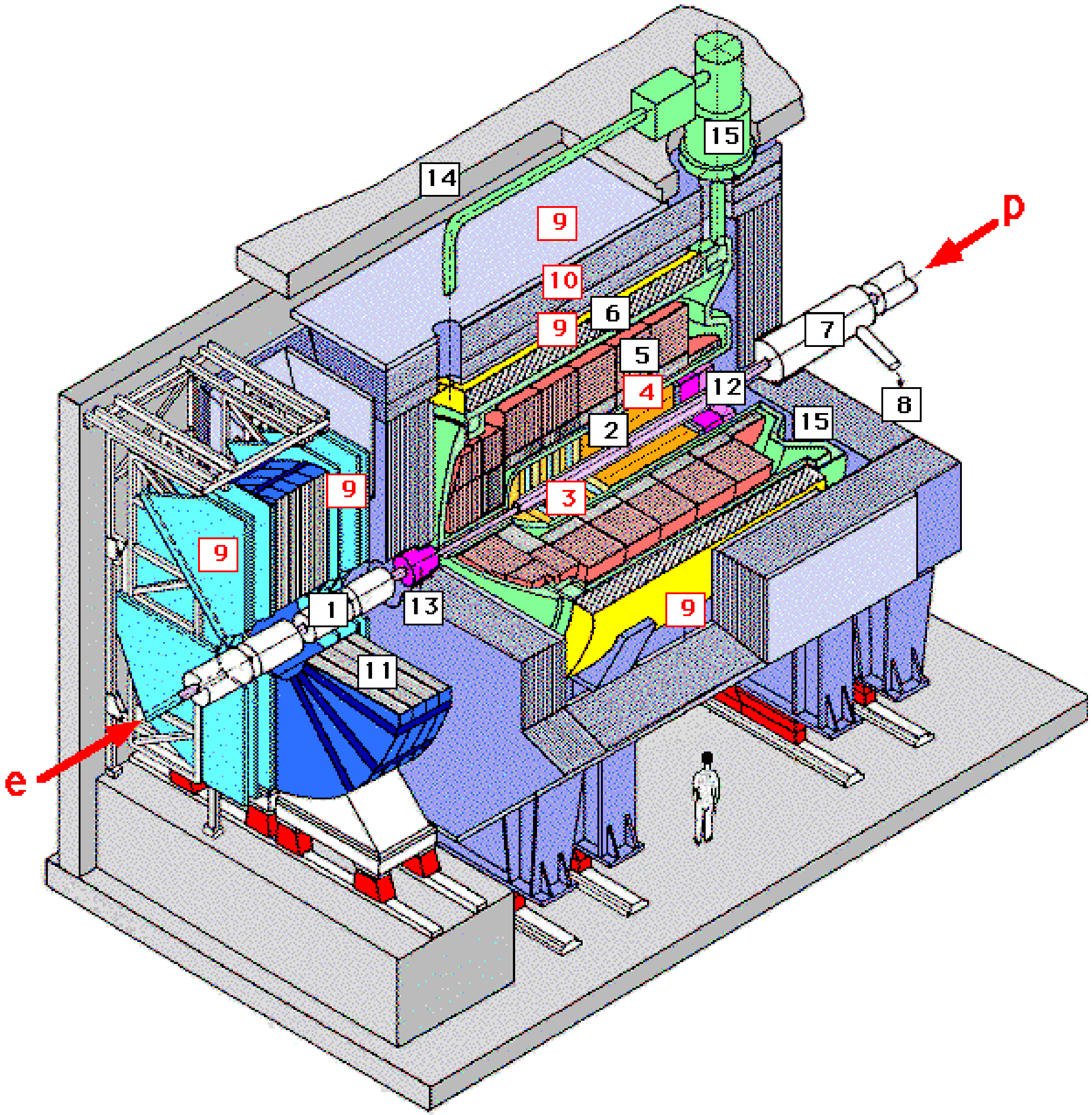

Central solenoid plus forward muon toroid to measure high energy muons between 3° and 17°

drift chamber planes before and after toroid

Toroidal magnet: 12 segments with 15 turns each (Cu), 150 A
$\rightarrow B = 1.6$ T filled with Fe core

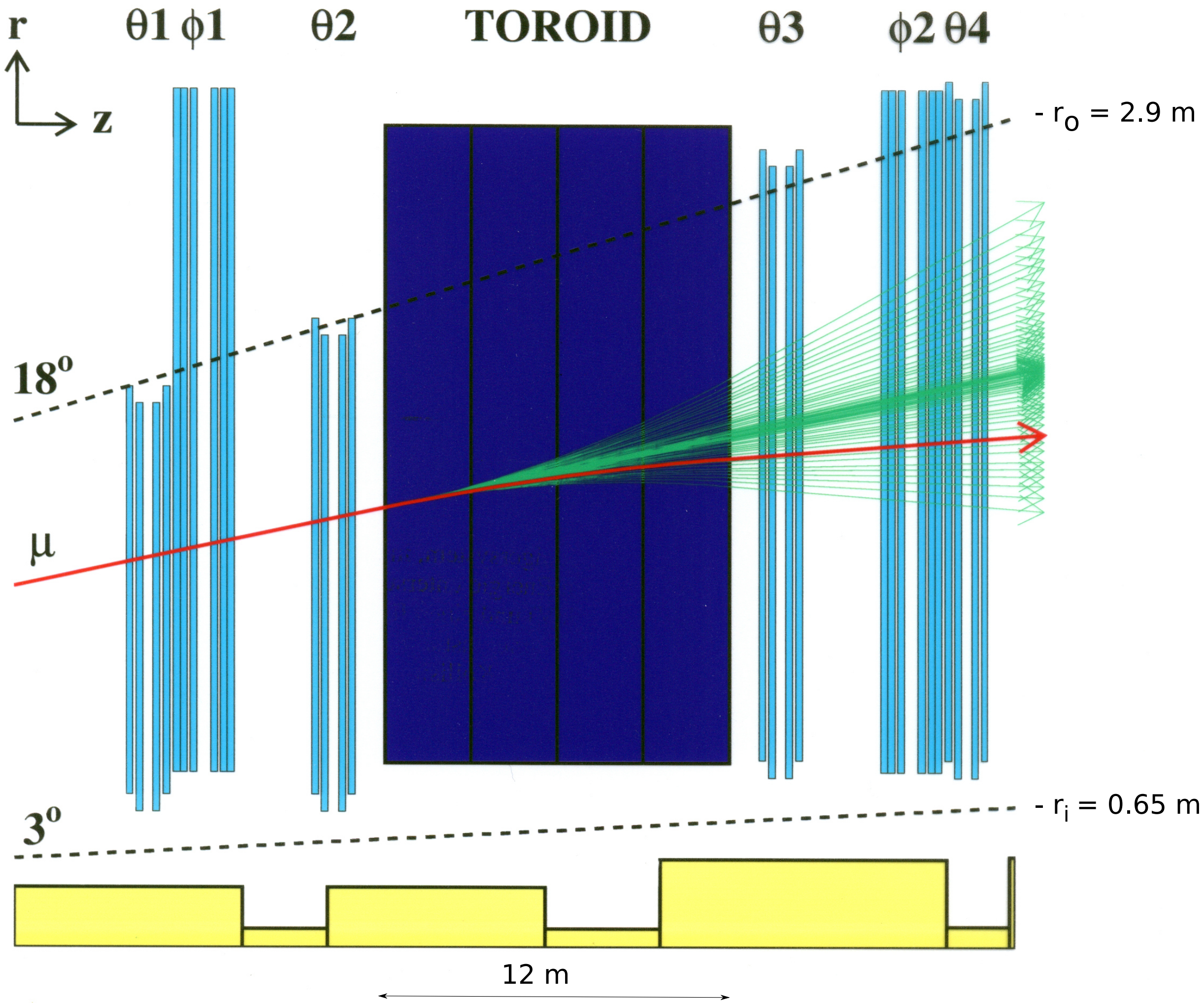

deflection in polar angle → momentum

$$\frac{\sigma_p}{p} = 24 - 36\%$$

$$\text{for } p = 5 - 200 \text{ GeV/c}$$

dominated by multiple scattering

$$\frac{\sigma_p}{p} = 0.24 \oplus 1.3 \cdot 10^{-3} p$$

ATLAS - A Toroidal LHC ApparatuS

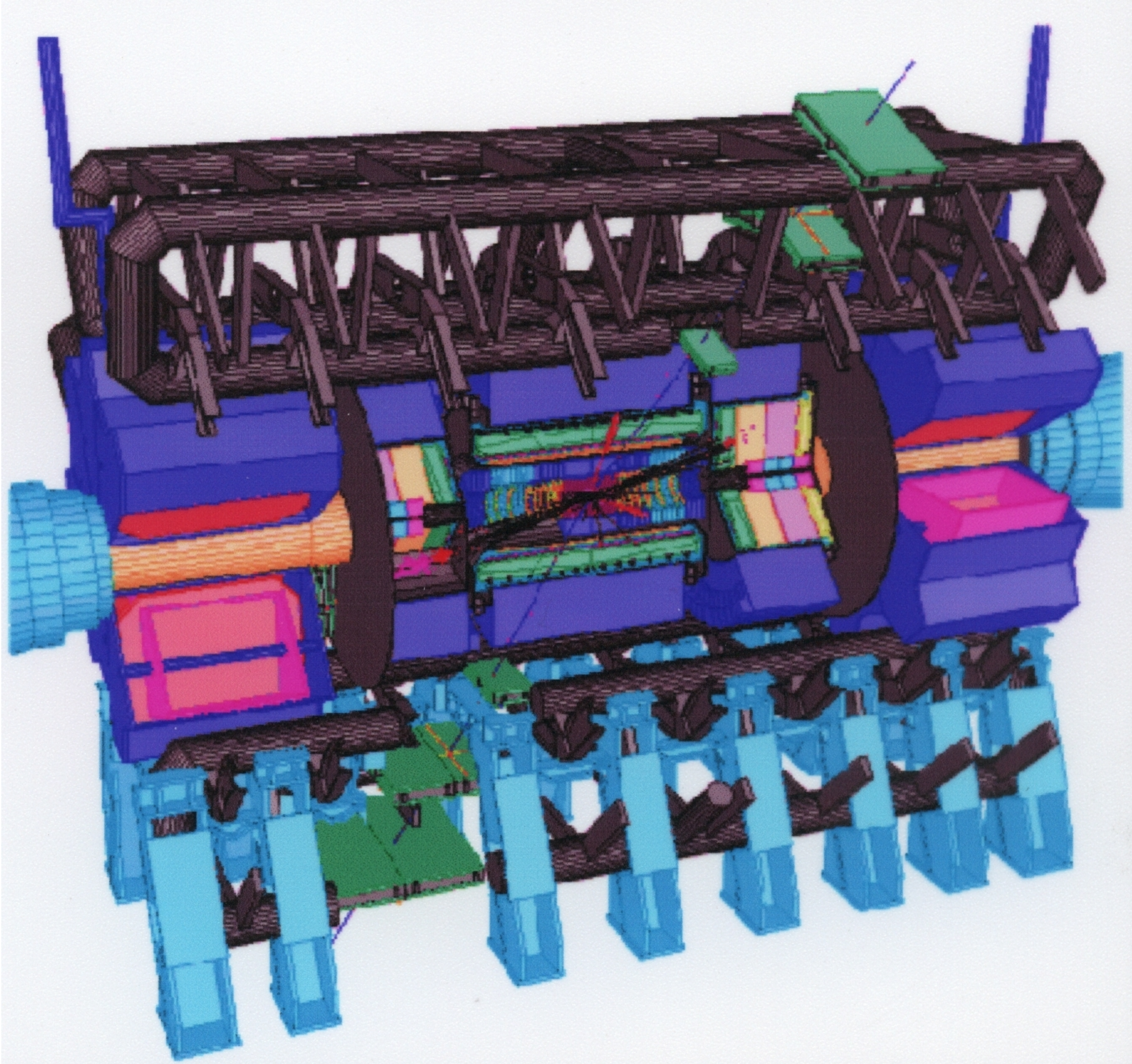

‘air core toroid’ central barrel

$L = 26$ m, $D_i = 9.4$ m, $D_0 = 19.5$ m

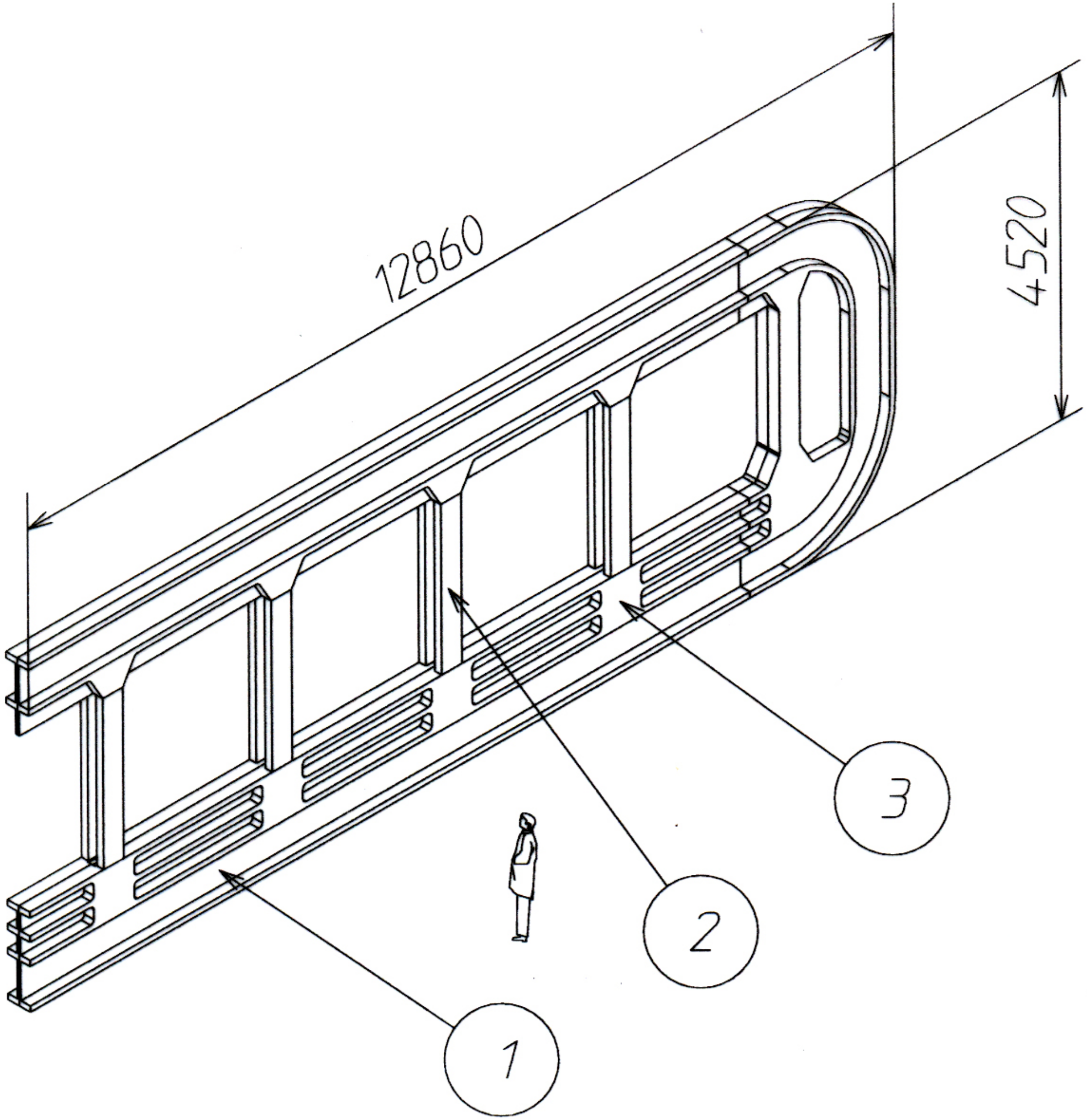

8 flat coils, super-conducting, 70 km super-conducting cable
20 kA, $\int BdL = 3 - 9$ Tm
energy stored in magnetic field 1490 MJ

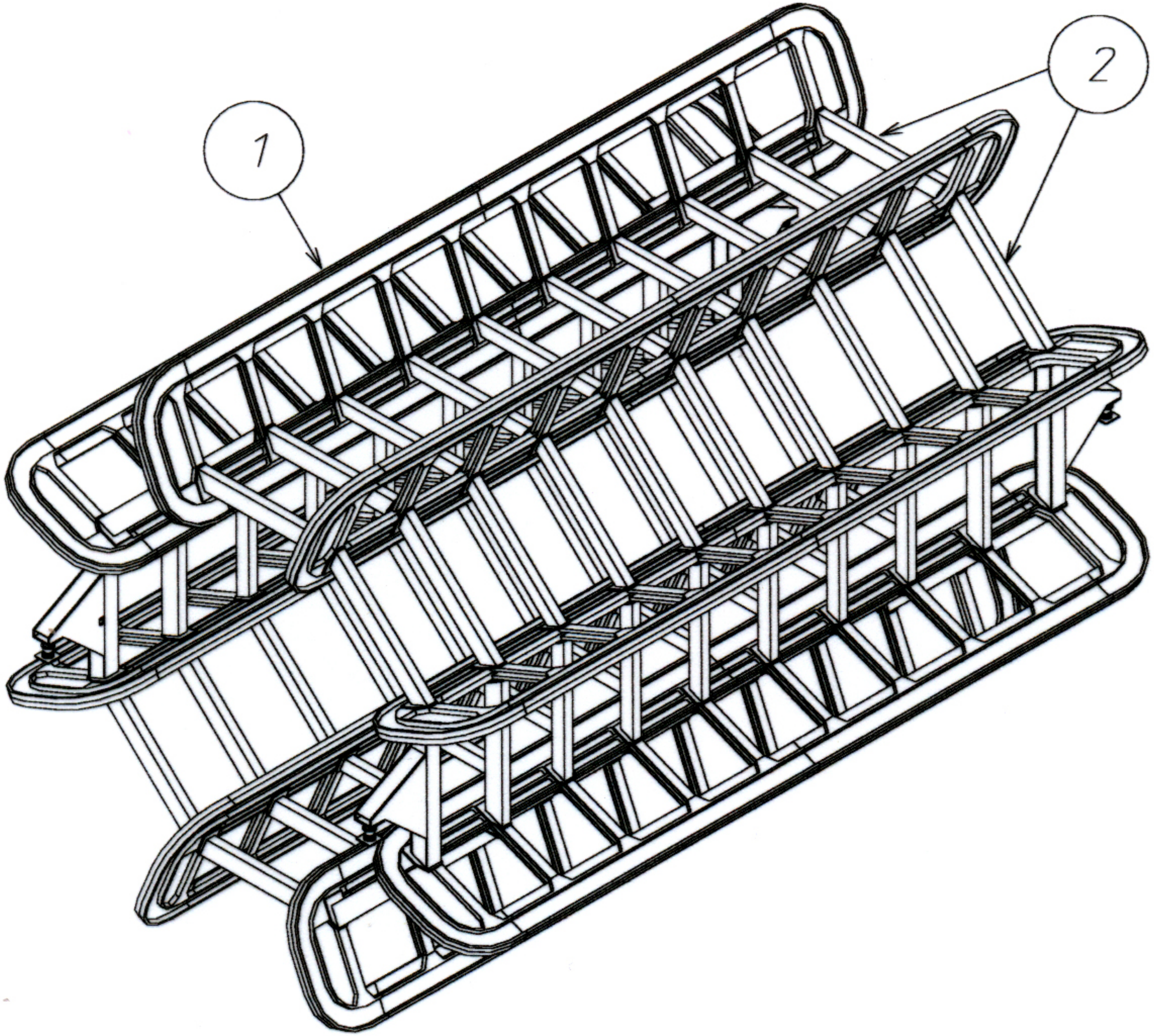

ATLAS cavern

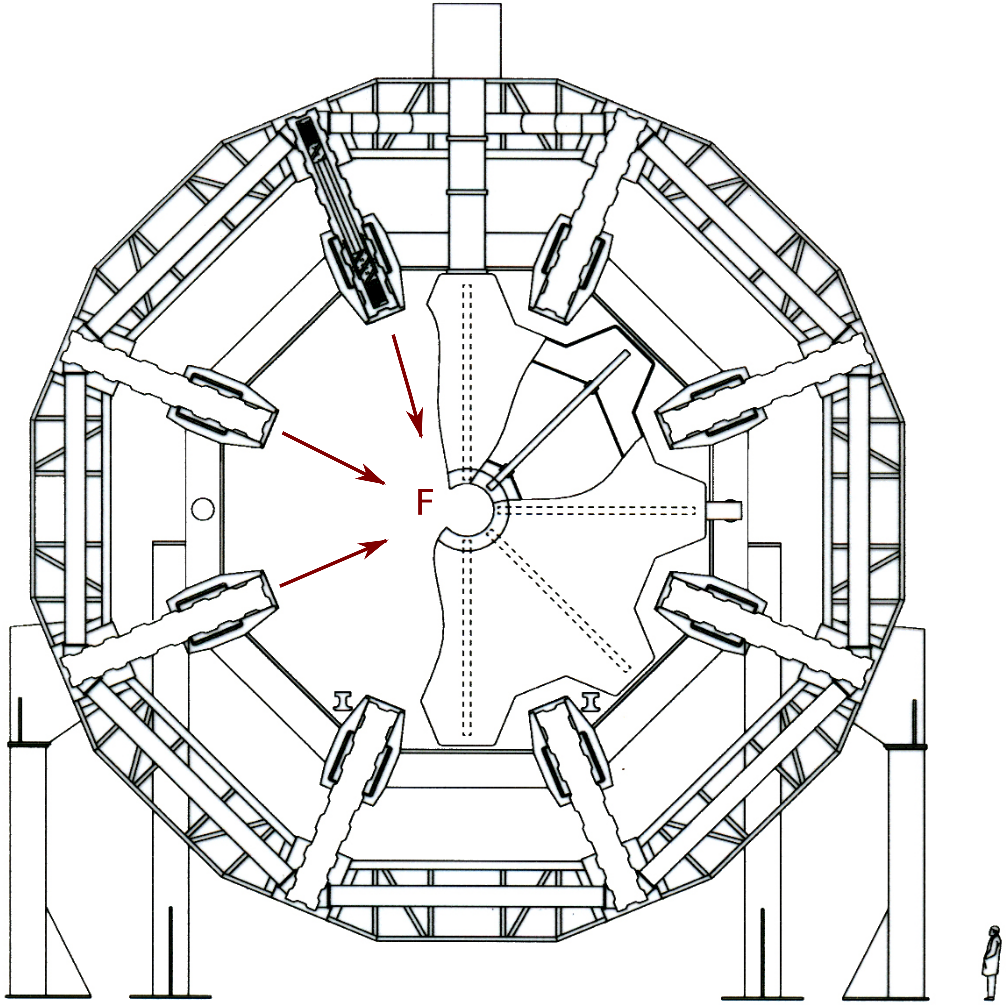

with 'current on' forces on coils radially inward

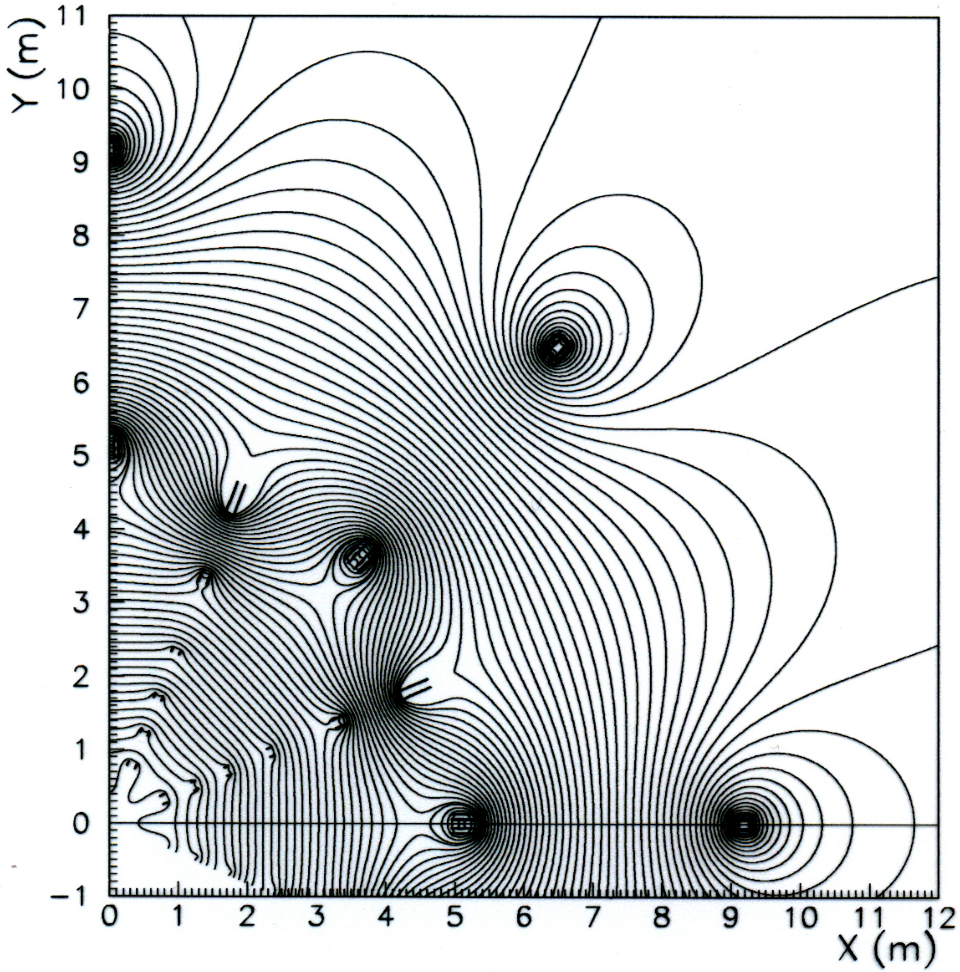

B-field monitored by 5000 Hall probes attached to muon chambers

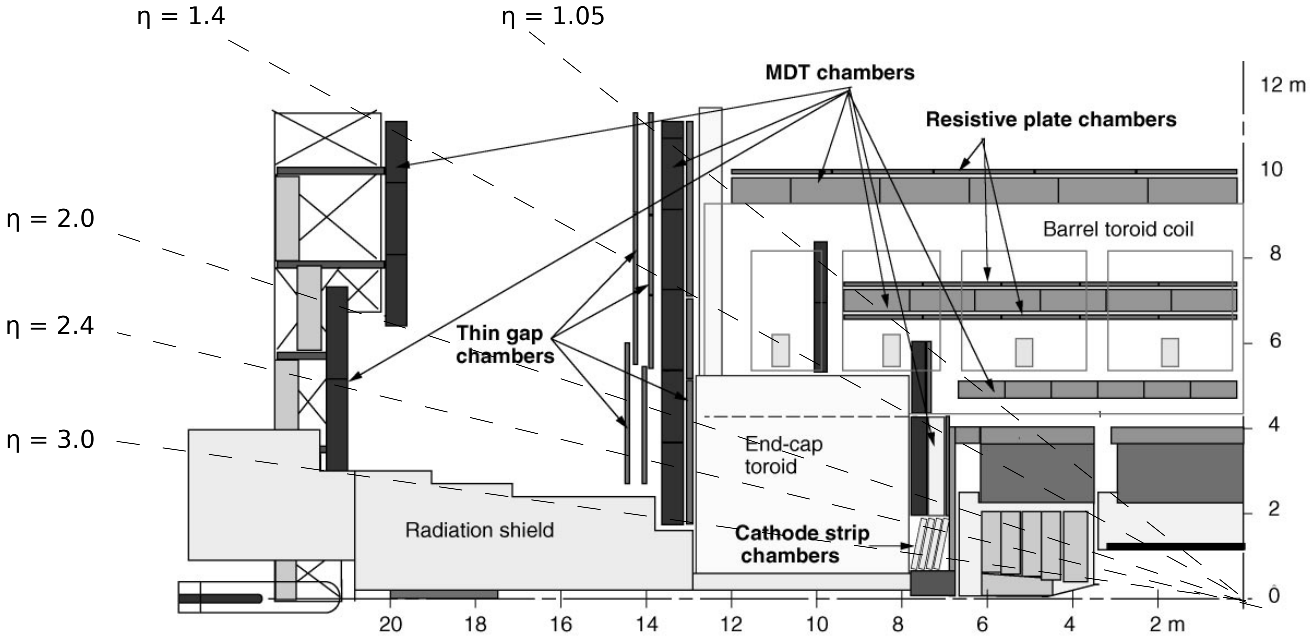

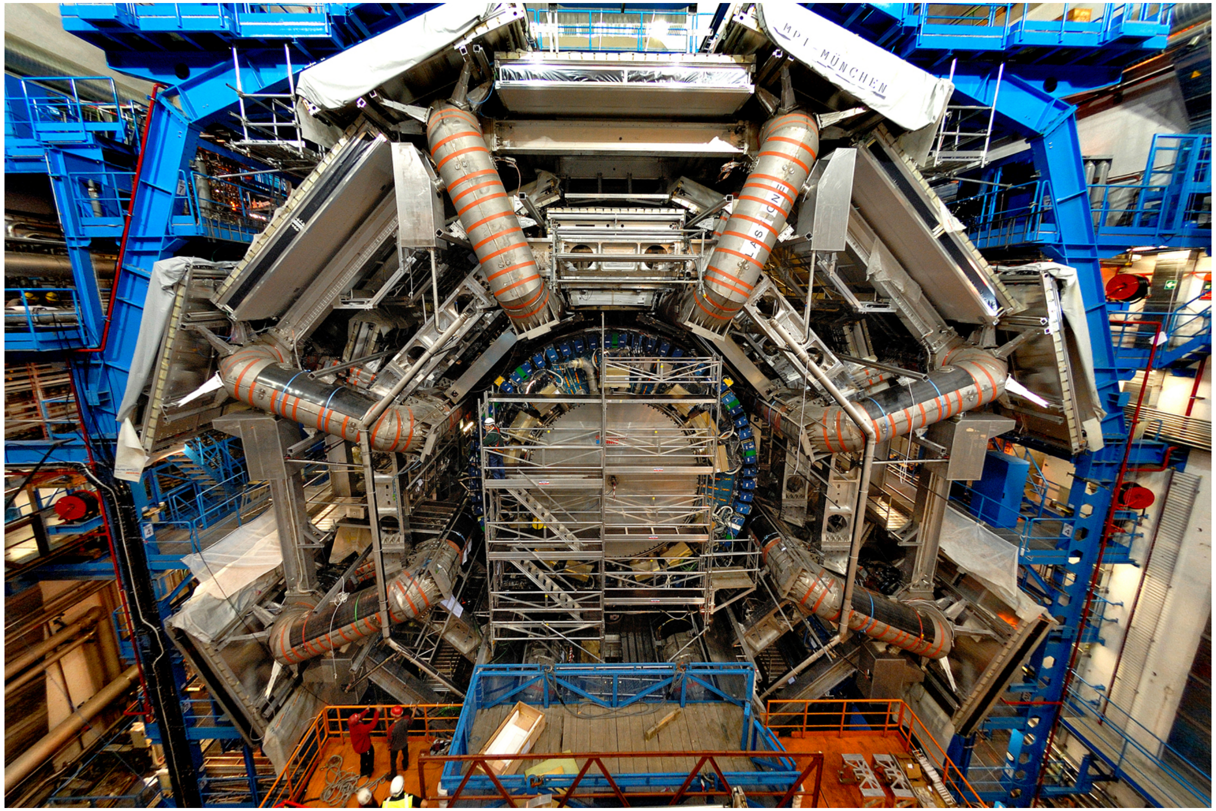

Principle of momentum measurement of muon tracks with monitored drift-tube array:

3 layers, each consisting of
2 multilayers

total 1200 muon chambers of 2×3.5 m^2

total 300000 channels

for 1 TeV muon sagitta S $= 500\ \mu$m
requirements: $\sigma_x = 50\mu$m
alignment known to 30 μm

ATLAS monitored drift tube arrays

two 3-layer multilayers of drift tubes
hard Al-Mn alloy (ALUMAN 100)
∅ 3 cm +0/-20 μm

400 ± 20 μm wall thickness

operation at 3 bar

$1.4 - 6.3$ m long 50 μm wire
centered in tube to 20 μm

drift time ≤ 600 ns

gas gain < 50000
(only 'streamers'
to avoid $\leftrightarrow$ 'aging')

gas: Ar/C_2H_6/CO_2/N_2
86 : 5 : 4 : 5

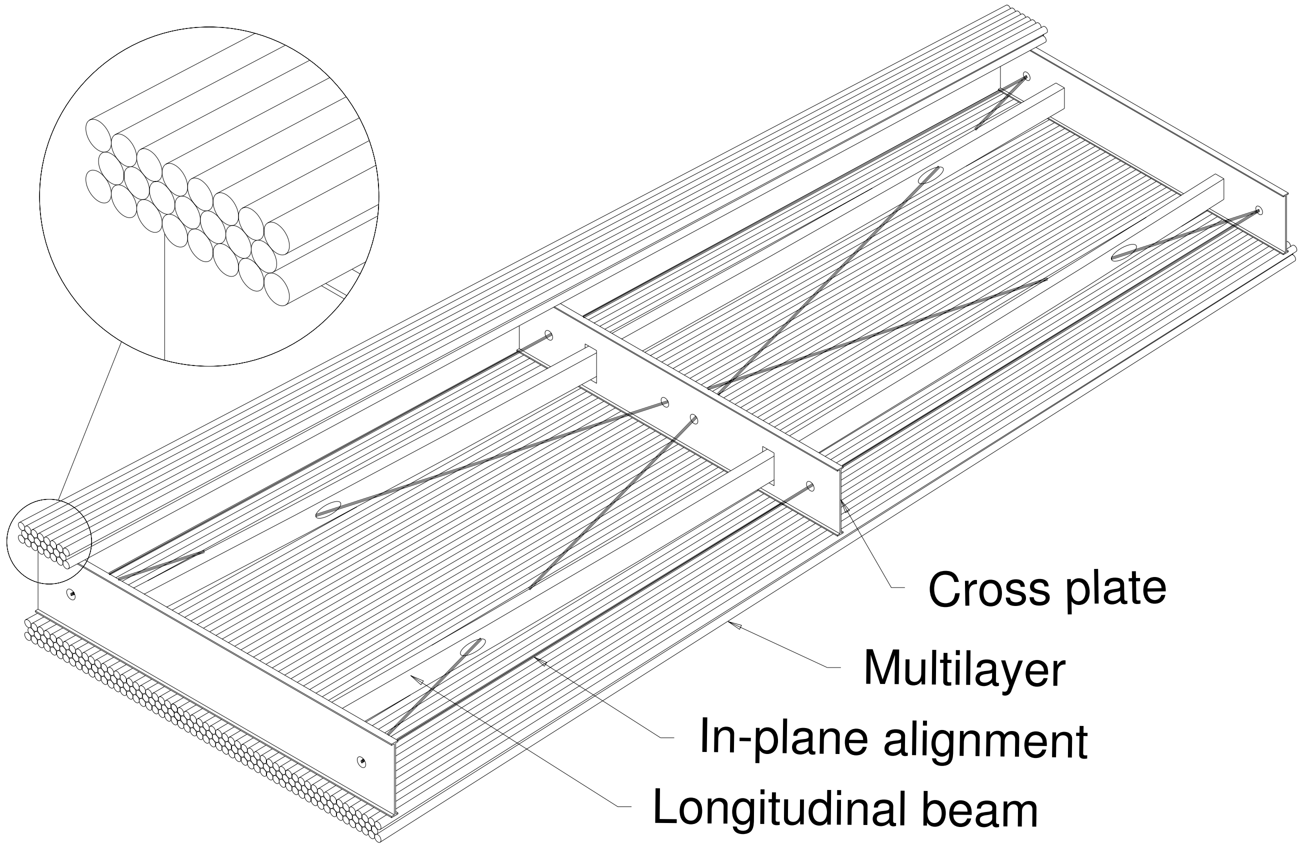

position resolution ATLAS monitored drift tube array

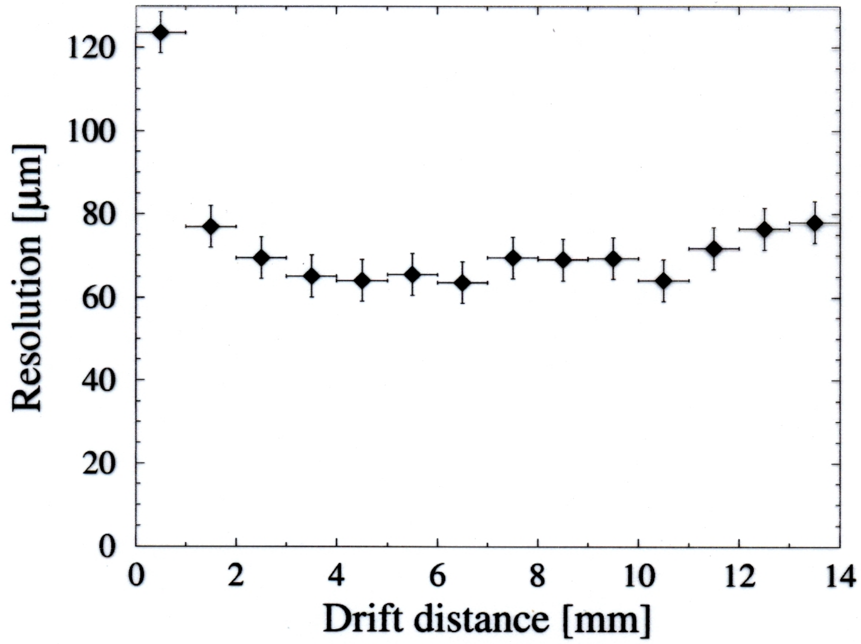

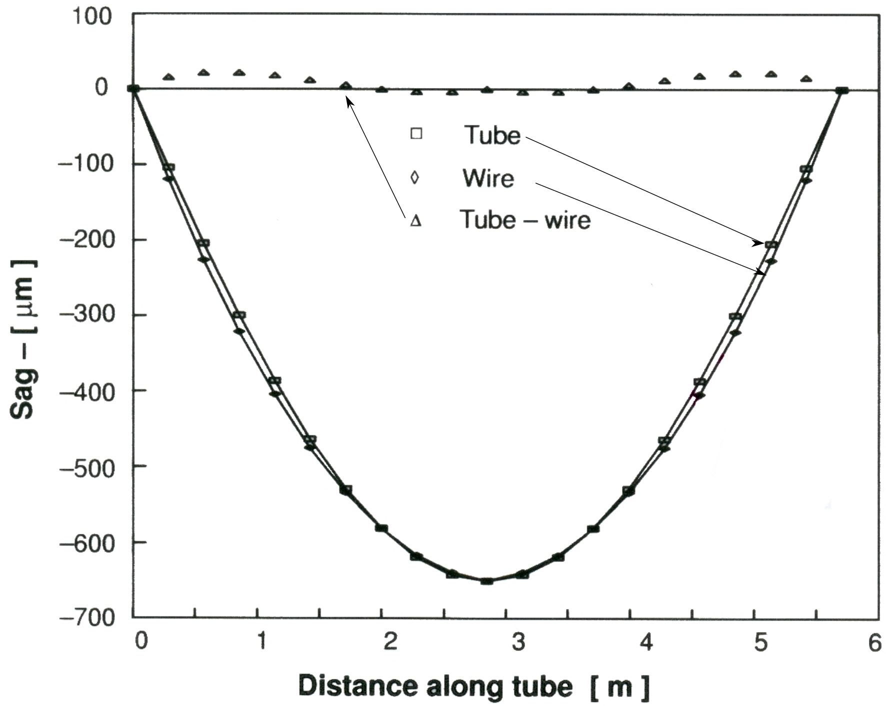

difficulty: gravitational sag of long tubes and wires

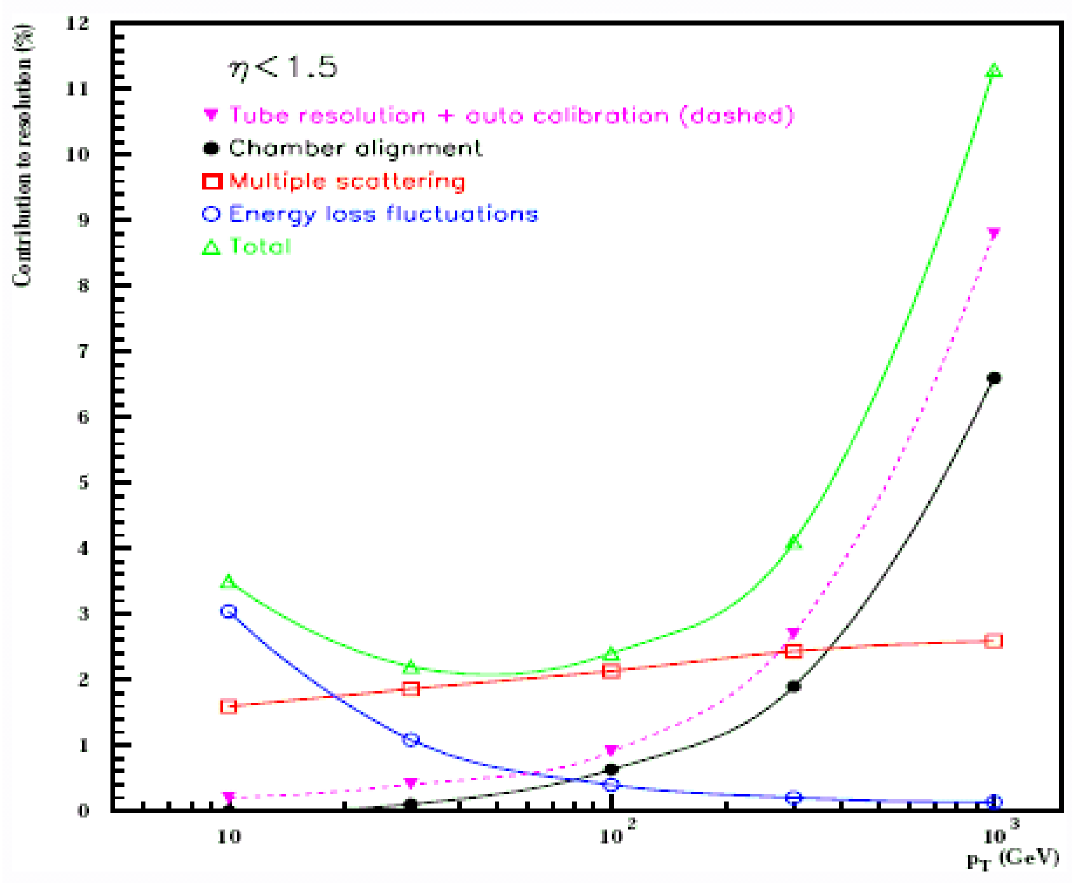

single tube position resolution 80 μm

$\rightarrow \sigma_{p_t}/p_t = 10\%$ at 1000 GeV

Need to know exactly where tubes and wires are!

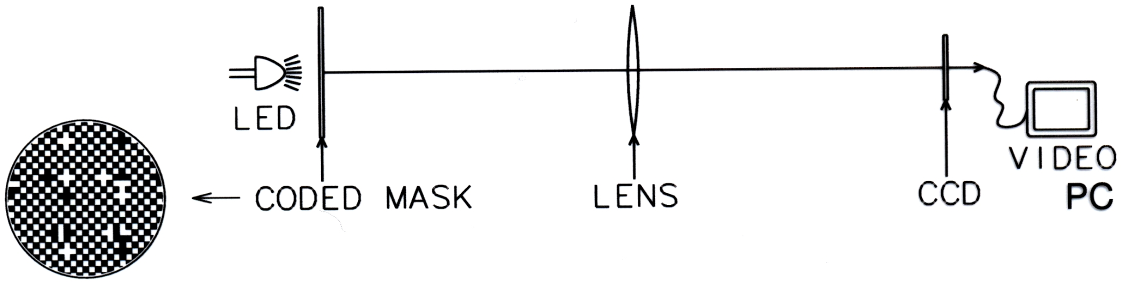

Rasnick System

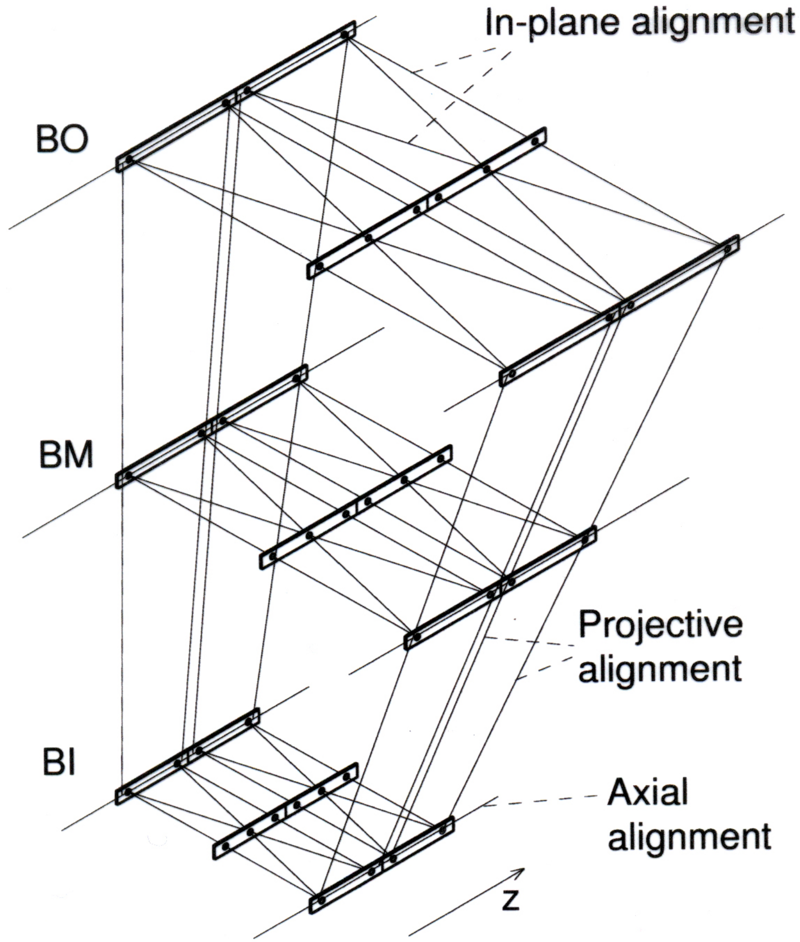

Alignment system for 3 layers of MDT's

13000 CCD cameras
→ align each muon chamber to 0.05 mm precision

Particle identification - parameters

in general, momentum of a particle measured in a spectrometer and another observable is used to identify the species

- velocity
  - time-of-flight $\tau \sim 1/\beta$
  - Cherenkov threshold $\beta > 1/n$
  - transition radiation $\gamma \gtrsim 1000$ for e/π separation
- energy loss
  - $-\frac{dE}{dx} \sim \frac{z^2}{\beta^2} \ln a\beta\gamma$
- energy measurement
  - calorimeter (chap. 8)

$$
\begin{aligned}
E &= \gamma m_0 c^2 \\
T &= (\gamma - 1) m_0 c^2 \quad (\text{deposited for } p, n, nuclei) \\
E_{dep} &= \gamma m_0 c^2 + m_0 c^2 \quad (\text{for } \bar{\mathrm{p}}, \bar{\mathrm{n}}, \ldots)
\end{aligned}
$$

Special signatures

photon

- total energy in crystal or electromagnetic sampling calorimeter
  + information on neutrality

neutron

- energy in calorimeter or scintillator with Li, B, or ^{3}He
  + information on neutrality

muon

- only dE/dx in thick calorimeter, penetrates thick absorber

K^0, Λ, Ξ, Ω, ...

- reconstruction of m_{inv} of weak decay products

neutrino

- only weak interaction with detector material,
  either as charged or neutral current

7.1 Time of flight τ

time difference between two detectors with good time resolution: ‘start’ and ‘stop’-counter

- typically scintillator or resistive plate chamber, also calorimeter (neutrons)
- coincidence set-up or put all signals as stop into TDC (time-to-digital converter) with common start (or stop) from ‘beam’ or ‘interaction’

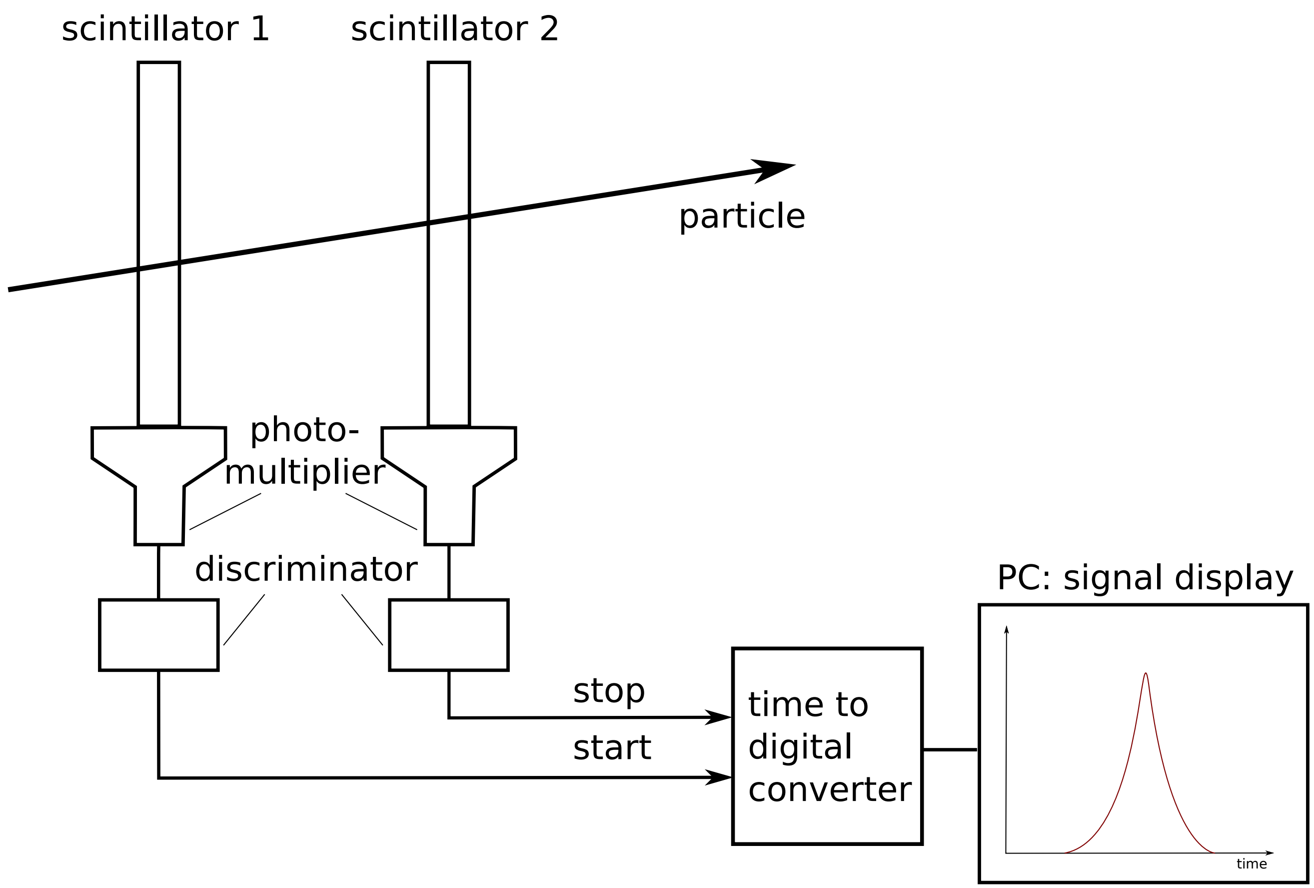

for known distance L between start and stop counters, time-of-flight difference of two particles with masses $m_{1,2}$ and energies $E_{1,2}$:

$$\Delta t = \tau_1 - \tau_2 = \frac{L}{c}\left(\frac{1}{\beta_1} - \frac{1}{\beta_2}\right)$$

$$\boxed{\Delta t = \frac{L}{c}\left(\sqrt{\frac{1}{1-(m_1c^2/E_1)^2}} - \sqrt{\frac{1}{1-(m_2c^2/E_2)^2}}\right)}$$

limiting case $\quad E \simeq pc \gg m_0c^2$ $\qquad \boxed{\Delta t = \frac{Lc}{2p^2}(m_1^2 - m_2^2)}$

require for clean separation e.g. $\Delta t \geq 4\sigma_t$

$\Rightarrow$ separation K/π at $L = 3$ m for $\sigma_t = 100$ ps possible up to $p = 3$ GeV/c

Cherenkov counter or RPC's $\quad \sigma_t \simeq 40$ ps
scintillator + PM $\quad \sigma_t \simeq 80$ ps

Difference in time-of-flight for $L = 1$ m

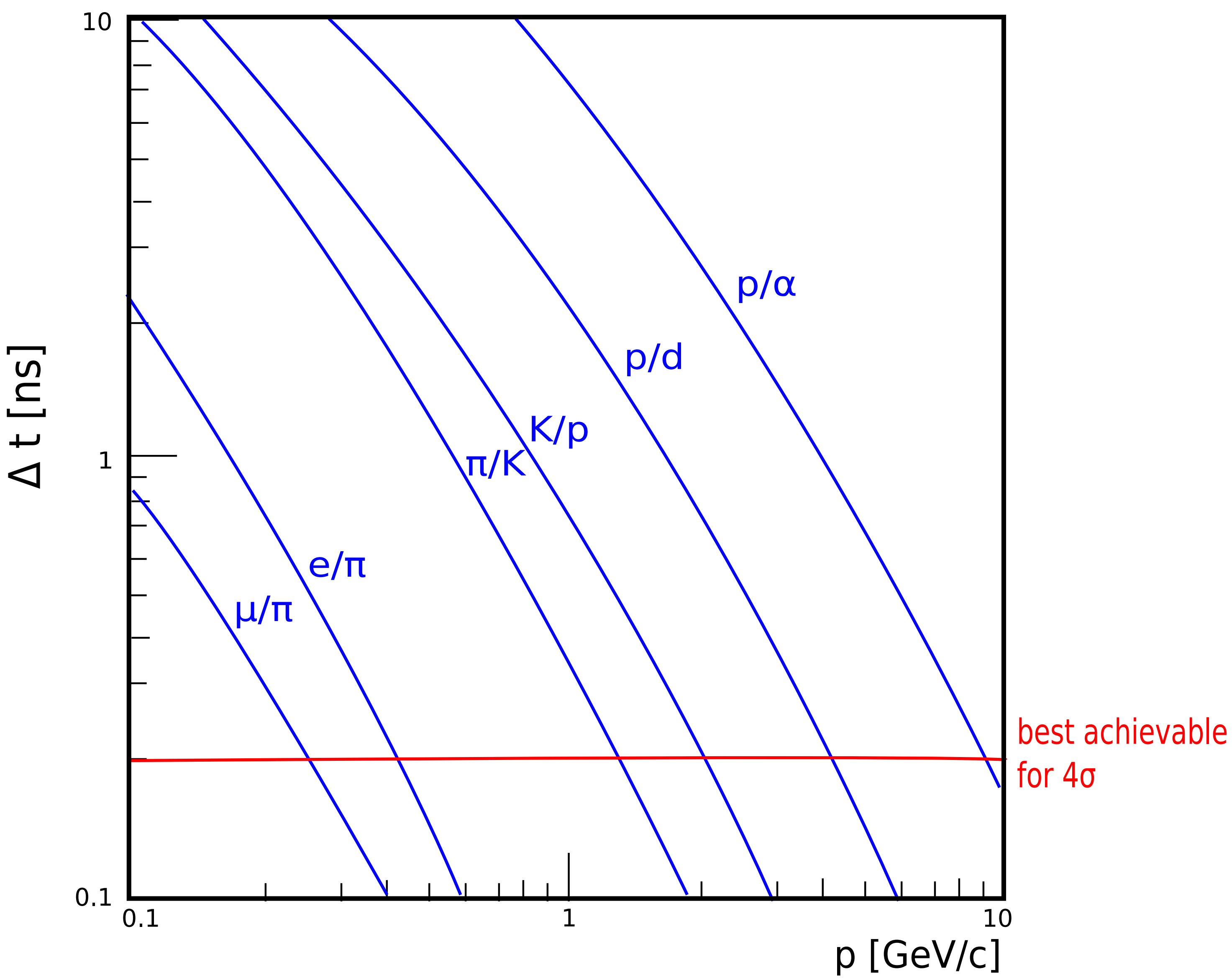

but of course distance L can be larger $$ detector area for a given acceptance

particle identification (PID) via time-of-flight at moderate momenta
$\rightarrow$ mass resolution:

$p = \beta\gamma m$ with rest mass m, $\beta = L/\tau$ (here exceptionally $c = 1$ for short notation)

$$
\begin{aligned}
\Rightarrow \quad m^2 &= p^2\left(\frac{\tau^2}{L^2} - 1\right) \\
\delta(m^2) &= 2p\delta p \underbrace{\left(\frac{\tau^2}{L^2} - 1\right)}_{m^2/p^2} + \underbrace{2\tau\delta\tau\frac{p^2}{L^2} - 2\frac{\delta L}{L^3}p^2\tau^2}_{\text{use } \frac{p^2\tau^2}{L^2} = m^2 + p^2 = E^2} \\
&= 2m^2\frac{\delta p}{p} + 2E^2\frac{\delta\tau}{\tau} - 2E^2\frac{\delta L}{L} \\
\sigma(m^2) &= 2\left(m^4\left(\frac{\sigma_p}{p}\right)^2 + E^4\left(\frac{\sigma_\tau}{\tau}\right)^2 + E^4\left(\frac{\sigma_L}{L}\right)^2\right)^{\frac{1}{2}}
\end{aligned}
$$

usually $\quad \frac{\sigma_L}{L} \ll \frac{\sigma_p}{p} \ll \frac{\sigma_\tau}{\tau}$

$\Rightarrow \quad \boxed{\sigma(m^2) \simeq 2E^2\frac{\sigma_\tau}{\tau}}$ error in time measurement dominates

7.1.1 Resistive plate chambers: gas detector for precise timing measurement

(material taken from talk by C. Williams on ALICE TOF)

how to get a good timing signal from a gas detector?

where is the problem?

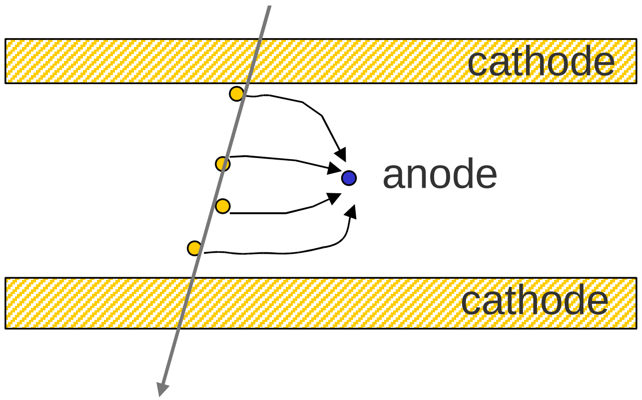

normally signal generated in vicinity of anode wire, timing determined by drift of primary ionization clusters to this wire, signal consists of a series of avalanches
spread over interval of order of 1 μs

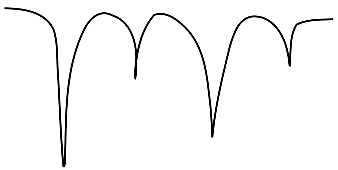

no way to get precision (sub-nanosecond) timing

idea: go to parallel plate chamber
(high electric field everywhere in detector)
clusters start to avalanche immediately
induced signal sum of all simultaneous avalanches

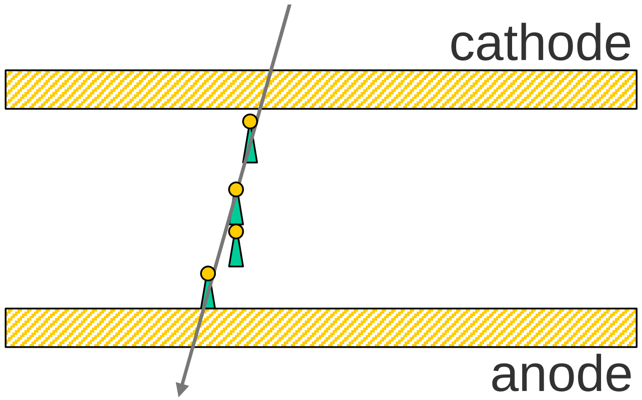

but in practice this is not so . . .

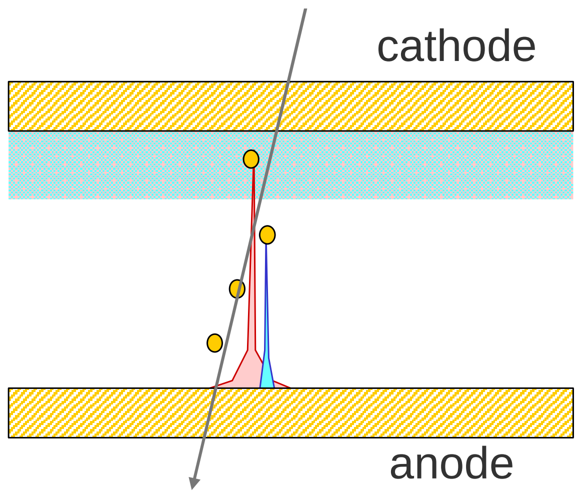

electron avalanche according to Townsend

$$N = N_0 e^{\alpha x}$$

only avalanches that traverse full gas gap will produce detectable signals $\Rightarrow$ only clusters of ionization produced close to cathode important for signal generation.
avalanche only grows large enough close to anode to produce detectable signal on pickup electrodes.

if minimum gas gain at 10^6 (10 fC signal)
and maximum gain at 10^8 (streamers/sparks produced above this limit), then sensitive region first 25% of gap

time jitter $\approx$ time to cross gap $\approx$ gap size/drift velocity

so

a) only a few ionization clusters take part in signal production
b) gap size matters (small is better)

first example: Pestov chamber (about 1975)

40 years ago Y. Pestov realized importance of size
planar spark chambers with localized discharge – gas gap of 100 μm gives time resolution $\approx$ 50 ps, first example of resistive plate chamber

glass electrode and metal electrode

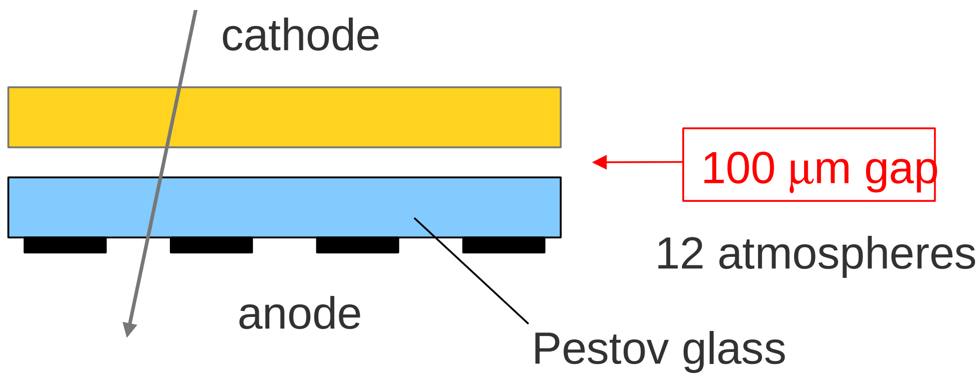

generally, excellent time resolution $\sim$ 50 ps or better!
but long tail of late events
mechanical constraints (due to high pressure)
non-commercial glass
$\rightarrow$ no large-scale detector ever built

how to make real life detector?

a) need very high gas gain (immediate production of signal)

b) need way of stopping growth of avalanches (otherwise streamers/sparks will occur)

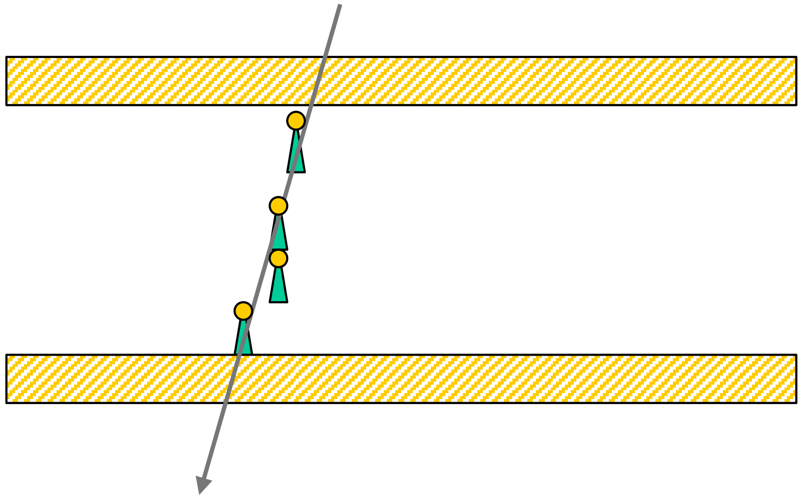

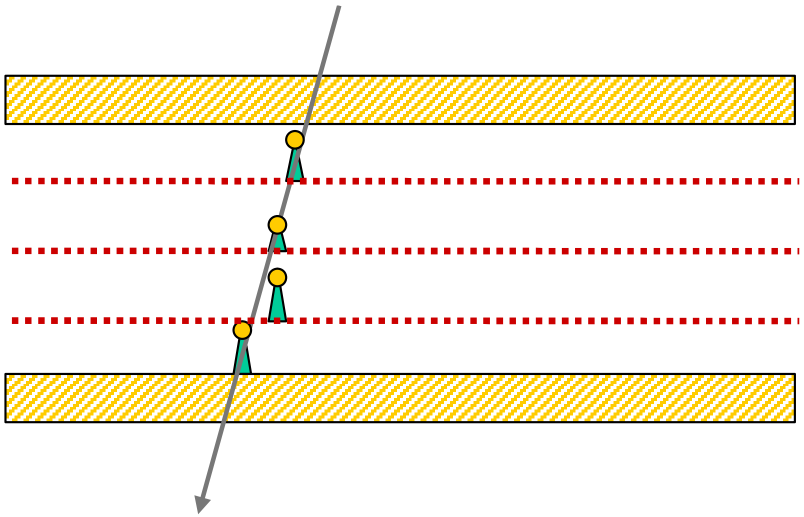

answer: add boundaries that stop avalanche development. These boundaries must be invisible to the fast induced signal - external pickup electrodes sensitive to any of the avalanches

from this idea the Multi-gap Resistive Plate Chamber was born

Multi-gap Resistive-Plate Chamber

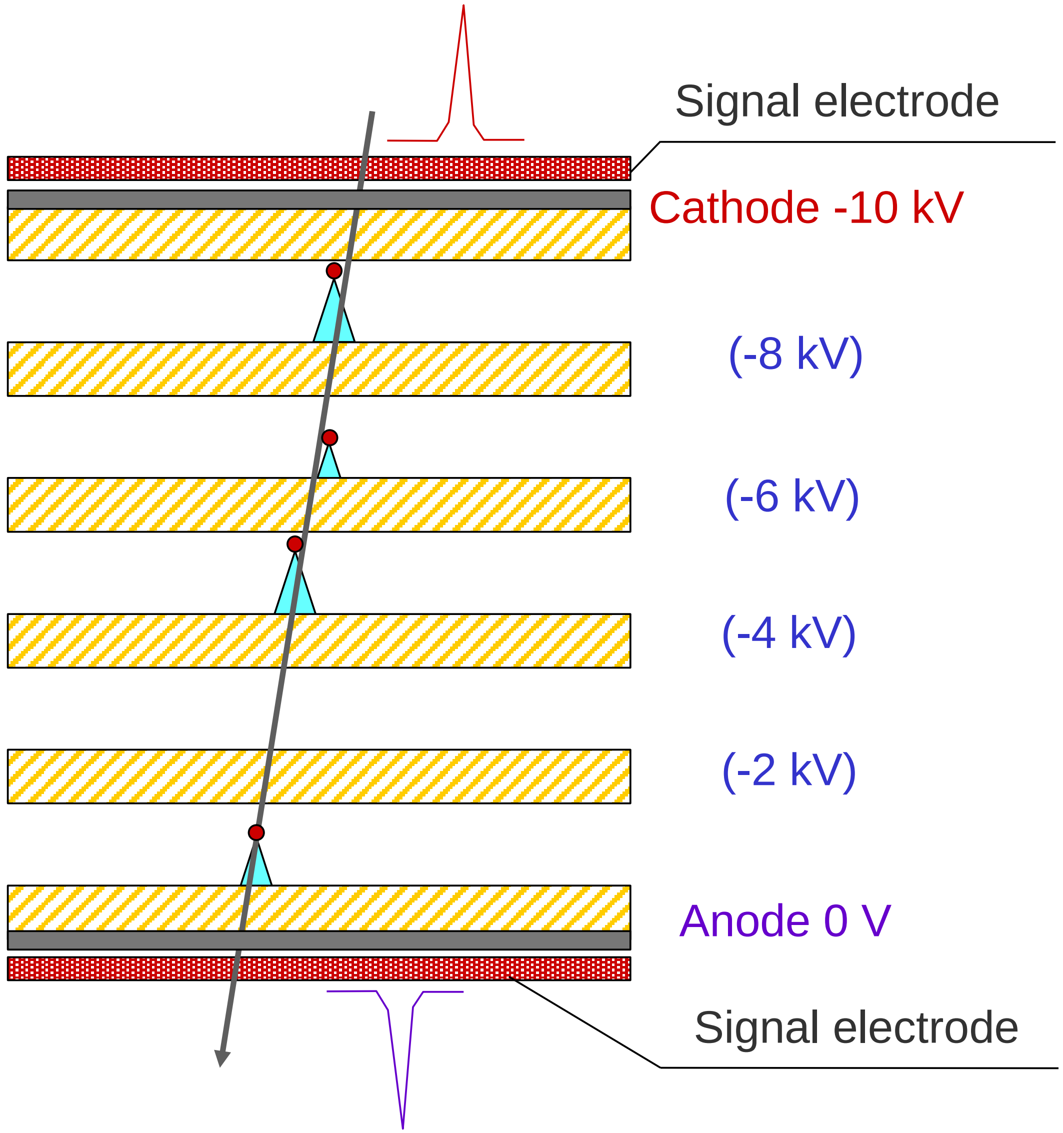

stack of equally-spaced resistive plates with voltage applied to external surfaces (all internal plates electrically floating)

pickup electrodes on external surfaces (resistive plates transparent to fast signal)

internal plates take correct potential – initially due to electrostatics but kept at correct potential by flow of electrons and positive ions - feedback principle that ensures equal gain in all gas gaps

Internal plates electrically floating!

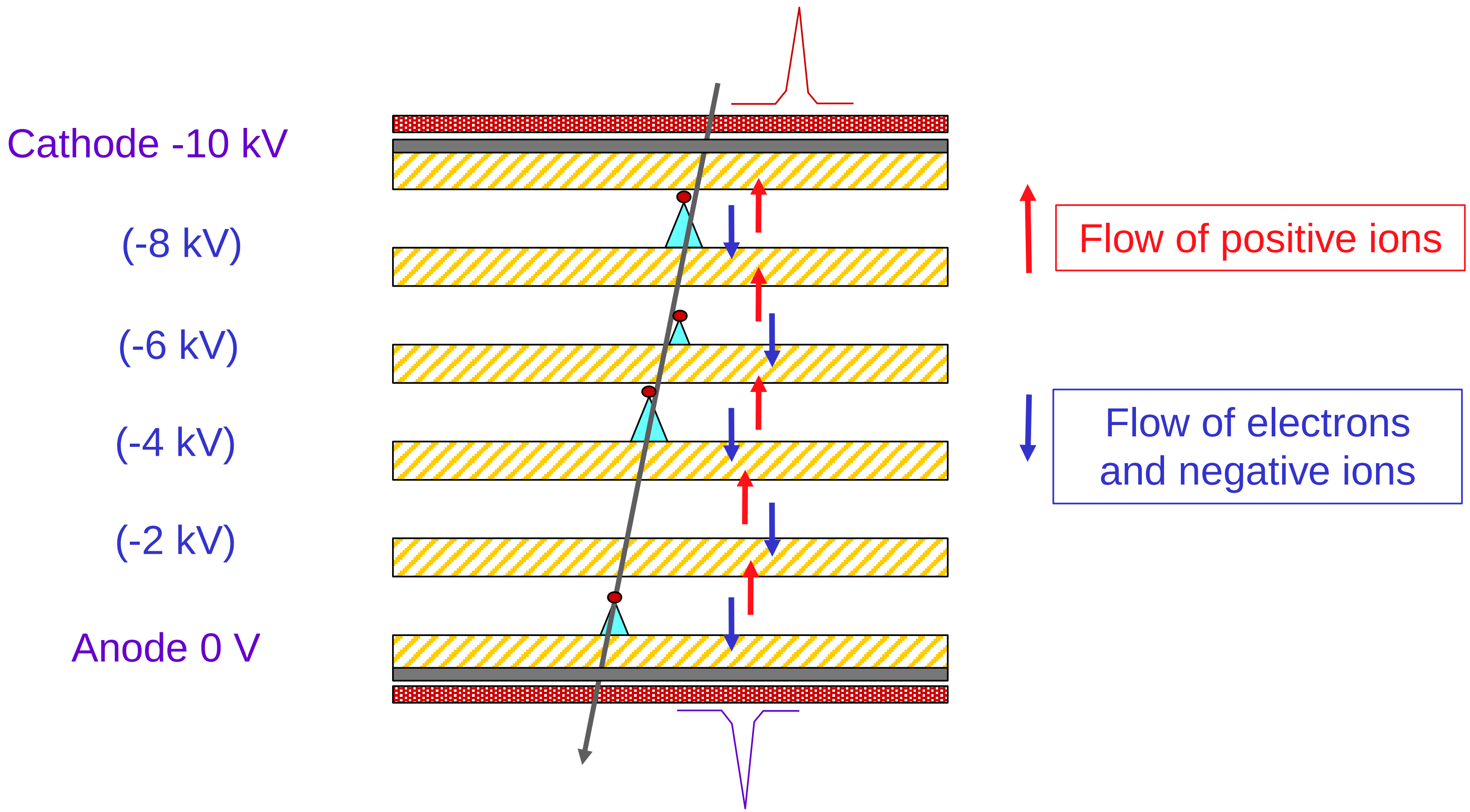

in this example: 2 kV across each gap (same E field in each gap)
since the gaps are the same size - on average - each plate has same flow of positive ions and electrons (from opposite sides of plate)
thus zero net charge flow into plate. STABLE STATE

What happens if a plate is at a wrong voltage for some reason?

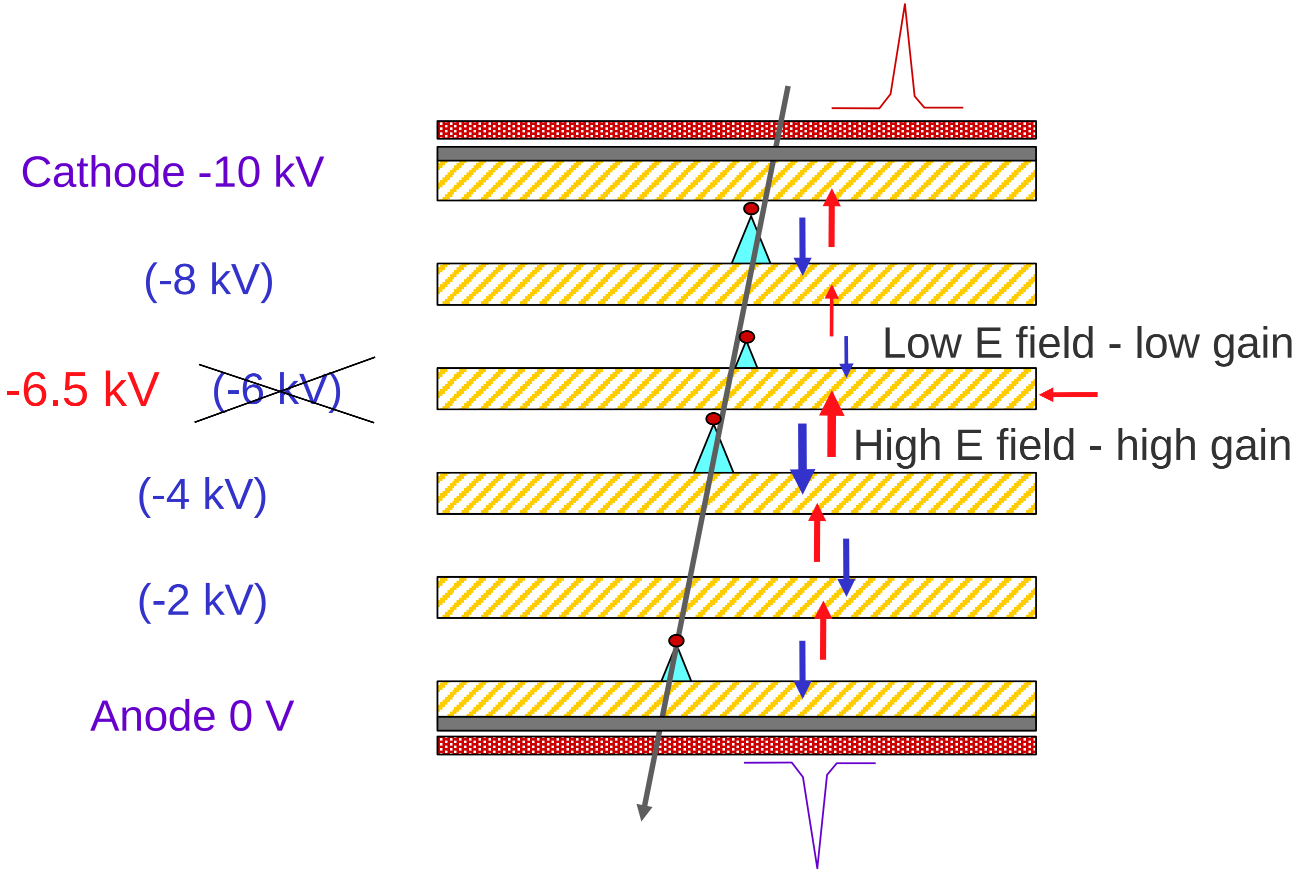

decreased flow of electrons and increased flow of positive ions – net flow of positive charge. This will move the potential on this plate more positive than −6.5 kV (i.e. towards 6 kV)

feedback principle that automatically corrects potentials on the resistive plates – stable situation is "equal gains in all gas gaps"

ALICE TOF prototypes

indeed one gets
sub 50 ps
time resolution

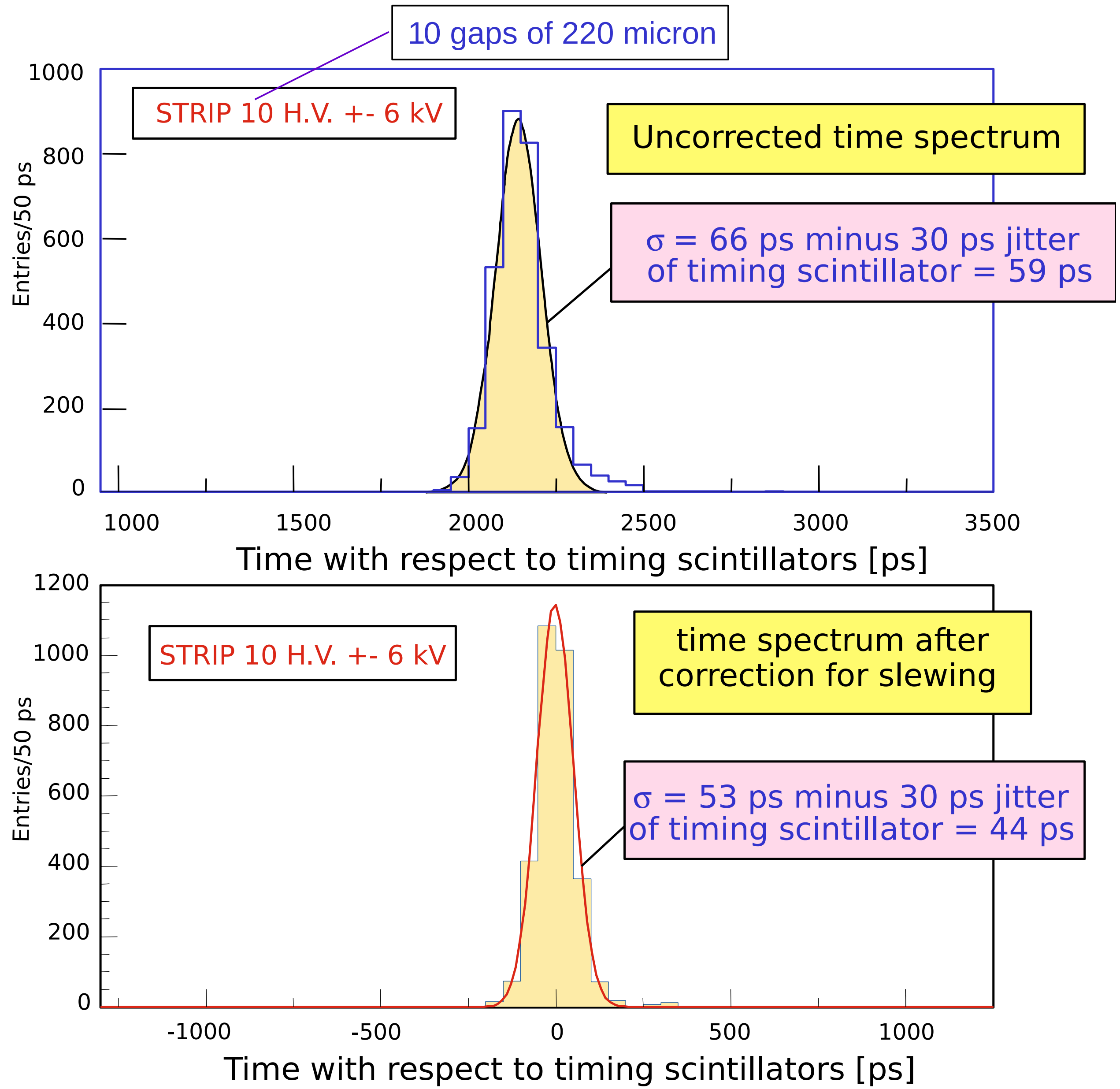

test of pre-production strip: 120×7 cm^2
read-out plane segmented into 3.5×3.5 cm^2 pads

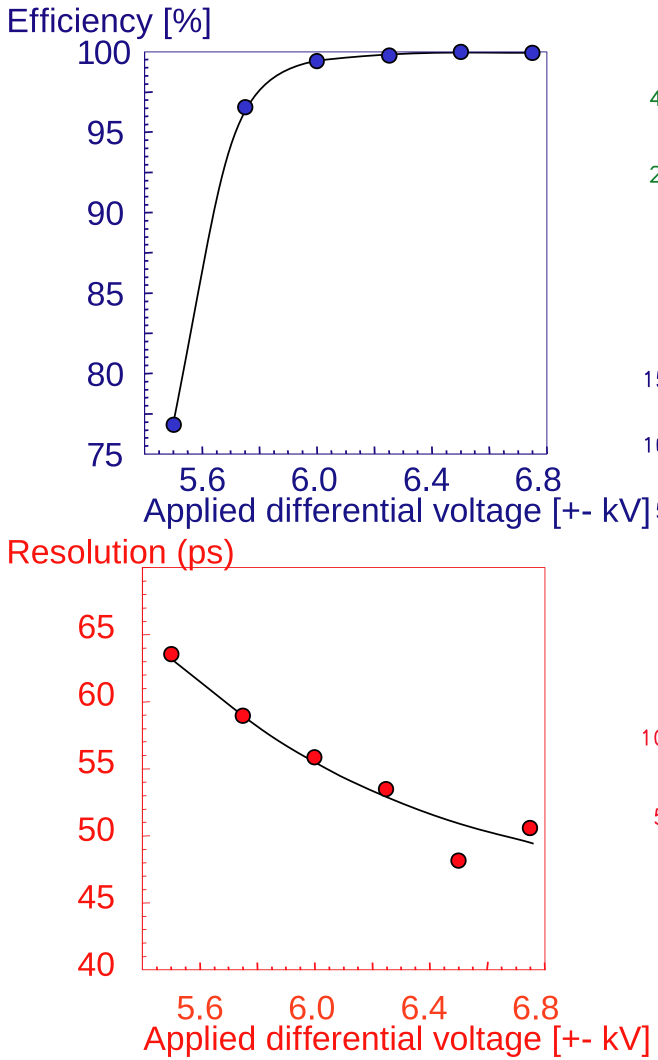

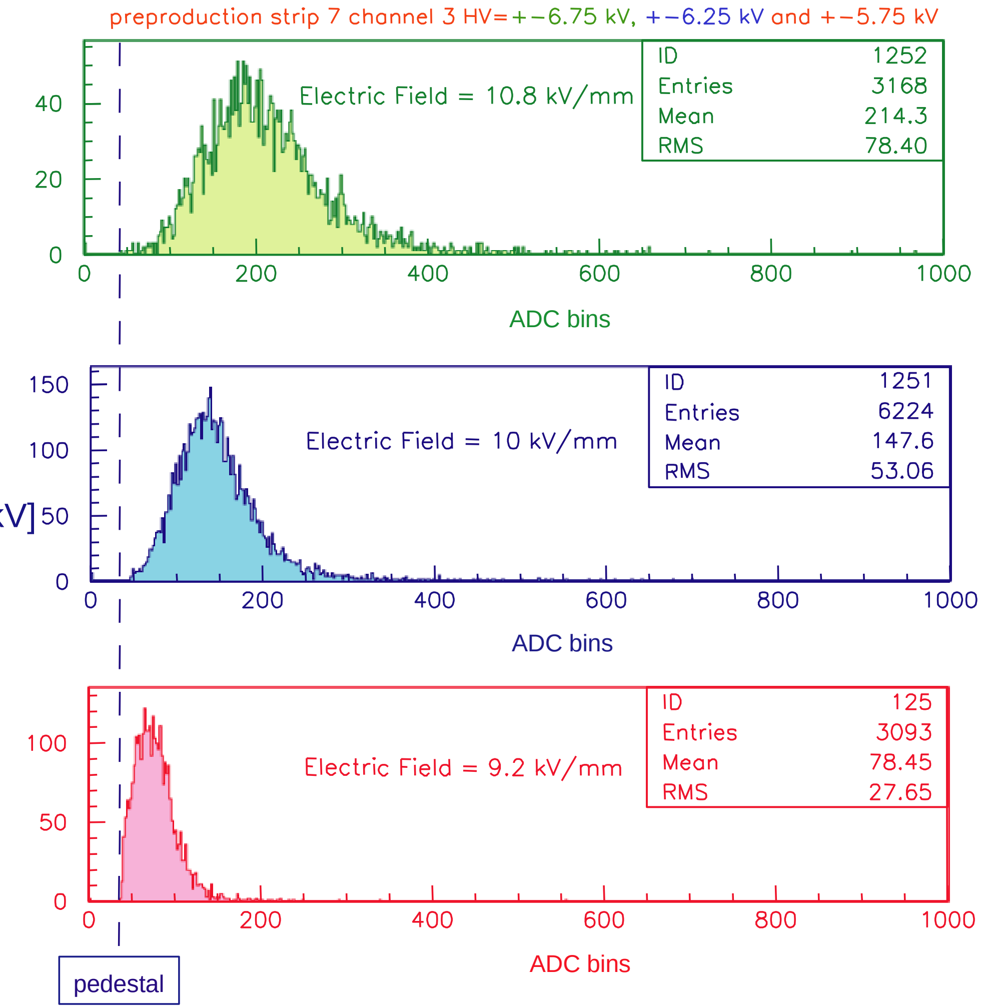

peak of charge spectra well separated from zero
no sign of streamers

but how precise do these gaps of 250 μm have to be?

gain not strongly dependent on gap size - actually loose mechanical tolerance - but why?

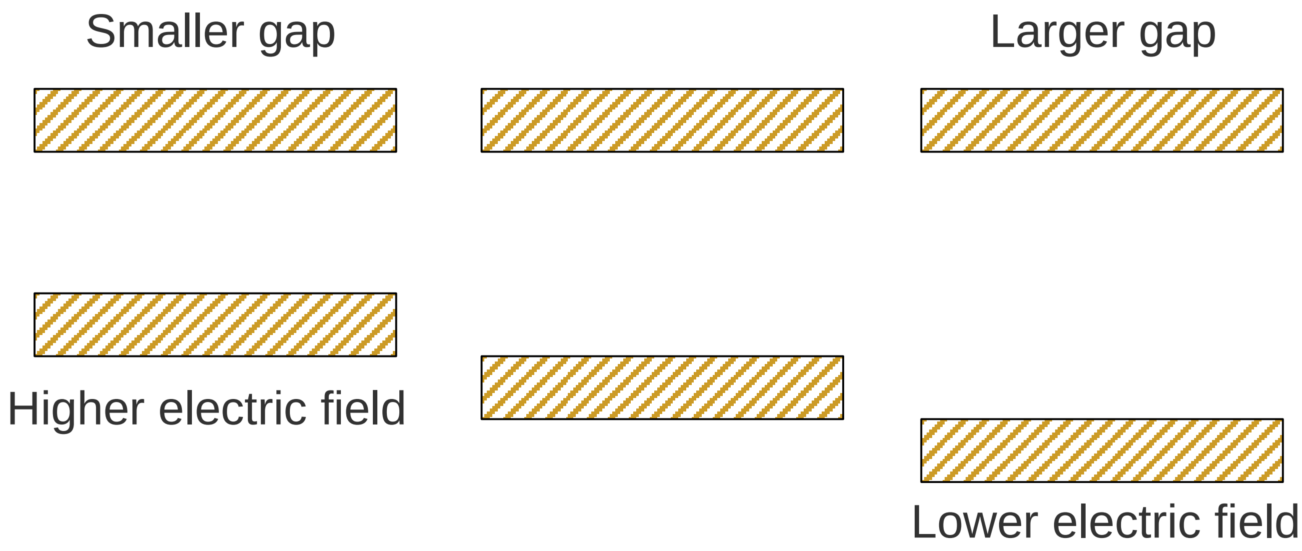

higher Townsend coefficient – higher gas gain but smaller distance for avalanche – lower gas gain

lower Townsend coefficient – lower gas gain but larger distance for avalanche – higher gas gain

with the gas mixture used (90% $C_2F_4H_2$, 5% SF_6, 5% isobutane) and with 250 μm gap size these two effects cancel and gap can vary by ± 30 μm

Cross section of double-stack MRPC – ALICE TOF

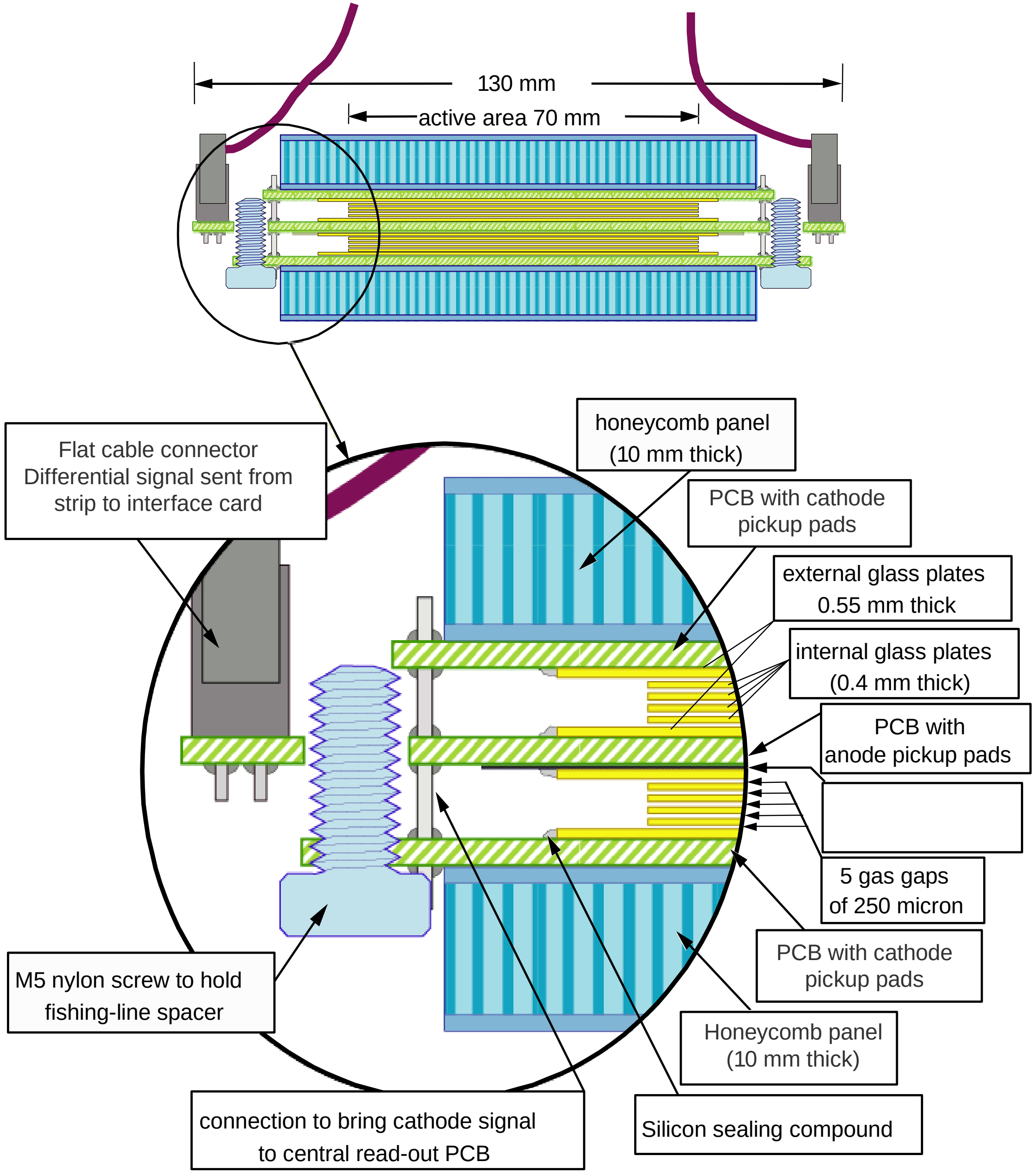

double stack
- each stack has 5 gaps (i.e. 10 gaps in total)

250 μm gap with spacers made from fishing line

resistive plates ‘off-the-shelf’
- soda lime glass

400 μm internal glass
550 μm external glass

resistive coating 5 MΩ/*square*

TOF with very high granularity needed!

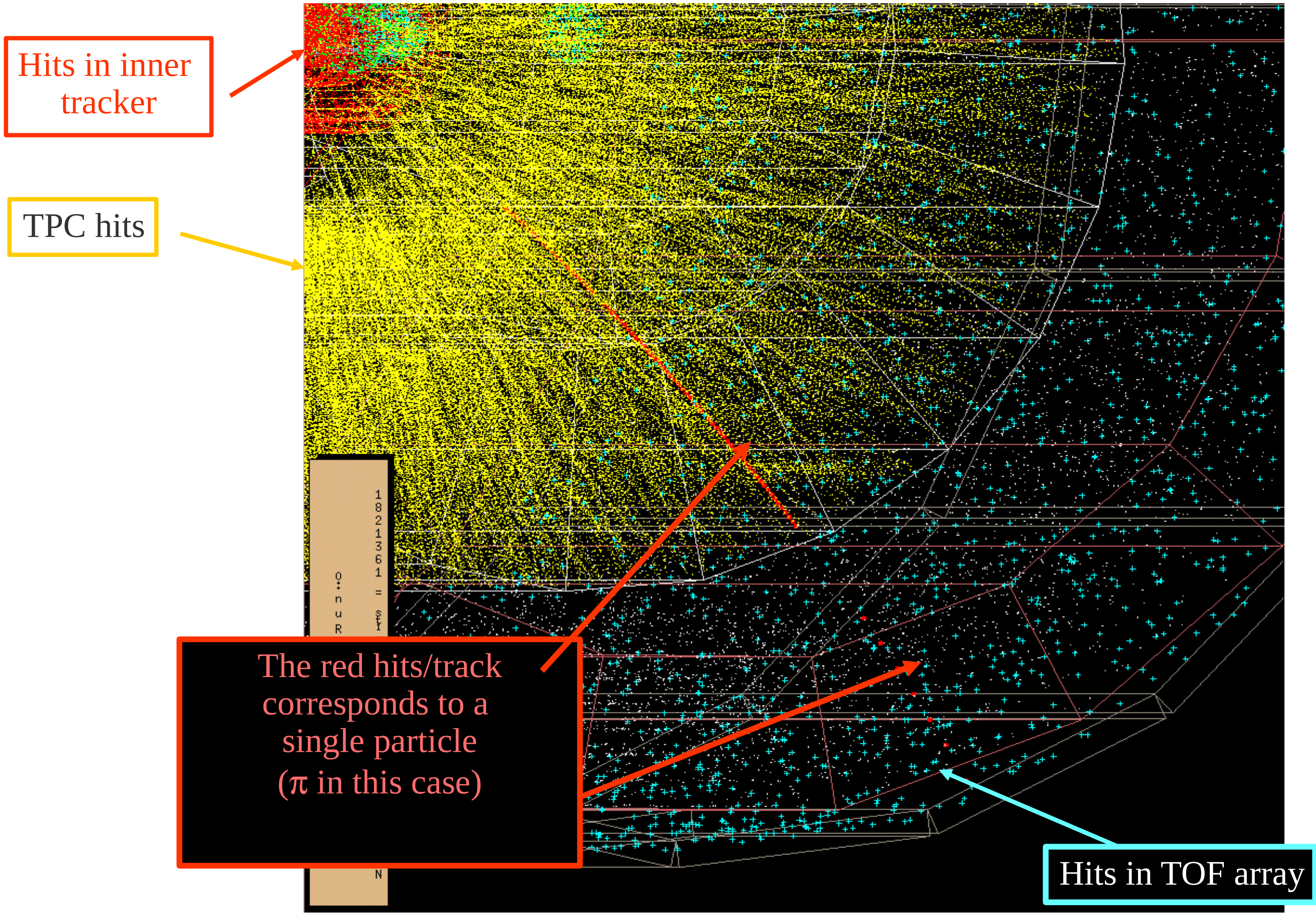

array to cover whole ALICE barrel - 160 m^2 and $\leq$ 100 ps time resolution
highly segmented - 160,000 channels of size 2.5 $\times$ 3.5 cm^2 gas detector is only choice!

modules need to overlap due to dead areas (frames) and noise

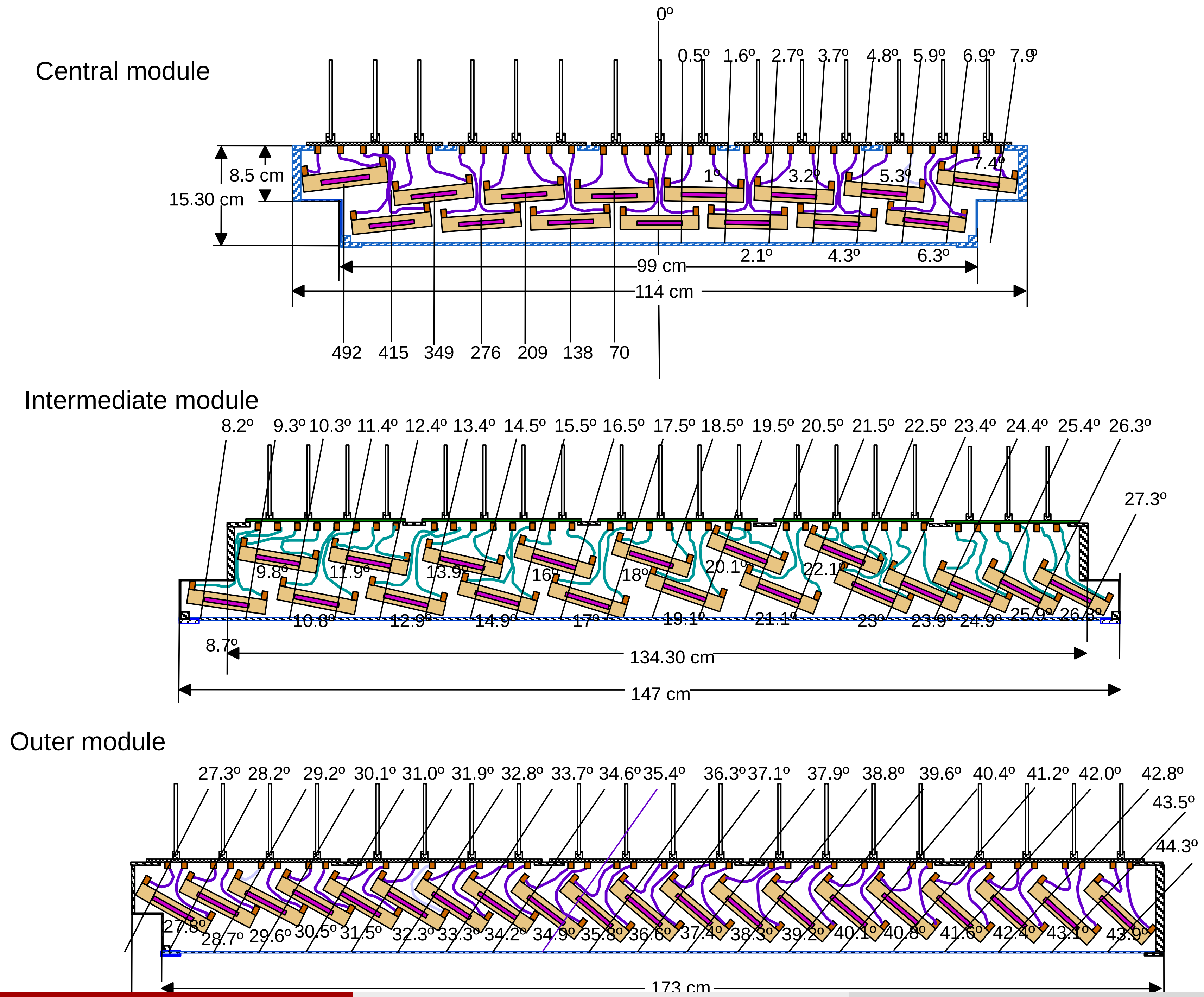

ALICE TOF time resolution

for full system one gets 80 ps resolution

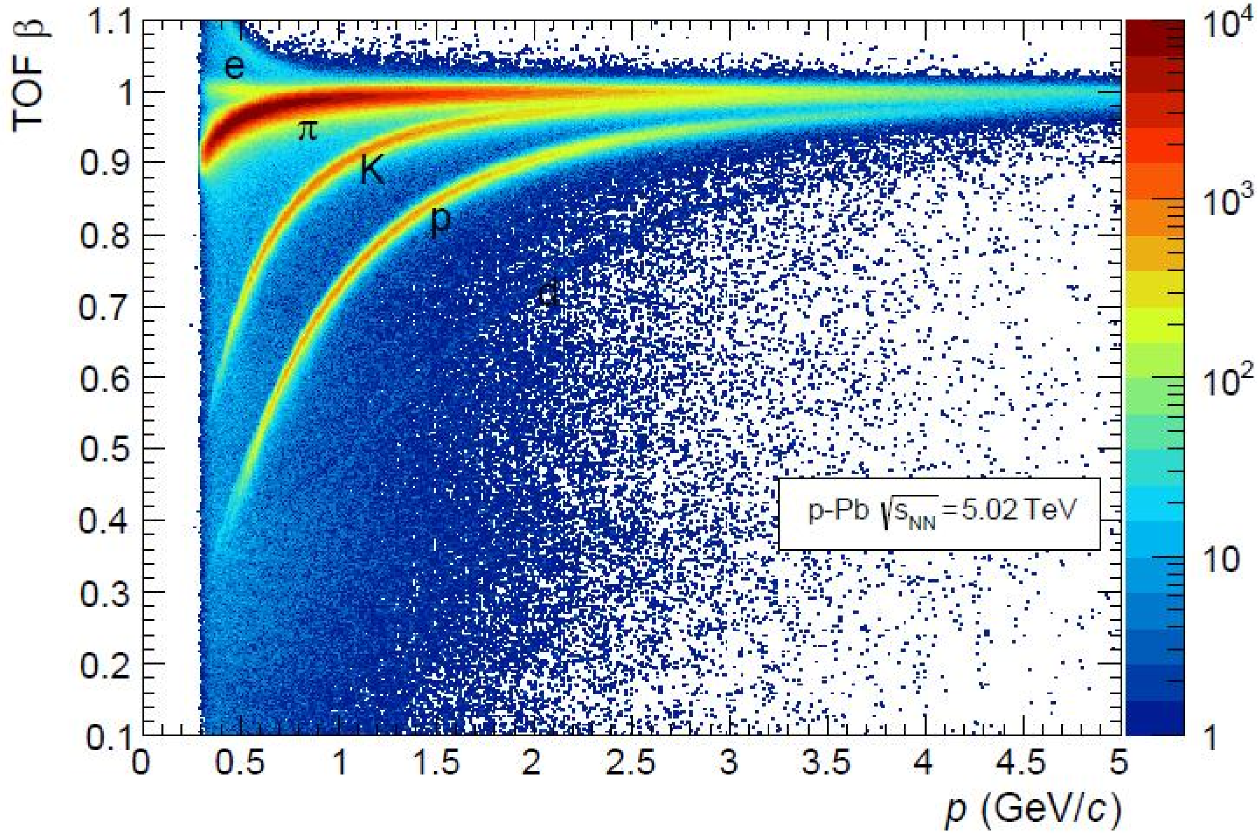

7.2 Specific energy loss

use drop and relativistic rise of d$E/$dx - easy at low momenta where differences are large

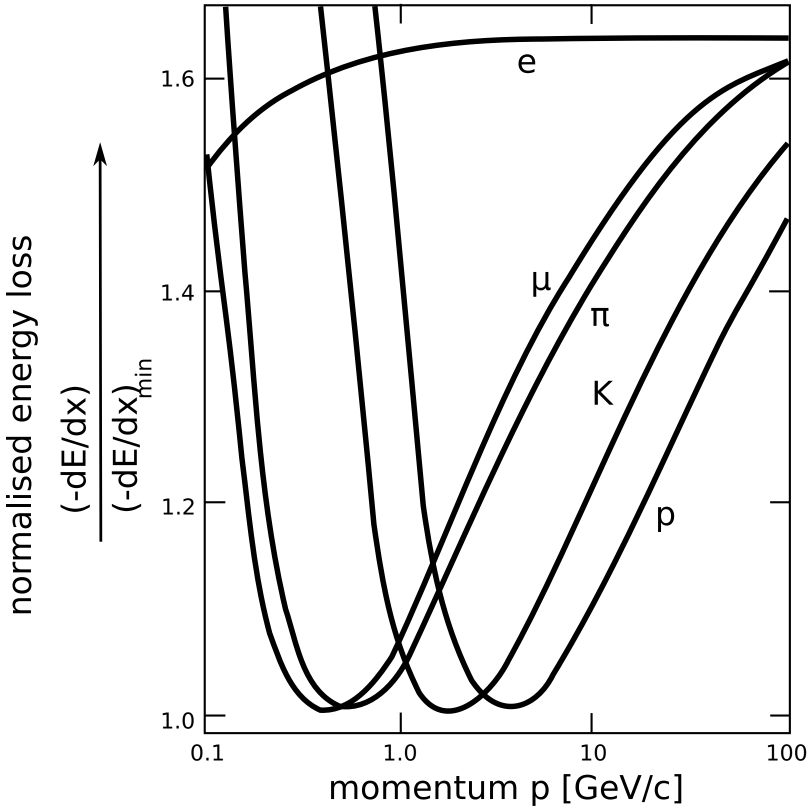

mean energy loss relative to minimum ionization, normally only μ/π separation excluded

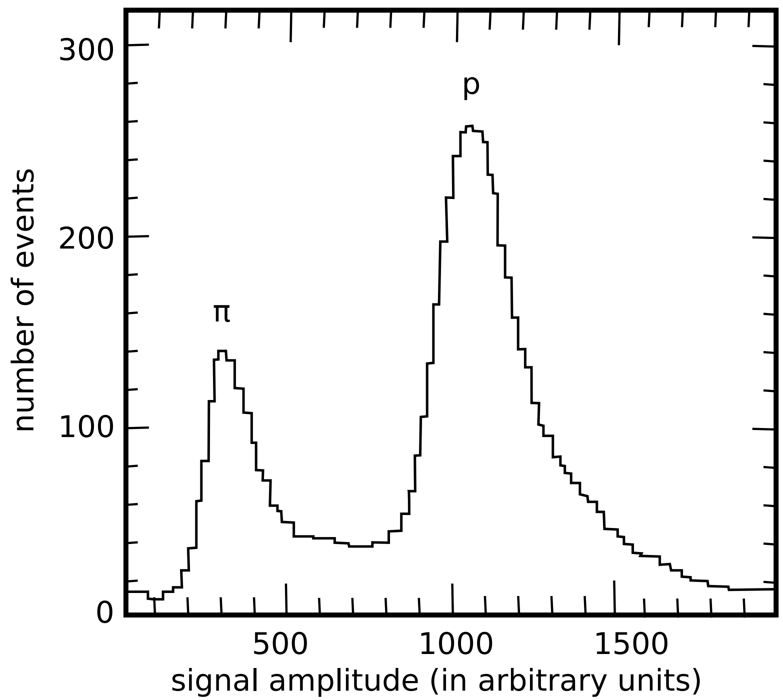

energy loss distribution for 600 MeV/c π and p in Si (3mm)
$p < p_{min.ion}$ for protons

is separation in region of relativistic rise possible?
normally, due to Landau tail, very large overlap of, e.g., pion and kaon

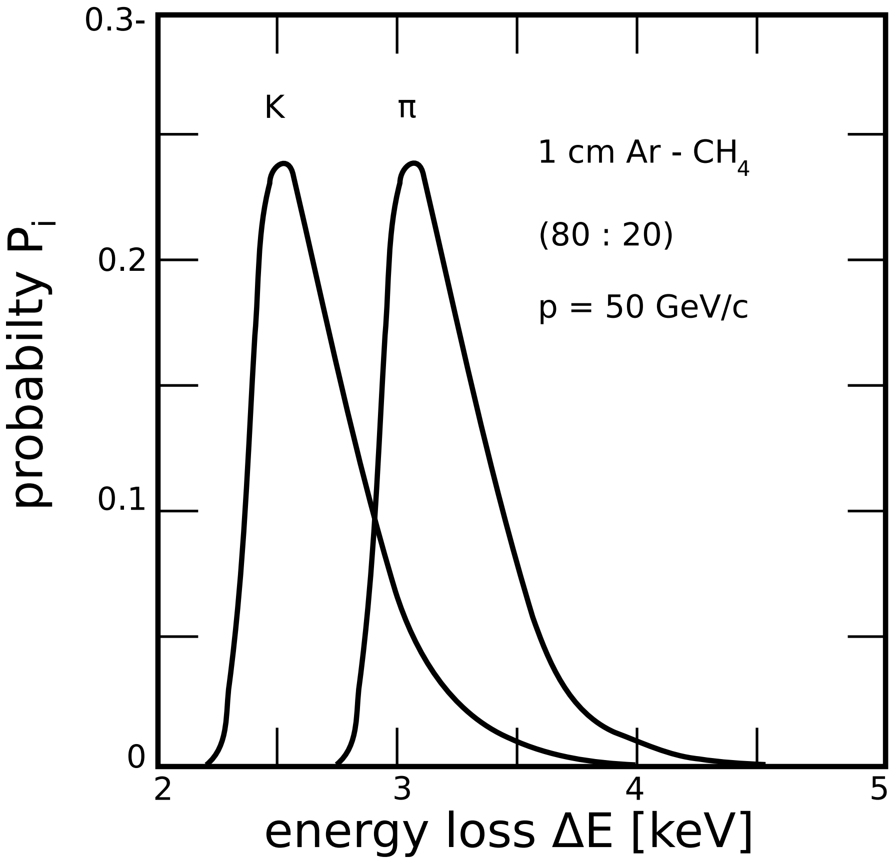

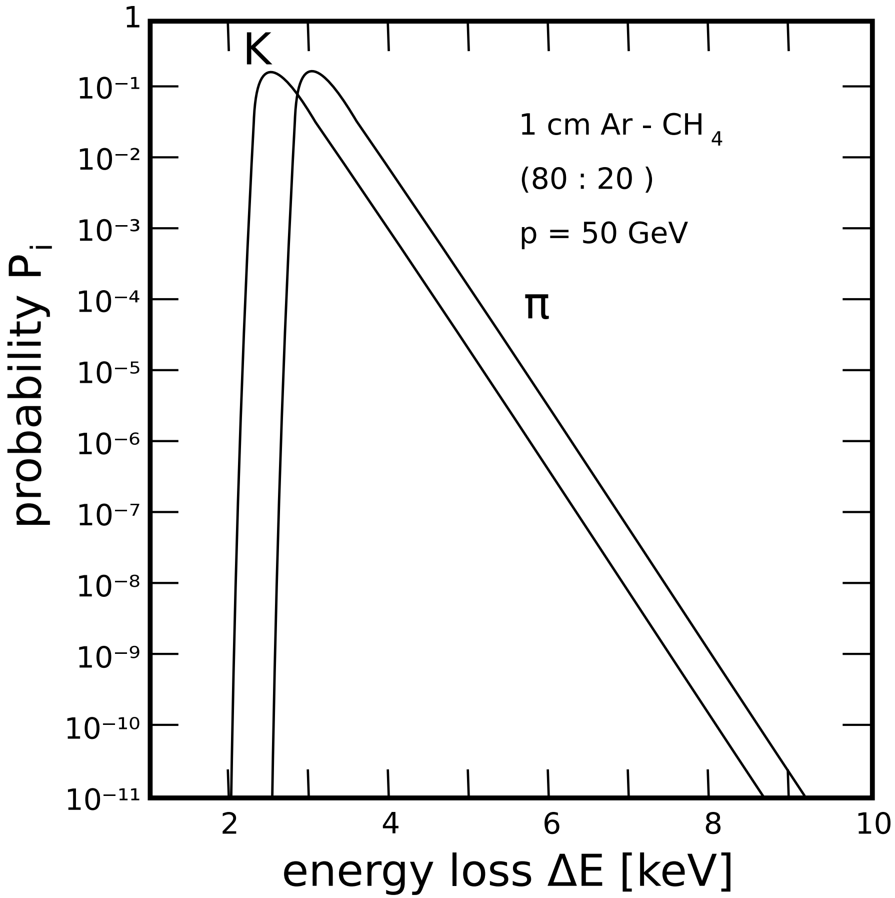

truncated mean method:
many measurements and truncation of the $30 - 50\%$ highest dE/dx values for each track

Alternative: 'likelihood'-method for several $\frac{dE}{dx}$-measurements

probability that pion produces a signal x: $p^i_\pi(x)$
for each particle measurements $x_1 \dots x_5$

probability for pion:

$$P_1 = \prod_{i=1}^{5} p^i_\pi(x_i)$$

probability for kaon:

$$P_2 = \prod_{i=1}^{5} p^i_K(x_i)$$

$$P_\pi = \frac{P_1}{P_1 + P_2}$$

$$\left.\begin{array}{l} P_1 = 7.1 \cdot 10^{-6} \\ P_2 = 1.5 \cdot 10^{-8} \end{array}\right\} \qquad P_\pi = 99.8\%$$

(see example on the right)

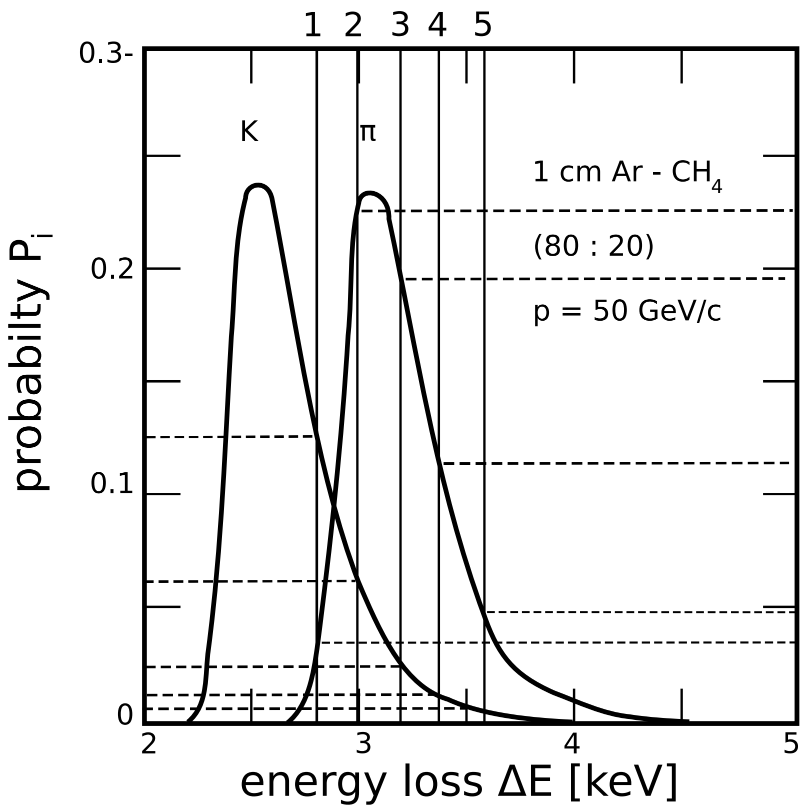

	1	2	3	4	5
p^i_K	0.123	0.061	0.025	0.013	0.006
p^i_π	0.031	0.236	0.192	0.108	0.047

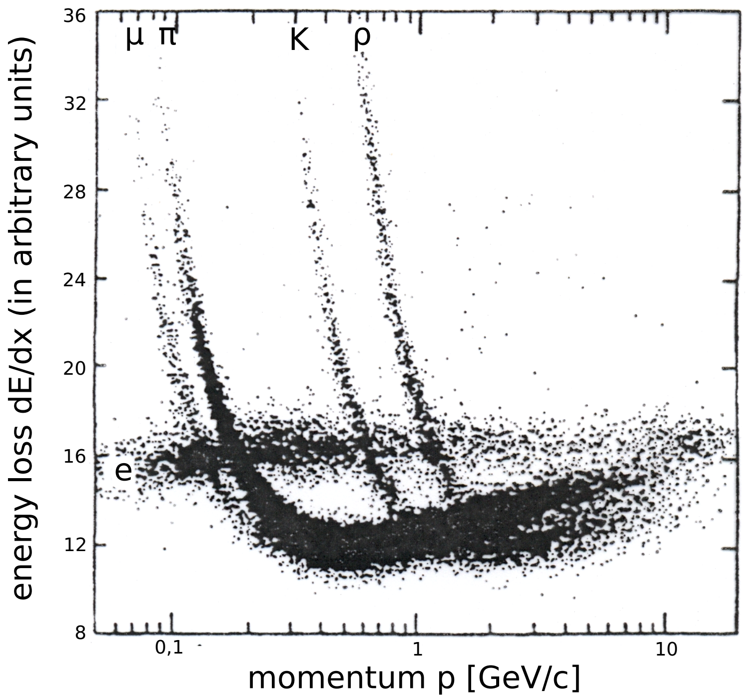

multiple energy loss measurement in TPC (TPC/Two-Gamma collaboration, LBNL 1988)

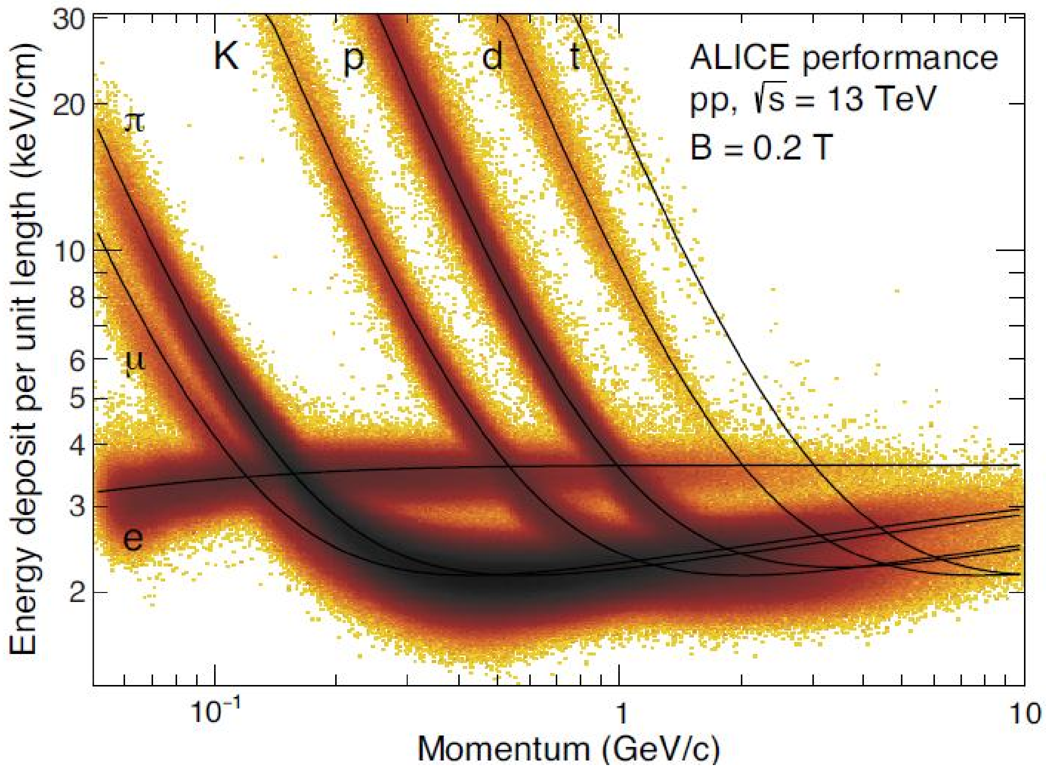

ALICE TPC $\sigma(dE/dx)/dE/dx$=5% ($Ne/C0_2/N_2$)

record: 3% have been reached (NA49 at SPS with Ar/CH_4, larger cells, and PEP-4/9 TPC at 8.5 bar)

7.3 Transition Radiation

effect: see chapter 2, particles with Lorentz factor $\gamma \gtrsim 1000$ emit X-ray photon when crossing from medium with one dielectric constant into another, probability of order α per boundary crossing

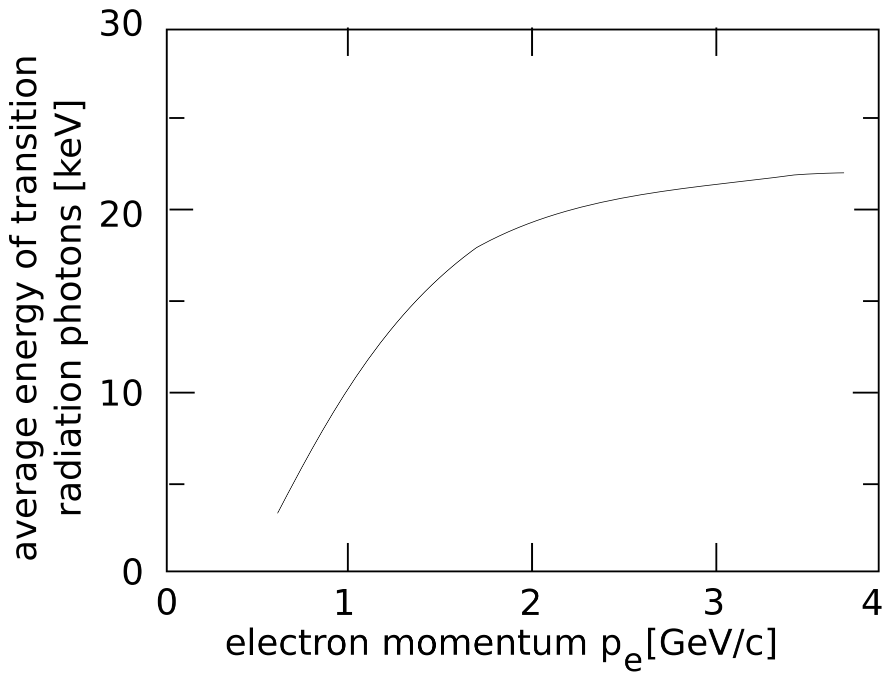

mean energy of transition radiation photon as function of electron momentum.

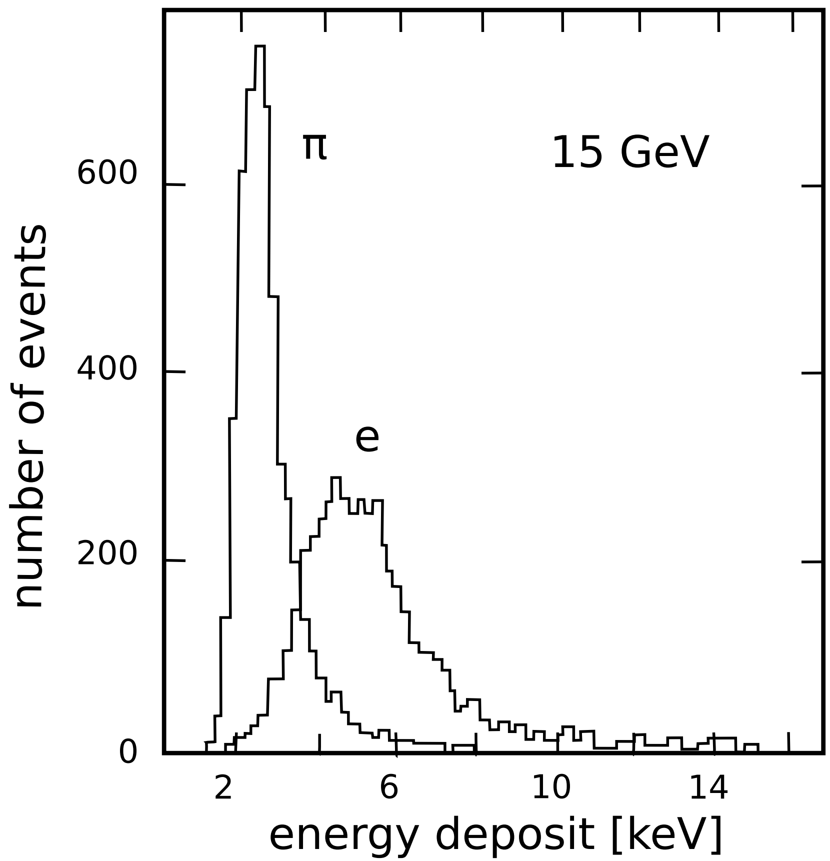

energy loss distribution for 15 GeV e, π in transition radiation detector

Transition radiation detector – TRD (schematic)

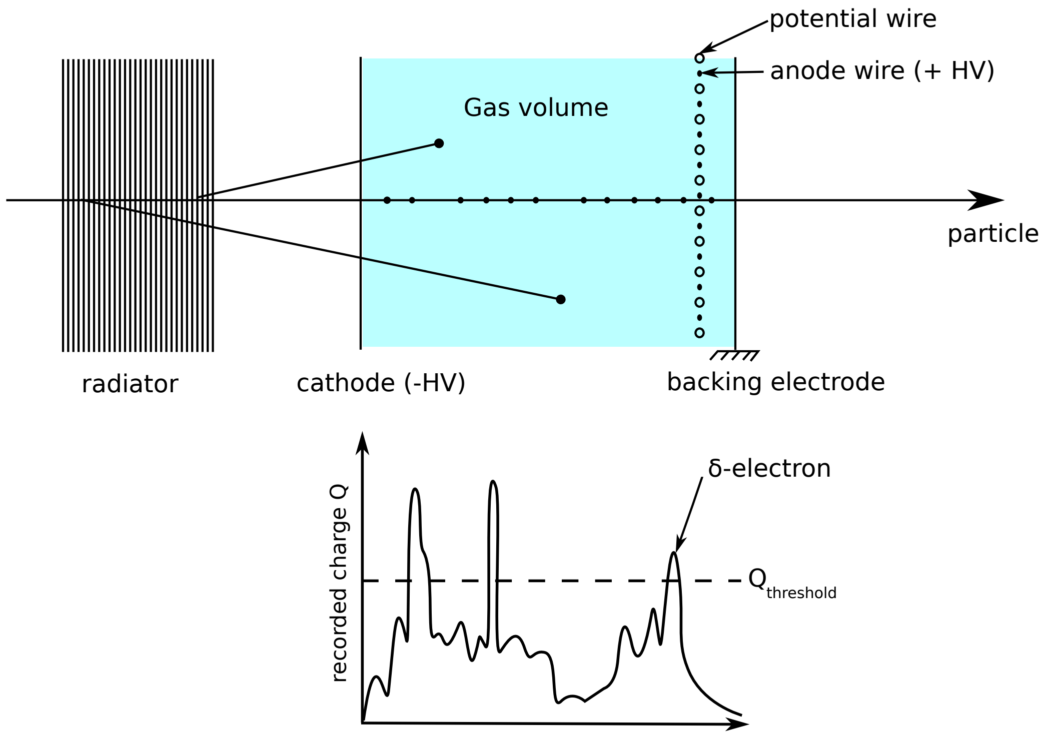

principle of separating ionization energy loss from the energy loss from emission of transition radiation photons

energy loss (excitation, ionization) plus transition radiation

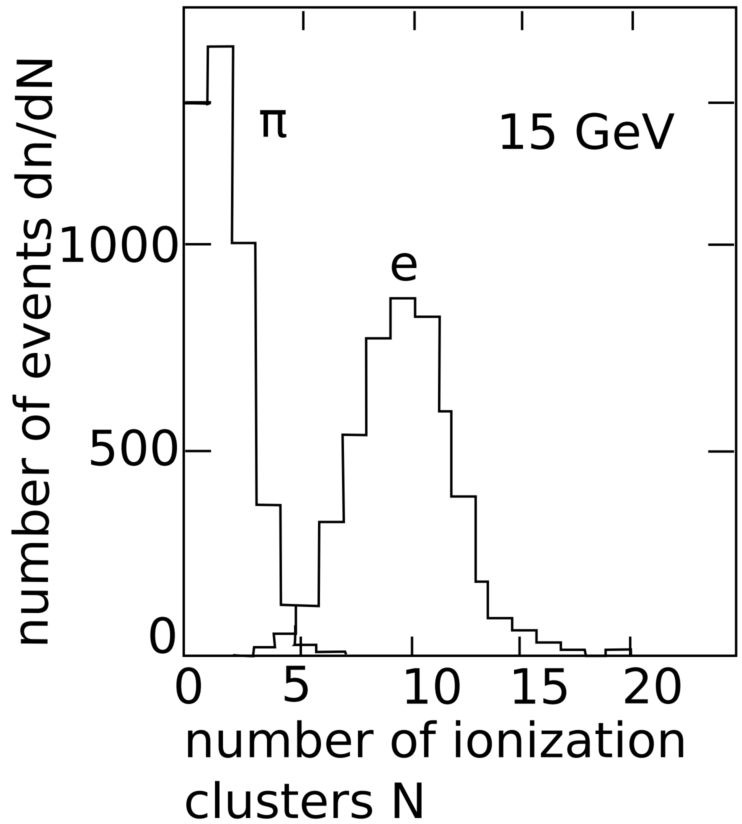

distribution of number of clusters above some threshold for 15 GeV e, π

e/π separation in a transition radiation detector

traditionally, two methods for electron discrimination

- total energy loss
- cluster counting method

novel type: ALICE TRD

- makes use of spatial information of TR absorption

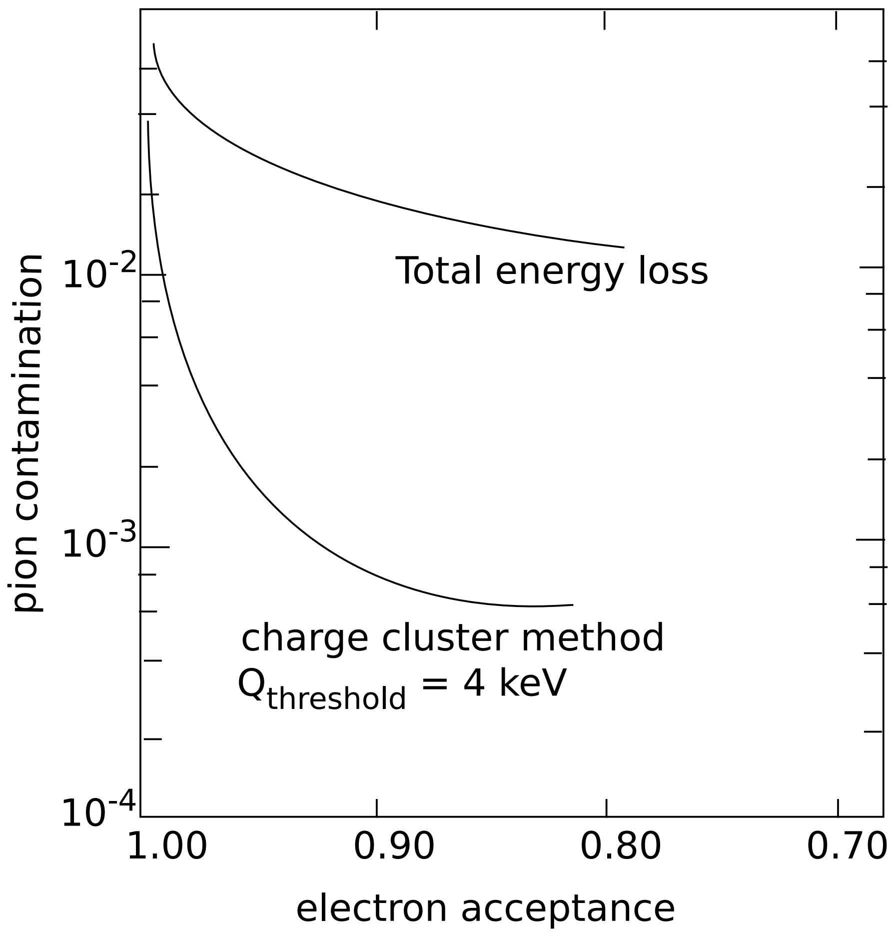

e/π separation at 15 GeV in a Li-foil radiator.

Application: ALICE TRD

radiator is followed by a gas detector that acts like a mini TPC: ionization and absorption of TR photon in 3 cm drift region, followed by amplification in MWPC with segmented cathode pad read-out, 20-30 time samples

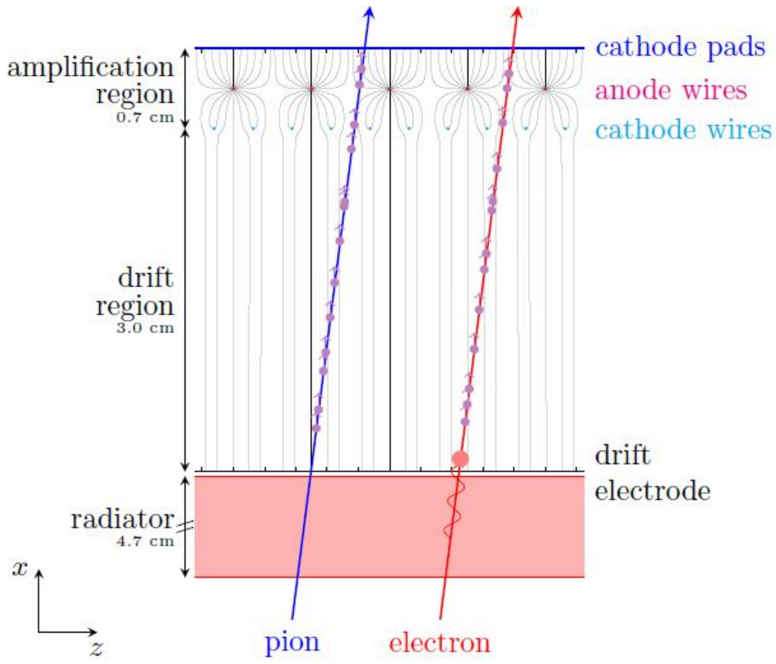

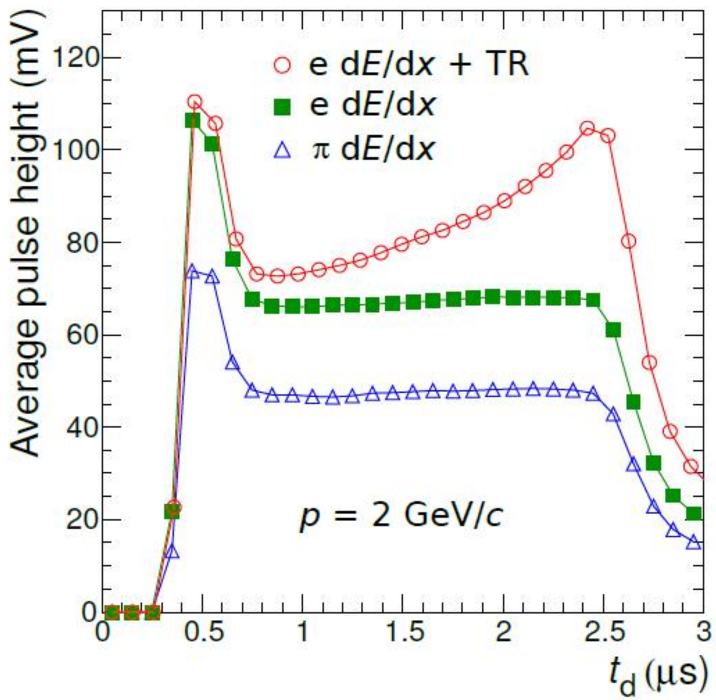

ALICE TRD performance

Combined energy loss by ionization and transition radiation
Nucl. Instr. Meth. **A881** (2018) 88-127, arXiv:1709.02743 [physics.ins-det]

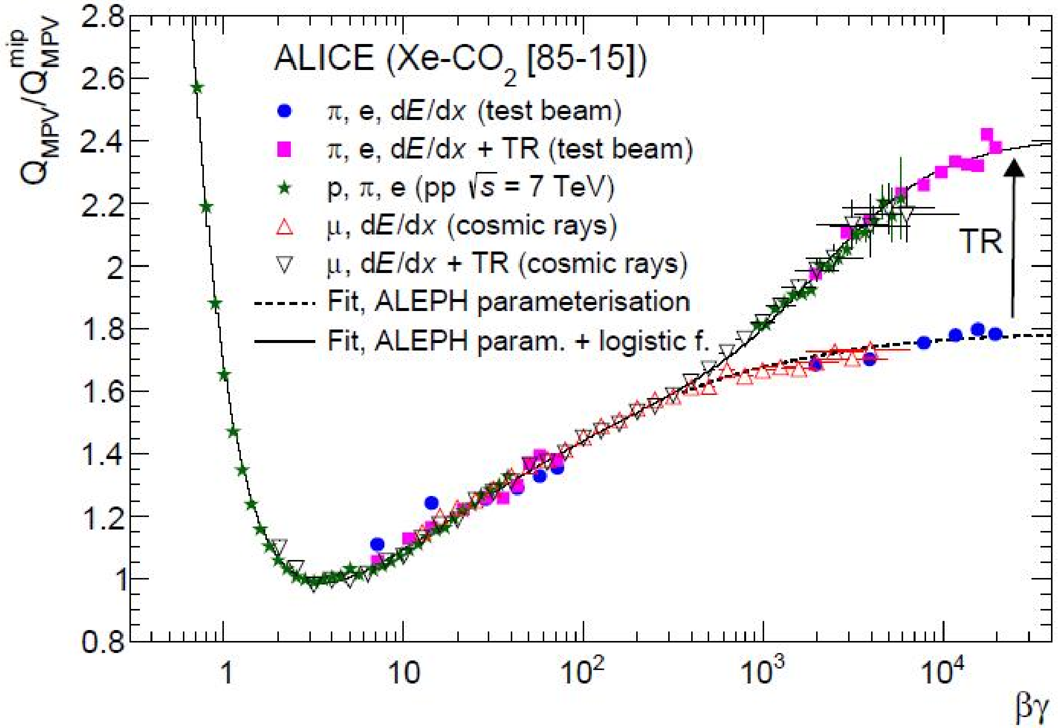

beyond $\beta\gamma = 500$ effect of transition radiation visible

ALICE TRD performance

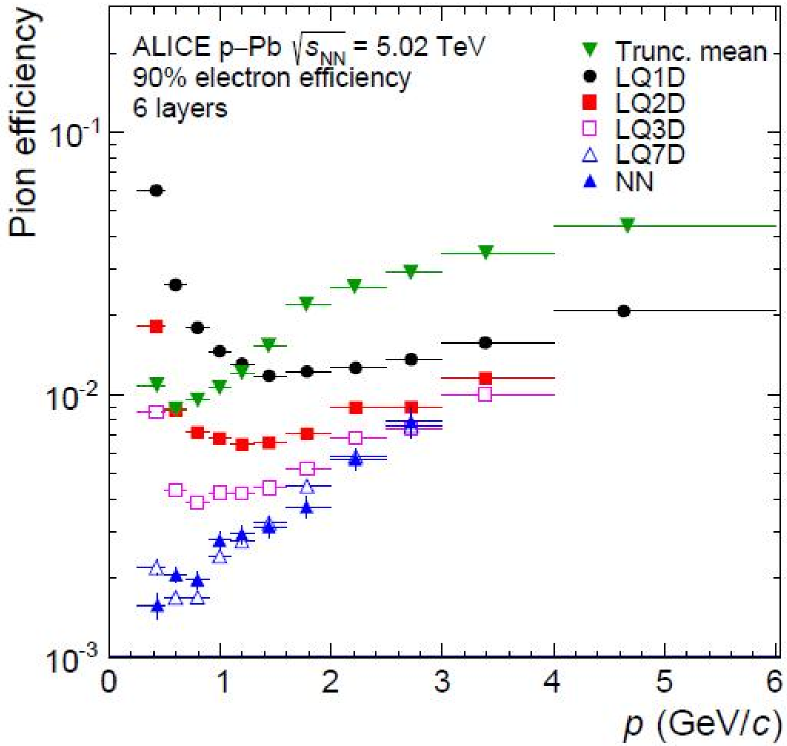

pion rejection with different algorithms around 1 GeV, pion supressed by 2 - 3 oom

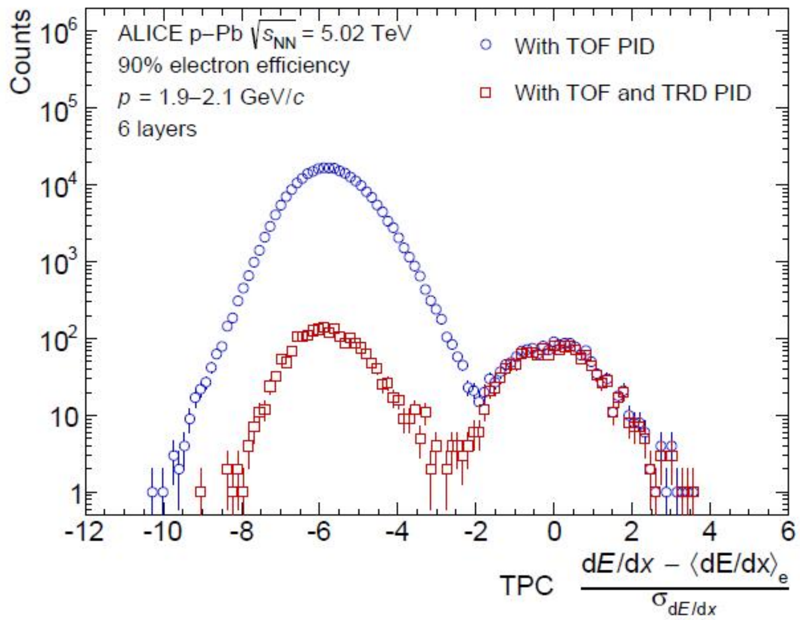

electron/pion identification with TPC, TRD, TOF

7.4. Cherenkov radiation

real photons emitted when $v > c/n$

$v < c/n$

induced dipoles symmetric, no net dipole moment

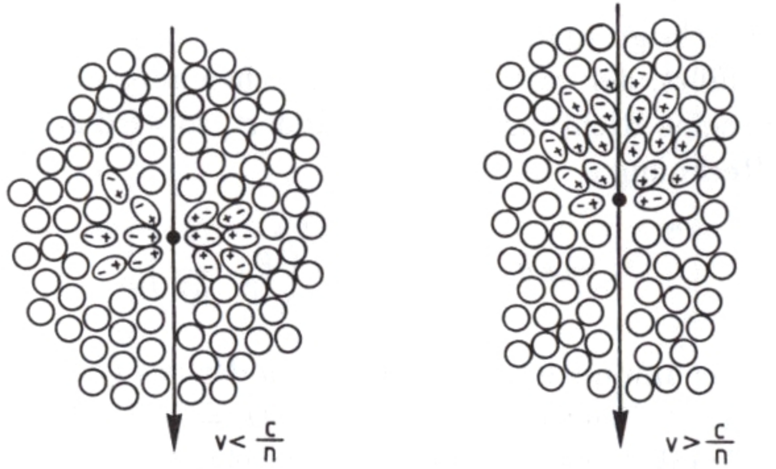

$v > c/n$

induced dipoles not symmetric $\rightarrow$ non-vanishing dipole moment

illustration of the Cherenkov effect

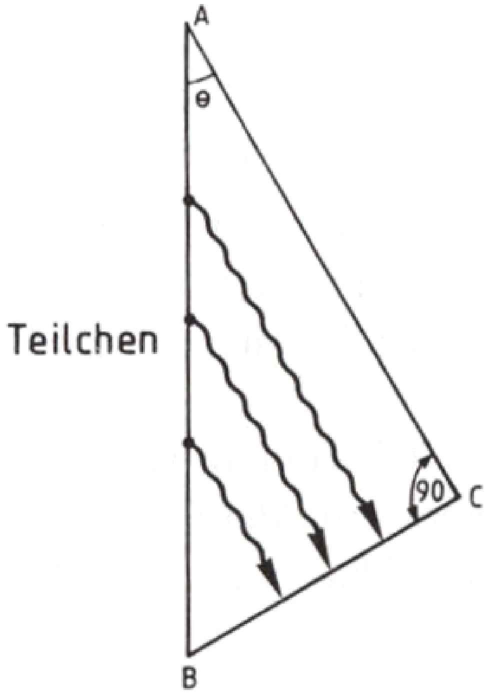

$$AB = \Delta t \beta c$$

$$AC = \Delta t \frac{c}{n}$$

$$\boxed{\cos\theta_c = \frac{1}{\beta n}}$$

simple geometric determination of the Cherenkov angle θ_c

threshold effect: radiation for $\beta > 1/n$, asymptotic angle $\theta_c = arc\cos\frac{1}{\beta n}$

number of Cherenkov photons per unit path length in interval $\lambda_1 - \lambda_2$ (see Chapter 2)

$$\frac{\mathrm{d}N_\gamma}{\mathrm{d}x} = 2\pi\alpha z^2 \int_{\lambda_1}^{\lambda_2}\left(1 - \frac{1}{n^2\beta^2}\right)\frac{d\lambda}{\lambda^2} \qquad (z = \text{charge in e})$$

in case of no dispersion (n const. in interval)

$$\frac{\mathrm{d}N_\gamma}{\mathrm{d}x} = 2\pi\alpha z^2 \sin^2\theta_c \frac{\lambda_2 - \lambda_1}{\lambda_1\lambda_2}$$

application of Cherenkov radiation for separation of particles with masses $m_1,\ m_2$ at constant momentum (say $m_1 < m_2$)

to distinguish: particle 1 above threshold $\beta_1 > 1/n$
particle 2 at most at threshold $\beta_2 = 1/n$ or $n^2 = \frac{\gamma_2^2}{\gamma_2^2 - 1}$

in $\lambda = 400 - 700$ nm range, lighter particle with $\gamma_1^2 \gg 1$ radiates

$$\frac{\mathrm{d}N_\gamma}{\mathrm{d}x} = 490\sin^2\theta_c$$

$$= 490\,\frac{(m_2c^2)^2 - (m_1c^2)^2}{p^2c^2}\text{photons per cm}$$

use $\sin^2\theta_c = 1 - \cos^2\theta_c = 1 - \frac{\gamma_2^2 - 1}{\beta_1^2\gamma_2^2} \approx \frac{1}{\gamma_2^2} - \frac{1}{\gamma_1^2}$

for radiator of length L in cm and quantum efficiency q of photocathode

$$N = 490 \frac{(m_2 c^2)^2 - (m_1 c^2)^2}{p^2 c^2} \cdot L \cdot q$$

and for threshold at N_0 photoelectrons

$$L = \frac{N_0 p^2 c^2}{490[(m_2 c^2)^2 - (m_1 c^2)^2] \cdot q} \text{ (cm)}$$

defines the necessary length of the radiator

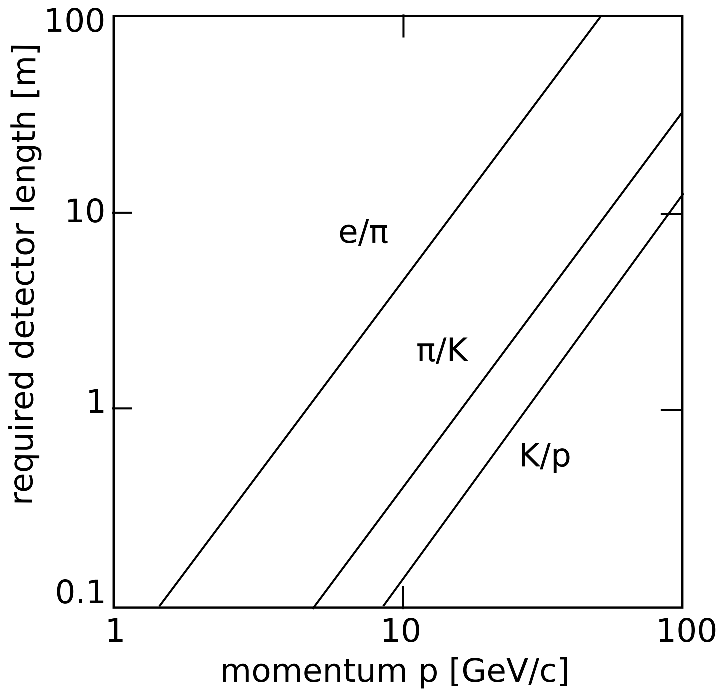

required detector length for $N_0 = 10$ and $q = 0.25$

π/K/p separation with Cherenkov detector: use several threshold detectors

p [GeV/c]	Particle	γ	$1/\beta$
10	π	71.9	1.0001
	K	20.3	1.0012
	p	10.6	1.0044

condition for no radiation:

$$\beta < \frac{1}{n} \quad \text{or}$$

$$\frac{1}{\beta} > n$$

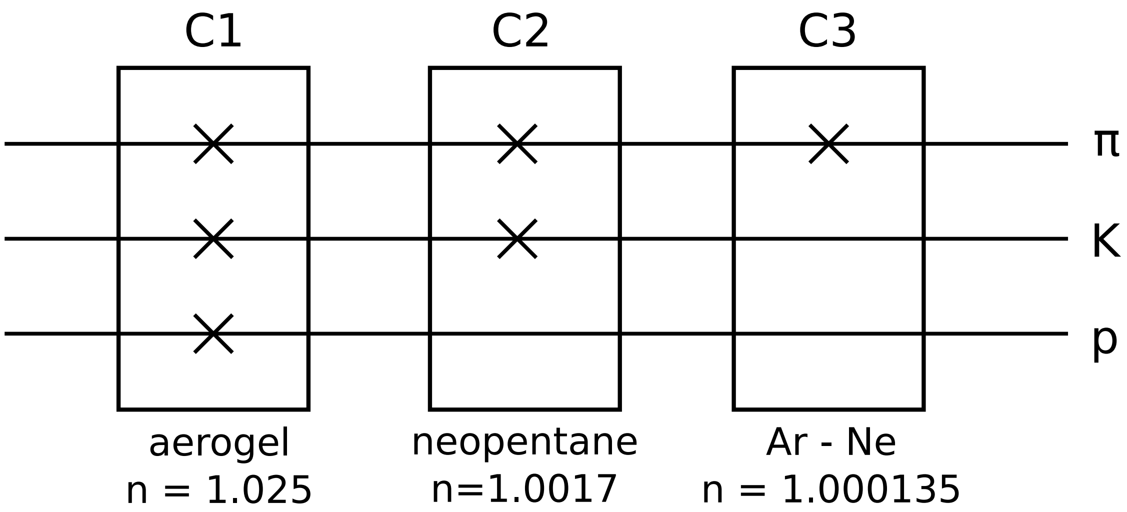

principle of particle identification by threshold Cherenkov counters (x represents production of Cherenkov photons)

π : $C1 \cdot C2 \cdot C3$ pion trigger
K : $C1 \cdot C2 \cdot \overline{C3}$ kaon trigger
p : $C1 \cdot \overline{C2} \cdot \overline{C3}$ proton trigger

Differential Cherenkov detectors

selection of velocity interval in which then actually velocity is measured
accept particles above threshold velocity $\beta_{min} = 1/n$
detect light for particles between β_{min} and a value β_t where light does not anymore propagate into (air) light guide by total reflection

$$\cos\theta_c = \frac{1}{n\beta}$$

the critical angle for total reflection:

$$\sin\theta_t = \frac{1}{n} \quad \rightarrow \quad \cos\theta_t = \sqrt{1 - \frac{1}{n^2}}$$

$$\Rightarrow \beta\text{-range} \qquad \frac{1}{n} < \beta < \frac{1}{\sqrt{n^2 - 1}}$$

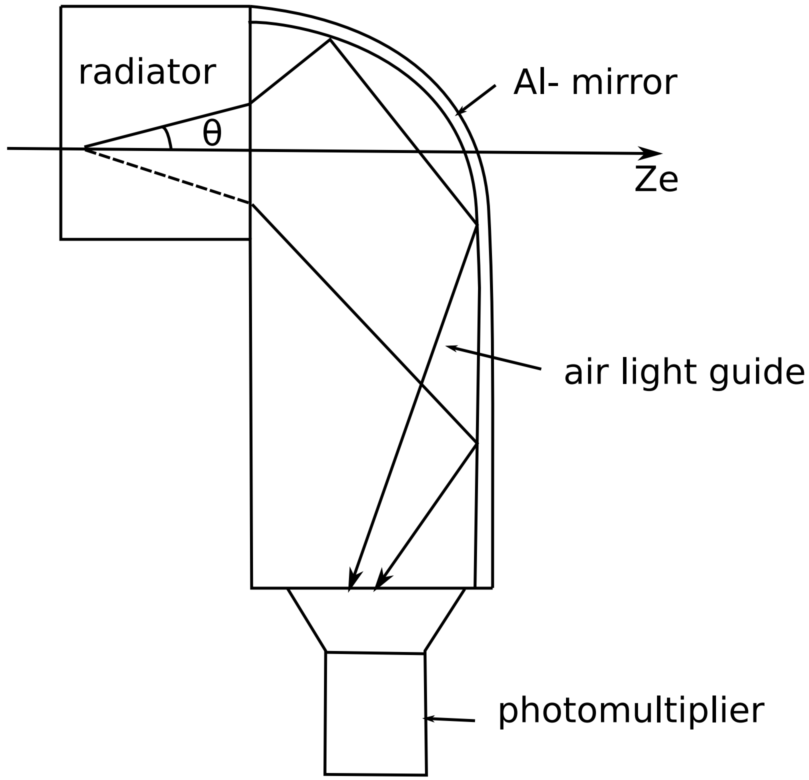

working principle of a differential Cherenkov counter

example: diamond $n = 2.42 \quad \Rightarrow \quad 0.41 < \beta < 0.454$, i.e. $\Delta\beta = 0.04$ window selected if optics of read-out such that chromatic aberrations corrected $\Rightarrow$ velocity resolution $\Delta\beta/\beta = 10^{-7}$ can be reached

principle of **DISC** (Discriminating Cherenkov counter)

Ring Imaging Cherenkov counter (RICH)

optics: such that photons emitted under certain angle θ form ring of radius r at image plane where photons are detected.
spherical mirror of radius R_S projects light onto spherical detector of radius R_D.

focal length of spherical mirror: $f = R_S/2$

place photon detector in focus: $R_D = R_S/2$

Cherenkov light emitted under angle θ_c

radius of Cherenkov ring at detector:

$$r = f \cdot \theta_c = \frac{R_s}{2}\theta_c$$

$$\Rightarrow \beta = \frac{1}{n\cos(2r/R_S)}$$

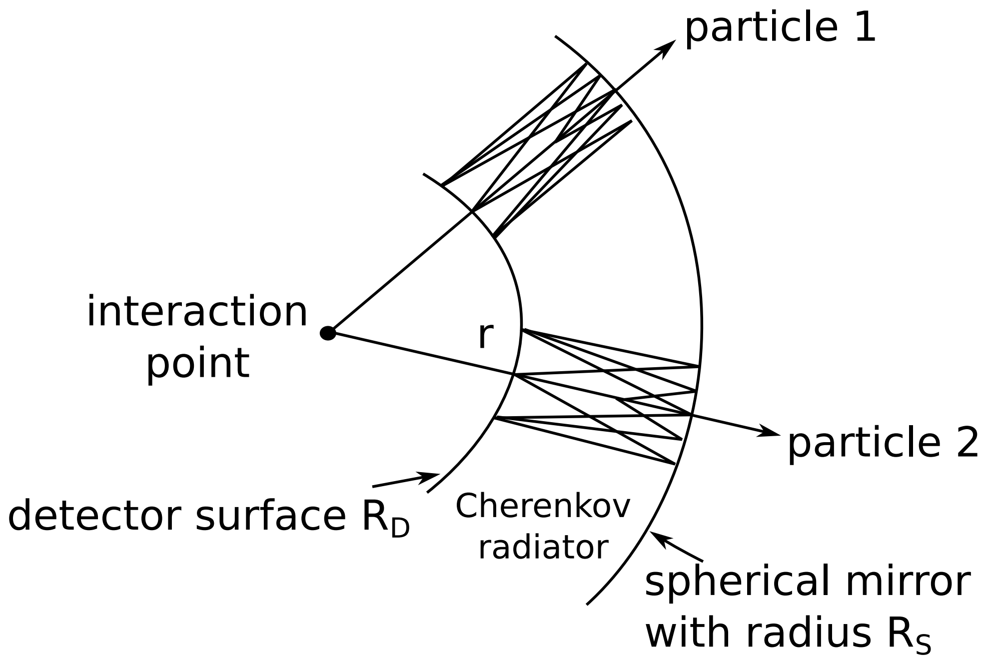

working principle of a RICH counter

photon detection:
- photomultiplier
- multi-wire proportional chamber or parallel-plate avalanche counter filled with gas that is photosensitive, i.e. transforms photons into electrons.
e.g. addition of TMAE vapor $(CH_3)_2N)_2C = C_5H_{12}N_2$ $E_{ion} = 5.4$ eV)
- or CsI coated cathode of MWPC (ALICE HMPID or hadron blind detector HBD in PHENIX)

example: K/π separation at $p = 200$ GeV/c

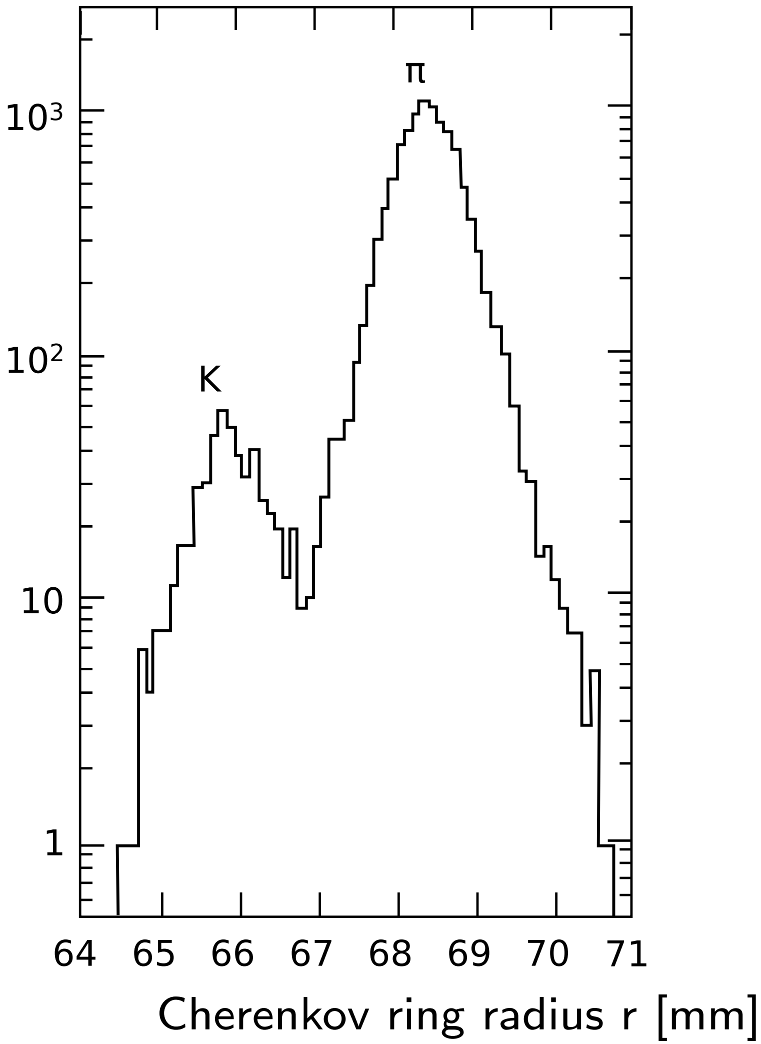

photons detected in MWPC filled with He (83%), methane (14%), TEA (triethyl-amine, 3%), CaF_2 entrance window (UV transparent)

event displays - CERES RICH

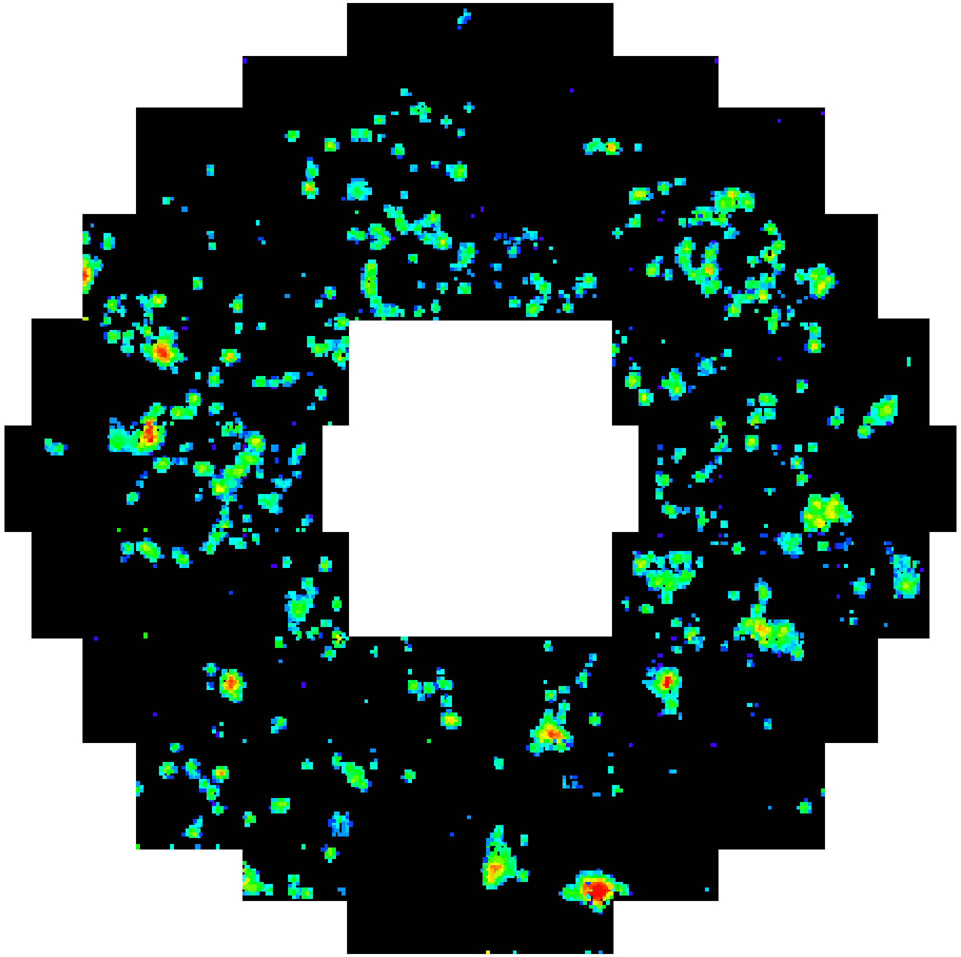

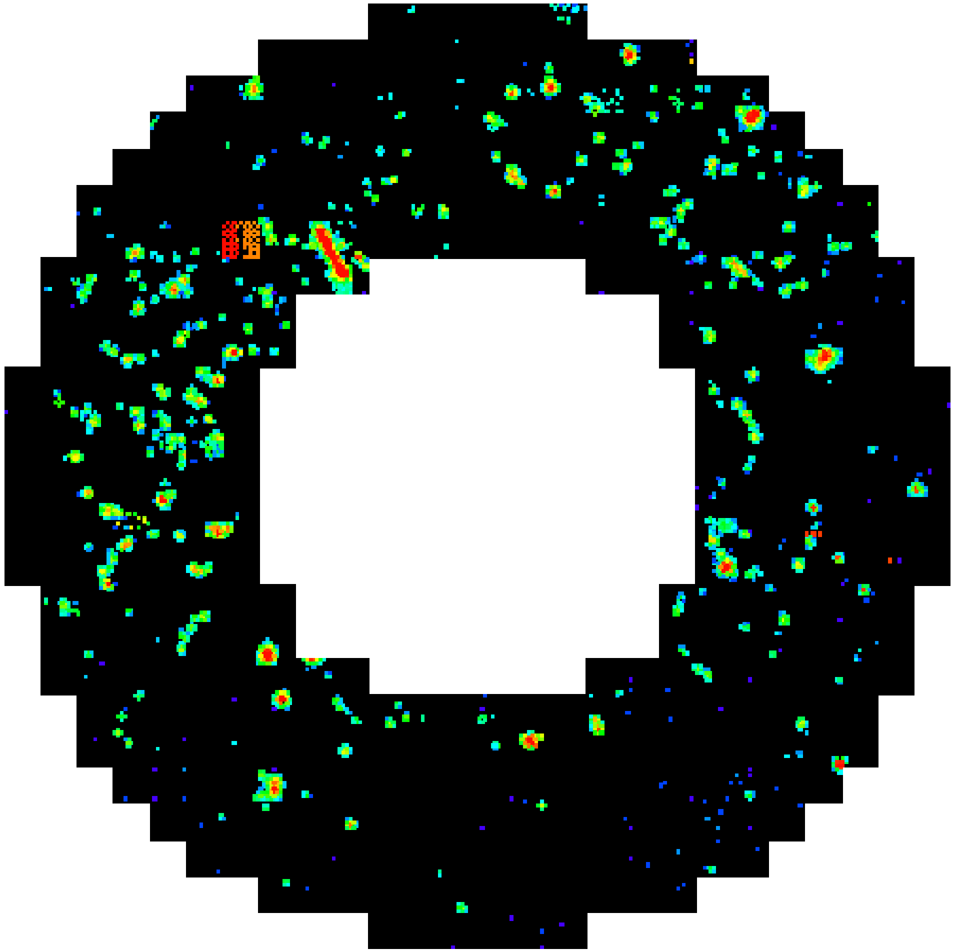

1 electron produces about 10 photons

CERES Electron Identification with TPC and RICH

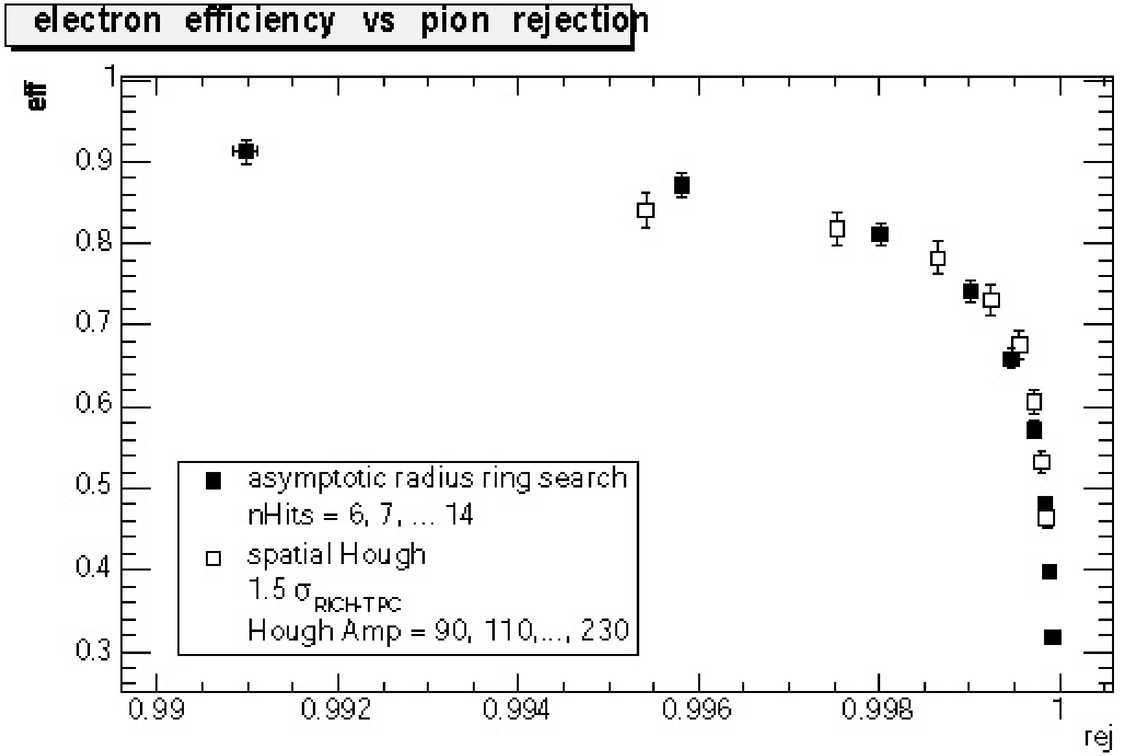

RICH π rejection vs. efficiency

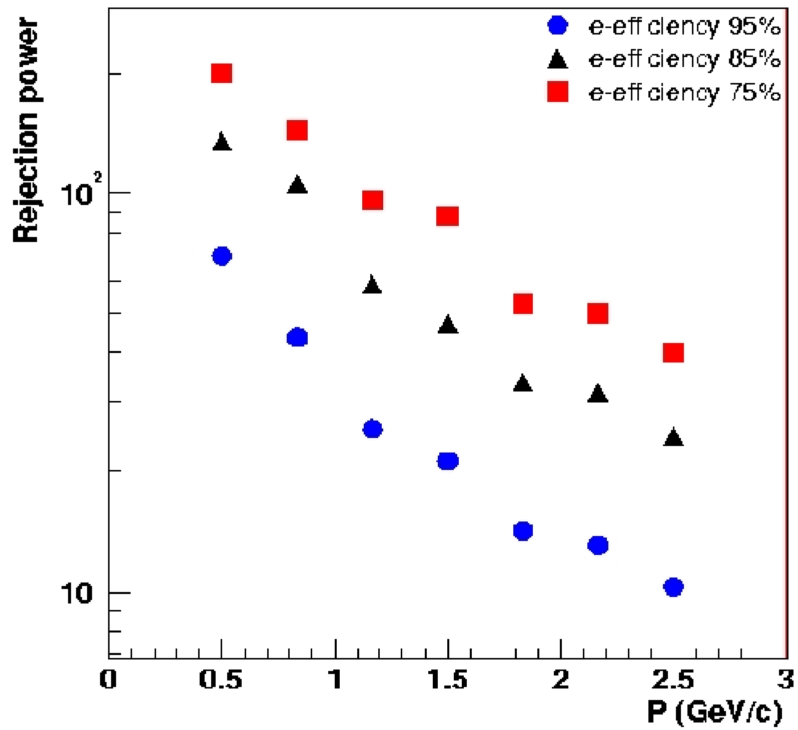

π rejection via TPC dE/dx

combined rejection - e.g. at 1.5 GeV/c at 67% e-efficiency $\rightarrow 4 \cdot 10^4$ π rejection

DIRC – Detection of Internally Reflected Cherenkov Light

collection and imaging of light from total internal reflection (rather than transmitted light)
optical material of radiator used in 2 ways simultaneously:
- Cherenkov radiator
- light guide for Cherenkov light trapped in radiator by total int. reflection

advantage: photons of ring image can be transported to a detector away from path of radiating particle
intrinsically 3d, position of hit $\rightarrow \theta_c, \phi_c$ and time $\rightarrow$ long. position

example: BABAR at SLAC

- rectangular radiator from fused silica
n=1.473
radiation hard, long attenuation length, low chromatic dispersion, excellent optical finish possible
- surrounded by nitrogen n≈1.00
- stand-off box filled with water n=1.346 (close to radiator)

NIM A538 (2005) 281

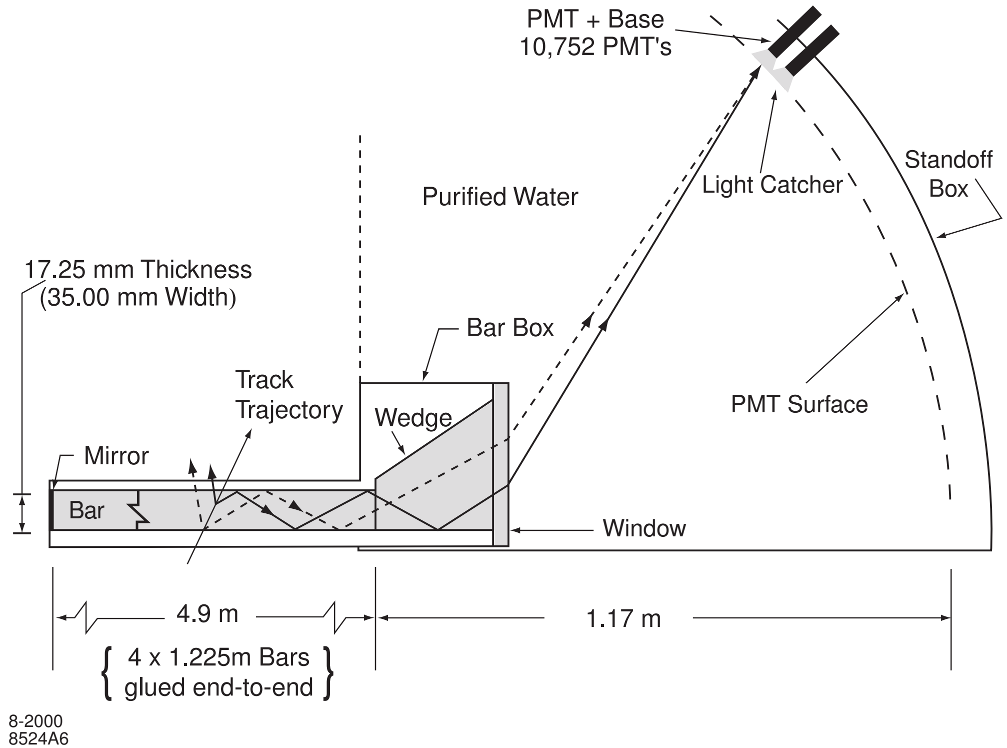

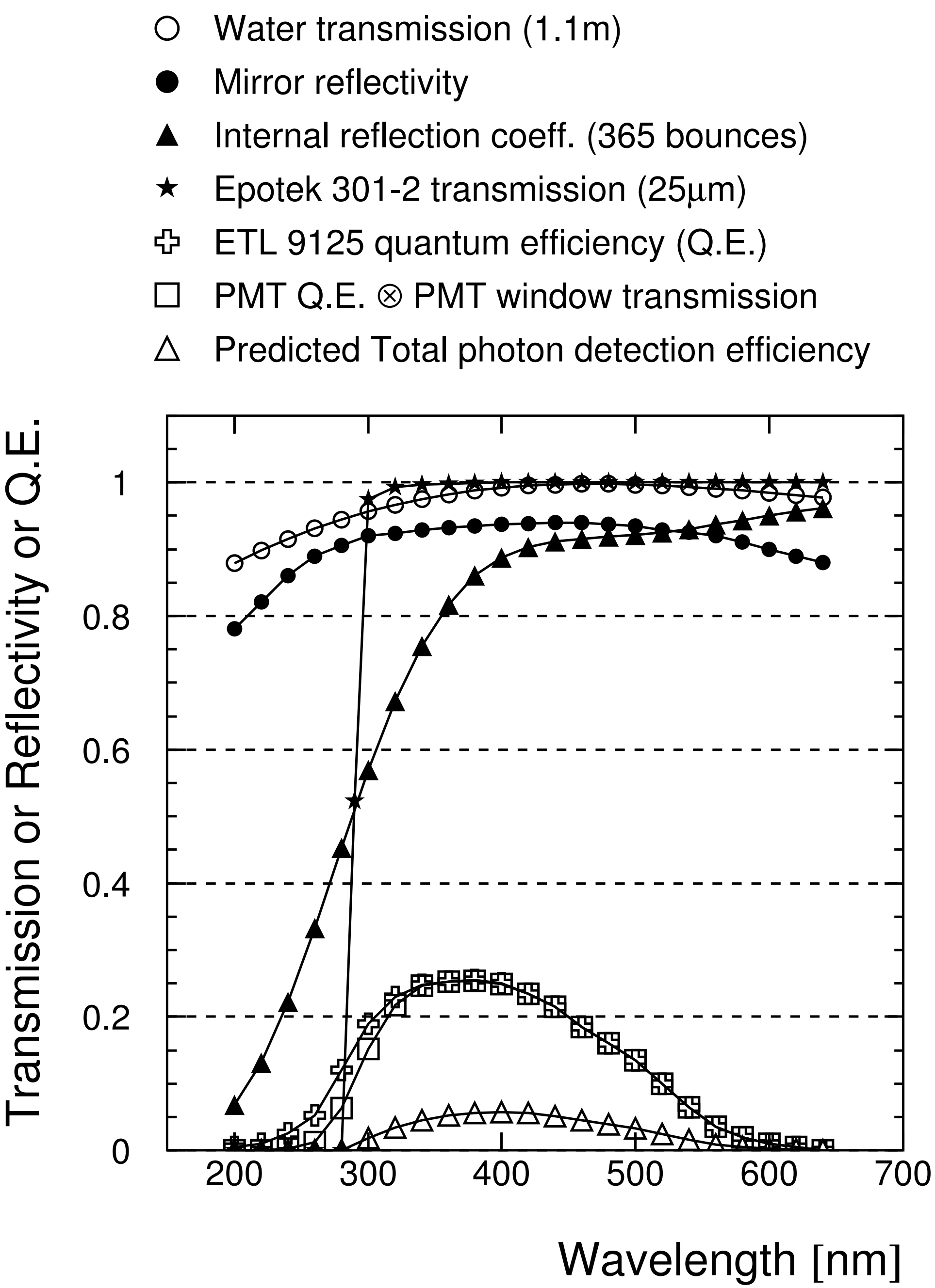

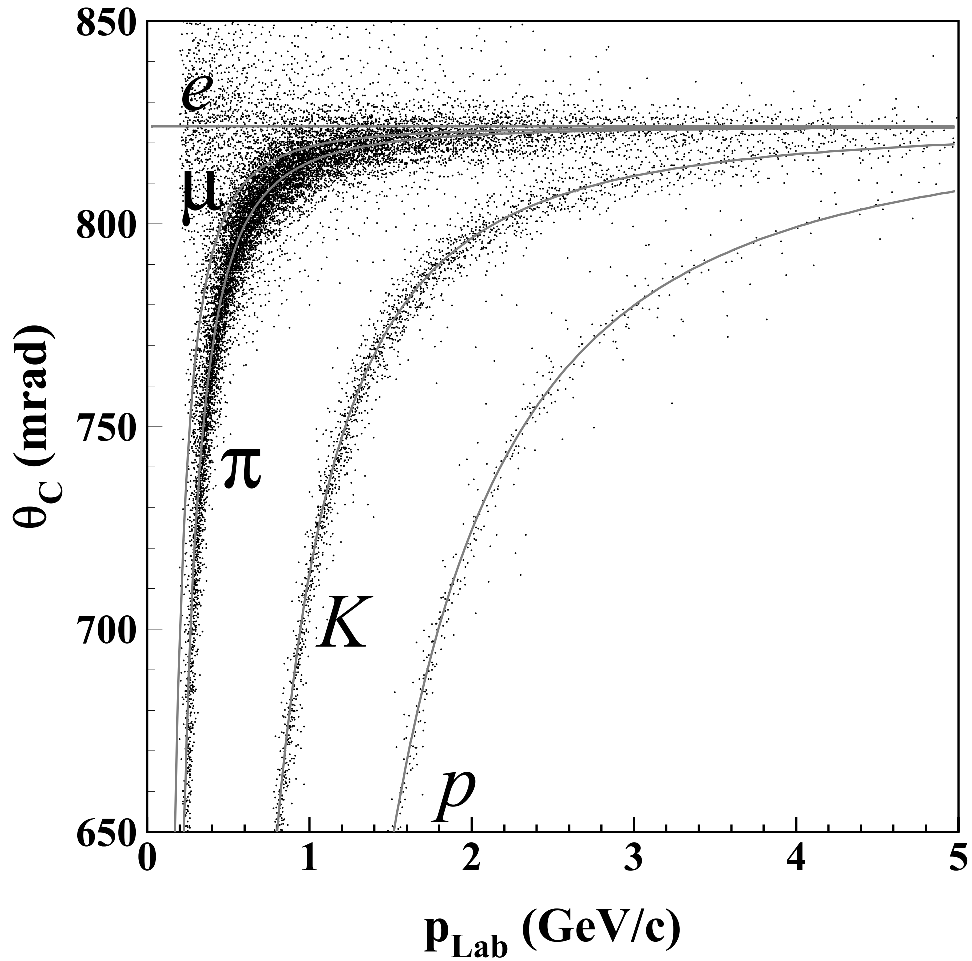

kaons can be separated up to 4 GeV/c

BABAR physics: decays of B^0 to study CP violation

b-tagging (78 % of $B^0 \to K^+ + X$)

golden channel for CP: $B^0 \to J/\psi + \phi$

and $\phi \to K^+ + K^-$

Comparision different PID methods for K/π separation

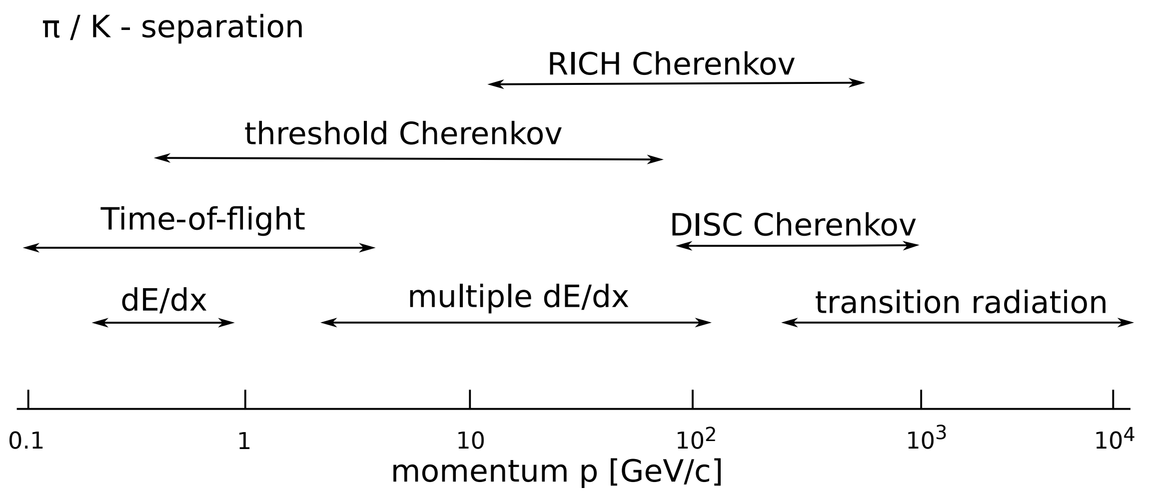

illustration of various particle identification methods for K/π separation along with characteristic momentum ranges.

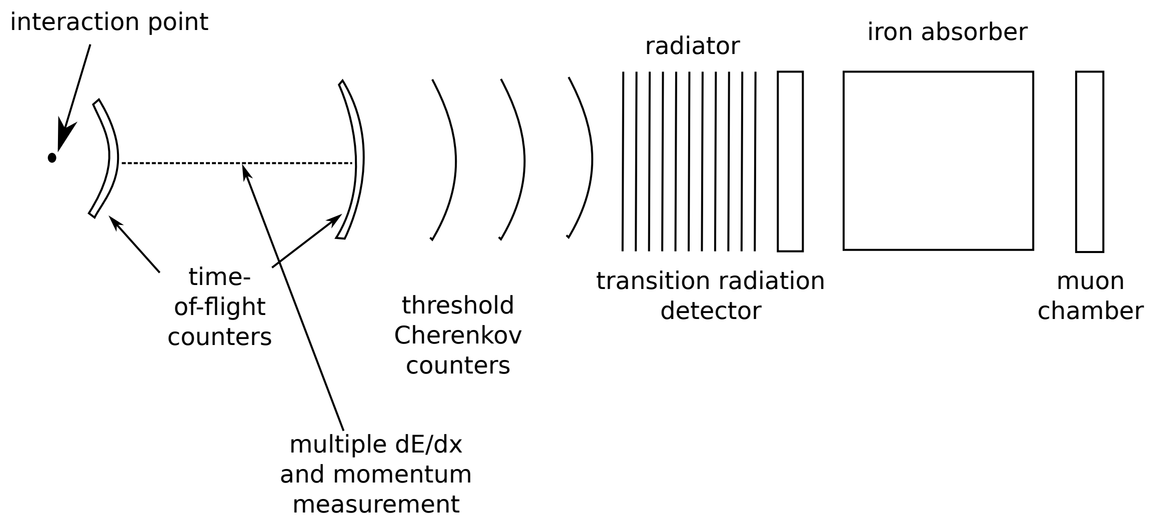

a detector system for PID combines usually several methods

8.1 General considerations - calorimeter

energy vs. momentum measurement

resolution:

calorimeter: $\frac{\sigma_E}{E} \propto \frac{1}{\sqrt{E}}$

tracking detectors: $\frac{\sigma_p}{p} \propto p$

e.g.: at $E \simeq p = 100$ GeV: $\frac{\sigma_E}{E} \simeq 3.5\%$ (ZEUS), $\frac{\sigma_p}{p} \simeq 6\%$ (ALEPH)

- at very high energies eventually have to switch to calorimeter because resolution improves with energy, while magnetic spectrometer resolution decreases
- depth of shower $L \propto \ln \frac{E}{E_0}$
- magnetic spectrometer (see chapter 6) $\frac{\sigma_p}{p} \propto \frac{p}{L^2} \rightarrow$ length would have to grow quadratically to keep resolution const. at high momenta
- calorimeter can cover full solid angle, for tracking in magnetic field anisotropy
- fast timing signal from calorimeter $\rightarrow$ trigger
- identification of hadronic vs. electromagnetic shower by segmentation in depth

8.2 Electromagnetic shower

alternating generations of pair formation and bremsstrahlung

reminder: electrons loose energy by excitation/ionization of atoms and by bremsstrahlung

for bremsstrahlung:
$$\begin{aligned} \frac{\mathrm{d}E}{\mathrm{d}x} &= -\frac{E}{X_0} \qquad \text{with } X_0 \equiv \text{ radiation length} \\ E &= E_0 \exp(-x/X_0) \end{aligned}$$

for sufficiently high energies: since $(\mathrm{d}E/\mathrm{d}x)_{ion} \propto 1/\beta^2$ falls until $\beta\gamma \approx 3$ towards high energies and the logarithmic rise is weak

$$\frac{\left(\frac{\mathrm{d}E}{\mathrm{d}x}\right)_{brems}}{\left(\frac{\mathrm{d}E}{\mathrm{d}x}\right)_{ion}} \approx \frac{ZE}{580\ \mathrm{MeV}}$$

critical energy E_c:
$$\left(\frac{\mathrm{d}E}{\mathrm{d}x}(E = E_c)\right)_{ion} = \left(\frac{\mathrm{d}E}{\mathrm{d}x}(E = E_c)\right)_{brems}$$

and for $E > E_c$ bremsstrahlung dominates

will see below that also transverse size is determined by radiation length via the Moliere Radius R_M:

$$R_M = \frac{21.2\ MeV}{E_c} \cdot X_0$$

Relevant parameters for electromagnetic shower

material	Z	X_0 [g cm^{-2}]	X_0 [cm]	E_c [MeV]	R_M [cm]
plastic scint.			34.7	80	9.1
Ar (liquid)	18	19.55	13.9	35	9.5
Fe	26	13.84	1.76	21	1.77
BGO		7.98	1.12	10	2.33
Pb	82	6.37	0.56	7.4	1.60
U	92	6.00	0.32	6.8	1.00
Pb glass (SF5)			2.4	11.8	4.3

Analytic shower Model

a high energy electron enters matter

- electron looses energy by bremsstrahlung
- photon is absorbed by pair production

Monte-Carlo simulation of electromagnetic shower

$$\begin{aligned} \gamma + \text{ nucleus} &\rightarrow e^+ + e^- + \text{ nucleus} \\ e + \text{ nucleus} &\rightarrow e + \gamma + \text{ nucleus} \end{aligned}$$

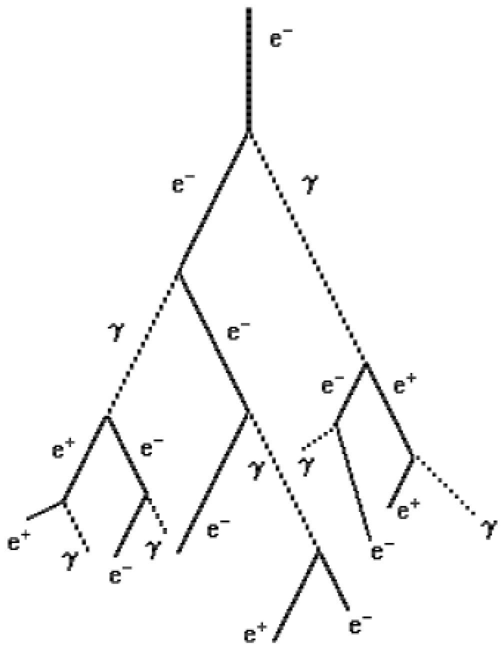

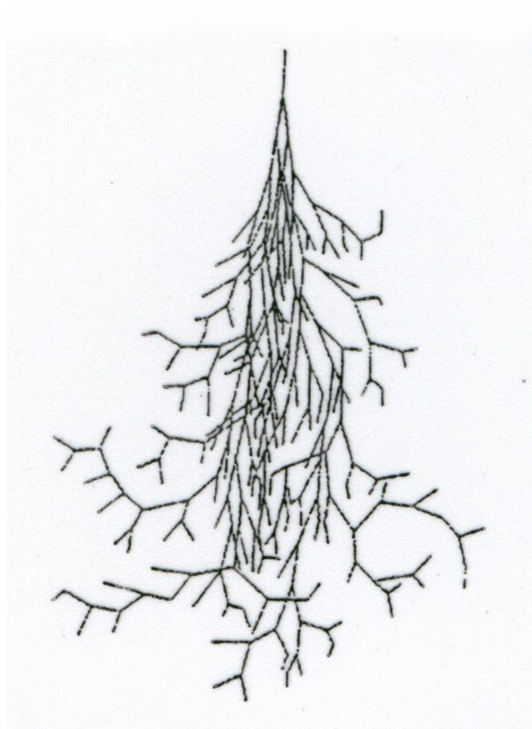

approximate model for electromagnetic shower

- over distance X_0 electron reduces via bremsstrahlung its energy to one half $E_1 = E_0/2$
- photon materializes as e^+e^- after X_0, energy of electron and positron $E_\pm \simeq E_0/2$ (precisely : $\mu_p = \frac{7}{9}X_0$ or pair creation probability in $X_0 \rightarrow P = 1 - \exp(-\frac{7}{9}) = 0.54$)

assume:
– for $E > E_c$ no energy loss by ionization/excitation
– for $E < E_c$ electrons loose energy only via ionization/excitation

- important quantities to characterize the em. shower

  number of particles in shower
  location of shower maximum
  longitudinal shower distribution
  transverse shower distribution (width)

introduce longitudinal variable $t = x/X_0$

number of shower particles after traversing depth t: $N(t) = 2^t$

each particle has energy $E(t) = \frac{E_0}{N(t)} = \frac{E_0}{2^t} \quad \rightarrow \quad t = \ln \frac{E_0}{E} / \ln 2$

total number of charged particles with energy E_1 $\quad N(E_0, E_1) = 2^{t_1} = 2^{\ln(E_0/E_1)/\ln 2} \simeq E_0/E_1$

number of particles at shower maximum $\quad N_{max}(E_0, E_c) \simeq E_0/E_c \propto E_0$

shower maximum located at $\quad t_{max} \propto \ln \frac{E_0}{E_c}$

– numerical values: for $E_0 = 1$ GeV in Fe $\rightarrow N_{max} \simeq 45$ and $t_{max} \simeq 5.5$ or $x_{max} \simeq 10$ cm

integrated track length of all charged particles in shower

$$T = X_0 \sum_{\mu=0}^{t_{max}} 2^\mu + t_0 X_0 N_{max} \qquad \text{with range } t_0 \text{ of electron with energy } E_c \text{ in units of } X_0$$

$$= (2 + t_0)\frac{E_0}{E_c} X_0 \propto E_0 \qquad \text{proportional to } E_0!$$

this was for all particles, for practical purposes for charged particles: $T = \frac{E_0}{E_c} X_0 F$ with $F < 1$

Transverse shower development

- emission of Bremsstrahlung under angle $\langle\theta^2\rangle \simeq \dfrac{1}{\gamma^2}$ small
- multiple scattering (in 3d) of electron in Moliere theory

$$\langle\theta^2\rangle = \left(\frac{19.2MeV}{\beta\ pc}\right)^2 t$$

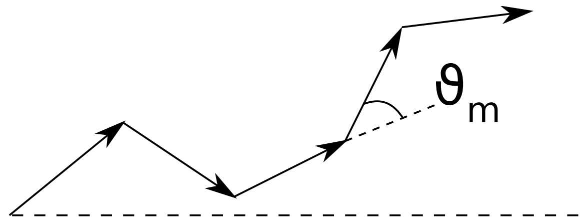

multiple scattering dominates transverse shower development
main contrib. from low energy electrons, assuming approximate range of electrons to be X_0

$$\text{Moliere radius}\quad R_M = \sqrt{\langle\theta^2\rangle_{x=X_0}}X_0 \approx \frac{19.2\text{ MeV}}{E_c}X_0$$

a 6 GeV electron in lead

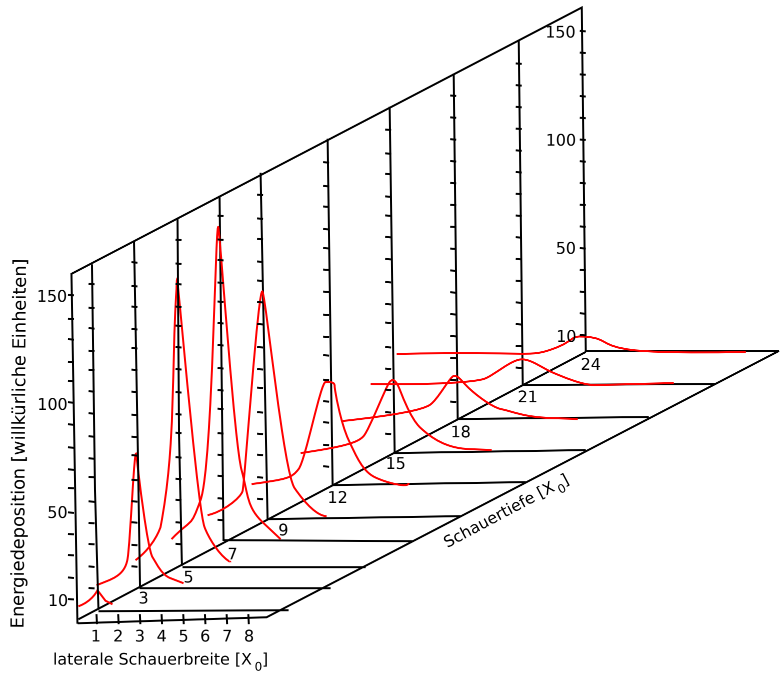

remember useful relations:

$$X_0 = \frac{180A}{Z^2}\ (\mathrm{g\ cm^{-2}})$$

$$E_c = \frac{580\ \mathrm{MeV}}{Z}$$

$$t_{max} = \ln\frac{E}{E_c} - \begin{cases} 1 & e \text{ induced shower} \\ 0.5 & \gamma \text{ induced shower} \end{cases}$$

95% of energy within

$$L(95\%) = t_{max} + 0.08\ Z + 9.6\ \ in\ X_0$$

$$R(95\%) = 2\ R_M$$

Longitudinal shower profile

parametrization (Longo 1975)

$$\frac{dE}{dt} = E_0 t^{\alpha} exp(-\beta t)$$

first secondaries increase
then absorption dominates

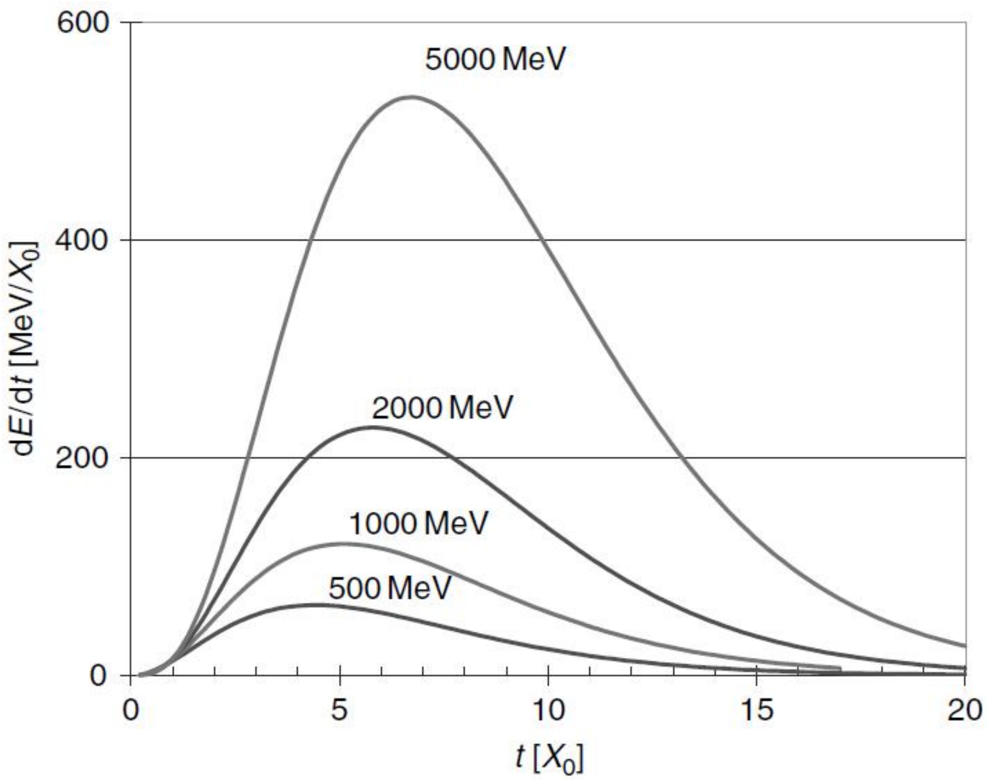

Transverse shower profile

parametrization as

$$\frac{dE}{dr} = E_0[\alpha exp(-r/R_M) + \beta exp(-r/\lambda_{min})]$$

with free parameters α, β
λ_{min} range of low energy photons and electrons
central part: multiple Coulomb scattering
tail: low energy photons (and electrons) produced in Compton scattering and photo effect

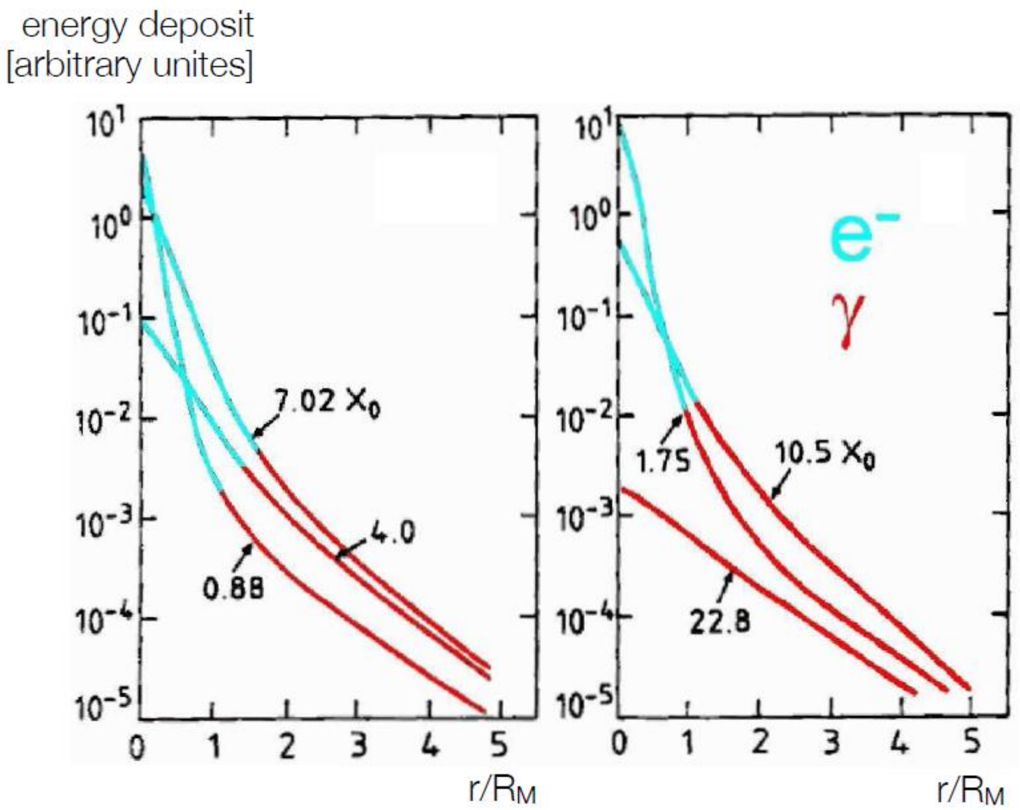

8.3 Electromagnetic calorimeter

(i) homogeneous shower detector

absorbing material $\equiv$ detection material
scintillating crystals (see chapter 5)

	NaI(Tl)	BGO	CsI(Tl)	$PbWO_4$
density (g/cm^3)	3.67	7.13	4.53	8.28
X_0 (cm)	2.59	1.12	1.85	0.89
R_M (cm)	4.5	2.4	3.8	2.2
dE/dx_{mip} (MeV/cm)	4.8	9.2	5.6	13.0
light yield (photons/MeV)	$4 \cdot 10^4$	$8 \cdot 10^3$	$5 \cdot 10^4$	$3 \cdot 10^2$
energy resolution σ_E/E	$1\%/\sqrt{E}$	$1\%/\sqrt{E}$	$1.3\%/\sqrt{E}$	$2.5\%/\sqrt{E}$

Energy resolution of homogeneous calorimeters

contributons to the energy resolution σ_E/E:

shower fluctuations (intrinsic)	$\propto \frac{1}{\sqrt{E}}$
photon/electron statistics in photon detector	$\propto \frac{1}{\sqrt{E}}$
electronic noise (noise)	$\propto \frac{1}{E}$
leakage, calibration	$\simeq const$

total energy resolution of electromagnetic calorimeter

$$\boxed{\frac{\sigma_E}{E} = \frac{A}{\sqrt{E}} \oplus \frac{B}{E} \oplus C}$$

PHOton Spectrometer (PHOS) in ALICE

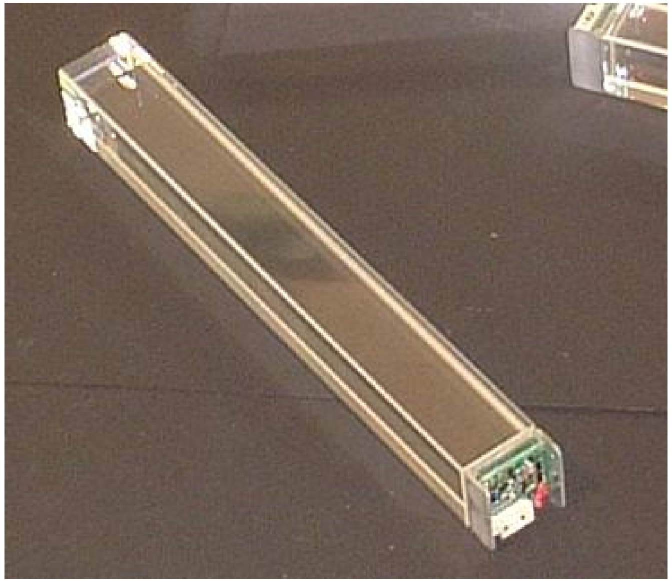

array of $22 \times 22 \times 180$ cm^3 $PbWO_4$ crystals, depth 20 X_0
in total about 18 000 (same type as CMS)

characteristics: dense, fast, relatively radiation hard

emission spectrum $420 - 550$ nm
read out with 5×5 mm^2 avalanche photodiodes, $Q = 85\%$
charge-sensitive preamplifier directly mounted on APD

light yield of $PbWO_4$ relatively low and strongly temperature dependent $\rightarrow$ operate detector at -25° C
(triple light yield vs 20° C)
but need to stabilize to 0.3° C
   (monitor with resistive temperature sensors)
crystals cold, electronics warm
   (liquid coolant, hydrofluoroether)

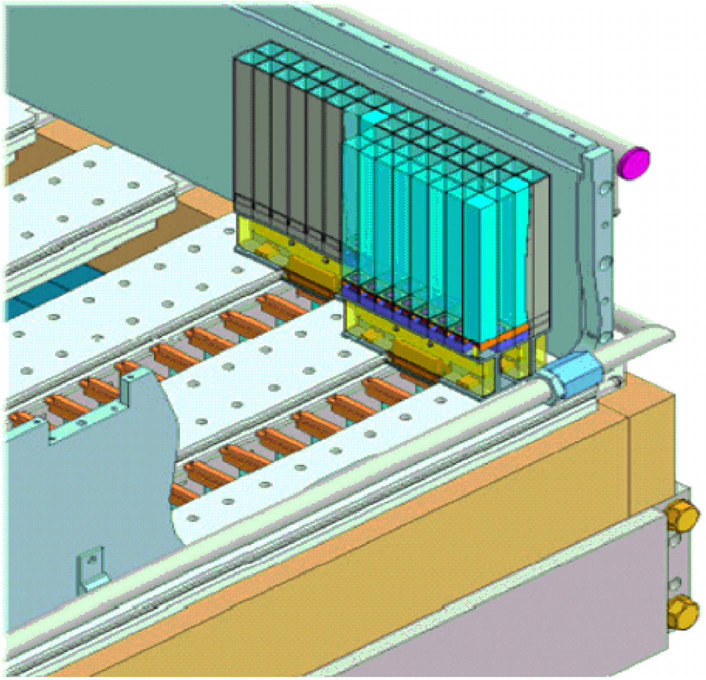

12.5 t of crystals covering 8 m^2 at 4 m from intersection point
in front: charged-particle veto (MWPC with cathode pad read-out)
test beams of pions and electrons at CERN PS and SPS: 0.6 – 150 GeV

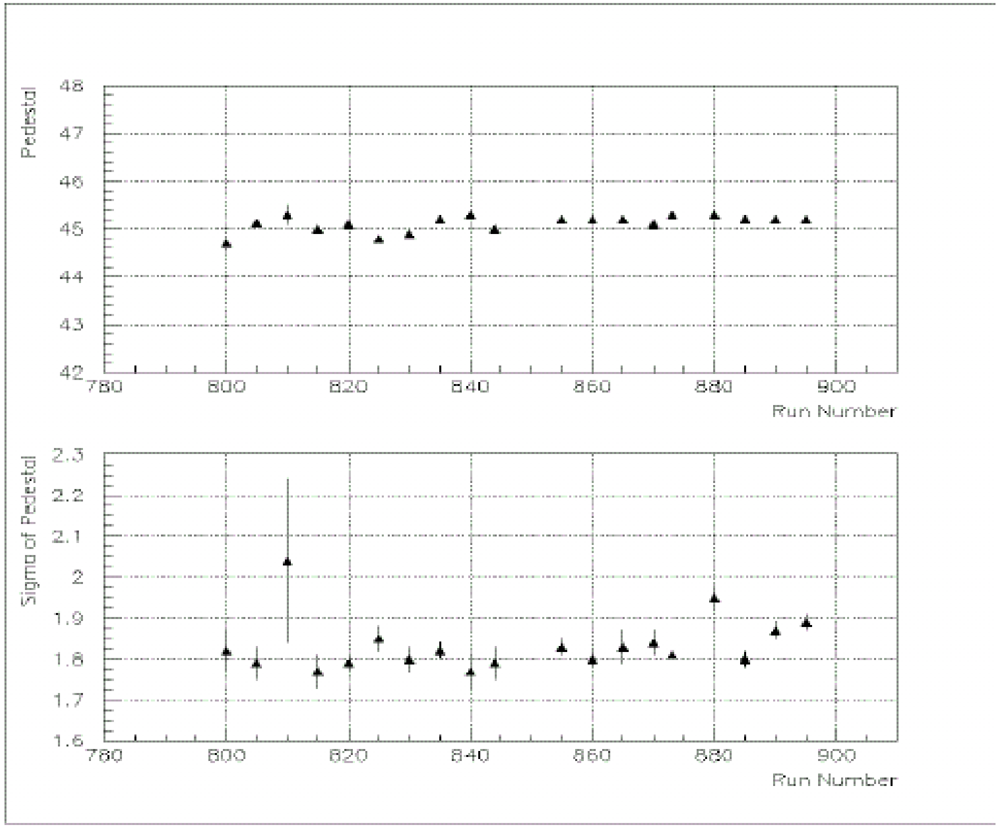

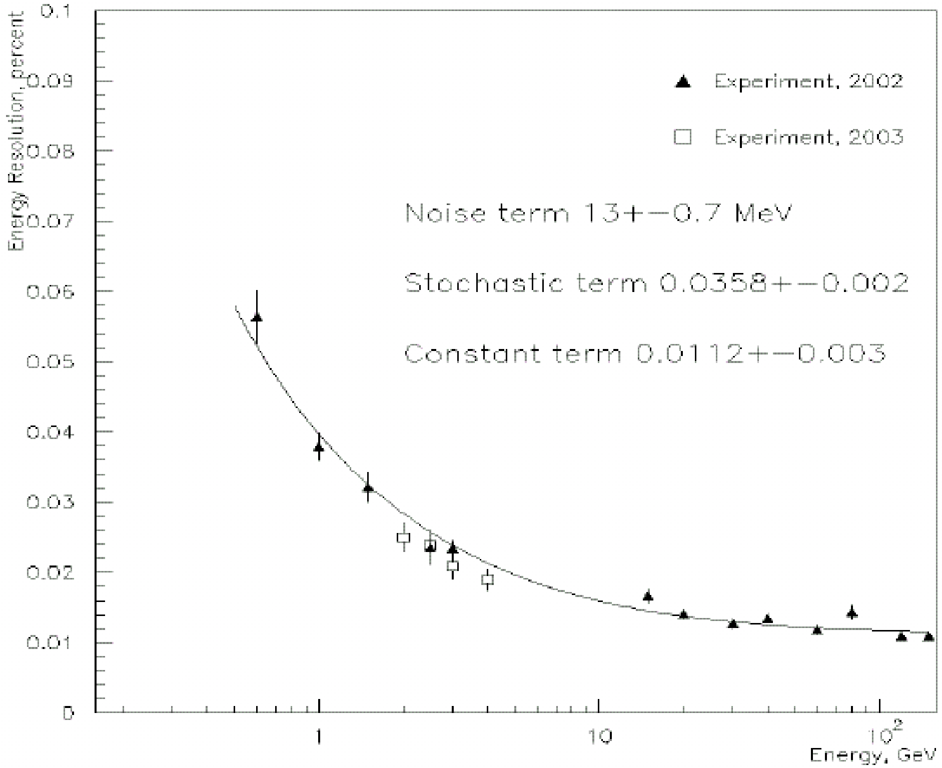

electronic noise:
1 ch = 400 e $\rightarrow$ noise about 700 e

$$\frac{\sigma_E}{E} = \frac{3.6\%}{\sqrt{E}} \oplus \frac{1.3\%}{E} \oplus 1.1\%$$

why does resolution matter so much?
when particles are reconstructed by invariant mass, peaks sit on combinatorial background, S/N strongly depends on resolution

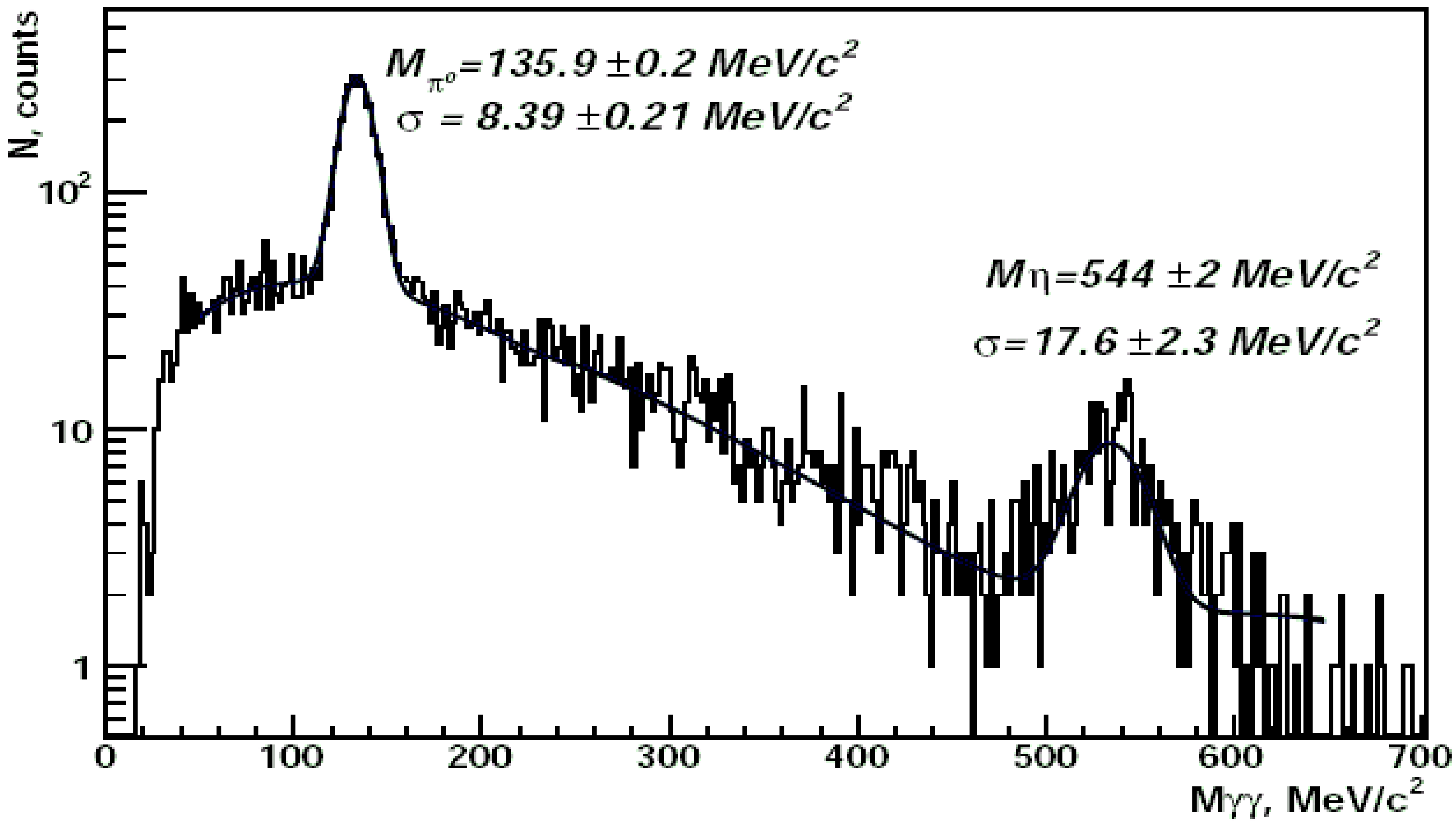

invariant-mass spectrum from the inclusive reaction 6 GeV/c $\pi^- + {}^{12}\mathrm{C} \rightarrow \pi^0 + X$, measured at a distance of 122 cm. The solid line is a fit of Gaussians plus 3rd order polynomials.

Higgs – CMS crystal calorimeter ($PbWO_4$)

decay H $\rightarrow \gamma\gamma$ for CMS the most important discovery channel

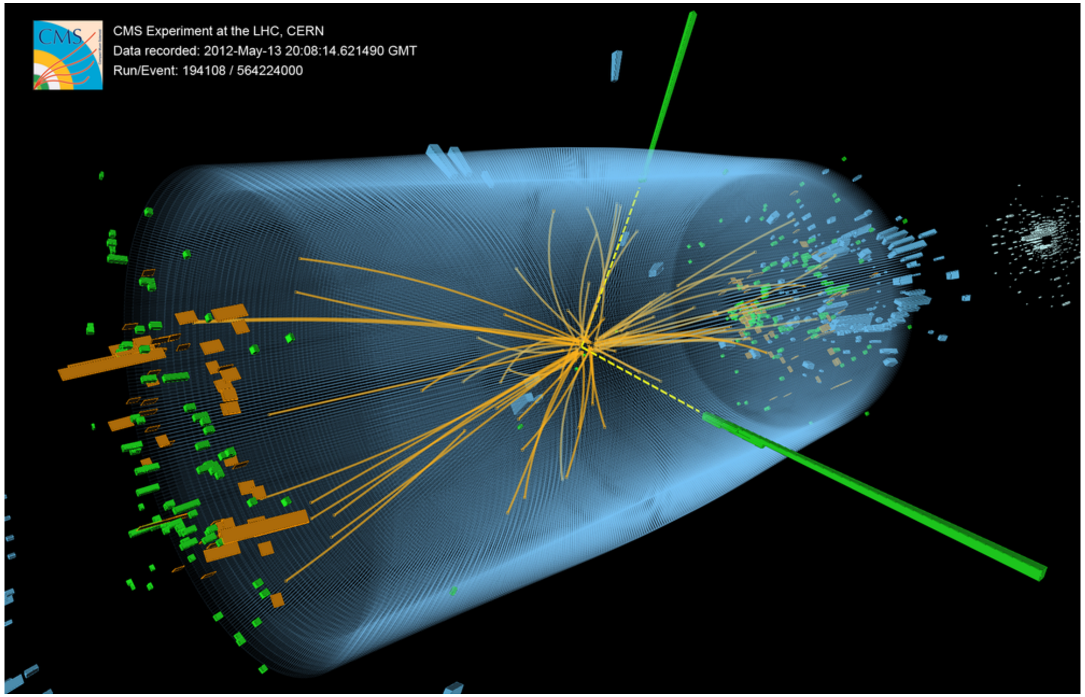

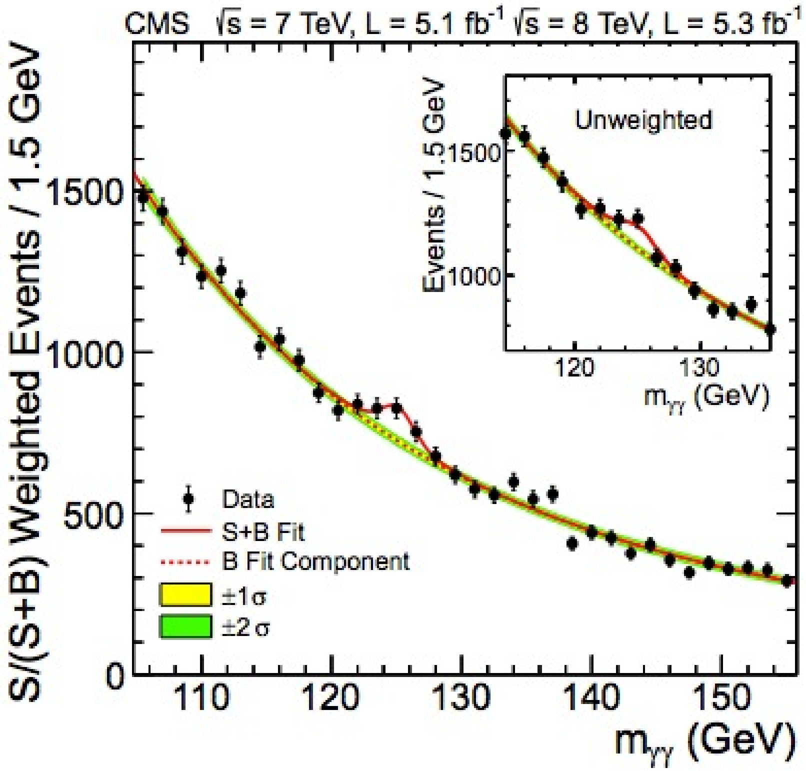

Alternative: instead of scintillating material use Cherenkov radiator

electrons and positrons of electromagnetic shower emit Cherenkov light

number of photons N_{ph} proportional to total path length T of electrons and positrons (see Ch. 2)

$$N_{ph} \propto T \propto E_0$$

remember: energy loss by Cherenkov radiation very small

$\rightarrow$ resolution limited by photoelectron statistics

typical: about 1000 photo electrons per GeV shower energy

mostly used: lead glass, e.g. SF5: $n = 1.67$ $\beta_{thr} = 0.6$ or $E_{thr} = 0.62$ MeV for electrons

blocks of typical size $14 \times 14 \times 42$ cm

$\rightarrow$ diameter: 3.3 R_M and depth: 17.5 X_0

read out with photomultipliers

typical performance: $\sigma_E/E = 0.01 + 0.05/\ t_{max} \simeq 5.5\sqrt{E(\text{GeV})}$

(ii) Sampling calorimeter

signal generated in material different from material where (main) energy loss occurs

shower (energy loss) is only ‘sampled’

converter medium: Pb, W, U, Fe $\leftarrow$ energy loss

detection medium: scintillator, liquid Ar $\leftarrow$ sampling of shower

often sandwich of absorber and detection medium

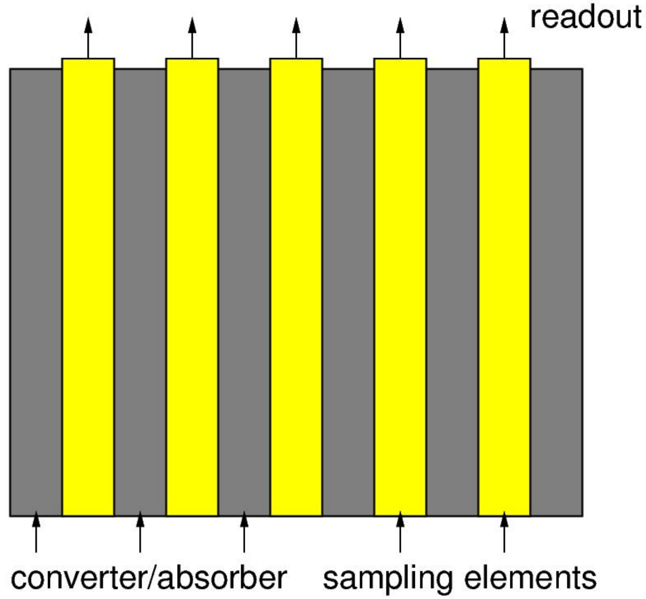

longitudinal shower development $\quad t_{max} = t_{max}^{abs} \dfrac{x+y}{x}$

transverse shower development $\quad R(95\%) = 2R_M \dfrac{x+y}{x}$

$x = \sum x_i$ absorber

$y = \sum y_i$ detection element

energy loss in absorber and detection medium varies event-by-event

‘sampling fluctuations’ $\rightarrow$ additional contribution to energy resolution

Sampling fluctuations

energy deposition dominated by electrons at small energies
range of 1 MeV electron in U: $R \simeq 0.4$ mm
for thickness d of absorber layers ≥ 0.4 mm: only fraction f of these electrons reaches detection medium

$$f(e, \mathrm{conv} \to \mathrm{det}) \propto \frac{1}{d} \propto \frac{1}{t_{conv}}$$

fraction of electrons generated in detection medium $f(e, \mathrm{det}) \propto \dfrac{t_{det}}{t_{conv}}$
number of charged particles in shower: $N \simeq E_0/E_c$

fluctuations $$\frac{\sigma_E}{E} \propto \frac{1}{\sqrt{N}} \quad \propto \quad \sqrt{\frac{E_c}{E}}\sqrt{\alpha t_{conv} + (1-\alpha)\frac{t_{conv}}{t_{det}}}$$

Fe: $(1-\alpha) \gg \alpha$ $$\frac{\sigma_E}{E} \propto \frac{1}{\sqrt{E}}\sqrt{\frac{t_{conv}}{t_{det}}}$$

Pb: $(1-\alpha) \ll \alpha$ $$\frac{\sigma_E}{E} \propto \frac{1}{\sqrt{E}}\sqrt{t_{conv}}$$

common parametrization: $$\frac{\sigma_E}{E} = 3.2\% \sqrt{\frac{E_c(MeV)}{F}}\sqrt{\frac{t_{conv}}{E(GeV)}}$$

good energy resolution for

- E_c small (Z large)
- t_{conv} small ($x < X_0$, fine sampling)

example of modern electromagnetic sampling calorimeter: PHENIX PbScint Calorimeter
alternating layers of Pb sheets and plastic scintillator sheets connected to PMT via scintillating fibres

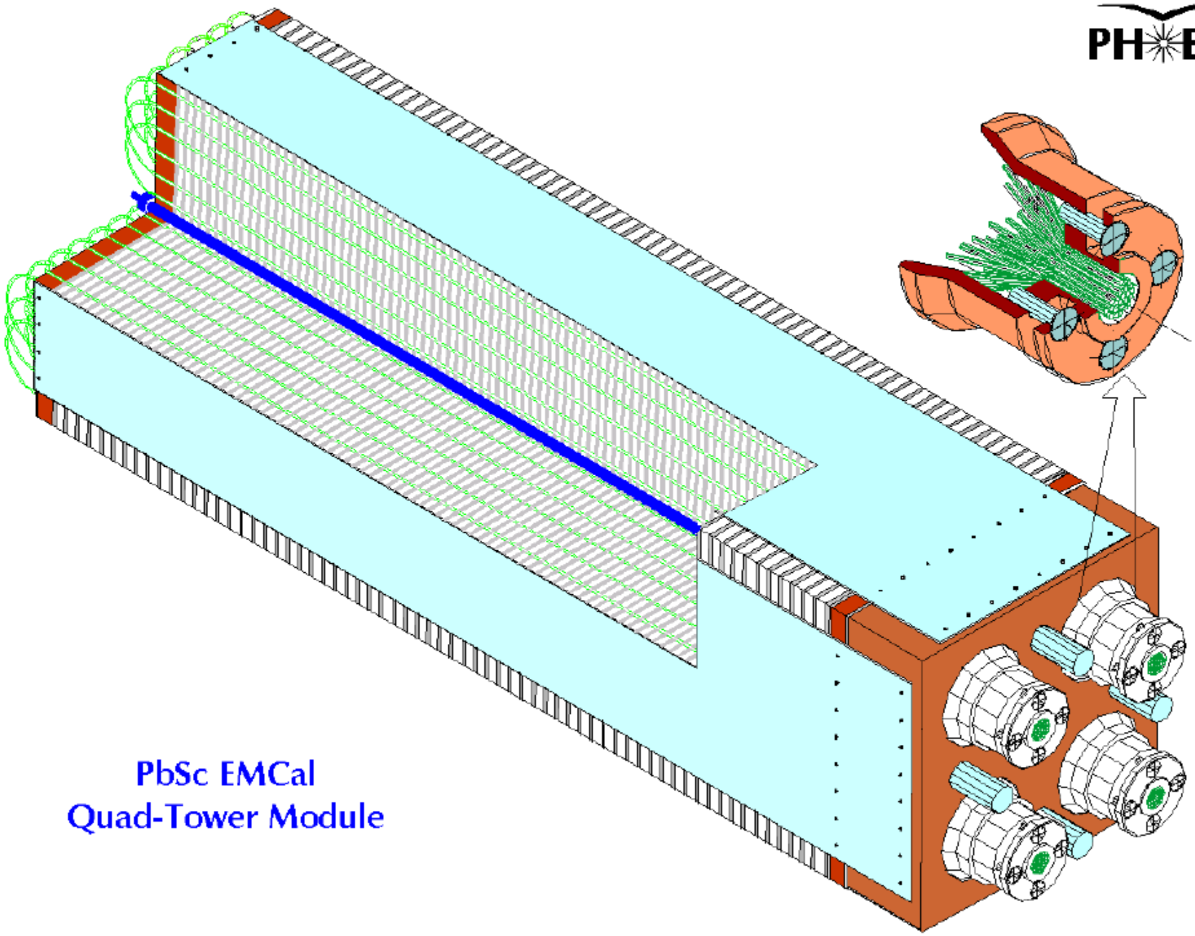

individual towers 5×5 cm^2

38 cm depth ($18 X_0$)
66 sampling cells

in total covering 48 m^2
in 15552 individual towers

Parameter	Value
Lateral segmentation	5.535 x 5.535 cm^2
Active cells	66
Scintillator	4 mm Polystyrene (1.5% PT/0.01% POPOP)
Absorber	1.5 mm Pb
Cell thickness	5.6 mm (0.277 X_0)
Active depth	
(mm)	375 mm
(Rad. length)	18
(Abs. length)	0.85
WLS Fiber	1mm, BCF-99-29a
WLS fibers per tower	36
PMT type	FEU115 M, 30 mm
Photocathode	Sb-K-Na-Cs
Rise time (25% - 80%)	$\leq$ 5 ns

one module of PHENIX EMCal

and entire WestArm

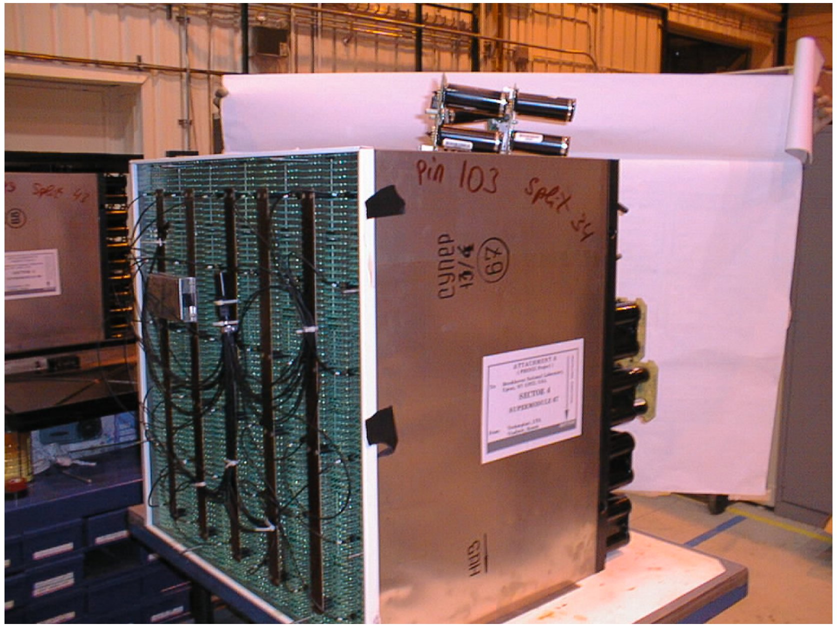

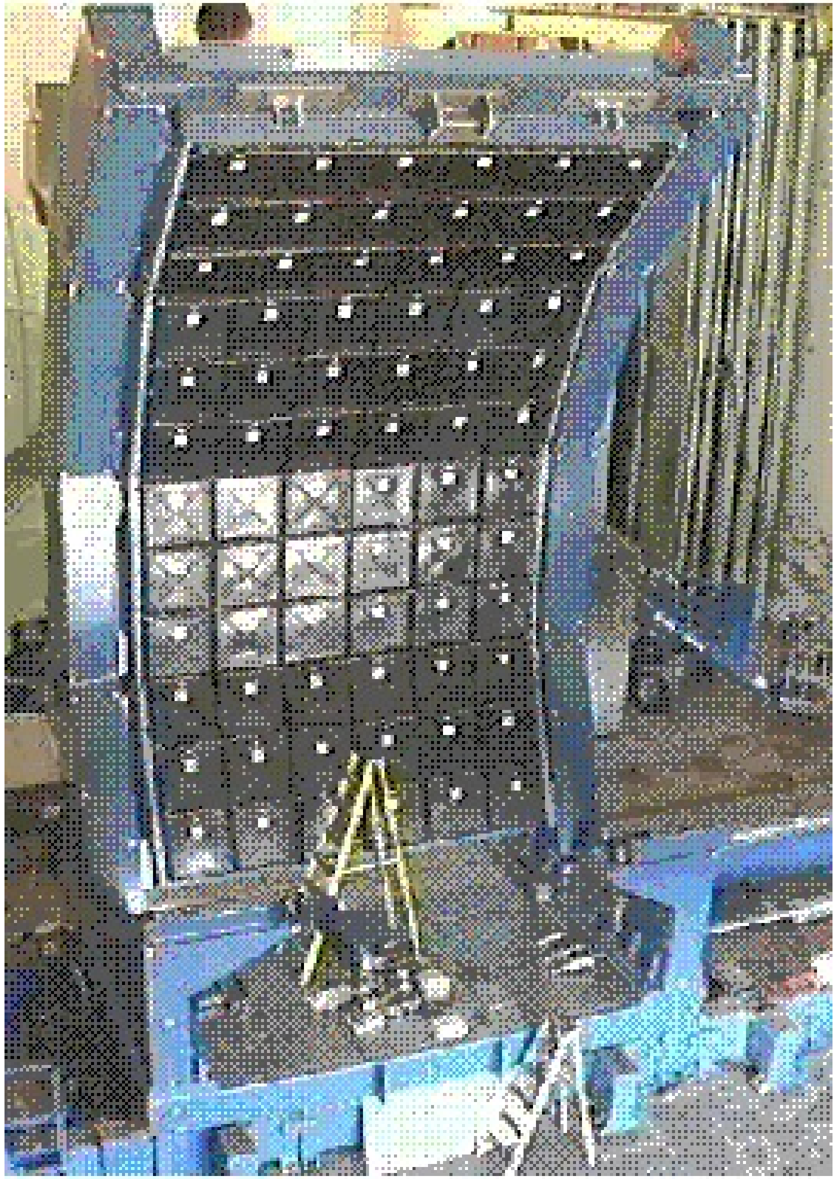

nominal energy resolution: stochastic term $8\%/\sqrt{E}$ and constant term: 2%
time resolution: 200 ps

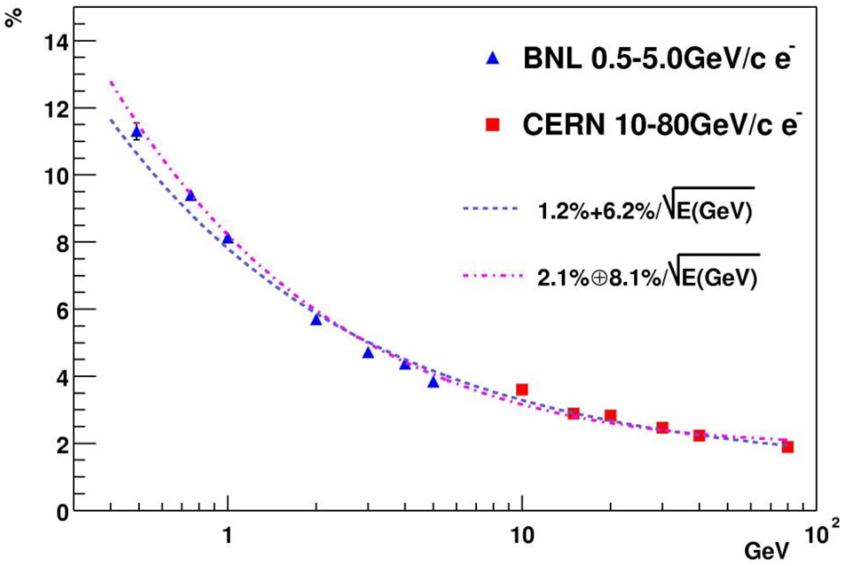

energy resolution

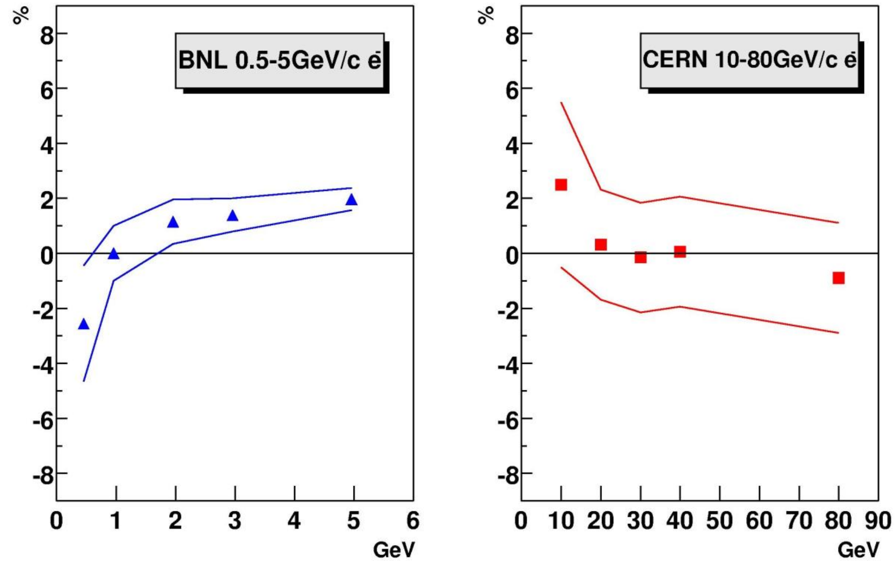

linearity of energy scale

lateral shower profile well understood → position resolution in mm range

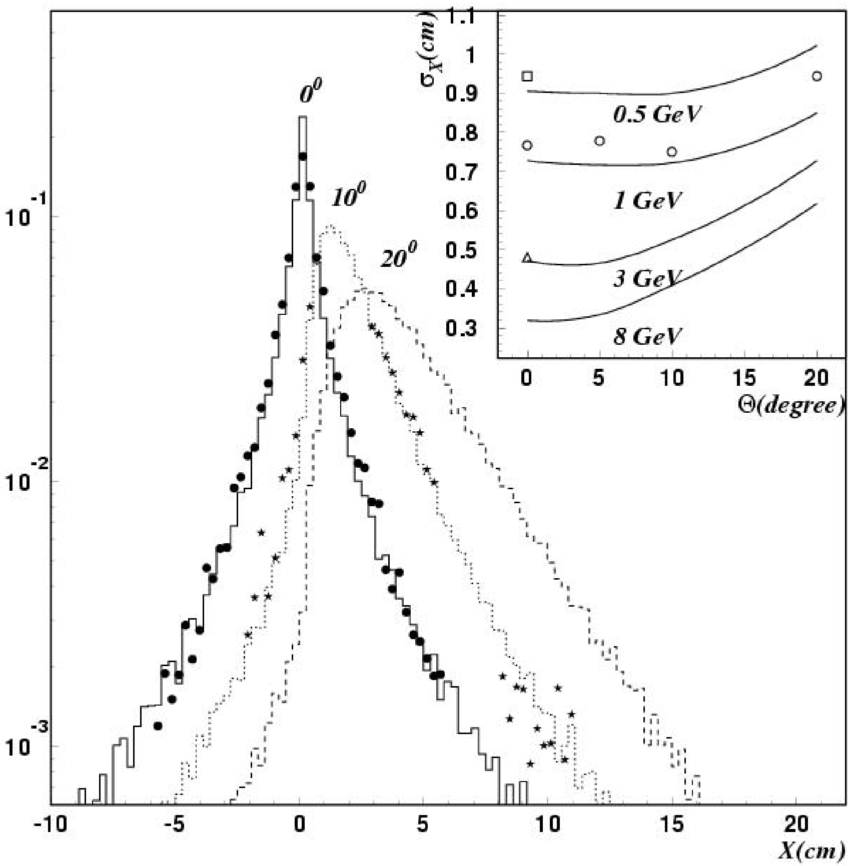

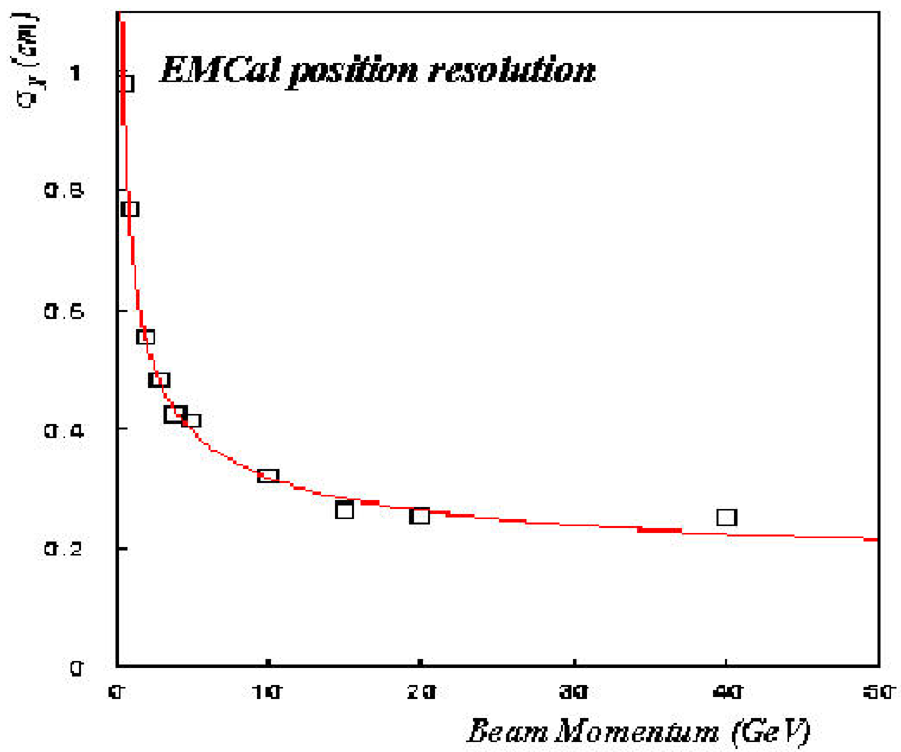

Liquid-Argon Sampling Calorimeter

instead of scintillator and optical readout: use of liquid noble gas and operation of sampling sections as ionization chamber

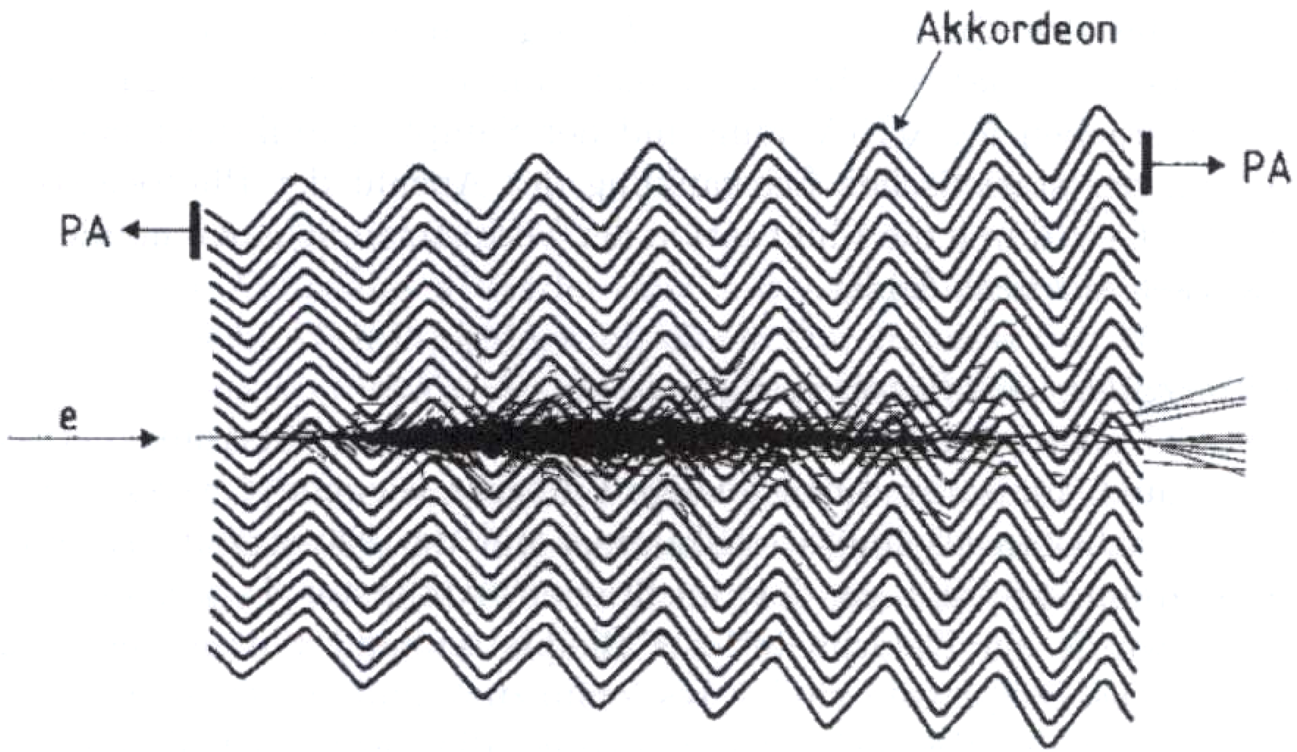

for faster readout: interleave electrodes between metal plates and electronics directly on electrodes inside liquid

example: electromagnetic calorimeter of ATLAS

9.1 Hadronic showers

Interaction of a hadron with nucleon or nucleus ($E \gtrsim 1$ GeV)

$$\left.\begin{array}{lll} \text{elastic} & p + N \rightarrow p + N & \sigma_{el} \\ \text{inelastic} & p + N \rightarrow X & \sigma_{inel} \end{array}\right\} \quad \sigma_{tot} = \sigma_{el} + \sigma_{inel} \quad \text{grows weakly with } \sqrt{s}$$

$\sqrt{s}$ (GeV)	σ_{tot} for pp (mb)
5	40
100	50
10000	100

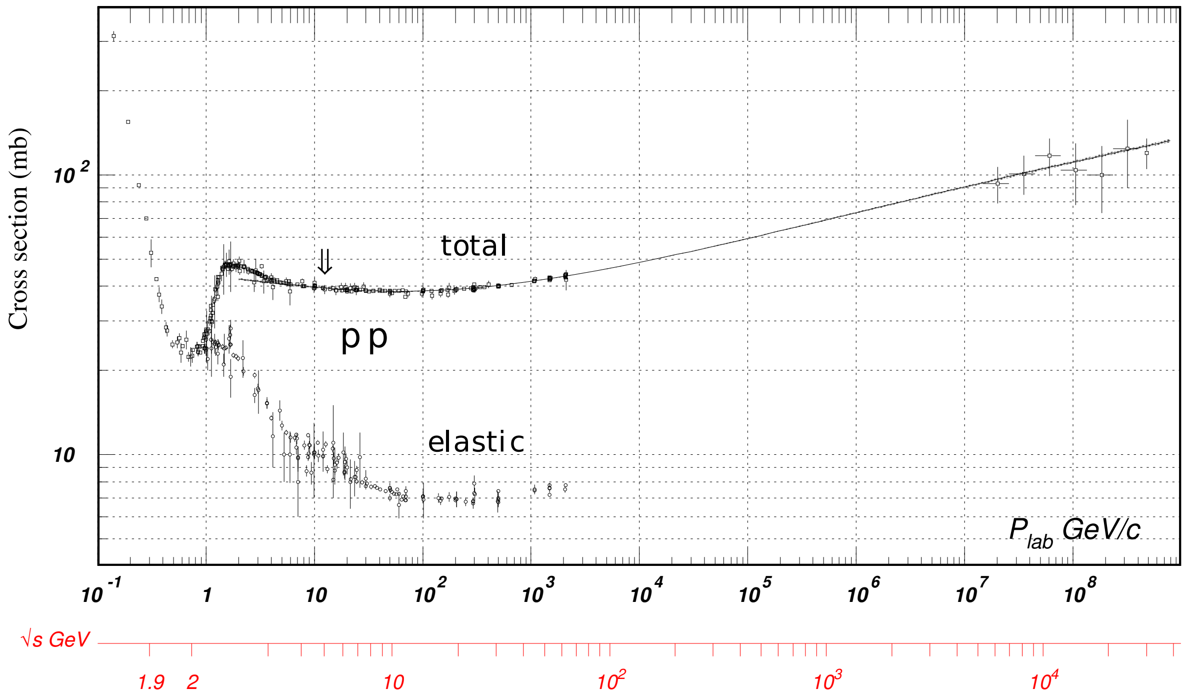

- elastic part about 10 mb
- at high energies also diffractive contribution (comparable to elastic)
- but majority of σ_{tot} is due to σ_{inel}
- pA: $\sigma_{tot}(pA) \simeq \sigma_{tot}(pp) \cdot A^{\frac{2}{3}}$

Hadronic interaction length:

$$\lambda_w = \frac{A}{N_A\,\rho\,\sigma_{tot}}$$

λ_w is the 'collision length' characterized by σ_{tot}
for inelastic processes $\rightarrow$

$$\lambda_A = \frac{A}{N_A\,\rho\,\sigma_{inel}} \qquad \text{'hadronic interaction length'}$$

$$N(x) = N_0 \exp\left(-\frac{x}{\lambda_A}\right)$$

$$\lambda_A \simeq 35 \cdot A^{\frac{1}{3}} (\mathrm{gcm}^{-2}) \qquad \text{for } Z \geq 15 \text{ and } \sqrt{s} \simeq 1 - 100 \text{ GeV}$$

	C	Ar (lq)	Fe	U	scint.
λ_A (cm)	38.8	85.7	16.8	11.0	79.5
X_0 (cm)	19.3	14.0	1.76	0.32	42.4

$\lambda_A \gg X_0$
$\rightarrow$ hadronic calorimeter needs more depth than electromagnetic calorimeter

will see below: typical longitudinal size for 95 % containment 9 λ_A
typical transverse size " 1 λ_A

Hadronic shower

- p + nucleus $\rightarrow\ \pi^+ + \pi^- + \pi^0 \cdots +$ nucleus*
  $\hookrightarrow$ nucleus 1 + n,p,α
  $\hookrightarrow$ nucleus 2 + 5p,n ...
  $\hookrightarrow$ fission
- secondary particles undergo further inelastic collisions with similar cross sections until they fall below pion production threshold
- sequential decays
  - $\pi^0 \rightarrow \gamma\gamma \rightarrow$ electromagnetic shower
  - fission fragments $\rightarrow \beta$-decay, γ-decay
  - nuclear spallation: individual nucleons knocked out of nucleus, de-excitation
  - neutron capture $\rightarrow$ nucleus* $\rightarrow$ fission (U)
- mean number of secondary particles $\propto \ln E$
  typical transverse momentum $\langle p_t \rangle \simeq 350$ MeV/c
- mean inelasticity (fraction of E in secondary particles) $\simeq 50\%$

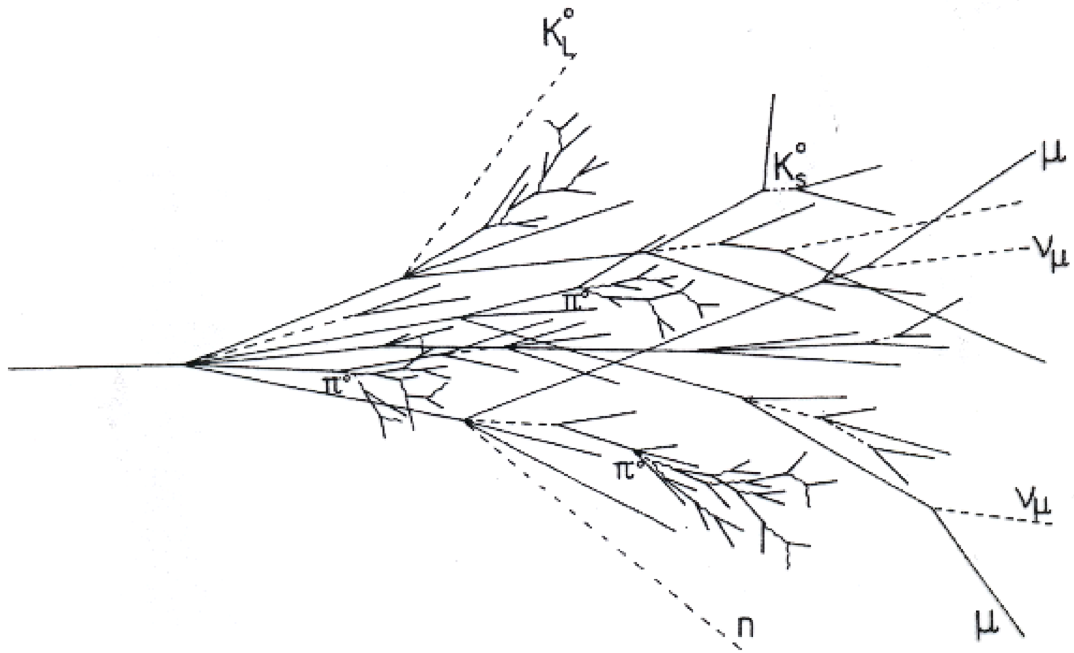

Shower development

rough estimates (data see below), qualitatively similar to em. shower, fluctuations are huge
variables: $t = x/\lambda_A$ depth in units of interaction length, $E_{thr} = 290\ MeV$

$$E(t) = \frac{E}{\langle n \rangle^t}$$

$$E(t_{max}) = E_{thr} \rightarrow E_{thr} = \frac{E}{\langle n \rangle^{t_{max}}}$$

$$\langle n \rangle^{t_{max}} = \frac{E}{E_{thr}} \quad \text{or} \quad t_{max} = \frac{\ln E/E_{thr}}{\ln \langle n \rangle}$$

number of particles in hadronic shower typically lower by a factor E_{thr}/E_C as compared to electromagnetic shower $\rightarrow$ intrinsic resolution worse by factor $\sqrt{E_{thr}/E_C}$

distribution of energy

example: 5 GeV proton in lead-scintillator calorimeter

	(MeV)	
ionization energy of charged particles (p, π, μ)	1980	40%
electromagnetic fraction (e, π^0, η^0)	760	15%
neutrons	520	10%
photons from nuclear de-excitation	310	6%
non-detectable energy (nuclear binding, $\nu, \ldots$)	1430	29%

Characteristics of hadronic shower

- strong fluctuations in energy sharing
- part of energy invisible, can be partly compensated by neutron capture leading to fission $\rightarrow$ release of binding energy
- variation in spatial distribution of energy deposition ($\pi^{\pm} \leftrightarrow \pi^{0}$ etc.)
- electromagnetic fraction grows with E
  $f_{em} \simeq f_{\pi^0} \propto \ln E$
- energetic hadrons contribute to electromagnetic fraction by e.g. $\pi^- + p \rightarrow \pi^0 + n$, but very rarely the opposite happens (a 1 GeV π^0 travels 0.2 μm before decay)
- below pion production threshold, mainly dE/dx by ionization

measurement of hadron energy by calorimetry considerably more difficult as compared to em. case

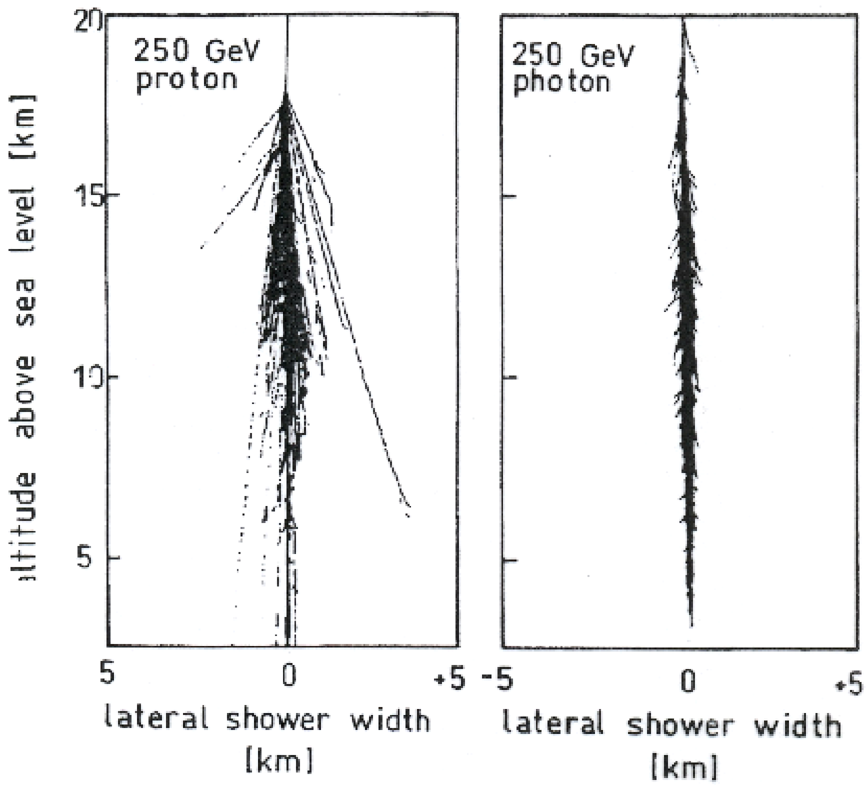

Monte-Carlo simulated air showers

shower simulations via intra- and inter-nuclear cascade models (GEISHA, CALOR, ...)

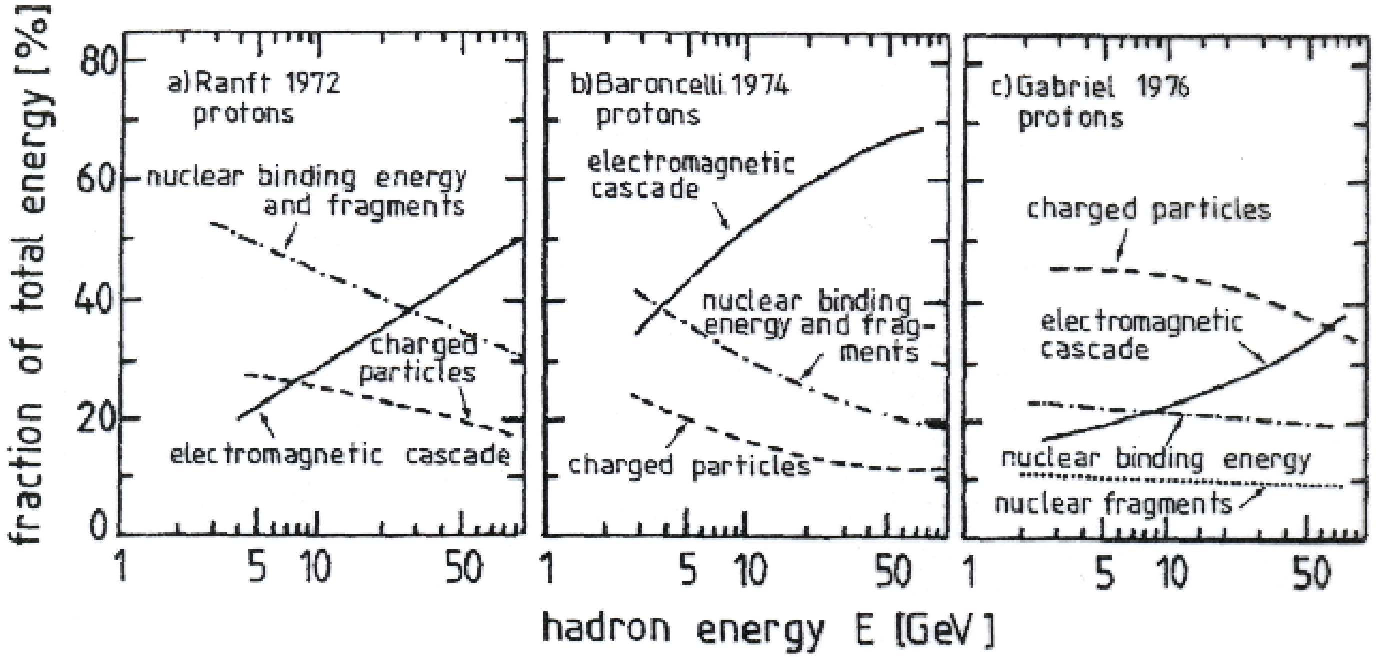

common features, but variations are significant! Need to tune to measured data in any case

Longitudinal shower development

- strong peak near hadronic interaction length λ_A
- followed by exponential decrease
- shower depth: $t_{max} \simeq 0.2 \ln E(\text{GeV}) + 0.7$
  95% of energy over depth $L_{95} = t_{max} + 2.5\lambda_{att}$
  $\lambda_{att} \simeq E^{0.3}$ (E in GeV, λ_{att} in units of λ_A)

example: 350 GeV $\pi^{\pm}$: $t_{max} = 1.9$ $L_{95} = 1.9 + 5.8$
need about $8\,\lambda_A$ to contain 95 % of energy
need about $11\,\lambda_A$ to contain 99 % of energy

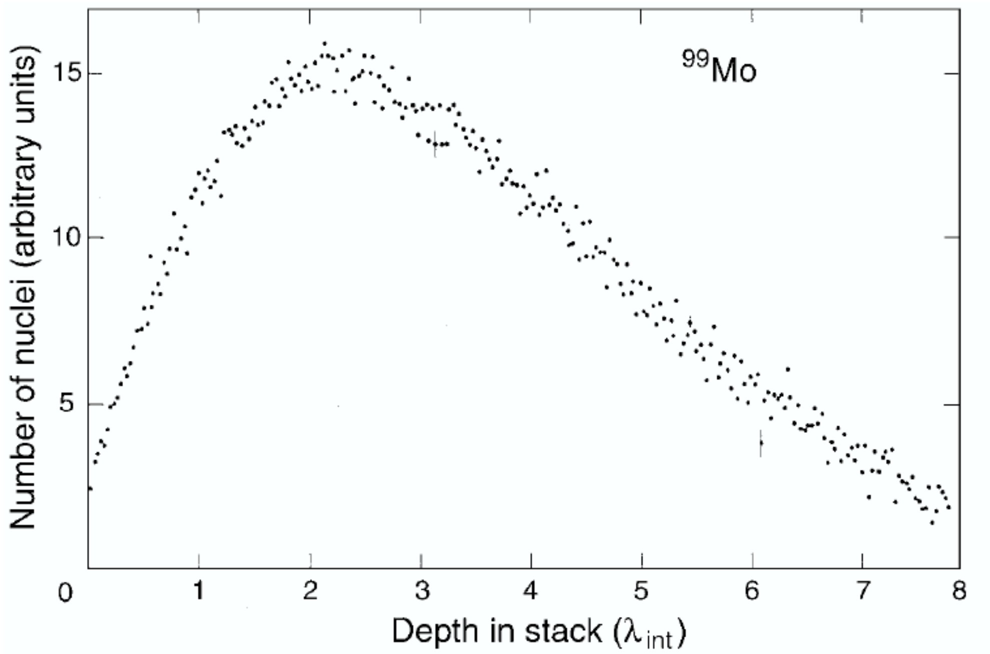

long. shower profile for 300 GeV π^- into block of U; measure radioactivity due to fission fragments

Longitudinal shower development

due to electromagnetic energy deposition rather sharp peak close to λ_A

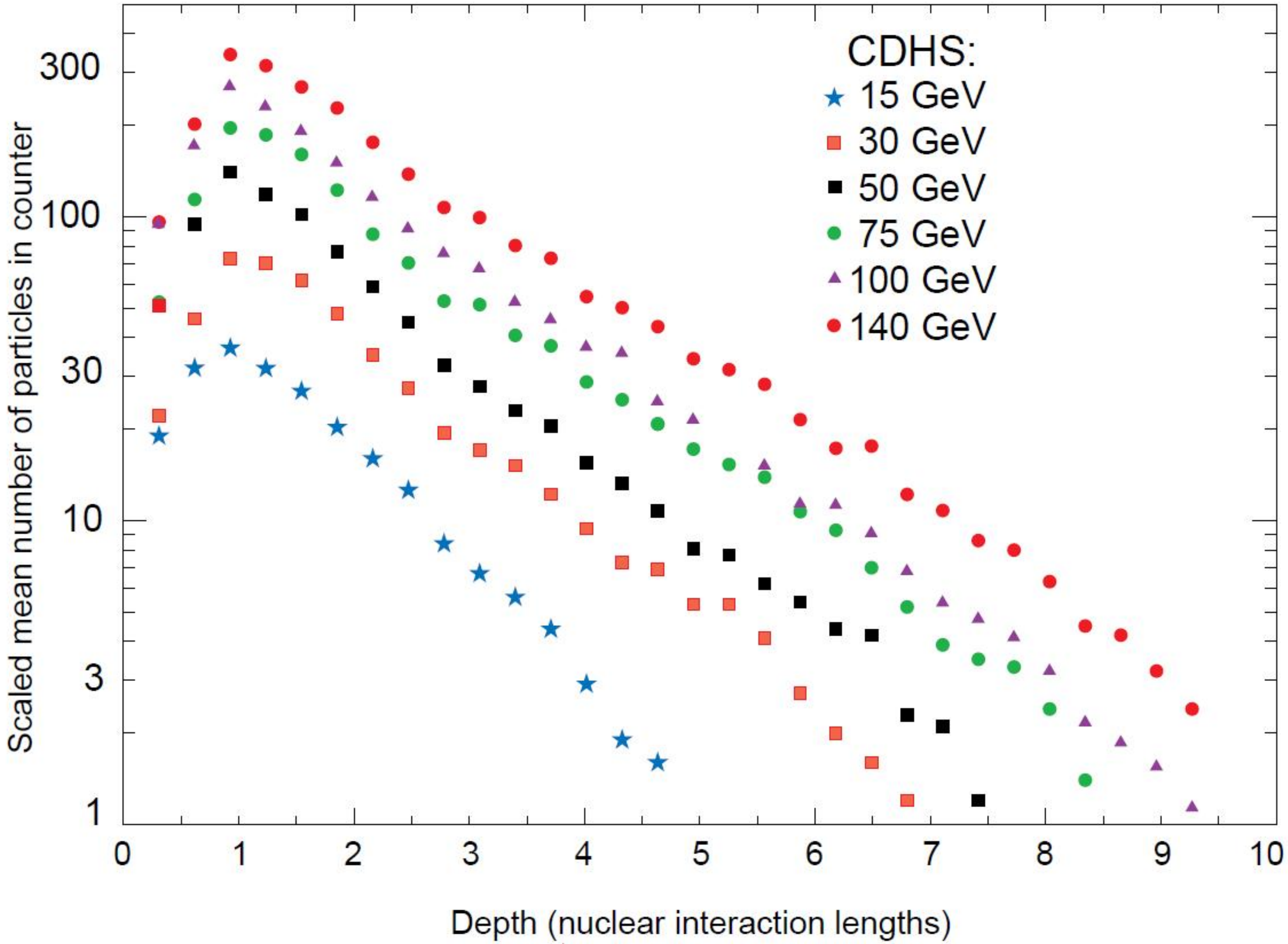

π^+ in the CDHS Fe-scintillator calorimeter

Lateral shower development

typical transverse momentum for secondary hadrons $\langle p_t \rangle \simeq 350$ MeV/c
lateral extent at shower maximum $R_{95} \simeq \lambda_A$
- relatively well defined core with $R \simeq R_M$ (electromagnetic component)
- exponential decay (hadronic component and fluct. in interaction point)

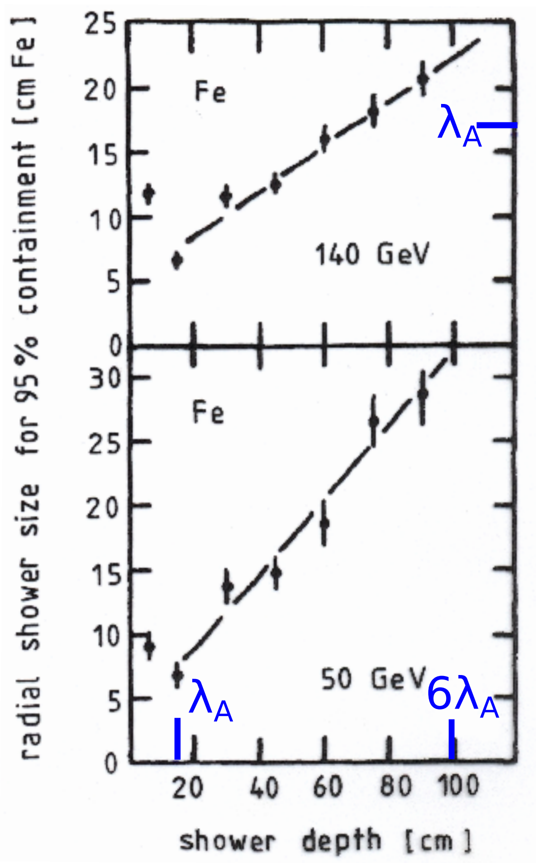

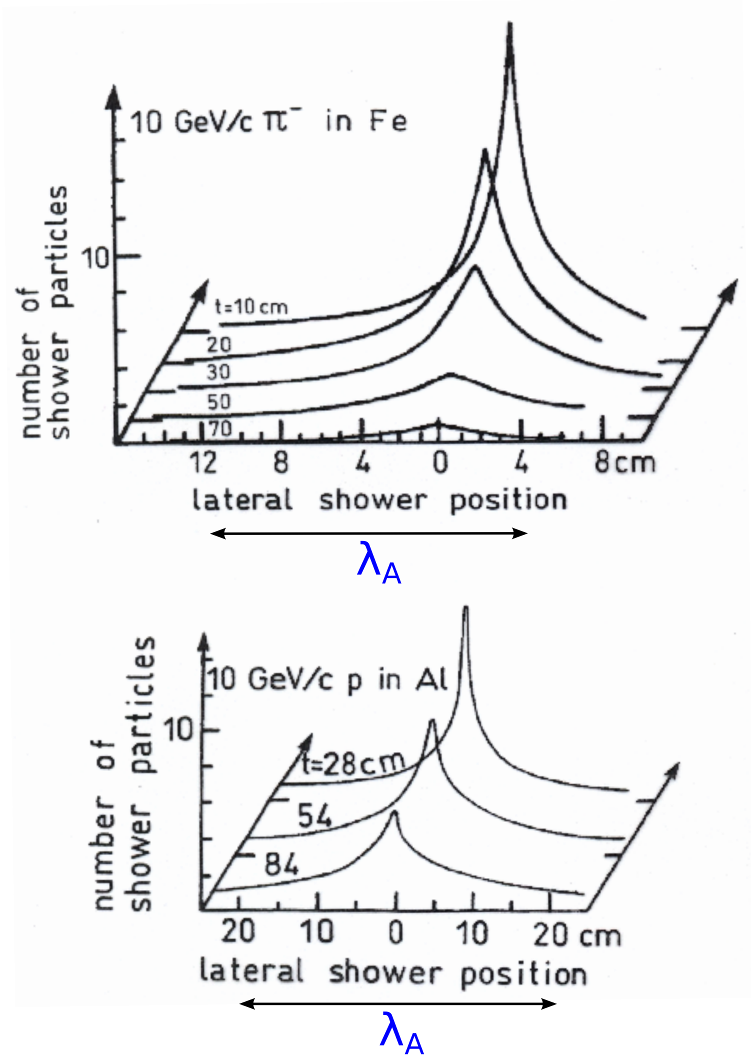

9.2 Hadronic Calorimeters

homogeneous calorimeter that could measure entire visible energy loss generally too large and expensive
in any case fluctuations of invisible component make this expense unnecessary

→ most common realization: **sampling calorimeter**
passive absorber (Fe, Pb, U) + sampling elements (scintillator, liquid Ar or Xe, MWPC's, layers of proportional tubes, streamer tubes, Geiger-Müller tubes, ...)

typical setup

- alternating layers of active and passive material
- also spaghetti or shish kebab calorimeter
(absorber with scintillating fibers embedded)

Typical arrangement of a sampling calorimeter

here: Fe/scint sampling calorimeter
also: separation of electromagnetic and hadronic component possible

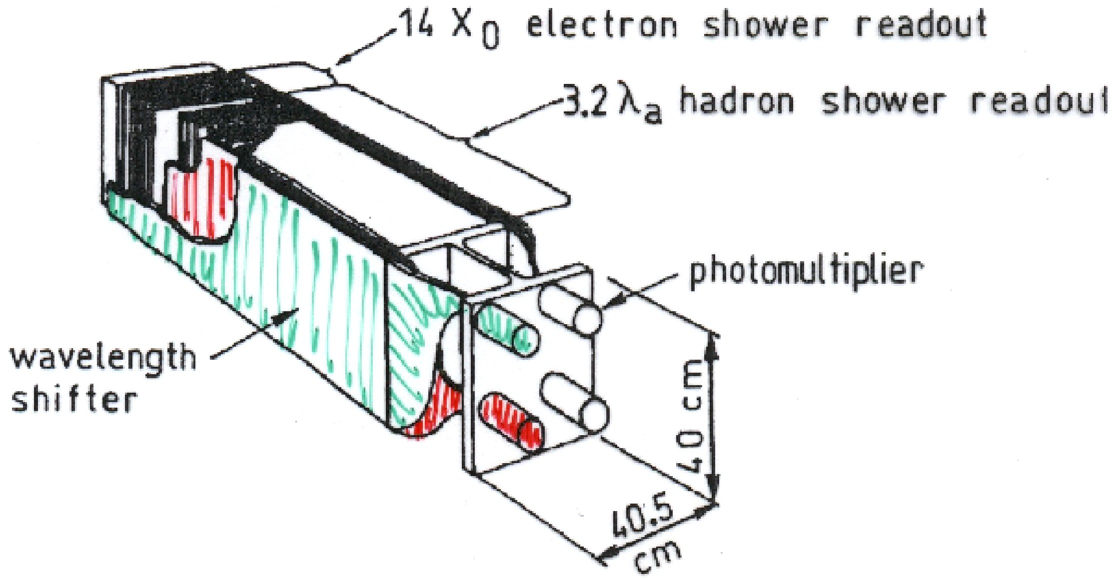

another example:
Fe / streamer tube sampling calorimeter

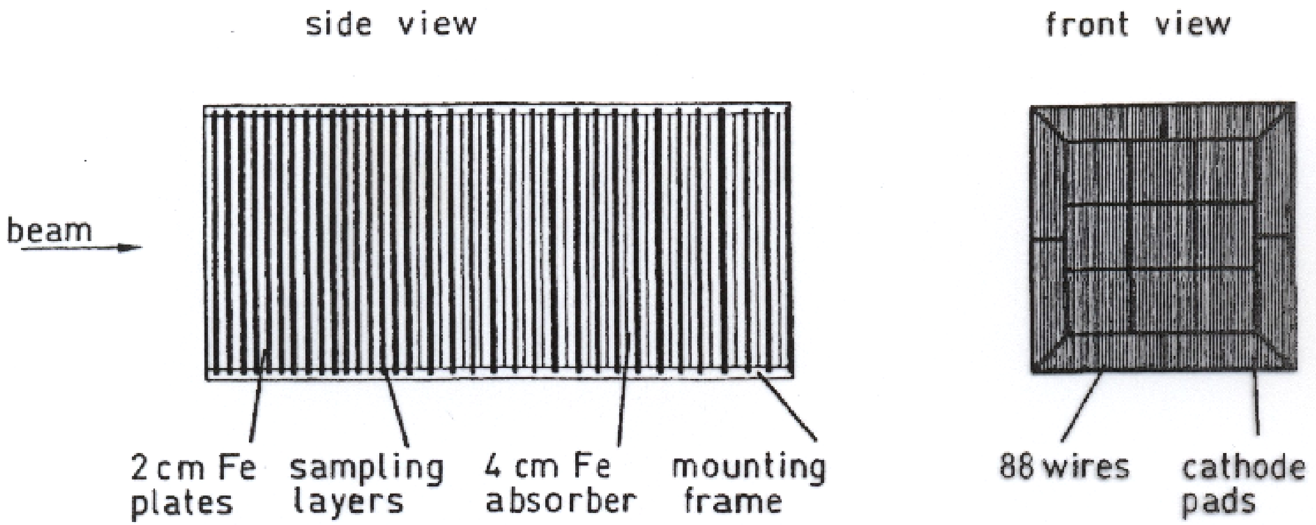

Quality of a calorimeter

- linear response: signal $\propto E$
- energy resolution: $\frac{\sigma_E}{E} = \frac{const}{\sqrt{E}}$ fluctuations Poisson, respectively Gaussian
- signal independent of particle species

because of complicated structure of hadronic shower, typically not all 3 conditions completely met

i) response not completely linear

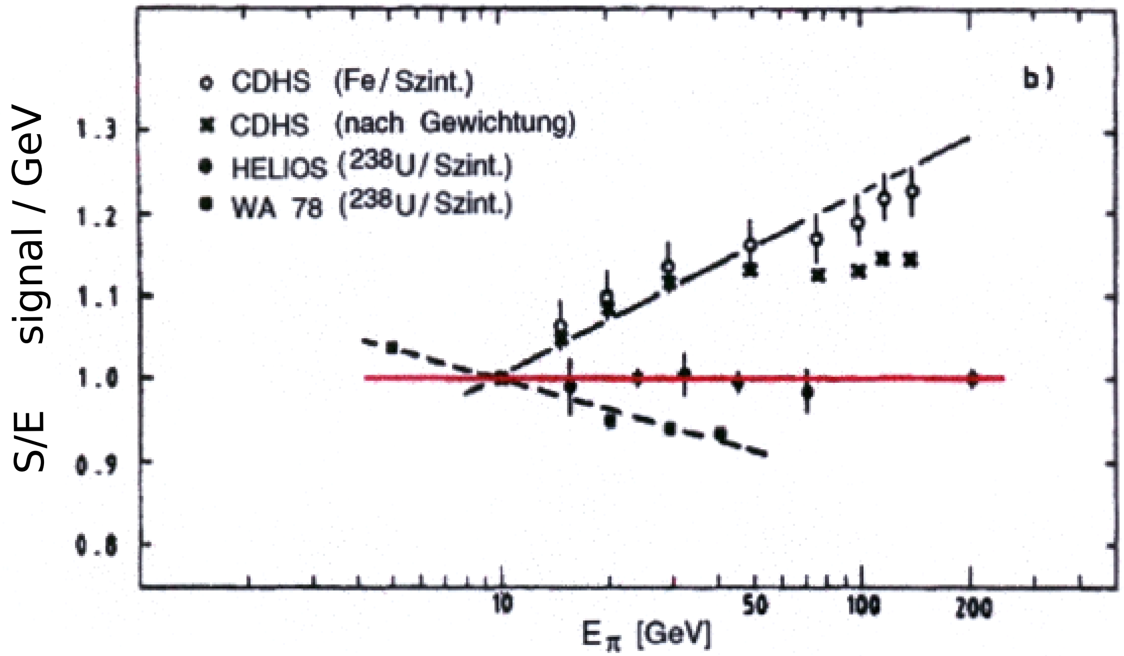

ii) resolution deviates somewhat from $const/\sqrt{E}$

iii) signal usually not completely Gaussian (tails), differences e vs h

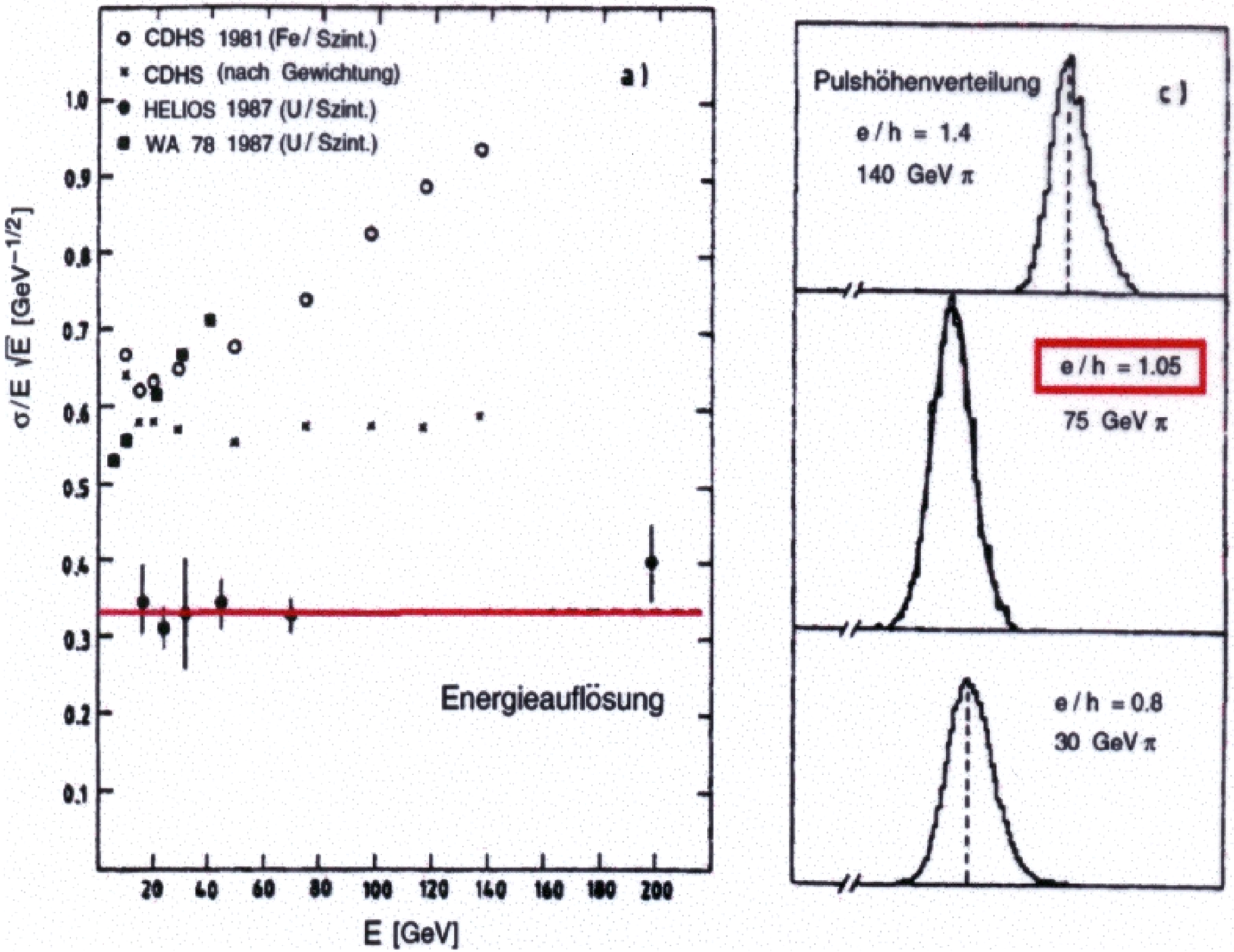

where do these differences come from?

need to understand in order to optimize to come close to ideal

e/π big issue

generally response to electromagnetic and hadronic energy deposition different

usually higher weight to electromagnetic component, since hadronic shower has invisible component i.e. '$e/h > 1$'

why is this important? want to measure total energy flow in an event without resolving and identifying origin or composition of individual showers

different calorimeters do very differently!

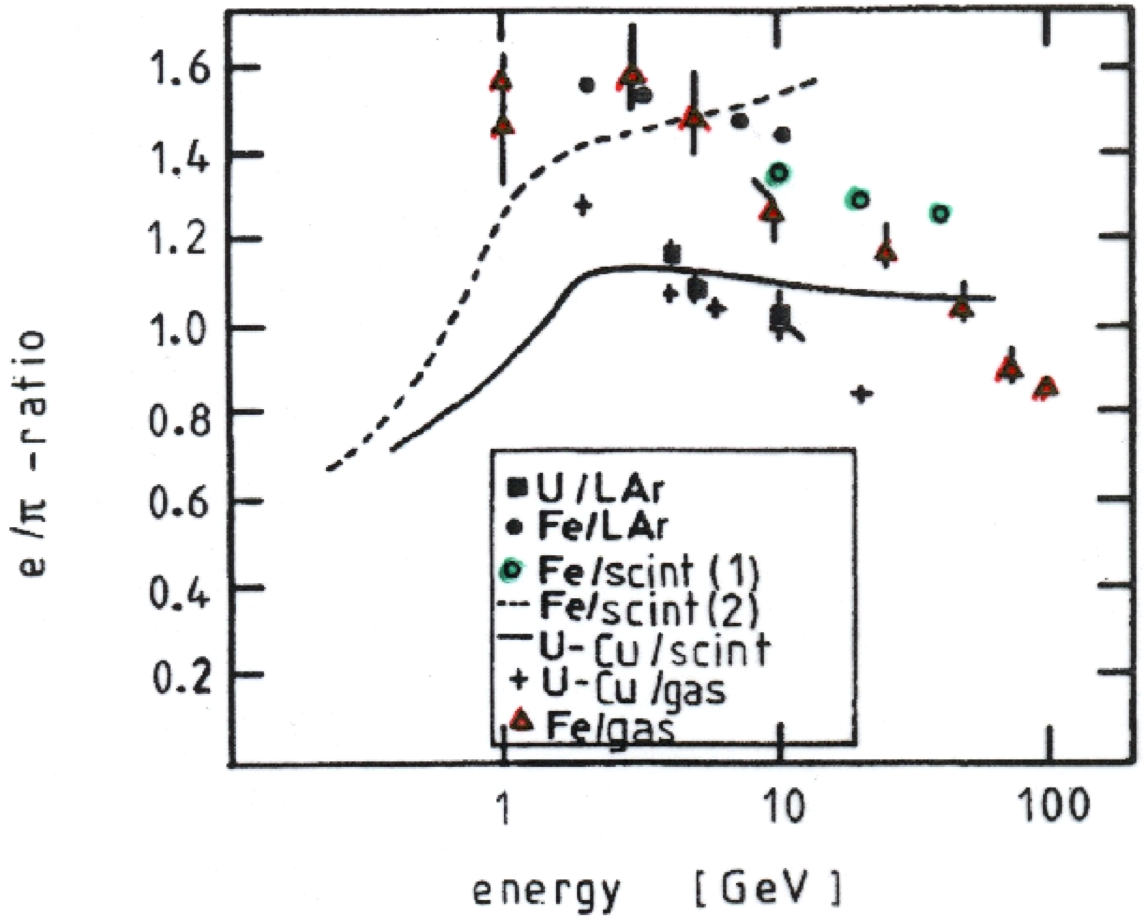

optimization:

'compensation' (see below)

'overcompensation' if $e/\pi < 1$

Energy resolution

- intrinsic contributions
  - leakage and it's fluctuations
    neutral and minimum ionizing particles:
    neutrons with $\lambda \gg \lambda_A$,
    muons,
    neutrinos 'leakage fluctuations'
  - fluctuations of electromagnetic portion
    π^0 fluctuations combined with $e/h \neq 1$
  - nuclear excitation, fission, spallation, binding energy fluctuations
  - heavily ionizing particles with $\mathrm{d}E/\mathrm{d}x \gg (\mathrm{d}E/\mathrm{d}x)_{min.ion} \rightarrow$ saturation

  all scale like $1/\sqrt{E}$ as statistical processes
- sampling fluctuations
  - dominate in electromagnetic calorimeter, nearly completely negligible in hadronic calorimeters: $\sigma_{sample}/S \propto \sqrt{d_{abs}/E}$ with d_{abs} = thickness of one absorber layer
- other contributions
  - noise: $\sigma_E/E = C/E$
  - inhomogeneities: $\sigma_E/E = const$

contributions add in quadrature

$$\boxed{\frac{\sigma_E}{E} = \frac{A}{\sqrt{E}} \oplus B \oplus \frac{C}{E}}$$

A: 0.5 – 1.0 (record: 0.35)
B: 0.03 – 0.05
C: 0.01 – 0.02

typically dominated by leakage fluctuations

9.3 Compensation

how to get from $e/h > 1$ to $e/h \simeq 1$?

need understanding of contributions to signal $\rightarrow$ allows optimization

particle i incident with energy $E(i)$

visible energy $$E_v(i) = E_{dep}(i) - \underbrace{E_{nv}(i)}_{\text{invisible}}$$

define visible fraction $$a(i) = \frac{E_v(i)}{E_v(i) + E_{nv}(i)}$$

compare various signals to those of a minimal ionizing particle:

electron $$\frac{e}{mip} = \frac{a(e)}{a(mip)}$$

hadronic shower component $$\frac{h_i}{mip} = \frac{a(h_i)}{a(mip)}$$

electron signal $$S(e) = k \cdot E \cdot \frac{e}{mip}$$

hadronic signal $$S(h_i) = k \cdot E \cdot \left[f_{em} \frac{e}{mip} + (1 - f_{em}) \frac{h_i}{mip} \right]$$

constant k determined by calibration
f_{em}: fraction of primary energy of a hadron deposited in form of electromagnetic energy
$\approx \ln(E/1 \text{ GeV})$

$$\text{in case} \quad \frac{e}{mip} \neq \frac{h_i}{mip} \quad \rightarrow \quad \frac{S(h_i)}{E} \neq \text{const.}$$

$$\frac{S(e)}{S(h_i)} \quad = \quad \frac{e/mip}{f_{em}(e/mip) + (1 - f_{em})(h_i/mip)}$$

$\rightarrow$ worsening of resolution in case $e/mip \neq h_i/mip$

$\rightarrow$ $S/E \neq$ constant

$$\text{aim for} \quad \frac{e}{mip} = \frac{h_i}{mip} \quad \rightarrow \quad \frac{S(e)}{S(h_i)} = 1$$

hadronic shower has various contributions to its visible energy

$$\frac{h_i}{mip} = f_{ion}\frac{ion}{mip} + f_n\frac{n}{mip} + f_\gamma\frac{\gamma}{mip} + f_b\frac{b}{mip}$$

f_{ion} fraction of hadronic component in charged particles, ionizing ($\mu^\pm, \pi^\pm, p$)
f_n fraction of neutrons
f_γ fraction of photons
f_b fraction of nuclear binding energy

example: 5 GeV proton

	Fe	U	
f_{ion}	57%	38%	← dominated by spallation products (protons)
f_γ	3%	2%	
f_n	8%	15%	} strongly correlated
f_b	32%	45%	

	Fe/Sci	Fe/Ar	U/Sci	U/Ar	determined by
ion/mip	0.83	0.88	0.93	1.0	d_{act}
n/mip	0.5-2	0	0.8 - 2.5	0	d_{act}/d_{abs}
γ/mip	0.7	0.95	0.4	0.4	d_{abs}
e/mip	0.9	0.95	0.55	0.55	d_{abs}

increase h_i/mip via increase of f_n, f_γ (materials) and $n/mip, \gamma/mip$ (layer thicknesses)

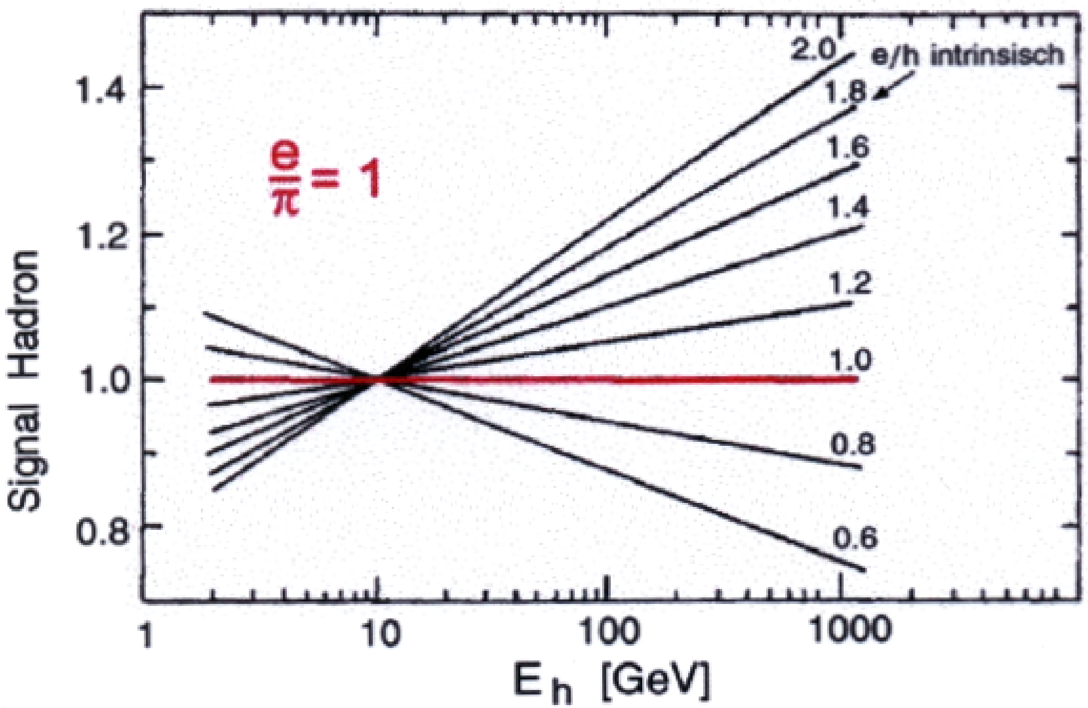

hadron signal in different sampling calorimeters

Software compensation

- segmentation in depth layers
- identify layers with particularly large $E_v \to \pi^0$ contribution
- small weight for these layers

$$w_i^* = w_i(1 - cw_i) \qquad w_i: \text{ measured, deposited energy} \qquad c: \text{weight factor}$$

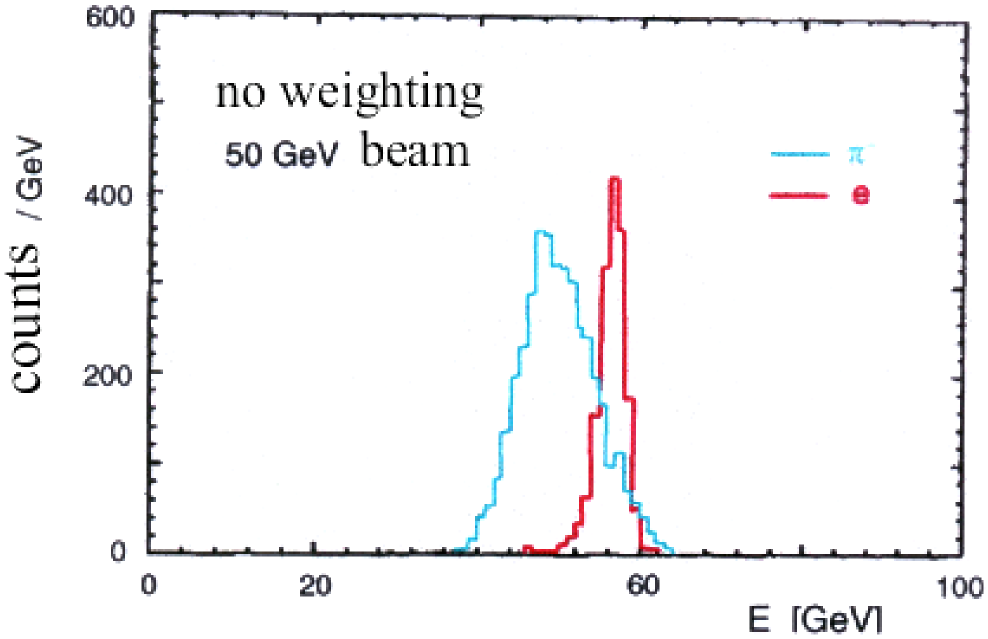

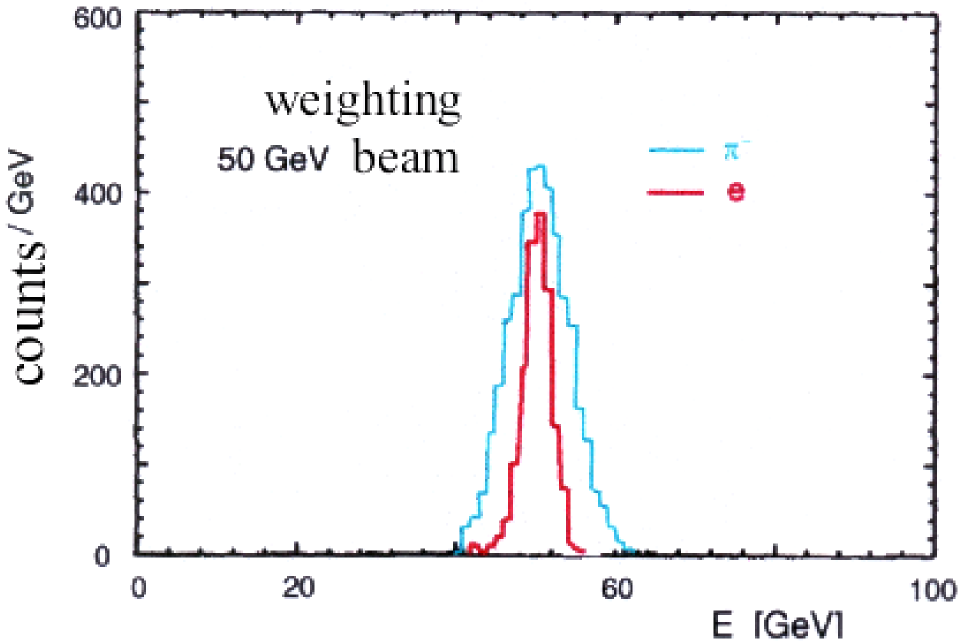

Energy resolution of non-compensating liquid-Ar calorimeter

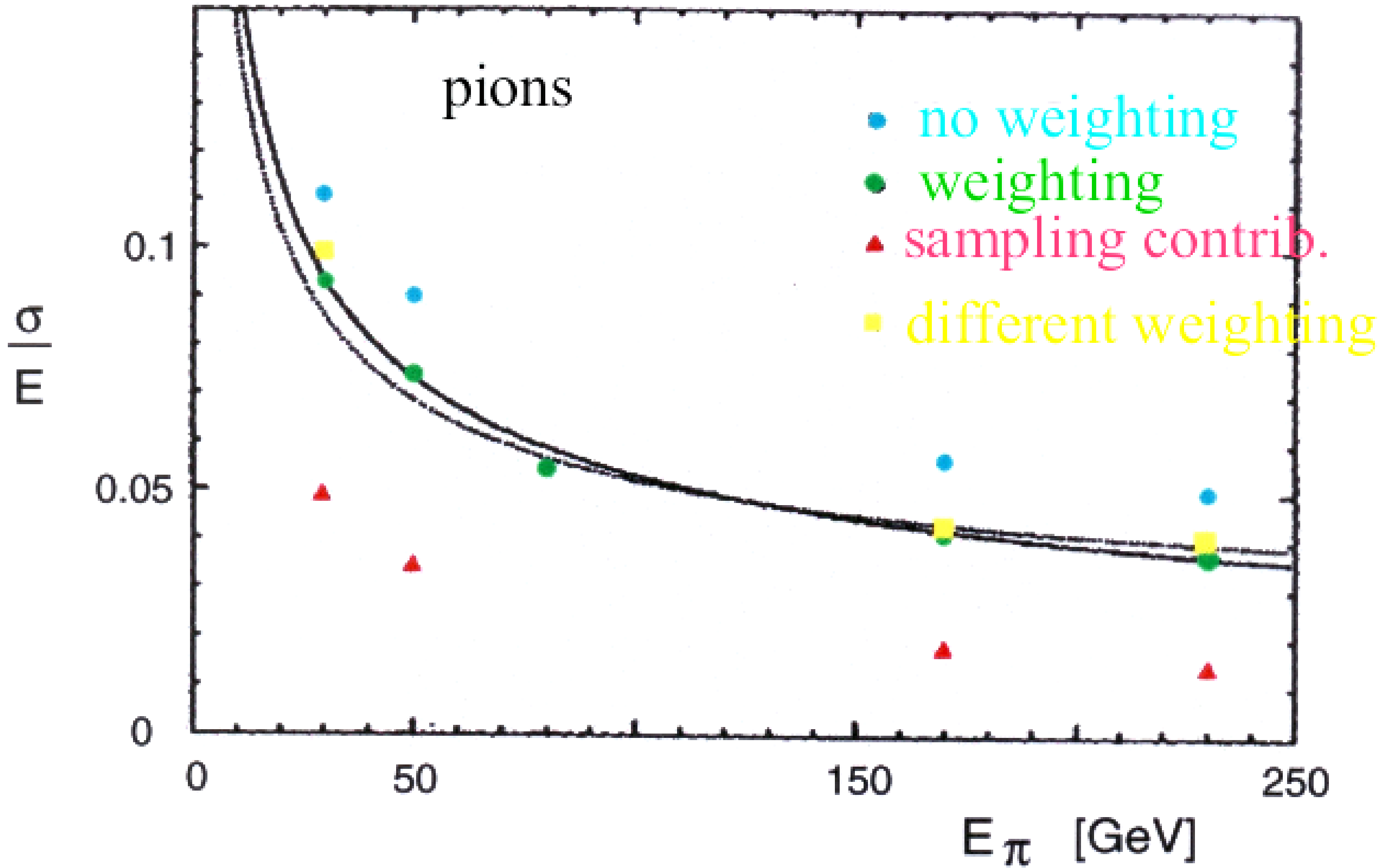

with weighting overall response more Gaussian, improved resolution, improved linearity

Hardware compensation

essential, if one wants to trigger!

increase of h/mip or decrease of e/mip

- increase of hadronic response via fission and spallation of ^{238}U

$$\uparrow \frac{ion}{mip} \text{ or } \frac{n}{mip}$$

- increase of neutron detection efficiency in active material $\rightarrow$ high proton content

$$Z = 1 \ \rightarrow \ \uparrow \frac{n}{mip}$$

- reduction of e/mip via high Z absorber and suitable choice of $\frac{d_{abs}}{d_{act}}$

$$Z_{abs} \uparrow \ \rightarrow \ \downarrow \frac{e}{mip} \ \leftarrow \uparrow \ d_{abs}$$

- long integration time $\rightarrow$ sensitivity to γ capture after neutron thermalization

$$t \text{ long } \ \rightarrow \ \uparrow \frac{n}{mip}$$

calorimeter response to protons

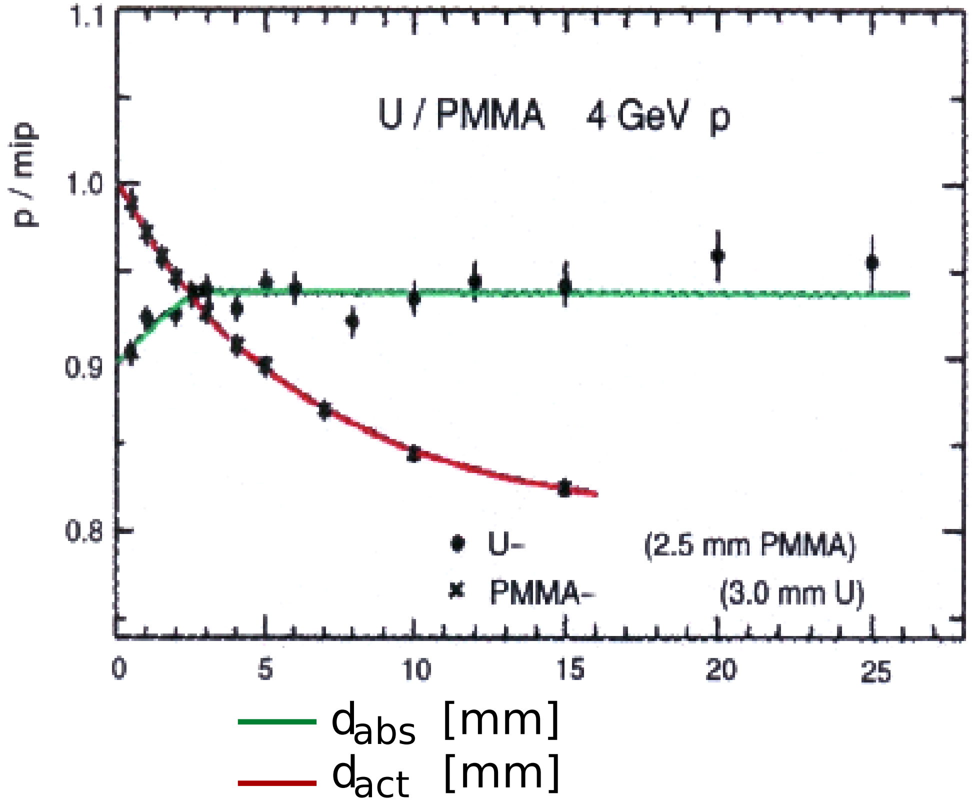

variation of plate thickness $\leftrightarrow$ variation of response p/mip

calorimeter response to neutrons

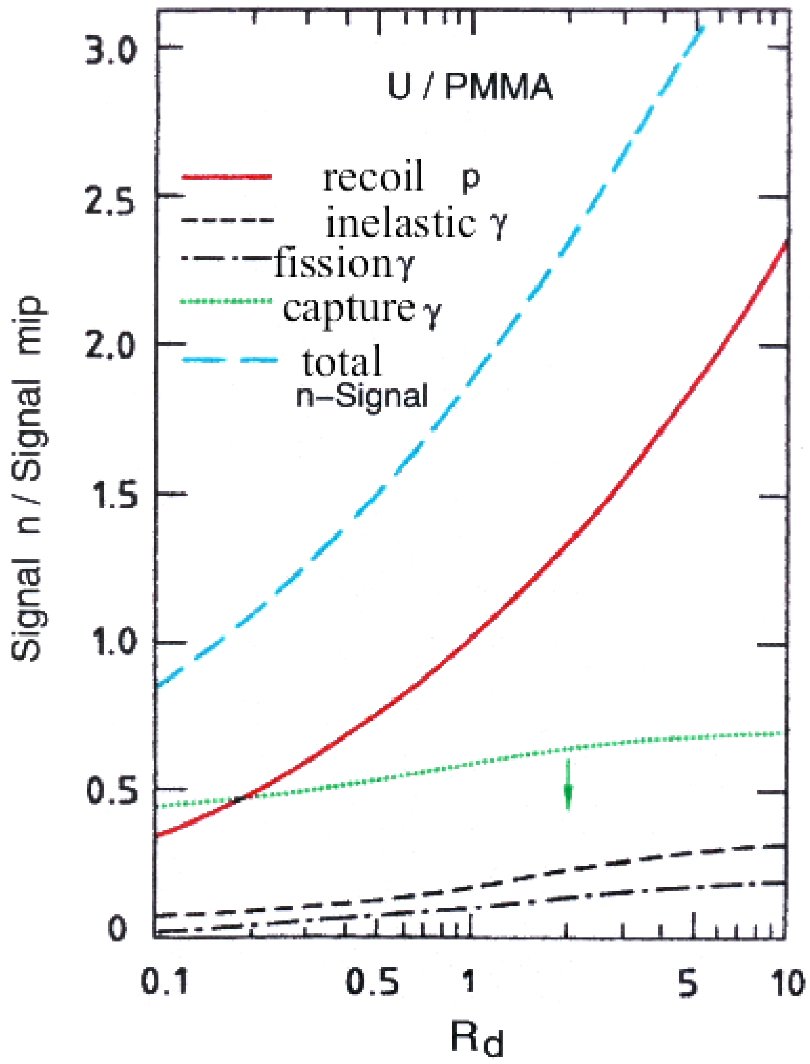

variation of contributions vs. $R_d = d_{abs}/d_{act}$

time structure different for electron and hadron showers

in em shower, all components cross detector within few ns (speed basically 30 cm/ns)
in hadronic shower component due to neutrons is delayed, need to slow down before they produce visible signal

signal width for 80 GeV e and π in spaghetti calorimeter

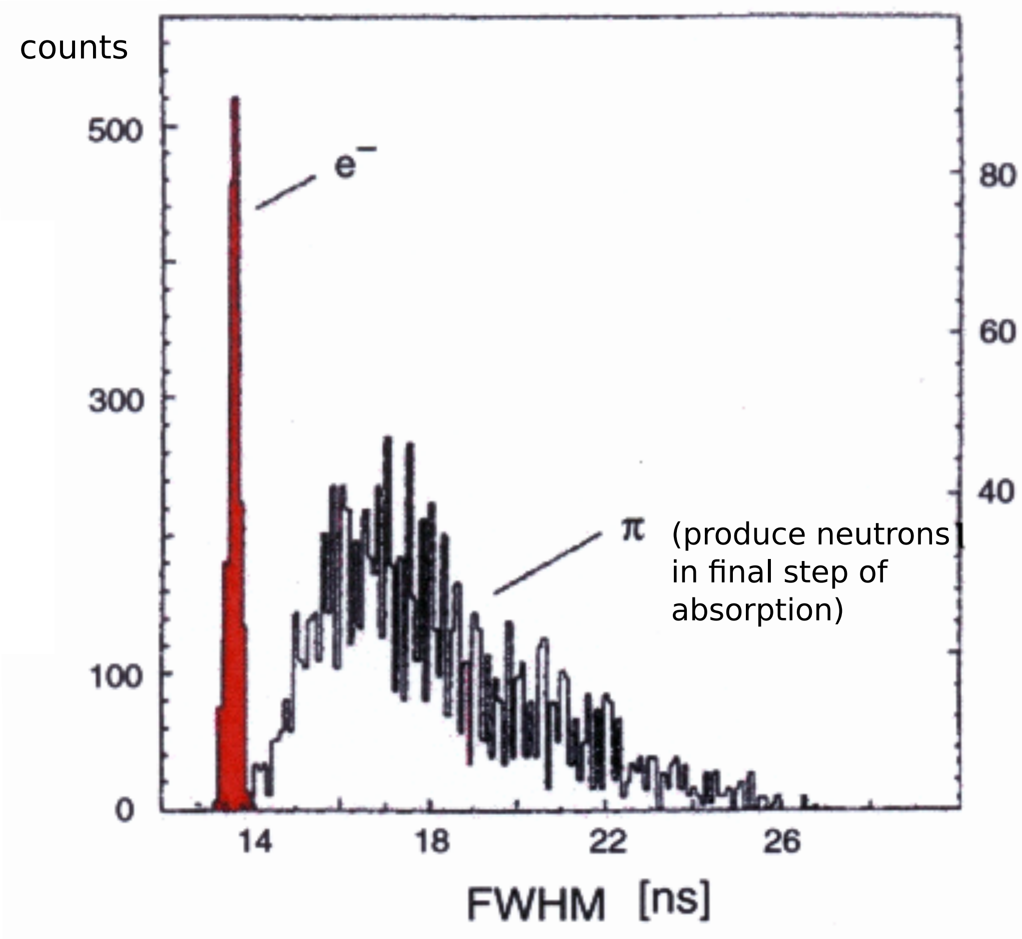

size of signal depends on integration time – variation in integration time of electronics can enhance hadronic signal (used in ZEUS calorimeter)

the e/π problem of hadronic calorimeters

U (3 mm) + Scintillator (2.5 mm)

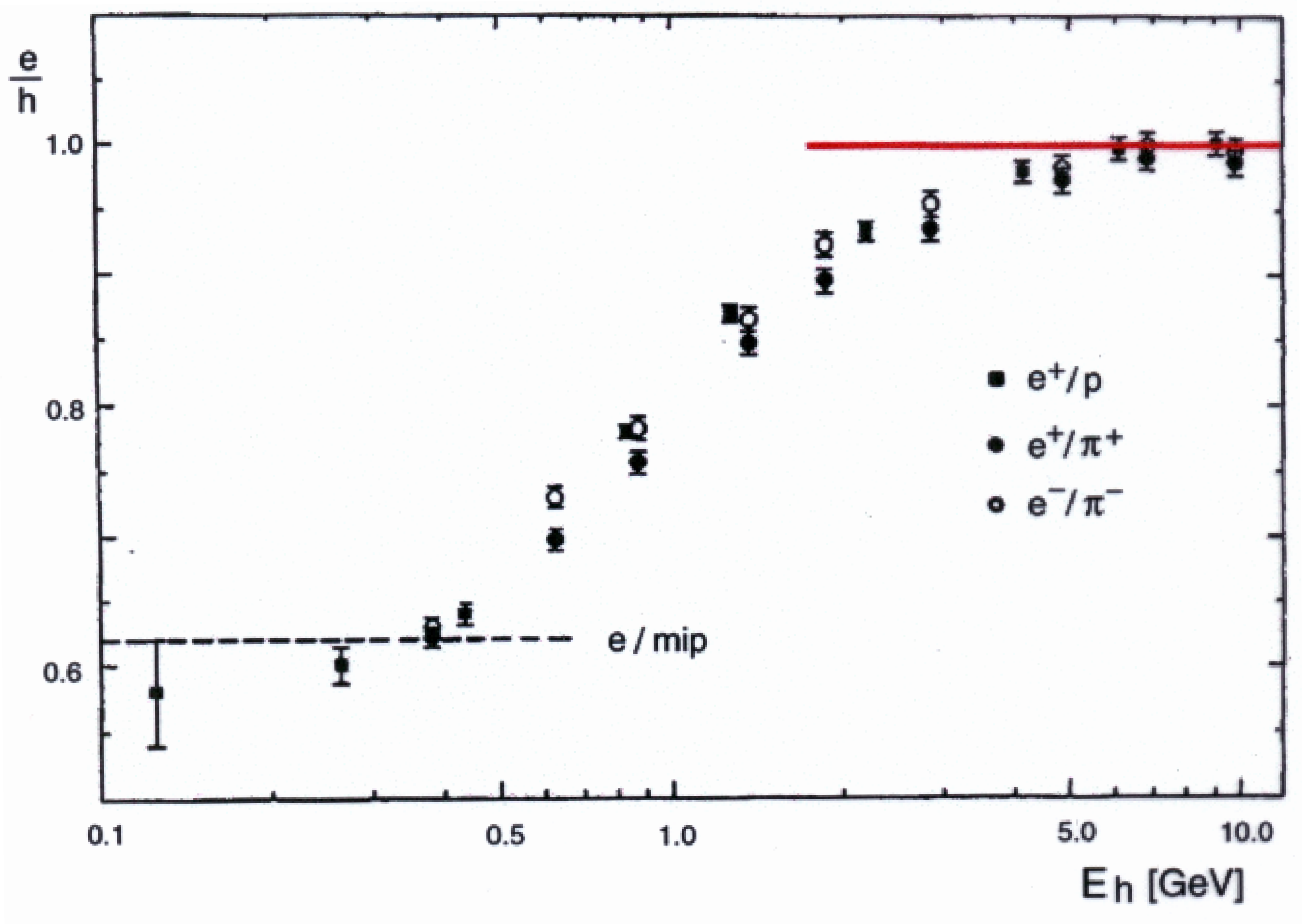

measured ratio of electron/pion signals at (ZEUS) for $E \geq 3$ GeV nearly compensated

9.4 Particle identification

electron/pion:

- use difference in transverse and longitudinal shower extent
- signal for electron is faster

hadron showers are deeper and wider and start later
PID based on likelihood analysis

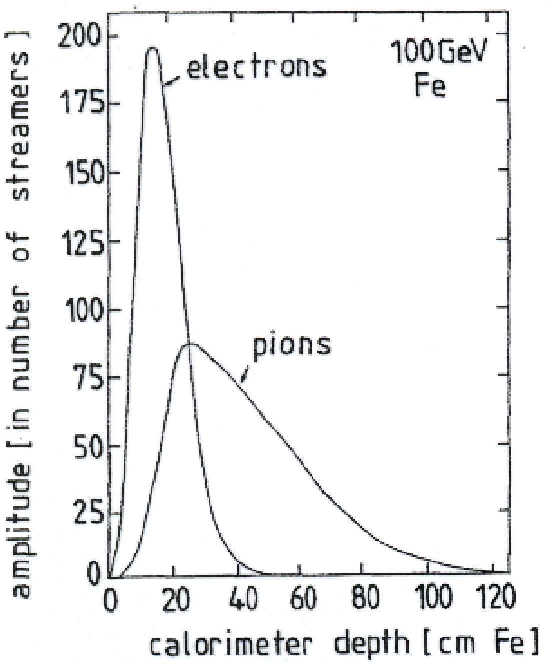

streamer tube calorimeter

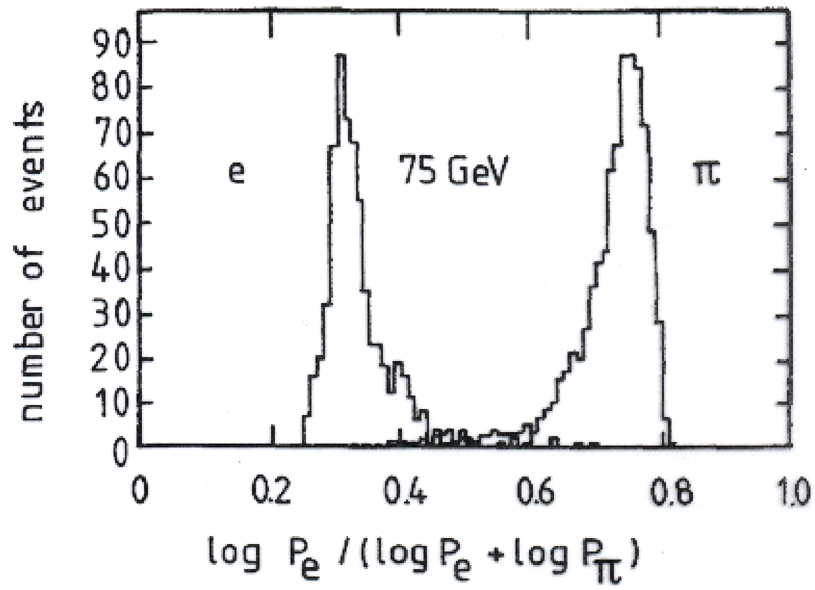

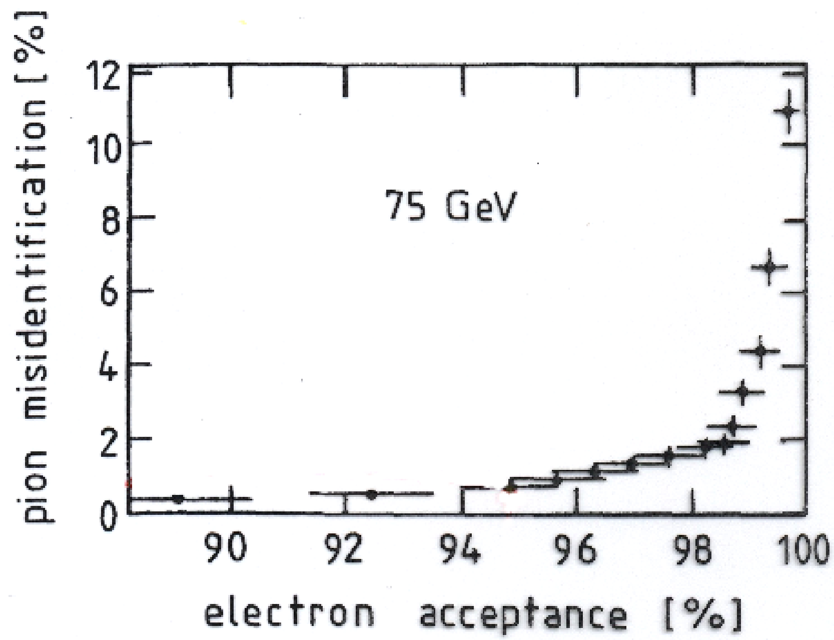

Muon vs pion/electron

low energy loss for muon

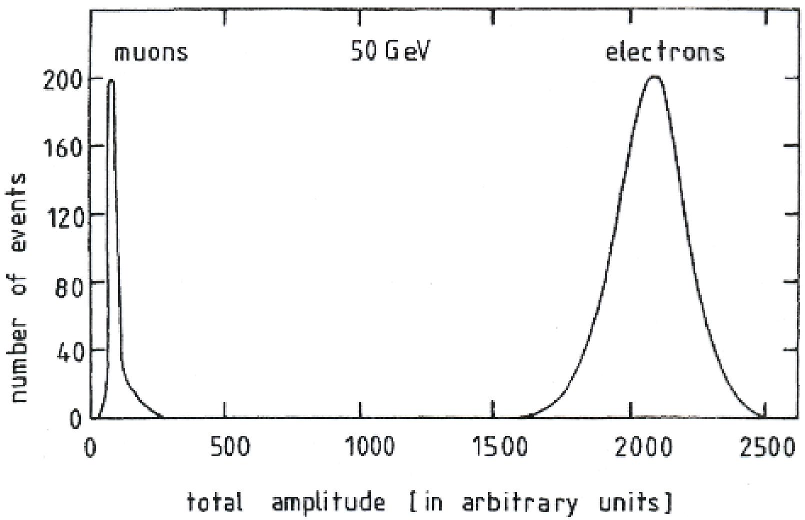

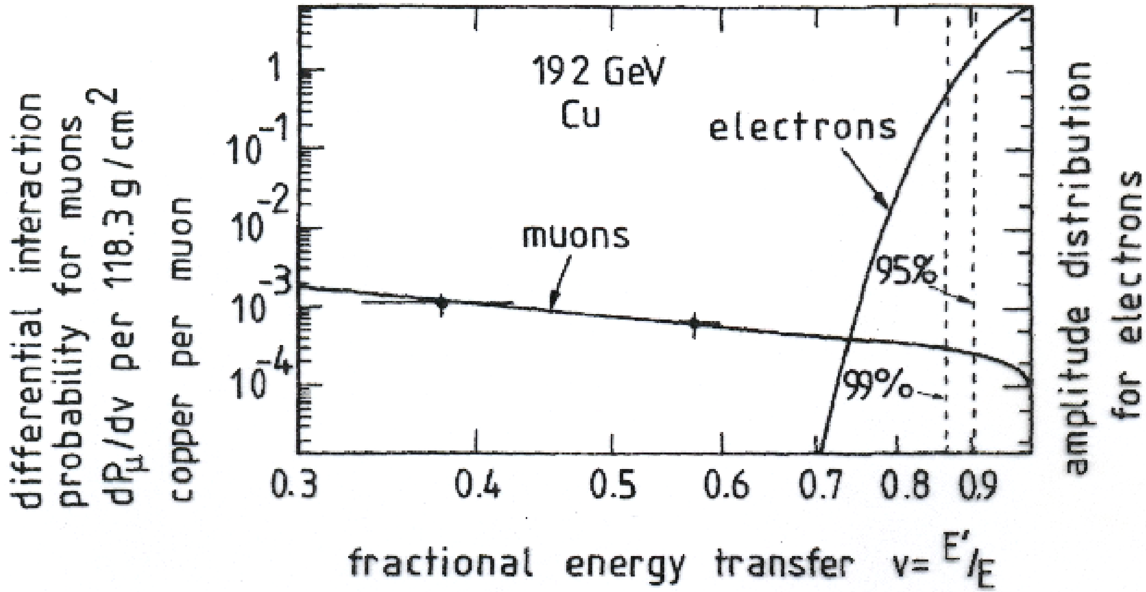

for 95% electron efficiency muon probability $1.7 \cdot 10^{-5}$

9.5 Role of (hadronic) calorimeters in large experiments

increasing importance compared to momentum measurement as energy increases

$$\frac{\sigma_p}{p} = A \oplus B \cdot p \qquad \text{good: } B = 0.1\%$$

$$\frac{\sigma_E}{E} = \frac{A}{\sqrt{E}} \oplus B \oplus \frac{C}{E}$$

ATLAS hadronic calorimeter $A \simeq 0.50,\ B \simeq 0.033,\ C = 0.018$

$$E = 1000\ \text{GeV} \quad \rightarrow \quad \frac{\sigma_E}{E} = 0.04$$

$$\frac{\sigma_p}{p} = 1.00$$

hadronic shower in ATLAS

- visible EM $\sim$ (50%)
  - $e,\ \gamma,\ \pi^0$
- visible non-EM $\sim$ (25%)
  - ionization of $\pi,\ p,\ \mu$
- invisible $\sim$ (25%)
  - nuclear break-up
  - nuclear excitation
- escaped $\sim$ (2%)

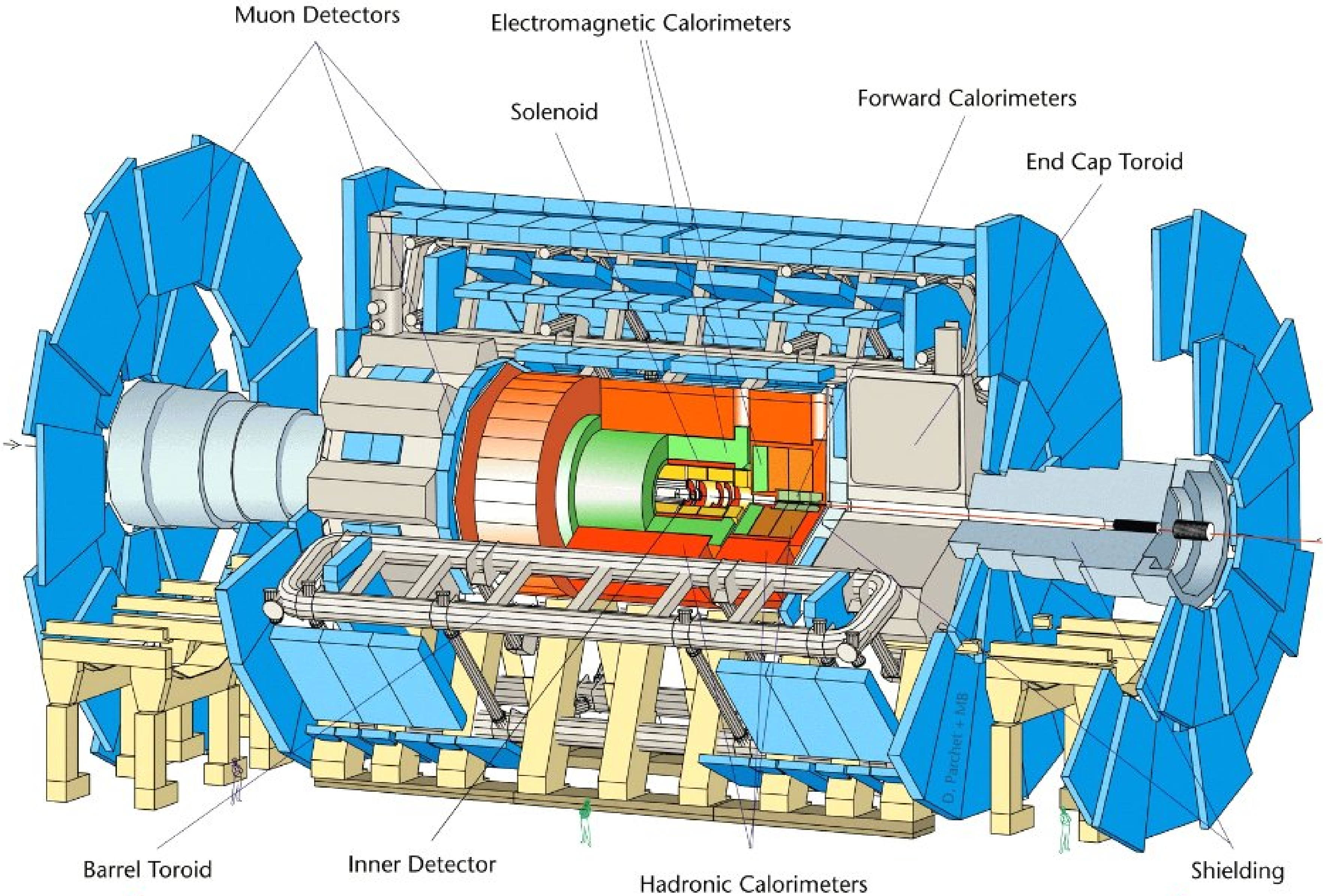

overall layout of the ATLAS detector

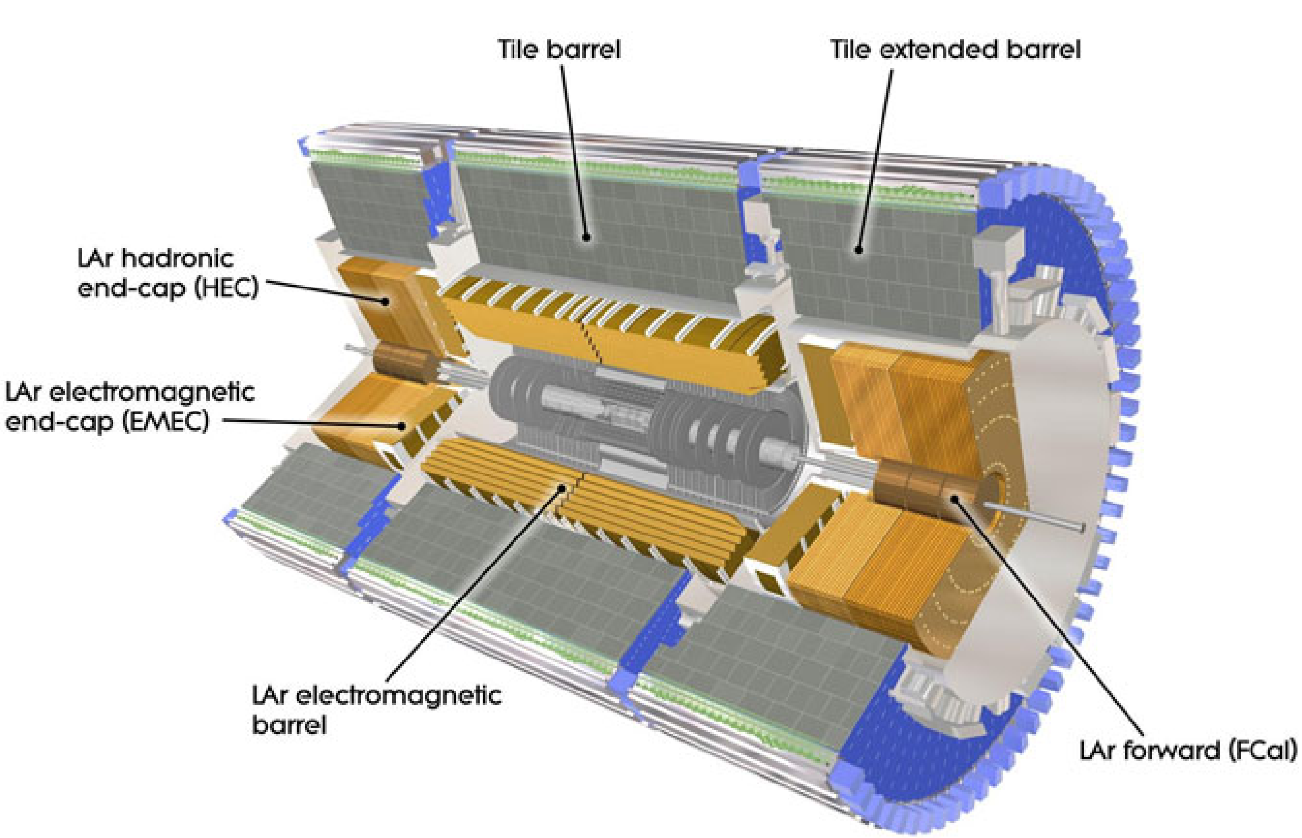

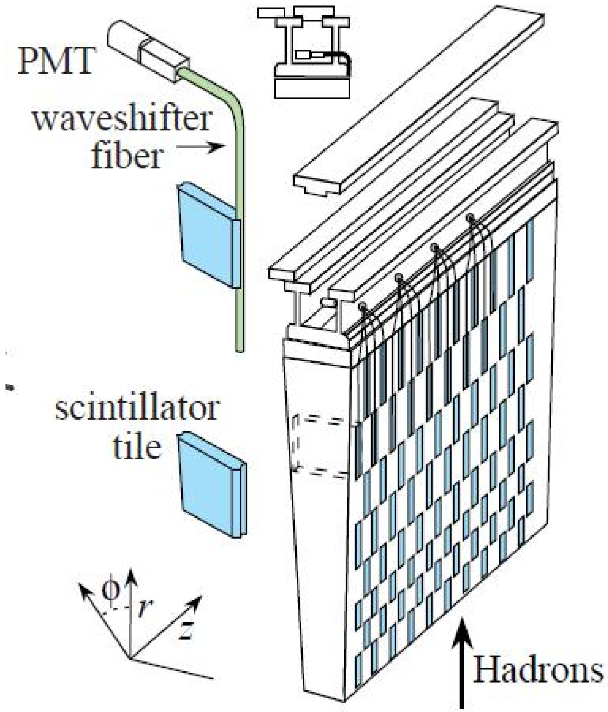

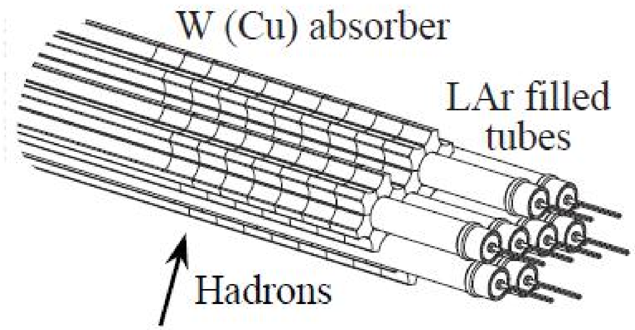

<ins>hadronic tile calorimeters:</ins>
steel sheets and scintillator tiles read out with wavelength-shifting fibers radially along outside faces into PMTs
<ins>forward hadronic calorimeters:</ins>
tubes with LAr embedded into tungsten matrix

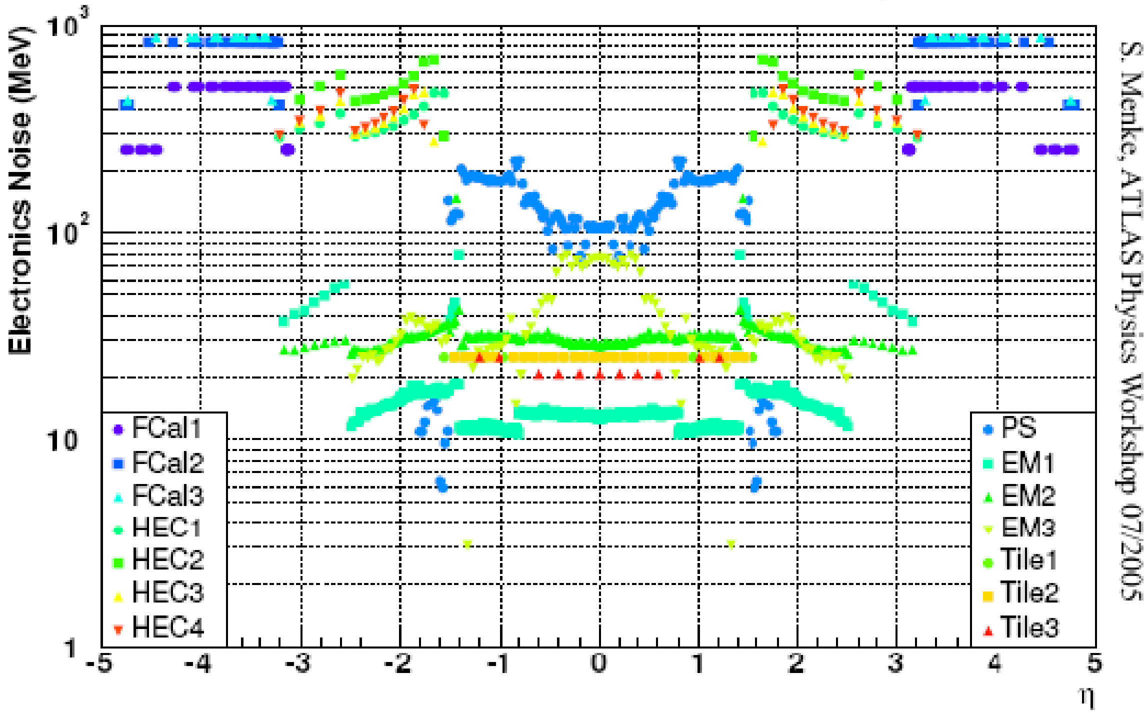

electronic noise in calorimeter cells

10 MeV – 850 MeV

pile-up noise in calorimeter cells

many events piling up on top of each other

introduces asymmetric cell signal fluctuations
from ∼ 10 MeV (rms, central region)
up to ∼ 40 MeV (rms, forward)

similar to coherent noise

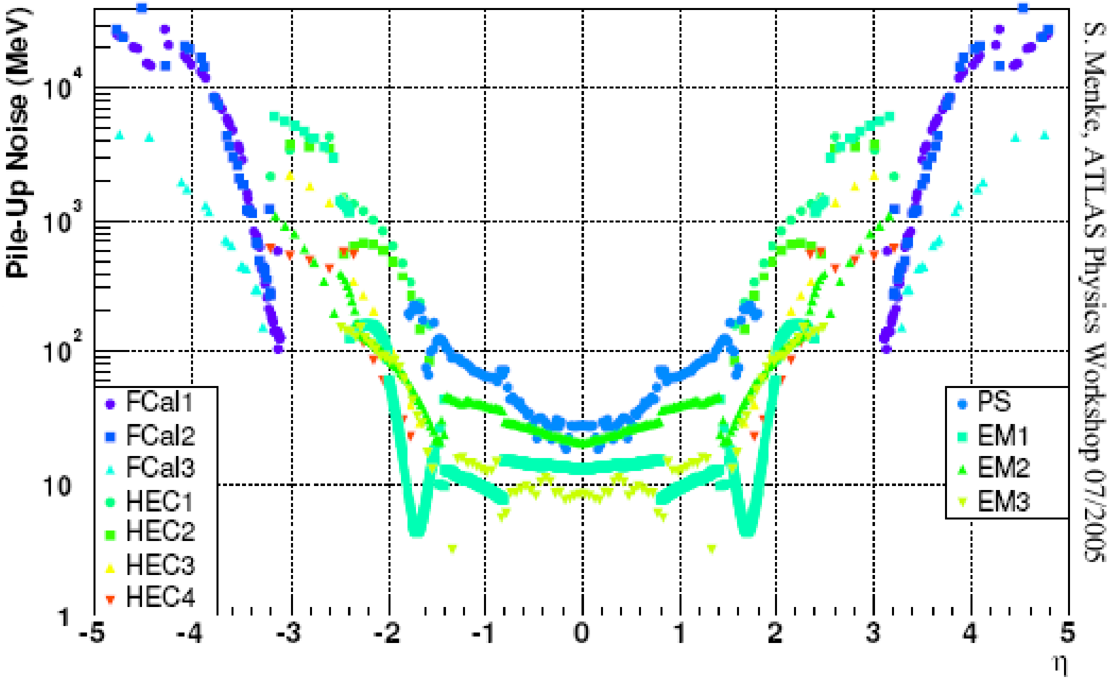

ATLAS tile calorimeter pion energy resolution

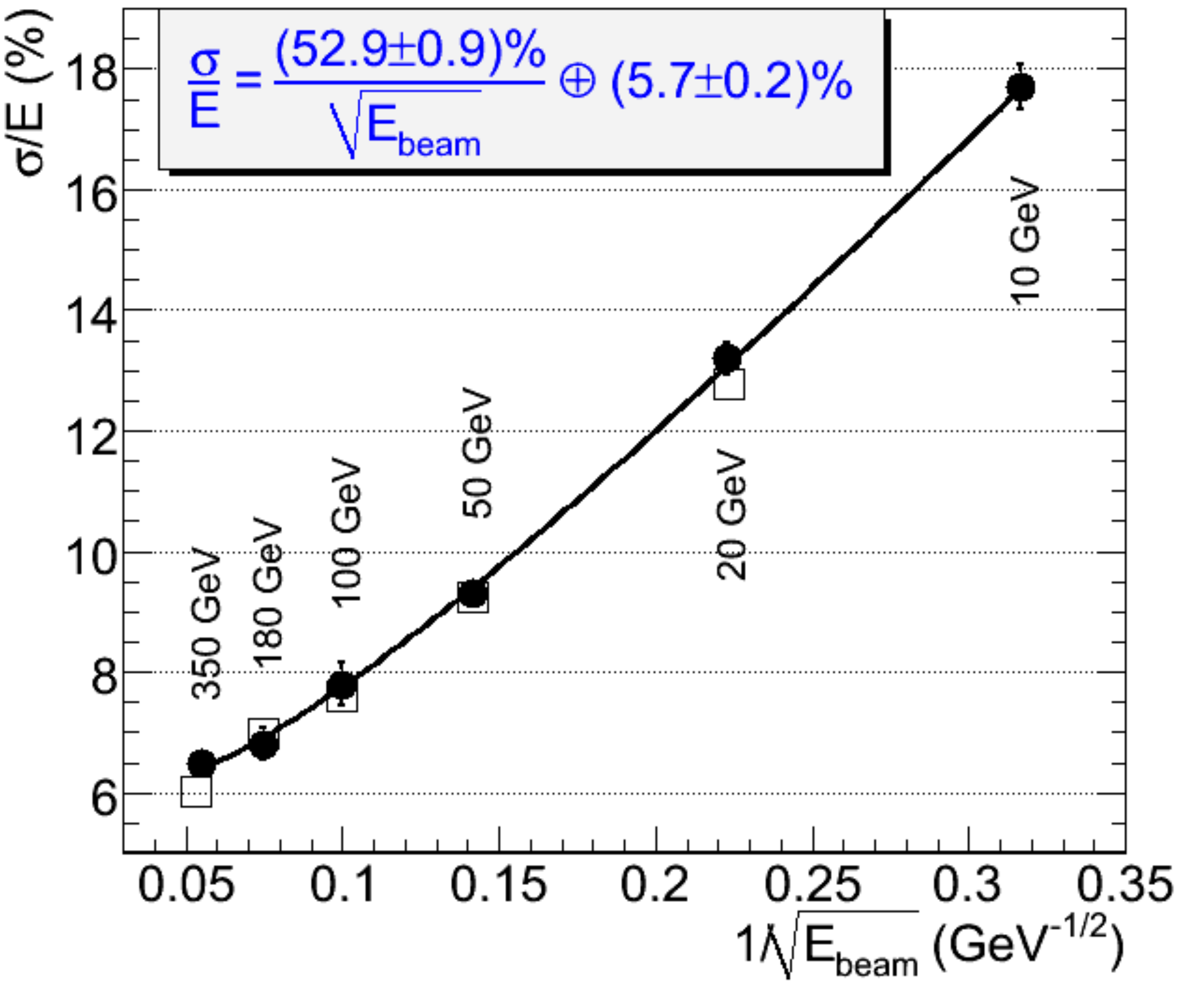

ATLAS tile calorimeter response to hadrons

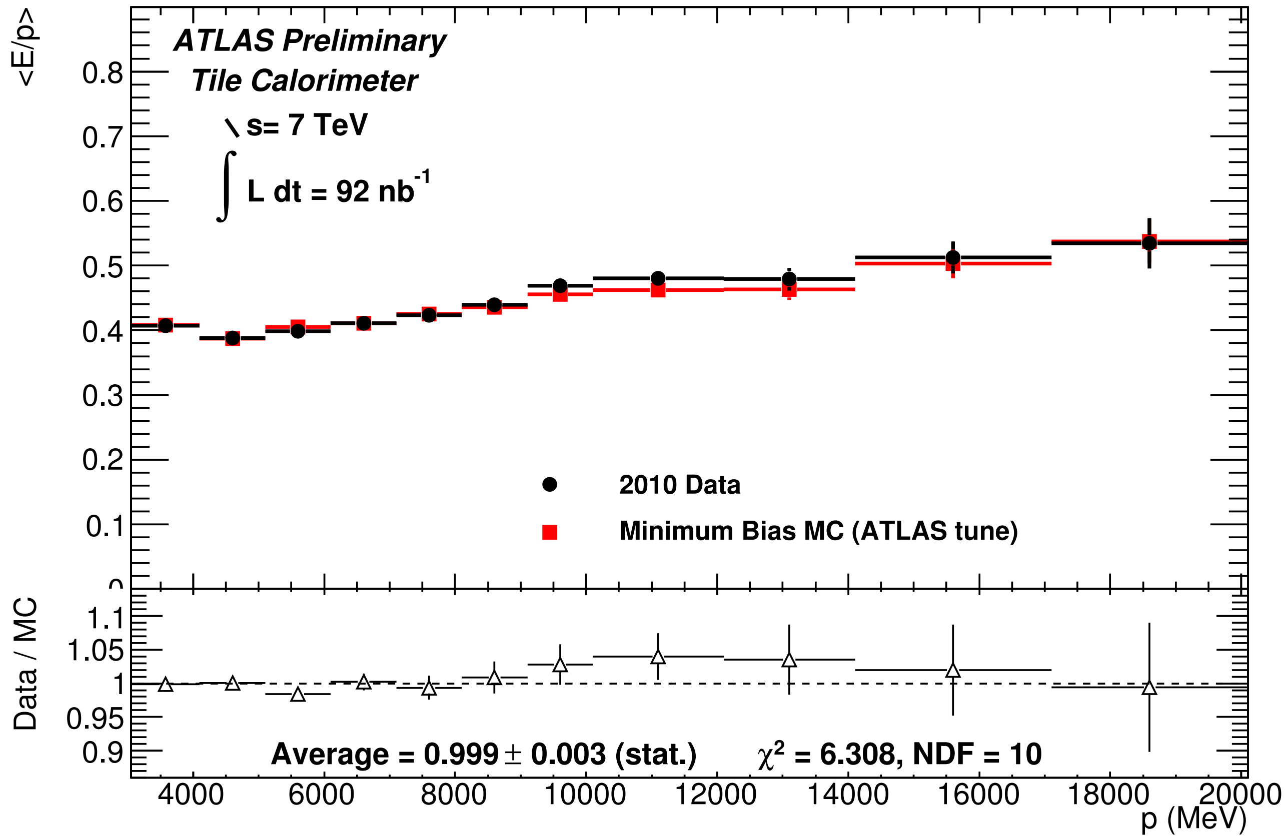

response for isolated tracks that look like mips in EMCal modification of similar chapter from H.C. Schultz-Coulon

10.1 Introduction

Electrically neutral particles do not interact via electromagnetic forces; for detection they are thus generally converted into charged particles.

Apart from the converting material, detectors for neutrals use essentially same techniques as those for charged particles.

Examples:

photons:	total energy deposited in electromagnetic shower use energy measurement, shower shape and information on neutrality (e.g. no track)
neutrons:	energy in calorimeter (high energy) or material with large neutron absorption cross section, such as Li, B, ^{3}He (low energy) and information on neutrality (e.g. no track)
K_0, Λ, ...	reconstruction of invariant masses
neutrinos:	identify products of charged and neutral current interactions

10.2 Detection of Neutrons

Neutron detection via nuclear interaction, interaction used varies with the neutron energy:

high energy	hadron calorimeter (see above) measure energy deposited in form of hadronic shower neutrality of incident particle has no effect on shower process
moderate energy	np-scattering detection of neutrons by scattering them from material containing appreciable amounts of hydrogen; recoiling proton is detected
low energy	exothermal nuclear processes use converter medium with large capture cross-section for slow neutrons; capture process results in unstable nuclei subsequent decay products give a detectable signal

Detection of Neutrons

Nuclear reactions used for neutron detectors:

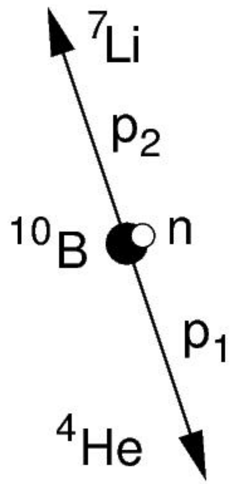

Helium:	$n + {}^3He$	$\rightarrow {}^3H \; + 1H$	$+ 0.76$ MeV	
Lithium:	$n + {}^6Li$	$\rightarrow {}^4He + {}^3H$	$+ 4.79$ MeV	
Boron:	$n + {}^{10}B$	$\rightarrow {}^7Li^* + {}^4He$	$+ 2.31$ MeV	(93%)
		$\rightarrow {}^7Li + 0.48$ MeV		
		$\rightarrow {}^7Li \; + {}^4He$	$+ 2.78$ MeV	(7%)
		charged nuclei	Q-value	

$$\vec{p}_1 = -\vec{p}_2 \qquad T({}^4He) = \frac{m_{\rm Li}}{m_{\rm Li}+m_{\rm He}} \approx \frac{7}{11}Q = 1.77 \text{ MeV}$$

$$\frac{\vec{p}_1^{\,2}}{2m_1} + \frac{\vec{p}_2^{\,2}}{2m_2} = \frac{-\vec{p}_1^{\,2}}{2m_1}\left(1 + \frac{m_1}{m_2}\right) = Q \qquad T({}^7Li) = \frac{m_{\rm He}}{m_{\rm Li}+m_{\rm He}} \approx \frac{4}{11}Q = 1.01 \text{ MeV}$$

Gadolinium:	$n + {}^{155}Gd$	$\rightarrow$	$Gd^* \rightarrow \gamma$-ray cascade (mostly continuum), total energy 8.5 MeV
	$n + {}^{157}Gd$	$\rightarrow$	$Gd^* \rightarrow \gamma$-ray cascade (mostly continuum), total energy 7.9 MeV
Uranium:	$n + {}^{235}U$	$\rightarrow$	fission fragments (T=170 MeV) + neutrons
Plutonium:	$n + {}^{239}Pu$	$\rightarrow$	fission fragments (T=176 MeV) + neutrons

Detection of Neutrons

cross section for neutron capture process (apart from resonances)

$$\sigma(E) \approx \sigma(E_{\rm th})\frac{v_{\rm th}}{v}$$

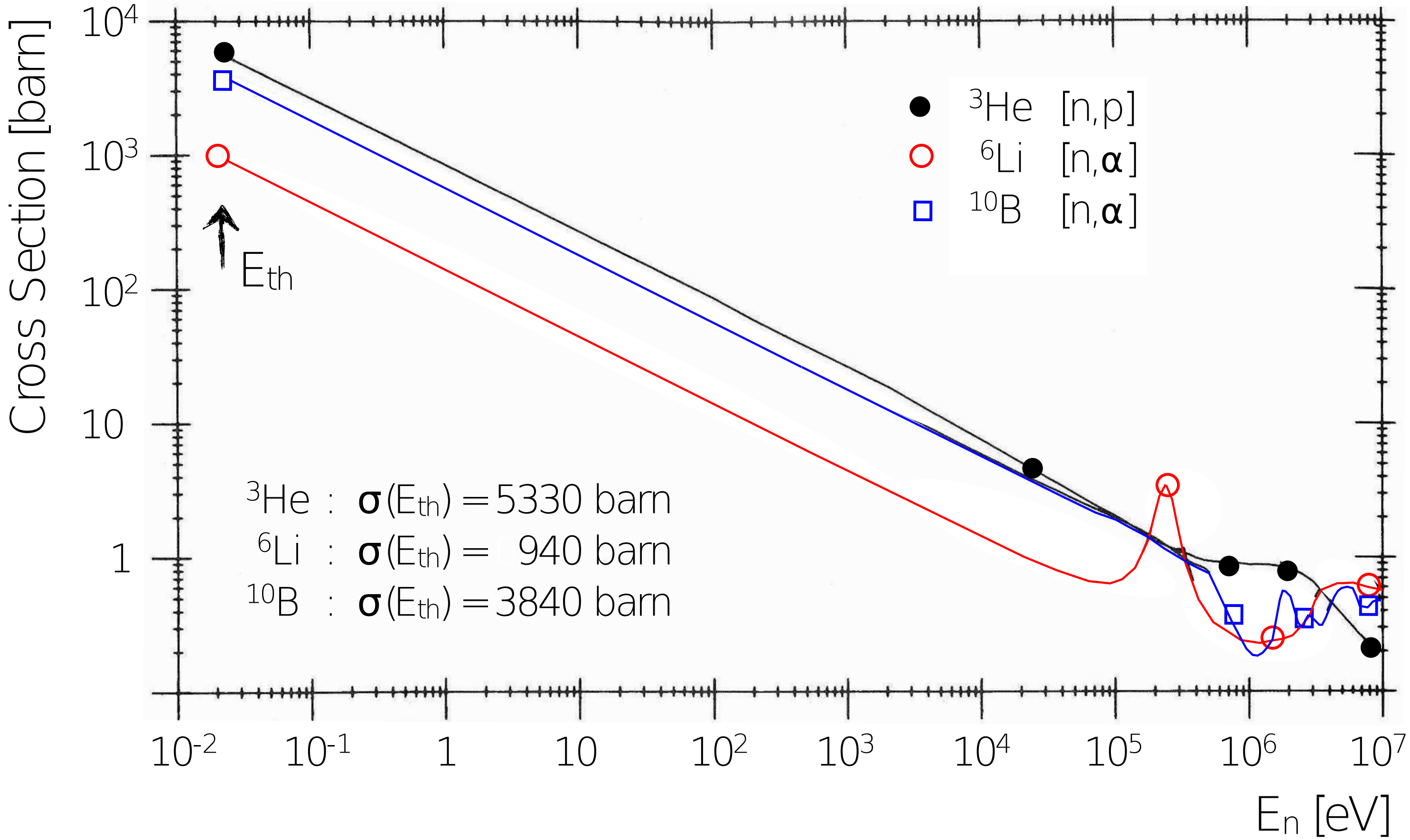

interpretation:

cross section increases with time neutron is close to absorbing nucleus

→ v^{-1}-dependence

Detection of Neutrons

scintillation detectors: detect scintillation light produced in capture process

e.g. Lithium glass:

$n + {}^6\mathrm{Li} \rightarrow {}^4\mathrm{He} + {}^3\mathrm{H} + 4.79$ MeV

common scintillators used for neutron detection

	density of ^{6}Li atoms [10^{22} cm^{-3}]	scintillation efficiency [in %]	photon wavelength [nm]	photons per neutron
Lithium glass (Ce)	1.75	0.45	395	7000
LiI(Eu)	1.83	2.8	470	51 000
ZnS(Ag)-LiF	1.18	9.2	450	160 000

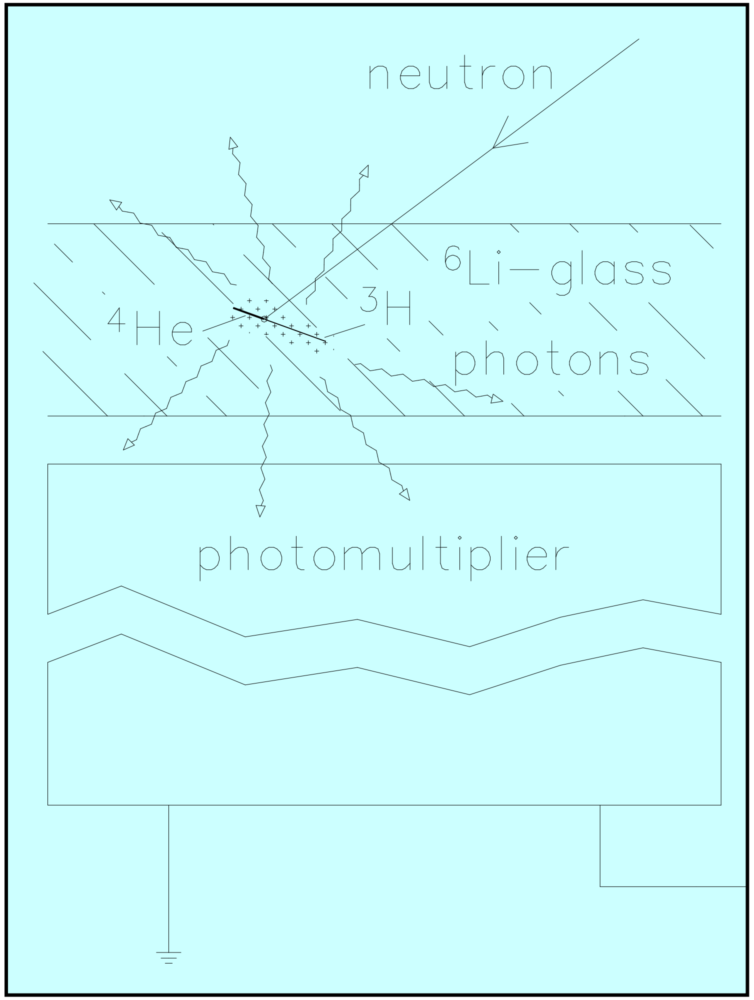

Detection of Neutrons

gas detectors: standard Geiger counter with ^{3}He or BF$_3$ gas

e.g. Helium: $n + {}^3He \rightarrow {}^3H + {}^1H + 0.76$ MeV
(about 25 000 ionizations produced per neutron, charge ≈ 4 fC)

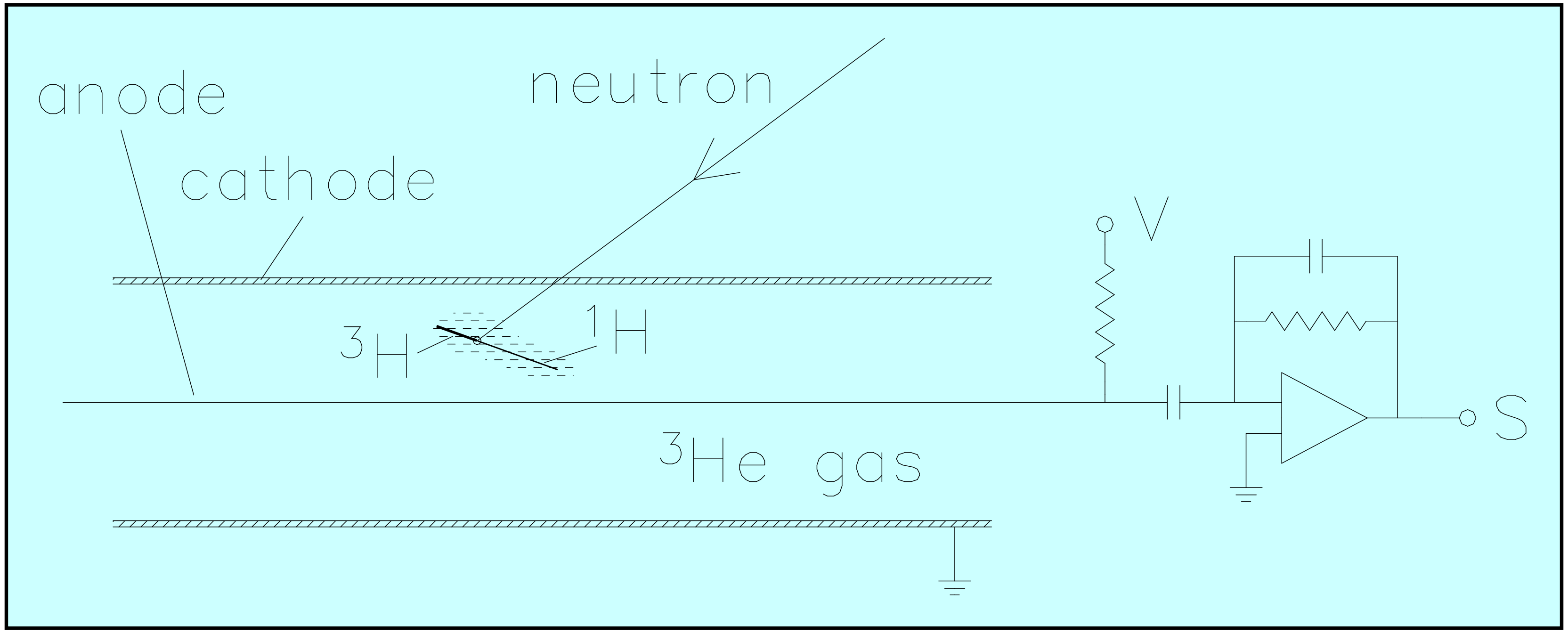

Detection of Neutrons

wall effect:
n + ^{3}He $\rightarrow$ ^{3}H + ^{1}H + 0.76 MeV

from mass ratio
T_p = 573 keV (p = ^{1}H)
T_t = 191 keV (t = ^{3}H)

ranges:

Si: $R_p \approx 6\mu$m, $R_t \approx 5\mu$m
gas: few mm ($\sim 1000 \times R_{\text{solid}}$)

remark: energy spectrum reflects detector response, not neutron energy

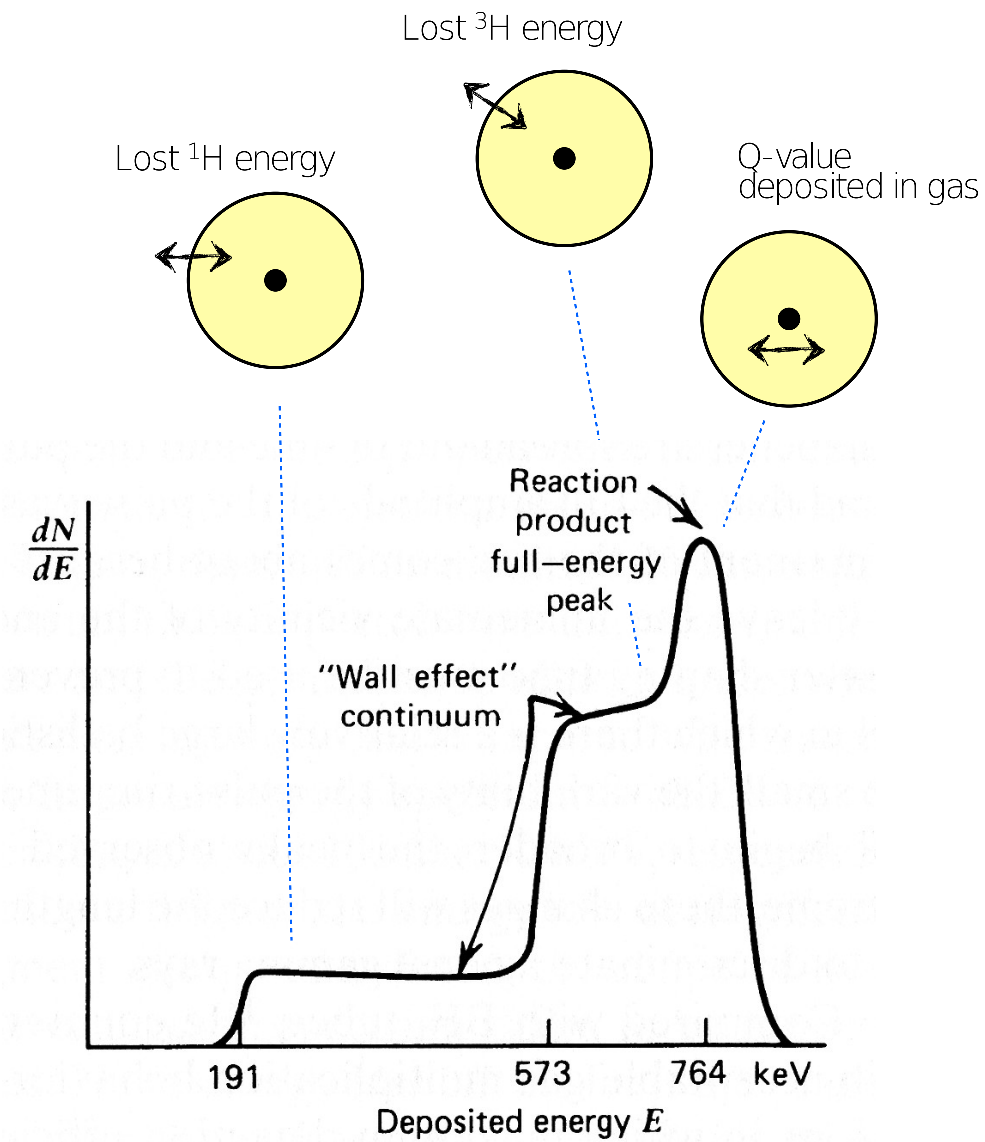

Detection of Neutrons

Fast Neutrons

generally, detection relies on observing neutron-induced nuclear reactions

capture cross sections for fast-neutron induced reactions are small compared to those at low energies; remember: $\sigma_{\text{cap}} \propto 1/v$

two approaches to detect fast neutrons:

- thermalize/moderate & capture as before, only providing count rates (i.e. neutron flux)
- elastic scattering off protons at high energy
  - protons are easy to detect in conventional detectors
  - observe recoils for time-of-flight (ToF), enables neutron energy measurements by measuring the velocity

Detection of Neutrons

Neutron Moderation

- moderate neutrons to increase efficiency in conventional slow-neutron detector
- hydrogen-rich materials: polyethylene or paraffin

optimum thickness between few cm to tens of cm
for energies of keV to MeV

trade-off between sufficient slow down
and detection cross section

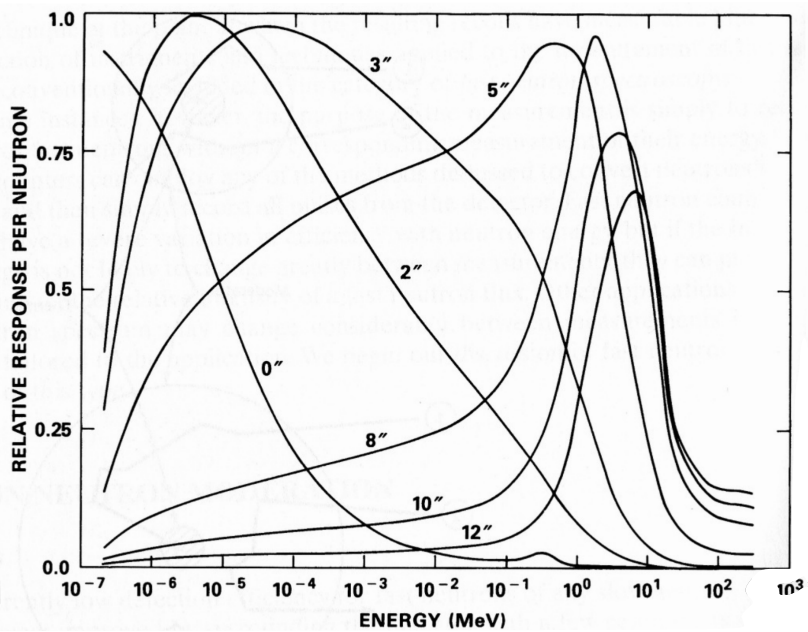

Relative response vs. energy for
various absorber thicknesses (in inch)

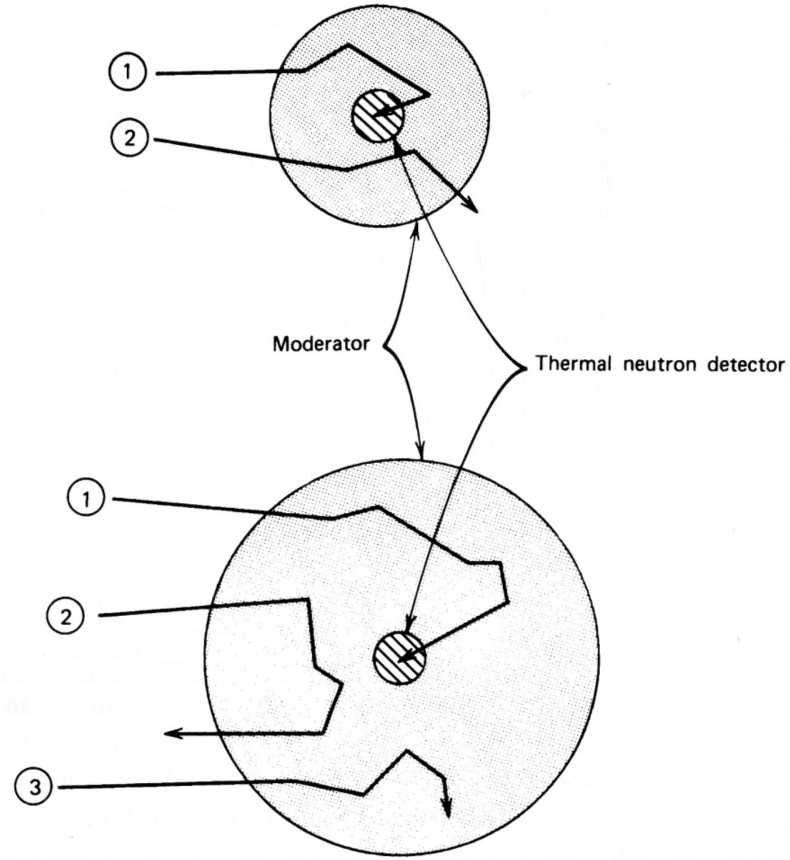

Detection of Neutrons

The Bonner Sphere - Tom W. Bonner et al., 1960

10-12" diameter moderator sphere with LiI(Eu) scintillator in center, has a similar response curve as the neutron rem dose curve in tissue

application:

several spheres of diff. size → neutron spectrum
single sphere of appropriate size: determination of dose equivalent due to neutrons with an unknown or variable neutron spectrum

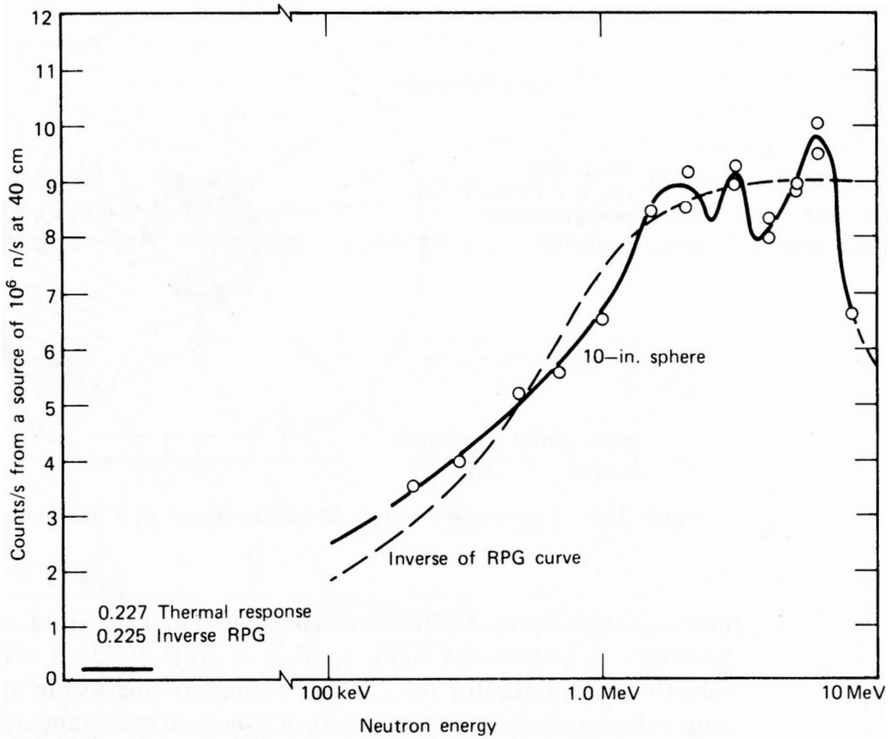

Detection of Neutrons

The Long Counter

neutron energy independent efficiency:
'flat response'

slow-neutron BF_3 detector in center of device
paraffin moderator, B_2O_3 absorber (shielding)

only sensitive to neutrons from one side

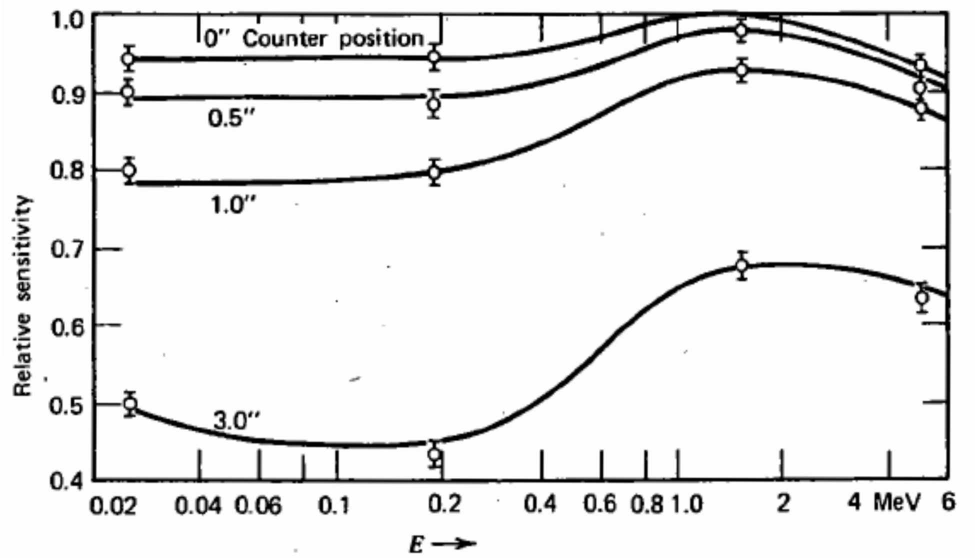

relative sensitivity of Long Counter

varied parameter is the distance of the end of the BF_3 tube if shifted in from the front of the moderator face

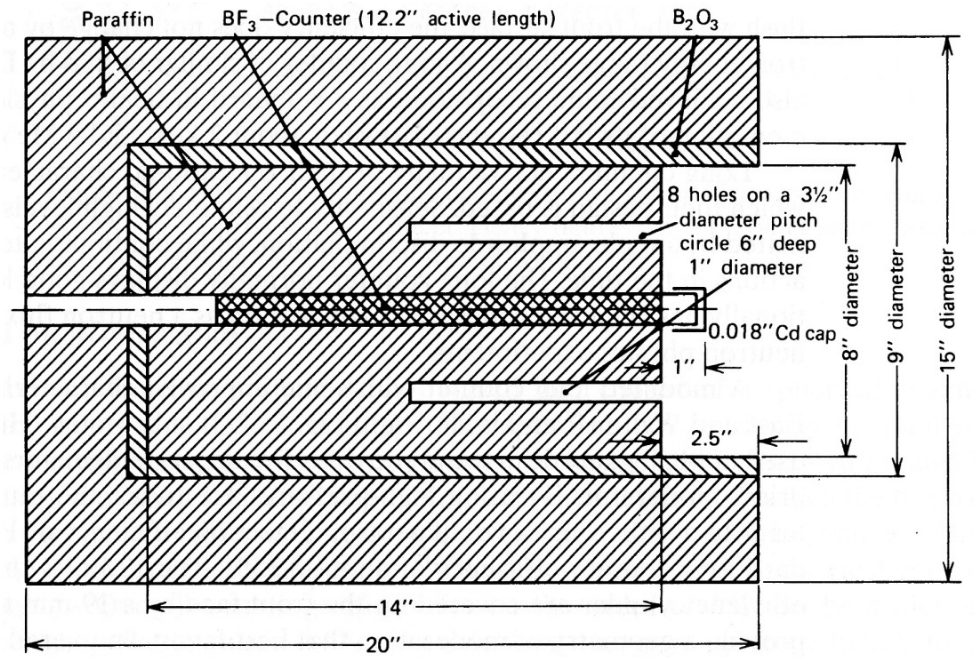

cross section of Long Counter

cencentric holes prevent efficiency reduction for neutrons with energies below 1 MeV

Detection of Neutrons

detector type	size	neutron active material	incident neutron energy	neutron detection efficiency[a] (%)	γ-ray sensitivity (R/h)[b]
plastic scintillator	5 cm thick	^{1}H	1 MeV	78	0.01
liquid scintillator	5 cm thick	^{1}H	1 MeV	78	0.1
loaded scintillator	1 mm thick	^{6}Li	thermal	50	1
Hornyak button	1 mm thick	^{1}H	1 MeV	1	1
CH_4 (7 bar)	5 cm Ø	^{1}H	1 MeV	1	1
^{4}He (18 bar)	5 cm Ø	^{4}He	1 MeV	1	1
^{3}He (4 bar), Ar (2 bar)	2.5 cm Ø	^{3}He	thermal	77	1
^{3}He (4 bar), CO_2 (5%)	2.5 cm Ø	^{3}He	thermal	77	10
BF_3 (0.66 bar)	5 cm Ø	^{10}B	thermal	29	10
BF_3 (1.18 bar)	5 cm Ø	^{10}B	thermal	46	10
^{10}B-lined chamber	0.2 mg/cm^3	^{10}B	thermal	10	10^3
fission chamber	1.0 mg/cm^3	^{235}U	thermal	0.5	$10^6 - 10^7$

[a] interaction probability for neutrons of the specified energy, normal incidence angle
[b] approximate upper limit of γ-ray dose that can be present with the detector still providing usable neutron output signals

Detection of Neutrons

Cascade Detector

capture process:

$$\begin{aligned} n + {}^{10}\mathrm{B} &\rightarrow {}^{7}\mathrm{Li}^{*} + {}^{4}\mathrm{He} + 2.31\ \mathrm{MeV}\ (93\%) \\ &\rightarrow {}^{7}\mathrm{Li} + {}^{4}\mathrm{He} + 2.78\ \mathrm{MeV}\ (7\%) \end{aligned}$$

Setup:

Boron layers on multiple GEM foils

GEMs:

- operated to be transparent for produced charges
- can be cascaded
- two Boron layers each
- last one: amplification layer
- high rate capability [10^7 Hz/cm^2]

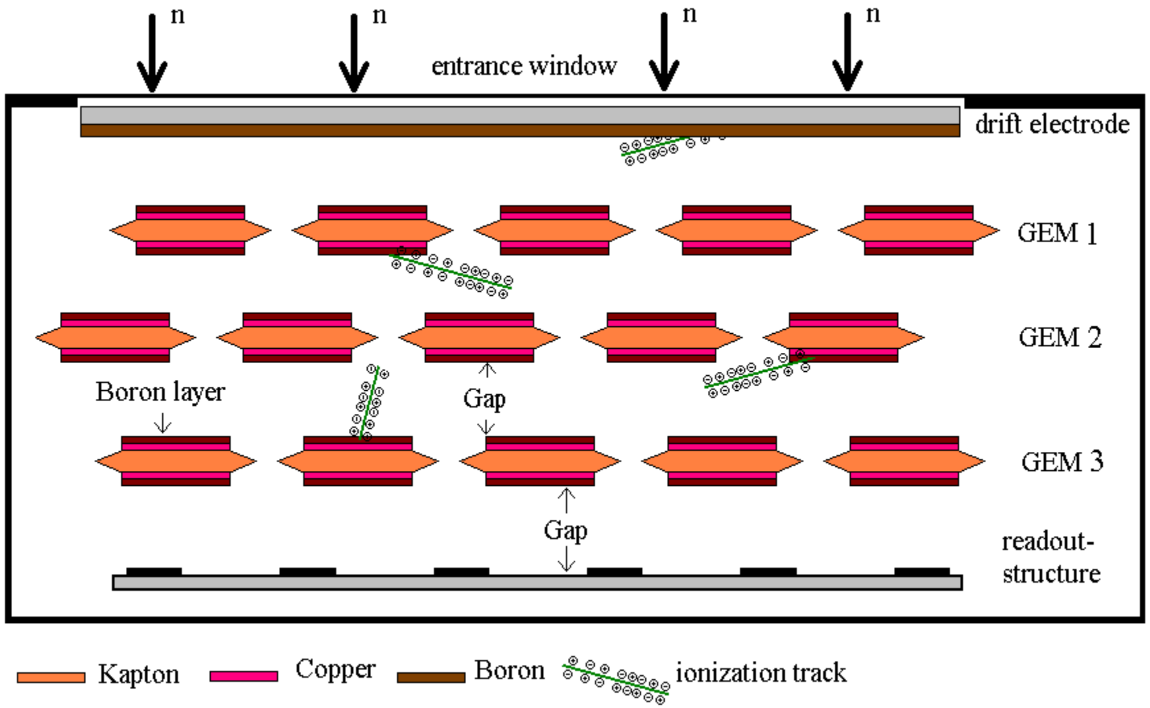

CASCADE neutron detector schematic

Detection of Neutrons

CASCADE Detector, M. Klein, C. Schmidt NIM A628 (2011) 9

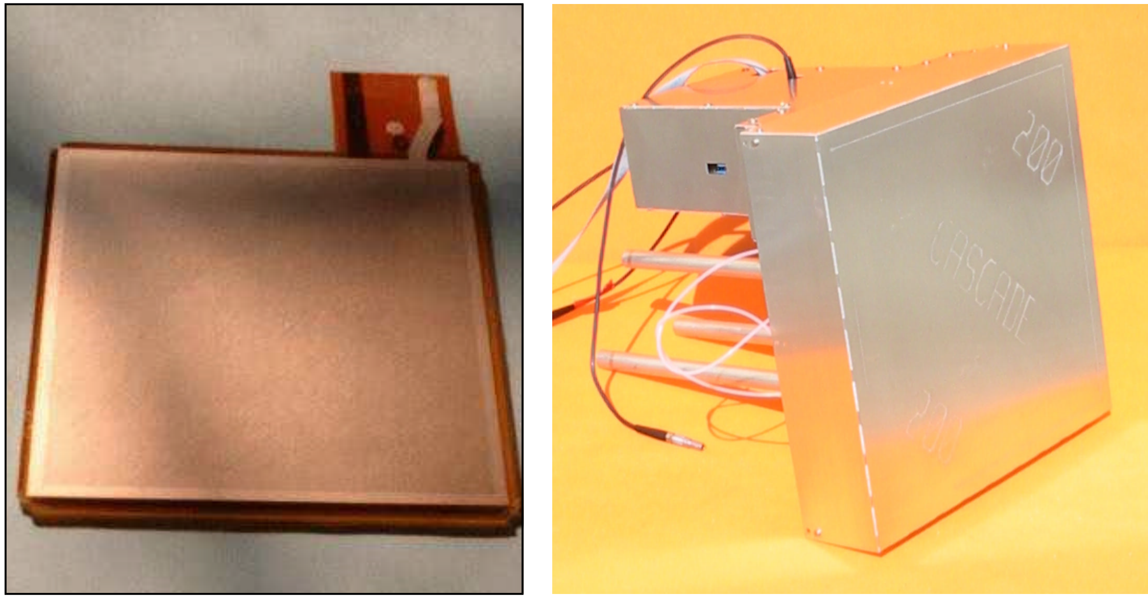

GEM foil glued to frame, complete CASCADE module

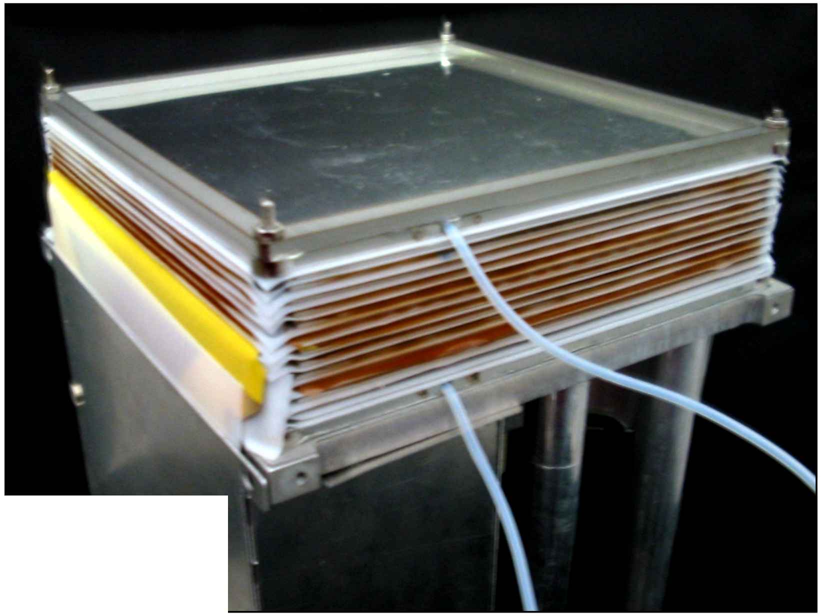

Cascade neutron detector: several GEM-modules stacked with drift electrodes and readout

10.3 Detection of Neutrinos

neutrino detection only via weak interaction

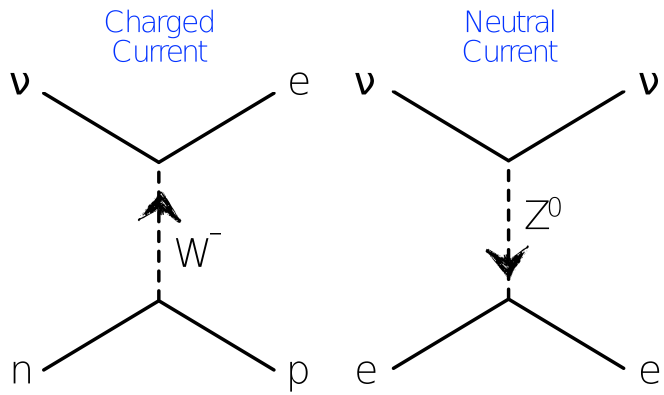

possible reactions:

charged current reactions:

$$\begin{aligned}
\nu_e &+ n \rightarrow e^- + p \\
\bar{\nu}_e &+ p \rightarrow e^+ + n \\
\nu_\mu &+ n \rightarrow \mu^- + p \\
\bar{\nu}_\mu &+ p \rightarrow \mu^+ + n \\
\nu_\tau &+ n \rightarrow \tau^- + p \\
\bar{\nu}_\tau &+ p \rightarrow \tau^+ + n
\end{aligned}$$

...

$$\begin{aligned}
\bar{\nu}_e &+ e^- \rightarrow \mu^- + \bar{\nu}_\mu \\
\bar{\nu}_e &+ e^- \rightarrow \tau^- + \bar{\nu}_\tau
\end{aligned}$$

neutral current reactions:

$$\begin{aligned}
\nu_e &+ e^- \rightarrow \nu_e + e^- \\
\nu_\mu &+ e^- \rightarrow \nu_\mu + e^- \\
\nu_\tau &+ e^- \rightarrow \nu_\tau + e^-
\end{aligned}$$

neutrino-nucleon cross section, examples:
10 GeV neutrinos: $\sigma = 7 \cdot 10^{-38}$ cm^2/nucleon
on 10 m Fe-target,
interaction probability $P = \sigma N_A d \rho = 3.2 \cdot 10^{-10}$
with $d = 10$ m, $\rho = 7.6$ g/cm^3

solar neutrinos (100 keV): $\sigma = 7 \cdot 10^{-45}$ cm^2/nucleon
through earth, interaction probability: $P = 2.8 \cdot 10^{-11}$
with $d = 12000$ km $= 1.2 \cdot 10^9$ cm, $\rho = 5.5$ g/cm^3

Neutrinos from the Sun (pp chain)

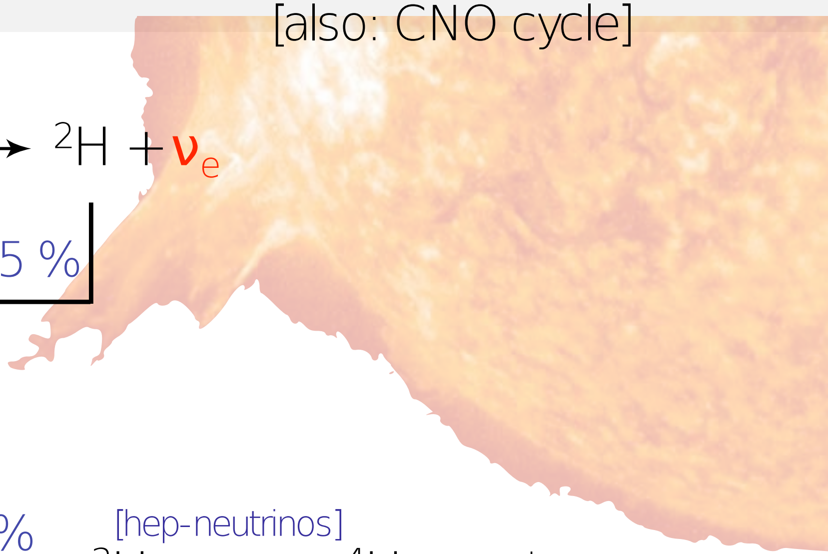

[also: CNO cycle]

[pp-neutrinos]
$p + p \rightarrow {}^{2}H + e^{+} + \nu_e$

[pep-neutrinos]
$p + e^{-} + p \rightarrow {}^{2}H + \nu_e$

99.75 % | 0.25 %

${}^{2}H + p \rightarrow {}^{3}He + \gamma$

85% | ~15% | ~10^{-5} %

${}^{3}He + {}^{3}He \rightarrow {}^{4}He + 2p$

${}^{3}He + {}^{4}He \rightarrow {}^{7}Be + \gamma$

[hep-neutrinos]
${}^{3}He + p \rightarrow {}^{4}He + e^{+} + \nu_e$

15.07 % | 0.02 %

${}^{7}Be + e^{-} \rightarrow {}^{7}Li + \gamma + \nu_e$
[^{7}Be-neutrinos]

${}^{7}Li + p \rightarrow \alpha + \alpha$

${}^{7}Be + p \rightarrow {}^{8}B + \gamma$

${}^{8}B \rightarrow {}^{8}Be^{*} + e^{+} + \nu_e$
[^{8}B-neutrinos]

Neutrinos from the Sun

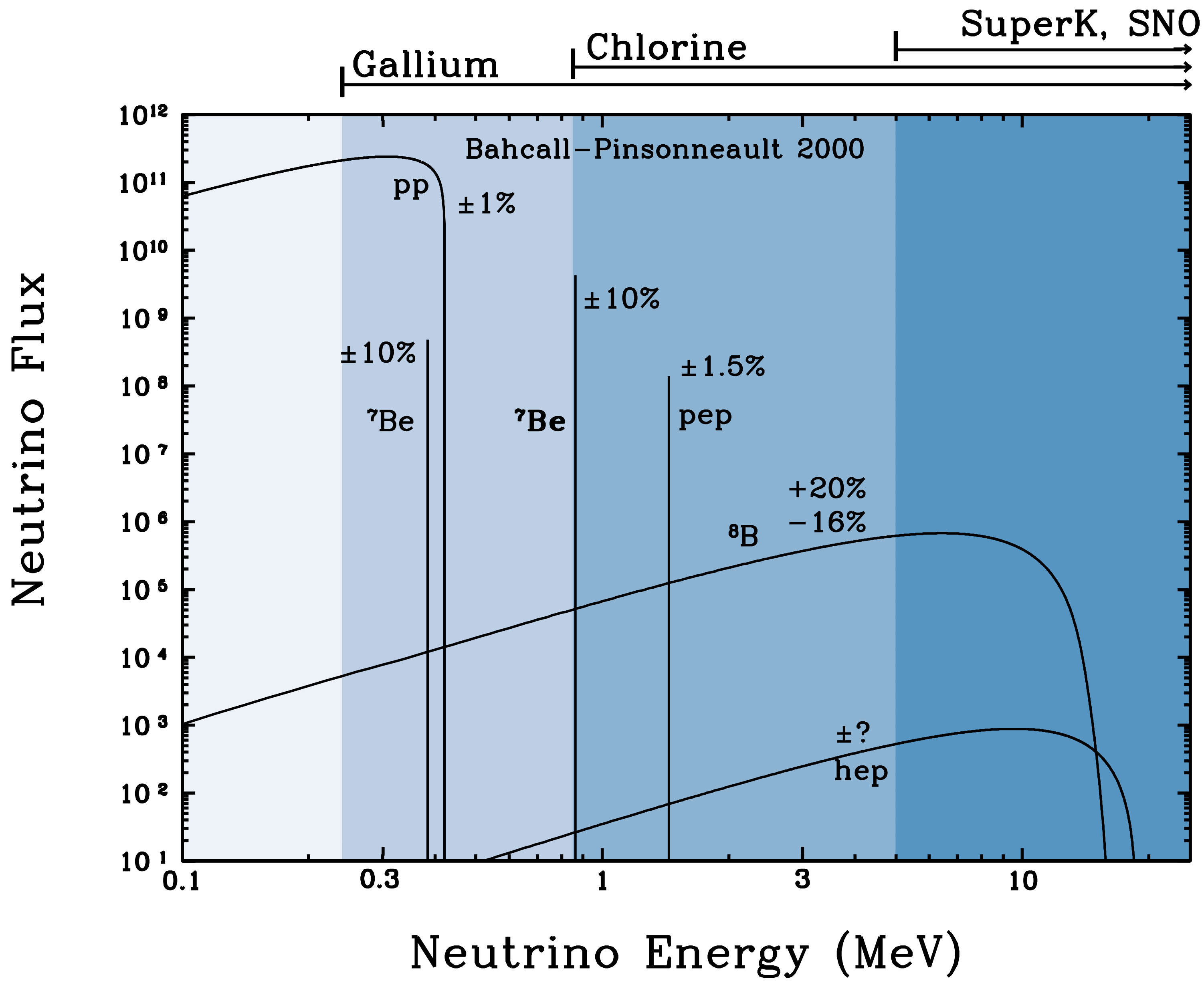

Solar Electron-Neutrino Problem

in SNU

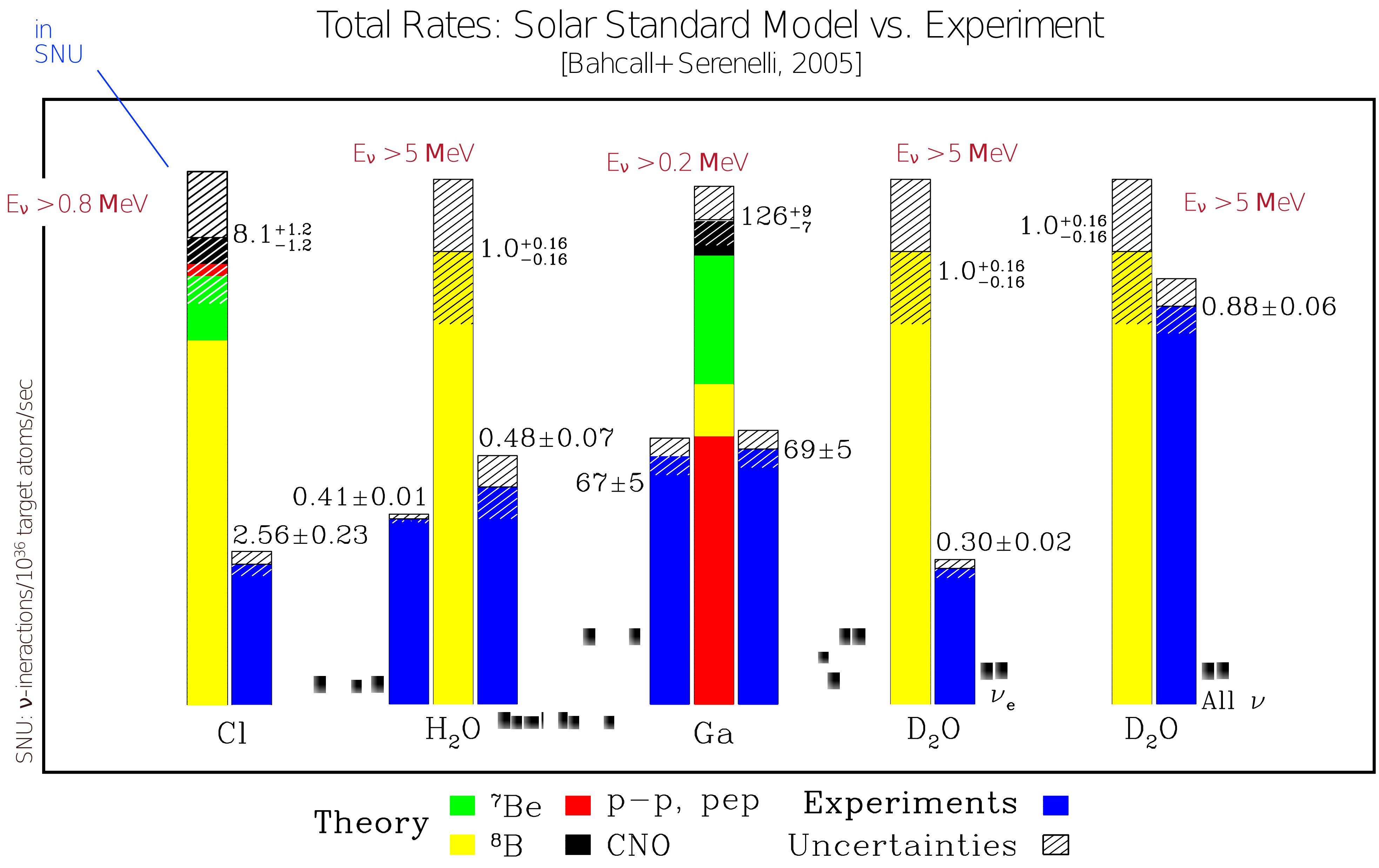

The Homestake Experiment

the Homestake Gold Mine in South Dakota

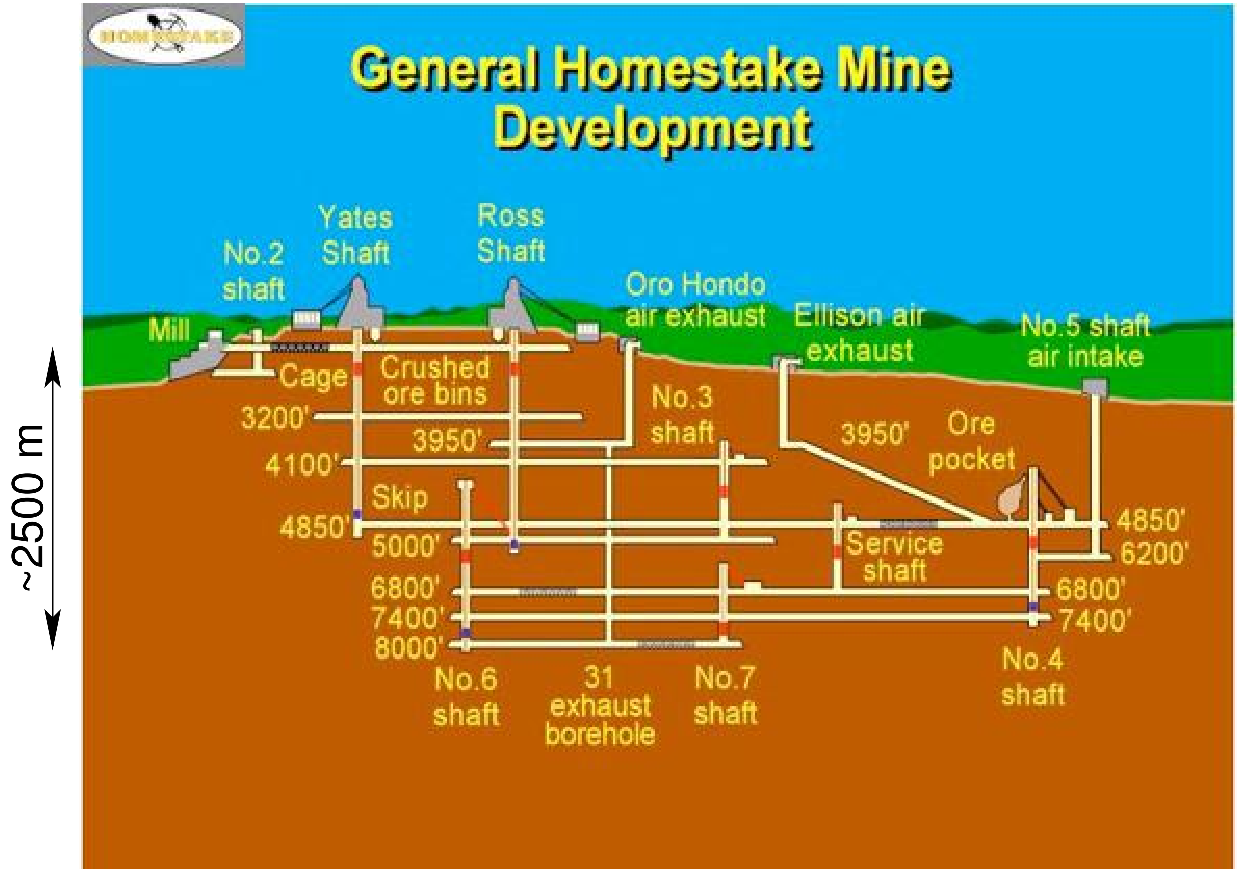

The Homestake Experiment

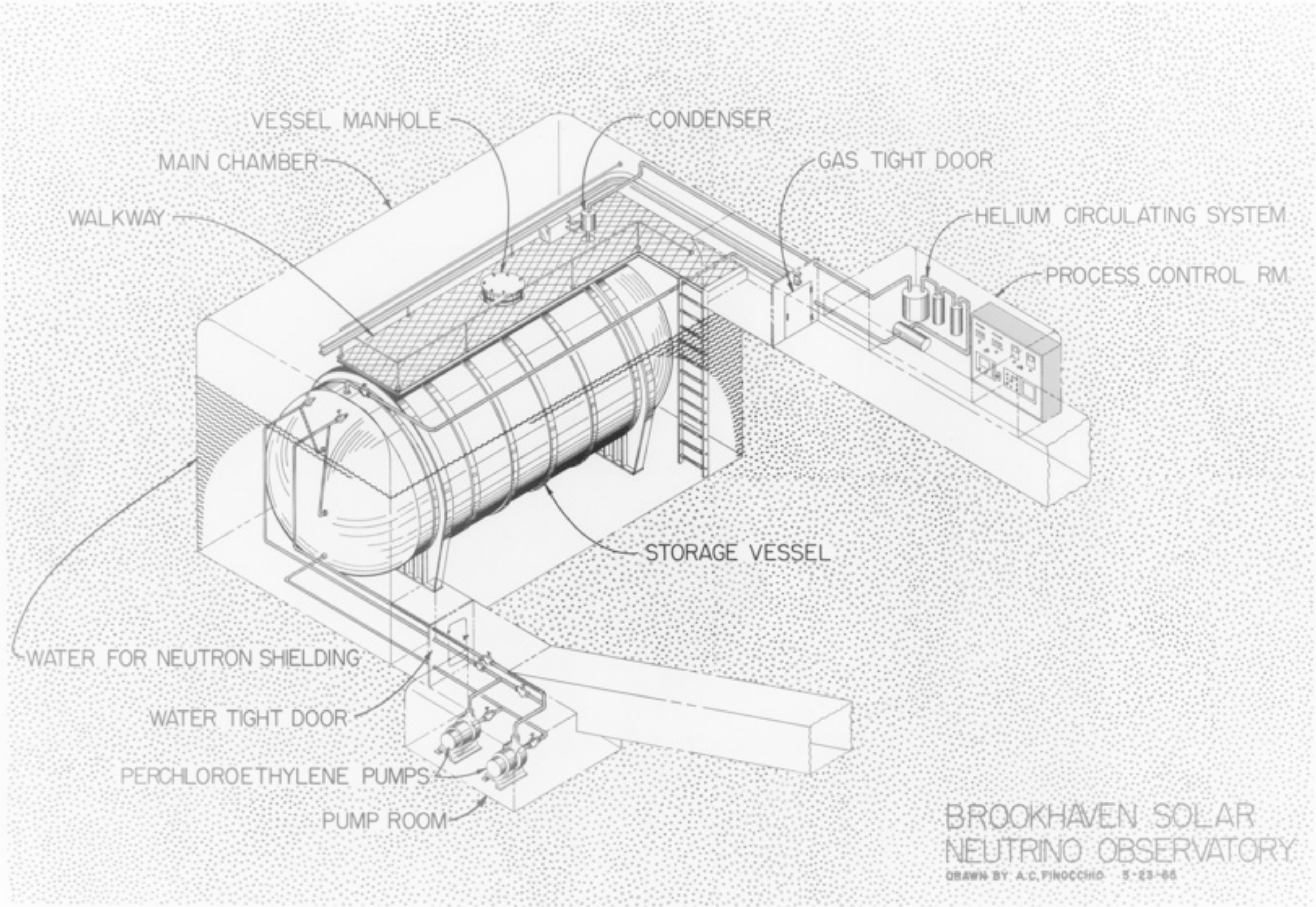

The Homestake Experiment

Raymond Davis Jr. construction of the Homestake Mine tank

The Homestake Experiment

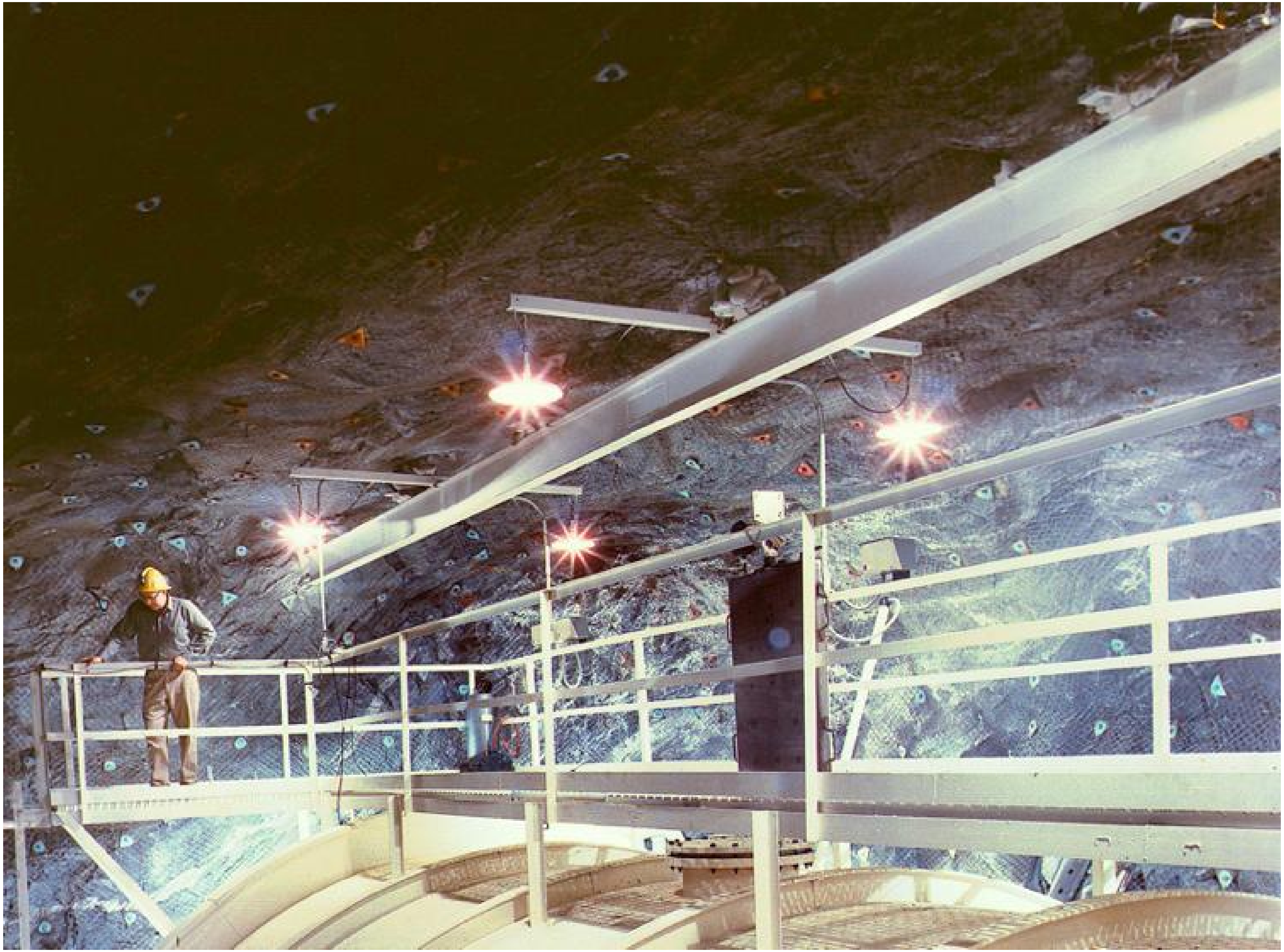

The Homestake Experiment

Raymond Davis Jr. the eductors being tested in swimming pool at BNL

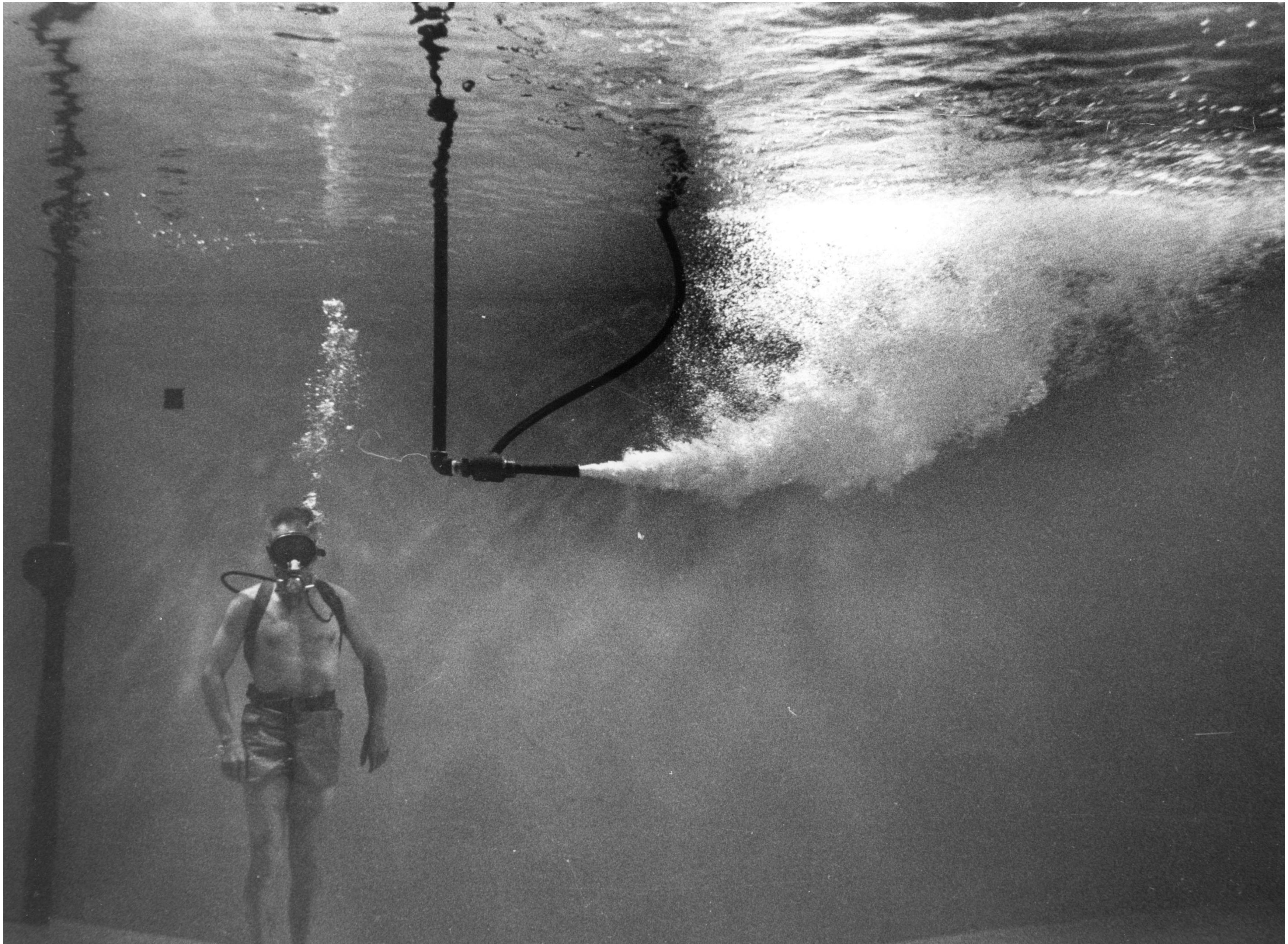

The Homestake Experiment

neutrino capture:

$^{37}\mathrm{Cl} + \nu_e \rightarrow {}^{37}\mathrm{Ar} + \mathrm{e}$

detection of ^{37}Ar via K-shell e$^-$-capture
[$^{37}\mathrm{Ar}(\mathrm{e},\nu_\mathrm{e})^{37}\mathrm{Cl}$] $\tau \approx 35$ d
resulting in a 2.82 keV Auger electron
detection after extraction in proportional counter

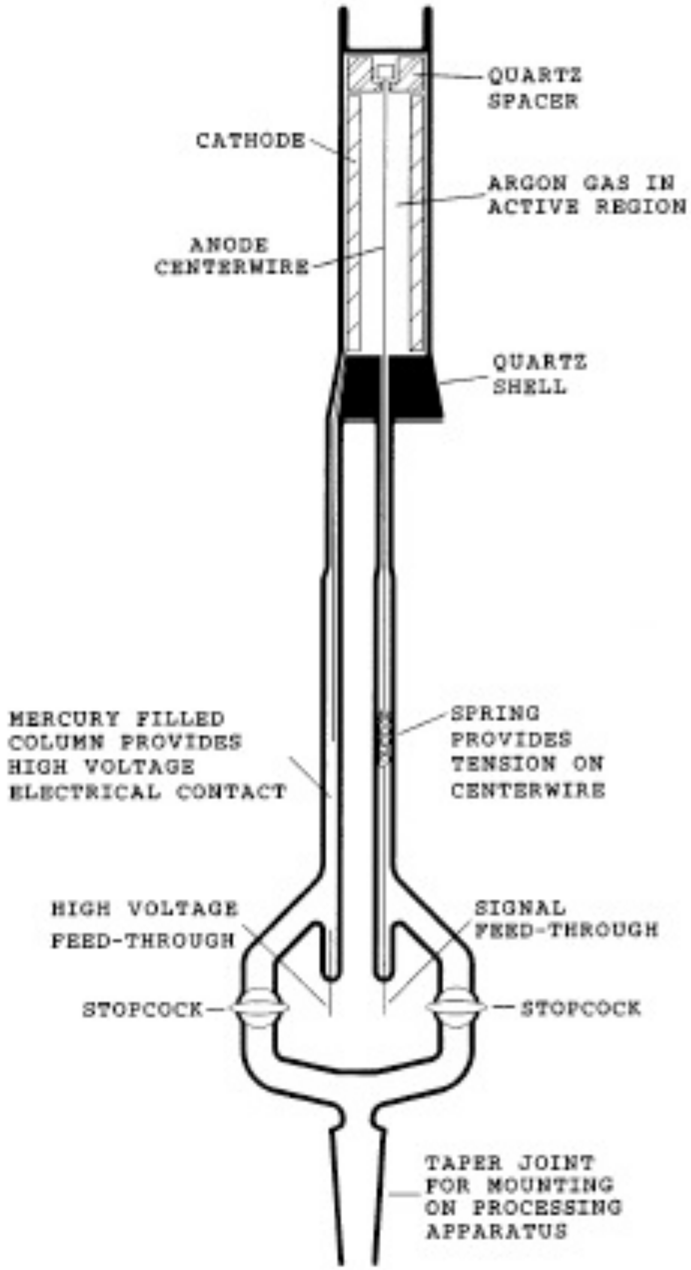

The Homestake Experiment

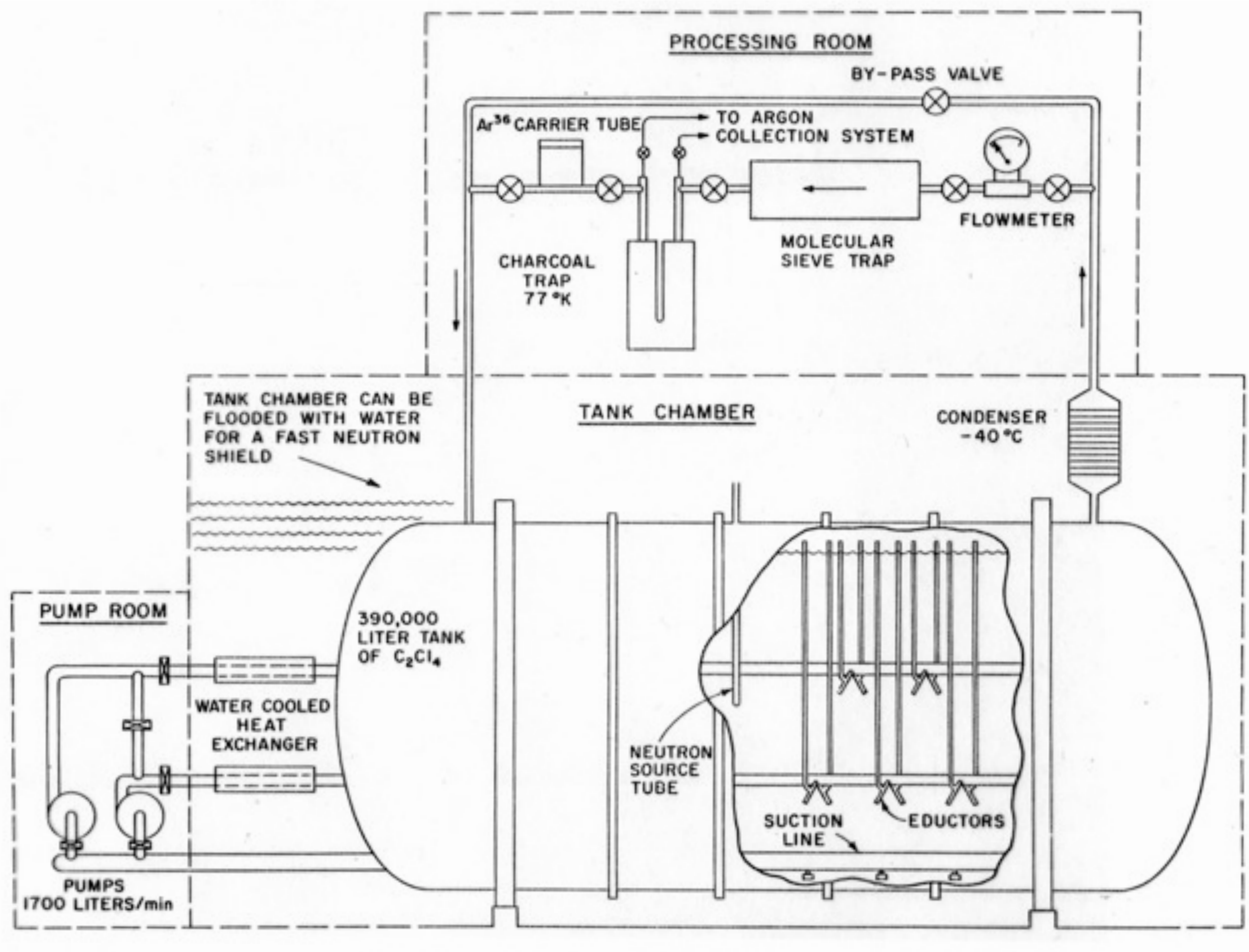

The Homestake Experiment

some approximate numbers

- 615 tons C_2Cl_4 (tetrachloro-ethylene)
- about $2 \cdot 10^{30}$ chlorine atoms (^{37}Cl)
- prediction: $7.5 \cdot 10^{-36}$ neutrino reactions/atom/s = 7.5 SNU
- considering half-life = 35 days, expect: 60 atoms every 2 months
- After 25 years: expectation: $\approx$ 5000 ^{37}Ar atoms expected
  observation: $\approx$ 2200 ^{37}Ar atoms produced

  [875 counted, 776 after background subtraction]

  ^{37}Ar extraction efficiency: $\approx$ 95%
  ^{37}Ar decay detection efficiency: $\approx$ 45%

The Homestake Experiment

Pulse height Spectra from first runs [1968]

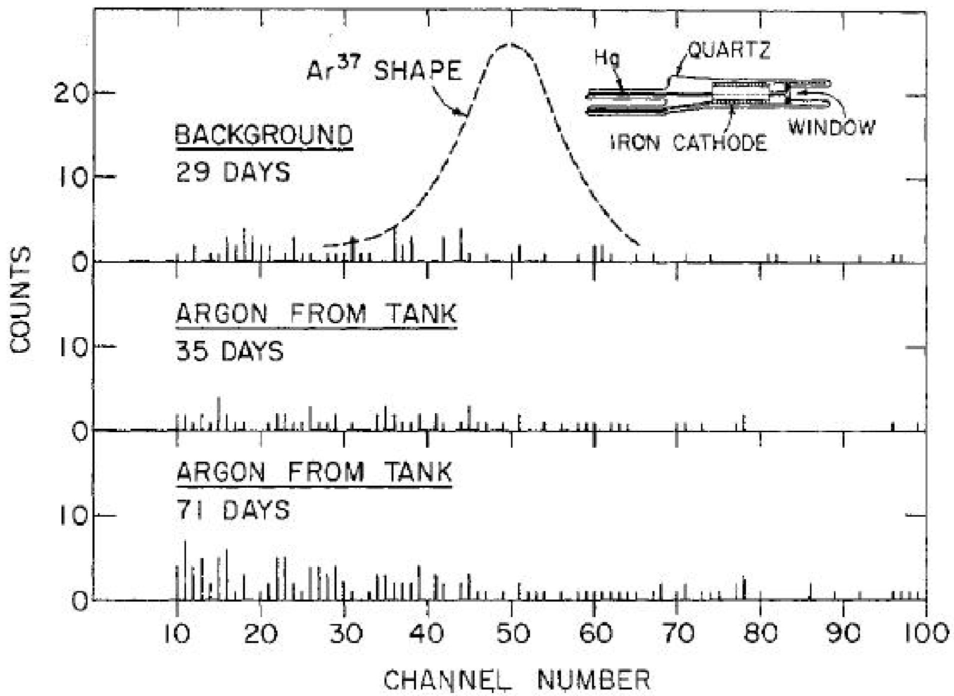

first runs 1968 produced only upper limit of 3 SNU with expectation of 7.5 $\pm$ 3 SNU
solution: pulse shape discrimination
signal: 2.82 keV e^- creating about 100 e-ion pairs in 100 μm
background: γ making Compton effect
1970 first observation of solar neutrinos

The Homestake Experiment

Result of 25 years of running

(after implementation of rise time counting)

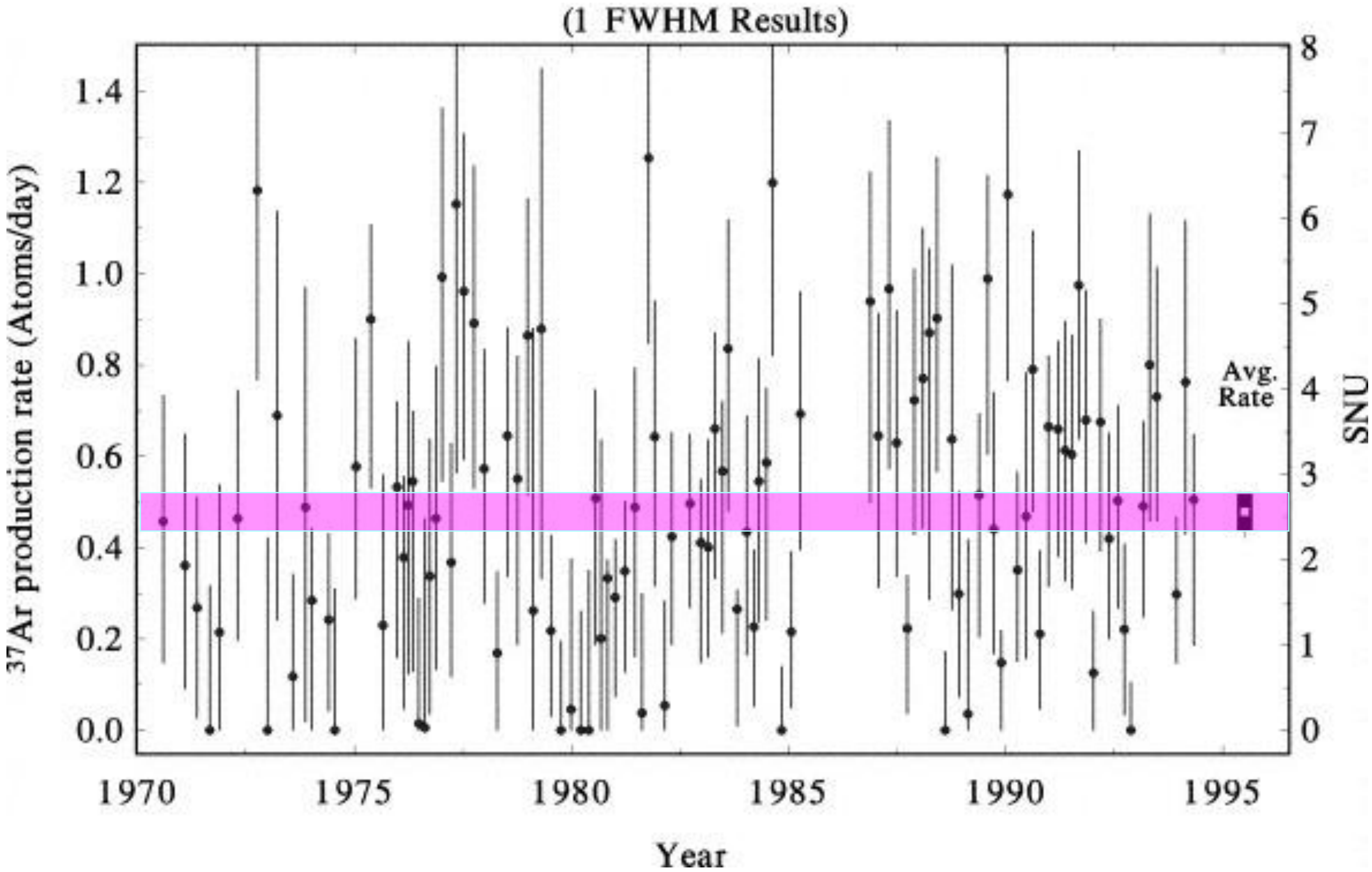

Nobel Prize 2002

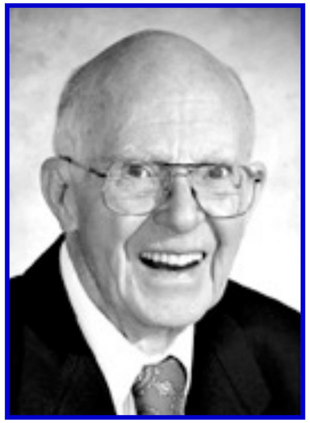

Raymond Davis Jr. [Homestake]

Masatoshi Koshiba [Kamiokande]

Riccardo Giacconi [X-Ray Sources]

Super-Kamiokande

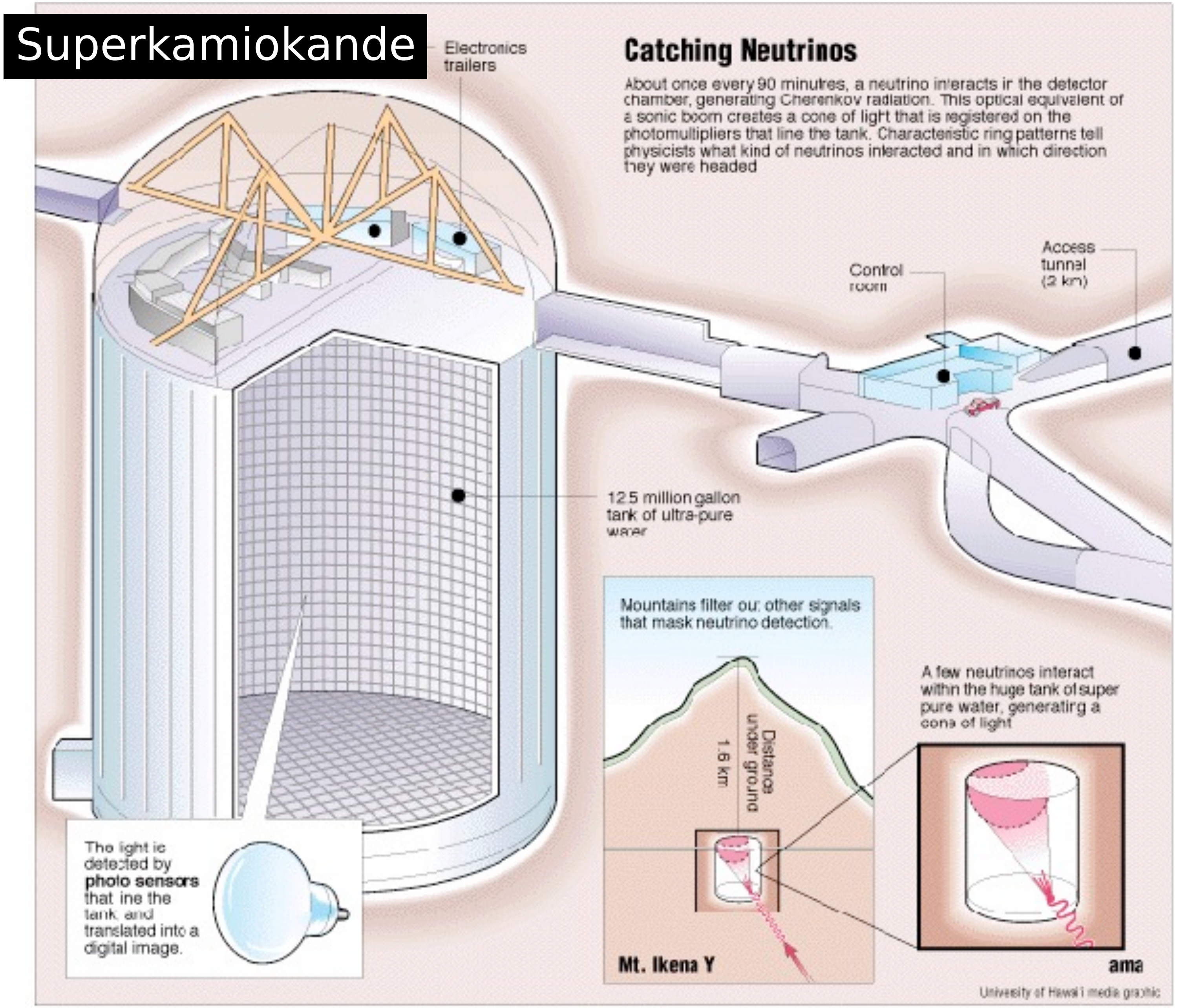

water tank
1.6 km below ground

50 million liter
ultra-pure water

1 neutrino interaction
every 1.5 hours

neutrino detection
via Cherenkov light

Super-Kamiokande

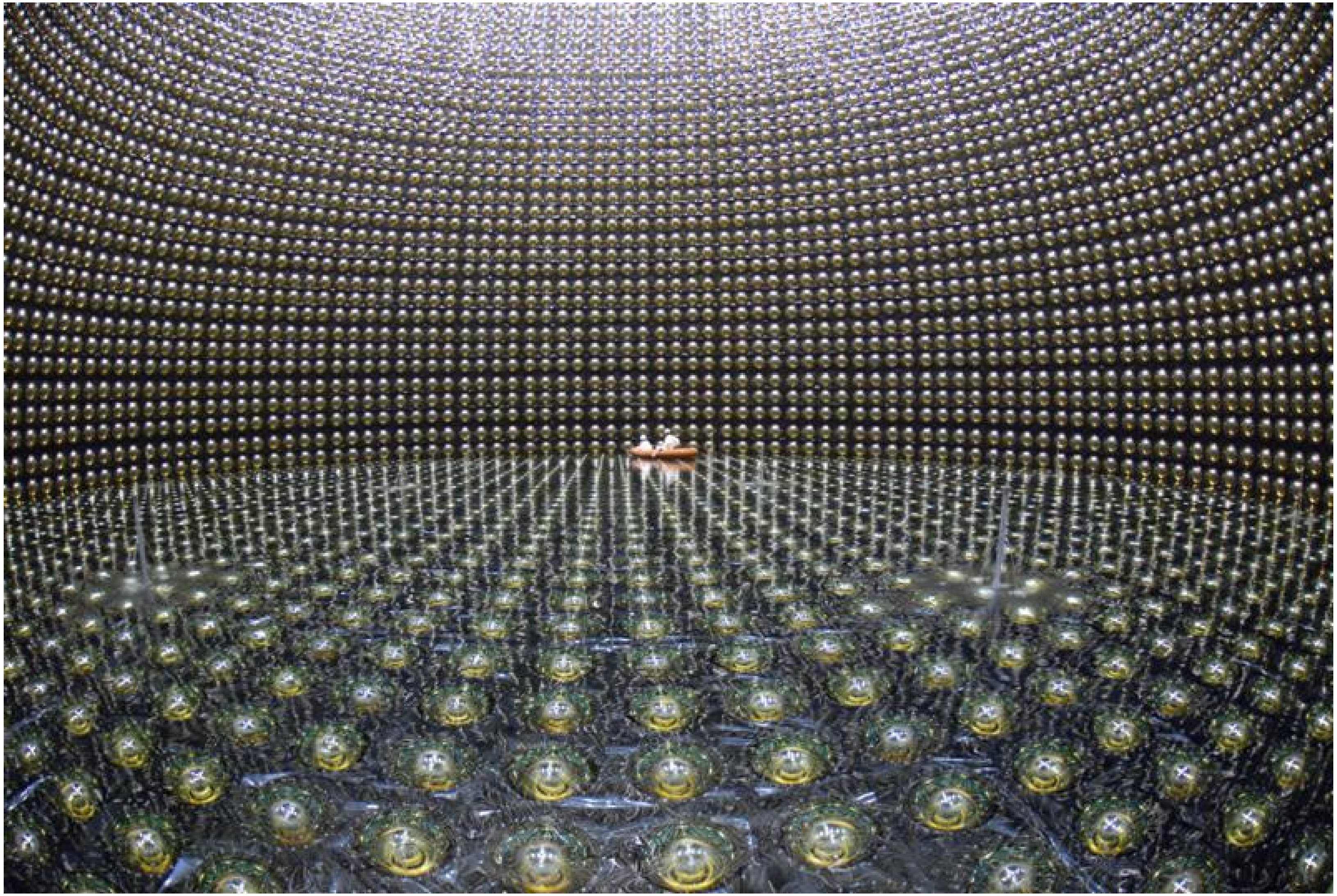

Super-Kamiokande

Mounting of Photomultiplier Tubes

total number of photomultipliers:

20 inch Ø	11,146
8 inch Ø	1,885

Super-Kamiokande

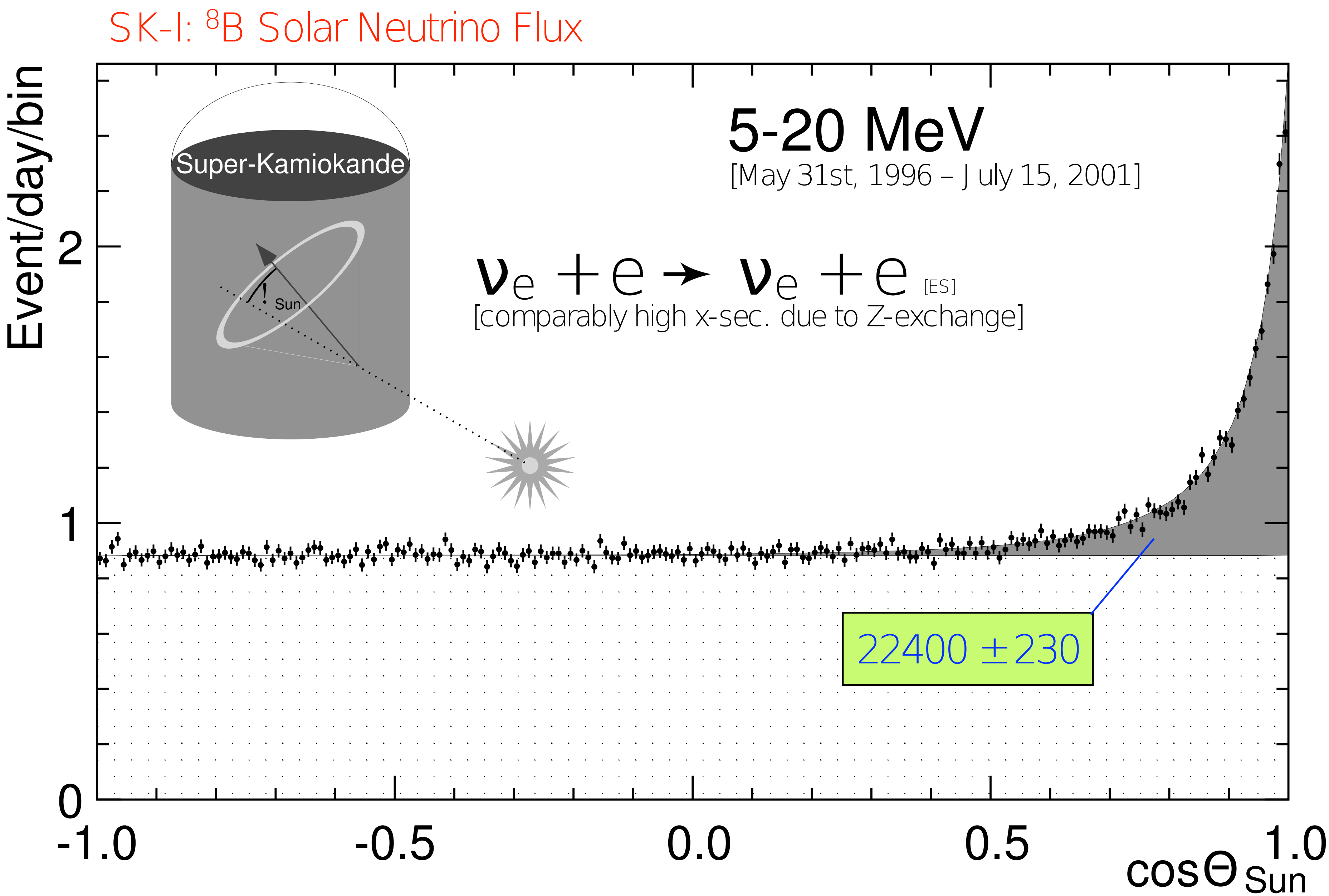

Super-Kamiokande

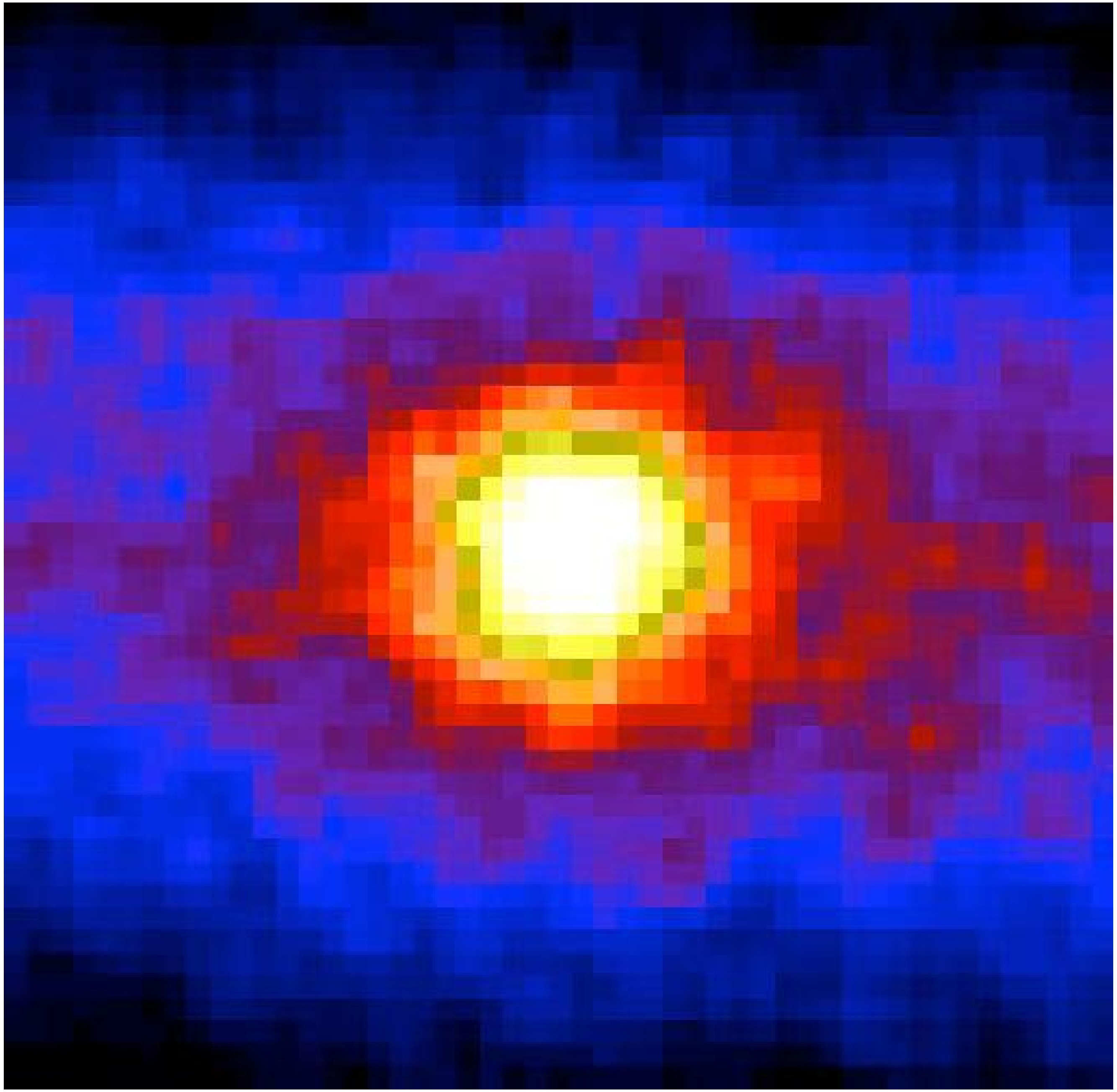

the sun seen through the earth in neutrino light

Super-Kamiokande

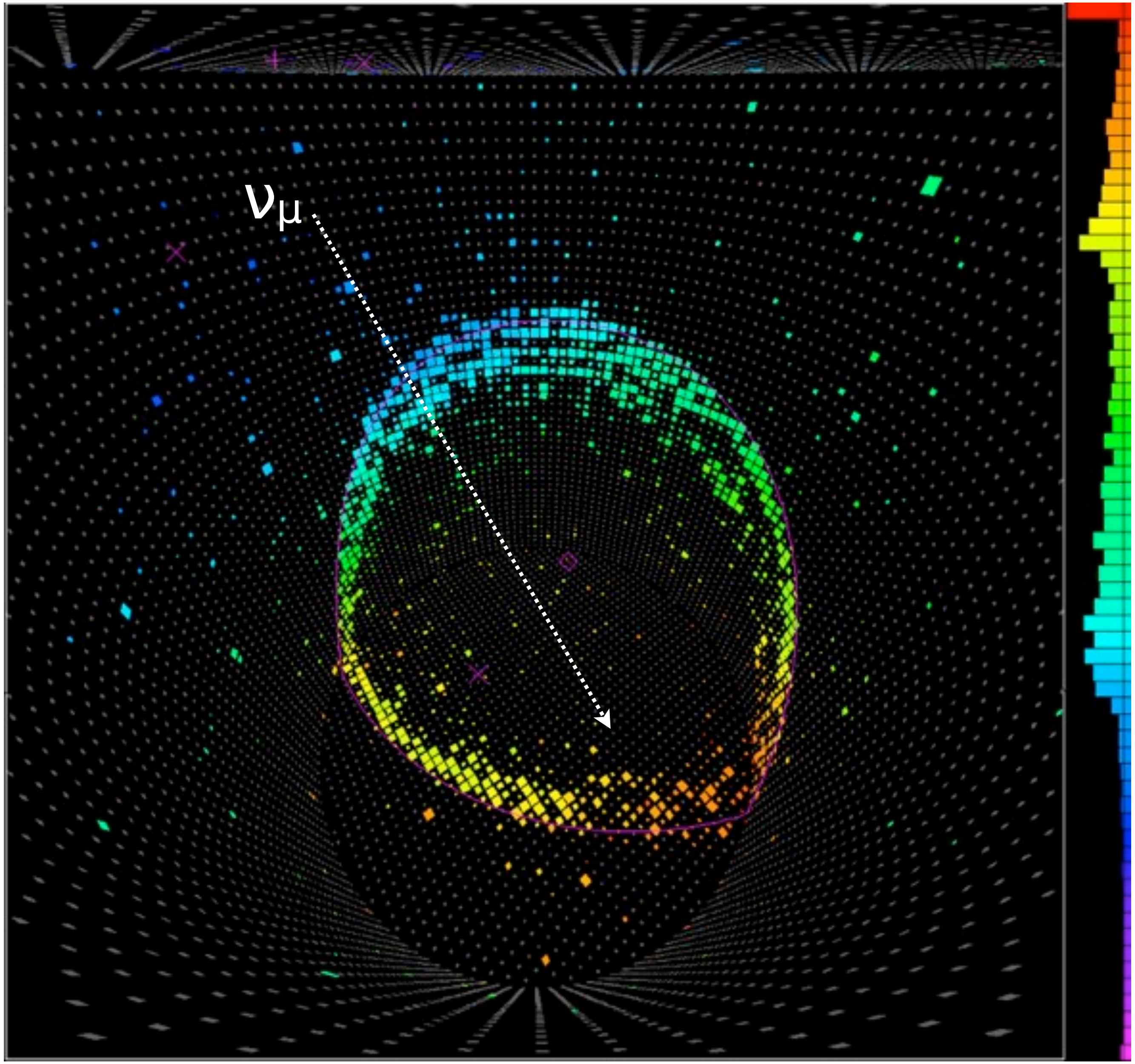

muon event (603 MeV)

observation of clean Cherenkov ring with sharp edges

flight direction from timing measurements
blue: early, red: late

energy from amount of light observed in PMs

Super-Kamiokande

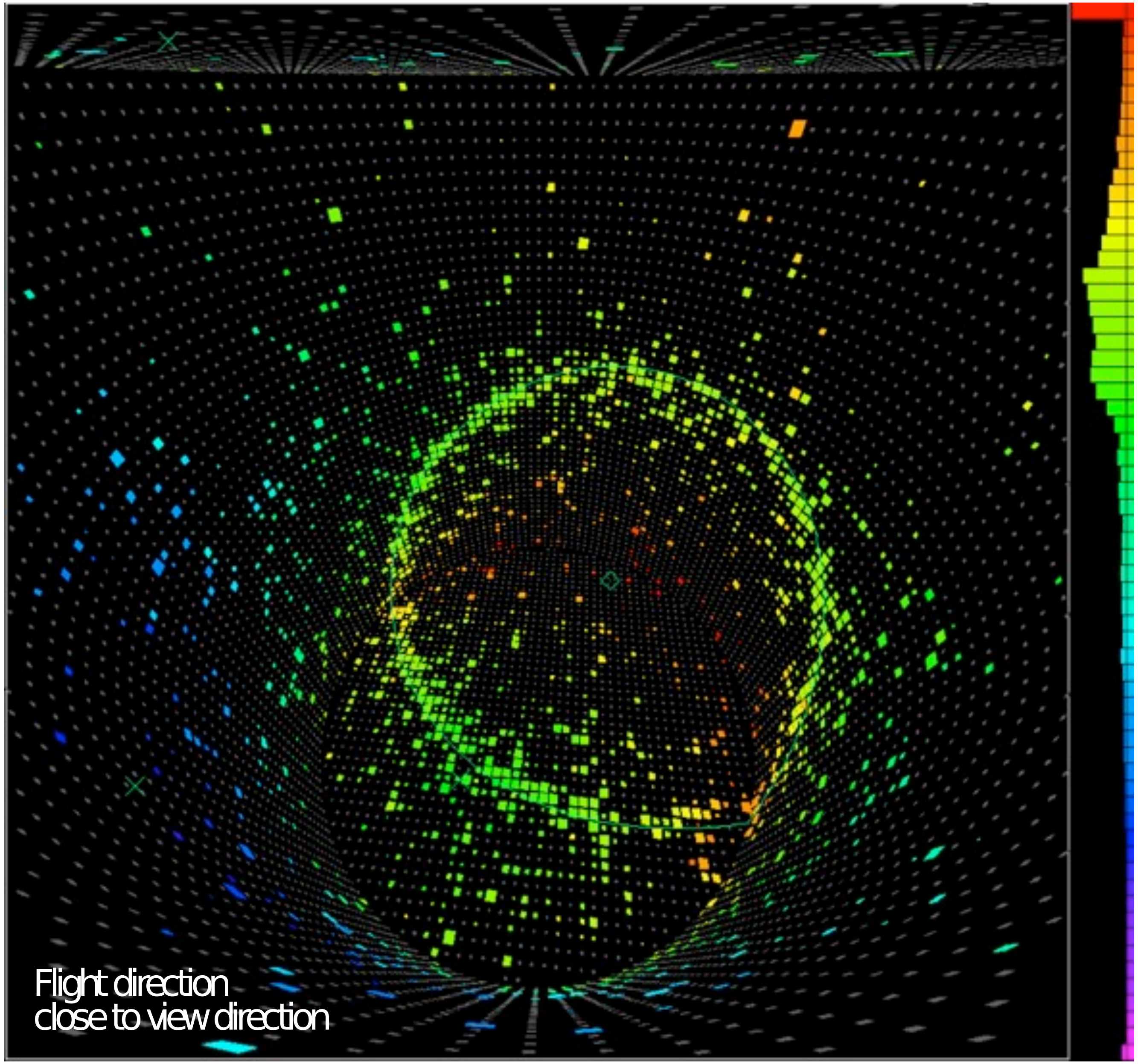

electron event (492 MeV)

observation of Cherenkov ring with fuzzy edge (bremsstrahlung)

flight direction from timing measurements
blue: early; red: late

energy from amount of light observed in PMs

Super-Kamiokande

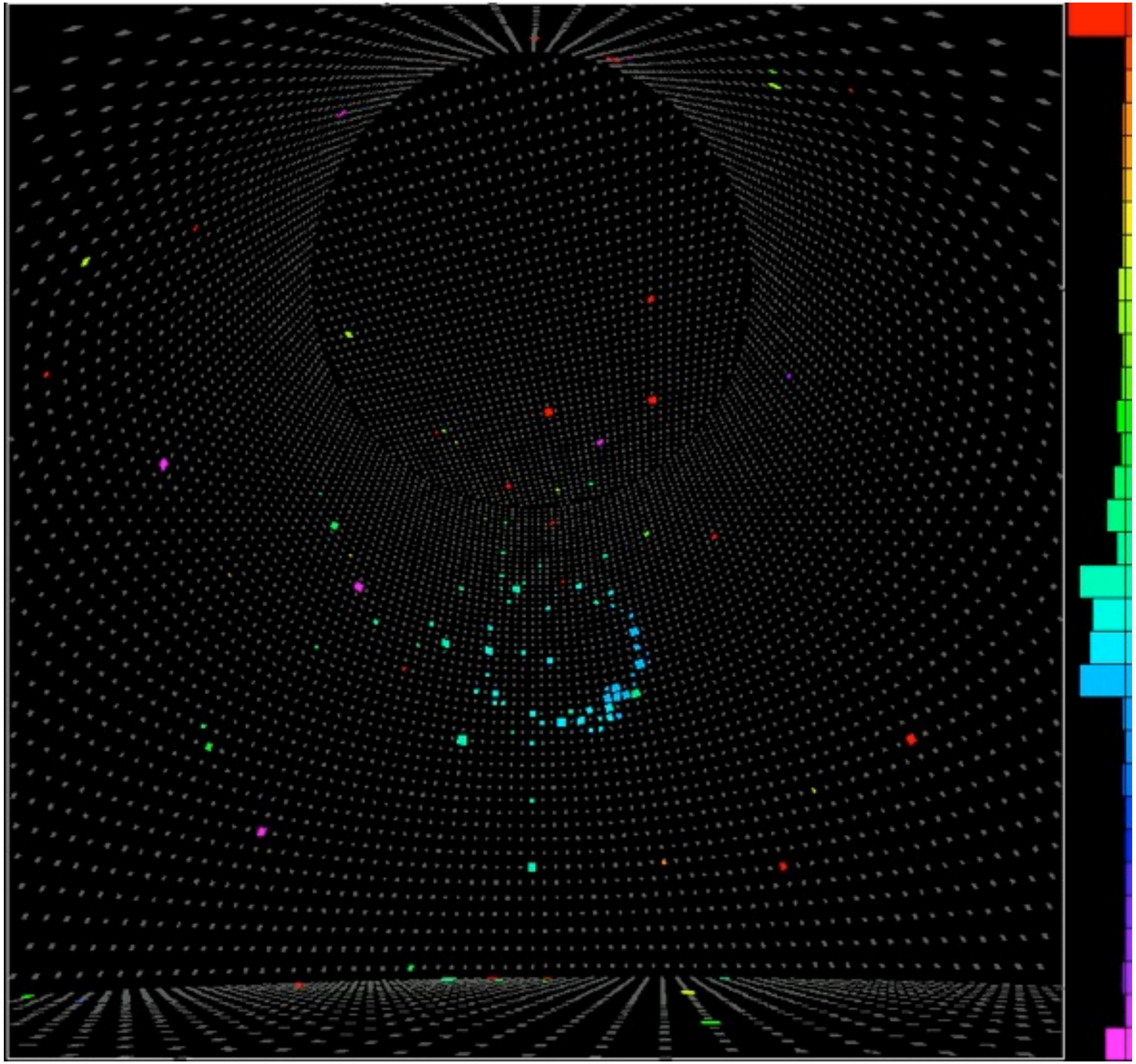

solar neutrino (12.5 MeV)

unusually nice, well-defined

flight direction from
timing measurements
blue: early; red: late

energy from amount of light
observed in PMs

Solar Electron-Neutrino Problem

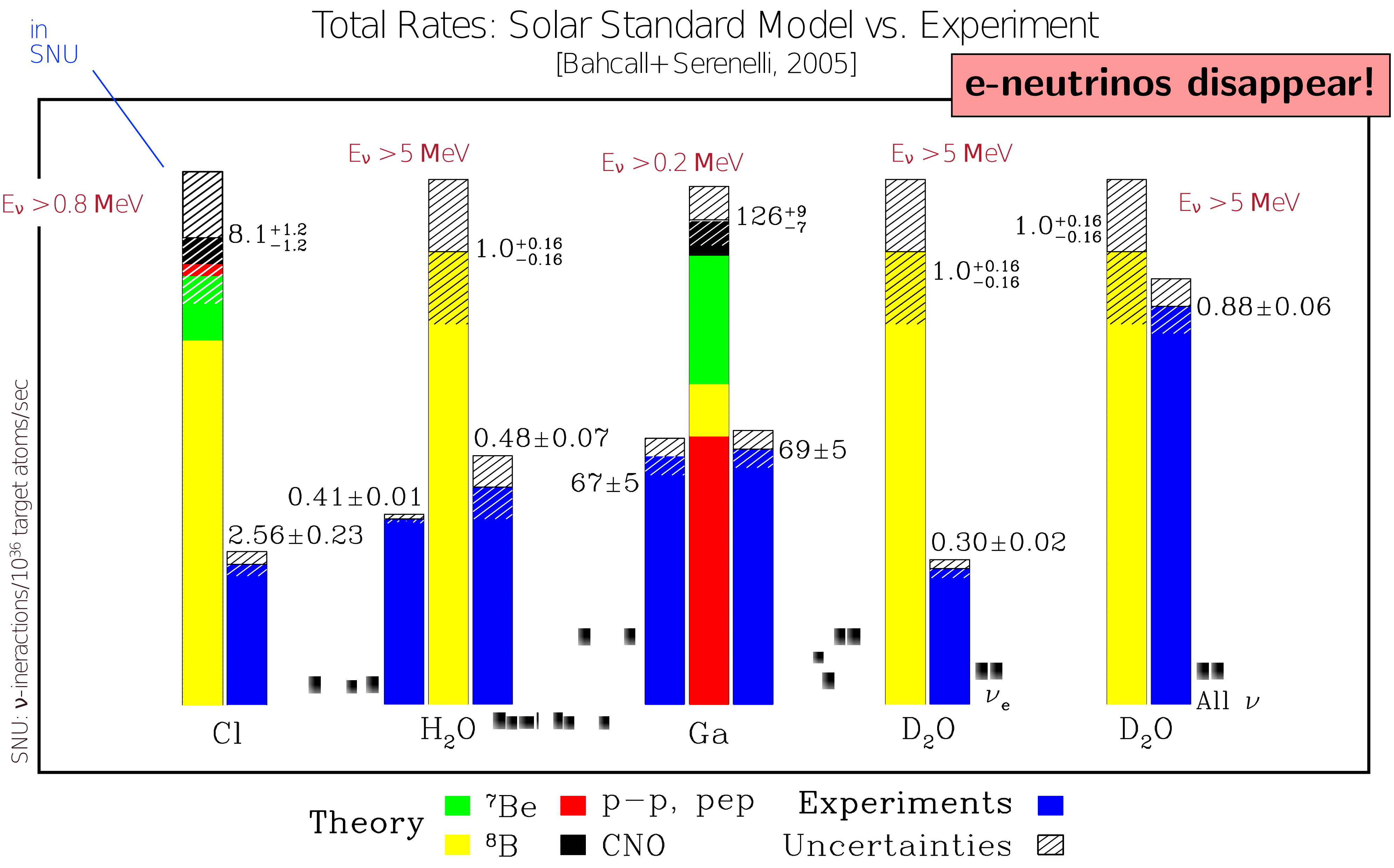

Different Solar Neutrino Experiments

different thresholds
all measure large deficit

- ^{37}Cl $\rightarrow ^{37}$Ar
  (Homestake)

  Exp: 2.6 SNU
  BS05: 8.1 SNU

- ^{37}Ga $\rightarrow ^{37}$Ge
  (Gallex, GNO, Sage)

  Exp: 70 SNU
  BS05: 126 SNU

- ^{8}B ν_e-flux
  (Kamiokande, SNO)

  Exp: 2.4 SNU
  BS05: 5.7 SNU

but SNO has a new twist ... deuterium

	^{37}Cl→^{37}Ar (SNU)	^{71}Ga→^{71}Ge (SNU)	^{8}B ν flux (10^{6}cm^{-2}s^{-1})
Homestake			
(CLEVELAND 98)[20]	2▹56 ∘ 0▹16 ∘ 0▹16	—	—
GALLEX			
(HAMPEL 99)[21]	—	77▹5 ∘ 6▹2$^{+4.3}_{-4.7}$	—
GNO			
(ALTMANN 05)[22]	—	62▹9$^{+5.5}_{-5.3}$ ∘ 2▹5	—
GNO+GALLEX			
(ALTMANN 05)[22]	—	69▹3 ∘ 4▹1 ∘ 3▹6	—
SAGE			
(ABDURASHI▹▹▹02)[23]	—	70▹8$^{+5.3+3.7}_{-5.2-3.2}$	—
Kamiokande			
(FUKUDA 96)[24]	—	—	2▹80 ∘ 0▹19 ∘ 0▹33†
Super-Kamiokande			
(HOSAKA 05)[25]	—	—	2▹35 ∘ 0▹02 ∘ 0▹08†
SNO (pure D_2O)			
(AHMAD 02)[4]	—	—	1▹76$^{+0.06}_{-0.05}$ ∘ 0▹09‡
	—	—	2▹39$^{+0.24}_{-0.23}$ ∘ 0▹12†
	—	—	5▹09$^{+0.44+0.46}_{-0.43-0.43}$$*$
SNO (NaCl in D_2O)			
(AHARMIM 05)[11]	—	—	1▹68 ∘ 0▹06$^{+0.08}_{-0.09}$‡
	—	—	2▹35 ∘ 0▹22 ∘ 0▹15†
	—	—	4▹94 ∘ 0▹21$^{+0.38}_{-0.34}$$*$
BS05(OP) SSM [13]	8▹1 ∘ 1▹3	126 ∘ 10	5▹69(1▹00 ∘ 0▹16)
Seismic model [18]	7▹64 ∘ 1▹1	123▹4 ∘ 8▹2	5▹31 ∘ 0▹6

The SNO Experiment

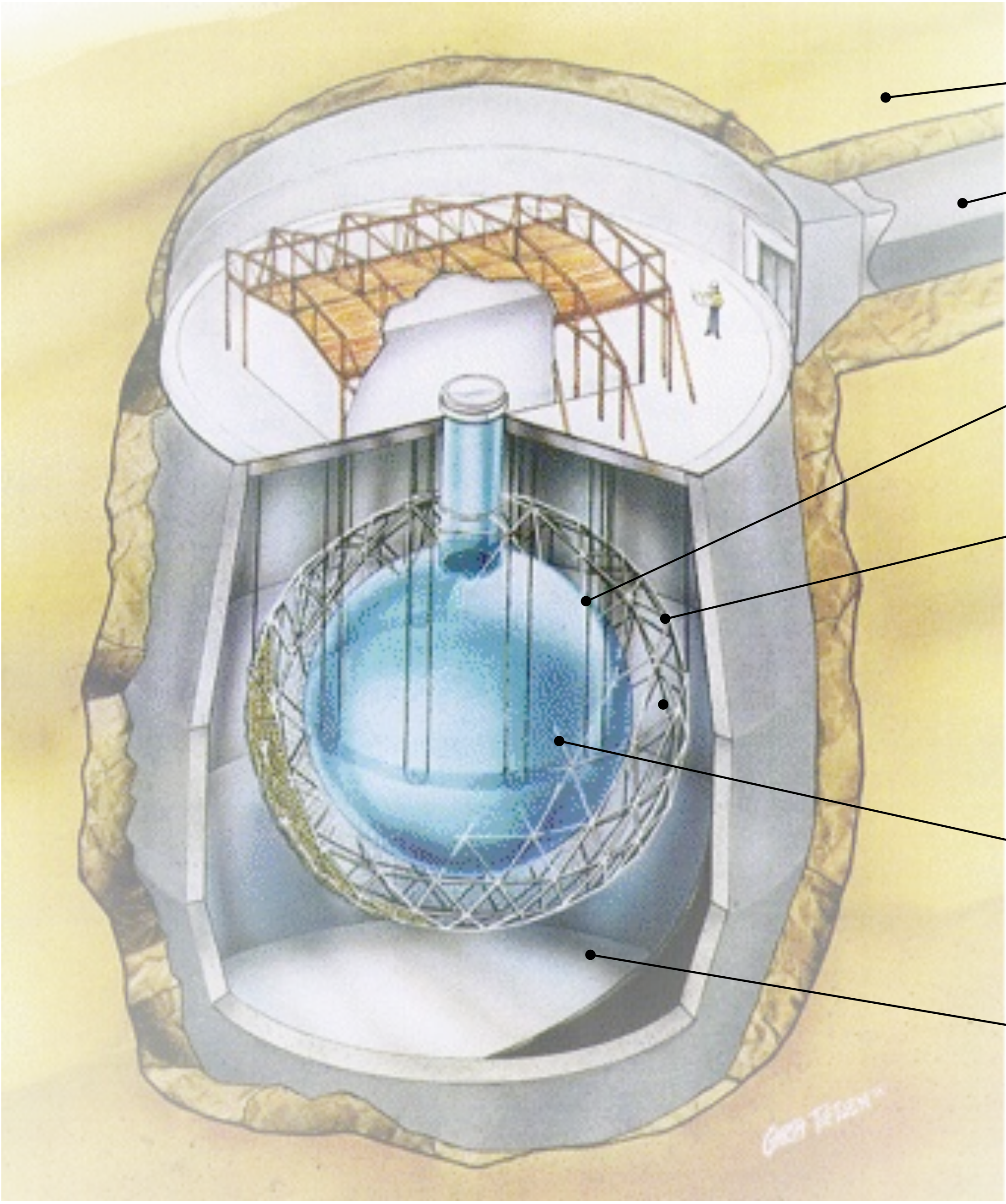

The SNO Experiment

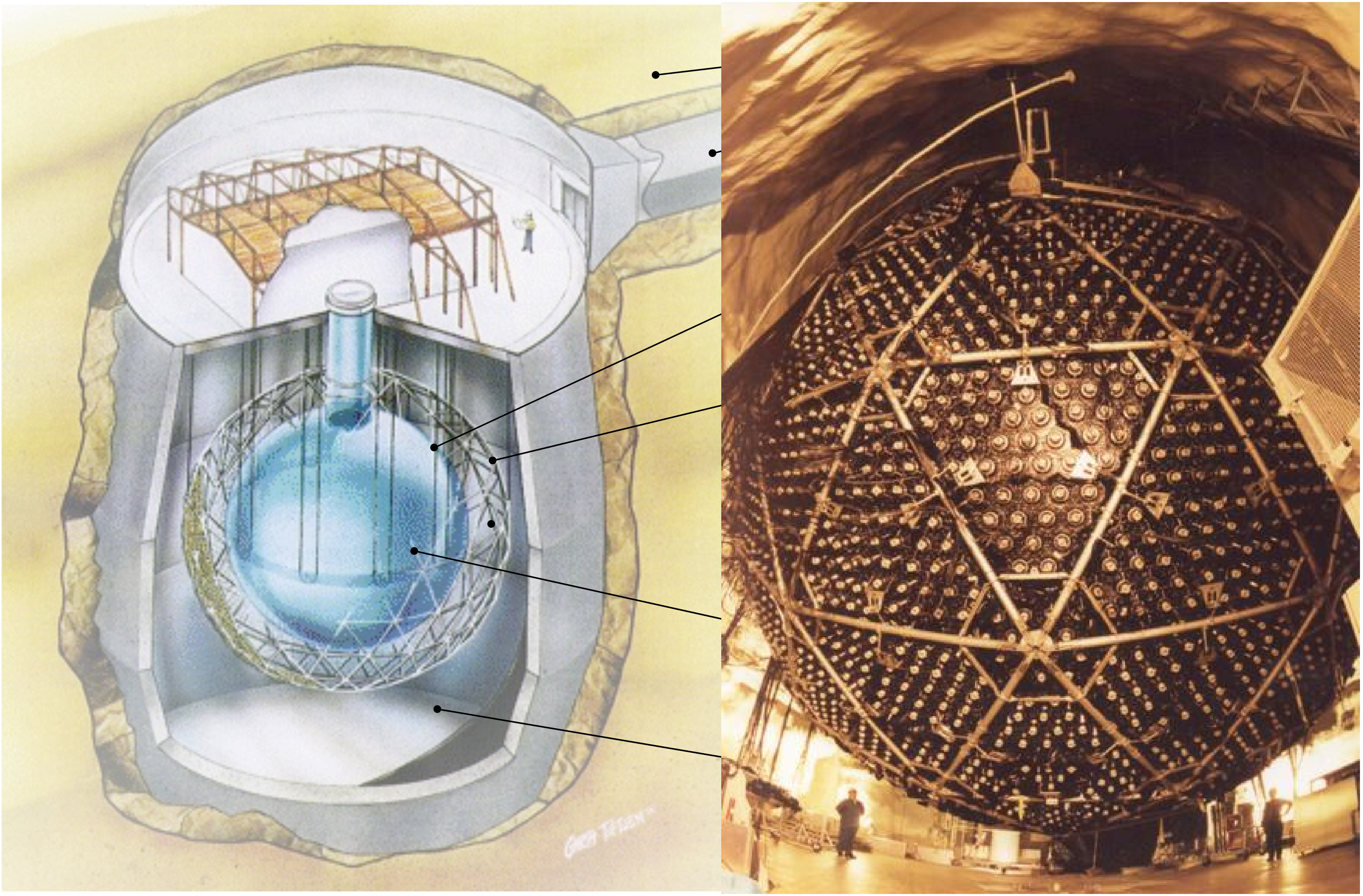

The SNO Experiment

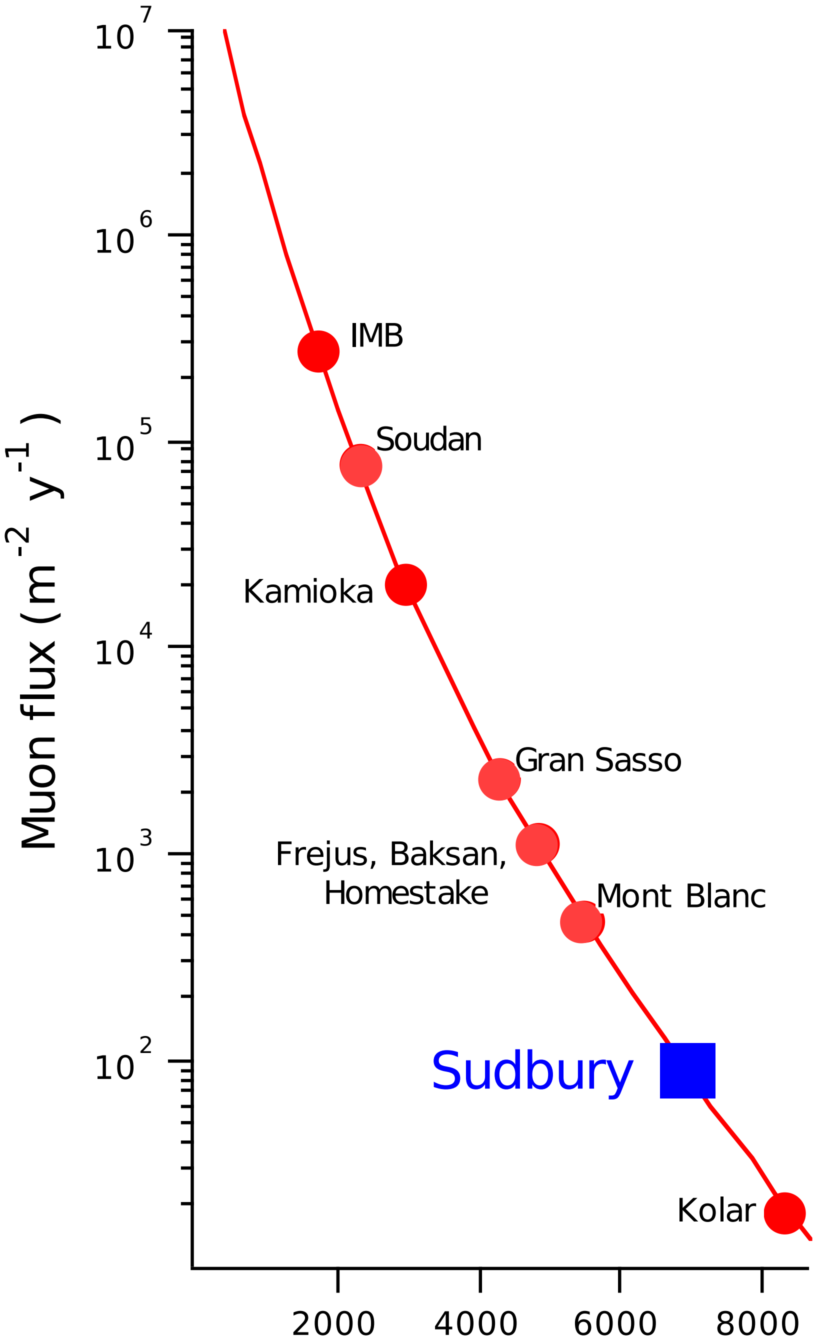

more than 3 km below ground
background < 100 muons/d

The SNO Experiment

charged current

$\nu_\mathrm{e} + \mathrm{d} \rightarrow \mathrm{p} + \mathrm{p} + \mathrm{e}^-$

measurement of ν_e energy spectrum
weak directionality: $0.34 < \cos\theta < 1$

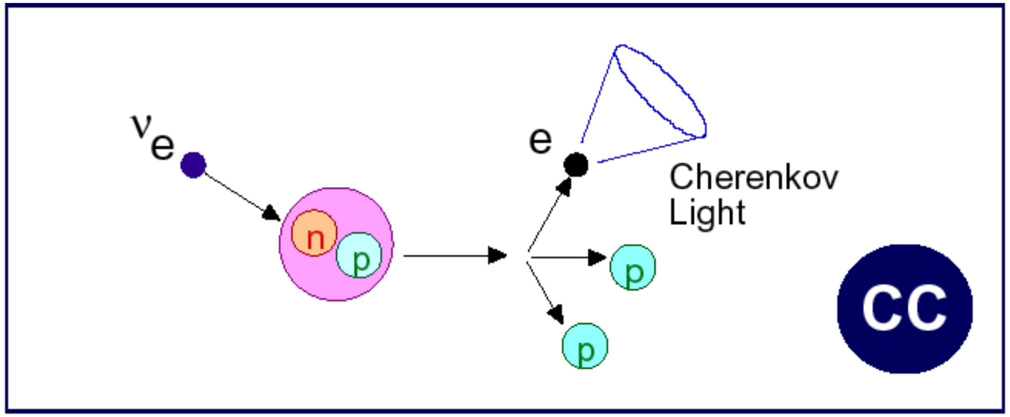

neutral currents

$\nu_\mathrm{x} + \mathrm{d} \rightarrow \mathrm{p} + \mathrm{n} + \nu_\mathrm{x}$

measure total ^{8}B neutrino flux from the sun
$\sigma(\nu_\mathrm{e}) = \sigma(\nu_\mu) = \sigma(\nu_\tau)$

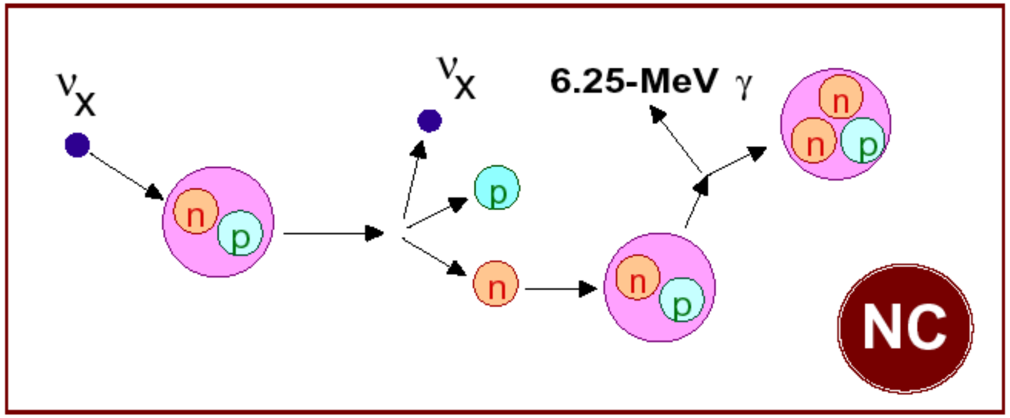

electron scattering

$\nu_\mathrm{x} + \mathrm{e}^- \rightarrow \nu_\mathrm{x} + \mathrm{e}^-$

low statistics
strong directionality: $\theta \leq 18^\circ$ ($T_\mathrm{e} = 10$ MeV)

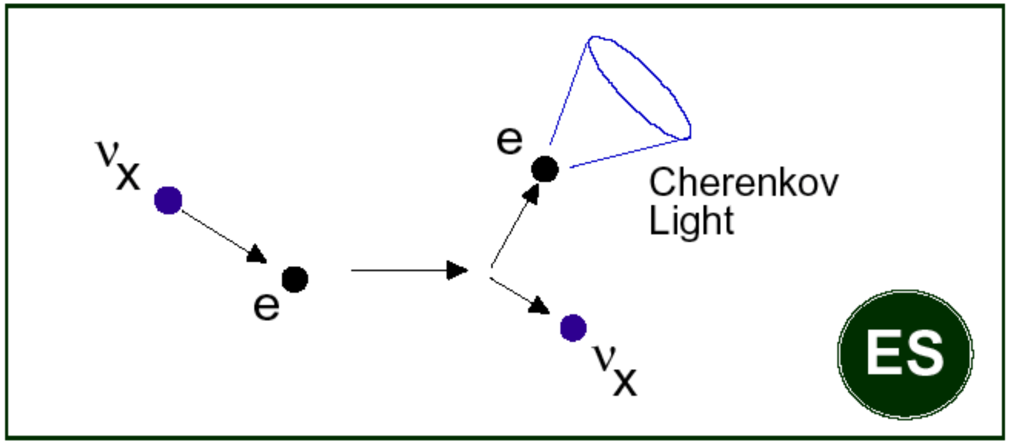

The SNO Experiment

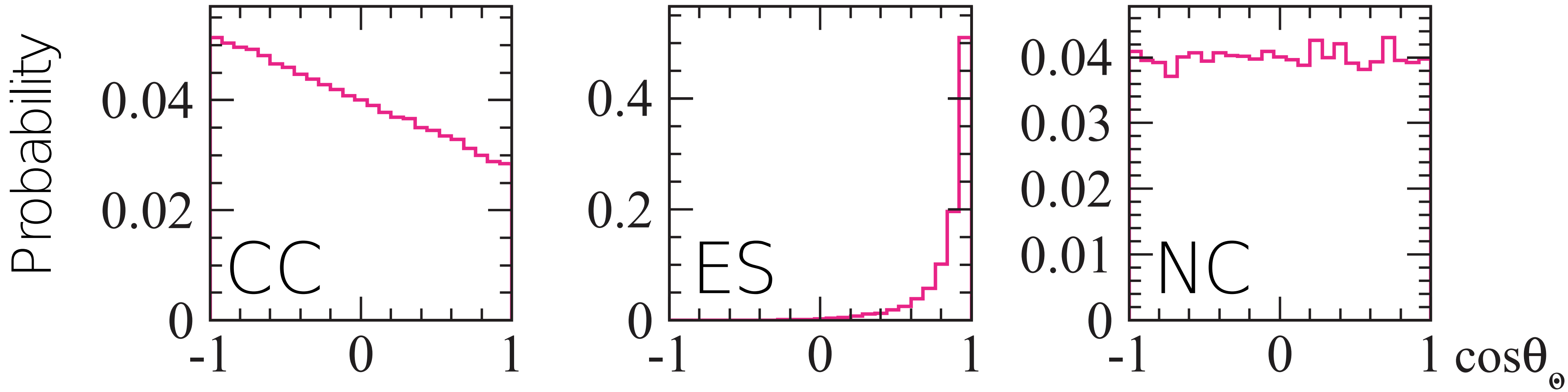

analysis strategy:

determine size of
CC, ES, and NC signals
via fit of the data
to probability distributions

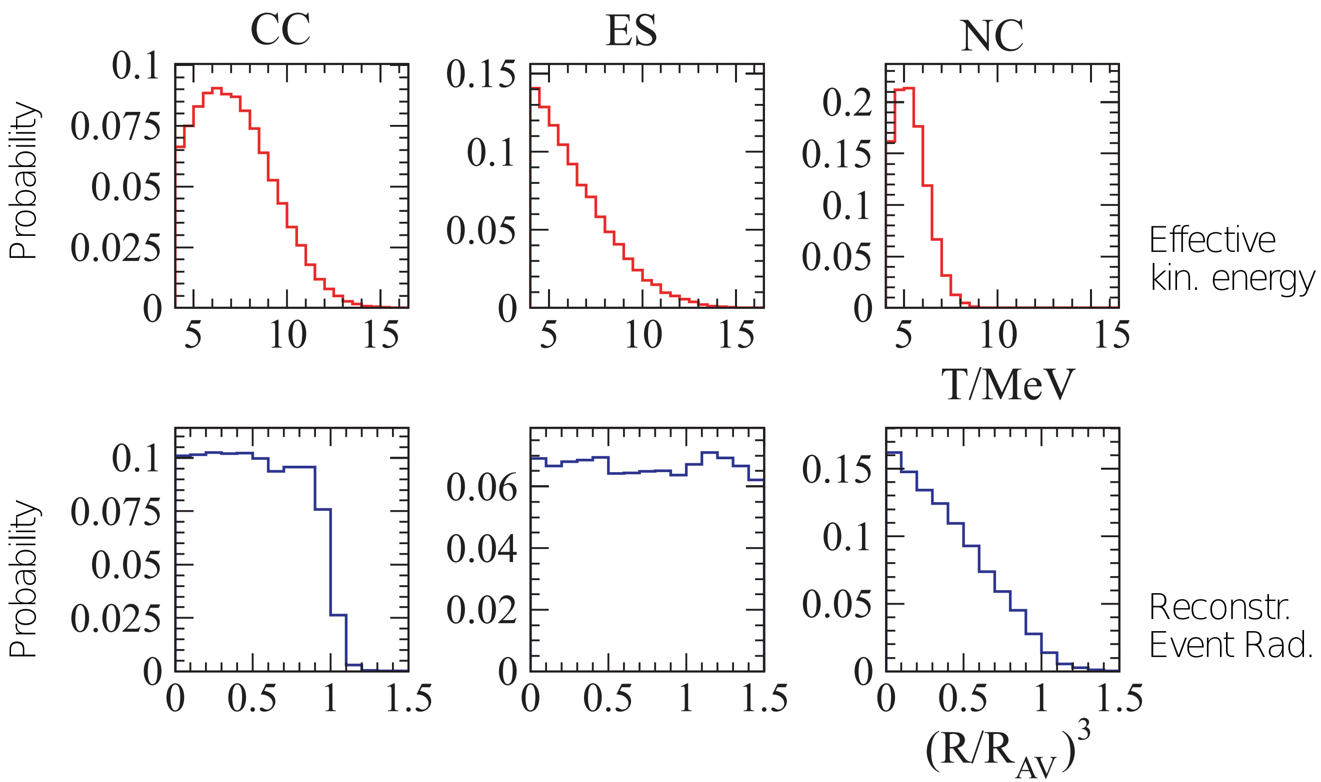

The SNO Experiment

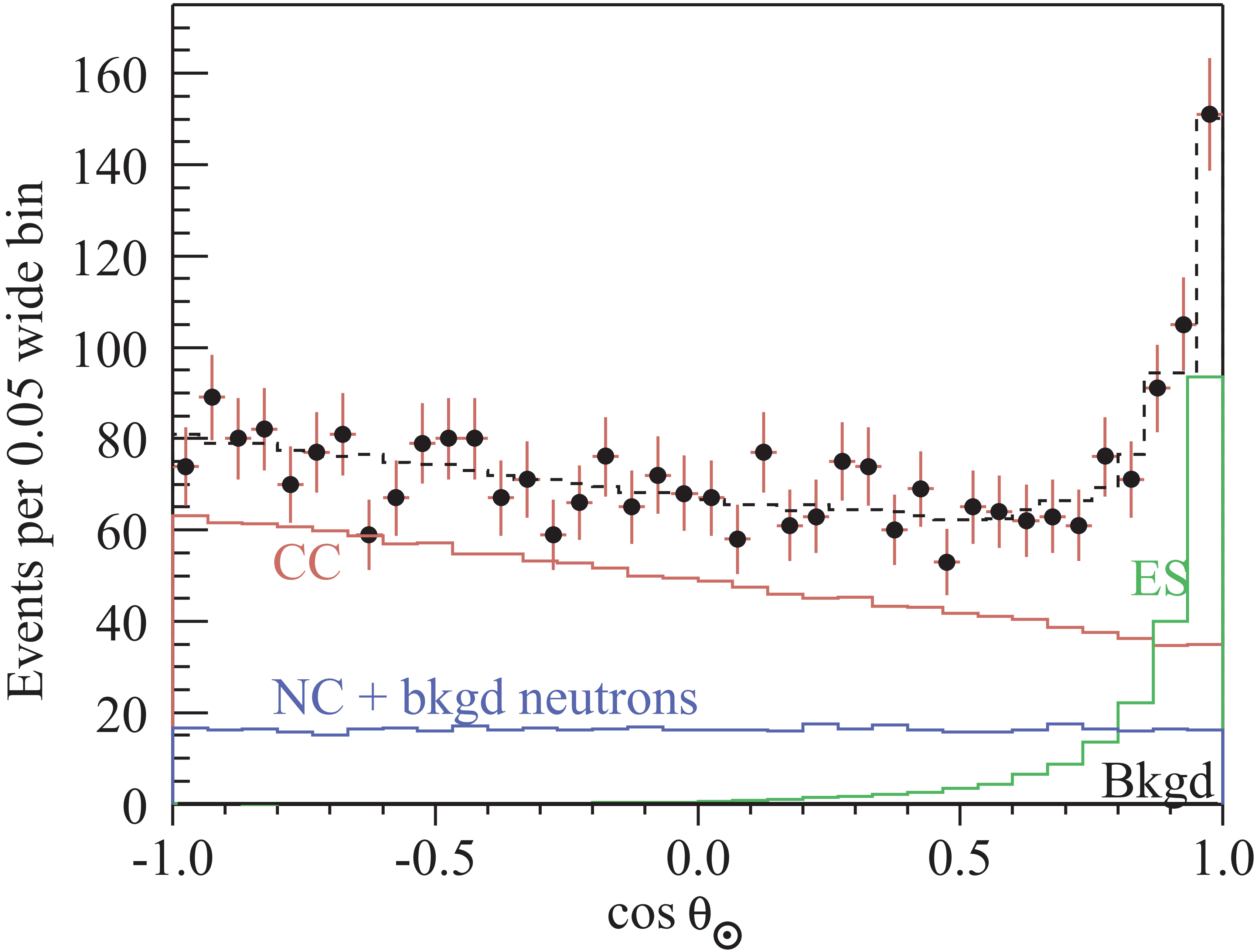

The SNO Experiment

$$\Phi_{CC} = 1.76\ {}^{+0.06}_{-0.05}(\text{stat.})\ {}^{+0.09}_{-0.09}(\text{syst.}) \cdot 10^6\ \text{cm}^{-2}\text{s}^{-1}$$
$$\Phi_{ES} = 2.39\ {}^{+0.24}_{-0.23}(\text{stat.})\ {}^{+0.12}_{-0.12}(\text{syst.}) \cdot 10^6\ \text{cm}^{-2}\text{s}^{-1}$$
$$\Phi_{NC} = 5.09\ {}^{+0.44}_{-0.43}(\text{stat.})\ {}^{+0.46}_{-0.43}(\text{syst.}) \cdot 10^6\ \text{cm}^{-2}\text{s}^{-1}$$

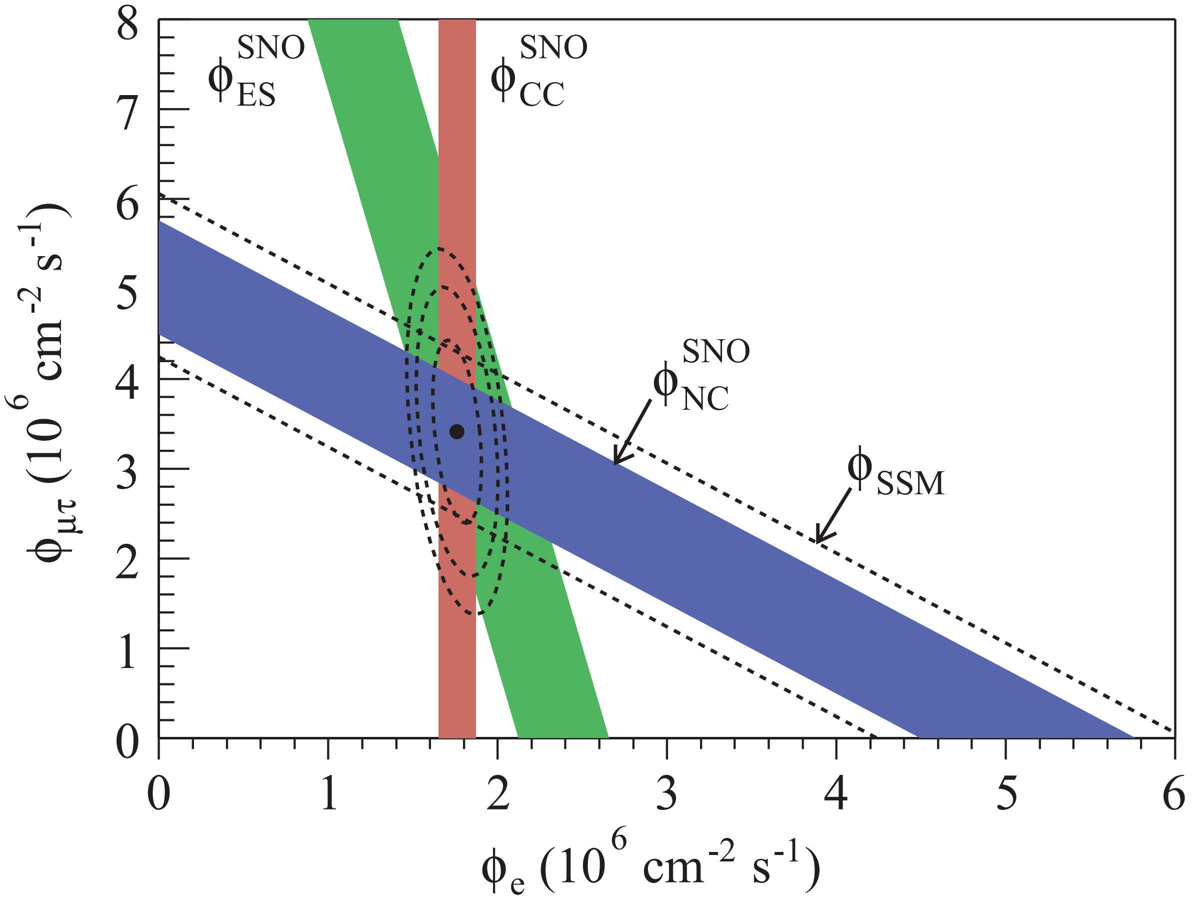

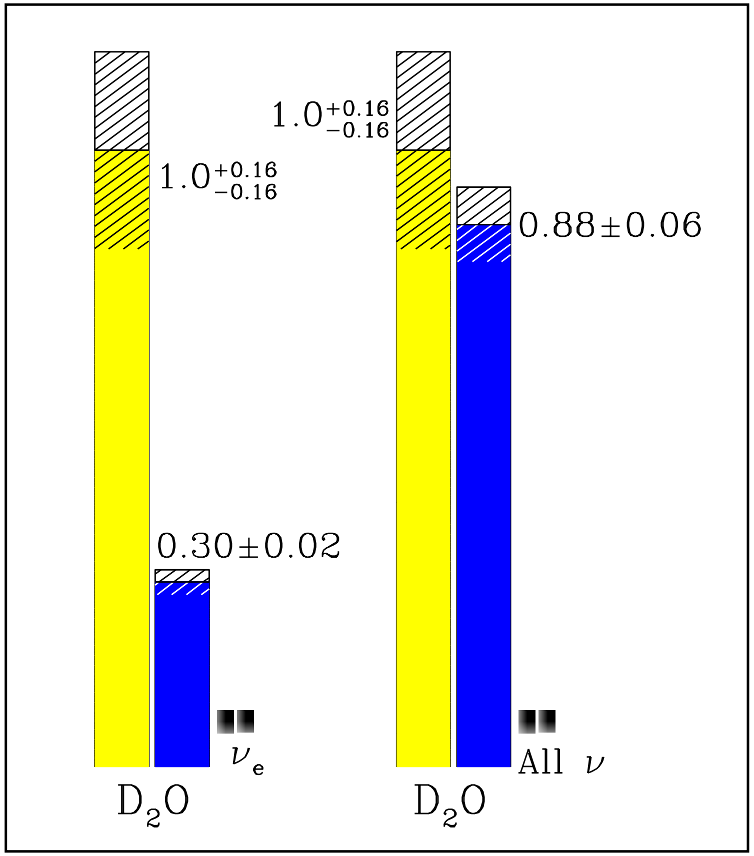

$$\Phi(\nu_e) = 1.76^{+0.05}_{-0.05}(\text{stat.})^{+0.09}_{-0.09}(\text{syst.})$$
$$\Phi(\nu_{\mu\tau}) = 3.41^{+0.45}_{-0.45}(\text{stat.})^{+0.48}_{-0.45}(\text{syst.})$$
$$\cdot 10^6\ \text{cm}^{-2}\text{s}^{-1}$$

Nobel Prize 2015

Art McDonald - SNO

Takaaki Kajita - Superkamiodande

for the discovery of neutrino oscillations, which shows neutrinos have mass

10.4 Cryogenic Detectors and Dark Matter Detection

motivation: **WIMP detection**

WIMPs = weakly interacting massive particles

dark matter particles:

must be neutral, i.e. must neither interact via electromagnetic nor strong interactions

WIMPs must be heavy, i.e. non-relativistic (cold dark matter) to allow for galaxy formation

assumed mass range: 10 GeV - 10 TeV

mass limits dependent on cross section, e.g.: $\sigma_{\chi \mathrm{p}} = 1.6 \cdot 10^{-7}$ pb yields $m_{\mathrm{WIMP}} > 60$ GeV

detection via elastic χp-scattering

assume WIMP velocity: $v_\chi \approx 300$ km/s, i.e. $\beta = 10^{-3}$

solar system speed w.r.t. to milky way: $v = 250$ km/s
velocity of earth moving w.r.t solar system: $v = 30$ km/s

maximum energy transfer for collision with nucleus N:

$$T_{\mathrm{N}}^{\mathrm{max}} = 2 \frac{m_\chi^2 M_{\mathrm{N}} c^2}{(m_\chi + M_{\mathrm{N}})^2} \beta^2 \quad (\approx 2 M_{\mathrm{N}} v_\chi^2 \text{ for } m_\chi \ll M_{\mathrm{N}})$$

for e.g. $M_{\mathrm{N}} = 100$ GeV: $\quad T_{\mathrm{N}}^{\mathrm{max}} \approx 100$ keV

Cryogenic Detectors

How to detect WIMPs

transferred energy of recoiling nuclei generally much smaller ($< 10\%$)

need detector that allows detection of recoil nuclei below keV range
energy resolution requires: $n_{\mathrm{excitation}} \gg 1$, i.e. $E_{\mathrm{excitation}} \ll 1$ eV

remember:	gases	–	ionzation energy ≈ 30 eV
	silicon	–	electron/hole pair creation ≈ 3 eV

better possibilities:

- phonon excitation:

  maximum phonon energy in Si is 60 meV,
  roughly 2/3 of the energy required for electron-hole formation goes into phonon excitation

- superconducting detectors:

  in superconductors the energy gap 2Δ is equivalent to the band gap in semiconductors
  absorption of energy $> 2\Delta$ (typically 1 meV) can break up a Cooper pair

Cryogenic detectors:

detect low energies with very good resolution

Cryogenic Detectors

Phonon Detectors

assume thermal equilibrium:

convert absorbed energy into phonons:

$$\Delta T = E/C$$

C: heat capacity of the sample
(specific heat $\times$ mass)
E: deposited energy

optimal detector: low heat capacity

example 1: Si-detector at room temperature

$C_{\mathrm{spec}} = 0.7$ J/gK
$E = 1$ keV, $m = 1$ g $\rightarrow \Delta T = 2 \cdot 10^{-16}$ K
not very practical, need lower specific heat and mass

example 2: Si-detector at low temperature

$C_{\mathrm{spec}} \propto (T/\Theta)^3$
$C_{\mathrm{spec}} = 2 \cdot 10^{-15}$ J/gK at $T = 0.1$ K
$E = 1$ keV, $m = 15$ μg $\rightarrow \Delta T = 0.04$ K (possible!)

basic configuration of cryogenic calorimeter

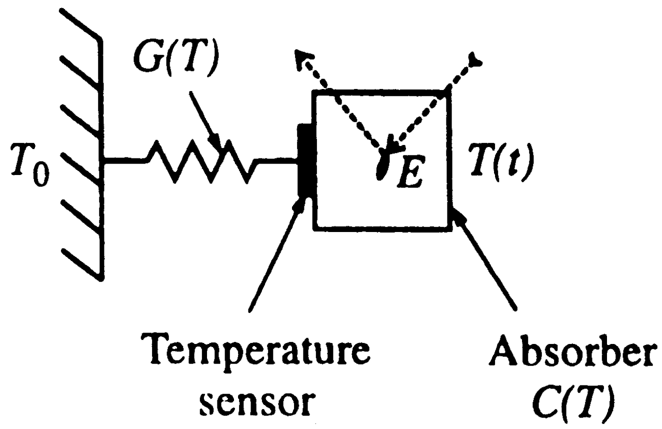

resolution:

$$\begin{aligned} n &= CT/kT = C/k \\ \sigma_0 &= kT\sqrt{n} = \sqrt{CkT^2} \\ \sigma_E &= \varepsilon\mathrm{Ph}\sqrt{E/\varepsilon Ph} = \sqrt{kTE} \\ \sigma^2 &= \sigma_0^2 + \sigma_E^2 \end{aligned}$$

yields: $\sigma < 0.2$ eV
(cf. Si semiconductor detector: $\sigma = 20$ eV)

Dark Matter Detection

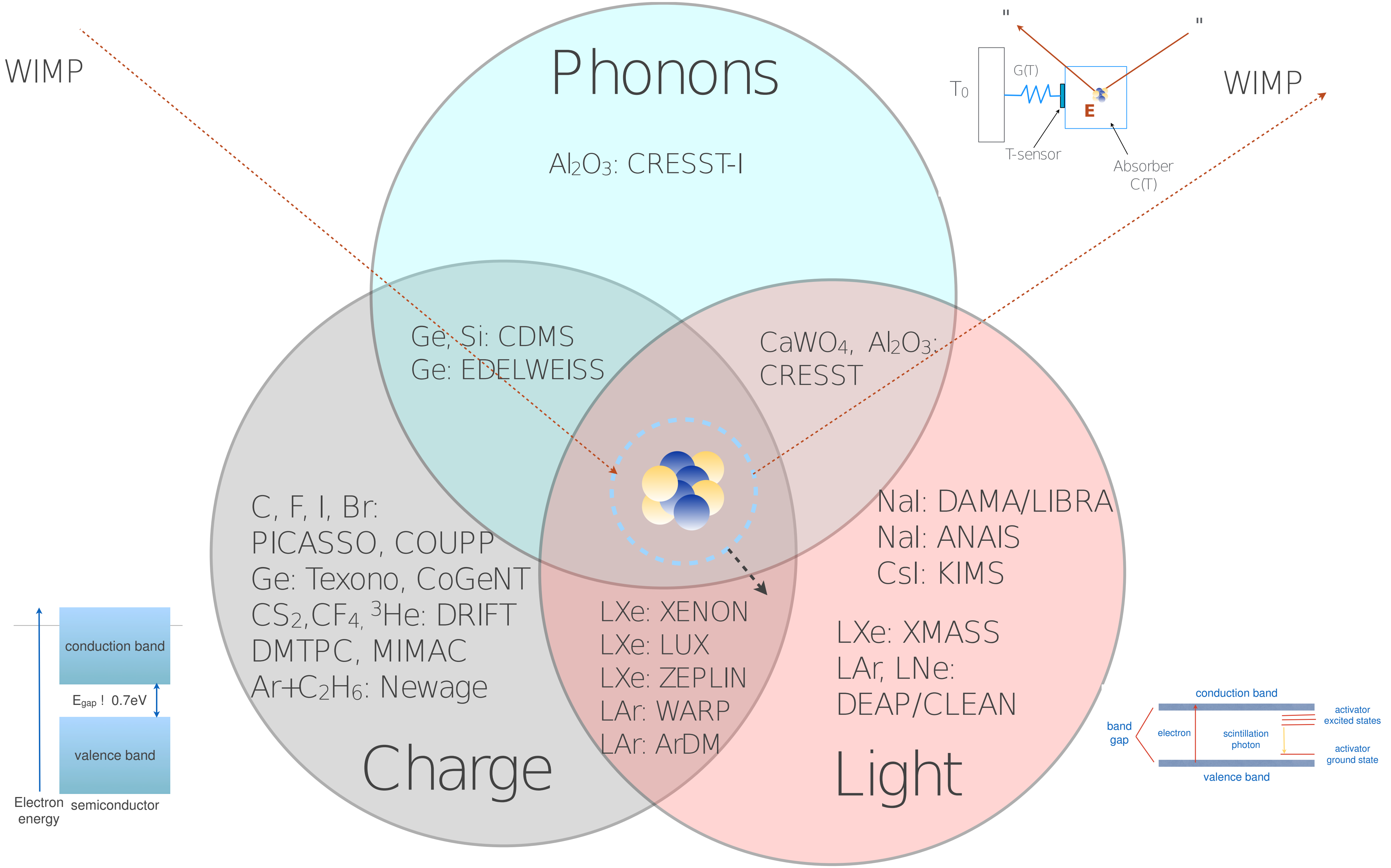

Dark Matter Detection

Example: CDMS

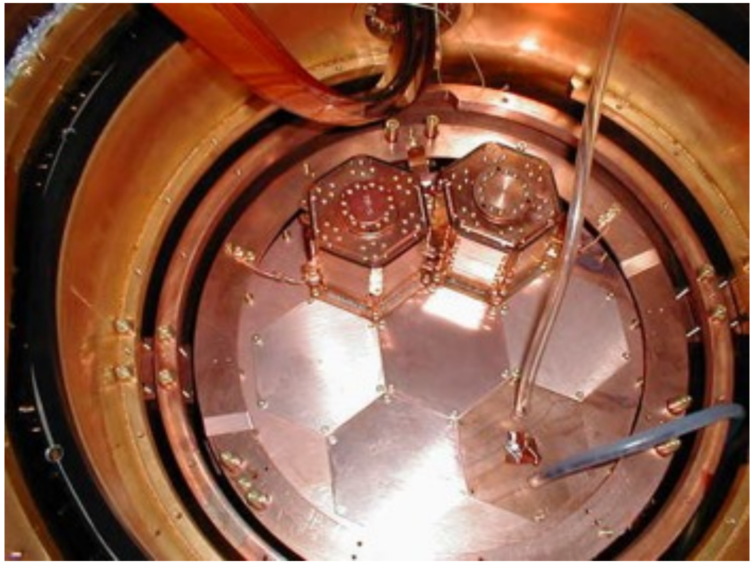

Soudan Underground Lab

5 towers with 6 Ge/Si detectors each
operated at $T \approx 20$ mK

Idea:

WIMPs (and neutrons) scatter off nuclei

most background noise sources (γ,e) scatter off electrons

ratio ionization/phonons differs for nuclear and electron recoils

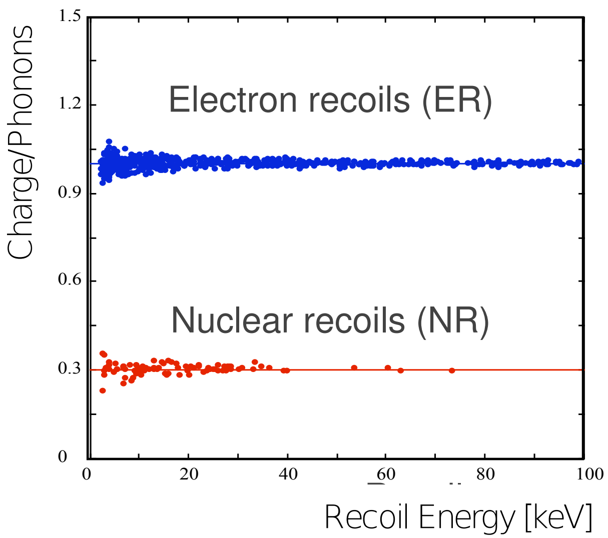

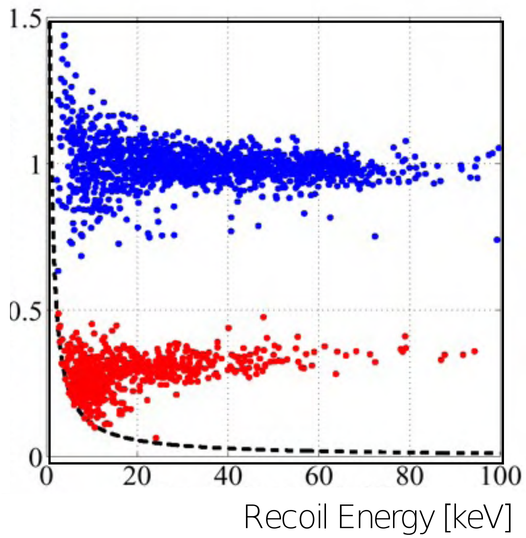

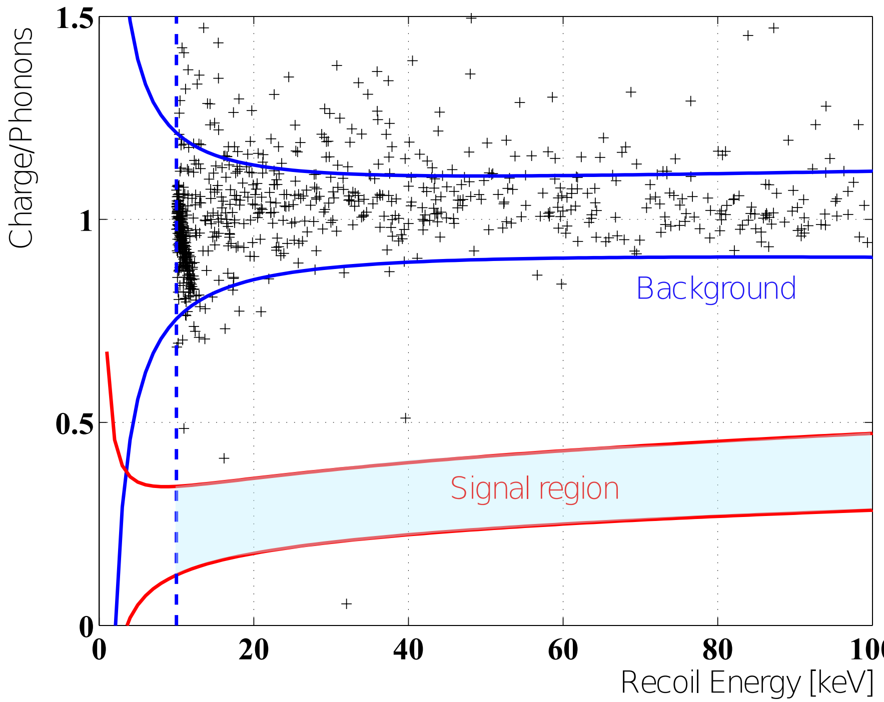

Dark Matter Detection

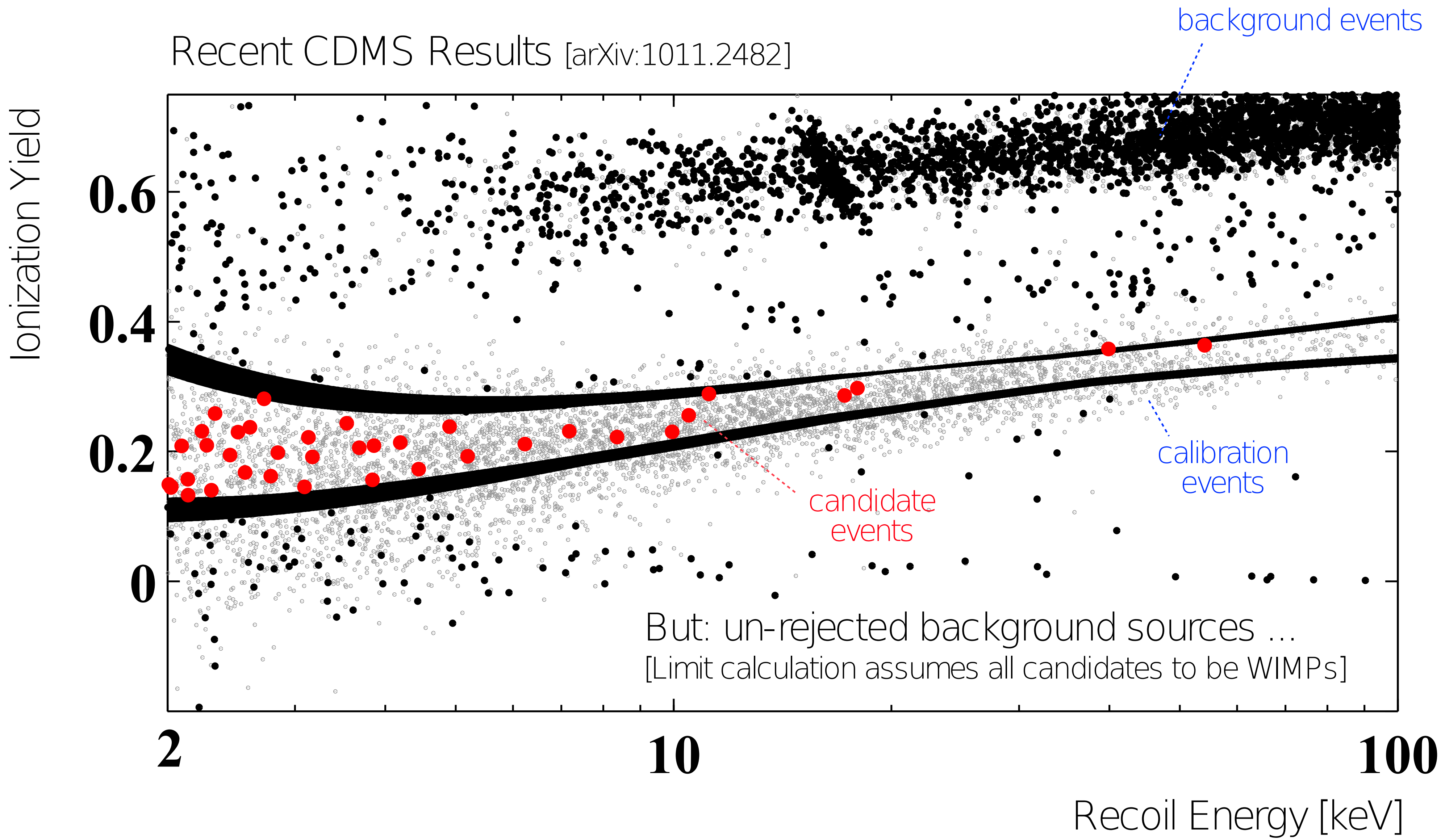

Dark Matter Detection

CDMS II Si 2013 Result

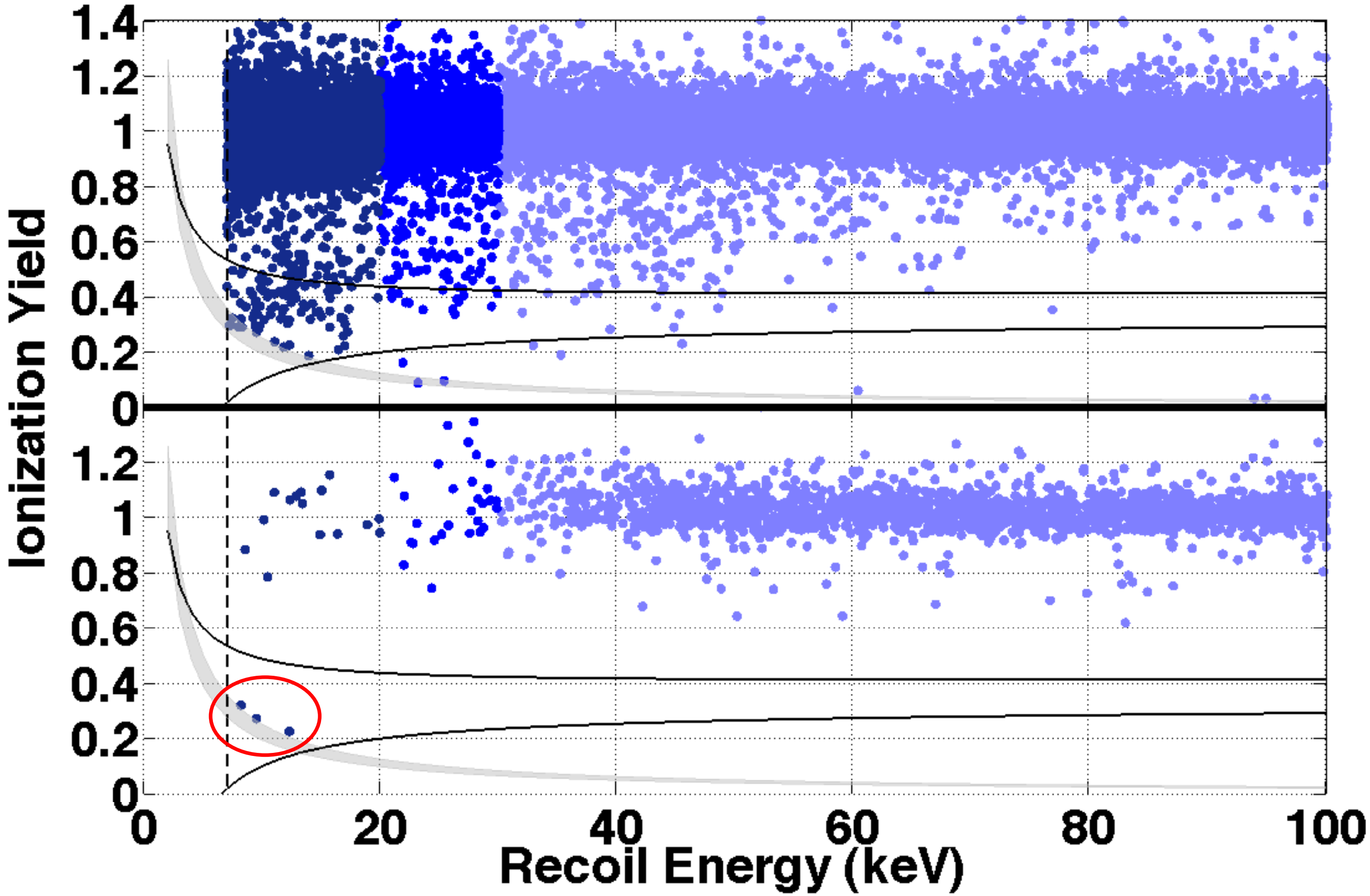

3 candidate WIMPs, ‘not yet a discovery’

Dark Matter Detection

Summary Dark Matter WIMP Searches